

0402594223



X-ray based machine vision system for distal locking of intramedullary nails

by

Faraz Junejo

A Doctoral Thesis
Submitted in partial fulfilment of the requirements
for the award of

Doctor of Philosophy
of Loughborough University

January 2009

© Faraz Junejo 2009



Acknowledgments

First of all I would like to thank my supervisors Dr. K. Bouazza-Marouf, Dr. D. Kerr, and Mr. A.J. Taylor for their valuable guidance, support, patience, and trust.

I would also like to thank the members of the technical staff, of the Department of Mechanical Engineering at Loughborough University, for their assistance towards this project.

Finally and above all, my deepest thanks are to my beloved parents Falak Sher Junejo and Khursheed Junejo, and my wife Wajiha Samma for all their support, encouragement, and prayers, without which I could have never come so far.

Abstract

In surgical procedures for femoral shaft fracture treatment, current techniques for locking the distal end of intramedullary nails, using two screws, rely heavily on the use of two-dimensional X-ray images to guide three-dimensional bone drilling processes. Therefore, a large number of X-ray images are required, as the surgeon uses his/her skills and experience to locate the distal hole axes on the intramedullary nail. The long term effects of X-ray radiation and their relation to different types of cancer still remain uncertain. Therefore, there is a need to develop a surgical technique that can limit the use of X-rays during the distal locking procedure.

A Robotic-Assisted Orthopaedic Surgery System has been developed at Loughborough University named Loughborough Orthopaedic Assistant System (LOAS) to assist orthopaedic surgeons during distal locking of intramedullary nails. It uses a calibration frame and a C-arm X-ray unit. The system simplifies the current approach as it uses only two near-orthogonal X-ray images to determine the drilling trajectory of the distal locking holes, thereby considerably reducing irradiation to both the surgeon and patient. The LOAS differs from existing computer-assisted orthopaedic surgery systems, as it eliminates the need for optical tracking equipment which tends to clutter the operating theatre environment and requires care in maintaining the line of sight. Additionally use of optical tracking equipment makes such systems an expensive method for surgical guidance in distal locking of intramedullary nails.

This study is specifically concerned with the improvements of the existing system. A potential problem with the existing System is the appearance of one or more of the opaque markers (embedded in the calibration frame plates) within or on the edge of the oval-shaped distal hole projection. An automatic technique has been implemented which removes the effect of such markers, thereby eliminating the need for repositioning the calibration frame or using a smaller number of opaque markers. Furthermore, the existing calibration frame is not suitable for use across wide range of patient physiologies. The cross-sectional images of the upper leg and anthropometric data are therefore used to propose a calibration frame which is suitable to be used for middle 95% of the population. In order to evaluate the robustness of the machine vision system using proposed calibration frame during clinical use, realistic trials using flesh-covered sheep femur were conducted. Based on the results obtained from the laboratory trials presented in this thesis, it has been shown that the proposed system provides the accuracy required for successful insertion of distal locking screws.

The adopted off-line modelling of the nail to generate look-up tables reduces the length of time for the computation of the drilling trajectory and thus has the potential for reducing the overall time required for the surgical procedure. Analysis has shown that once Lateral and AP x-ray image acquisition is performed, around 20 seconds are taken for computation of drilling trajectory of the distal locking hole. Furthermore, it allows modelling of any shape of intramedullary nail accurately; therefore nails from different manufacturers can be modelled. Also, the system uses robust machine vision features to reduce the surgeon's interaction with the system, thus reducing the overall operating time. Laboratory test results have shown that the proposed system is very robust in the presence of variable noise and contrast in the X-ray images and in terms of variable magnification.

In summary, the LOAS, which is also applicable to other osteosynthesis procedures, such as tibial distal locking and humeral shaft fracture treatment, has the potential to reduce the surgical time and to make the procedure more consistent, irrespective of variations in the skill levels and experience of clinical staff.

Keywords: robotic/computer-assisted orthopaedic surgery, intramedullary nailing, distal locking


 Loughborough University Pilkington Library
Date 08 / 10
Class
Acc. No. 0402594223

Table of contents

TABLE OF CONTENTS.....	VI
LIST OF FIGURES	IX
LIST OF TABLES	XIV
LIST OF ACRONYMS.....	XV
GLOSSARY OF TERMS.....	XVII
1 INTRODUCTION	1
1.1 ORTHOPAEDIC SURGERY	3
1.2 INTRODUCTION TO THE PROBLEM	4
1.3 LIMITATIONS OF THE CURRENT TECHNIQUES USED FOR DISTAL LOCKING	5
1.4 THE LOUGHBOROUGH UNIVERSITY ROBOTIC-ASSISTED ORTHOPAEDIC SURGERY SYSTEM (LOAS) 6	
1.5 AIM OF THE RESEARCH.....	10
1.6 PROPOSED APPROACH.....	10
1.7 SUMMARY.....	11
2 FEMORAL SHAFT FRACTURE TREATMENT.....	13
2.1 FEMORAL FRACTURES	13
2.1.1 <i>Internal fixation</i>	15
2.2 INTRAMEDULLARY NAILING (IMN)	15
2.2.1 <i>Closed Antegrade Intramedullary Nailing</i>	17
2.2.2 <i>Closed Retrograde intramedullary nailing</i>	26
2.3 ANTEGRADE V/S RETROGRADE INTRAMEDULLARY NAILING	30
2.4 LOCKED INTRAMEDULLARY NAILING	31
2.4.1 <i>Dynamic locking</i>	33
2.4.2 <i>Static locking</i>	34
2.5 REAMED V/S UN-REAMED NAILING.....	35
2.6 DISTAL LOCKING	36
2.7 SUMMARY.....	38
3 REVIEW OF TECHNIQUES AVAILABLE FOR ASSISTANCE IN DISTAL LOCKING	39
3.1 NAIL MOUNTED DISTAL TARGETING DEVICES	39
3.2 IMAGE INTENSIFIER MOUNTED TARGETING DEVICES.....	45
3.3 FREE HAND TECHNIQUE	49
3.3.1 <i>Proposed modifications of the free hand technique</i>	53
3.3.2 <i>Devices to reduce surgeon's irradiation while using the free hand technique</i>	57
3.4 USE OF FLUOROSCOPY FOR DISTAL LOCKING	58
3.4.1 <i>Prolonged radiation exposure to surgeons</i>	59
3.5 PHOTOGRAMMETRY.....	61
3.5.1 <i>X-Ray Photogrammetry</i>	63
3.6 FLUOROSCOPY	64
3.6.1 <i>Pincushion distortion</i>	65
3.6.2 <i>Vignetting</i>	66
3.6.3 <i>Geomagnetic Distortion</i>	67
3.7 DISTORTION CORRECTION OF X-RAY IMAGES	68
3.7.1 <i>Global distortion correction approach</i>	68
3.7.2 <i>Localized distortion correction approach</i>	69
3.8 ROBOTIC/COMPUTER ASSISTED ORTHOPAEDIC SURGERY (RAOS/CAOS).....	70

3.8.1	Hull University Robotic Assistance Orthopaedic Surgery System	71
3.8.2	Hebrew university Robotic Assistance Orthopaedic Surgery System.....	78
3.9	COMPUTER ASSISTANCE ORTHOPAEDIC SURGERY	84
3.10	THE LOUGHBOROUGH UNIVERSITY ROBOTIC ASSISTANCE ORTHOPAEDIC SURGERY SYSTEM 88	
3.11	NOVELTY OF THIS THESIS.....	91
3.12	SUMMARY.....	92
4	X-RAY IMAGE ACQUISITION AND ANALYSIS.....	94
4.1	CAPTURE OF INTRAOPERATIVE X-RAY IMAGES.....	94
4.2	FIDUCIAL RECOGNITION	97
4.2.1	Thresholding.....	98
4.2.2	Procedure.....	100
4.2.3	Check for partially imaged fiducials.....	113
4.3	LOCALIZED DISTORTION CORRECTION	115
4.4	LOCATION OF X-RAY SOURCE.....	115
4.4.1	Selection of three closest fiducials.....	116
4.5	RECOVERY OF THE NAIL AXIS IN SPACE.....	121
4.5.1	Nail border detection in the Lateral view image.....	122
4.5.2	Nail border detection in the AP view image.....	128
4.6	DETERMINATION OF THE DRILLING AXIS FOR DISTAL HOLES.....	134
4.6.1	Extraction of distal hole projection.....	139
4.6.2	Fiducial within the oval.....	142
4.6.3	Fiducial at the edge of the oval.....	144
4.7	GUI DEVELOPMENT.....	154
4.7.1	Software flowchart of GUI.....	156
4.8	DETERMINATION OF NAIL SPECIFICATIONS FROM THE INTRAOPERATIVE X-RAY IMAGE....	158
4.9	SUMMARY.....	160
5	MODELLING OF INTRAMEDULLARY NAILS	161
5.1	SELECTION OF THE CAD PACKAGE.....	162
5.2	TOOLS USED FOR MODELLING	163
5.2.1	AutoCAD.....	163
5.2.2	Autodesk Mechanical Desktop	163
5.2.3	AutoLISP	164
5.3	CONSTRUCTION OF AN INTRAMEDULLARY NAIL MODEL	164
5.4	CONSTRUCTION OF DELTA NAIL	170
5.5	SELECTION OF CHARACTERISTIC MEASUREMENTS	178
5.6	BUILDING OF LOOK-UP TABLES	180
5.7	ACCURACY EVALUATION OF NAIL MODELLING	180
5.7.1	Determination of nail rotation angle θ	181
5.8	SUMMARY.....	183
6	ACCURACY EVALUATION OF THE MACHINE VISION SYSTEM	185
6.1	THEODOLITE	185
6.1.1	The triangulation technique	186
6.2	ACCURACY EVALUATION OF MACHINE VISION SYSTEM USING Γ CALIBRATION FRAME	187
6.2.1	Determination of drilling trajectory using theodolites.....	191
6.2.2	Determination of positional and angular error of machine vision drilling trajectory.	204
6.3	EFFECT OF X-RAY SOURCE POSITION ON THE LATERAL VIEW IMAGE	207
6.4	INFLUENCE OF CONTRAST AND NOISE VARIATIONS ON IMAGE ANALYSIS	208
6.5	SUMMARY.....	212
7	DESIGN OF A ROBUST CALIBRATION FRAME	213
7.1	INVESTIGATION INTO FIDUCIAL LAYOUT	213
7.1.1	First stage investigation.....	213
7.1.2	Second stage investigation.....	217
7.2	ADAPTABILITY FOR PATIENT PHYSIOLOGY.....	228
7.2.1	Swelling.....	244

7.3	DESIGN OF A MODULAR CALIBRATION FRAME	248
7.4	PROPOSED FIDUCIAL LAYOUT	251
7.4.1	<i>Fiducial layout for Lateral calibration plates</i>	252
7.4.2	<i>Fiducial layout for AP calibration plates</i>	254
7.5	SUMMARY.....	256
8	IMAGE ANALYSIS AND ACCURACY EVALUATION OF THE PROPOSED CALIBRATION FRAME	257
8.1	IMAGE ANALYSIS PROTOCOL FOR LATERAL CALIBRATION PLATES	257
8.2	IMAGE ANALYSIS PROTOCOL FOR AP CALIBRATION PLATES	269
8.3	ACCURACY EVALUATION OF MACHINE VISION SYSTEM USING PROPOSED CALIBRATION FRAME 276	
8.4	ROBUSTNESS EVALUATION OF MACHINE VISION SYSTEM FOR CLINICAL USE.....	280
8.5	SUMMARY.....	285
9	CONCLUSIONS AND FUTURE WORK	286
9.1	CONCLUSIONS.....	286
9.1.1	<i>Modelling of the IMN</i>	286
9.1.2	<i>Automated machine vision system</i>	287
9.1.3	<i>Design of a robust calibration frame</i>	288
9.1.4	<i>Computation of drilling trajectory</i>	288
9.2	CONTRIBUTIONS	289
9.3	FUTURE WORK	290
9.3.1	<i>Proposed Calibration frame configurations</i>	290
9.3.2	<i>LOAS Commercialization</i>	292
	REFERENCES.....	294
	APPENDIX A: FUNCTIONAL ANATOMY OF THE FEMUR.....	309
A.1	PROXIMAL FEMUR	310
A.2	FEMORAL SHAFT OR DIAPHYSIS	311
A.3	DISTAL FEMUR	311
	APPENDIX B: TYPES OF FEMORAL SHAFT FRACTURE	313
B.1	FEMORAL SHAFT FRACTURE	313
B.2	COMPLICATIONS OF FEMUR FRACTURE	317
	APPENDIX C: FEMORAL SHAFT FRACTURE TREATMENT.....	319
C.1	SKELETAL TRACTION	319
C.2	CAST OR FUNCTIONAL BRACING.....	320
C.3	EXTERNAL FIXATION.....	321
	APPENDIX D: OVERVIEW OF THE X-RAY IMAGING	323
D.1	X-RAY TUBE.....	323
D.2	X-RAY IMAGE INTENSIFIER.....	325
	APPENDIX E: SOFTWARE DETAILS.....	327
	APPENDIX F: THEODOLITE MEASUREMENT PROCEDURE	338
	APPENDIX G: CMM MEASUREMENTS ON CALIBRATION FRAME	341
G.1	LATERAL XRII CALIBRATION PLATE.....	343
G.2	LATERAL SOURCE CALIBRATION PLATE.....	346
G.3	AP XRII CALIBRATION PLATE.....	349
G.4	AP SOURCE CALIBRATION PLATE.....	352
	APPENDIX H: PUBLICATIONS	355

List of figures

FIGURE 1-1 INTRAMEDULLARY NAIL	1
FIGURE 1-2 FEMORAL SHAFT FRACTURE TREATMENT USING CLOSED INTRAMEDULLARY NAILING.....	2
FIGURE 1-3 PERFECT CIRCLE APPROACH.....	5
FIGURE 1-4 CALIBRATION FRAME.....	7
FIGURE 1-5 LATERAL VIEW IMAGE ACQUISITION DURING DISTAL LOCKING.....	7
FIGURE 1-6 AP VIEW IMAGE ACQUISITION DURING DISTAL LOCKING.....	8
FIGURE 1-7 TYPICAL LATERAL AND AP X-RAY IMAGES.....	8
FIGURE 1-8 PRESENCE OF FIDUCIAL AT THE EDGE OF THE OVAL	9
FIGURE 2-1 INTRAMEDULLARY NAILING TREATMENT OF A FEMORAL SHAFT FRACTURE.....	16
FIGURE 2-2 FEMUR ANATOMY (ANTERIOR VIEW) [1].....	18
FIGURE 2-3 LATERAL DECUBITUS POSITION [37].....	19
FIGURE 2-4 SUPINE POSITION [37].....	20
FIGURE 2-5 SKIN INCISION AT GREATER TROCHANTER [22].....	21
FIGURE 2-6 (A) INTRAMEDULLARY NAIL INSERTED USING THE PIRIFORM FOSSA (B) INTRAMEDULLARY NAIL INSERTED USING THE TROCHANTERIC TIP [38].....	22
FIGURE 2-7 INSERTION OF THREADED GUIDE PIN AT TROCHANTERIC FOSSA TO DETERMINE ENTRY POINT [22]	22
FIGURE 2-8 INTRODUCTION OF GUIDE ROD TO THE LEVEL OF FRACTURE [22].....	23
FIGURE 2-9 USE OF INTERNAL FRACTURE ALIGNMENT DEVICE [22].....	23
FIGURE 2-10 DETERMINATION OF THE NAIL LENGTH USING GUIDE ROD [22].....	23
FIGURE 2-11 DETERMINATION OF NAIL LENGTH USING NAIL GAUGE [22].....	24
FIGURE 2-12 REAMING OF FEMORAL CANAL OVER GUIDE ROD [22].....	24
FIGURE 2-13 FLUOROSCOPIC IMAGES SHOWING THE STEPS OF CLOSED INTRAMEDULLARY NAILING (A) OPENING OF THE MEDULLARY CANAL (B) ALIGNMENT OF BONE FRAGMENTS (C) INSERTION OF THE NAIL (D) DISTAL LOCKING [39].....	25
FIGURE 2-14 THIGH SUPPORT FOR RETROGRADE NAILING.....	27
FIGURE 2-15 GUIDE PIN PLACEMENT DURING RETROGRADE NAILING [41].....	27
FIGURE 2-16 FEMORAL TARGETING DEVICE FOR DISTAL LOCKING DURING RETROGRADE NAILING [42].	28
FIGURE 2-17 INTRAMEDULLARY NAIL LOCKING USING INTERNAL LOCKING MECHANISM [52].....	31
FIGURE 2-18 AO/ASIF UNIVERSAL FEMORAL NAIL [37]	32
FIGURE 2-19 INTERLOCKING OF AN INTRAMEDULLARY NAIL.....	33
FIGURE 2-20 DYNAMIC LOCKING TO TREAT PROXIMAL TRANSVERSE FRACTURE.....	34
FIGURE 2-21 COMPARISON BETWEEN ROTATION OF THE NAIL ABOUT ITS LONG AXIS FOR SOLID AND SLOTTED NAIL.....	37
FIGURE 3-1 NAIL MOUNTED DISTAL TARGETING DEVICE [52].....	40
FIGURE 3-2 OPENING OF LATERAL CORTEX.....	41
FIGURE 3-3 THE NAIL SLIDES DOWN OVER THE GUIDE ROD WITHOUT ROTATING AND INTERLOCKS WITH THE DISTAL DRILL BIT.....	41
FIGURE 3-4 ENGAGEMENT OF GUIDE ROD WITH TRANSVERSE DRILL BIT, AND THE DRILL SLEEVE IS INSERTED THROUGH THE GUIDE ROD AND DISTAL DRILL SLEEVE GUIDE.....	42
FIGURE 3-5 SELF-GUIDED INTERLOCKING SYSTEM RESEMBLING A RECTANGLE [72]	43
FIGURE 3-6 H-SHAPED DEVICE [71]	44
FIGURE 3-7 (A) INTRODUCTION OF K-WIRE USING EXTERNAL GUIDE NAIL. (B) DEFINING RECTANGLE BY HOLES DRILLED ON THE ANTERIOR CORTEX OF THE DISTAL FEMUR [73].....	45
FIGURE 3-8 TARGET DEVICE INSERTED INTO THE CONSOLE, WHICH IS SECURED TO THE X-RAY TUBE HOUSING [28]	46
FIGURE 3-9 IMAGE INTENSIFIER MOUNTED TARGETING DEVICE [68]	47
FIGURE 3-10 ALIGNMENT OF X-RAY IMAGING AXIS WITH WIRE CROSS INTERSECTION [69].....	48
FIGURE 3-11 LASER PLANES INTERSECTION FOR DEFINING PATH OF X-RAY IMAGING AXIS [69].....	49
FIGURE 3-12 PERFECT CIRCLE APPROACH.....	50
FIGURE 3-13 DETERMINATION OF ENTRY POINT.....	51

FIGURE 3-14 CONFIRMATION OF DRILLING TRAJECTORY	51
FIGURE 3-15 X-RAY FLUOROSCOPIC IMAGES TAKEN DURING DISTAL LOCKING [77]	52
FIGURE 3-16 DIRECT X-RAYS EXPOSURE TO SURGEON'S HAND [78]	52
FIGURE 3-17 DEVICES USED TO IMPLEMENT FLAG AND GRID TECHNIQUE [25]	53
FIGURE 3-18 ATTACHMENT OF THE METALLIC GRID TO FEMUR WITH AN ADHESIVE DRAPE [25]	54
FIGURE 3-19 LATERAL VIEW PERFECT CIRCLE IMAGE WITH HEMOSTATIC CLAMP (I.E. STAR) [25]	54
FIGURE 3-20 3D RECONSTRUCTION OF AN OBJECT POINT USING Γ FRAME [3]	62
FIGURE 3-21 X-RAY IMAGE FORMATION PROCESS	63
FIGURE 3-22 SIEMENS SIREMOBIL 2 MOBILE X-RAY IMAGE INTENSIFIER [78]	65
FIGURE 3-23 PINCUSHION DISTORTION CAUSED BY X-RAY IMAGE INTENSIFIER	66
FIGURE 3-24 S-DISTORTION WHEN IMAGE INTENSIFIER IS PARALLEL TO MAGNETIC FIELD [78]	67
FIGURE 3-25 S-DISTORTION WHEN IMAGE INTENSIFIER ORIENTED TRANSVERSE TO THE MAGNETIC FIELD [78]	68
FIGURE 3-26 OVERVIEW OF RAOS DEVELOPED BY HULL UNIVERSITY [113]	72
FIGURE 3-27 END-EFFECTOR HOLDING THE CALIBRATION FRAME [116]	73
FIGURE 3-28 LATERAL VIEW IMAGE [116]	75
FIGURE 3-29 AP VIEW IMAGE [116]	75
FIGURE 3-30 LOCATION OF THE LONG AXIS OF THE INTRAMEDULLARY NAIL [116]	76
FIGURE 3-31 BONE MOUNTED MARS ROBOT CARRYING THE TARGETING DRILL GUIDE [119]	79
FIGURE 3-32 FLUOROTRAX ATTACHED TO C-ARM'S IMAGE INTENSIFIER [118]	80
FIGURE 3-33 TYPICAL INTRAOPERATIVE X-RAY IMAGE [119]	81
FIGURE 3-34 TARGETING DRILL GUIDE IDENTIFICATION [119]	82
FIGURE 3-35 DISTAL LOCKING HOLE IDENTIFICATION [119]	83
FIGURE 3-36 REGISTRATION OF DISTAL LOCKING HOLE WITH NAIL REFERENCE BASE PRIOR TO NAIL INSERTION	86
FIGURE 3-37 HIP BOX PROTOTYPE (L.H.S) AND Γ FRAME (R.H.S)	89
FIGURE 3-38 FIDUCIAL OCCLUSION PHENOMENA	90
FIGURE 4-1 SET-UP FOR LATERAL VIEW IMAGE ACQUISITION	95
FIGURE 4-2 SET-UP FOR THE AP VIEW IMAGE ACQUISITION	95
FIGURE 4-3 (A) CALIBRATION FRAME (B) TYPICAL LATERAL AND AP X-RAY IMAGES	96
FIGURE 4-4 TEST RIG USED TO SIMULATE NAIL'S ROTATION	96
FIGURE 4-5 FLOWCHART OF IMAGE ANALYSIS	97
FIGURE 4-6 SUMMARY OF FIDUCIAL RECOGNITION PROGRAM	101
FIGURE 4-7 (A) INTRAOPERATIVE AP VIEW IMAGE (B) AP VIEW IMAGE AFTER APPLYING OTSU'S THRESHOLDING	102
FIGURE 4-8 INVERTED THRESHOLDED LATERAL VIEW IMAGE	103
FIGURE 4-9 IDENTIFICATION OF SIX LARGEST OBJECTS BASED ON THEIR AREA	105
FIGURE 4-10 SELECTED SUB-REGION WITH FIDUCIAL	107
FIGURE 4-11 INVERTED IMAGE OF SELECTED REGION	108
FIGURE 4-12 2D NORMAL DISTRIBUTED GAUSSIAN PROBABILITY DENSITY FUNCTION	109
FIGURE 4-13 CROPPED REGION CONTAINING WASHERS AND CENTRAL MARKER IN THE LATERAL VIEW	110
FIGURE 4-14 FIDUCIAL RECOGNITION IN THE LATERAL VIEW IMAGE	112
FIGURE 4-15 FIDUCIAL RECOGNITION IN AP VIEW IMAGE	112
FIGURE 4-16 LATERAL VIEW X-RAY IMAGE	113
FIGURE 4-17 CROPPED REGION CONTAINING THE PARTIALLY IMAGED FIDUCIAL AT THE EDGES OF THE X-RAY IMAGE	114
FIGURE 4-18 (A) THRESHOLDED IMAGE OF THE CROPPED REGION CONTAINING FIDUCIAL AT THE NAIL EDGES (B) THRESHOLDED IMAGE OF THE CROPPED REGION CONTAINING COMPLETELY VISIBLE FIDUCIAL	114
FIGURE 4-19 DIVISION OF INTRAOPERATIVE IMAGE INTO TRIANGULAR SUB-REGION	116
FIGURE 4-20 DETERMINATION OF THREE CLOSEST FIDUCIALS FOR A GIVEN IMAGE POINT	117
FIGURE 4-21 FLOWCHART OF ALGORITHM FOR SELECTING THE BOUNDING TRIANGLE FOR A GIVEN IMAGE POINT	118
FIGURE 4-22 IDEAL CASE OF THE FOCAL POINT DETERMINATION	119
FIGURE 4-23 DETERMINATION OF POINT OF INTERSECTION BETWEEN TWO FOCAL LINES USING POINT OF CLOSEST APPROACH	119
FIGURE 4-24 SELECTION OF IMAGE POINTS FROM XR11 PLATE FOR FOCAL POINT DETERMINATION	121
FIGURE 4-25 LINE PROFILE ACROSS THE NAIL FOR NAIL BORDER DETECTION	122
FIGURE 4-26 CROPPING OF IMAGE TO DETERMINE NAIL WIDTH	123

FIGURE 4-27 DETERMINATION OF APPROXIMATE NAIL WIDTH.....	124
FIGURE 4-28 DIVISION OF LINE PROFILE IN TWO HALVES.....	124
FIGURE 4-29 DETERMINATION OF NAIL EDGE USING GRADIENT.....	125
FIGURE 4-30 DETERMINATION OF NAIL DIAMETER.....	127
FIGURE 4-31 DETECTION OF NAIL EDGES AND NAIL CENTRELINE IN THE LATERAL VIEW.....	128
FIGURE 4-32 (A) AP VIEW IMAGE (B) CROPPING OF THE AP VIEW IMAGE TO LOCATE THE NAIL USING CENTRAL AND ORIENTATION MARKERS.....	129
FIGURE 4-33 LOCATION OF NAIL IN THE AP VIEW, WHEN FIDUCIALS ON EXTREME R.H.S. OF THE ORIENTATION MARKER ARE HIDDEN BENEATH THE NAIL.....	129
FIGURE 4-34 DETERMINATION OF STARTING POINT FOR DRAWING LINE PROFILES.....	130
FIGURE 4-35 DRAWING LINE PROFILE ACROSS THE NAIL TO AVOID A DISTAL HOLE.....	131
FIGURE 4-36 DETECTION OF NAIL EDGES AND NAIL AXIS IN THE AP VIEW.....	132
FIGURE 4-37 RECOVERY OF THE NAIL AXIS IN SPACE USING EXTRAPOLATION TECHNIQUE [5, 85].....	134
FIGURE 4-38 ANGLE BETWEEN THE MAJOR AXIS OF THE OVAL AND THE NAIL AXIS. (A) CONCEPT (B) IMPLEMENTATION USING IMAGE ANALYSIS.....	135
FIGURE 4-39 LOCATION OF THE CENTRE OF THE DISTAL HOLE PROJECTION IN IMAGE PLANE.....	136
FIGURE 4-40 DETERMINATION OF DISTAL HOLE'S CENTRE AND ANGLE ϕ	137
FIGURE 4-41 ROTATION OF THE NAIL ABOUT ITS LONG AXIS.....	139
FIGURE 4-42 LATERAL VIEW IMAGE BEFORE AND AFTER THRESHOLDING.....	140
FIGURE 4-43 LATERAL VIEW X-RAY IMAGE WITH NAIL COMPLETELY ACROSS THE CALIBRATION FRAME.	141
FIGURE 4-44 OVAL BEFORE AND AFTER THRESHOLDING.....	142
FIGURE 4-45 PRESENCE OF FIDUCIAL WITHIN THE OVAL.....	143
FIGURE 4-46 INVERTED THRESHOLDED IMAGE.....	143
FIGURE 4-47 REMOVAL OF THE FIDUCIAL WITHIN THE OVAL. (A) ORIGINAL (B) AFTER FIDUCIAL REMOVAL AND BINARIZATION.....	144
FIGURE 4-48 (A) LATERAL INTRAOPERATIVE X-RAY IMAGE (B) CROPPED REGION.....	145
FIGURE 4-49 (A) OVAL WITH GAPS ALONG ITS BOUNDARY (B) CLOSED OVAL OBTAINED USING ADAPTIVE THRESHOLDING.....	146
FIGURE 4-50 STARTING POINT FOR THE ORDERED EDGE CO-ORDINATES.....	147
FIGURE 4-51 USE OF GRADIENT DIRECTION FOR DETECTION OF FIDUCIAL LOCATION AT THE OVAL EDGES.	148
FIGURE 4-52 PLOT OF SIX LARGEST ORIENTATION TRANSITIONS ALONG THE EDGES OF THE OVAL.....	149
FIGURE 4-53 USE OF ORIENTATION GRADIENT FOR DETECTION FOR FIDUCIAL LOCATION AT THE OVAL EDGES.....	150
FIGURE 4-54 STARTING POINTS USED DURING TWO PASSES FOR LOCATING FIDUCIAL.....	151
FIGURE 4-55 CONVEX HULL OF A SET OF POINTS.....	152
FIGURE 4-56 INTRODUCTION OF FIDUCIAL AT THE EDGE OF THE OVAL.....	153
FIGURE 4-57 GUI FOR DISTAL LOCKING PROCEDURE.....	156
FIGURE 4-58 MATLAB SOFTWARE FLOWCHART.....	157
FIGURE 4-59 INTRAOPERATIVE TRAJECTORY ANALYSIS USING VB AND MATLAB INTERFACE.....	158
FIGURE 5-1 LOOK-UP TABLE FORMAT.....	161
FIGURE 5-2 MODELLING OF THE NAIL USING AUTOCAD MECHANICAL DESKTOP.....	165
FIGURE 5-3 FRONT VIEW OF DISTAL END OF THE INTRAMEDULLARY NAIL.....	166
FIGURE 5-4 SHADED REGION REPRESENTING PROJECTION OF DISTAL LOCKING HOLE.....	167
FIGURE 5-5 ROTATION OF THE NAIL ABOUT ITS OWN AXIS AT $\theta = 0$	168
FIGURE 5-6 SMALL HOLE PROJECTION RESULTING IN TERMINATION OF ANGLE " θ " INCREMENT.....	169
FIGURE 5-7 FLOWCHART OF INTRAMEDULLARY NAILING PROCEDURE.....	170
FIGURE 5-8 DISTAL END OF THE DELTA NAIL.....	171
FIGURE 5-9 DELTA NAIL MODEL.....	172
FIGURE 5-10 CREATION OF TWO CYLINDERS TO REPRESENT DISTAL END OF THE NAIL.....	173
FIGURE 5-11 POLAR ARRAY OF RECTANGULAR BOX TO OBTAIN DELTA SHAPE.....	173
FIGURE 5-12 RIGHT VIEW OF THE DELTA NAIL.....	174
FIGURE 5-13 FRONT ISOMETRIC VIEW OF DISTAL END OF DELTA NAIL.....	174
FIGURE 5-14 COMPARISON BETWEEN SMALL DIAMETER DELTA AND CYLINDRICAL NAIL AT $\phi = 5^\circ$..	175
FIGURE 5-15 COMPARISON BETWEEN SMALL DIAMETER DELTA AND CYLINDRICAL NAIL AT $\phi = 10^\circ$..	176
FIGURE 5-16 COMPARISON BETWEEN SMALL DIAMETER DELTA AND CYLINDRICAL NAIL AT $\phi = 15^\circ$..	176
FIGURE 5-17 COMPARISON BETWEEN LARGE DIAMETER DELTA AND CYLINDRICAL NAIL AT $\phi = 5^\circ$..	177

FIGURE 5-18 COMPARISON BETWEEN LARGE DIAMETER DELTA AND CYLINDRICAL NAIL AT $\phi = 15^\circ$.	178
FIGURE 5-19 GRAPHICAL COMPARISONS OF DIFFERENT OVAL MEASUREMENTS WITH ANGULAR ROTATION " θ " OF THE NAIL.	179
FIGURE 5-20 MATCHING BETWEEN X-RAY IMAGE AND CAD MODEL.	182
FIGURE 5-21 ROTATION ANGLE ACCURACY OBTAINED USING THE MAJOR ANGLE METHOD.	182
FIGURE 5-22 ROTATION ANGLE ACCURACY OBTAINED USING THE AREA METHOD.	183
FIGURE 6-1 INTERNAL CONSTRUCTION OF THEODOLITE.	186
FIGURE 6-2 APPLICATION OF TRIANGULATION TECHNIQUE.	187
FIGURE 6-3 EXPERIMENTAL SET UP IN THE VICINITY OF CALIBRATION FRAME.	188
FIGURE 6-4 SOKISHA DT5 THEODOLITE.	188
FIGURE 6-5 STANDARD NORMAL DISTRIBUTION GRAPH.	190
FIGURE 6-6 POSITIONING OF SPECIFIED ORIGIN OF CALIBRATION FRAME.	192
FIGURE 6-7 THEODOLITE MEASUREMENTS ON THE CALIBRATION FRAME.	193
FIGURE 6-8 SOLID CYLINDER WITH CIRCULAR DISC.	194
FIGURE 6-9 INSERTION OF SOLID CYLINDER INTO THE DISTAL LOCKING HOLE.	194
FIGURE 6-10 FERRANTI MERLIN 750 CO-ORDINATE MEASUREMENT MACHINE.	195
FIGURE 6-11 POINTS TO BE MEASURED ON THE SURFACE OF THE CIRCULAR DISC.	196
FIGURE 6-12 DRAWING OF SEVERAL CHORDS ON DISC SURFACE TO DETERMINE DISC'S CENTRE	196
FIGURE 6-13 DATUM COORDINATE SYSTEM OF CALIBRATION FRAME	199
FIGURE 6-14 CALIBRATION FRAME IN POSITION FOR CMM MEASUREMENTS (FRONT VIEW).	205
FIGURE 6-15 RESULTS FROM ACCURACY EVALUATION OF THE MACHINE VISION SYSTEM.	206
FIGURE 6-16 POSITIONING OF THE X-RAY SOURCE RELATIVE TO CALIBRATION FRAME.	207
FIGURE 6-17 IMAGES AT DIFFERENT SNR RATIOS [134].	209
FIGURE 6-18 INFLUENCE OF X-RAY PENETRATION ON IMAGE CONTRAST [135].	210
FIGURE 6-19 MACHINE VISION ANALYSIS ON THE LATERAL VIEW IMAGE WITH VARIABLE NOISE AND CONTRAST.	211
FIGURE 6-20 MACHINE VISION ANALYSIS ON THE AP VIEW IMAGE WITH VARIABLE NOISE AND CONTRAST.	211
FIGURE 7-1 REMOVAL OF CENTRE FIDUCIALS IN THE LATERAL VIEW IMAGE.	214
FIGURE 7-2 FIDUCIAL USED IN STANDARD PRACTICE IMAGE ANALYSIS.	215
FIGURE 7-3 DISCARDING OF FIDUCIALS IMMEDIATELY ABOVE AND BELOW THE INTRAMEDULLARY NAIL.	216
FIGURE 7-4 FIDUCIALS USED IN THE LATERAL VIEW IMAGE FOR SCENARIO 1.	218
FIGURE 7-5 FIDUCIALS USED IN THE AP VIEW IMAGE FOR SCENARIO 1.	218
FIGURE 7-6 FIDUCIALS USED IN THE LATERAL VIEW IMAGE FOR SCENARIO 2.	219
FIGURE 7-7 FIDUCIALS USED IN THE AP VIEW IMAGE FOR SCENARIO 2.	220
FIGURE 7-8 FIDUCIALS USED IN THE LATERAL VIEW IMAGE FOR SCENARIO 3.	221
FIGURE 7-9 SCHEMATIC VIEW OF FIDUCIAL LAYOUT ON THE LATERAL VIEW USING SCENARIO 3.	222
FIGURE 7-10 FIDUCIALS USED IN THE AP VIEW IMAGE FOR SCENARIO 3.	223
FIGURE 7-11 SCHEMATIC VIEW OF FIDUCIAL LAYOUT ON AP VIEW IMAGE USING SCENARIO 3.	223
FIGURE 7-12 FIDUCIAL USED IN THE LATERAL VIEW FOR SCENARIO 4.	224
FIGURE 7-13 FIDUCIAL USED IN THE LATERAL VIEW FOR SCENARIO 4.	225
FIGURE 7-14 FIDUCIAL USED IN THE LATERAL VIEW IMAGE FOR SCENARIO 5.	226
FIGURE 7-15 FIDUCIAL USED IN THE AP VIEW IMAGE FOR SCENARIO 5.	226
FIGURE 7-16 FIDUCIAL USED IN THE LATERAL VIEW IMAGE FOR SCENARIO 6.	227
FIGURE 7-17 FIDUCIAL USED IN THE AP VIEW IMAGE FOR SCENARIO 6.	228
FIGURE 7-18 FEMUR CROSS-SECTION OF LEFT LEG.	229
FIGURE 7-19 MEASUREMENT LOCATION OF THIGH DEPTH, BEHIND THE KNEE	230
FIGURE 7-20 STANDARD NORMAL DISTRIBUTION GRAPH.	231
FIGURE 7-21 MEASUREMENT LOCATION OF THIGH DEPTH(MAXIMUM, SITTING) FOR OLDER ADULTS [139]	232
FIGURE 7-22 MEASUREMENT LOCATION OF THIGH DEPTH(MAXIMUM, SITTING) FOR OLDER CHILDREN [147]	235
FIGURE 7-23 FRONT VIEW OF THE UPPER LEFT LEG [148].	237
FIGURE 7-24 FEMUR CROSS SECTION, JUST BEHIND THE KNEE REGION [148].	238
FIGURE 7-25 DISTAL FEMUR CROSS SECTION [148].	239
FIGURE 7-26 FRONT VIEW OF THE UPPER RIGHT LEG.	241
FIGURE 7-27 CROSS SECTIONAL VIEW OF THE DISTAL FEMUR [149].	242
FIGURE 7-28 FEMUR LOCATION DIMENSIONS WITH RESPECT TO OUTSIDE AND TOP OF THE LEG.	244
FIGURE 7-29 CALIBRATION FRAME DIMENSIONAL REQUIREMENTS.	248

FIGURE 7-30 ASSEMBLED MODULAR CALIBRATION FRAME [156]	249
FIGURE 7-31 DESIRED PATIENT POSITION DURING THE LATERAL IMAGE ACQUISITION.	250
FIGURE 7-32 SEPARATION BETWEEN LATERAL AND AP PLATES ALONG THE X-AXIS.....	251
FIGURE 7-33 FIDUCIAL LAYOUT FOR LATERAL CALIBRATION PLATES.	253
FIGURE 7-34 FIDUCIAL LAYOUT FOR AP CALIBRATION PLATES (MEDIUM FRAME).	254
FIGURE 7-35 FIDUCIAL LAYOUT FOR AP CALIBRATION PLATES (LARGE FRAME).....	255
FIGURE 8-1 DIVISION OF FIDUCIALS ON LATERAL CALIBRATION PLATES INTO TWO REGIONS.	257
FIGURE 8-2 LATERAL VIEW IMAGE.....	258
FIGURE 8-3 CROPPED LATERAL VIEW IMAGE.....	258
FIGURE 8-4 CROPPING OF THE IMAGE TO OBTAIN NAIL'S LOCATION	259
FIGURE 8-5 (A) LATERAL VIEW IMAGE WITH EXTERNAL OBJECT (B) CROPPED REGION TO OBTAIN NAIL'S LOCATION.....	260
FIGURE 8-6 DISCARDED LATERAL IMAGE DUE TO INSUFFICIENT NUMBER OF FIDUCIALS.	261
FIGURE 8-7 DISCARDED LATERAL IMAGE DUE TO ABSENCE OF FIDUCIALS WITH UNIQUE SPACING.....	262
FIGURE 8-8 LATERAL VIEW IMAGE WITH FIDUCIALS VERY CLOSE TO EACH OTHER.....	263
FIGURE 8-9 X-RAY IMAGING AXIS WITH RESPECT TO CALIBRATION FRAME FOR THE LATERAL IMAGE ACCUSATION (TOP VIEW).....	263
FIGURE 8-10 FIDUCIAL OVERLAPPING IN LATERAL VIEW IMAGE.....	264
FIGURE 8-11 USEFUL LATERAL VIEW IMAGE	264
FIGURE 8-12 LATERAL IMAGE'S UPPER REGION.....	265
FIGURE 8-13 DETERMINATION OF HORIZONTAL AND VERTICAL SPACINGS.	266
FIGURE 8-14 ESTABLISHMENT OF STARTING POINTS ON SOURCE PLATE.....	266
FIGURE 8-15 FIDUCIAL RECOGNITION IN LATERAL VIEW UPPER REGION.....	267
FIGURE 8-16 FIDUCIAL RECOGNITION IN LATERAL VIEW UPPER REGION WHEN XRII LINE2 IS IN CLOSE PROXIMITY OF THE NAIL.	268
FIGURE 8-17 FIDUCIAL RECOGNITION LATERAL VIEW LOWER REGION	268
FIGURE 8-18 LATERAL VIEW IMAGE ANALYSIS	269
FIGURE 8-19 AP VIEW IMAGE	270
FIGURE 8-20 CROPPED AP VIEW IMAGE.....	270
FIGURE 8-21 AP VIEW UPPER REGION	271
FIGURE 8-22 AP VIEW LOWER REGION.....	271
FIGURE 8-23 SELECTION OF INITIAL STARTING POINT	272
FIGURE 8-24 SELECTION OF STARTING POINT.....	273
FIGURE 8-25 DISTINCTION BETWEEN LINE 2, 3 OR 4 OF SOURCE PLATE	273
FIGURE 8-26 AP VIEW IMAGE ANALYSIS WITH STARTING POINT CHOSEN IN UPPER REGION	274
FIGURE 8-27 SELECTION OF STARTING POINT FROM LOWER REGION.....	275
FIGURE 8-28 AP VIEW IMAGE ANALYSIS WITH STARTING POINT CHOSEN IN LOWER REGION.....	276
FIGURE 8-29 NAIL AND CALIBRATION FRAME SET-UP DURING LABORATORY TRIALS.....	277
FIGURE 8-30 THEODOLITE SET-UP FOR OPTICAL MEASUREMENT DURING LABORATORY TRIALS.....	277
FIGURE 8-31 RESULTS OBTAINED FOR SMALL CYLINDRICAL NAIL DURING ACCURACY EVALUATION OF THE MACHINE VISION SYSTEM.	278
FIGURE 8-32 RESULTS OBTAINED FOR LARGE CYLINDRICAL NAIL DURING ACCURACY EVALUATION OF THE MACHINE VISION SYSTEM.	279
FIGURE 8-33 INSERTION OF DISTAL END OF THE NAIL INTO SHEEP FEMUR.....	280
FIGURE 8-34 X-RAY IMAGES ACQUIRED WITH FLESH-COVERED SHEEP FEMUR.....	281
FIGURE 8-35 (A) INITIALLY CROPPED UPPER REGION (B) FURTHER CROPPING OF THE UPPER REGION ..	282
FIGURE 8-36 (A) INITIALLY CROPPED LOWER REGION (B) FURTHER CROPPING OF THE LOWER REGION.	282
FIGURE 8-37 IMAGE ANALYSIS ON THE LATERAL VIEW IMAGE.	283
FIGURE 8-38 IMAGE ANALYSIS ON THE AP VIEW IMAGE.	283
FIGURE 8-39 RESULTS OBTAINED DURING ACCURACY EVALUATION OF THE MACHINE VISION SYSTEM FOR CLINICAL USE.	284
FIGURE 9-1 PROPOSED MODULAR CALIBRATION FRAME CONFIGURATIONS.....	291

List of Tables

TABLE 3-1 RADIATION EXPOSURE DURING DISTAL LOCKING PROCEDURES.....	60
TABLE 4-1 XRII PLATE REFERENCE MARKER IDENTIFICATION BASED ON AREA IN THE LATERAL VIEW	104
TABLE 4-2 XRII PLATE REFERENCE MARKER IDENTIFICATION BASED ON AREA IN AP VIEW	104
TABLE 4-3 XRII PLATE REFERENCE MARKER IDENTIFICATION BASED ON AREA IN AP VIEW FOR NOISY X- RAY IMAGE	104
TABLE 4-4 SOURCE PLATE REFERENCE MARKER IDENTIFICATION BASED ON AREA.....	111
TABLE 4-5 INVESTIGATION INTO CHANGE IN THE CENTRE OF THE OVAL.	138
TABLE 4-6 ESTIMATION OF EXPECTED FIDUCIAL LOCATIONS USING DIRECTION OF THE GRADIENT.....	149
TABLE 4-7 FIRST SIX LARGEST ORIENTATION GRADIENTS.	150
TABLE 4-8 COMPARISON BETWEEN PROPOSED AND CONVEX HULL APPROACH.	154
TABLE 6-1 THEODOLITE READINGS TO DETERMINE SAMPLE STANDARD DEVIATION.	191
TABLE 6-2 THEODOLITE MEASUREMENTS.....	197
TABLE 6-3 DISC'S CENTRE OBTAINED USING PERPENDICULAR BISECTOR METHOD.	197
TABLE 7-1 ANTHROPOMETRIC DATA FOR THIGH DEPTH (MM), BEHIND KNEE WHILE SITTING [137]	230
TABLE 7-2 THIGH DEPTH IN MM (MAXIMUM, SITTING) ANTHROPOMETRIC DATA FOR OLDER ADULTS [139]	231
TABLE 7-3 THIGH DEPTH IN MM (MAXIMUM, SITTING) ANTHROPOMETRIC DATA FOR ADULTS.	232
TABLE 7-4 GENERAL TREATMENT GUIDELINES IN CHILDREN WITH FEMORAL SHAFT FRACTURES.....	233
TABLE 7-5 THIGH DEPTH IN MM (MAXIMUM, SITTING) ANTHROPOMETRIC DATA FOR MALE OLDER CHILDREN [147].....	234
TABLE 7-6 THIGH DEPTH IN MM (MAXIMUM, SITTING) ANTHROPOMETRIC DATA FOR FEMALE OLDER CHILDREN [147].....	235
TABLE 7-7 DETERMINATION OF MM/SQUARE RATIO	238
TABLE 7-8 DEPTH AND WIDTH DIMENSIONS FOR DISTAL END OF THE LEG.....	240
TABLE 7-9 DEPTH AND WIDTH DIMENSIONS AT THE DISTAL SECTION FOR MIDDLE 95 TH PERCENTILE POPULATION.	240
TABLE 7-10 DETERMINATION OF MM/SQUARE RATIO	242
TABLE 7-11 DEPTH AND WIDTH DIMENSIONS FOR DISTAL END OF THE LEG.....	243
TABLE 7-12 DEPTH AND WIDTH DIMENSIONS AT THE DISTAL SECTION FOR MIDDLE 95 TH PERCENTILE POPULATION.	243
TABLE 7-13 GENERAL TREATMENT GUIDELINES FOR FEMORAL SHAFT FRACTURES USING IMN.	247

List of Acronyms

AAOS	: American Academy of Orthopaedic Surgery
ACR	: American college of Radiology
AIS	: Abbreviated Injury Scale
AO/ASIF	: Arbeitsgemeinschaft fuer Osteosynthesefragen / Association for The Study of Internal Fixation
AP	: Anterior-Posterior
API	: Application programming interface
ARDS	: Acute respiratory distress syndrome
ASPRS	: American Society for Photogrammetry and Remote Sensing
AVN	: Avascular necrosis.
CAD	: Computer-aided design
CAOS	: Computer assisted orthopaedic system
CCD	: Charge-coupled device
CMM	: Co-ordinate Measuring Machine
CSV	: Comma Separated File
CT	: Computerized Tomography
GUI	: Graphical User Interface
ICRP	: International Commission on Radiological Protection
I.I.	: Image intensifier
IMN	: Intramedullary nailing
ISS	: Injury Severity Score
LEDs	: Light Emitting Diodes
LUT	: Look-up table
MPD	: Maximum permissible dose
MRI	: Magnetic Resonance Imaging
NHS	: National Health Service
OT	: Operating theatre
PCI	: Peripheral Component Interconnect

RAOS	: Robotic assisted orthopaedic system
SNR	: Signal-to-Noise ratio
UCS	: Universal co-ordinate system
VB	: Visual Basic
WBC	: White blood cells
WCS	: World co-ordinate system

Glossary of Terms

Anterior: It denotes the front surface of a structure.

Anterior-Posterior (AP): In x-ray imaging, it denotes taken or viewed from front to back through the body.

Acute respiratory distress syndrome (ARDS): It is a life-threatening condition that causes lung swelling and fluid build up in the air sacs. This fluid inhibits the passage of oxygen from the air into the bloodstream.

Aseptic technique: It is a technique to protect against infection by pathogenic micro-organisms.

Autologous graft: It is transfer of a tissue from one site to another site in the same individual.

Bone Healing: As soon as a fracture occurs, the body acts to protect the injured area, as soon after the fracture, the blood vessels constrict, stopping any further bleeding. Within a few hours after the fracture, the extravascular blood cells, known as a "hematoma", form a blood clot. All of the cells within the blood clot degenerate and die. Some of the cells outside of the blood clot, but adjacent to the injury site, also degenerate and die. Within this same area, the "fibroblasts" i.e. connective tissue cells survive and replicate. Over a period of time new "threads" of bone cells start to grow on both sides of the fracture line. These threads grow toward each other, resulting in bone healing i.e. solid union of the fracture.

Bounding box: It describes the rectangle containing the region i.e. [ul_corner width], where, "ul_corner" is in the form [x y] and specifies the upper left corner of the bounding box in terms of x & y co-ordinates, and "width" is in the form [x_width y_width] and specifies the width of the bounding box along x & y axis.

Carcinogenic: It implies producing or tending to produce cancer.

Centering: It involves, loosening of the tripod screw, and slowly translating the theodolite until it is exactly centred over the survey point, then tightening of the screw.

Congenital: It implies existing at or before birth usually through heredity, such as congenital deafness.

Cortical bone: It is the dense outer surface of bone that forms a protective layer around the internal cavity. It is also known as compact bone.

Distal: It refers to the part of the structure furthest away from the centre of the body.

Endosteal: It is the thin layer of cells lining the medullary cavity of a bone.

Haematoma: It is a mass of clotted blood that forms in a tissue, organ, or body space as a result of a broken blood vessel.

Hemostat: It is a surgical tool which resembles a set of scissors.

Ipsilateral: It is located on or affecting the same side of the body.

Injury Severity Score (ISS): It is an anatomical scoring system that provides an overall score for patients with multiple injuries. Each injury is assigned an Abbreviated Injury Scale (AIS) score and is allocated to one of six body regions (Head, Face, Chest, Abdomen, Extremities (including Pelvis) and External). Only the highest AIS score in each body region is used. The 3 most severely injured body regions have their score squared and added together to produce the ISS score.

Laparotomies: It is a surgical incision into the abdominal wall.

Malunion: It means incomplete union or union in a faulty position after a fracture or wound. Types of malunion include overlap and shortening, angulation, rotation and cross-union i.e. union to an adjacent bone. The most common reasons for malunion are poor reduction of the original fracture, poor holding of an originally well reduced fracture, soft tissue contracture, and gradual collapse of the fracture due to comminuted or osteoporotic bone.

Medial: It implies in or toward the middle; nearer the middle of the body. Lying or extending in the middle; especially of a body part for example lying or extending toward the median axis of the body, such as the medial surface of the femur.

Millirem (mrem): It is a unit used to measure the effect of radiation on the human body.

Necrosis: It implies death of bone tissue due to impaired or disrupted blood supply as that caused by traumatic injury or disease.

Percutaneous: It pertains to any medical procedure where access to inner organs or other tissue is done via needle-puncture of the skin, rather than by using an "open" approach where inner organs or tissue are exposed.

PeopleSize: It is an anthropometry dataset which gives data on human sizes for design ergonomics.

Posterior: It refers to the back surface of a structure.

Proximal: It refer to the part of a structure closest to the centre of the body

Radiolucent: Anything that permits the penetration and passage of X-rays or other forms of radiation.

Septic arthritis: It is an infection of the joints characterized by pain, fever, chills, inflammation, and swelling in one or more joints, and loss of function in those joints. It is also known as infectious arthritis or pyogenic arthritis.

Sv: It is a unit 100 times larger than "mrem", i.e. $1\text{mSv} = 100\text{mrem}$.

Trabecular or cancellous bone: It is spongy, and makes up the bulk of the interior of most bones.

Valgus: It describes a deformity where, in the case of a leg, the limb is bent toward the midline of the body.

Varus: It describes a deformity where, in the case of a leg, the limb is bent away from the midline of the body.

1 Introduction

The femur or thigh bone is the longest, largest (by volume) and strongest bone of the human body [1]. A femoral shaft fracture is therefore regarded as an orthopaedic emergency and requires immediate medical attention to preserve the patient's limb and to minimize complications [2]. Femoral-shaft fractures occur usually due to trauma. Motor vehicle accidents, pedestrian-versus-vehicle accidents, falls, and gunshot wounds are among the most common causes. Pathologic fractures in adults are most often the result of osteoporosis, a disease in which the bones become extremely porous and thus subject to fracture, and heal slowly. Nowadays, closed intramedullary nailing (IMN) is the best available method for femoral shaft fracture treatment. It involves passing the intramedullary nail, shown in Figure 1-1, from proximal (hip) to distal (knee) end of the femur as shown in Figure 1-2.

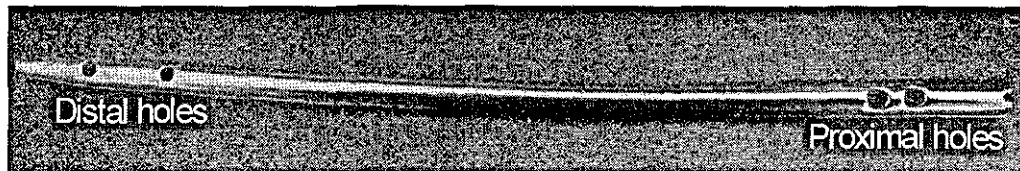


Figure 1-1 Intramedullary nail

The intramedullary nail is in the form of a stainless steel tube with fixation holes at the proximal and distal ends as shown in Figure 1-1.

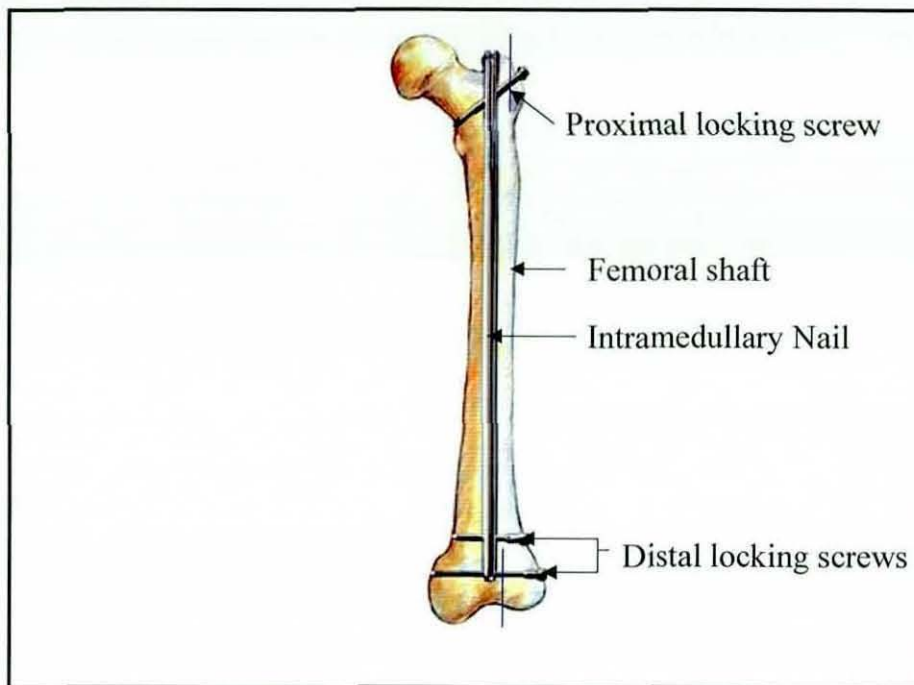


Figure 1-2 Femoral shaft fracture treatment using closed intramedullary nailing.

Following nail insertion, the problems associated with the location of the distal holes and correct screw placements are well known. Numerous techniques and devices have been proposed to aid distal locking, in attempts to overcome the associated problems. However, all of these devices and techniques have deficiencies. For example, they lack versatility (i.e. are only selectively applicable), are not easy to use, are time consuming or are not sufficiently accurate. A Robotic-Assisted Orthopaedic Surgery System has been developed at Loughborough University named Loughborough Orthopaedic Assistant System (LOAS) to assist orthopaedic surgeons during internal fixation of hip fractures and distal locking of intramedullary nails by Bouazza-Marouf et al [3-7]. The goal of this thesis is to review existing system and develop a robust LOAS by addressing problems which are currently faced.

Given the goal of the thesis, this chapter provides an overview of both the orthopaedic and engineering aspects of the thesis. Section 1.1 provides a brief insight into Orthopaedic surgery. Section 1.2 starts with a generalised discussion about the use of closed IMN for femoral shaft fracture treatment, followed by a succinct description of the need of distal locking during IMN. Section 1.3 introduces the limitations associated with current techniques used for distal locking. Section 1.4 begins with brief description about the Robotic-Assisted Orthopaedic Surgery System that has

been developed at Loughborough University to assist orthopaedic surgeons. Towards the end of section 1.4 limitations of the existing system are discussed. In the light of these limitations, the objectives of this thesis are described in Section 1.5. This is followed by a description of the proposed approach in Section 1.6.

1.1 Orthopaedic Surgery

The term orthopaedic was first introduced by N. Andry in 1741. It comes from two Greek words: "*ortho*" meaning straight, upright or free from deformity and "*paedia*" meaning children [8]. His proposal was that prevention of deformity in adults lies in the development of straight children [9]. Therefore, initially, orthopaedic surgeons only dealt with bone deformities in children; they used braces to straighten the child's bones. However, with the introduction of anaesthesia and an understanding of the importance of aseptic techniques in surgery, orthopaedic surgeons extended their role to include surgery involving bones and their related nerves and connective tissue. According to the American Academy of Orthopaedic Surgery (AAOS), *Orthopaedic surgery* is "a medical specialty concerned with diagnosis, care, treatment, rehabilitation, and prevention of injuries and diseases of the body's musculoskeletal system, i.e. the complex system that includes: bones, joints, ligaments, tendons, muscles and nerves". A large proportion of an orthopaedic surgeon's workload is related to the treatment of fractures of bony structures or tissue directly connected to bones.

A *fracture* is a complete or incomplete break in a bone resulting from the application of excessive force. The Orthopaedic treatment of bone fractures initially involves a *reduction* stage, in order to restore the bone fragments to their normal anatomical position. Then *stabilisation* of the reduced fracture site is carried out; this involves the insertion of mechanical fixation devices, for example use of the intramedullary nail for femoral shaft fracture treatment (shown in Figure 1-2) to prevent occurrence of any misalignment while the natural *bone healing* process takes place.

1.2 Introduction to the problem

Treatment of femoral shaft fractures has undergone significant evolution over the past century. In the past, the definitive method for treating femoral shaft fractures was *traction* or *splinting* that involved the insertion of a metal wire or pin through the bone, so as to exert a continuous pull in the long axis of the bone for the reduction of a fracture. Prior to the evolution of modern fracture treatment and techniques these injuries were often disabling or fatal. However, *traction* or *splinting* as a treatment option has many drawbacks, including poor control of the length and alignment of the fractured bone, development of pulmonary insufficiency, and joint stiffness due to supine positioning (i.e. lying on the back).

Intramedullary nailing of femoral shaft fractures was first introduced by H.Groves in 1918. Initially, it involved the use of unlocked thin, flexible rods, which were introduced through the fracture site. However, the introduction of image intensifiers in the operating room has enabled surgeons to perform both the reduction and stabilisation procedures without opening the fracture site (i.e. closed surgery). In 1940, G. Kuntscher [10] introduced the antegrade IMN technique, in which the nail is inserted into the bone from the proximal end in order to avoid the complications of opening the fracture site, thereby reducing further damage to the traumatized area. This resulted in low blood loss, low infection risk, and short hospitalisation time. Since then, reamed or unreamed closed nailing has become the standard treatment for femoral shaft fractures [11], as this method extends the use of IMN to severely comminuted, oblique, and spiral fractures as well as to fractures complicated by loss of bone. During conventional closed IMN, the locking of the nail is achieved by inserting screws at the proximal end of the nail. Although the conventional closed IMN provides adequate stabilization of mid-shaft fractures, problems can be encountered when the technique is applied to more distal shaft fractures. Therefore, in order to overcome such problems and hence to extend the scope of IMN, the concept of *distal locking* was introduced. Distal locking, as shown in Figure 1-2 involves rigidly attaching the nail to bone fragments at the distal end of the femoral shaft, in order to provide more effective fixation i.e. rotational and axial stability. During the distal locking of an intramedullary nail, surgeons typically drill the distal locking

holes freehand, using fluoroscopic views of the distal part of the femur to aid in the positioning of the drill bit. The limitations of this technique are discussed below.

Although nowadays 3-D imaging modalities, such as computerised tomography (CT) or magnetic resonance imaging (MRI), are available they are usually used in pre-operation stages to provide static information on the anatomic or pathological structure of the patients. Their intraoperative use is not feasible due to their high cost, time consumption, and excessive radiation exposure. Therefore, the use of 2D X-ray imaging still remains the main choice to perform the distal locking procedure during femoral shaft fracture treatment.

1.3 Limitations of the current techniques used for distal locking

A number of problems are faced by orthopaedic surgeons during distal locking of an intramedullary nail, the most serious being:

1. During the surgery, X-rays must be used in pulse-continuous mode so that the C-arm can be precisely aligned with the intramedullary nail axis for an optimal view (i.e. the distal locking nail holes appear as circles rather than ellipses, as shown in Figure 1-3), commonly known as the perfect circle approach. Details on the perfect circle approach are given in Section 3.3.

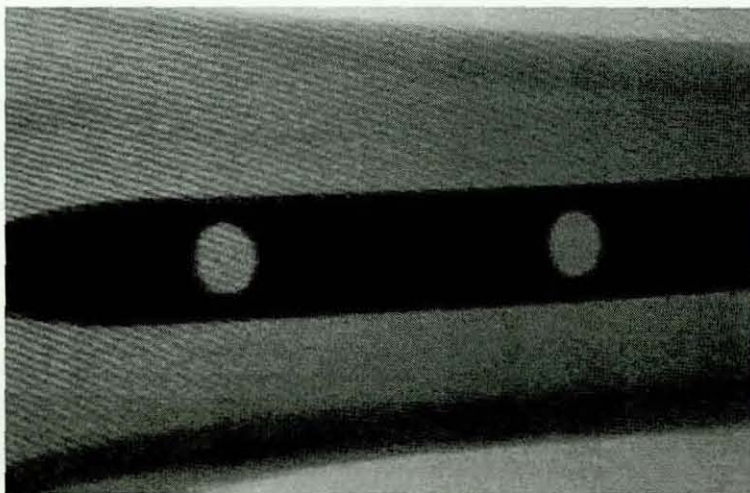


Figure 1-3 Perfect circle approach

2. The use of two-dimensional X-ray images to guide three-dimensional bone drilling procedures means that a large number of X-ray images are required. The surgeon has to mentally correlate the surgical tool and desired drilling trajectory without direct visual feedback [12]. Hence sets of X-ray images must be frequently acquired to ascertain each new position of the surgical tool resulting in an increased radiation exposure to both surgeons and patients, which can prove hazardous, particularly to surgeons who perform this operation on a regular basis [13].
3. The nail deforms by several millimetres during passage through the medullary canal to conform to the bone canal shape [14]. Without compensation for nail deformation, it is impossible to place the distal locking screws correctly using an external guide attached to the proximal end of the nail, as is used for proximal locking screws.

In summary, the current techniques employed for distal locking are limited by the amount of radiation exposure due to the large number of X-ray images required during each step, as well as variability of results that largely depend upon the surgeon's skills and experience. These difficulties make the insertion of the distal locking screws the most demanding step of the closed IMN operation [14]. Distal locking of intramedullary nails therefore remains a surgical challenge. Since the long term effects of X-ray radiations and their relation to different types of cancer still remain unknown [15-17], there is a need to develop surgical techniques that can limit the use of fluoroscopy (X-rays) during distal locking.

1.4 The Loughborough University Robotic-Assisted Orthopaedic Surgery System (LOAS)

The Loughborough Orthopaedic Assistant System (LOAS) uses a calibration frame, shown in Figure 1-4, and a C-arm X-ray unit. The calibration frame contains two Lateral and two AP (Anterior-Posterior) calibration plates, with each plate containing an array of embedded fiducial markers (stainless steel balls).

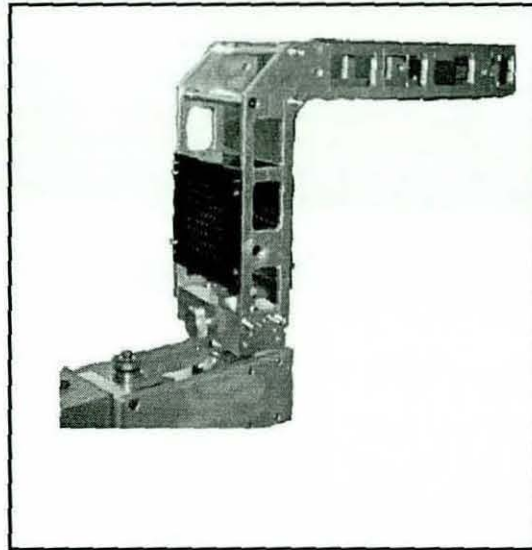


Figure 1-4 Calibration frame

The system simplifies the current approach as the drilling trajectory of the distal locking holes is computed from two near orthogonal intraoperative X-ray images thus reducing the irradiation (i.e. exposure to radiation) to both surgeon and patient significantly. Intraoperative X-ray images (i.e. Lateral and AP) are taken with the calibration frame in position around the body part of interest as shown in Figure 1-5 and Figure 1-6 respectively.

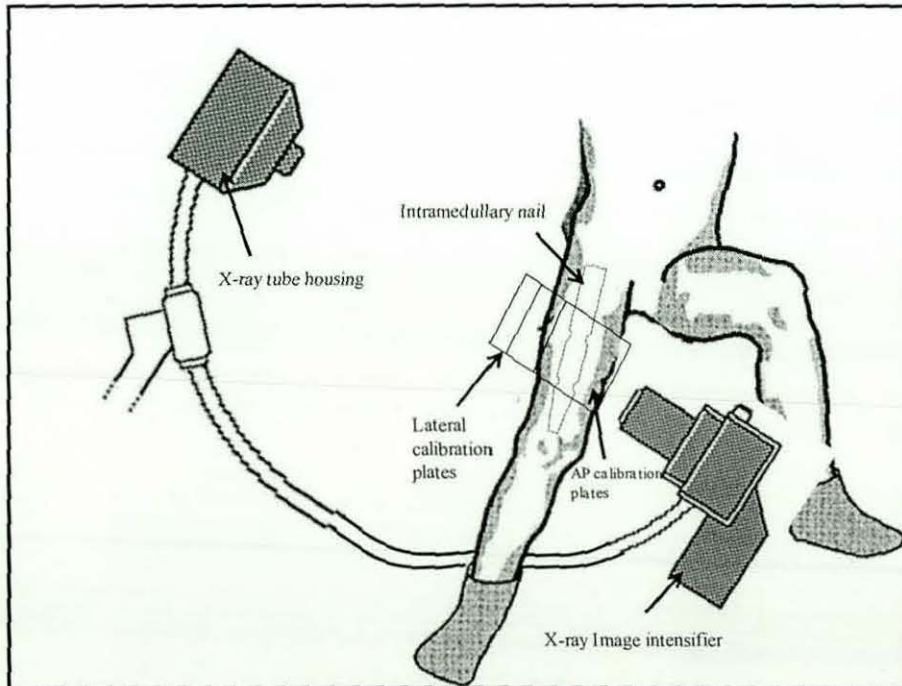


Figure 1-5 Lateral view image acquisition during distal locking

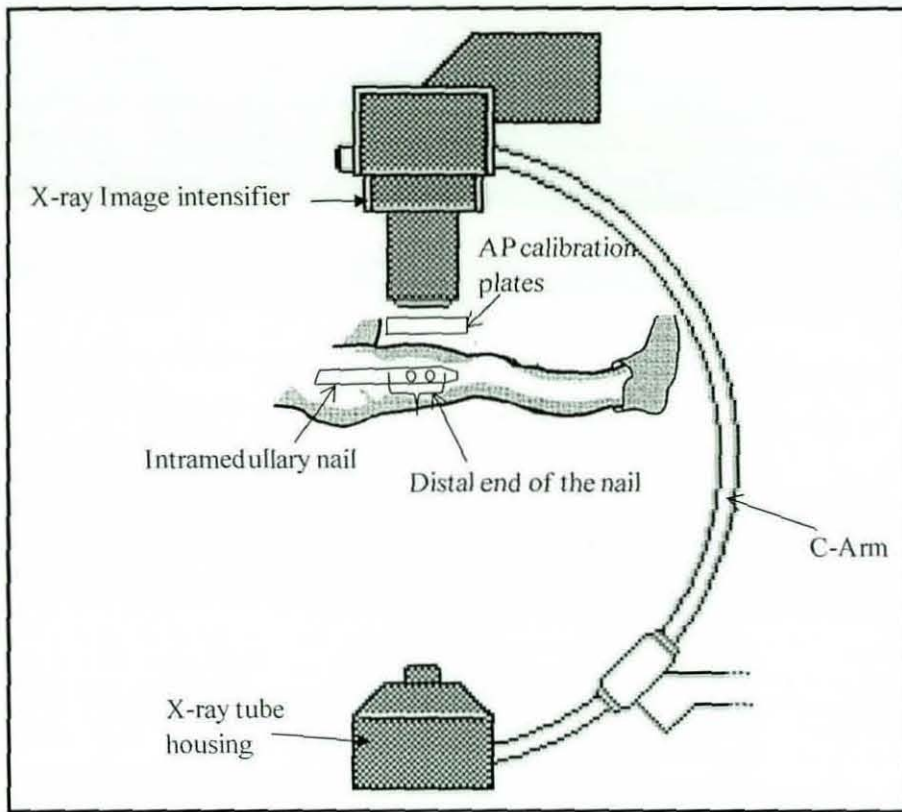


Figure 1-6 AP view image acquisition during distal locking

The radiopaque reference markers (inserted in the radiolucent plates of the calibration frame) which are visible on each X-ray view (as shown in Figure 1-7) and image points of interest are used to establish the drilling trajectory with respect to the calibration frame co-ordinate system.

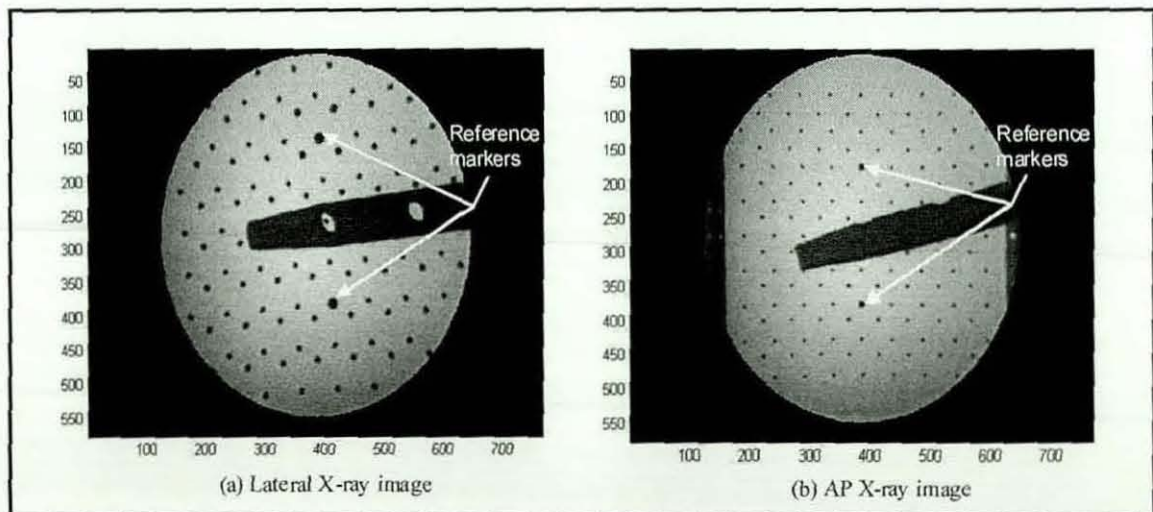


Figure 1-7 Typical Lateral and AP X-ray images.

The existing system has some limitations, which are discussed below.

A potential problem with the existing system is the appearance of one or more of the opaque markers (embedded in the calibration frame plates) within or on the edge of the oval-shaped distal hole projection as shown in Figure 1-8. This phenomenon can cause error in determining the centre and the major axis of the distal locking hole, since these features are required to determine the drilling trajectory of the distal locking holes, therefore occurrence of such phenomenon can induce error in drilling trajectory calculation.

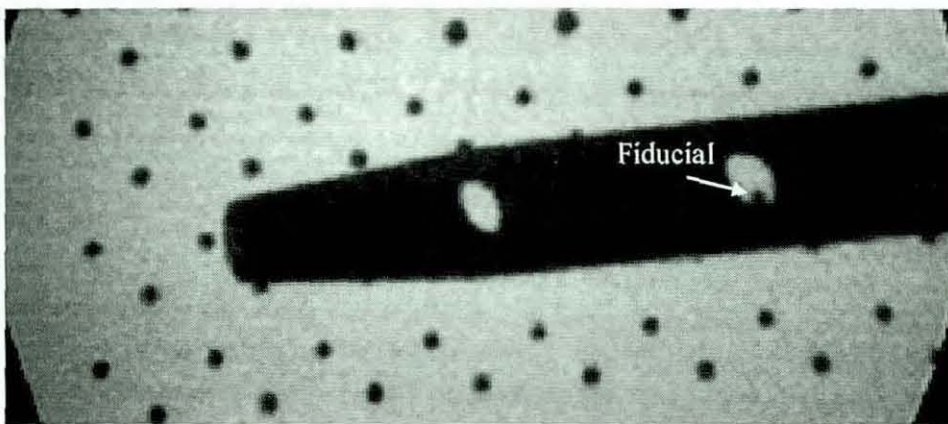


Figure 1-8 Presence of fiducial at the edge of the oval

Furthermore, the system employs reference markers (large diameter ball bearings), shown in Figure 1-7, to accomplish unique identification of each marker visible in field of view. This implies that calibration frame should be positioned around the body part of interest such that these reference markers should always be visible in the field of view as shown in Figure 1-7. The existing calibration frame is therefore not suitable for use across wide range of patient physiologies. Also, the system requires the surgeon (or user) to manually select some features i.e. reference markers, shown in Figure 1-7, and nail edges on both the Lateral and AP images, and oval shaped distal hole projection in the Lateral view image. The accuracy of the system is therefore largely dependent upon the input from the surgeon (or user).

1.5 Aim of the research

Speed, accuracy, robustness, reliability, and repeatability are of paramount importance when introducing any new technology into the operating theatre. The aim of this study is therefore to review the existing system to develop a robust computer assisted orthopaedic system (CAOS) that will assist orthopaedic surgeons in performing distal locking during closed IMN, and hence will:

- Improve the outcome of the distal locking procedure by ensuring that the drill bit and the distal hole axes are in alignment during drilling, thereby reducing the occurrence of screw misplacement.
- Make outcome of the procedure more consistent irrespective of variations in the skill levels and experience of the clinical staff.
- Reduce surgical time.
- Be adaptable for different patient physiology.

1.6 Proposed approach

During closed IMN, direct access to the patient's skeleton is limited to the extent of the surgical incision; therefore the patient's location with respect to the robotic manipulator must be determined indirectly using X-ray images. This registration or calibration process requires the extraction of 3-D measurements from 2-D X-ray images and, therefore, falls within the scope of a field of research known as *X-ray Photogrammetry*.

Unlike the majority of X-ray photogrammetry research, the current study involves an intraoperative application i.e. distal locking of an intramedullary nail during femoral shaft fracture treatment. 3-D measurements must therefore be performed in the operating theatre at the time of surgery. In addition to the need for complying with surgical sterility it is essential that the 3-D measurement process does not delay the surgical procedure. As a result, the use of machine vision, i.e. digital image

processing techniques has been proposed as a means of providing the drilling trajectory of the distal locking holes intraoperatively.

Digital image processing allows the use of complex algorithms for image processing, and hence can offer more sophisticated performance at simple tasks and the implementation of methods which would be impossible by analogue means. These applications operate on data to be presented visually or to extract image features for several tasks such as object detection, tracking, and classification.

In orthopaedics, increasing demands on a patient's early mobilisation combined with early weight bearing capability have made digital image processing one of the key technologies of modern orthopaedic surgical procedures. The use of digital image processing methods results in [18]:

- Better precision and repeatability,
- Process automation, as surgical procedures benefit from the reliability provided by automatic processing, such as vision guided surgery,
- Accurate prediction of the surgical tool due to the ability of providing improved medical treatment.

In this study, after capturing two nearly orthogonal intraoperative X-ray images using a standard C-arm, processing of images is done using X-ray photogrammetry techniques in the Matlab Image Processing environment. The results from image analysis are then used in conjunction with off-line CAD modelling of the intramedullary nails to determine the drilling trajectory of the distal locking hole.

1.7 Summary

At present IMN is the standard surgical procedure to treat femoral shaft fractures. The concept of distal locking during IMN has been introduced to provide more effective fixation. Conventional techniques use fluoroscopy for screw placement in distal locking. However, the accurate placement of the distal interlocking screws is the most difficult part of the procedure due to the deformation of the nail during its insertion

into the medullary canal and the use of 2-D X-rays images during drilling. The locking thus can be time consuming and involve a significant amount of irradiation to the patient and the operating staff. A Robotic-Assisted Orthopaedic Surgery System named LOAS has been developed at Loughborough University to assist orthopaedic surgeons during distal locking, however it has some limitations. The aim of this study is therefore to review the existing system and address these limitations to develop a robust system. In order to achieve this aim, a novel approach based on the use of a calibration frame in conjunction with offline modelling of the nail and an automated X-ray based machine vision system is proposed. To implement this approach, Matlab's digital image processing toolbox and AutoCAD Mechanical Desktop have been used for image analysis and intramedullary nail modelling respectively. In the following chapter, a detailed insight into the background for this research is given by describing the use of closed intramedullary nailing (IMN) for femoral shaft fracture treatment, its history and advantages.

2 Femoral shaft fracture treatment

The femur (thigh bone) is a structure for standing and walking. It is tubular, containing a cavity i.e. the medullary canal which is filled with marrow. The wall or cortex of the tube consists of the cortical or lamellar bone, while the closed ends of the tube are built of the trabecular or cancellous bone. The femur is subject to many forces during walking, including axial loading, bending, and torsional forces. In fact, the femur is the largest and most dense bones in the body which requires a great amount of force to overcome its mechanical strength and cause breakage or fracture. Accidents that may cause a femur fracture usually involve falling from a height, high-speed collisions etc. In elderly people *Osteoporosis*, a disease of bone in which the amount of bone is decreased and the strength of trabecular bone is reduced, cortical bone becomes thin, dramatically increasing the risk of femoral fracture [19]. **APPENDIX A** provides an overview of the anatomy of the femur and associated orthopaedic terminologies.

2.1 Femoral Fractures

A fracture is a break in the structural continuity of a bone. It may be no more than a crack, a crumpling or a splintering of the cortex; more often the break is complete and the bone fragments are displaced. If the overlying skin remains intact it is a closed or simple fracture; if the skin or one of the body cavities is breached, then it is termed as an open or compound fracture, liable to contamination and infection [20]. This injury is most common among persons younger than 25 years and those older than 65 years [21]. Details about different types of femoral shaft fractures and their associated complications are given in **APPENDIX B**.

The successful treatment of bone fractures initially requires the restoration of the broken bone fragments to their normal anatomical positions and alignment. This process is referred to as *reduction* of the fracture, and involves either a manipulative or a surgical procedure. Nowadays closed reduction is preferred to open reduction

[22, 23] in order to avoid disturbing the fracture haematoma, to lower the risk of infection and to incur less interference with the process of fracture union. For example, in the case of a fractured femur in which both fractured ends of the bone lie beside one another, after the muscles have relaxed, these parts of the bone must be pulled away from one another and held stationary before being precisely positioned end to end to allow internal fixation. There is always the danger of physical overshoot, resulting in unnecessary muscle, tissue, and ligament strain during the manipulation process; therefore, successful closed reduction is one of the demanding steps during fracture treatment. A *stabilisation* technique is then applied, in order to ensure that the bone fragments maintain this anatomically correct position throughout the natural *bone healing* process. The continuity of the bone is then restored by the formation and progressive hardening of a callus at the fracture site [3].

In the case of femoral shaft fractures, poor reduction/stabilisation of the fracture site can lead to serious complications because, when the femoral shaft is fractured, the muscles attached to the bone fragments contract, resulting in shortening of the leg. In order to prevent prolonged disability it is, therefore, essential that normal limb length is restored. Misalignment of the bone fragments, which can alter the biomechanics of the hip and knee joints, must also be avoided in order to prevent joint disorders such as *osteoarthritis* (a form of arthritis, occurring mainly in older persons, that is characterized by chronic degeneration of the cartilage of the joints) developing.

Since the thigh is so heavily padded with muscle, an external plaster cast can not provide the required level of stabilization. Therefore, treatment of femoral shaft fractures is limited to: skeletal traction, cast bracing, external fixation and internal fixation, with the final decision being made on the grounds of fracture (type and location, degree of comminution, open or closed, etc) and patient's age, general health, severity of any additional injuries, etc [9, 24].

Since, treatments of diaphyseal fractures using techniques that require prolong immobilization of the extremity results in limitation of joint motion, and malunion or non-union may occur. Therefore, at present, intramedullary nailing is the preferred choice of treatment for femoral shaft fractures [25-27], as it offers better control of the limb length and the rotational alignment, as well as early mobilization and short

hospitalization time. Hence, this study is concerned with intramedullary nailing of femoral shaft fractures, which is an internal fixation technique; therefore details of only internal fixation are discussed here. However, details of other techniques mentioned above are given in **APPENDIX C**.

2.1.1 Internal fixation

Internal fixation is a surgical procedure that stabilizes and joins the ends of fractured bones by mechanical devices such as metal plates, pins, rods, wires or screws. It enables a reduced fracture to be held securely so that activity (although not weight bearing) can begin immediately. The internal fixation devices are inserted surgically to ensure the bones remain in an optimal position during and after the healing process. It is particularly useful for fractures in elderly patients, those with multiple injuries or who are difficult to nurse.

In the context of femoral shaft fracture, the most effective form of internal fixation device is an intramedullary nail. One of the significant advantages of intramedullary nailing over other methods of internal fixation is that an intramedullary nail shares the load with the bone by being closer to the weight bearing axis (i.e. femoral shaft axis) rather than entirely supporting the bone, as some force or stress within the callus is essential to the healing process. Because of this, patients are able to walk soon after the surgical operation and as such better (stronger) bone healing results.

2.2 Intramedullary nailing (IMN)

IMN was originally performed using thin, flexible rods, which were introduced through the fracture site. However, the initial unlocked design was modified to allow proximal and distal locking [2, 28-30] as shown in Figure 2-1, thereby eliminating the problems of angulation, rotation and leg shortening.

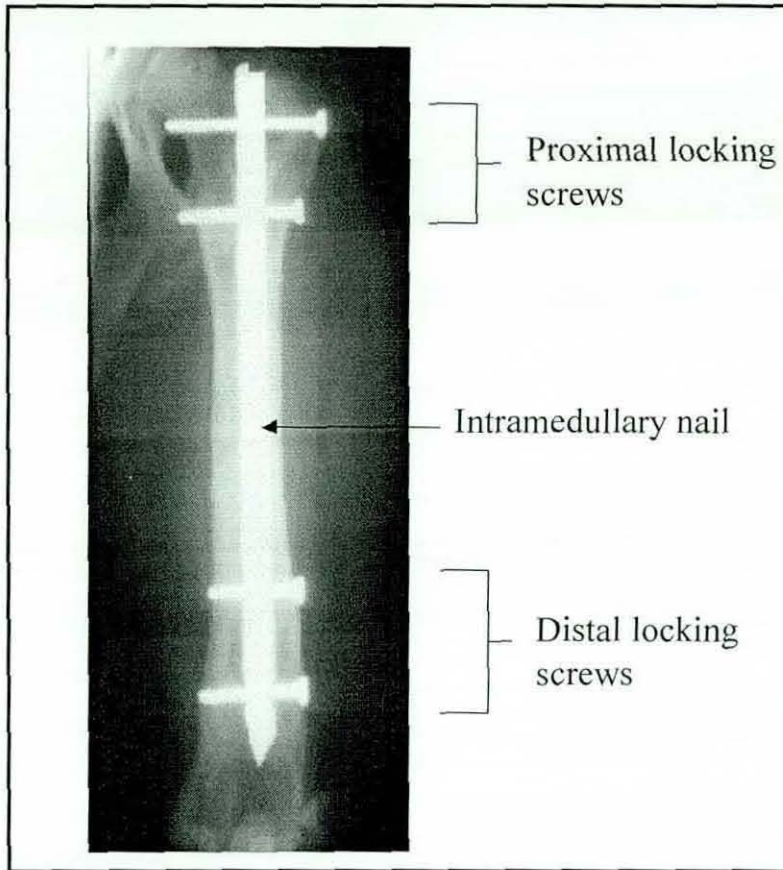


Figure 2-1 Intramedullary nailing treatment of a femoral shaft fracture.

Enthusiasm for minimally invasive surgery has led to an ever-increasing number of procedures being done percutaneously (i.e. done through the skin). The concept behind closed fracture surgery is to perform internal fixation of the fracture without surgically opening the fracture site of the femur, thereby avoiding additional damage to the already traumatized area. Less soft-tissue trauma, lower infection rates, minimal blood loss, smaller incisions and reduced morbidity are some of the advantages of these procedures. However, it should be noted that occasionally if reduction and reaming cannot be accomplished by closed means then open nailing is performed. It involves reaming of the distal and proximal fragments of the medullary canal through fracture site to determine the nail diameter. Once the proximal and distal medullary canal fragments are reamed to a satisfactory diameter, a cork borer or similar centering device is placed in the proximal fragment of the medullary canal, and a guide pin is then introduced through it. Guide pin is then drilled proximally through the upper end of the femur until it emerges just proximal to the greater trochanter. Without exposing the trochanter a small incision is made over the protruding point of

the guide pin, allowing it to emerge. A reamer is then placed over the guide pin to drill hole in correct alignment with medullary canal. Intramedullary nail is then inserted into the proximal medullary canal over the guide pin. When the nail reaches the fracture site, guide pin is removed and fracture is reduced under direct vision. Nail is then driven into the distal fragment of the medullary canal while holding firm pressure against the flexed knee to maintain reduction and prevent distraction at the fracture site. Before closing of the wound, placement of the intramedullary nail in the distal end of the femur is checked using Lateral and AP fluoroscopic views. During open nailing no interlocking is carried out, therefore if the nail is too tight or loose it must be withdrawn and replaced with a nail which conforms to medullary canal size [22]. In addition to above mentioned disadvantages of open surgery, open nailing also results in decreased rate of union in comparison to closed nailing because fracture haematoma which is important in fracture healing is removed. Generally, use of open nailing has therefore been abandoned in favour of closed nailing [22, 28, 31].

Closed IMN has shown its efficacy in the treatment of diaphyseal (i.e. shaft of a long bone) fractures of long bones especially of the complex fractures of the femur. It has been reported by S.T. Canale in [22] that, for femoral shaft fracture treatment, incidence of infection with closed nailing is less than 1% in comparison to 10% with open nailing. The closed IMN operation is guided by fluoroscopy for fracture reduction, proximal locking and distal locking. There are two types of closed IMN procedures, namely:

- Closed antegrade intramedullary nailing, and
- Closed retrograde intramedullary nailing.

2.2.1 Closed Antegrade Intramedullary Nailing

Closed antegrade nailing involves passing the intramedullary nail from proximal to distal end of the femur as shown in Figure 2-1. It has a high rate of fracture union (99%), and low rate of infection, malunion (less than 1%) and shortening. Therefore, it is currently the treatment of choice for femoral shaft fractures [2, 28, 32-36]. The following overview of preoperative planning and patient positioning for antegrade IMN is based on information provided by [22, 34, 37].

2.2.1.1 Preoperative Planning

The choice of the appropriate length of the nail is very important because the leg is shortened by the tension of the muscles. Assuming that only one of the femurs is fractured, preoperative radiographs of the uninjured leg must be taken to estimate the dimensions of the nail (length, diameter) and the expected amount of reaming [22, 34]. To determine the approximate length of the intramedullary nail before the surgery, the distance from the tip of the *greater trochanter* to the *patellar surface* of the knee (shown in Figure 2-2) on the patient's uninjured side is measured, and subtracted by 20-30mm. Intramedullary nails of the resultant length and the next longer and shorter lengths are selected before the operation, as only after reduction direct measurement is possible [37].

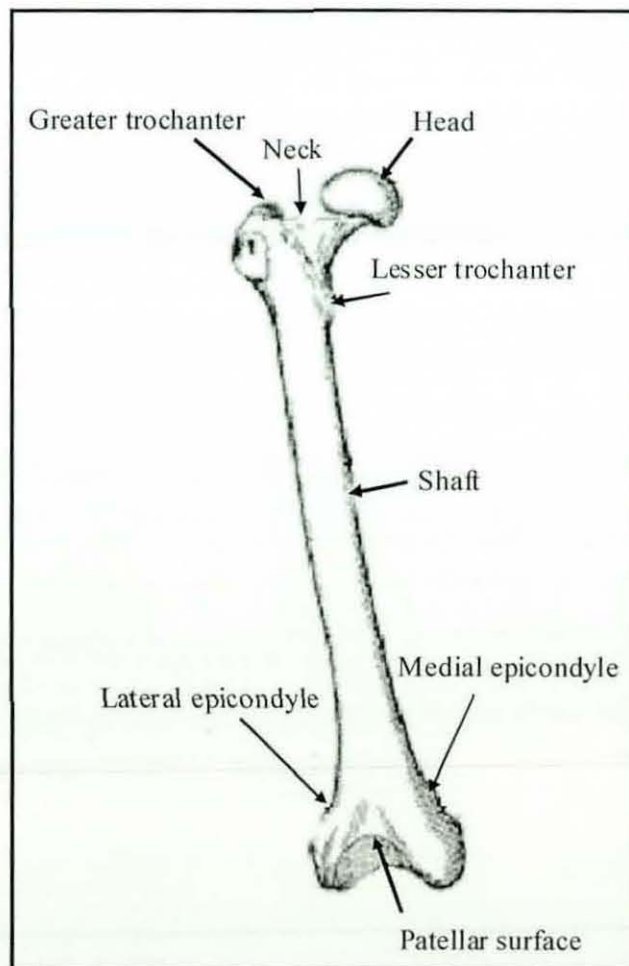


Figure 2-2 Femur anatomy (Anterior view) [1]

2.2.1.2 Patient positioning and preparation

In line with most closed *osteosynthesis* procedures (i.e. the process of mechanically bringing the ends of a fractured bone close together using a metal plate), intramedullary nailing is heavily reliant upon intraoperative fluoroscopy. As a result, the patient must be positioned on the operating table in a “C-arm compatible” pose. In other words, the operating table and the patient’s uninjured limb must not obstruct the movement of the mobile C-arm unit, and must not appear within the field-of-view when fluoroscopic images in Anterior-Posterior (AP) and Lateral views of the fractured femur are acquired. The need to apply skeletal traction intraoperatively, to allow reduction of the fracture, also creates problems in relation to patient positioning when using a conventional operating table. Ideally, an orthopaedic fracture table should therefore be used during closed IMN procedures. These modified operating tables incorporate adjustable extensions for securing the patient’s legs, and a padded perineal post to prevent movement of the pelvis/hip joint when traction is applied. The bottom one-third of the table is also significantly shortened to allow direct fluoroscopic visualisation of the fracture site. The nailing procedure can actually be performed with the patient in either the *lateral decubitus* (shown in Figure 2-3) or the *supine* position (shown in Figure 2-4) on the fracture table.

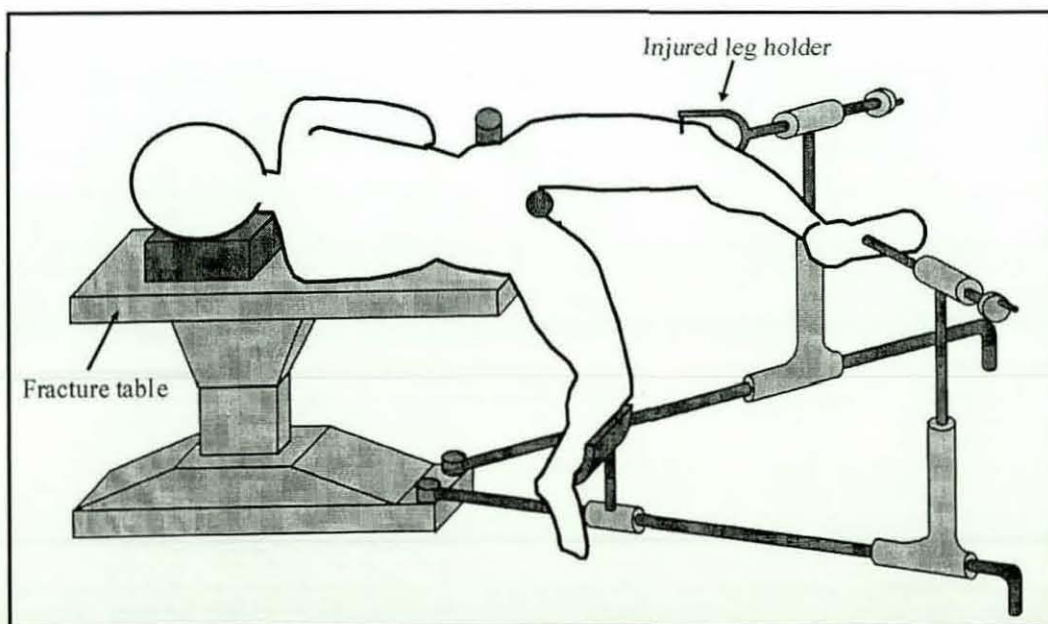


Figure 2-3 Lateral decubitus position [37]

As depicted in Figure 2-3, the *lateral decubitus* position involves laying the patient on their uninjured side, thereby affording easy access to the greater trochanter of the fractured femur (i.e. the nail's insertion point). In practice, obtaining this position can be difficult, and special table attachments may be required to safely support the patient's weight. By contrast, the supine position depicted in Figure 2-4 simply involves laying the patient on their back, and is therefore more suitable for patients with multiple injuries. However, the supine position offers limited access to the trochanter of the fractured femur, making insertion of the intramedullary nail more difficult.

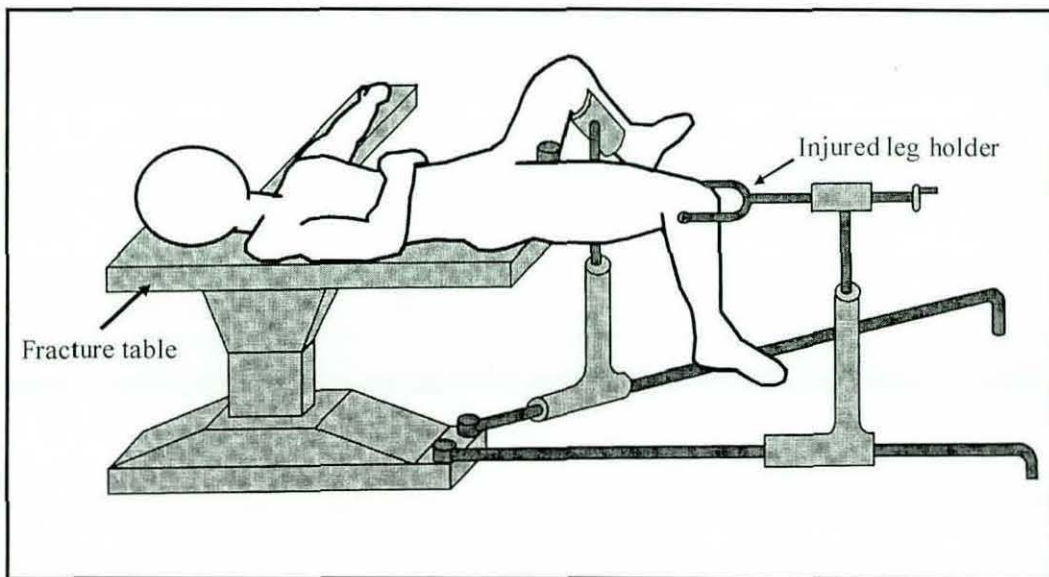


Figure 2-4 Supine position [37]

Once the patient is in position, skeletal traction is applied via a femoral pin, and a closed reduction of the fracture is attempted. This fluoroscopically monitored process involves the manual application of localised pressure to both sides of the fracture site.

2.2.1.3 Intraoperative Procedure

In antegrade nailing the surgeon initially makes an incision as shown in Figure 2-5.

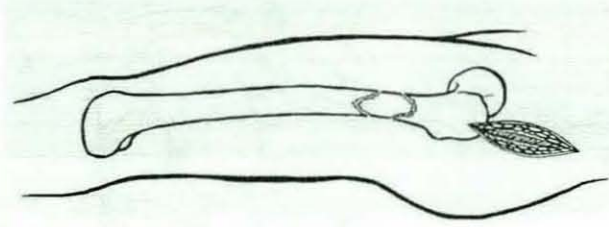


Figure 2-5 Skin incision at greater trochanter [22]

The surgeon then determines the entry point to pass the intramedullary nail. A widely recommended entry point for antegrade nailing is the piriform fossa, which as shown in Figure 2-6 (a) is perfectly in line with the medullary canal so that a straight nail can be inserted. However, sometimes, access to the piriform fossa is technically demanding and can result in rarely reported complications such as fracture of the femoral neck, avascular necrosis (AVN) marked by severe pain in the affected region and by weakened bone that may flatten and collapse called also osteonecrosis of the femoral head and septic arthritis from intra-articular penetration [38]. Therefore, in situations where access to the piriform fossa is difficult, tip of greater trochanter, shown in Figure 2-5(b) is used as entry point. The tip of the greater trochanter, however is lateral to the central axis of the medullary canal, and the nail insertion therefore must be performed at an angle of approximately 6° to enter the canal, as shown in Figure 2-6 (b). Therefore, an intramedullary nail with a proximal bend, as shown in Figure 2-6(b), is used when the trochanter tip is chosen as entry point.

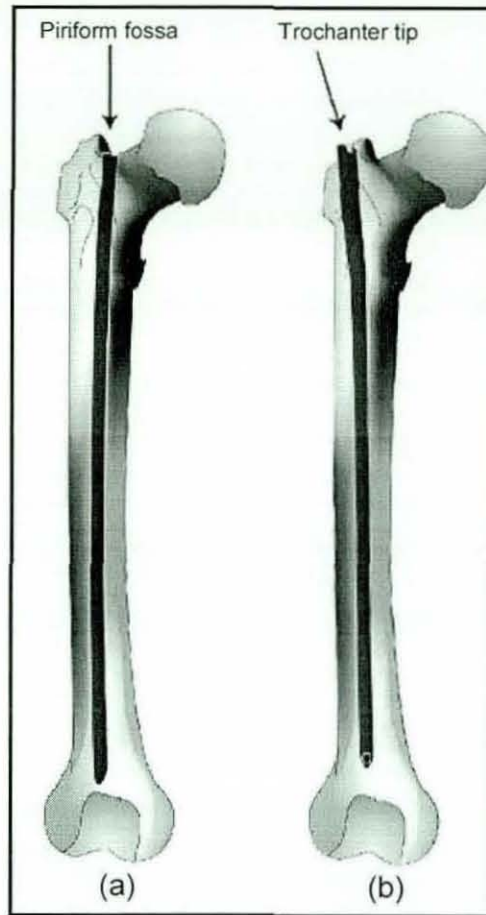


Figure 2-6 (a) Intramedullary nail inserted using the piriform fossa (b) Intramedullary nail inserted using the trochanteric tip [38]

A threaded guide pin is inserted at the trochanteric fossa. X-ray images from both Lateral and AP fluoroscopic views are then analysed to ensure that the guide pin is in the centre of the femur as shown in Figure 2-7.

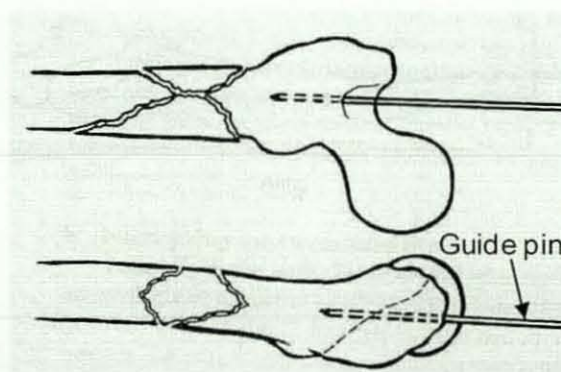


Figure 2-7 Insertion of threaded guide pin at trochanteric fossa to determine entry point [22]

The surgeon then reams the canal to enlarge the entry portal. A guide rod (usually of 3.2mm) is then introduced by means of the guide rod holder to the level of fracture as shown in Figure 2-8.

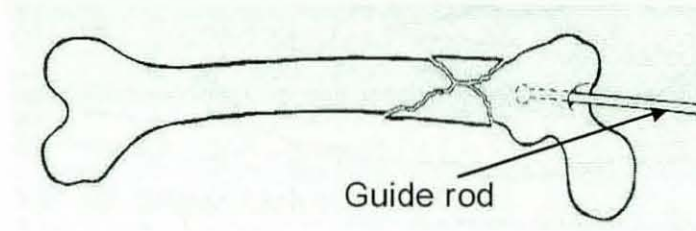


Figure 2-8 Introduction of guide rod to the level of fracture [22]

The surgeon reduces the fracture by manipulating the proximal and distal bone fragments and by using an internal fracture alignment device as shown in Figure 2-9.

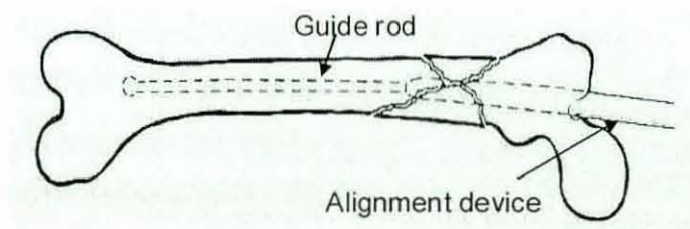


Figure 2-9 Use of internal fracture alignment device [22]

The guide rod is then advanced until it reaches the epiphyseal scar as shown in Figure 2-9. The exact nail length can be determined by using either the guide rod or a nail length gauge as described below:

Guide rod method

A second guide rod is overlapped on the reduction guide rod extending proximally from the femoral entry point. Subtracting the length (say XX mm, as shown in Figure 2-10) of the overlapped guide rod from its overall length yields the nail length.

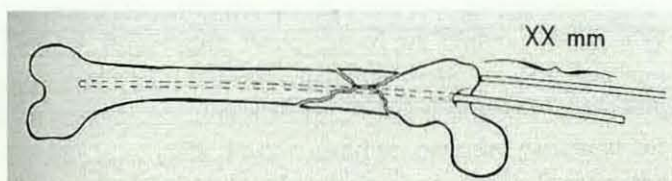


Figure 2-10 Determination of the nail length using guide rod [22]

Nail length gauge method

The nail gauge is positioned anterior to the femur (unaffected femur preoperatively, affected femur intraoperatively) with its distal end between the proximal pole of the patella and distal femoral physal scar as shown in Figure 2-11.

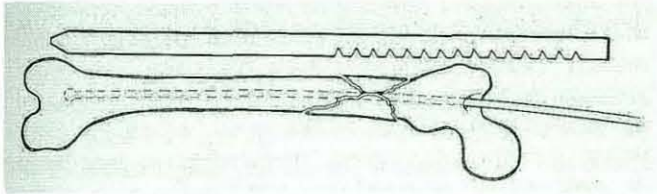


Figure 2-11 Determination of nail length using nail gauge [22]

The C-arm is then moved to the proximal end of the femur and an AP image is taken, the nail length can be read from the stamped measurements on the nail gauge. For reamed insertion, the entire femur is then reamed over the guide rod in 0.5mm increments until the desired diameter is achieved as shown in Figure 2-12. It is essential to ream 1mm over the selected nail diameter. Generally, the proximal 4 to 6cm of the femur is always reamed up to 3mm more than the diameter of the nail being used to permit easy insertion of the nail.

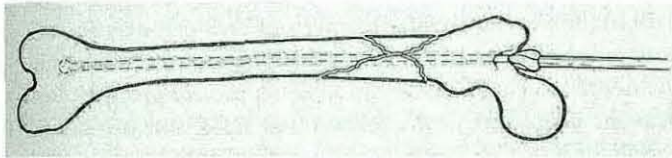


Figure 2-12 Reaming of femoral canal over guide rod [22]

The nail is then inserted over the guide rod before the guide rod is removed. In most cases, the surgeon also inserts lateral proximal and distal locking screws to prevent fragment rotation and bone shortening. The procedure is performed under X-ray fluoroscopy. Figure 2-13 shows fluoroscopic images showing the different steps in closed intramedullary nailing.

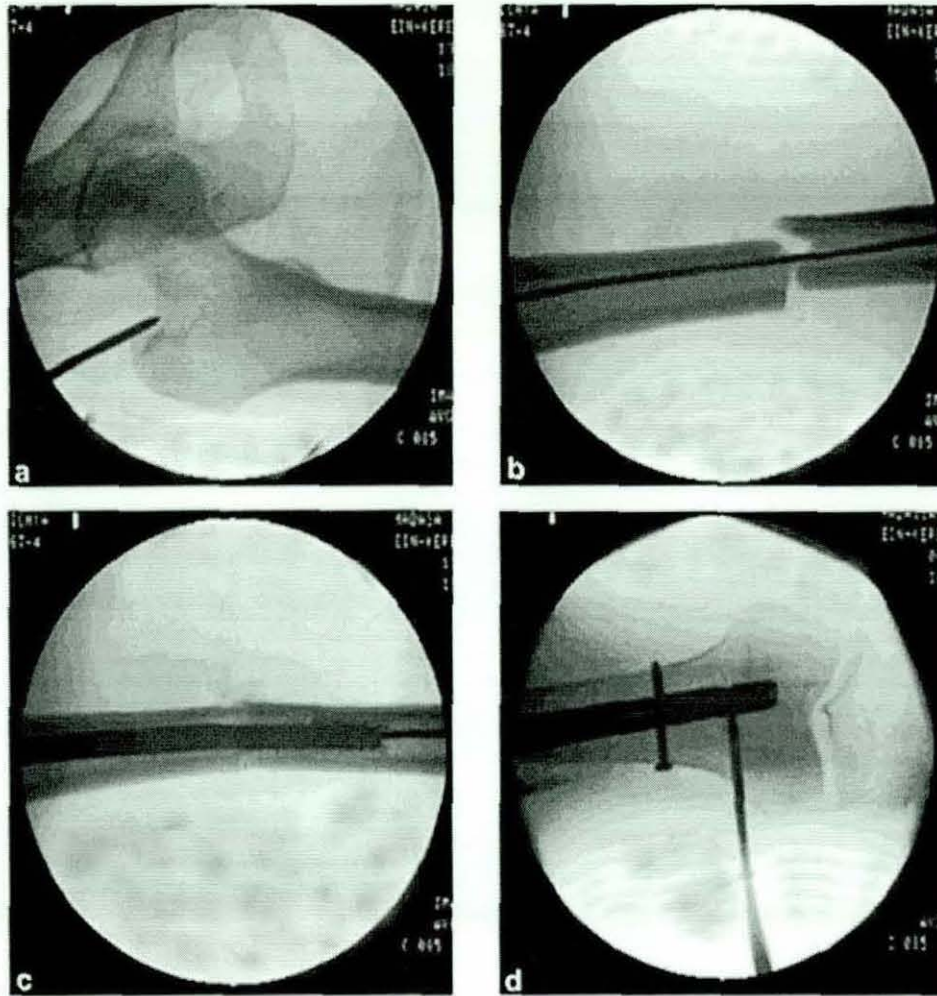


Figure 2-13 Fluoroscopic images showing the steps of closed intramedullary nailing (a) Opening of the medullary canal (b) Alignment of bone fragments (c) Insertion of the nail (d) Distal locking [39]

Many fluoroscopic images are necessary, especially during distal locking because the intramedullary nail is concealed within the femur, and the blind drilling of distal screw holes can only be performed under continuous fluoroscopic guidance [5, 39, 40]. Generally distal interlocks should be inserted prior to the proximal interlocks; as this allows the leg to be rotated in the most advantageous position for interlock insertion and allows more efficient compression across the fracture site (by gently tapping the proximal nail assembly proximally). As antegrade IMN is the standard treatment of choice for femoral shaft fracture treatment, this procedure is therefore discussed further in section 2.4.

2.2.1.4 Postoperative procedure

During the first or second postoperative week, the patient is encouraged to start walking with the aid of crutches (i.e. walking without weight-bearing). In the following weeks, a program of physiotherapy exercises is undertaken to strengthen the quadriceps (thigh muscles) and regain the full range of knee joint motions. Following radiographic confirmation of the formation of a satisfactory callus, progressive weight bearing then can begin. Assuming that full weight-bearing is achieved, whenever possible, a second surgical procedure to remove the locking screws and the intramedullary nail, will then be performed during the second postoperative year [37].

2.2.2 Closed Retrograde intramedullary nailing

Closed retrograde nailing involves passing the intramedullary nail from distal to proximal end of the femur with the nail being inserted through the supercondylar notch of the distal femur.

The following overview of patient positioning and intraoperative procedure for retrograde IMN is based on information provided by [22, 41].

2.2.2.1 Preoperative planning and patient positioning

The patient is placed in a supine position on a radiolucent operating table in such a way that allows visualization from the hip joint to the knee. A bolster is placed under the knee to allow knee flexion, as shown in Figure 2-14. This allows easy access to the entry site.



Figure 2-14 Thigh support for retrograde nailing.

2.2.2.2 Intraoperative procedure for retrograde IMN

A percutaneous incision is made in the region between the lower side of the patella (Knee cap) to the upper edge of the tibial tubercle. The anterior cruciate ligament is then exposed by retracting the patellar tendon. A guide pin or K-wire is then placed into the notch and the entry point for retrograde nail insertion is made by centering the guide pin or Kirschner Wire (K- wire) anterior to the intercondylar notch. The K-wire is then advanced manually or with the slotted Hammer approximately 10cm confirming its placement within the center of the distal femur, its position is verified using AP and Lateral X-ray images, as shown in Figure 2-15.

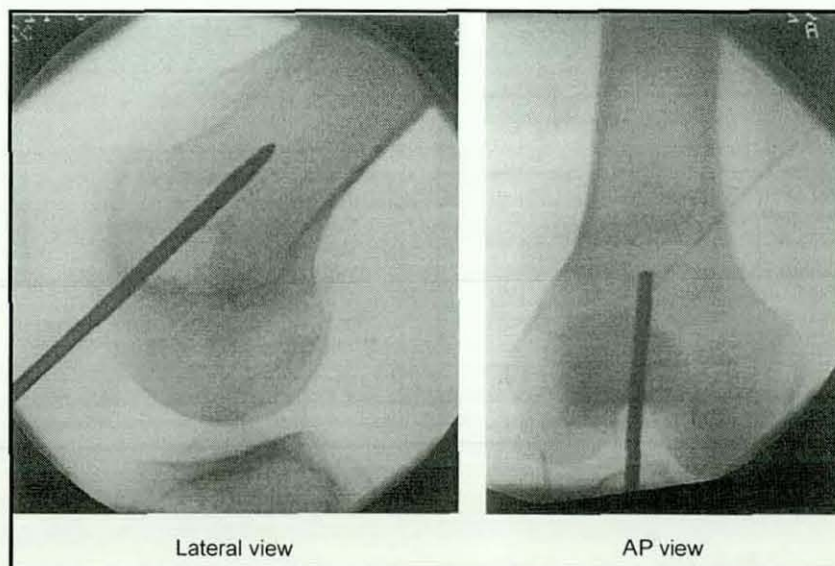


Figure 2-15 Guide pin placement during retrograde nailing [41]

It can be seen from Figure 2-15 that, on the AP view, the pin is placed so that it lies centered in the intercondylar notch and in the centre of the femoral shaft, in order to ensure proper varus-valgus alignment especially in distal one-third femur fractures. The guide pin is then advanced into the medullary canal and a reamer is inserted over the guide pin to open the distal femur to an appropriate size to accept the distal portion of the nail. Both the guide pin and reamer are then removed while irrigating all loose fragments (i.e. cartilaginous and bony debris) from the knee. A radiolucent ruler is then used to estimate the length of the nail required, by measuring the distance from 1cm proximal to the intercondylar notch to the upper side of the lesser trochanter. The diameter of the selected nail should be 1mm smaller than that of the last reamer used. The nail is then placed into the notch and is advanced towards the fracture. The fracture is then reduced, and the nail is driven across the fracture and seated at the level of lesser trochanter. Distal locking is achieved using a target device, for example the femoral target device shown in Figure 2-16 from Stryker® [42].

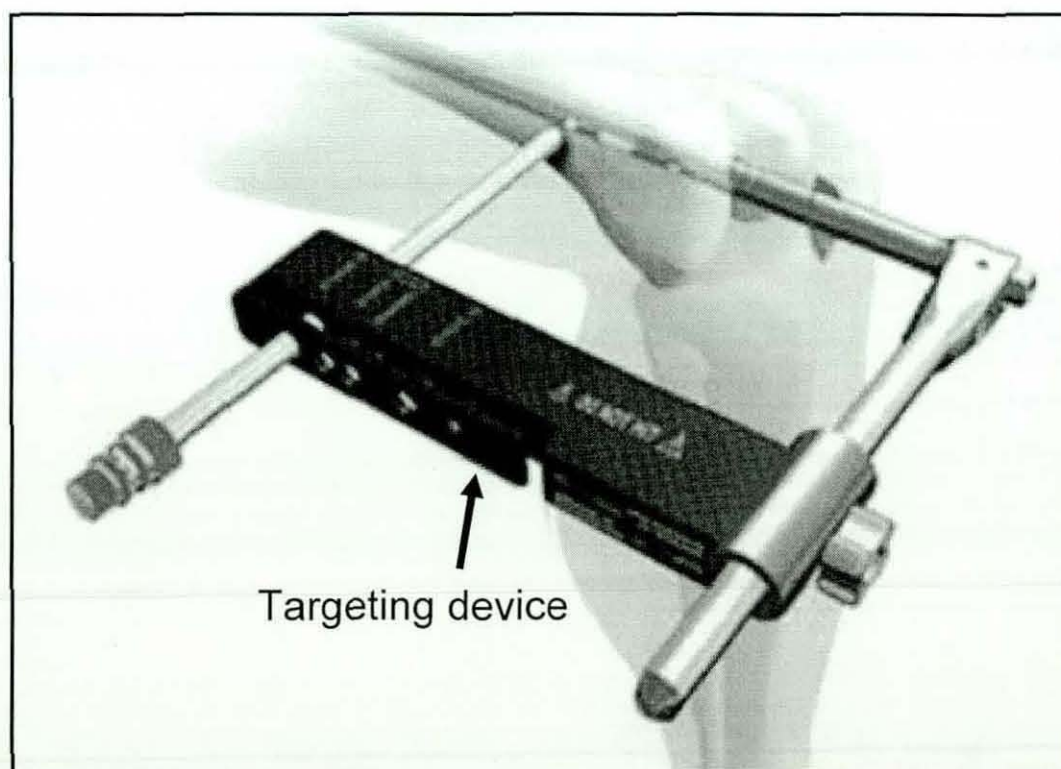


Figure 2-16 Femoral targeting device for distal locking during retrograde nailing [42]

Proximal locking is performed by using the free hand technique, which uses the perfect circle approach discussed in section 3.3. With employment of a reamed, canal sized implant one proximal screw is sufficient. For easier placement of proximal screws, the ipsilateral pelvis is raised by placing a bump under it, so that a true Lateral view X-ray image of the proximal end can be obtained. A 2 to 3 cm incision is made after determining the hole's location radiographically. A hemostat is used to spread through the adipose tissue and quadriceps muscle down to the bone. A drill is inserted with its point centered in the hole. Drilling proceeds through the anterior cortex nail hole and posterior cortex. Screw length is determined by using a depth gauge or by noting the relative size of the nail in the femoral canal in the Lateral view image, for example, if a 10 mm nail takes up about 1/3rd of the femoral shaft diameter than the proper screw length would be about 30 to 32 mm; a screw with the appropriate length is then inserted.

It has been reported by [22, 34, 41, 43-45] that retrograde nailing is preferred over antegrade nailing under the following clinical situations:

- For treating pregnant patients, because the radiation exposure to the fetus is reduced.
- Ipsilateral femoral neck and shaft fracture to allow the use of separate fixation devices for the shaft and the neck fractures,
- Floating knee injuries to allow fixation of both femoral and tibial fractures through the same anterior longitudinal incision,
- Multiple trauma patients to decrease operative time by not using a fracture table, which allows multiple injuries to be treated simultaneously,
- Often, patients with chest tubes, laparotomies with associated intestinal obstruction, and head injuries have physicians and other apparatuses surrounding the proximal parts of the patient. These necessary live saving procedures are absolutely essential, but they can impede antegrade nailing. Therefore, the use of a retrograde nailing allows the orthopaedic surgeon to perform the femoral fixation through a remote area i.e. area around the knee joint.

- Fractures of the distal third of the femoral shaft may be better suited for retrograde nailing, as they have a lower rate of malalignment. Antekeier *et al* [45] conducted a study to determine the safe distance for distal femoral fractures relative to the distal locking screws in antegrade intramedullary femoral nailing. It was reported that an antegrade nail is safe to use when the fracture is ≥ 3 cm from the more proximal of the two distal locking screws.

2.3 Antegrade v/s retrograde intramedullary nailing

Tornetta *et al* [46] conducted a randomised, controlled trial with 1 year of follow-up on 68 patients (mean age of 32 years), who had femoral shaft fracture. It was found out that patients treated with retrograde reamed nailing had similar rates of and time to union but with increased rates of shortening, longer operating time, and more immediate postoperative complaints of pain, when compared with patients treated with antegrade nailing.

One potential disadvantage of retrograde nailing is that it contaminates a further compartment of the limb, namely the intra-articular contents of the knee, as it requires the creation of an intra-articular entry hole [46-48]. There is concern about the long-term effect of such an entry hole in patients as well as the potential for infection of the joint in patients with an open fracture. The long-term effects and complications of retrograde femoral IMN on knee joint function and disorders are still unknown [43]. Furthermore, malunion is more frequent after retrograde nailing than it is after antegrade nailing. Papadokostakis *et al* [49] and Ostrum *et al* [50] demonstrated a higher prevalence of delayed union and non-union after retrograde nailing. At present, it is agreed upon that studies with larger numbers and long term follow-up are needed before the current recommendations for the use of retrograde nails can be extended, thereby antegrade nailing remains the standard surgical technique for the treatment of femoral shaft fractures [24, 34, 46, 51].

Therefore, this study is aimed at femoral shaft fracture treatments using closed antegrade IMN, as it still remains the standard treatment of choice for treatment of such fractures. The remainder of this chapter discusses antegrade nailing in detail, and

from here onwards as in general practice, the term IMN will be used to refer to antegrade IMN.

2.4 Locked Intramedullary nailing

Intramedullary nail locking designs are generally categorized as using either an internal or an external locking mechanism. In the case of internal locking systems, the locking mechanism is integral to the nail's design as shown in Figure 2-17, which depicts the instrumentation supplied with the Grosse-Kempf locking nail [52].

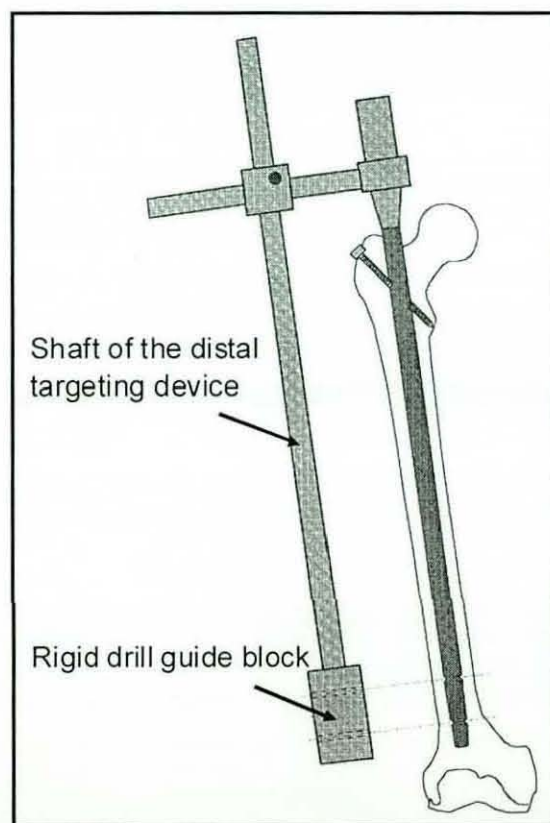


Figure 2-17 Intramedullary nail locking using internal locking mechanism [52]

This mechanical jig system is initially assembled prior to insertion of the intramedullary nail. The assembly is then screwed into the proximal end of the nail, and adjustments are made to bring the holes in the drill guide block into alignment with the distal holes in the nail. The assembly is then removed, and reapplied following insertion of the nail. Theoretically the drill guide block could then be used to assist drilling of the distal holes. However, in reality, an intramedullary nail

deforms by several millimetres to conform to the bone canal shape [14], resulting in holes in the drill guide block no longer being aligned with the distal holes in the nail, therefore, without compensation for the intramedullary nail deformation, it is impossible to place the distal interlocking screws correctly. As a result the use of interlocking mechanism has generally been abandoned.

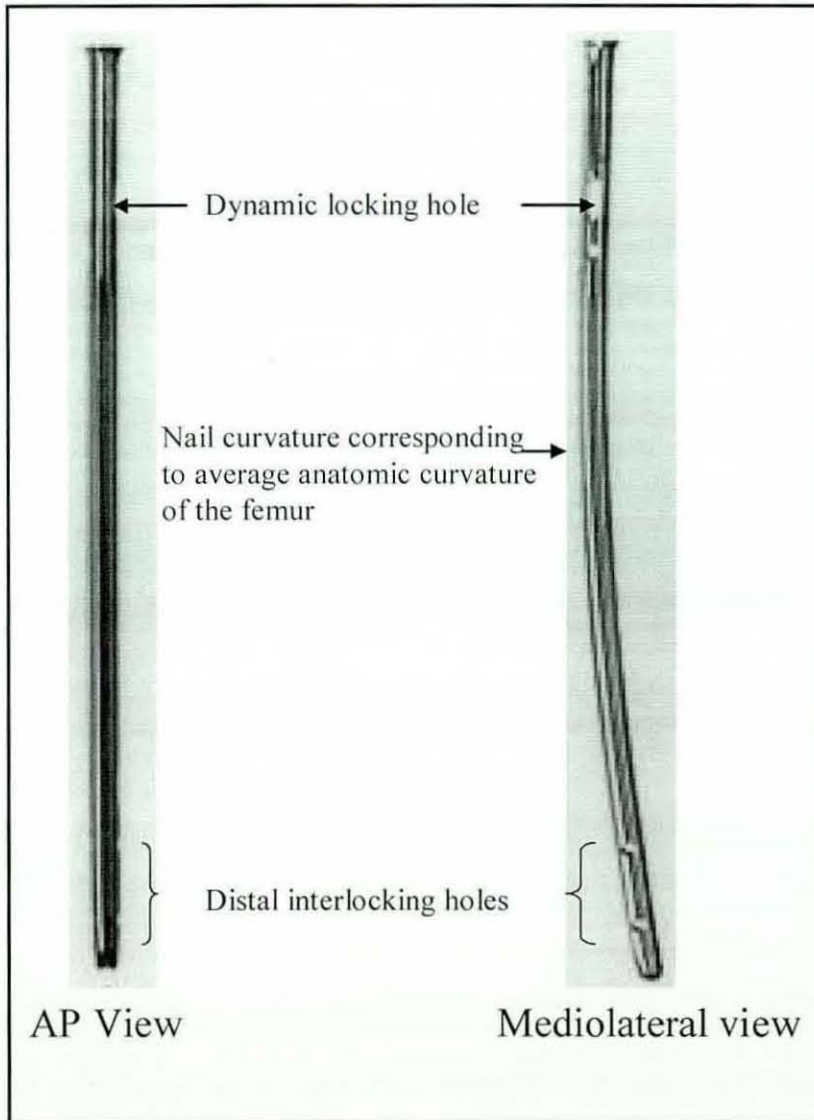


Figure 2-18 AO/ASIF Universal femoral nail [37]

The AO/ASIF Universal femoral nail [37], shown in Figure 2-18 is a typical example of an externally locked intramedullary nail i.e. intramedullary nail without integrated locking mechanism. It consists of a hollow stainless steel tube, which is pre-bent to match the curvature of the femur. Interlocking of the AO/ASIF intramedullary nail is achieved by inserting screws in the manner shown in Figure 2-19. Accordingly, the

nail's design includes a pair of holes at both the distal and proximal ends. This arrangement allows two possible modes of fixation, which are referred to as *static* and *dynamic* locking [37], which are discussed below.

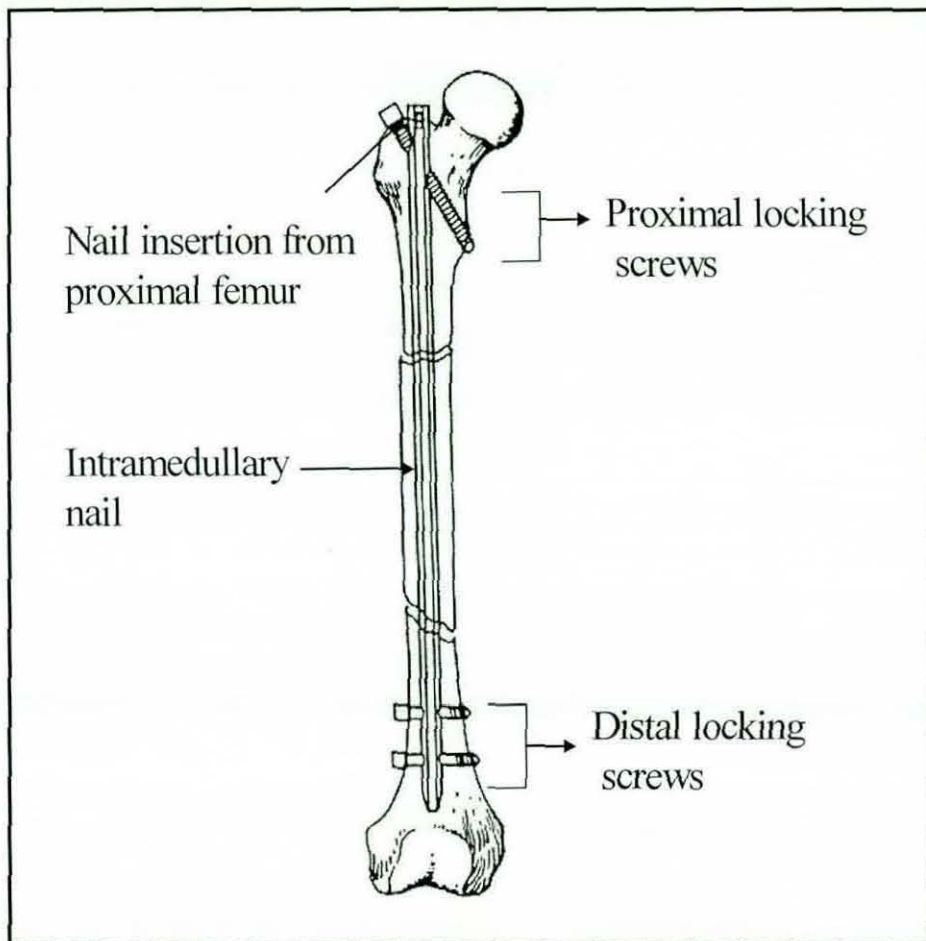


Figure 2-19 Interlocking of an intramedullary nail.

2.4.1 Dynamic locking

Dynamic locking involves insertion of only screws through the proximal end of the nail (shown in Figure 2-20) using a drill guide incorporated in the insertion handle. Dynamic locking controls bending and rotational deformation and allows nearly full axial load transfer by the bone. However, dynamic locking is not applicable in the case of long oblique, spiral or comminuted fractures or fractures that are located towards the distal widening of the medullary canal as it cannot control the rotation of the bone fragments [28]. Treatment of an unstable fracture by dynamic locking results in complications such as leg shortening (on average 2cm) and malrotation that usually

requires re-operation. Dynamic intramedullary stabilization of the femur should, therefore, be reserved for axially stable, transverse or short oblique fractures.

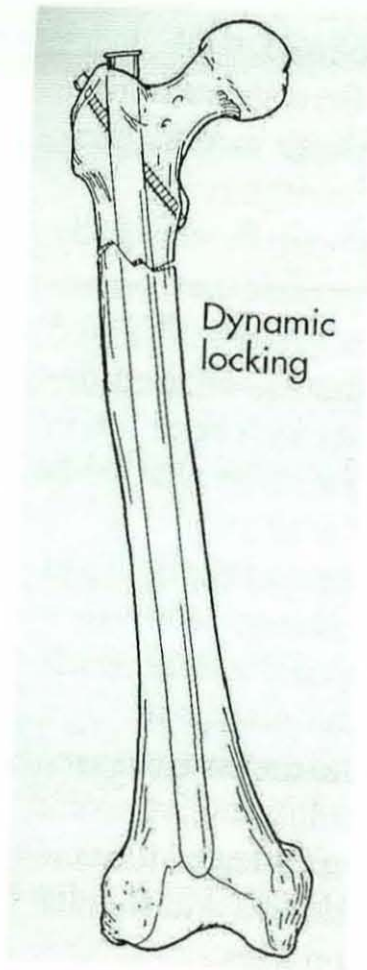


Figure 2-20 Dynamic locking to treat proximal transverse fracture.

2.4.2 Static locking

Static locking as shown in Figure 2-19, involves insertion of the screw through both proximal and distal ends of the nail, and is used to prevent axial compaction of severely comminuted and unstable fractures as it controls rotation, bending, and axial loading [28]. It makes the implant a more load-bearing device with a potential for a reduced fatigue life [22]. Brumback *et al* [53] treated 100 femoral fractures with statically locked Russell-Taylor nails. Postoperative analysis showed that all fractures were united.

2.5 Reamed v/s Un-reamed nailing

Intramedullary nailing is the standard treatment for femoral shaft fractures in most medical centres in the UK. However, whether to ream or not to ream remains controversial [22, 54].

There are three main reasons for the improved healing with reamed nailing. Firstly, the reamed nailing allows insertion of larger diameter nails, which improves cortical contact and stability. A larger nail with larger locking bolts allows earlier or immediate weight bearing even in the presence of a comminuted fracture [55].

Secondly, reaming also increases the contact area between the nail and the endosteal bone through the deposition of bone from the reaming at the fracture site, which acts like an autologous bone graft resulting in quick healing time in comparison to unreamed nailing as it results in a stiffer fracture construct [55-57]. Thirdly, although reaming disrupts the blood flow to the cortex, reaming induces a six-fold increase in the periosteal blood flow. This overcomes the lack of endosteal blood flow and may improve fracture healing. Clatworthy *et al* [58] showed that a group of patients treated with reaming had a faster time to union i.e. 28.5 weeks compared with 39.4 weeks for the group without reaming. They also showed that the group treated without reaming required substantially more secondary procedures, such as bone-grafting to achieve union. Several studies have demonstrated that use of a locked intramedullary femoral nail with reaming leads to a union rate of 97% to 100% [53, 59]. Theoretically reaming results in the removal of bone, thereby decreasing the overall bone strength. However, the outer diameter of the cortex is the primary contributor of strength of the bone; thus reaming removes the bone that contributes least to the overall strength yet allows a substantially stronger nail to be inserted [34]. Although, according to Forster *et al* [54], unreamed femoral nails are quicker to insert (by approximately 30 min) and are associated with less blood loss (approximately 140 ml less) in comparison to reamed nails. However, without reaming the nail and, consequently, the screws must be of smaller diameter, which leads to hardware-related complications such as screw or even nail breakage, and rules out early weight bearing. It has been reported by Forster *et al* [54] and Giannoudis *et al* [60] that reaming improves fracture healing, significantly reduces the time to union (by around 7 weeks) and significantly reduces the incidence of non-union (from 7% to 1%) when compared with unreamed nailing.

According to CA. Christian in [22], clinical data shows no difference in infection rates after reamed and unreamed femoral nailing .

Therefore, locked IMN with reaming is currently the standard treatment for severely comminuted, oblique and spiral fractures in the proximal and distal ends of the femoral shaft [61-63] as it results in quicker union, lower implant failure, fewer non-unions and consequently fewer re-operations in comparison to unreamed nailing. However, excessive reaming should be avoided as it significantly weakens the bone and increases the risk of thermal necrosis.

2.6 Distal Locking

Although conventional IMN (i.e. dynamic locking) provides adequate stabilization of femoral shaft fractures, problems can be encountered when the technique is applied to more distal/proximal shaft fractures. Recent reports [64, 65] suggest that distal locking is also necessary to prevent pathological fractures through the bone lesion even during subtrochanteric fracture treatment. In particular, when torsional forces are applied to the femur, friction between the nail and the bone can be insufficient to control rotation of bone fragments. In order to rectify these problems and hence to extend the scope of IMN, the concept of distal locking shown in Figure 2-19, has therefore been introduced. This technique involves rigidly attaching the nail to bone fragments at the distal end of the femoral shaft in order to provide more effective fixation i.e. rotational and axial stability.

However, the deformation of the nail during passage through the medullary canal and use of two-dimensional X-ray images, to guide three-dimensional bone machining processes makes the insertion of the distal locking screws the most difficult part of the closed IMN procedure [27, 66]. Krettek *et al* [66] used a three-dimensional motion tracking system, consisting of a magnetic field source and two field sensors, to quantify insertion related nail deformation in both solid and slotted nails.

Since, solid nails have higher area moment of inertia and hence more resistance to rotation than slotted nails, therefore insertion related force is decreased. This results in significantly smaller rotation about the long axis of the solid nail in comparison to that of slotted nails as shown in Figure 2-21.

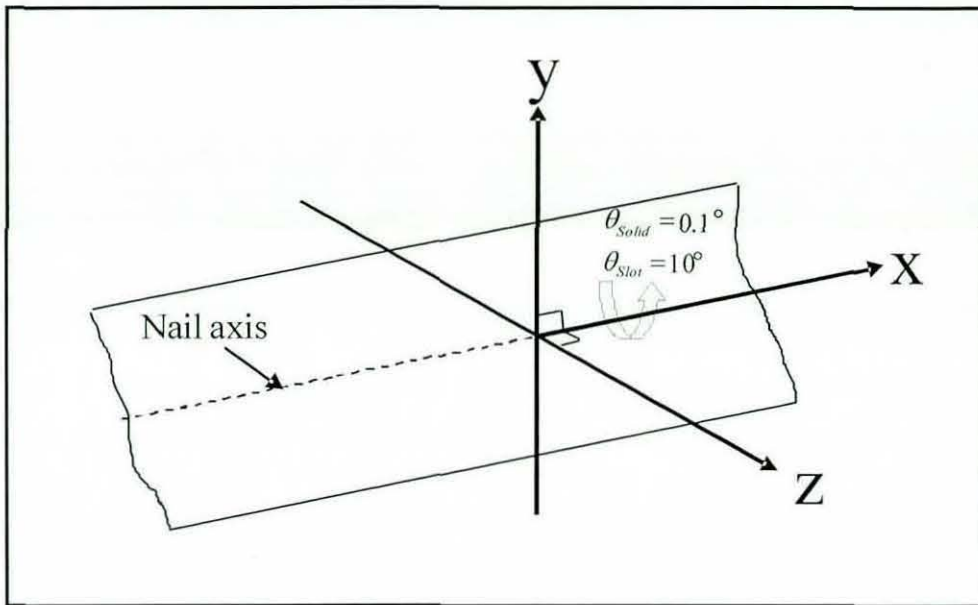


Figure 2-21 Comparison between rotation of the nail about its long axis for solid and slotted nail.

However, large medial-lateral i.e. along y- axis (axis perpendicular to both the nail and the distal hole axes) and anterior-posterior i.e. along z-axis (distal hole axis) translations were found for both solid (i.e. mean of 3.1mm and 8.2mm respectively) and slotted nails (i.e. mean of 0.3mm and 21.5 mm respectively). Therefore it is not possible to place the distal locking screws of an intramedullary nail accurately without compensating for its deformation. However, it should be noted that the implants used in this study were 9mm solid nails and 13mm slotted nails. Since, diameter of the nail could be expected to influence insertion related nail deformation, therefore experimental results obtained in this study does not represent true comparison between solid and slotted nails in terms of insertion related nail deformation. Authors concluded this technique should be used to study solid and slotted nails of same diameter from different manufacturers before definitive conclusions regarding insertion related nail deformation can be made.

The two main reasons for failure in distal locking are incorrect entry point on the bone and wrong orientation of the drill. If either of these two factors is wrong, then the drill will not go through the nail hole. An inaccurate entry point also compounds the problem as the rounded end of the drill bit often slips and it is then difficult to place another drill hole next to the earlier one. Inaccurate distal locking leads to premature

failure with breakage of the nail through the nail hole, breakage of the screw or the breaking of the drill bit within the bone.

2.7 Summary

Femoral shaft fractures are generally caused by high-energy forces and, therefore are regarded as a medical emergency. At present, most of the femoral shaft fractures are treated surgically with IMN. The goal of treatment is reliable anatomic stabilization, while allowing mobilization as soon as possible. The traditional IMN technique has been modified by introducing distal locking to obtain better fixation. However, nail deformation during its insertion into the medullary canal makes distal locking the most difficult part of the IMN procedure. In the next chapter, numerous techniques and devices that have been proposed to aid distal targeting are discussed in detail.

3 Review of techniques available for assistance in distal locking

Since the introduction of intramedullary locking nails there have been several technical aids put forward to assist and simplify the insertion of distal locking screws. Many devices have been developed to assist orthopaedic surgeons to locate the centre of the distal locking holes and the drilling trajectory during distal locking. Examples include proximally mounted targeting devices [67], image intensifier mounted devices [28], laser devices [68, 69], stereo fluoroscopy [70] and mechanical guides [71]. However, all of these devices and techniques have deficiencies, such as they are only selectively applicable, are cumbersome and difficult to use, time consuming, or are not sufficiently accurate, and thus fail to significantly reduce surgeons' radiation exposure during distal locking and the likelihood of patient complications. In general, three types of distal targeting techniques have been proposed:

- The use of target devices mounted onto the nail i.e. proximally mounted devices,
- The use of target devices mounted onto the image intensifier and
- Various free hand techniques with the use of various instruments.

3.1 Nail mounted distal targeting devices

The nail mounted targeting device shown in Figure 3-1 depicts the instrumentation supplied with Russell-Taylor interlocking nail [52]. This instrumentation is assembled intraoperatively, with the proximal drill guide initially being attached to assist intramedullary nail insertion. Following acquisition of the perfect circle image (discussed in section 3.3), the shaft of the distal targeting device is then inserted through the adapter block, until a position which corresponds to the individual nail's length is obtained. The shaft is then locked into position (parallel to the nail) by tightening a grub-screw in the adaptor block. The adjustment instrument is then used

to align the distal targeting device with the more proximal of the two distal holes, by making several fluoroscopically-guided fine adjustments.

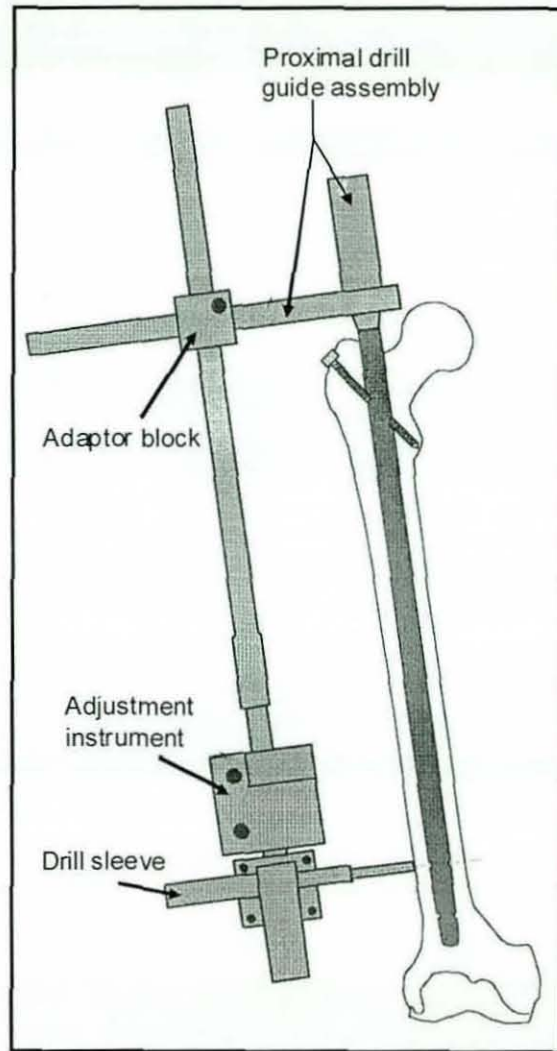


Figure 3-1 Nail mounted distal targeting device [52]

As an alternative to an externally positioned solution, a self guiding intramedullary nail system was developed by Azer *et al* [72]. Once reaming of the medullary canal is performed, the lateral cortex at the distal end of the femur is exposed through a 4cm incision, and the dissection is made for placement of distal screw as shown in Figure 3-2.

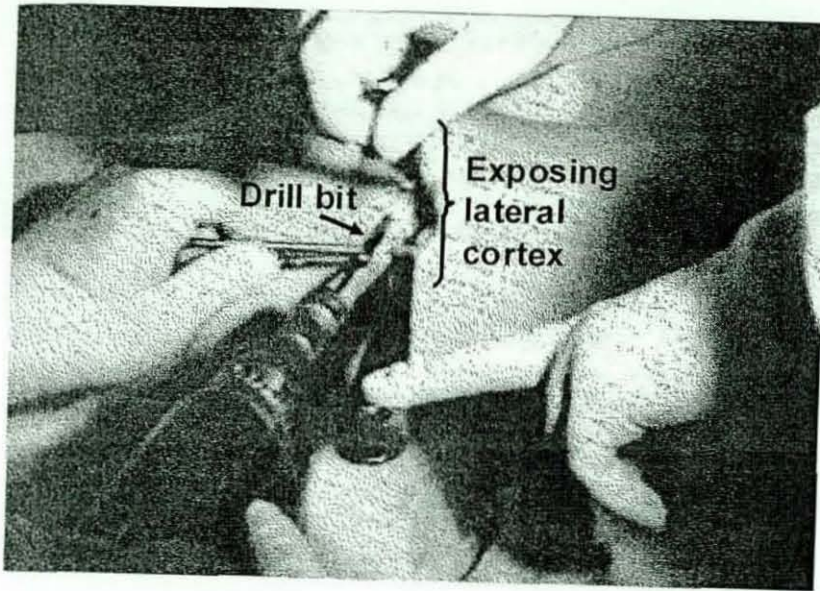


Figure 3-2 Opening of lateral cortex.

The center of the femur is approximated and a drill bit is placed perpendicular to the long axis of the femur as shown in Figure 3-3. The transverse drill bit is drilled through both cortices and left in place. The position and perpendicularity of the drill bit is checked by using fluoroscopy.

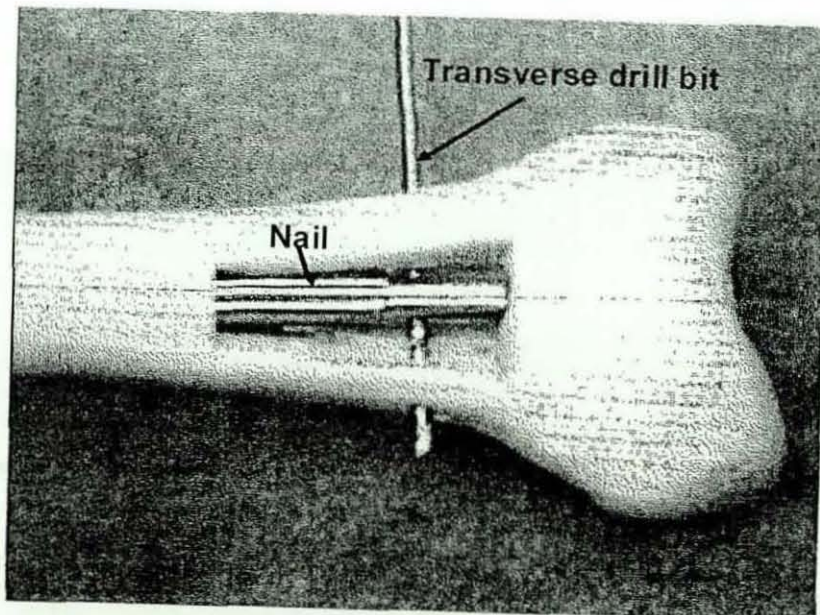


Figure 3-3 The nail slides down over the guide rod without rotating and interlocks with the distal drill bit.

A guide rod with a “distal bifurcation” (similar distal end to that of an intramedullary nail, i.e. containing two distal holes) is inserted down the reamed canal just proximal to the transverse drill bit. The guide rod is considerably smaller in diameter than the reamed canal; therefore the surgeon can rotate it to intersect and capture the transverse drill bit in the distal bifurcation. The engagement of the guide rod onto the transverse drill bit is confirmed by using fluoroscopy. The length of the nail is then determined from the marking on the guide rod at the level of nail entry point. The self guiding nail is inserted over the guide rod by tapping using an impactor. To prevent rotation between the nail and the guide rod during insertion, outer diameter of the guide rod is chosen slightly smaller than the inner diameter of the nail. The nail is then engaged with the transverse drill bit as shown in Figure 3-3. The guide rod is then withdrawn while maintaining the nail firmly against the transverse drill bit. The guide rod is then inserted into an external guide positioned laterally to the nail. The guide rod is slid down externally to intersect again with the transverse drill bit. Then a drill sleeve is inserted through the guide rod’s hole proximal to the transverse drill bit and through the distal drill guide down to the lateral cortex as shown Figure 3-4.

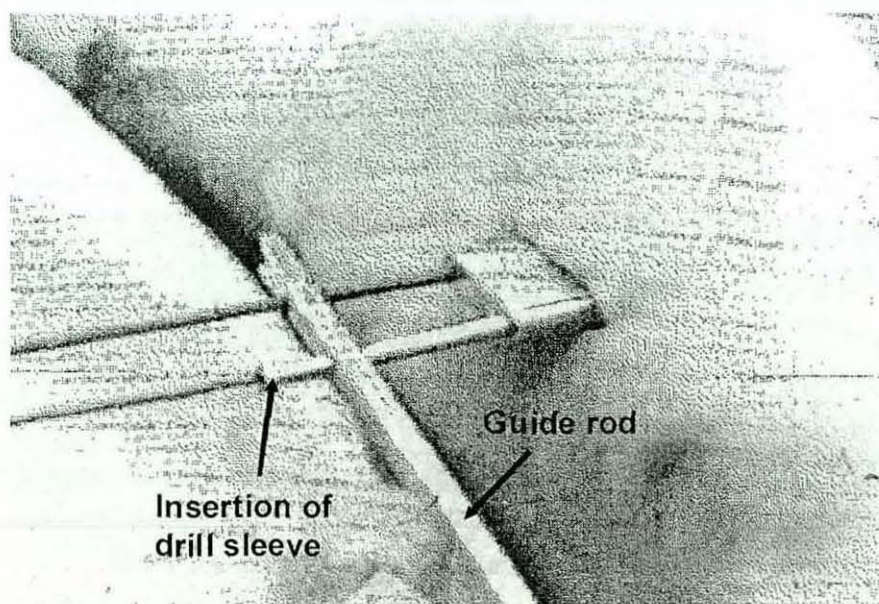


Figure 3-4 Engagement of guide rod with transverse drill bit, and the drill sleeve is inserted through the guide rod and distal drill sleeve guide.

The assembly now resembles a rectangle, as shown in Figure 3-5, with drill sleeve parallel to the transverse drill bit and at a distance equal to the distance between holes

in the nail and guide rod. A second drill bit is then inserted into the drill sleeve and drill through the cortex, nail, and medial cortex. Confirmation of the drill placement is made using the fluoroscopy. The drill, drill sleeve, parallel guide, and guide rod are then removed prior to screw insertion in the hole proximal to the transverse drill bit. Afterwards, the transverse drill bit is removed and second screw is inserted. The interlocking of the nail is then confirmed using the fluoroscopy.

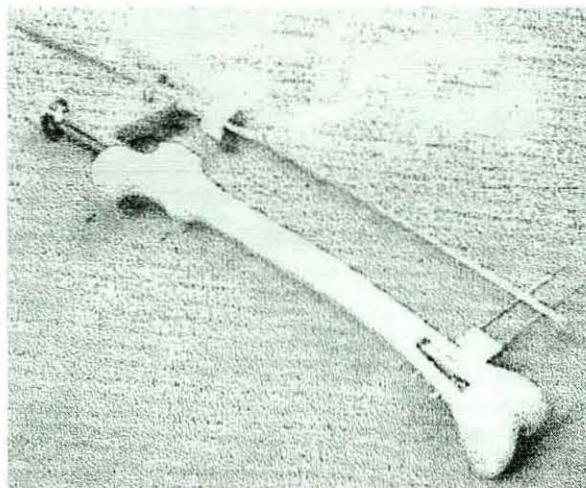


Figure 3-5 Self-guided interlocking system resembling a rectangle [72]

An H-shaped device, as shown in Figure 3-6, described by Steriopoulos *et al.*[71], aids distal locking in intramedullary nailing by holding two similar intramedullary nails parallel to one another. Following the insertion of one of the nails into an overreamed medullary canal, the free nail situated external to the patient is used as a guide. The device could not be used for obese patients due to the depth of the site of the insertion of the nail. Authors concluded that distal locking procedure was time-consuming due to insertion related nail deformation, and the proposed device can perform better if the possible deformation of the nail could be predicted.

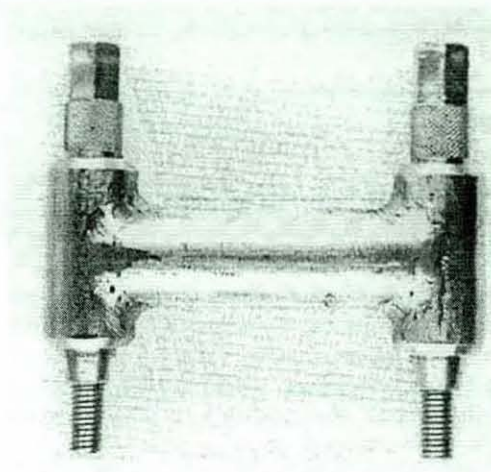


Figure 3-6 H-shaped device [71]

In situations where an image intensifier is unavailable intraoperatively (a situation which exists in many of the third world countries), Kanellopoulos *et al* [73] propose performing distal locking through a window of length 3- 4 cm and width 1.5- 2 cm cut through the distal anterior femoral cortex. The cortical window provides a direct line of sight to the distal holes. In summary, once the intramedullary nail is inserted, an external nail of the same length is placed side by side on the lateral surface of the patient's thigh. Alignment between the two nails at the proximal end is achieved using the nail's insertion instrument. A K-wire is then introduced through the proximal of the two distal locking holes of the external "guide nail" as shown in Figure 3-7(a). The K-wire is then engaged onto the lateral femoral cortex, and the "guide nail" is withdrawn. Using the location of the K-wire with respect to the most proximal of the two distal locking holes, a rectangle is then defined on the exposed anterior aspect of the distal femur by drilling 2mm diameter holes, as shown in Figure 3-7(b) to expose the distal end of the nail. Two screws are then inserted through the distal holes of the intramedullary nail and the wound (i.e. rectangular cut-out bone section) is closed in layers.

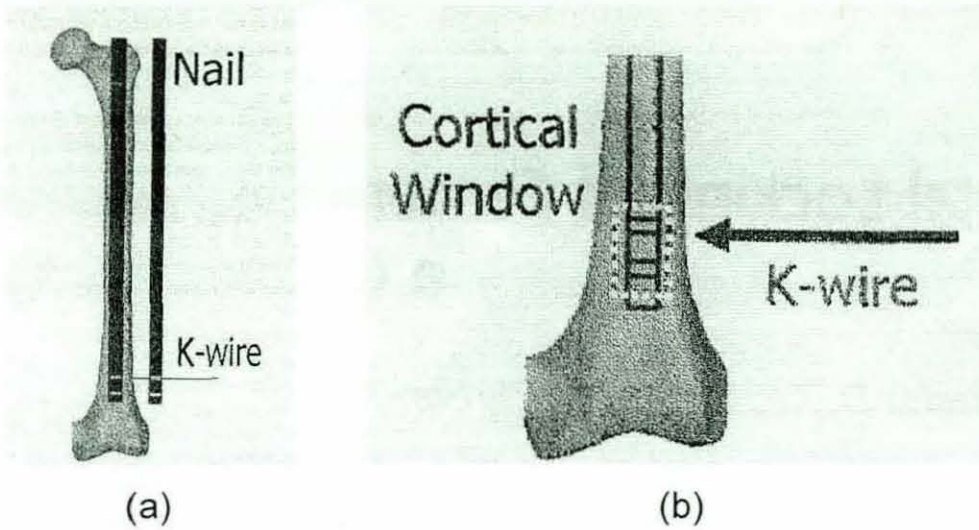


Figure 3-7 (a) Introduction of K-wire using external guide nail. (b) Defining rectangle by holes drilled on the anterior cortex of the distal femur [73]

It is reported that it takes about 10 minutes to complete this procedure. According to Kanellopoulos *et al* [73] all fractures and cortical windows healed uneventfully.

Although the above mentioned systems are rather simple to apply, they have not been applied for general clinical use, as these devices do not compensate for deformation of the nail during insertion, due to bending and rotational forces, thereby making this technique unreliable [66, 74] as up to 15% misplaced screws have been reported. In addition to this, the proximally mounted device is specific to the type of the nail being used. It is not as versatile as a free hand locking device, which can be applied to more than one locking nail system.

3.2 Image Intensifier mounted targeting devices

Image intensifier mounted targeting devices were introduced as a means of reducing the radiation exposure to both surgeons and patients. A device resembling a double pronged fork is described by Kempf *et al* [28]. This device is inserted into a bracket attached to the X-ray tube housing (prior to image accusation) as shown in Figure 3-8. The surgical incision is then made, and the drill guide incorporated into the targeting device is brought into alignment with one of the distal holes. This is accomplished by mounting the targeting device on a hinged bracket, in such a way that the drill guide is

aligned with X-ray imaging axis when the targeting device is lowered into a horizontal position as shown in Figure 3-8. Once a perfectly circular image of the distal hole alignment with the sighting barrel's hole is obtained, the targeting is complete i.e. first distal hole is locked. The procedure is then repeated for locking the second distal hole.

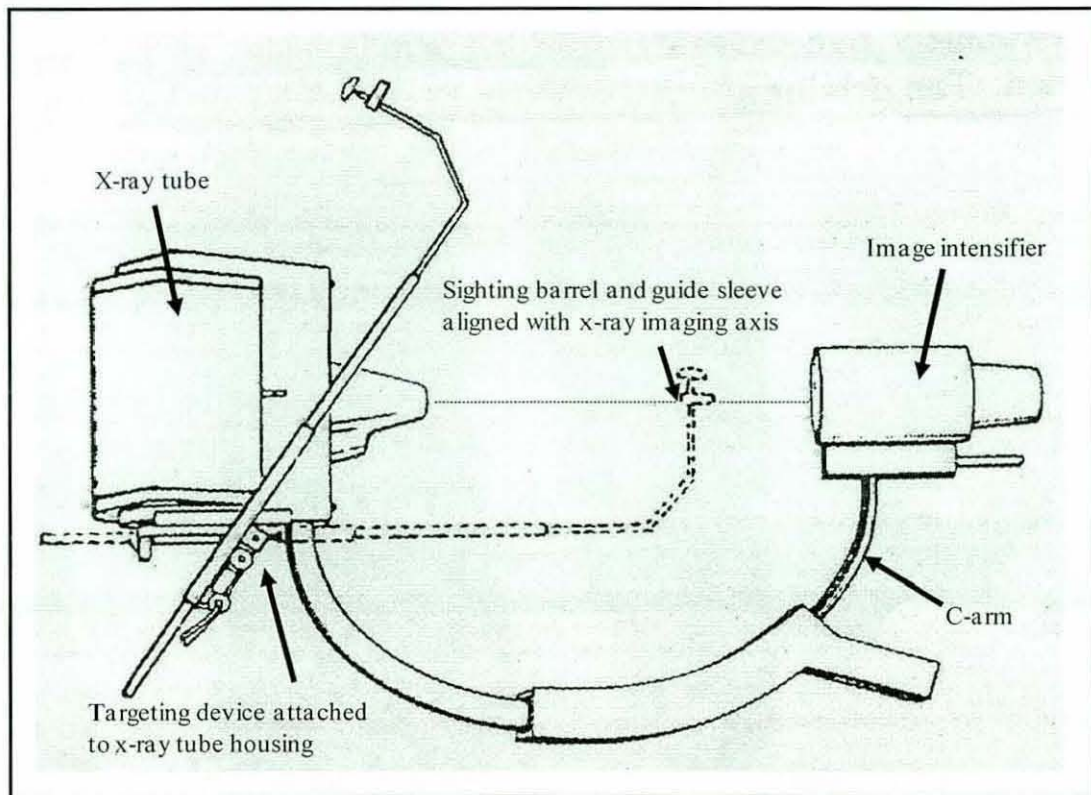


Figure 3-8 Target device inserted into the console, which is secured to the X-ray tube housing
[28]

The procedure requires an expert radiographer as it involves the manipulation of the C-arm by the radiographer, to align the hole in the sighting barrel with the nail's distal hole. Many surgeons have found that the drill guide is easily displaced from its planned trajectory. This is caused by the bending of the long lever arm of the targeting device when manual pressure is applied during drilling process.

Goodall *et al* [68] developed a system that uses a laser enclosed in an aluminium case, which is mounted on the image intensifier. The visible laser beam is aligned with the X-ray axis of the C-arm by focusing it via mirrors. The C-arm is then adjusted until the distal locking hole appears as a circle (instead of an ellipse) to

acquire a perfect circle image. Once the perfect circle image is obtained the laser beam is centred through the distal hole resulting in the laser as a dot on the skin marking the incision site as shown in Figure 3-9. Now drilling of the distal locking hole can be performed without fluoroscopic guidance, resulting in reduction of radiation exposure to both surgeon and patient. However, extreme care must be taken to avoid direct exposure of laser to eyes.

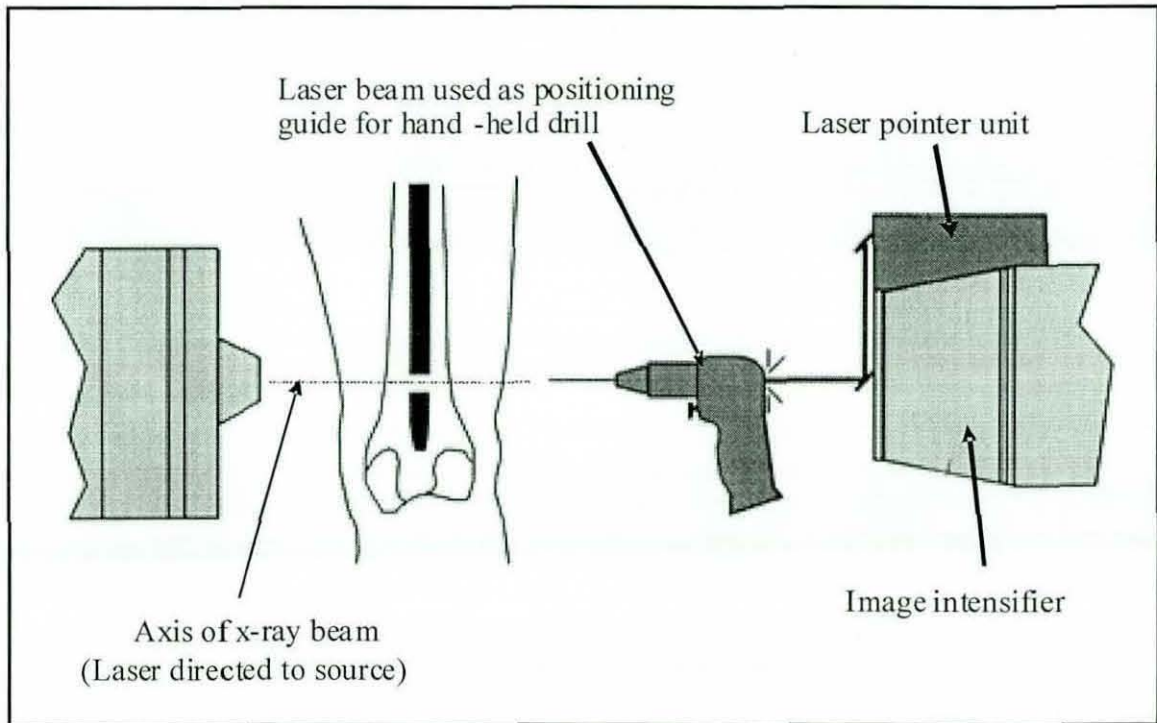


Figure 3-9 Image Intensifier mounted targeting device [68]

Goulet *et al* [69] have proposed a laser guidance system in which the centre of the X-ray beam i.e. X-ray imaging axis is marked on the image intensifier by placing a 90° wire cross directly on the image intensifier as shown in Figure 3-10. This projects a cross on the centre of the CRT monitor screen.

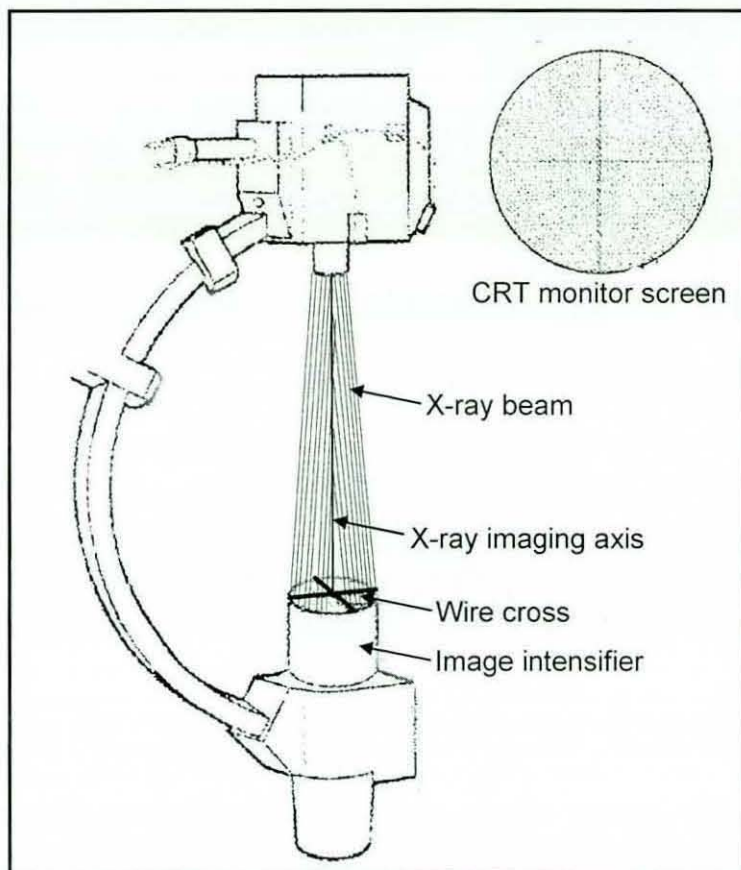


Figure 3-10 Alignment of X-ray imaging axis with wire cross intersection [69]

The path of the X-ray imaging axis is then defined by aligning the planes of two laser lights mounted on the cathode tube of the image intensifier such that intersection of the light planes is parallel to and coaxial with the X-ray imaging axis as shown in Figure 3-11. This allows direct visualization of the path of the X-ray imaging axis.

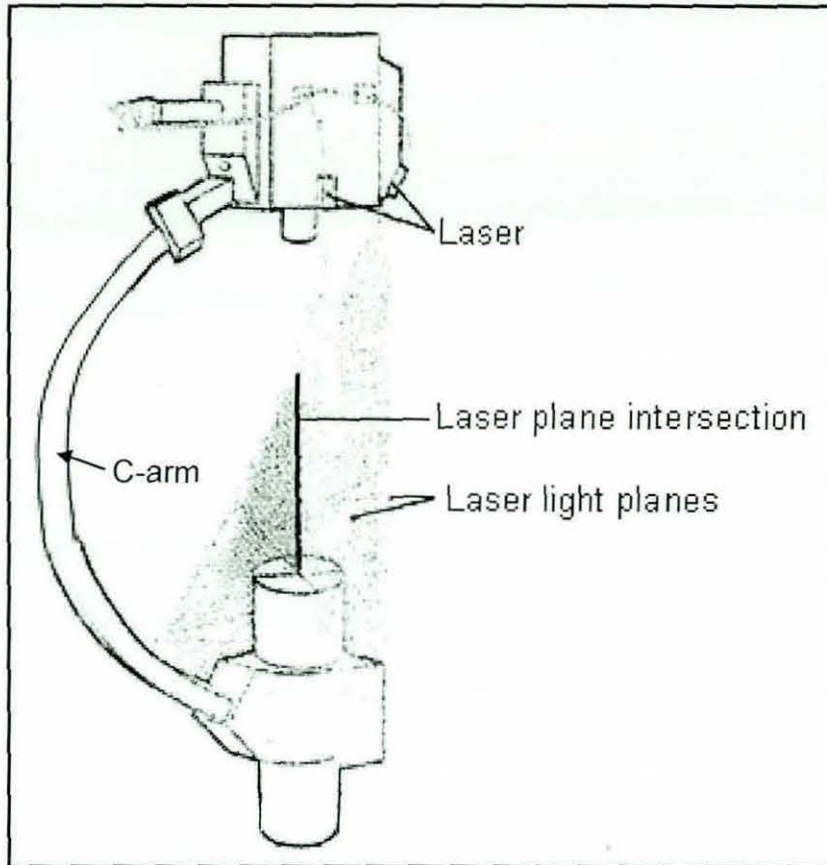


Figure 3-11 Laser planes intersection for defining path of X-ray imaging axis [69]

The C-arm is then moved until the distal nail holes are aligned centrally with the cross on the screen allowing the laser to guide the direction and angle of the drill.

Although these devices offer good protection from the radiation, they have not been generally accepted, mainly because of their instability, as these devices can only move with the image intensifier, which is not constructed to perform minute movements.

3.3 Free hand technique

The failure of proximally mounted targeting devices during the distal locking process resulted in the introduction of free hand techniques for completion of the distal locking process. Due to their simplicity, free hand techniques are used nowadays by most of the surgeons as the best available method for distal locking [75]. The simplicity of these technique results from the use of a surgical instrument as the aiming device. Mostly, this surgical instrument is a form of K-wire, drill bit or guide

wire [76], which is inserted into the chuck of an air-powered surgical drill. Free hand techniques use the *perfect circle approach*. It involves the following stages:

- **Acquisition of near-perfect circle image**

In order to obtain a near-perfect circle image, i.e. an image in which the distal locking holes appear as perfect circle rather than an ellipse, the position of the C-arm is adjusted until the two distal holes appears as near perfect circles as shown in Figure 3-12.

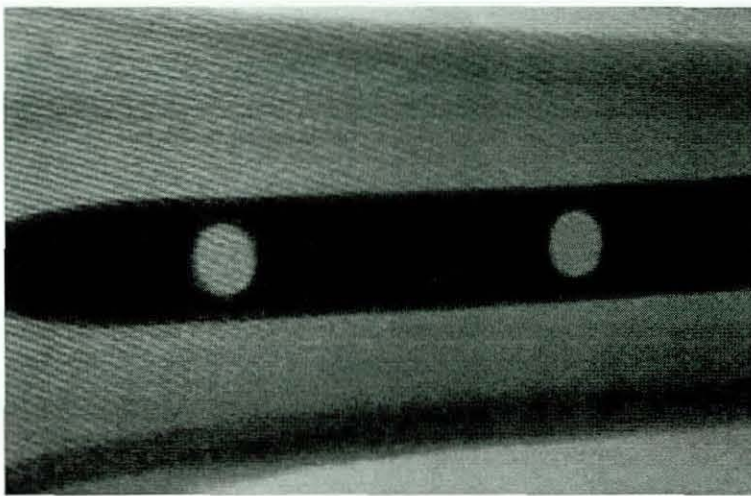


Figure 3-12 Perfect circle approach.

- **Determination of entry point**

After obtaining a near perfect circle, the surgical tool (K-wire, drill bit or guide wire) is then held within the image intensifier field of view, with the tip of the surgical instrument in contact with the lateral femoral cortex. Determination of the entry point is done by centring the tip of the surgical tool onto one of the distal locking holes, while taking x-rays in continuous mode. During this procedure, the surgical tool must be held at approximately 45° to the femoral shaft, to ensure visualization as shown in Figure 3-13. This entry point is then marked by drilling few millimetres into the lateral femoral cortex.

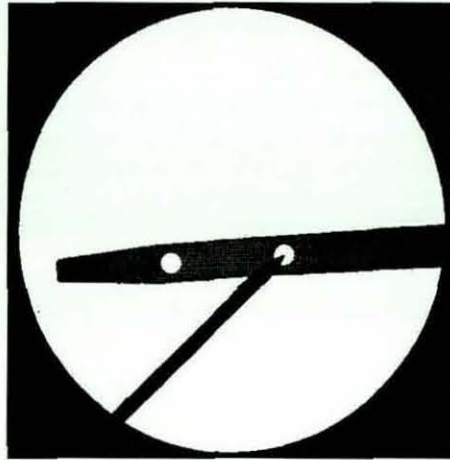


Figure 3-13 Determination of entry point.

- **Determination of drilling trajectory**

The orientation of the surgical tool is then checked on the AP view by holding the surgical tool perpendicular to the femoral shaft without moving its tip, which is centred onto the distal locking hole, as shown in Figure 3-14.

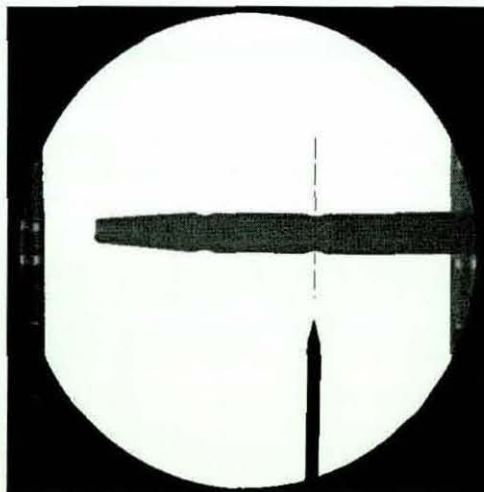


Figure 3-14 Confirmation of drilling trajectory.

Having checked the drilling trajectory on both views, the distal hole can then be drilled. In summary, by repeatedly alternating between AP and Lateral X-ray fluoroscopic views, the surgeon adjusts the entry point and orientation of the drill so that its axis coincides with the corresponding distal hole axis. Drilling proceeds incrementally, with each advance verified with a new pair of X-ray fluoroscopic

images. Once the pilot hole passing through the distal locking nail's hole has been drilled, the locking screw is fastened as shown in Figure 3-15.

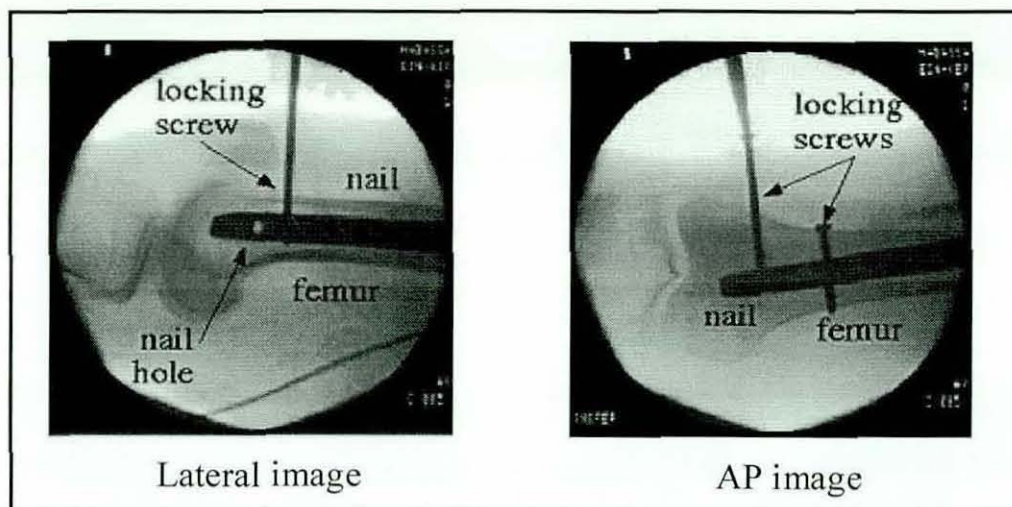


Figure 3-15 X-ray fluoroscopic images taken during distal locking [77]

The major disadvantage of the free hand technique is direct exposure of the surgeon's hands to X-ray radiation, as shown in Figure 3-16, and since the process of obtaining near perfect circle image is time consuming, both surgeon and patient are subjected to excessive irradiation. The outcome of the procedure is heavily dependent on the surgeon's skill and experience. S. Madan *et al* [13] demonstrated that the average time of radiation exposure during intramedullary nailing reduces to about one-third when performed by a consultant (0.52 minutes) rather than a middle-grade surgeon (1.61 minutes).

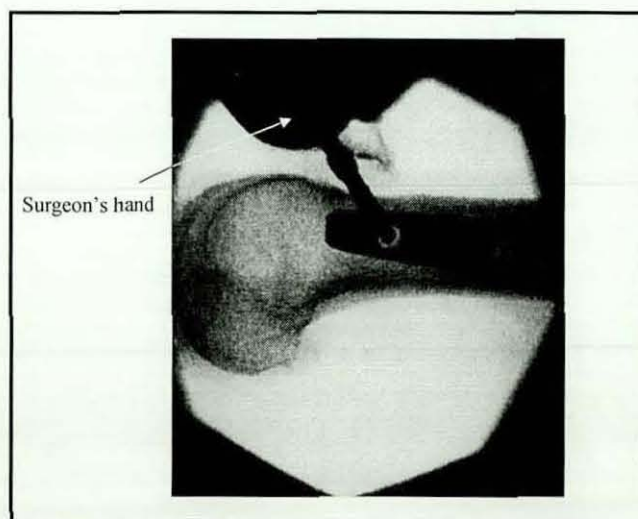


Figure 3-16 Direct X-rays exposure to Surgeon's hand [78].

3.3.1 Proposed modifications of the free hand technique

Yiannakopoulos *et al* [25] proposed a modification of the "perfect circles" free-hand technique by employing a Flag and Grid technique. It involves the use of a stainless steel "grid" of 20 by 10cm (internal dimensions of the grid's quadrants are 10 by 10mm), and a "flag", which consists of a 20 cm long and 3 to 4mm diameter Steinmann pin (depending upon the core diameter of the locking screws) with a metallic handle attached to the pin's proximal end, as shown in Figure 3-17. The metallic handle is used to make holding of the pin easier and to keep the surgeon's hand further away from X-rays.

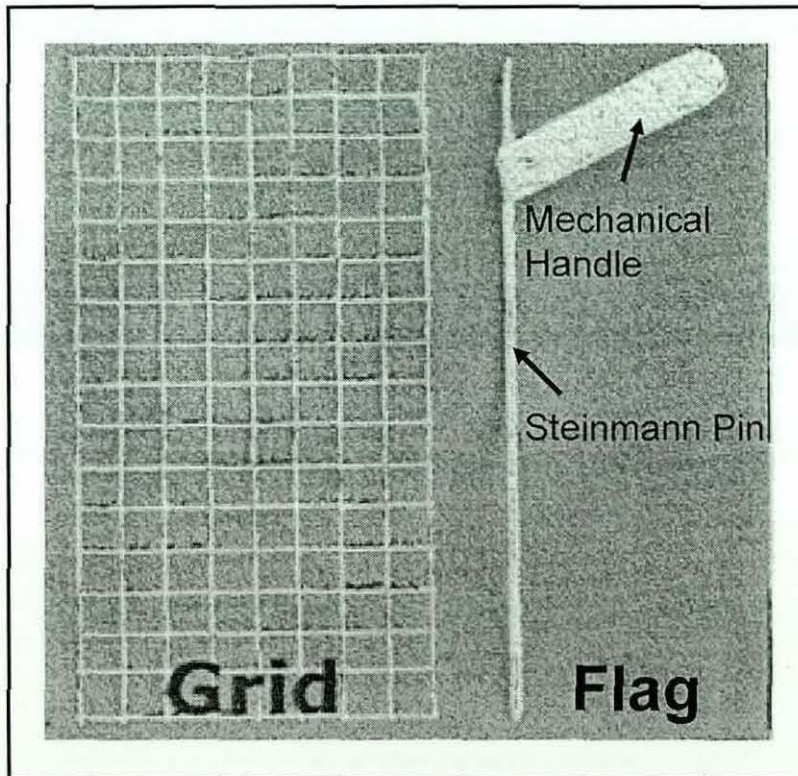


Figure 3-17 Devices used to implement Flag and grid technique [25]

After the nail insertion, the grid is temporarily attached to the skin of the lateral surface of the femur (i.e. corresponding to the distal nail holes) using a plastic adhesive drape as shown in Figure 3-18.

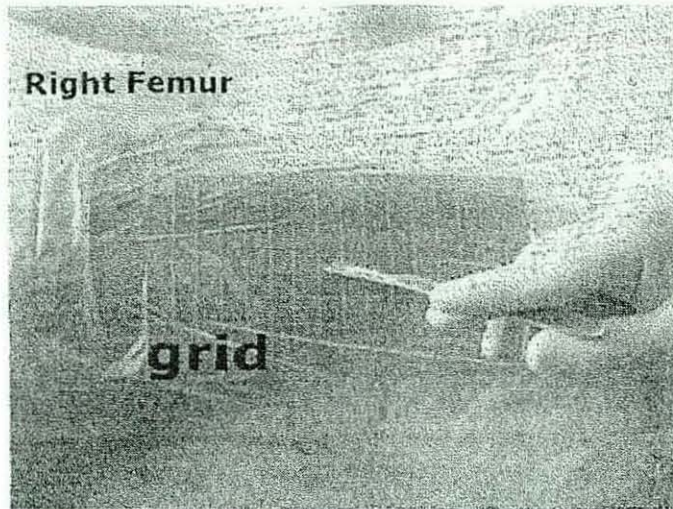


Figure 3-18 Attachment of the metallic grid to femur with an adhesive drape [25]

A haemostatic clamp (star) is attached to the grid (shown in Figure 3-19) to provide reference. Once the perfect circle fluoroscopic image is obtained, as shown in Figure 3-19, the position of the distal holes in relation to the grid is determined by referring to the grid' quadrant. A 0.5 to 1 cm long skin incision is performed at the appropriate quadrant. Through the skin incision the tip of the "flag" is then used to locate the approximate centre of the distal hole using fluoroscopic verification. Subsequently, the tip of the "flag" is positioned parallel to X-ray imaging axis, and advanced through the cortex and the nail with hammer blows. The "flag" is then removed and a screw of appropriate length is inserted.

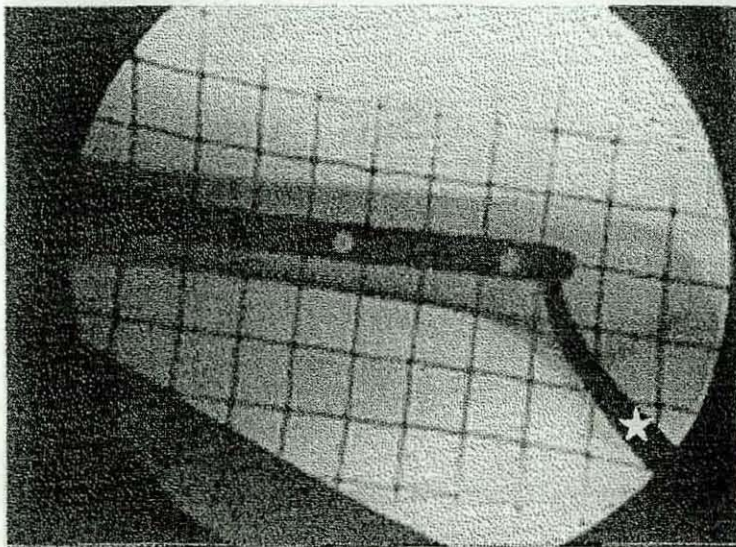


Figure 3-19 Lateral view perfect circle image with hemostatic clamp (i.e. star) [25]

A comparison of the proposed "Flag and Grid" technique with the free-hand technique showed that use of the proposed technique during distal locking resulted in reduction of radiation exposure, as only 5 to 9 radiographs (mean 6.2) were required in comparison to 17 to 52 radiographs (mean 28.4). Furthermore, total distal locking operating time was also reduced while using "Flag and Grid" technique in comparison to free-hand technique, as only 5.1 ± 2.7 minutes were required in comparison to 19 ± 7.1 minutes.

Another drawback of the free-hand technique is the effect of the introduction of a large defect into the cortex during the initial penetration by the trocar, or drill, if an accurate position has not been achieved, i.e. if the hole has been positioned incorrectly, it may hinder a new hole being drilled in a corrected path, as the drill may slide into the first off-centre hole [79]. The placement of two holes in close proximity produces an area of stress concentration and the repeated drilling may lead to screw loosening. The creation of a large defect may also weaken the bone.

Modifications to the free-hand technique have addressed the problem of initial cortical penetration prior to the achievement of an accurate position. Most of these modified techniques use a Steinmann pin, K-wire, or guide pin for primary insertion into the cortex. This has the advantage that cortical defects are not produced if multiple attempts are required to locate the nail hole. If the wire is incorrectly sited, a second wire will take its own path and not slip into a previously made hole [80]. It has also been found by Owen *et al* [81] that during X-ray imaging it is easier to determine, when the tip of a K-wire is aligned with the centre of the nail hole compared with a larger diameter drill. According to Knudsen *et al* [80] it is usually easier to pass a small diameter wire through a screw hole than a drill.

Knudsen *et al* [80] developed a technique using a 3 mm Kirschner wire (K-wire), an air drill and an image intensifier. Implementation of this technique does not require any assistant or aiming device. At first, the C-arm is adjusted until the X-ray image shows two distal locking holes as perfect circles, following which the air drill is loaded with the K-wire. The tip of the wire is then positioned on the lateral cortex and moved until located in the centre of the proximal of the two distal locking holes. The wire is then inserted perpendicular to the femur in the proximal of the two holes. The

orientation is checked using the AP view by holding the K-wire perpendicular to the femoral shaft without moving its tip. The K-wire is then driven through the bone using the Lateral view X-ray image. Once it is confirmed that the proximal K-wire is correctly sited, a second K-wire is inserted into the most distal hole using a similar technique. The proximal Kirschner wire is then removed and replaced with the definitive drill bit, and the hole is drilled using the distal K-wire as a visual guide to show the line of passage. The same procedure is used for the second distal hole. A disadvantage to this technique is the removal of the guide wire prior to drilling. While testing this method, Owen *et al* [81] found the procedure of reinserting the drill across the nail is difficult and took longer than trials using a cannulated drill bit.

MacMillan and Grosse [79] describe a method using a 2mm diameter Steinmann pin, attached to the handle of a disposable suction unit to distance the surgeon from the radiation field. The image intensifier is used to view the distal nail holes as perfect circles. The pin is aligned, driven through the bone, and engaged in the opposite cortex. A 6.0 mm cannulated reamer is placed over the Steinmann pin and the lateral cortex is reamed up to the nail. With the guide in place the guide pin is then removed, followed by drilling and screw insertion.

Owen *et al* [81] conducted a trial to compare the free-hand method with a method similar to that recommended by MacMillan and Grosse, using a K-wire and cannulated drill instead of a reamer. They found that the proposed technique reduced the average operating time for distal locking from 30 minutes to 18 minutes and radiation exposure time to the surgeon from 8.13 minutes to 4.7 minutes.

Although the above mentioned techniques reduce the problems of radiation and cortical defects there are still difficulties to be addressed. These include involuntary movements that occur during the change from locating the holes to aiming the drill bit, or wire, and drilling the hole; additionally, the path of the drill bit is difficult to monitor.

3.3.2 Devices to reduce surgeon's irradiation while using the free hand technique

The use of lead-impregnated gloves has been tried to limit surgeon's irradiation while performing distal locking procedures using the free hand technique, however they have not been successful as they limit movements of the surgeon's hand considerably. Wagner *et al* [82] evaluated gloves from four different manufacturers and reported that exposure reduction of only 7% to 50% at most, whereas at higher energy levels, the gloves were even less effective. It was also concluded that wearing protective gloves might give a false sense of security that could increase the risk of the surgeon placing his/her hand directly in the path of the X-ray beam. Another proposed solution is the use of radiolucent drills in order to minimize the radiation dose, however, their use still resulted in sizeable radiation exposure to surgeons' hand [83]. Skjeldal *et al* [84] proposed the use of a long-handled tool holder, which ensures the surgeon's hands are removed from the x-rays zone to reduce surgeon's irradiation.

In addition to the above-mentioned techniques, other alternatives have also been proposed to assist orthopaedic surgeons in performing distal locking procedures. For example Takashi *et al* [70] have proposed the use of stereo fluoroscope i.e. X-ray images are alternately taken from left and right X-ray sources to provide a 3-D view in real time, to assist surgeons during distal locking. However, this technique still relies on the perfect circle approach, hence results in lengthy operation time and thereby excessive irradiation to both surgeon and patient. Also the stereo fluoroscope is large, heavy and expensive in comparison to the traditional 2-D fluoroscope and therefore is not suitable for use in the operating room during surgery.

All of the above-mentioned distal targeting techniques used by orthopaedic surgeons involve the following three major distinct steps:

- Adjust the position of the C-arm fluoroscopy image intensifier so that the distal holes appear as perfect circles on the X-ray image.
- Using a visual based targeting approach to drill a pilot hole for the locking screw is an example of "the placement of an object (guide wire, screw, tube, or scope) at a specific site within a region, via a trajectory which is planned from one or more

imaging modalities and governed by 3-D anatomical constraints", referred to as "*The Basic Orthopaedic Principle*"[85].

- Implement the "*The Basic Orthopaedic Principle*"[85] to insert the locking screw.

The problems encountered with existing techniques of distal locking include, length of the time required for locking the distal screw, excessive radiation exposure to surgeon and patient and misplacement of screws.

3.4 Use of fluoroscopy for distal locking

Fluoroscopy, known to most people as x-ray, is the oldest and most frequently used form of medical imaging. The current trend in osteosynthesis, as in other branches of medicine, is to minimise the trauma associated with gaining access to the surgical site. Therefore, many of the "open" osteosynthesis techniques, which require large incisions and retraction to expose the fracture site, are being superseded by "closed" surgery counterparts in which the fracture site is not directly exposed [86]. Without direct visualisation of the fracture site, X-ray imaging often becomes the only means of guidance during orthopaedic surgery. Although closed surgery allows the orthopaedic surgeon to use a minimally invasive or percutaneous approach in order to minimize the additional trauma associated with surgical exposure of the fracture site, but it also results in a marked increase in the use of intra-operative fluoroscopic imaging.

For acquisition of fluoroscopic images, the C-arm is currently the imaging instrument of choice because it gives valuable in situ two-dimensional projection information on the relative position of surgical tools, bones, and implants. Nowadays, during closed IMN for femoral shaft fracture treatment, surgeons' usually drill the distal locking holes using the free-hand technique as describe in **Section 3.3**. However use of fluoroscopy for intraoperative guidance has some drawbacks, such as it may result in prolong radiation exposure to surgeons.

3.4.1 Prolonged radiation exposure to surgeons

The introduction of closed surgery has resulted in an increase in the use of intraoperative fluoroscopy during certain surgical procedures. One pitfall of this growing reliance on fluoroscopy, is an excessive radiation exposure to orthopaedic surgeons and patients [87-89], as according to the American college of Radiology (ACR), fluoroscopy gives some of the highest doses of diagnostic radiation to both patients and surgeons [90]. Therefore, there is a concern among orthopaedic surgeons about the increasing levels of exposure to radiation associated with intraoperative C-arm fluoroscopy [91-93]. The maximum permissible dose (MPD), recommended by the International Commission on Radiological Protection (ICRP), is 5,000mrem (or 50mSv) per year for the head, neck, trunk, eyes, bone marrow and gonads. Whereas, the maximum permissible dose (MPD) for the hands and feet is 50,000mrem (or 500mSv) per year [13, 91, 94]. During the closed IMN operation a lead apron provides adequate protections for the trunk and gonads of the surgeon but the surgeons' hands are more susceptible to radiation exposure due to their proximity to the primary radiation and lack of shielding[88]. Blattert *et al* [95] showed that the surgeon's hands were exposed to markedly higher doses, which ranges from 0-2.88 mSv and 0-11.94 mSv for senior and junior surgeon groups respectively compare to the measurements taken at the trunk and head which ranged from 0-0.27 mSv and 0-0.38 mSv for these groups. According to [85, 89, 95-99], the total radiation exposure time for femoral IMN, with proximal and distal locking, varies between 3.1 and 31.4min with distal locking alone occupying up to 30 to 50 percent of the total radiation exposure time [95, 97, 99].

A number of studies [13, 89, 93] have quantified the actual radiation exposure received by orthopaedic surgeons during IMN, and have proposed that the maximum number of permissible IMN procedures performed by a surgeon during one year period should be limited to between 247 and 750 as depicted by Table 3-1.

Author (Year)	Radiation dose (mSv)	Average fluoroscopy time (min) per operation	Maximum allowed IMN operations per Year
Coetzee (1992)	1.42	4.64	352
Muller	2.02	4.6	247
Sanjeev (2002)	1.27	1.61	394

Table 3-1 Radiation exposure during distal locking procedures.

Although reaching the yearly limit for hands' radiation exposure for an individual orthopaedic surgeon seems unlikely, however the long term effects of X-ray radiations and their relation to different types of cancer still remains unknown [100]. There is evidence that carcinogenic potential exists from low-dose, low-energy radiations [101]. Therefore, risk of significant intraoperative radiation to orthopaedic surgeons has been the impetus for many clinicians to develop surgical techniques and/or recommendations that would limit the need for fluoroscopy.

Furthermore, the use of two-dimensional X-ray images, to guide three-dimensional bone machining processes, means that a large number of X-ray images are required. As achievement of optimum positioning of fracture fixation devices involves a certain amount of trial-and-error and surgeons rely heavily on their hand-eye coordination during the entire procedure. Both the duration and outcome of the procedure are, therefore, highly dependent upon the skill and experience of the surgeon. In addition to this, bringing the fluoroscope into position to visualize the surgical manoeuvre often hinders the surgeon's access to the injured extremity [86, 102]. Also the importance of an experienced X-ray technician in the operating room cannot be underestimated, because the quality of the image and the frequent changes in the C-arm position around the patient directly influences total radiation exposure time.

3.5 Photogrammetry

According to the American Society for Photogrammetry and Remote Sensing (ASPRS), the term *photogrammetry* is defined as “the art, science, and technology of obtaining reliable information about physical objects and the environment through the processes of recording, measuring, and interpreting photographic images and patterns of [90]electromagnetic radiant energy and other phenomena” [103] or in simple terms “the science or art of obtaining reliable measurements by means of photographs” [104].

It is evident from the term “photogrammetry” that initially photogrammetric techniques were developed for camera-based applications, generally referred as “*classical photogrammetry*”. Although these classical techniques achieved high levels of accuracy, however the amount of unavoidable delay caused by film development process, and further delays which are incurred during reconstruction process that involved manual extraction of image coordinates from a pair of photographs, meant that these techniques are not suitable for real-time applications.

Recently, due to the huge advancements in the field of computer vision, PC-based frame grabber cards and CCD video cameras are easily available at low price. By using these PCI-bus frame grabbers with digital image processing, algorithms allows both the acquisition and analysis of digital images in almost real time. Due to the nature of digital images the automation of data processing is an inherent characteristic of digital photogrammetric data processing thereby eliminating problems, such as lengthy film development process and manual reconstruction associated with “*classical photogrammetry*”. Also by using digital images, image enhancement can be applied hence making “*digital photogrammetry*” a viable option for real time or on-line applications [105, 106].

Photogrammetry tries to reconstruct 3D object from its two or more 2D images; for example, the image of an object consists of the “projections” of all object points through “lines-of-sight”, therefore, the image plane is just a section of this bundle of rays in space. Although, along every “line-of-sight” a corresponding object point can be determined, but since all the space points along each “line-of-sight” will be

projected at the same point on the image plane, therefore, this determination is not unique and the 3D coordinates of the object point cannot be determined. However, by introducing another image of the same object from a different view as shown in Figure 3-20, the object point will be uniquely defined as the intersection of the two corresponding rays, additional images of the object point will result in more rays, but the point will still be the unique intersection of all the rays.

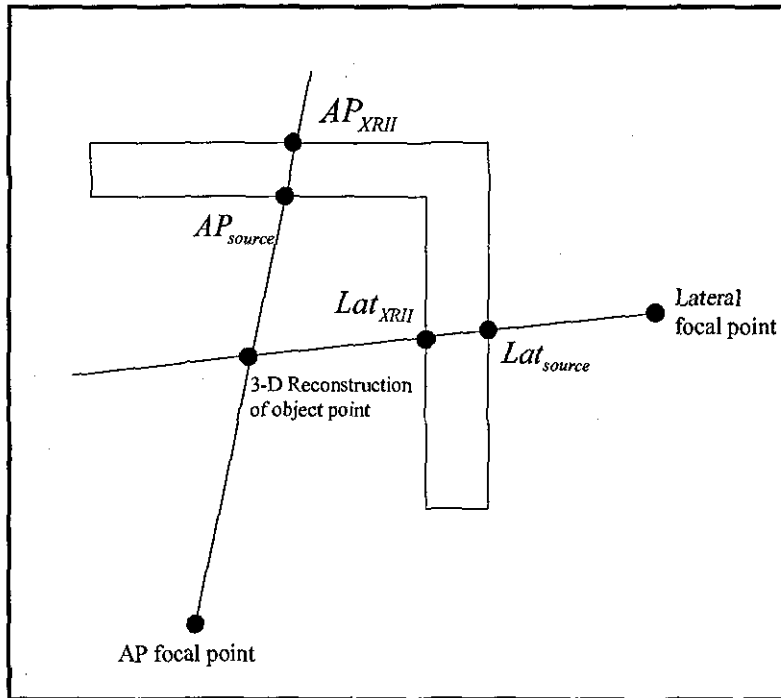


Figure 3-20 3D reconstruction of an object point using Γ Frame [3].

The most important feature of photogrammetry is the fact, that the objects are measured without being touched. Therefore, photogrammetry's primary advantage in the medical field is because of its reliance on imaging; as an imaging technique, it offers short patient involvement times as well as avoids contact with the patient and thereby avoids the risk of deforming the area of interest and spreading infection [107]. Moreover, image acquisition is generally a simple process, using standardized equipment that is not daunting to patients, such as the C-arm image intensifier for taking X-ray images during distal locking. Nowadays the term "remote sensing", is also being used by some authors instead of photogrammetry.

3.5.1 X-Ray Photogrammetry

The basis for X-ray photogrammetry is the central projection of a bundle of X-rays from a focal point (i.e. X-ray source, located in the x-rays generating tube) through an object and onto the film plane. Figure 3-21 shows the schematic of the relationship of the perspective centre i.e. X-ray source, the image plane and the imaged object. Since, the imaged object lies between the focal point and the film plane as in the case of back lighting photography technique. The image is therefore larger than the object being x-rayed. The extents of this magnification depends upon the ratio of the source-to-object and source-to-image distance, and as a result object points nearer to the X-ray source experience more magnification in comparison to the objects points nearer to the image plane, this phenomenon is commonly known as “*perspective distortion*”.

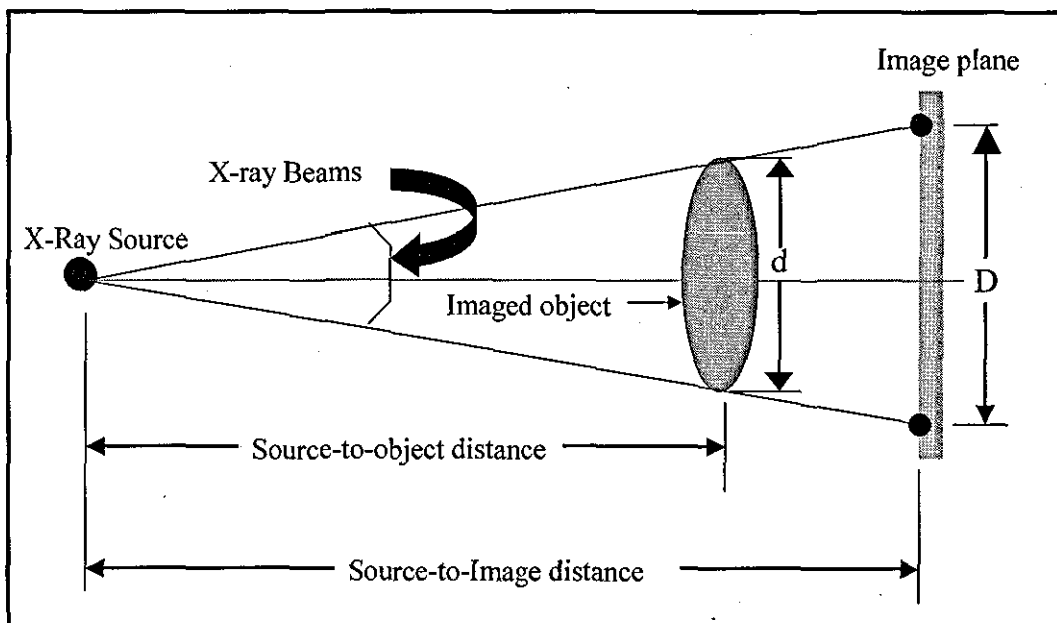


Figure 3-21 X-Ray image formation process

Close range photogrammetry

The term “*close range photogrammetry*” is used to describe photogrammetric applications in which the extent of the object to be measured or analyzed is less than 300 meters away from the camera [106, 108]. Since, during the distal locking of an intramedullary nail, the distance of the object (intramedullary nail) and camera (X-ray tube) is always less than 300 meters, therefore, it belongs to the close range photogrammetry application. The results of close range photogrammetry must

generally be made available very quickly after acquiring images, so that they can be used for further processing related to the measured object. In this study the drilling trajectory must be provided to surgeons intraoperatively, shortly after acquisition of X-ray images, so that drilling of distal locking holes can proceed.

3.6 Fluoroscopy

Fluoroscopy is an imaging technique that takes live X-ray images of the body by passing a continuous X-ray beam through the object being studied using a fluoroscope. A fluoroscope, shown in Figure 3-22, utilizes an *X-ray tube* and fluorescent screen, with the object to be studied placed between the screen and the tube. This immediate imaging, when coupled with an image intensifier, is invaluable in several intraoperative medical applications such as neurosurgery, bone fracture treatment etc.

In the past, traditional fluoroscopy employed a simple fluorescent screen to produce instantaneous X-ray images. The fluorescent screen consists of a plastic base coated with a thin layer of fluorescent material, which in turn is mounted onto a lead glass plate. The lead glass plate was used to provide protection from radiation. The resulting images can be viewed directly through the glass plate. However, low brightness of the resulting images meant it could only be viewed in a darkened room [109]. Therefore, modern fluoroscopy employs a device called "*image intensifier tube*", in order to produce a brighter image than that of a simple fluorescent screen.

Since fluoroscopy is a primary radiographic technique during several intraoperative orthopaedic surgical procedures. Therefore, an imaging system is required that does not clutter the operating theatre environment, i.e. an imaging system that can be easily manoeuvred, facilitate wide range of projection angles and does not obstruct the surgeon's access to the patient. Therefore, manufacturers of medical imaging equipment have developed mobile C-arm units, which are specific for use in operating theatres. As shown in Figure 3-22, the mobile C-arm employs a counterbalanced C-arm geometry and a wheeled base unit. The X-ray tube and image intensifier housings are placed at a fixed distance from each other on opposite ends of the C-arm arc.

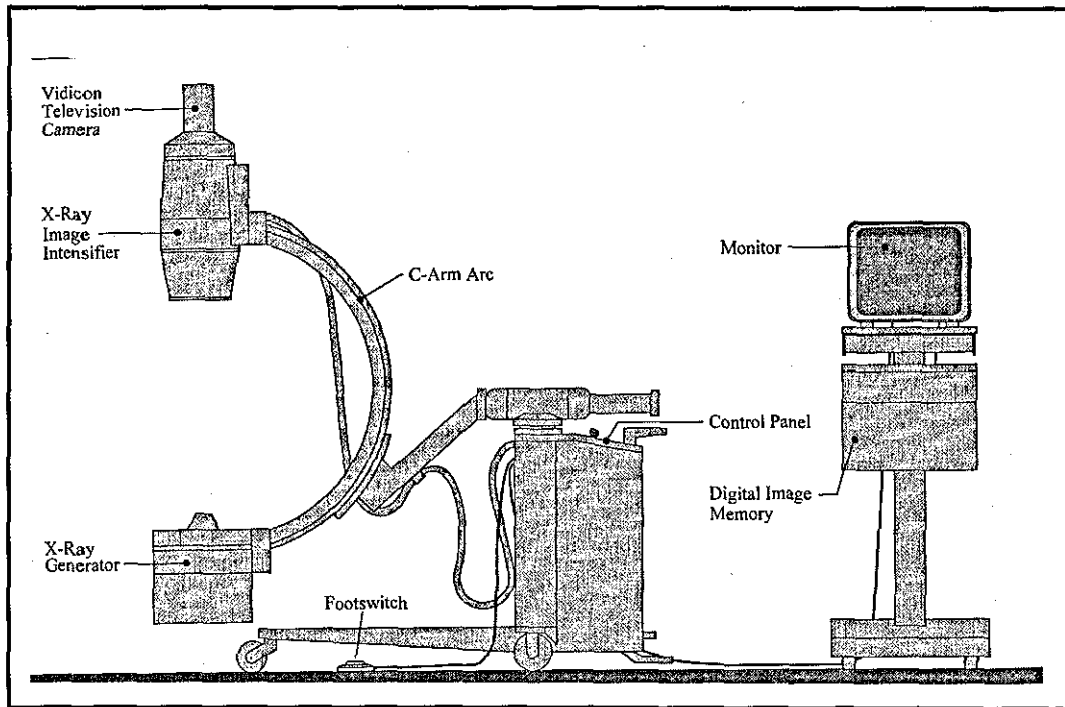


Figure 3-22 Siemens Siremobil 2 Mobile X-ray image intensifier [78]

Details about the working mechanisms of X-ray tube and image intensifier are given in APPENDIX D.

X-ray images obtained from the image intensifier tube inherent different forms of image distortion, such as pincushion distortion and vignetting. These are discussed below.

3.6.1 Pincushion distortion

Image distortion due to photocathode curvature is generally referred as *Pincushion distortion* [110]. Spatial distortion observed in the displayed fluoroscopic image obtained from image intensifier tube is mainly due to the focusing of accelerated electrons from the curved input fluorescent screen onto a curved photocathode surface, followed by mapping onto a flat output window. The central electrons are therefore more accurately focused than the more peripheral ones. The peripheral electrons also tend to flare out from their ideal course. This mapping causes larger object magnification at the periphery of the image than at the centre of the image and thus pincushion distortion arises, as shown in Figure 3-23. The pincushion distortion is dependent on the X-ray source-to-image intensifier distance.

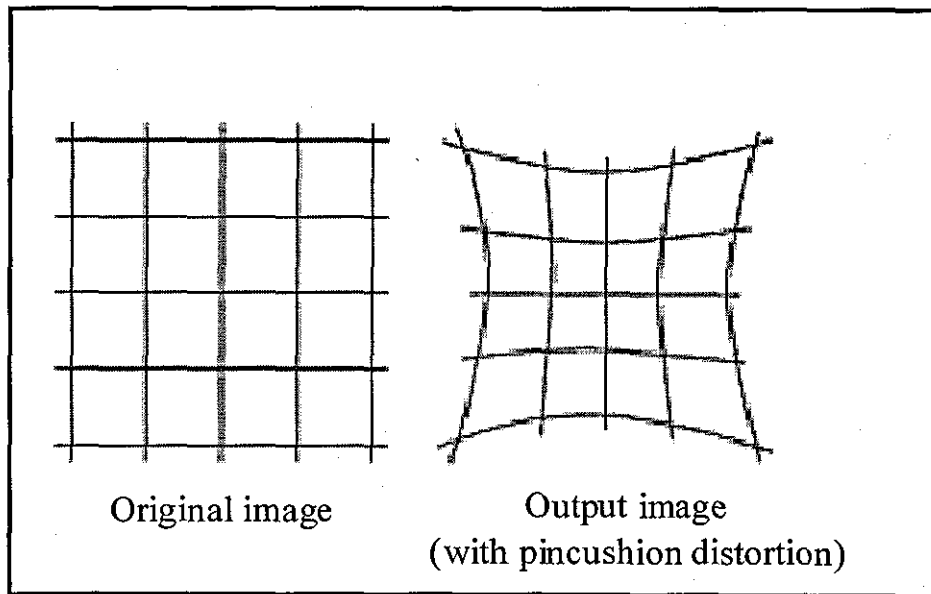


Figure 3-23 Pincushion distortion caused by X-ray Image intensifier.

Generally, correction for pincushion distortion in detectors is achieved by imaging a regular calibration grid, consisting of small ball bearings [111, 112], which represent the control points, and are used to compute the correction coefficients. An interpolation function, either global or localized, is then used to provide the mapping between input (undistorted) and output (distorted) pixel locations. Since, for the image intensifier only data related to output image is available, therefore, input (undistorted) data is usually obtained by acquiring a reference image of the calibration frame (usually, containing a repeating grid pattern). The calibration frame is placed as near as possible to the image intensifier window, to obtain the sharpest possible edges.

3.6.2 Vignetting

In addition to pincushion distortion, a fluoroscopic image also suffers from brightness non-uniformity, with the centre of the image being brighter than the periphery. This image distortion phenomenon is generally referred to as *Vignetting*. It occurs as a direct consequence of pincushion distortion as the increased magnification at the edges of the image means that a given area element (i.e. a grid square) is projected onto a larger area at the periphery of the image. The increased size of the element area leads to a corresponding decrease in intensity, since the X-ray beam is spread over a larger area [78].

3.6.3 Geomagnetic Distortion

Geomagnetic distortion or S- distortion, shown in Figure 3-24, is introduced by the electron optics of the image intensifier and their interaction with external magnetic fields, mainly with the earth magnetic field. When an electron travels through a magnetic field, it experiences an induced force which, in accordance with *Lorentz force law*, acts at right angles to both its velocity and the magnetic field. In the case of the image intensifier tube, this induced force deflects electrons from their true trajectories and therefore represents an additional source of image distortion [3]. The geomagnetic distortion effect does depend on the orientation of the image intensifier in the earth's magnetic field, and changes considerably in pattern and magnitude as the position of the image intensifier is changed during its rotation [111]. Therefore, in order to achieve distortion correction of geomagnetic distortion, spatial orientation of the C-arm must be taken into account. When the image intensifier tube is parallel to geomagnetic field, a magnetic field component parallel to the image intensifier affects velocity of radial electrons velocity in the image intensifier, which causes a rotation of the image.

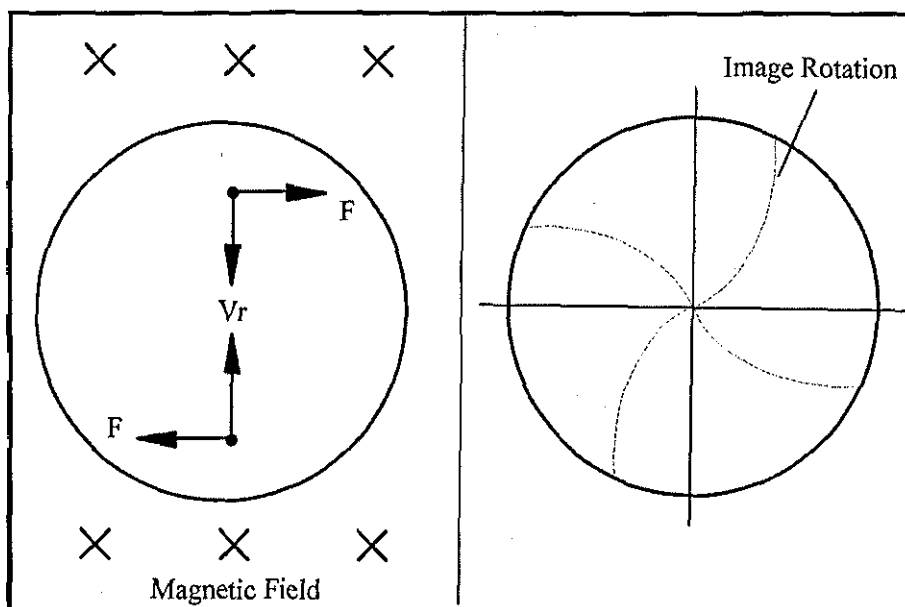


Figure 3-24 S-distortion when Image intensifier is parallel to magnetic field [78]

Whereas, when the image intensifier tube is perpendicular to the geomagnetic field, a transverse magnetic field component acts on the longitudinal velocity of electrons that translates the image as shown in Figure 3-25.

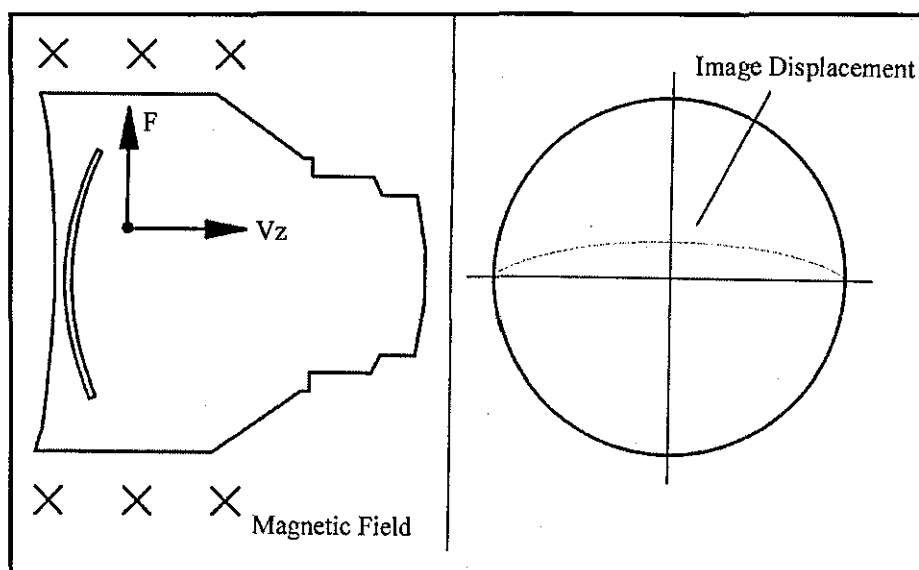


Figure 3-25 S-distortion when Image intensifier oriented transverse to the magnetic field [78]

In addition to the geomagnetic distortion effect, the possibilities of additional magnetic influences in the operating room cannot be overlooked. The image intensifier housing of the C-arm unit is by necessity frequently placed in close proximity to large metallic objects, for example the operating table. Therefore, electromagnetic interferences caused by operating room equipment are also widely acknowledged as being a significant problem. In relation to the mobile C-arm fluoroscopy unit, these magnetic-related image distortion effects are therefore highly unpredictable and, as such, can not be modelled off line i.e. preoperatively.

3.7 Distortion Correction of X-ray Images

In order to be able to extract quantitative data from the X-ray images, distortion correction is needed. For a distorted image, two types of corrections are used, namely: global correction methods and local methods. Both local and global methods have their advantages and disadvantages, which are discussed in the following section.

3.7.1 Global distortion correction approach

While applying a global approach, it is assumed that the image distortion is uniform i.e. symmetrical; over the entire field-of-view, therefore, a global polynomial function of a high-order polynomial, usually a 4th or 5th-order polynomial is used to determine a relationship between the output (distorted) and input (undistorted) image

coordinates [32, 110, 113]. Since, in the case of the image intensifier, only data pertaining to the distorted output image is available, therefore, the "input image" data is usually created by acquiring a reference image of a calibration target containing a repeating grid pattern. It is standard practice for this calibration target to be placed as near as possible to image intensifier input window to ensure a sharpest possible image as well as simulating the image plane. A dewarping function is then calculated by comparing the locations of the centres of the calibration markers (i.e. fiducials) of the input image with their projected locations in the output image. However, the resulting dewarping function is only valid for a specific gantry angle (i.e. specific orientation of the C-arm), for which the output image is taken, whereas usually fluoroscopy during surgical procedures involves the arbitrary panning and scrolling of the image intensifier, and, it is not always possible to use a standard gantry angle for many oblique fields. Consequently, the global methods do not allow correction of local distortions that may appear in the acquired image and require an excessive calibration of the system. Therefore, a method of distortion correction is required that is applicable to any arbitrary orientation of the image intensifier.

3.7.2 Localized distortion correction approach

Previous research has shown that image distortion is non-uniform across the entire image, thereby application of the global distortion correction approach results in errors and occasionally can also result in unacceptably high errors. One way to avoid high errors is to use a localized distortion correction approach [111]. In localized distortion correction methods, the image is divided into many small areas (usually rectangular or triangular) and then distortion correction interpolation functions are found for each localized area. Localized correction can also be very effective in correcting geomagnetic distortion, which depends upon orientation of Image intensifier.

One of the main criticisms for the localized approach is that although, localized approach results in better distortion correction of X-ray images in comparison to the global approach, it also results in lengthy computational time, as before correction can be applied, it is necessary to identify the triangular/rectangular region for each reference markers whose coordinates are to be corrected. However, with recent

advancement in processing speeds, it only results in delay of milliseconds, which can easily be overlooked due to the advantages of the localized method. Furthermore, the discontinuities occurring along the edges of the neighbouring regions, where different correction equations are used, represent the major problem in localized correction methods. However, in this study while applying the localized approach for distortion correction, it has been made sure that there are no discontinuities along the edges of neighbouring regions, by only selecting reference markers, for triangulation, that are in middle of the calibration frame, and not at the edges.

3.8 Robotic/Computer Assisted Orthopaedic Surgery (RAOS/CAOS)

Orthopaedics is particularly well suited for RAOS/CAOS, as the bones and *periarticular* soft tissues (i.e. tissues surrounding a joint) can be evaluated easily and accurately by diagnostic technologies such as radiographs. The bony and soft tissue structures can subsequently be reconstructed to create three-dimensional images. These images can then be used for simulating surgical procedures.

Intraoperative complications during distal locking of intramedullary nails have prompted research in RAOS/CAOS to improve the accuracy of this fluoroscopy-based orthopaedic procedure. Inserting the screw for locking the nail is an example of implementing "*The Basic Orthopaedic Principle*" [85].

RAOS/CAOS can thus be defined as the application of computer-based technology which aims to assist surgeons in improving their free hand capabilities during surgery, and thereby, allowing surgeons to perform more accurate and minimally invasive techniques, which in turn results in substantial reduction in intraoperative irradiation and an improvement in the overall outcome of surgical treatment [114, 115].

3.8.1 Hull University Robotic Assistance Orthopaedic Surgery System

Phillips *et al* [113, 116, 117] developed a prototype robotic assisted orthopaedic system (RAOS) to assist surgeons in distal locking of intramedullary nails. The RAOS comprises of the following equipment:

RAOS trolley: It contains a PC-based computer system, a separate computer system for an optical tracking system (Optotrak), monitor, keyboard, mouse, and a frame grabber to obtain video feed from C-arm image intensifier.

Optotrak: It is an optical tracking system that uses two CCD camera array to track the position of Infrared LEDs in a 3-D space. The central co-ordinate system for the RAOS, known as *operating theatre* (OT) space, is based around the Optotrak.

End-effector: The end-effector is in the form of a drill bit guide, it is held by a passive lockable arm. Passive arm is rigidly mounted on the side bar of the operating table. For optical tracking, the end-effector is fitted with an arrangement of seven Infrared LEDs. The end-effector is used to position an H-shaped registration phantom and drill guide.

In order to determine the drilling trajectory for the distal locking holes and its implementation, RAOS comprises of three independent modules (shown in Figure 3-26), namely:

- Intelligent image intensifier,
- Trajectory tactician and
- Intelligent trajectory guide.

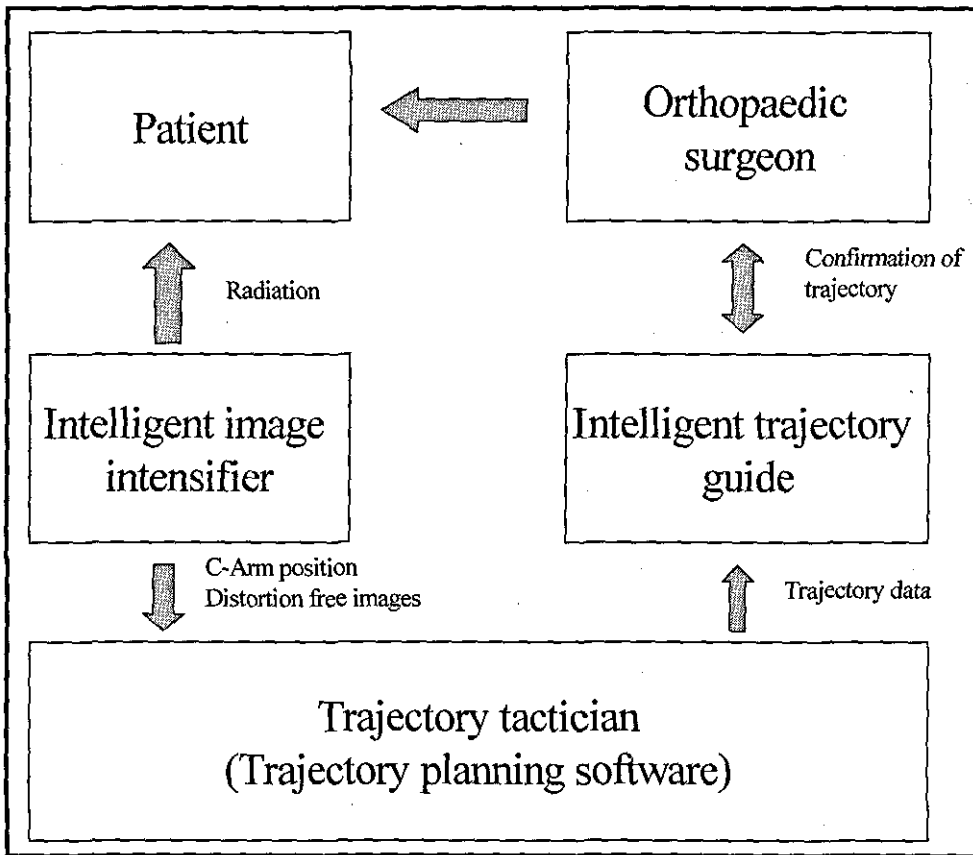


Figure 3-26 Overview of RAOS developed by Hull University [113].

3.8.1.1 Intelligent image intensifier

The intelligent image intensifier has been used to provide distortion free X-ray images of the operation site using the globalized distortion correction approach, i.e. by creating a mapping between the displayed (distorted) output image and a hypothetical (undistorted) input image for the correction of image distortion. This distortion correction is achieved by using a phantom (radiolucent calibration plate equipped with Infrared LEDs) that is placed against the input window of the image intensifier housing. This phantom contains a grid of 64 X 64 ball bearings which when imaged, allows an image dewarping function to be derived. By applying this dewarping function to subsequent intraoperative images, the RAOS system defines distortion correction for each pixel of the image. For this calibration and all subsequent measurements, this calibration plate, referred to as "virtual screen"[113], is used to define the location of the image intensifier.

3.8.1.2 Registration Strategy of RAOS

In order to allow 3-D reconstruction of features appearing in both AP and Lateral X-ray images, it is essential to determine the position of the X-ray source in terms of image intensifier space. Therefore, registration of the X-ray source with the image intensifier space is obtained by placing a phantom (an H-shaped calibration frame) in the fluoroscopic image using an optically tracked end-effector as shown in Figure 3-27.

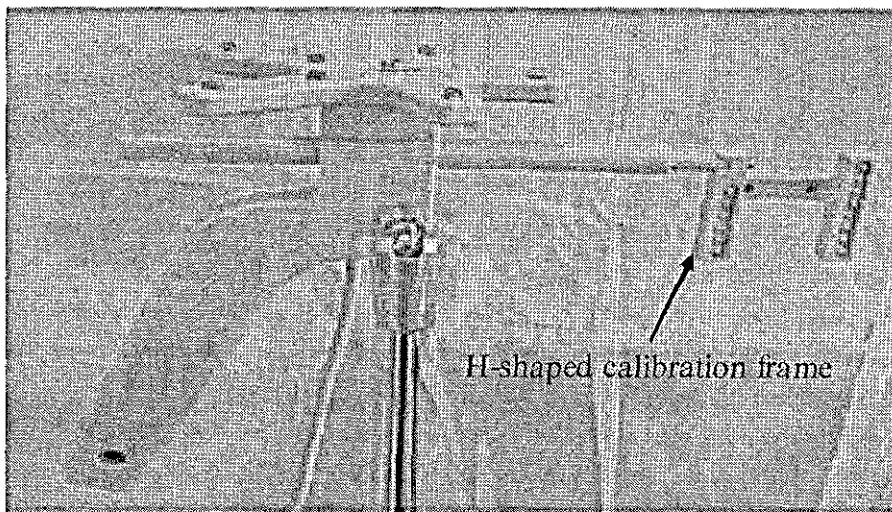


Figure 3-27 End-effector holding the calibration frame [116].

The phantom is placed as far away from the image intensifier as possible because as the distance of the phantom from the X-ray source increases, the pixel/mm ratio decreases i.e. a small error in pixels will cause large reconstruction errors in millimetres. Therefore the phantom position is chosen as close to the X-ray source as possible, provided that a minimum number of fiducials required for the X-ray source location are visible. For each visible marker on the phantom, a line-of sight which passes through each radiopaque fiducial marker and its corresponding imaged point (transformed into virtual screen coordinates) can then be reconstructed. Intersecting these line-of-sight results in the determination of the X-ray source location with respect to the image intensifier space.

Since the virtual screen must be removed while taking diagnostic Lateral and AP view X-ray images to avoid splattering of the image by calibration markers. Therefore, the

registration of the image intensifier with the OT coordinate space is established by attaching infrared diodes onto the image intensifier. The 3-D position of these diodes allows a transformation matrix between the image intensifier space and OT space to be calculated. Those infrared diodes attached during registration to the image intensifier remain attached throughout the distal locking procedure. The use of Optotrak, to continuously monitor the location of the image intensifier allows the mobile C-arm unit to be freely moved without invalidating registration, as long as the infrared diodes mounted on the image intensifier housing remain clearly visible to the Optotrak. Having measured the image intensifier position with respect to the OT space, the corresponding X-ray source position is determined in terms of the OT coordinate system by using the transformation obtained by calibration process. Knowledge of the X-ray source and image intensifier locations in terms of the OT space, then allows 3-D reconstruction of the features appearing in both AP and Lateral X-ray images. However, this registration can be invalidated by patient motion.

3.8.1.3 Trajectory tactician

A trajectory tactician (a procedure specific software module) has been used to select the surgical trajectory. This software extracts features of interest from the operation site and uses their location to calculate the 3-D trajectory required for locking screws. It requires the reconstruction of three geometrical positions:

1. Location of the long axis of the intramedullary nail,
2. The angle of rotation of the intramedullary nail about its long axis and
3. A point on the intramedullary nail axis, which corresponds to the centre of the distal locking hole.

Location of the long axis of the intramedullary nail

- In order to locate the long axis of the intramedullary nail in terms of the OT space, intramedullary nail edge boundaries are interactively extracted from both the Lateral and AP X-ray images as shown in Figure 3-28 and Figure 3-29 respectively.

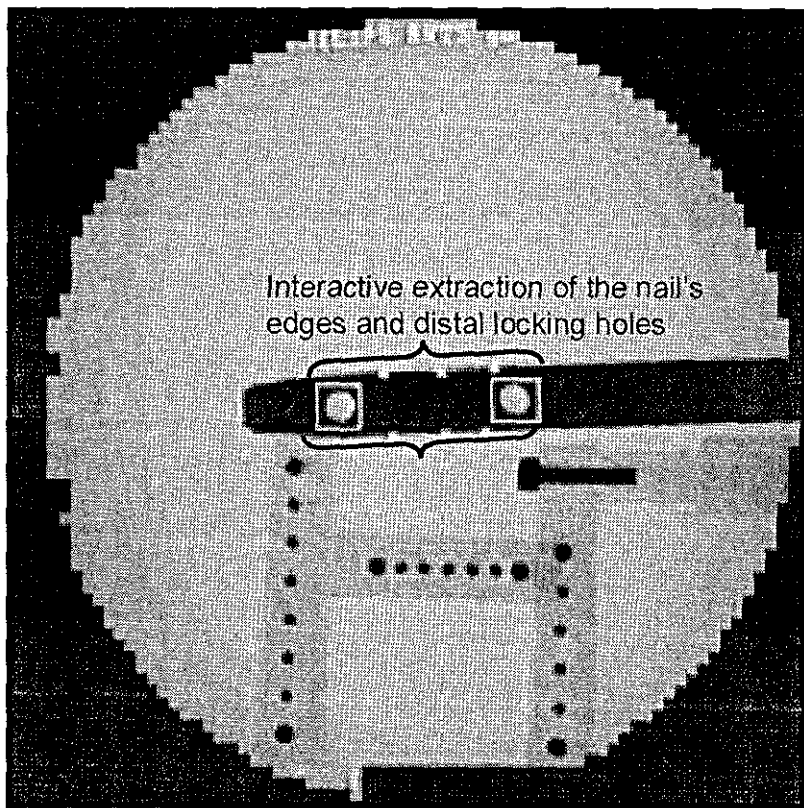


Figure 3-28 Lateral view image [116].

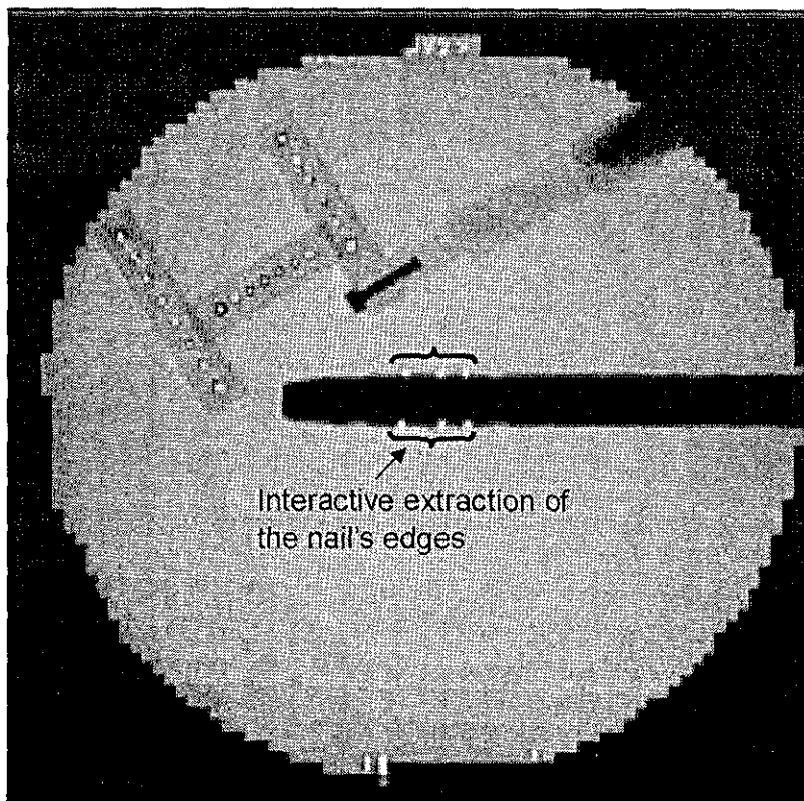


Figure 3-29 AP view image [116].

- In each view, bisecting the two nail boundaries results in 2-D projection of the nail axis, which when combined with a known source point for that particular view, allows a projection plane that passes through the actual nail axis to be defined.
- After such projection planes are defined in the Lateral and AP images, their intersection defines the nail axis in terms of the OT space as shown in Figure 3-30.

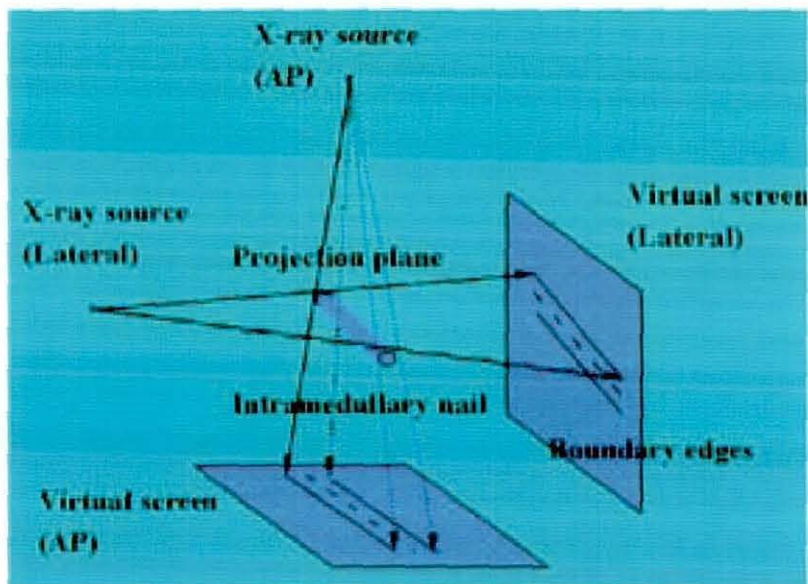


Figure 3-30 Location of the long axis of the intramedullary nail [116].

Determination of the nail angle of rotation about its long axis

- An area of interest (A.O.I), containing hole profile is interactively selected from the Lateral view image as shown in Figure 3-28.
- A gradient-based edge detection algorithm is then applied to segment the boundaries of the hole.
- The hole is then mapped onto a spherical surface i.e. Best fit approach, in order to compensate for perspective distortion (i.e. distortion resulting from central projection, experienced by all forms of radiography. It occurs when points nearer to the X-ray source experience more magnification than points on the opposite i.e.

points on the image plane side of the object). The major axis of this corrected hole is then measured using least square optimisation technique.

- Comparing major axis measurement with a mathematical model [117], designed for registration of the nail geometry, allows the desired angle of rotation to be determined.

Derivation of a point on the nail axis, which corresponds to the centre of the distal locking hole

The centre of mass of the oval area is also the projection of the centre of the distal hole in 3-D space. Therefore, the centre of the distal locking hole is then determined in terms of OT space as the intersection of the nail axis with the line-of-sight joining the oval centre on the virtual screen with the X-ray source location.

3.8.1.4 Registration of the passive manipulator with OT space

As with the intelligent image intensifier, there is a registration set-up step that determines a transformation matrix between the coordinate space of intelligent trajectory guide and OT space. The passive manipulator has optical encoders incorporated into each of its joints. The passive manipulator is then registered with OT space by using the Optotrak to locate a group of IR-LED's mounted on an especially designed end-effector.

3.8.1.5 Intelligent trajectory guide

Having established intra-operative registration, the intelligent drill guide is then used to align a drill guide with the optimal trajectory. The surgical guidance system comprises a custom built, passive manipulator arm, and a real time graphical display. The graphical display, on a monitor, gives visual cues to the surgeon about the relative difference between the actual position of the surgical instrument attached to the passive arm and the required trajectory. The surgeon is therefore required to manipulate the passive arm until the displayed drill guide location is coincident with the displayed trajectory. An electromagnetic braking system then allows the arm to be locked in position, prior to manual completion of the drilling process. It is claimed

that the intelligent trajectory guide shows a maximum deviation of 0.25mm in placing the surgical instrument along the given trajectory.

3.8.1.6 Summary of Hull robotic assisted orthopaedic system

This system does not depend on obtaining a perfect circle image. However, the main disadvantage with this system is the need for a 3-D line-of-sight optical tracking system (Optotrak). Use of optical tracking equipment clutters the operating theatre environment and requires care in maintaining the line-of-sight. Furthermore, the system is user dependent, as identification of the nail boundaries is accomplished interactively by selecting 6 points in each view, and region containing the oval shaped distal hole projection is also cropped manually.

3.8.2 Hebrew university Robotic Assistance Orthopaedic Surgery System

Joskowicz *et al* [118, 119] at Hebrew University, Israel have developed a robot-based system to assist orthopaedic surgeons in performing distal locking of the intramedullary nail during femoral shaft fracture treatments. The system consists of:

- Sterilized robotically controlled targeting device,
- An image calibration ring for distortion correction of fluoroscopic images.

3.8.2.1 Robotically controlled targeting device

The robotically controlled targeting device, shown in Figure 3-31, consists of:

- A miniature robot, named "MARS". MARS is a $50\text{mm} \times 50\text{mm} \times 70\text{mm}$ parallel manipulator of 150grams in weight with 6 Degree-of-freedom.
- A robot base plate, used to mount the miniature robot. The length of this plate is adjustable, so that it can be adjusted to roughly equal with the length of the intramedullary nail, and
- A targeting guide, which is mounted on the top of the robot. It consists of a *head*, *connecting block* and a *targeting drill guide*. The head is mounted directly on the

robot top. Both the connecting block and the targeting drill guide are made of radiotransparent Derlin. The targeting drill guide is $40\text{mm} \times 55\text{mm} \times 15\text{mm}$ block with two guiding holes. The two guiding holes are 30mm apart similar to the spacing between to distal locking holes. For the spatial localization of targeting drill guide, it has been embedded with 32 stainless steel fiducials (each of 2mm diameters).

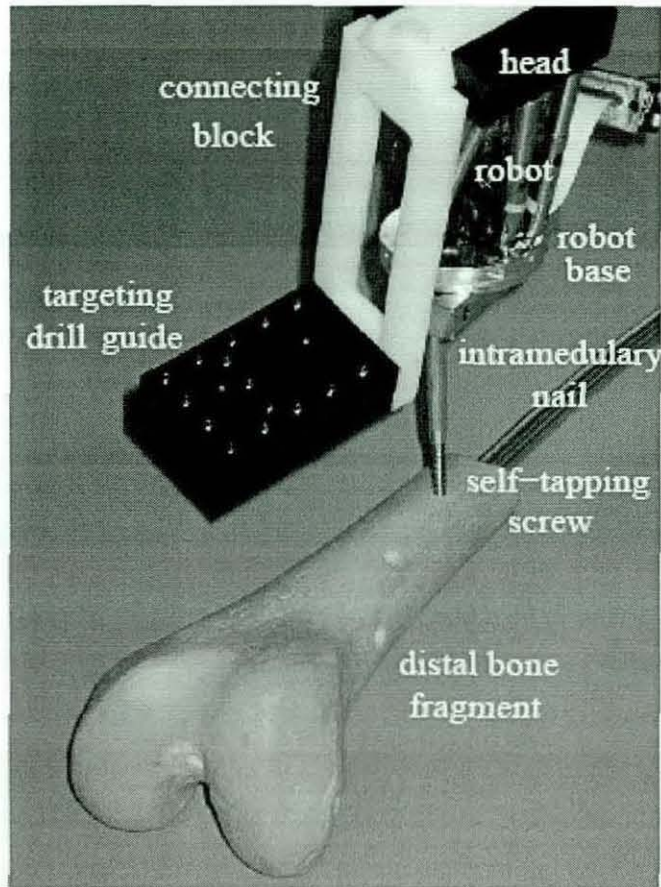


Figure 3-31 Bone mounted MARS robot carrying the targeting drill guide [119]

3.8.2.2 Image Calibration ring (FluoroTrax)

The image calibration ring is a C-arm calibration phantom which attaches to the C-arm's image intensifier as depicted by Figure 3-32. It consists of two parallel radiotransparent calibration plates. These plates are 76mm apart from each other, and are embedded with 120 fiducials of 2 and 3mm diameters. The small fiducials having a spacing of 20mm are arranged in a regular Cartesian grid pattern, whereas all 21

large fiducials (i.e. of 3mm diameter steel balls) are all embedded onto upper the calibration plate and form a U-shaped pattern.

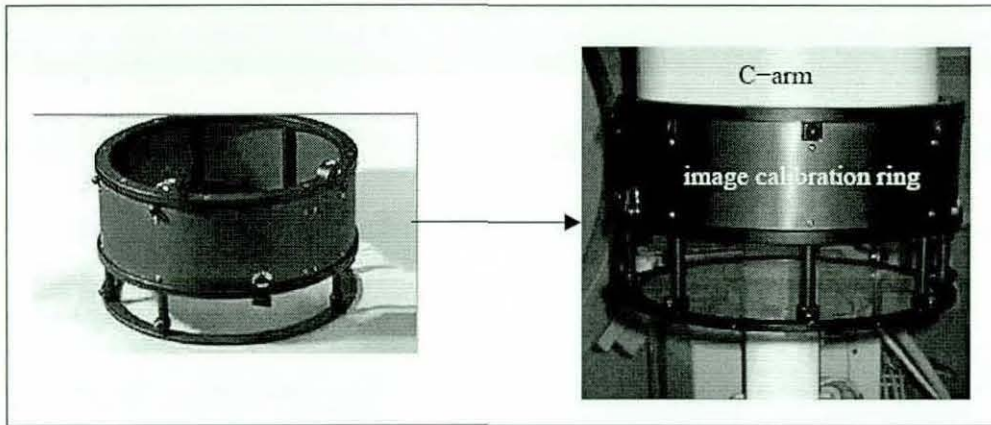


Figure 3-32 FluoroTrax attached to C-arm's image intensifier [118]

3.8.2.3 Surgical procedure

The surgical procedure employed is as follows:

- Once the nail has been inserted to its desired position, the image calibration ring (FluoroTrax) is mounted on the C-arm image intensifier.
- The robot is then rigidly placed in the vicinity of the distal locking holes by either mounting it to the distal bone or the nail's head.
- Distal bone mounting of the robot is achieved using a Lateral X-ray image showing the distal locking holes, the surgeon determines the location of two self-tapping screws onto which the robot base will be mounted. The location is selected such that their axis is roughly parallel to the axes of the distal holes and in close proximity of the distal locking holes. The surgeon then using a hand held jig drills two parallel pilot holes along the nail axis. The screws are then fastened to mount robot base on them as shown in Figure 3-31.
- Intramedullary nail head mounting of the robot is accomplished using a U-shaped adaptor. One end of a U-shaped adaptor is directly screwed onto the nail's head, whereas the other end is used to mount the robot base plate. It is claimed that this fixation is rigid unless the bone is osteoporotic.

- The targeting drill guide is then mounted on the robot top base as shown in Figure 3-31.
- Orientation of the C-arm is then adjusted until the distal locking holes appear, as near perfect circles in the Lateral X-ray image. This is being done, so that later on axes of the distal locking holes can coincide with the axes of two guiding holes on the targeting drill guide.
- Once, the perfect circle image is obtained, an intraoperative X-ray image is acquired as shown by Figure 3-33.

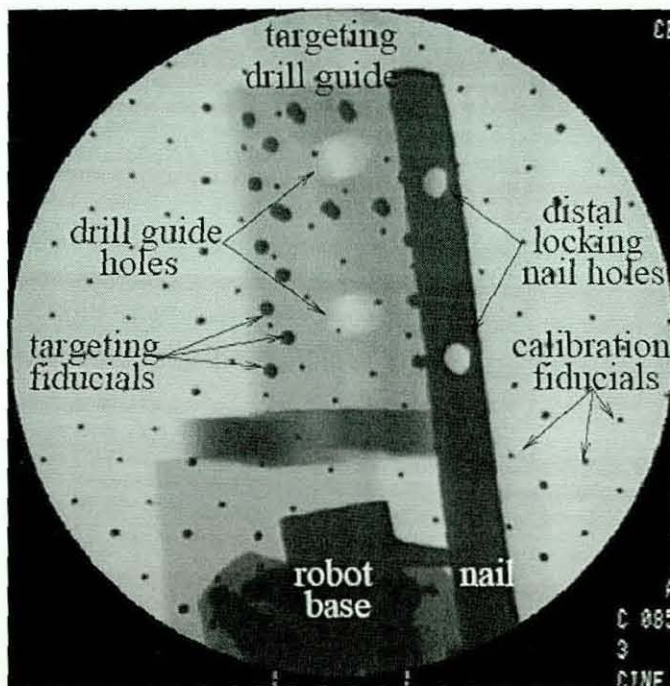


Figure 3-33 Typical intraoperative X-ray image [119]

- Distortion correction of the intraoperative image is then carried out in the following manner:

At first, a background image is obtained by morphologically removing fiducials from the intraoperative X-ray image, by using a median filter on the intraoperative image. Since, the grey level values of the pixels occupied by fiducials in the intraoperative image are lower than that of the background image, therefore, after subtraction grey level values of pixels occupied by fiducials will be negative, and hence these pixels are potential candidate for fiducial location. Two circle templates are then created one

for small fiducials (2mm diameter) and other for large fiducials (3mm diameter). Fiducial's cluster recognition is then accomplished using two circle templates, with each cluster defining the location of an individual fiducial. The center of the fiducial is determined by finding the center of mass, of the cluster defining a fiducial. The large fiducials forming a U-shape pattern are identified by analyzing the weight of each cluster (i.e. number of pixels forming the cluster). Once the fiducials have been detected, a dewarping function is then determined for the entire image (i.e. Global approach) by comparing the locations of the fiducial centres of input image with their projected locations in the image.

- Camera calibration is then carried out to determine internal (focal length or principal axis distance, image centre co-ordinates, horizontal and vertical pixel scales) and external camera (location of X-ray source) parameters.
- The targeting drill guide is then localized by identifying its fiducials and their pattern in the image. Two orthogonal pairs of parallel lines define the targeting drill guide pattern as shown in Figure 3-34.

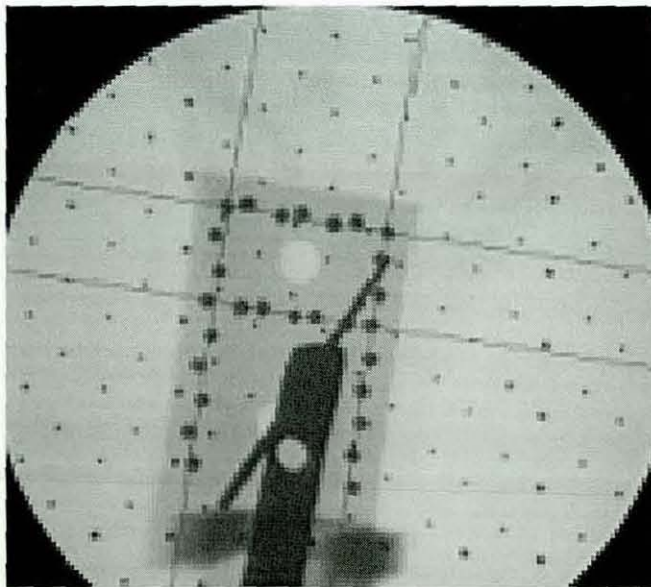


Figure 3-34 Targeting drill guide identification [119]

- In order to locate the distal locking holes, at first the nail's edges are detected using the canny edge detector, then location of the distal locking holes is determined by running a parallelepiped window within the nail contour, as

illustrated by Figure 3-35. The size of the parallelepiped window is equal to that of the nail width.

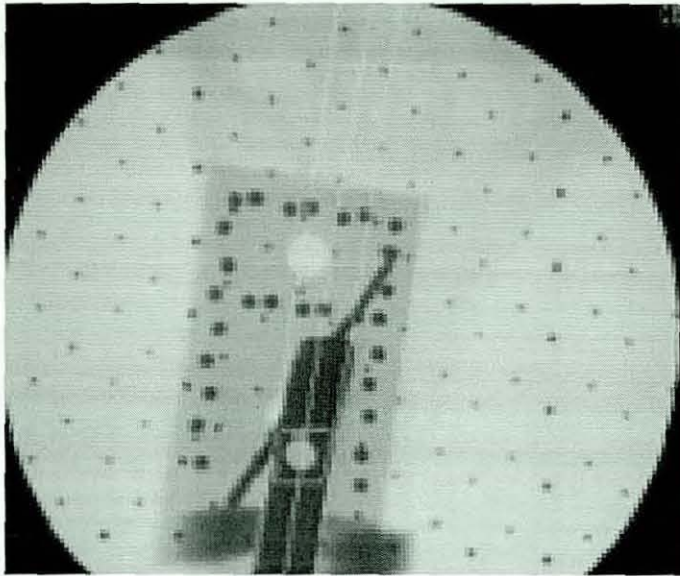


Figure 3-35 Distal locking hole identification [119]

The transformation that will make the axes of the guide holes and the axes of the distal locking holes coincide is then obtained in following manner:

- As the targeting drill guide is pre-calibrated, therefore, the transformation from the robot's coordinate system to the targeting drill guide is known.
- Whereas, the transformation between the targeting drill guide and the C-arm X-ray source (i.e. the Lateral X-ray source with respect to drill guide co-ordinate system) is determined from the external camera parameters (i.e. spatial position and orientation of X-ray source) and known geometry of targeting drill guide.
- Then, in order to ensure that the axes of the guide holes and the axes of the distal locking holes coincide, the robot is oriented in such a way that both the axes of the guide holes and imaging axis of the C-arm are aligned. The guide hole axis is defined by the centre of drill guide hole and the Lateral focal point, which are both known in terms of drill guide coordinate system. The C-arm imaging axis is defined by the centre of distal locking hole and the Lateral focal point, in this way it is ensured that the axes of the guide holes are parallel with the axes of the distal

holes, as the axes of the distal holes are already in alignment with the imaging axis due to the perfect circle approach.

- Then the guide holes are translated until their centres coincide with those of the distal locking holes i.e. when the centre of the guide holes coincide with the centre of the distal locking holes, since both are known in terms of the drill guide co-ordinate system using triangulation technique (described in section 4.4) in the Lateral view X-ray image.

It is claimed that the system yields a worst-case deviation of 1.5mm and 2° between the axes of the drill guide holes and the axes of the distal holes at the screw entry point.

3.8.2.4 Summary of Hebrew University RAOS

By mounting the robot directly on the patient's bone this system eliminates the need for leg immobilization and real-time tracking. However a rigid attachment of the miniature robot to the bone is absolutely essential. This system has some drawbacks. There is a reliance on the perfect circle approach. A globalized approach is used for distortion correction, which does not allow correction of local distortions that may appear in the acquired image.

3.9 Computer Assistance Orthopaedic Surgery

As discussed earlier the use of fluoroscopy for intraoperative guidance has some drawbacks such as excessive irradiation to operating room personnel and lack of spatial information. Therefore, nowadays in order to overcome these problems there is trend of applying virtual fluoroscopy/ surgical navigation technique in orthopaedic surgery, especially for distal locking of the intramedullary nail for treating femoral shaft fractures.

Nolte *et al* [12, 120] developed a computer-assisted free-hand navigation system that uses intraoperative X-ray images as a basis for real-time navigation of surgical tools. It separates image acquisition from the surgical procedure. The system consists of the following equipment:

- An optical tracking system, which emits and receives infrared signals,
- A computer unit and monitor,
- Optically tracked calibration grid attached to the image intensifier of the C-arm,
- Optically tracked frames placed on implant and surgical tool.

The basic principles of virtual fluoroscopy are distortion correction of fluoroscopic images and real-time tracking. During surgery, X-ray images of the bone being operated are acquired, for each image the position of patient/implant and the C-arm are recorded. During surgery the position of the surgical instrument and the bone are optically tracked via Infrared LEDs attached to them. This allows the software to produce virtual fluoroscopic images by overlaying real time positioning of the surgical tool in the stored fluoroscopic images, and hence reduce irradiation to the surgeon during the surgical procedure.

N. Suhm *et al* [100, 121], have used a SurgiGATE based CAOS system for distal locking procedures. SurgiGATE (Medivision, Switzerland) is a surgical navigation system that offers continuous intraoperative guidance to surgeons by using stored fluoroscopic images. These images are acquired intraoperatively, i.e. after the nail is inserted into the medullary canal. The SurgiGATE navigation system employs Optotrak, to track the C-arm Image intensifier, a compact air drive and the nail insertion handle, which are all equipped with Infrared LEDs. The computer-assisted distal locking is performed as follows:

- In order to obtain the perfect circle image (i.e. alignment between C-arm and axes of the distal holes), prior to insertion of the nail into the femur, the nail is rigidly attached to the nail reference base, which is fitted with Infrared LEDs. Optotrak is then used to track the position of the distal locking holes and their major axes relative to the nail reference base. This is accomplished by inserting the referenced nail pointer (which is fitted with Infrared LEDs as well) into the distal locking holes as shown in Figure 3-36. This information is then transferred to the workstation; this procedure is referred as “collecting”.

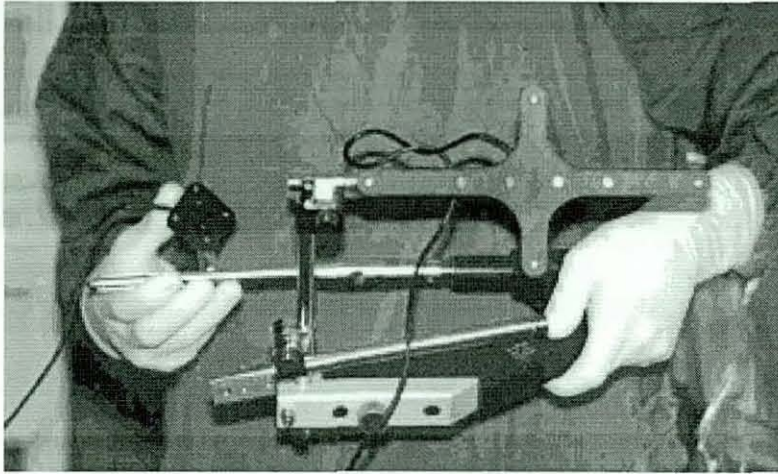


Figure 3-36 Registration of distal locking hole with nail reference base prior to nail insertion.

- Once the nail is inserted into the femur, a computer animation on a workstation screen guides the radiographer to position the C-arm relative to the intramedullary nail in such a way that distal locking holes can be imaged as perfect circles rather than ellipses. This computer animation is based on the data obtained during the “collecting” procedure (i.e. prior to the insertion of the nail). Therefore, this data does not take into account the nail’s deformation its insertion into the medullary canal, which can impair the ability of the system to provide precise alignment required to obtain the perfect circle image.

In computer animation (virtual C-arm image), defined points (i.e. registration of the axes of the distal holes relative to the nail reference base) are represented by a graphical object that is rendered through the cone beam projection model onto the virtual C-arm image. Each distal locking hole is represented by a pair of small circles, whereas the nail axis is represented by a long straight line, and the large circle represents the field of view of the C-arm image. Once two circles belonging to a distal hole are overlapped over each other and are located in the centre of the field of view, the desired C-arm alignment is achieved to obtain perfect circle image.

- The result of the alignment process is confirmed by using a Lateral image. If a perfect circle image is obtained, then the Lateral image is transferred to the workstation. However, in case of the hole being imaged elliptical, the C-arm is repositioned manually, until the perfect circle image is obtained.

- After acquisition of the Lateral view perfect circle image, the AP view image is acquired, and the C-arm is removed. At the time of image acquisition, the relative position of the nail reference base and the C-arm is measured; this allows defining the desired C-arm orientation with respect to the patient i.e. the nail reference base. The images are then calibrated to remove distortions and account for magnification.
- Once the image acquisition is finished, Optotrak is used to track the drill and the nail reference base. This allows computation of the spatial relationship between the drill and the nail reference base. The position of the drill is then projected onto workstation screen (i.e. graphical display of the drill bit is overlaid on the stored images in real time).
- The drill is then introduced through an incision until it contacts bone. The drill bit is then moved along the surface of the bone, until its projection on the computer screen is located in the centre of the distal locking hole. The entrance point is then obtained by impression of drill bit onto the bone. The drill axis is then aligned with the distal locking hole's axis using the trajectory displayed on workstation screen.

It is claimed that the total fluoroscopy time to insert one distal locking screw is reduced from 108 (± 61) seconds to only 7.3 (± 6.4) seconds using the fluoroscopy-based surgical navigation system in comparison to the fluoroscopic guidance system. Although, additional time was required to set-up the navigation system, and it was observed that the technical reliability was better with fluoroscopic guidance system compared to fluoroscopy-based surgical navigation system. There were 5 "major technical related intraoperative problems ¹" out of 23 procedures using the surgical navigation system. For accuracy evaluation of the proposed system, 39 distal locking insertions were made. There was one failure² and eight minor-precision problems.

There are other commercially available computer-assisted fluoroscopy based surgical navigation systems, such as Fluoronav (Medtronic, USA).

¹ Major technical problem: Technical problems were rated as major when they could not be solved within 10 minutes during the procedure, such as incorrect distortion of stored x-ray images from navigation system, invisibility of nail's reference base used for nail registration etc.

² Failure : Failure means complete failure in distal locking.

3.9.1.1 Summary of surgical navigation system

Radiation exposure to surgeon is significantly reduced, as only few X-ray images are acquired. However, although these surgical assist systems reduce the irradiation to the surgeon they may result in a longer overall procedure time in comparison to the free-hand technique [114]. The use of these systems also requires expertise and additional personnel. Furthermore, these systems require an unobstructed line-of-sight between the optical tracking cameras and infrared LEDs mounted on the image intensifier and the surgical tool (or drill guide), resulting in a limitation of free movement by the surgical personnel.

3.10 The Loughborough University Robotic Assistance Orthopaedic Surgery System

The Loughborough University approach under the supervision of Dr. K Bouazza Marouf [3-7], differs from existing RAOS/CAOS systems, as it uses a calibration frame for calibration and registration purposes. Thereby, it eliminates the need for optical tracking equipment such as Optotrak, which tends to clutter the operating theatre environment and requires care in maintaining the line of sight.

Ian Browbank [78], designed a calibration frame known as Hipbox (enclosed measurement volume = $225\text{mm} \times 225\text{mm} \times 225\text{mm}$), prototype of the Hipbox is shown in Figure 3-37. It consisted of two parts forming a sleeve which is then put around the knee. However, for intraoperative application this arrangement proved to be rather cumbersome and heavy. Therefore in order to achieve a quicker set up time another calibration frame, known as the "Gamma" (Γ) Frame, shown in Figure 3-37, was developed by Schanbler [4].

However, the use of the Γ Frame has one obvious drawback compared to the Hipbox. The patient's leg is not situated within the calibration plates for the Γ Frame. Therefore, reconstruction of the target points located inside the patient's leg must be done on extrapolation instead of intrapolation basis. Hence, a small error in positioning of calibration plates can cause significant errors in reconstruction of points in space. This limitation makes the Γ Frame slightly less accurate than the

Hipbox, but analysis showed that it provides reconstruction errors of better than 1mm, which is within the desired accuracy requirement of 1mm for guide wire insertion and distal locking procedure.

It should be noted that to avoid fiducial overlapping robotic positioning of Γ Frame can be achieved with ease as well as required calibration images can also be obtained without excessive repositioning of the Γ Frame. Furthermore, the Γ Frame is less sensitive to rotations in comparison to the Hipbox resulting in visibility of most of the fiducials required for calibration and registration purposes. Therefore, as a result the use of the Γ Frame is preferred over the Hipbox due to its ease of use, which makes it more compatible for intraoperative application.

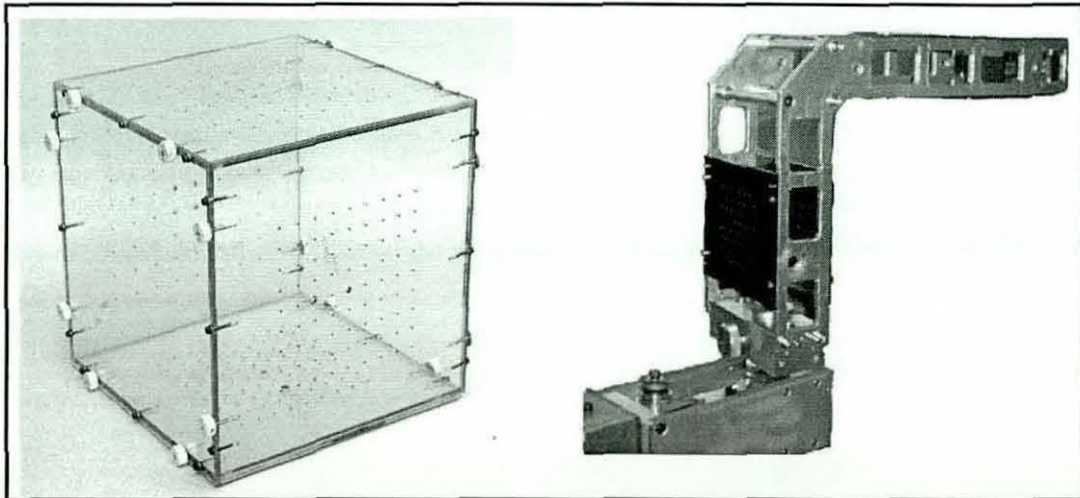


Figure 3-37 Hip box prototype (L.H.S) and Γ frame (R.H.S).

In total there are four Perspex calibrations plates fixed on the Γ frame. Since in order to obtain good results, a large number of fiducials should be visible for better distortion correction, therefore, the aim of the arrangement was to find such grid pattern so that almost no fiducials are superimposed on the image plane, i.e. to avoid projection of ball bearings from both plates in a view onto the same image point as shown in Figure 3-38.

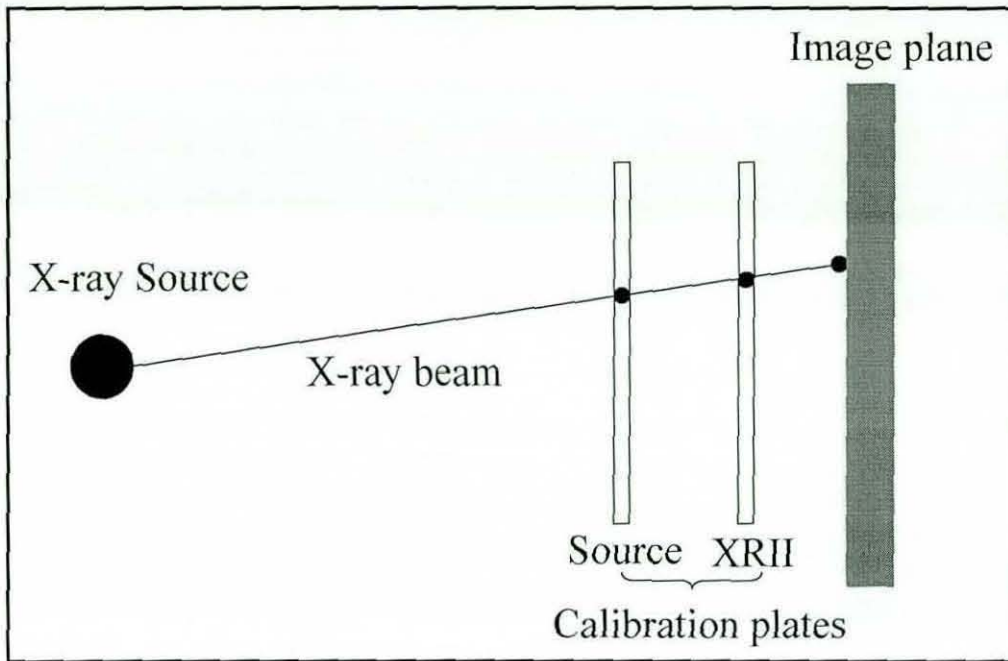


Figure 3-38 Fiducial occlusion phenomena.

In Figure 3-38 it should be noted that XRII calibration plate refers to the calibration plate nearest to the X-ray image intensifier, whereas Source calibration plate refers to the calibration plate nearest to the X-ray source.

The fiducial patterns used on the calibration plates are as follows:

XRII plate – Lateral view

A nine-by-nine grid (10mm grid spacing) of 2 mm diameter ball bearings. Grid central marker (5mm diameter ball bearing) and orientation marker (6mm diameter ball bearing) are also provided. A distinctive hole in the centre of the orientation marker makes it easier for the user to distinguish between the centre and orientation markers.

Source plate – Lateral view

An eight-by-eight grid (9mm grid spacing) of 3 mm diameter ball bearings. Four small washers (4mm outside diameter) are used to mark the centre of the grid. There is no difference between these washers. Therefore, they can be easily distinguished from the central marker of XRII plate.

XRII plate – AP view

A nine-by-nine grid (14mm grid spacing) of 2 mm diameter ball bearings. A grid central marker (5mm diameter ball bearing) and an orientation marker (6mm diameter ball bearing) are also provided.

Source plate –AP view

An eight-by-eight grid (13mm grid spacing) of 3 mm diameter ball bearings. Four small washers (4mm outside diameter) are used to mark the centre of the grid.

Use of Reference markers

Since the position of the calibration frame is not fixed with respect to C-arm, and there is a need to identify each fiducial appearing within the field of view individually. This can be accomplished by introducing reference markers within the field of view. As they provide both in-plane angular orientation of the calibration frame and a grid pattern in pixels. In addition to this, it is easier for the user to differentiate between the reference marker and other fiducials due to their different sizes.

3.11 Novelty of this thesis

The novelty of the work presented in this thesis lies in the robustness of the machine vision system and the offline CAD modelling of the intramedullary nails. These contributions to an existing system allow the proposed system to determine the drilling trajectory of the distal locking holes with respect to the calibration frame using a novel approach based on offline modelling of the nail and an automated machine vision system.

Look-up tables (LUTs) are obtained by off-line CAD modelling of nails of different shapes and dimensions, and all the steps involved during image analysis have been fully automated to make the machine vision system user independent and very efficient in terms of time taken to determine the drilling trajectory.

The adopted machine vision system is shown in Chapter 6 and Chapter 7 to be very robust in the presence of variable noise and contrast in the X-ray images and in terms of variable magnification. Therefore, the benefits of this approach are:

- The use of off-line modelling of the nail reduces the length of time of the surgical procedure.
- The method allows accurate modelling of any shape of intramedullary nail; therefore nails from different manufacturers can be modelled.
- User independent image analysis, and
- Robustness of the machine vision system.

Furthermore, in order to make the existing Γ calibration frame more robust, a review of the calibration frame design is made on the following basis:

- To investigate the optimal number of fiducials and their spatial distribution necessary to provide the required accuracy of 1mm and 1° i.e. maximum allowable positional and angular misalignment respectively from the entry point (centre of the distal locking hole).
- Design issues such as robustness and ease of manufacture.
- Adaptability for different patient physiology.

3.12 Summary

Distal locking is the most difficult part during IMN procedure due to, deformation of the nail during its insertion and use of 2D X-ray images to guide 3D bone drilling procedures. Therefore, many clinicians and researchers have proposed a variety of targeting devices to assist surgeons during distal locking, and to reduce irradiation to patient and operating staff during distal locking of intramedullary nails, with varying success. The three main approaches are the devices assisting free-hand technique, nail mounted guides and guides attached to an image intensifier. However, each of these devices has its advantages and disadvantages; consequently the free-hand technique

remains the main method used by orthopaedic surgeons. Hence, the surgical time and outcome of the procedure are very much dependent upon the skill and experience of the surgeon.

Current trend is to use RAOS/CAOS for distal locking. It is a fairly new area of development and many of the systems described in this chapter are at a prototype stage. Although these surgical assist systems reduce the irradiation to the surgeon they may result in a longer overall procedure time in comparison to the free-hand technique. Furthermore, these systems require an unobstructed line-of-sight between the optical tracking cameras and infrared LEDs mounted on the image intensifier and the surgical tool (or drill guide), resulting in a limitation of free movement by the surgical personnel. Therefore, there is a need to develop a surgical system/technique that can, reduce the irradiation to patient and operating staff, improve the outcome of the procedure and make surgical time more consistent. Towards, the end of the chapter, the system developed at Loughborough University for robotic assisted orthopaedic surgery is explained followed by a description about the novelty of this thesis. In the following chapter, a comprehensive description of the machine vision system developed for analysing X-ray images acquired using Loughborough system is presented.

4 X-ray image acquisition and analysis

Medical information is often not provided by raw spatial data, for example intraoperative X-ray images taken during distal locking of an intramedullary nail do not provide the drilling trajectory of distal locking holes. Therefore, all medical photogrammetric applications require the use of further analysis and interpretation to allow meaningful information to be given to the end-user i.e. surgeon. Only if this additional information is provided, can photogrammetry be utilised in practice. This chapter discusses the application of image analysis on raw intraoperative X-ray images obtained during laboratory trials to determine the drilling trajectory of the distal locking holes.

4.1 Capture of Intraoperative X-ray images

In laboratory trials, two approximately orthogonal (Lateral and AP) X-ray images of the distal end of the intramedullary nail were taken with the calibration frame in position as shown in Figure 4-1 and Figure 4-2 for Lateral and AP view respectively. Here it should be noted the term approximately orthogonal is used as no device is mounted onto the C-arm which can be used to quantify rotation of the C-arm and hence ensure that Lateral and AP X-ray images are taken orthogonal to each other. Here it should be noted that proposed system does not rely on Lateral and AP view images taken orthogonally to each other. In image intensifier used in this study i.e. Siemens Siremobil 2N, a videcon camera is used in combination with a digital image processor, thus ensuring that the image intensifier/TV system is fully digitised. The result of continuous, pulsed, or snapshot (single-pulse) fluoroscopy examinations can therefore be enhanced prior to display on a monitor mobile viewing station. It should be noted that frame grabber produces images with pixel resolution of 768 by 576, and contrast resolution of 8 bit i.e. grey level values ranges between 0 and 255.

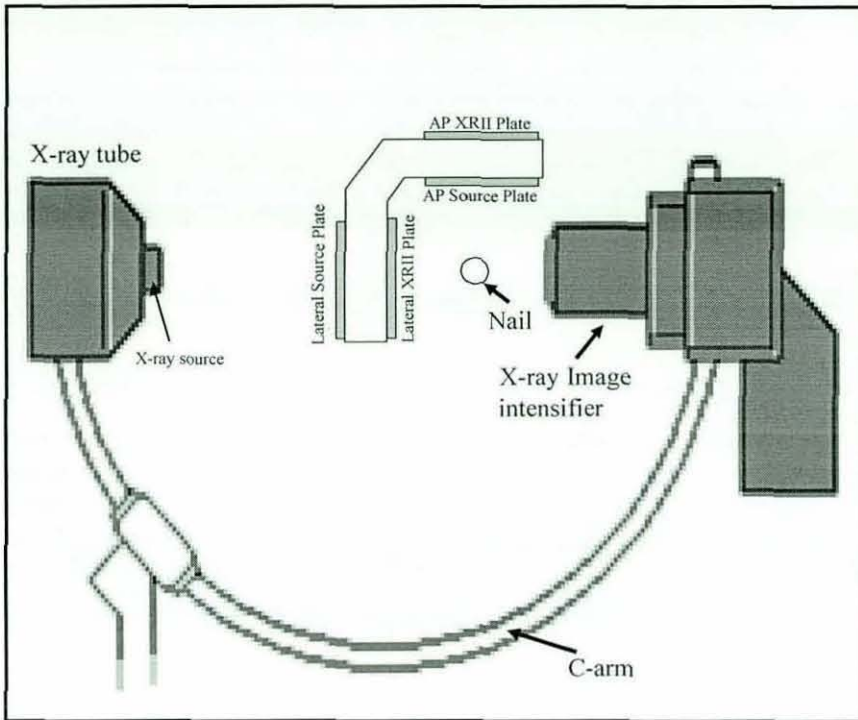


Figure 4-1 Set-up for Lateral view image acquisition.

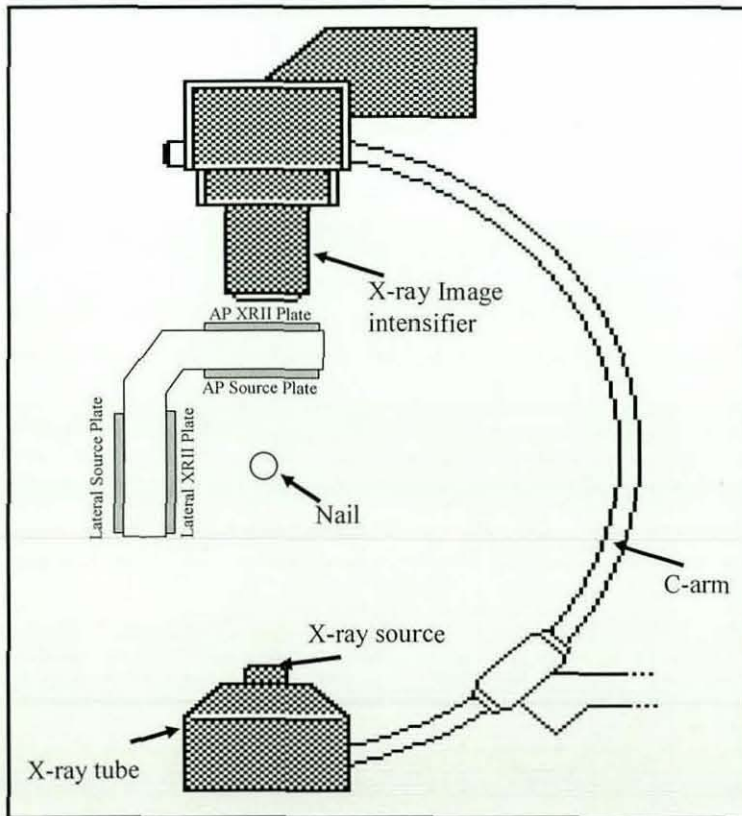


Figure 4-2 Set-up for the AP view image acquisition.

The calibration frame and typical X-ray images are shown in Figure 4-3. It should be noted that from here onwards all dimensions along x-axis (i.e. horizontal axis of the image) and y-axis (i.e. vertical axis of the image) are in pixels unless specified otherwise.

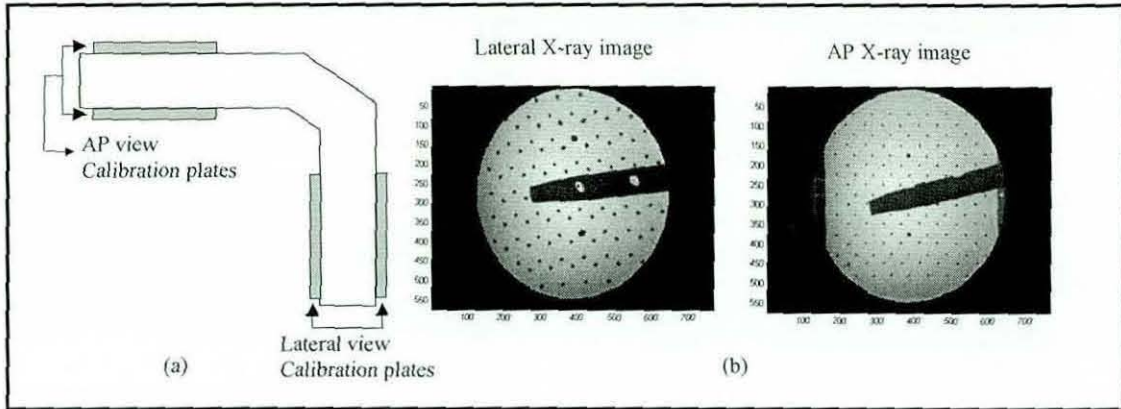


Figure 4-3 (a) Calibration frame (b) Typical Lateral and AP X-ray images.

Simulation of the distal locking procedure was performed using a specially designed test-rig incorporating a cylindrical nail of 14mm diameter containing two distal holes of 7mm diameter spaced 30mm apart to represent a typical intramedullary nail. The nail can be rotated accurately by known angles using a specially designed test-rig as shown in Figure 4-4, so that results obtained from image analysis can then be verified. It should be noted that the test-rig has an angular resolution of 1° and can be positioned with an accuracy of around 0.2° .

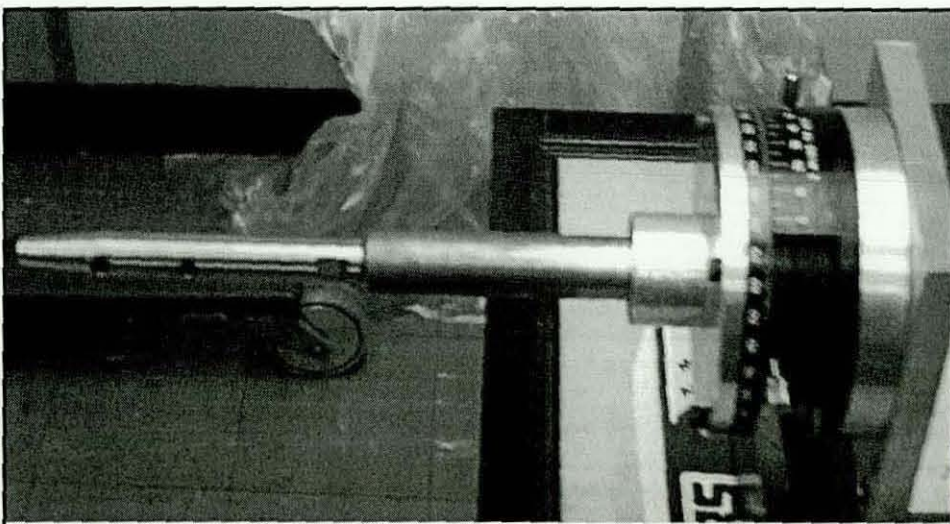


Figure 4-4 Test rig used to simulate nail's rotation.

The image analysis protocol depicted by the flow diagram of Figure 4-5 was followed once the Lateral and AP intra-operative X-ray images were acquired. In order to determine the drilling axis for the distal locking holes, the image analysis protocol depicted by the flow diagram of Figure 4-5 was followed once the Lateral and AP X-ray images were acquired

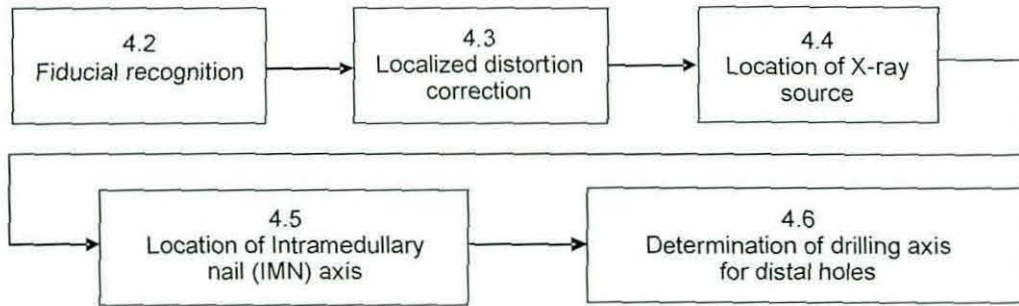


Figure 4-5 Flowchart of Image analysis.

4.2 Fiducial Recognition

Registration is the process of establishing a spatial relationship between certain locations on the images and the corresponding locations on the actual patient anatomy in the surgical field. A key element in registration is the use of steel ball bearings as artificial calibration markers or *fiducials* [122]. X-ray Photogrammetry techniques work by introducing fiducials in radiographic images to reconstruct 3D locations of imaged object points. The extraction of accurate quantitative 3-D data from a conventional pair of radiographs is complicated by:

- Perspective transformation (i.e. from 3D to 2D)
- Image distortion
- Lack of easily identifiable anatomical landmarks in the human body.

However, all these problems can be overcome by the introduction of artificial calibration features into the X-ray images, in this case by surrounding the anatomical region of interest with a radiotransparent frame into which an array of fiducial markers have been inlaid. The CAOS system functions in two worlds; the real, or

patient world and the virtual, or computer world. Calibration markers (fiducials) are used to link these two worlds, as they are present in both. Therefore, most surgical robot systems to date have used such fiducials [123].

In order to calibrate the system internally or externally, the positions of the fiducials in the calibration frame must be determined with sub-pixel accuracy, as error in the measured coordinates of any fiducial induces an error in the location of other image points.

The main goal of the fiducial recognition program was to recognize the maximum number of fiducials within the field of view. Although the grey scale values of the fiducials differ significantly from the background, global greyscale thresholding may not be able to segment all the fiducials, as the threshold value for a given fiducial varies with its respective position due to non-uniform brightness across the X-ray image, with the centre of the image being brighter than the edges of the image. This phenomenon cause low contrast at the image edges. Therefore, for fiducial recognition, this study employs a localized thresholding approach by dividing the whole image into small sub-regions in which each fiducial was processed individually. Localized thresholding is superior to global thresholding as the former computation is adaptive to local image characteristics. Localized thresholding may result in extra computational time, as it is necessary to identify the rectangular sub-regions for each fiducial whose centre is to be computed. However, with recent increased processing speeds, such delays are insignificant at the image resolution used and are far outweighed by the advantages of the technique.

4.2.1 Thresholding

In many applications of image processing, the grey levels of pixels belonging to the object are quite different from the grey levels of the pixels belonging to the background. In such cases, thresholding then becomes a simple but effective tool to separate objects from the background [124, 125]. Thresholding is regarded as one of the most powerful tools for image segmentation. Examples of thresholding applications are in document image analysis [126] or in scene processing [127]. In

this study thresholding will be used to extract the fiducials from the intraoperative X-ray images.

The output of the thresholding operation is a binary image whose grey level of 0 (black) pixels correspond to background and a grey level of 1 (white) pixels correspond to foreground or vice versa. The main difficulties associated with the thresholding operation in medical imaging applications include strong illumination gradient, variance of the grey levels within the object and the background and inadequate contrast.

The thresholding method used in this study for individual fiducial recognition is "Otsu thresholding" [128], in which the grey level histogram of the image is divided into two groups and the threshold is determined when the variance between the two groups is a maximum. This method provides good results even when the histogram of a grey level image does not have two obvious peaks. Therefore, it is regarded as one of the most powerful methods for bi-level thresholding and is used in many thresholding applications [129].

4.2.1.1 Implementation of Otsu's thresholding method in Matlab

- Firstly maximum and minimum grey level values of the image were determined.
- Then a minimum grey level value is chosen as the initial threshold (T_0). Based on this threshold, all the pixels of the image were divided into two groups, say C_0 i.e. pixels with grey level value smaller or equal to initial threshold and C_1 i.e. pixels with grey level value greater than initial threshold.
- If N_0 and μ_0 and N_1 and μ_1 are the number of pixels and the average grey level value of groups C_0 and C_1 respectively, the average grey level value of all the pixels in the image can be given by:

$$M_T = \frac{N_0\mu_0 + N_1\mu_1}{N_0 + N_1}$$

- Now the between class variance (BCV) between the two groups of pixels for threshold value T_0 can be determined as follows:

$$\sigma^2(T_0) = \{N_0(\mu_0 - M_T) + N_1(\mu_1 - M_T)\}$$

- The required threshold value T is then chosen corresponding to the maximum value of $\sigma^2(T)$ i.e. the threshold value for which BCV is maximum.

4.2.2 Procedure

In this study, the image analysis procedure adopted to perform automatic fiducial recognition is summarized by the flow diagram shown in Figure 4-6.

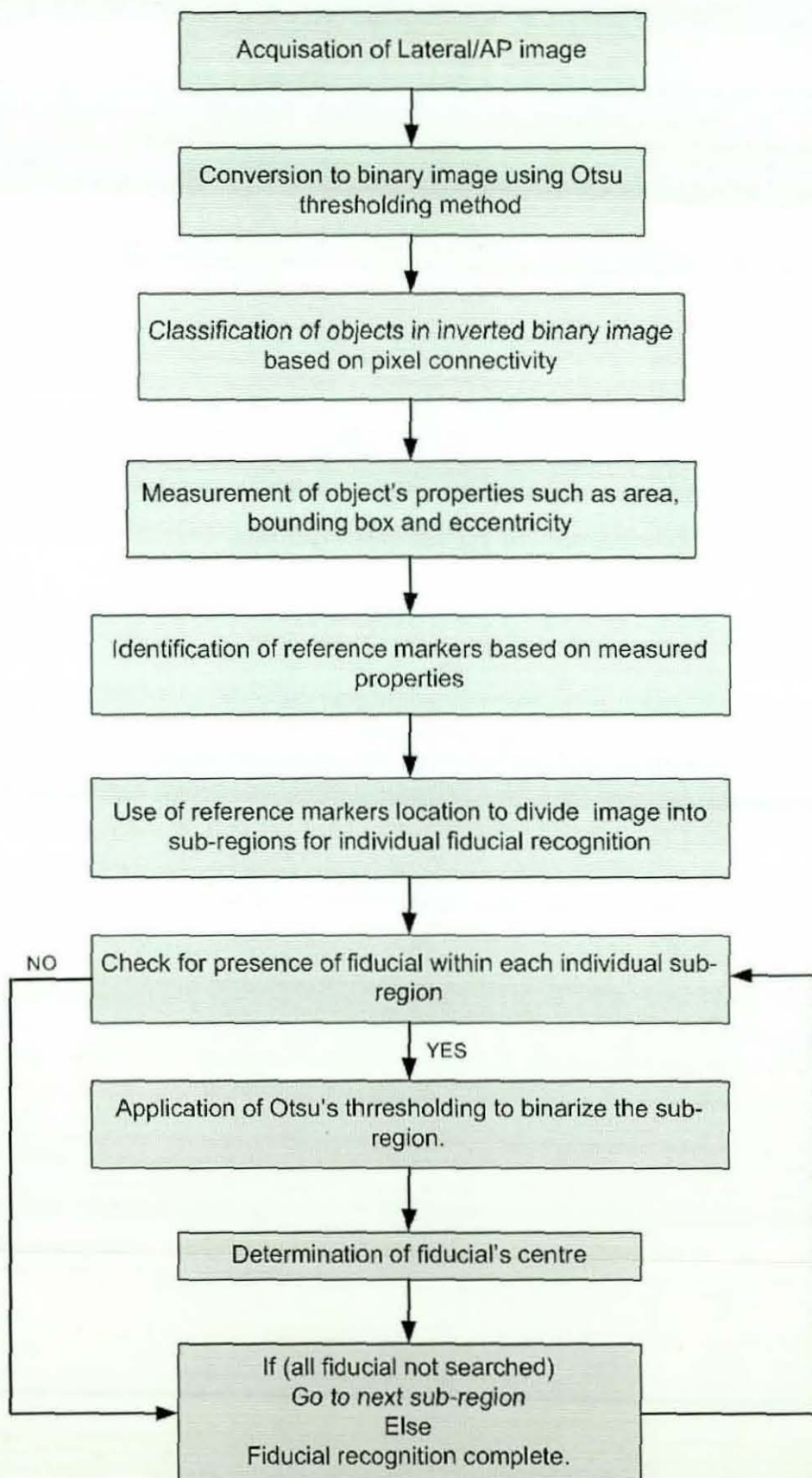


Figure 4-6 Summary of fiducial recognition program.

Detailed description of the procedure implemented to carry out automatic fiducial recognition is described in the following sub-sections:

Initially, the X-ray image was converted to a binary image by applying Otsu's thresholding technique, which calculates the thresholding value corresponding to maximum variance between a black & white group of pixels. Figure 4-7 (a) and Figure 4-7 (b) represents the original image and thresholded image respectively.

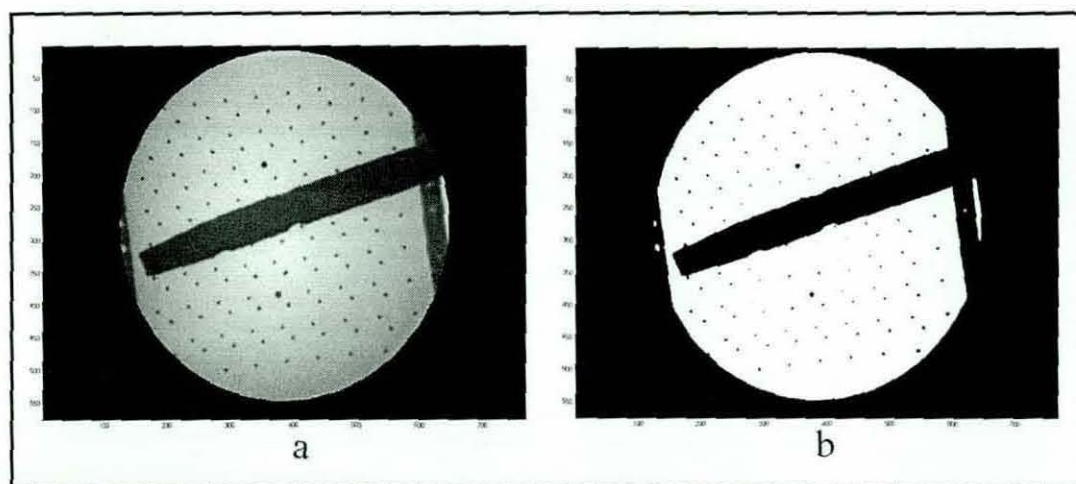


Figure 4-7 (a) Intraoperative AP view image (b) AP view image after applying Otsu's thresholding.

- In binary images, pixels with a value of 1 i.e. white pixel represent a point on the object; whereas pixels with a value 0 i.e. black pixels represent the background. Since the aim was to determine each visible fiducial's centre, the binary image was inverted, shown in Figure 4-8, so that fiducials can be classified as objects.
- Pixel connectivity was then used for extraction of connected components in the inverted binary image for individual identification of objects. This was accomplished by using Matlab function Image Processing toolbox "bwlabel.m". For this purpose, 8-connectedness was used to define the neighbourhood of a given image pixel as in addition to horizontal and vertical movements between adjacent pixels, it also uses diagonal connections. Then objects properties such as area, bounding box and circularity were determined.

- The objects were then sorted in descending order based on their area (number of white pixels), with the nail having the largest area among all objects, as depicted by Figure 4-8.

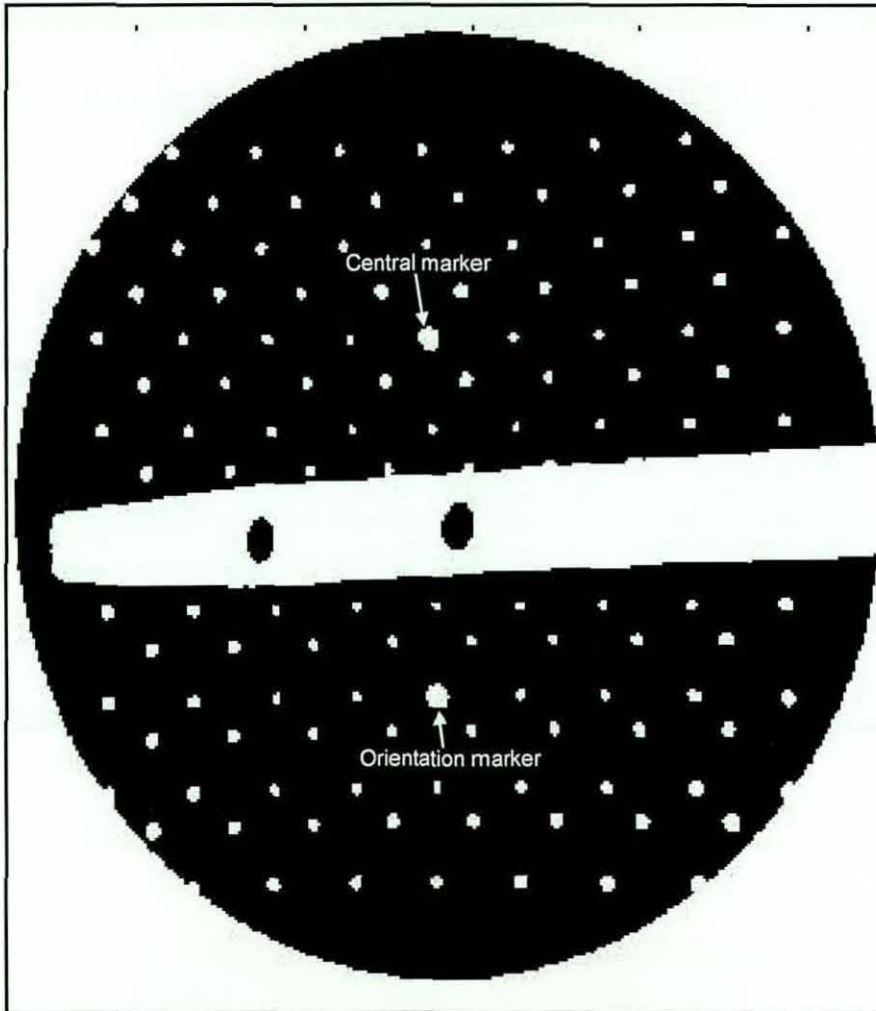


Figure 4-8 Inverted thresholded Lateral view image.

- It is obvious from Figure 4-8 that the nail will have the largest area, whereas the two reference markers (i.e. central and orientation markers) will each have an area value less than the nail but greater than the area value of any other fiducials on the calibration plates. For typical Lateral and AP view X-ray images, values of area obtained for the six largest objects in the inverted image are shown as an example in Table 4-1:

Object Name	Intramedullary Nail	Reference marker 1	Reference marker 2	Fiducial	Fiducial	Fiducial
Area (Pixels)	250768	125	117	66	65	65

Table 4-1 XRII plate reference marker identification based on area in the Lateral view

Object Name	Intramedullary Nail	Reference marker 1	Reference marker 2	Fiducial	Fiducial	Fiducial
Area (Pixels)	250768	69	62	47	45	44

Table 4-2 XRII plate reference marker identification based on area in AP view

Although reference markers on both Lateral and AP views have the same dimensions, it can be seen from Table 4-1 and Table 4-2 that for the AP view image the area of the reference markers is considerably smaller in comparison to that for the Lateral view image. This is due to the positioning of Lateral and AP calibration plates with respect to Lateral and AP X-ray source as depicted by Figure 4-1 and Figure 4-2 respectively.

It can be seen from Figure 4-1 and Figure 4-2 that during the Lateral image acquisition, due to the design of the Γ frame, the Lateral X-ray source is closer to the Lateral XRII plate, which contains the reference markers. Therefore, Lateral calibration plates experience more magnification in comparison to AP calibration plates.

It can also be noted from Table 4-2 that the difference in area of the reference markers from other fiducials is relatively small in the AP view, therefore there is a possibility that due to the presence of noise, fiducials at the edges may not be detected accurately, and may have an area greater than that of the reference markers as shown in Table 4-3.

Object Name	Intramedullary Nail	Reference marker 1	Reference marker 2	Fiducial	Fiducial	Fiducial
Area (Pixels)	256995	73	64	94	74	56

Table 4-3 XRII plate reference marker identification based on area in AP view for noisy X-ray image

In order to locate the reference markers reliably, the six largest objects (i.e. based on their area) excluding the nail were considered. It can be seen from Table 4-1 to Table 4-3 that doing so results in reliable identification of the reference markers. Once the six largest objects excluding the nail were selected, the following procedure was adopted to distinguish between reference markers and fiducials:

- The location of reference markers on the Lateral/AP XRII calibration plate implies that the difference in their image x-coordinates will be a minimum. Therefore, the bounding box (the smallest rectangle containing the object) of each of the six objects was determined as shown in Figure 4-9. The bounding box of each object was derived from a Matlab object labelling process.

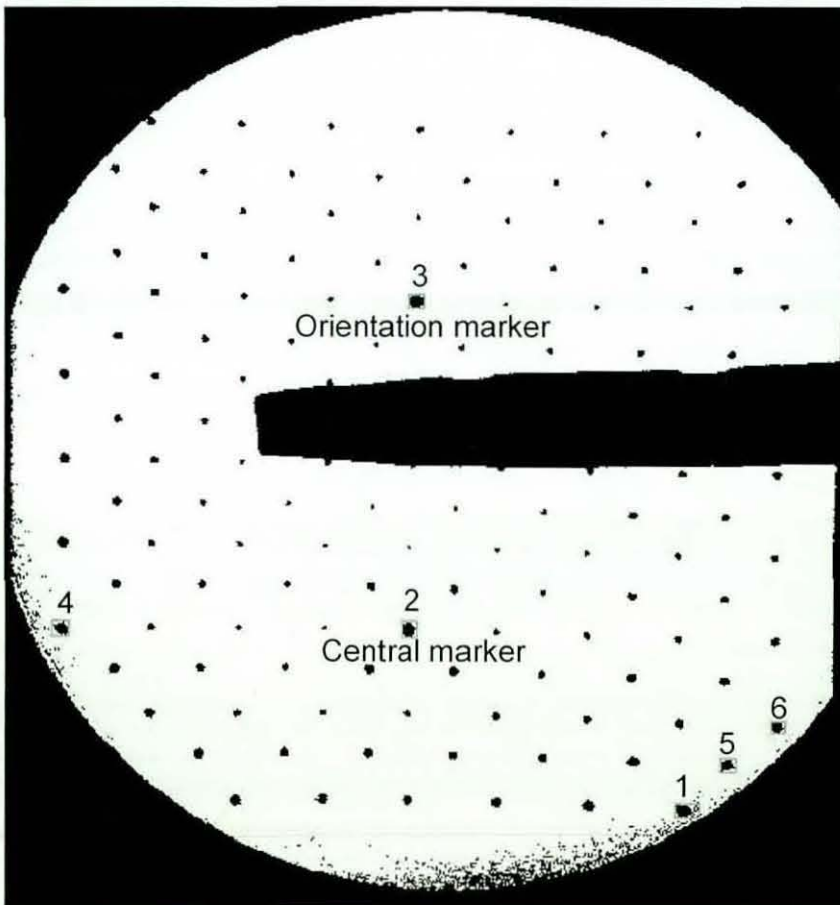


Figure 4-9 Identification of six largest objects based on their area.

- The image co-ordinates ($\min x_i, \min y_i$) of each object's bounding box were obtained. Then the difference in the x co-ordinates of the bounding box between each of the objects was then determined as follows:

$diff_{12} = abs(minx_1 - minx_2);$ *ie. difference in x-coordinates of 1st & 2nd object,*

$diff_{13} = abs(minx_1 - minx_3);$ *ie. difference in x-coordinates of 1st & 3rd object,*

....

....

....

$diff_{45} = abs(minx_4 - minx_5);$ *ie. difference in x-coordinates of 4th & 5th object,*

$diff_{46} = abs(minx_4 - minx_6);$ *ie. difference in x-coordinates of 4th & 6th object,*

$diff_{56} = abs(minx_5 - minx_6);$ *ie. difference in x-coordinates of 5th & 6th object,*

Among the six objects, two objects with least difference between their x co-ordinates were identified by arranging " $diff_{12} diff_{13} diff_{14} \dots \dots \dots diff_{45} diff_{46} diff_{56}$ " in descending order. These two objects were classified as an initial estimate for the location of reference markers, as ideally the distance along the x-axis should be a minimum between the central and orientation markers, due to their positioning on the XRII calibration plate.

Then to make sure that the two markers selected are true reference markers, the difference in their y co-ordinates of the starting point of the bounding box was determined. Several X-ray images have been measured, and it has been found that the two reference markers are always at least 150 pixels apart along the y-axis. This value was obtained by measuring Lateral and AP view images with maximum magnification i.e. X-ray images obtained by positioning the X-ray source such that it was at the smallest possible distance from the calibration plates in each view. Once this condition was satisfied, for confidence measure a final check was made to avoid the selection of a fiducial at the edge of the image being selected as a reference marker. This involves a comparison between the circularity of the two markers, which is given as:

$$Circularity = \frac{4\pi A}{P^2}$$

where,

$A = Area,$

$P = Perimeter$

Circularity was used as any fiducial detected with background noise will have a low circularity value in comparison to reference markers due to it being non-circular. Therefore, in the case of circularity of the any of the two selected markers being lower than 1, the whole process was repeated until all the above mentioned conditions are met to determine the location of the two reference markers.

Processing of several intraoperative X-ray images has shown that by using the above procedure the two reference markers on the XRII calibration plate are located reliably. Once the two reference markers were located, the distinction between the central and orientation marker was made based on their bounding boxes. Then the predicted locations of the other fiducials on the XRII calibration plate were computed. Since photogrammetric reconstruction techniques work by establishing image-world point pairs, the image vision system must be able to uniquely identify each fiducial visible in the field of view. In order to accomplish this task, both the horizontal and vertical grid spacings were obtained using the image coordinates of the two reference markers. These grid spacings yield the increments required to determine the locations of the remaining fiducials on the XRII calibration plate. The program uses this information to divide the image into sub-regions, as shown in Figure 4-10, and processes each fiducial individually. A typical picture of a fiducial, which must be recognized in that sub-region, is shown in Figure 4-10. It should be noted that for individual fiducial recognition on the XRII calibration plate raw grey scale image is used.”

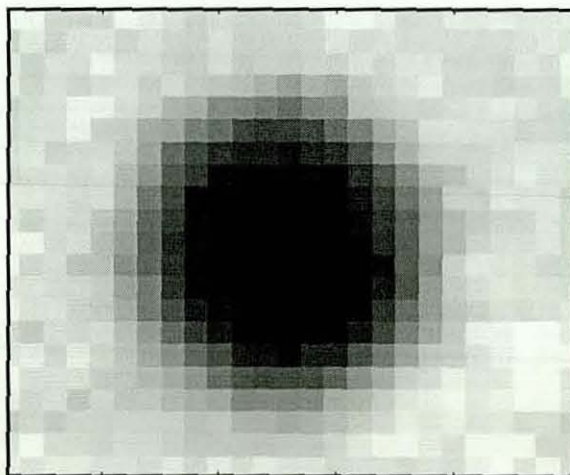


Figure 4-10 Selected sub-region with fiducial.

Processing of grey levels of the selected region was carried out in the following manner:

- The inverted image of the selected region, shown in Figure 4-11, was obtained.

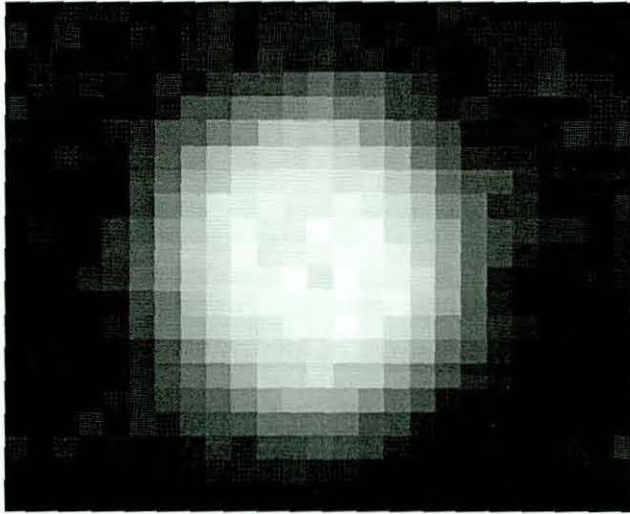


Figure 4-11 Inverted image of selected region.

The inverted image was then converted into a binary image, the coordinates of the fiducial's centre of mass (\bar{x}, \bar{y}) were determined from the set of N white pixels of coordinates (x_i, y_i) which makes up the fiducial as follows:

$$\bar{x} = \frac{1}{N} \sum_{i=1}^N x_i$$

$$\bar{y} = \frac{1}{N} \sum_{i=1}^N y_i$$

It was decided to check whether using grey-scale variations would be more accurate than binarising these images (for example, shown in Figure 4-11) before calculating the centre of mass. Surface fitting can be used for measurement purposes when the object of interest has a known or assumed function form. For example, fiducials on the X-ray image can be modelled as 2D Gaussians. This is because the X-ray distribution of an image of a ball bearing have similar shape to that of 2D Gaussian

surface (shown in Figure 4-12), as the thickness is maximum at the centre of the ball bearing and decreases towards its periphery.

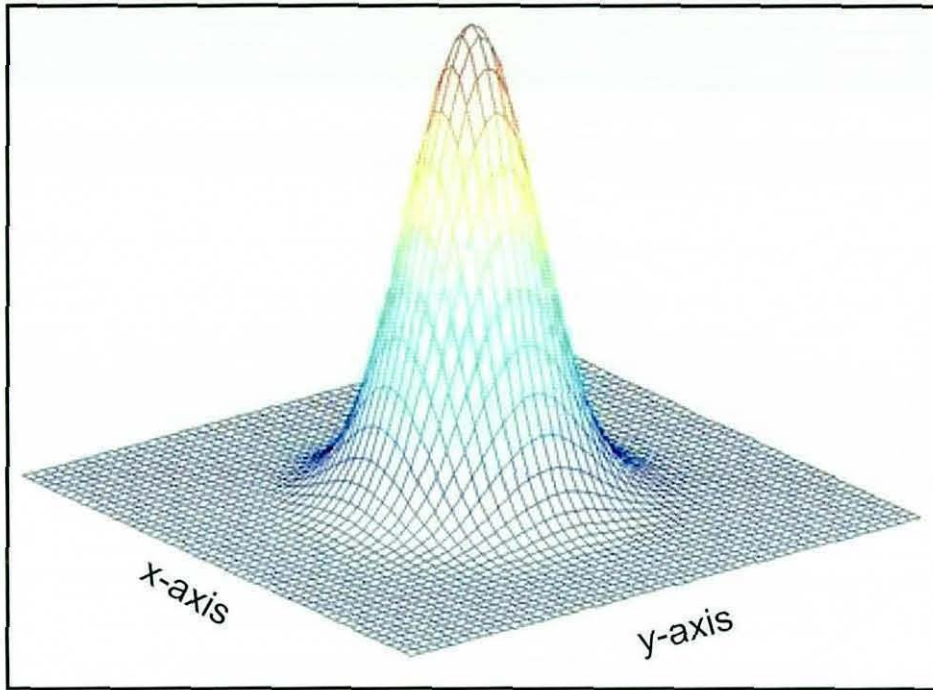


Figure 4-12 2D normal distributed Gaussian probability density function.

Therefore, 2D Gaussian surface fitting based on the X-ray absorbance characteristic of the inverted image (shown in Figure 4-11) was performed, the peak of which yields the location of the fiducial centre. The equation of the 2D Gaussian is:

$$\text{gauss_fit} = A e^{-\left[\frac{(x_i - x_o)^2}{2\sigma_x^2} + \frac{(y_i - y_o)^2}{2\sigma_y^2} \right]}$$

where,

$A = \text{Peak}$, i.e. the maximum gray level value ,

$(x_i, y_i) = \text{image co-ordinates}$,

$(x_o, y_o) = \text{mean position}$,

$(\sigma_x, \sigma_y) = \text{Standard deviation (radii) in x and y direction respectively}$.

However, processing of several X-ray images have shown that no improvement in terms of overall accuracy of the system was achieved while employing 2D Gaussian surface fitting to find the fiducials centre.

It should be noted that for each fiducial the algorithm checks the predicted fiducial location against the image's field-of-view i.e. (576 x 768) pixels. If a fiducial expected location does not lie within the field-of-view, the image coordinates for that fiducial were written as (0,0). The algorithm (described using Fig. 4.10 and Fig. 4.11 for individual fiducial recognition on XRII calibration plate) was then used to perform fiducial recognition on the Source calibration plate.. The grid spacings for the Source plate were different than that of the XRII calibration plate due to perspective distortion. Therefore, reference makers for the Source calibration plate are of different shape, as four washers were used to determine the grid spacings. Since these washers lie in the vicinity of the central marker, location of the central marker and grid spacings obtained for the XRII calibration plate were used to crop a region that contains the central marker and the four washers, as shown in Figure 4-13.

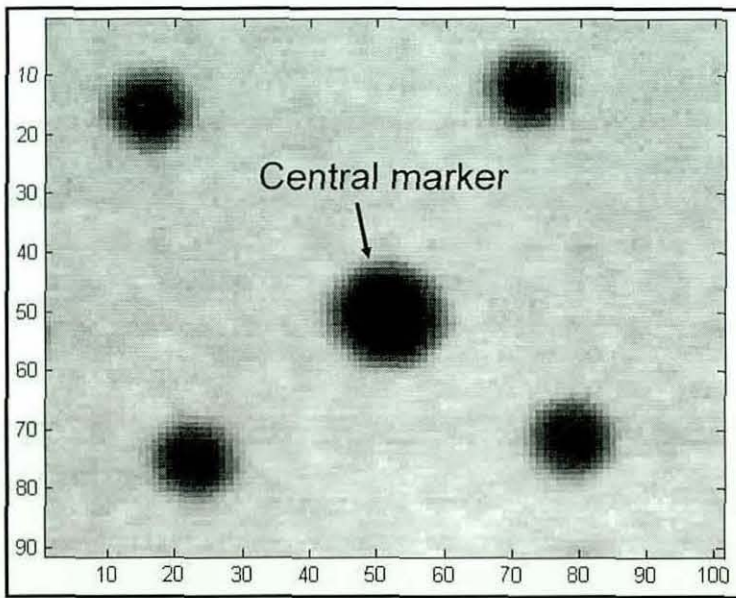


Figure 4-13 Cropped region containing washers and central marker in the Lateral view.

Four washers of 4mm outside diameter are used on Source plate as reference markers to distinguish from the central marker (5mm diameter) of XRII plate, thereby distinction can be made between Source and XRII plates during fiducial recognition. The cropped region was inverted so that the reference markers can be classified as objects. It is obvious from Figure 4-13 that the central marker will have the largest area, whereas the four washers will each have an area value less than the central

marker. Therefore, the objects were sorted in descending order based on their area as shown in Table 4-4.

Object Name	Central Marker	Washer 1	Washer 2	Washer 3	Washer 4
(Pixels)	242	140	137	133	130

Table 4-4 Source plate reference marker identification based on area.

It can be seen that it is fairly easy to distinguish between the central marker and the four washers based on their areas. The bounding box of each of the four washers was then determined. Then x and y co-ordinates of the bounding box for each washer were used to uniquely identify each washer. The image coordinates of the washers were used to obtain grid spacings for the Source calibration plate. Once the grid spacings for the Source calibration plate were known, the program uses this information to divide the image into sub-regions, and processes each fiducial individually. The image coordinates for each fiducial were then written to a file. Figure 4-14 and Figure 4-15 shows results of fiducial recognition in typical Lateral and AP X-ray images respectively.

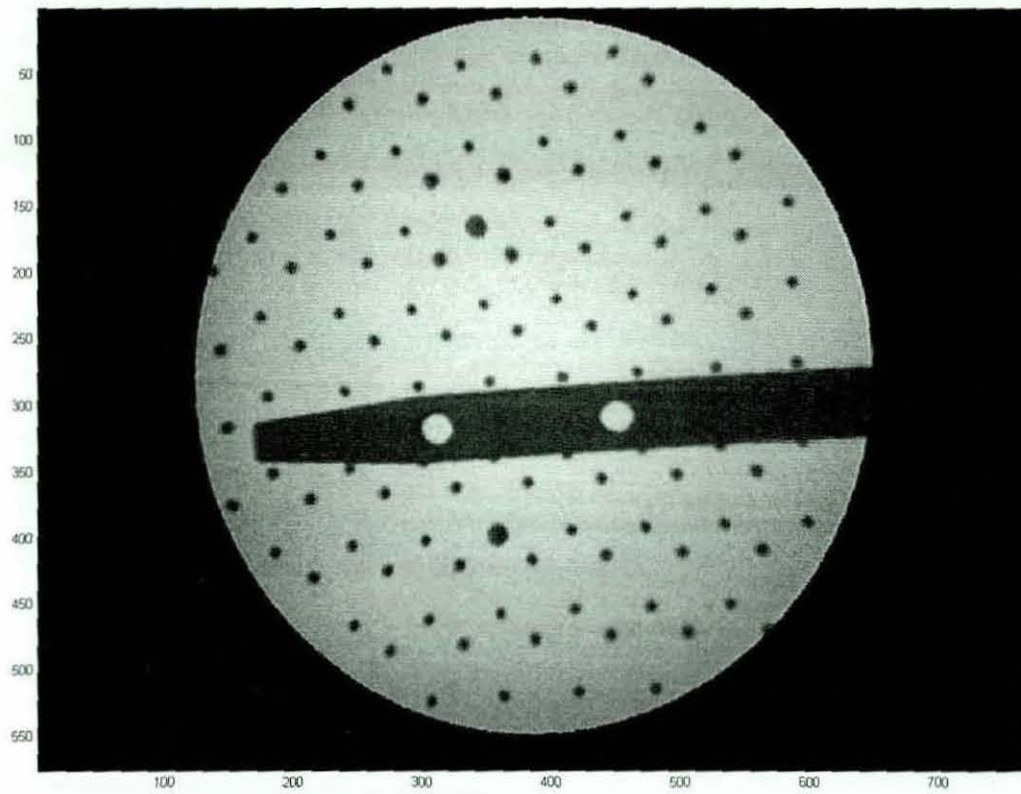


Figure 4-14 Fiducial recognition in the Lateral view image.

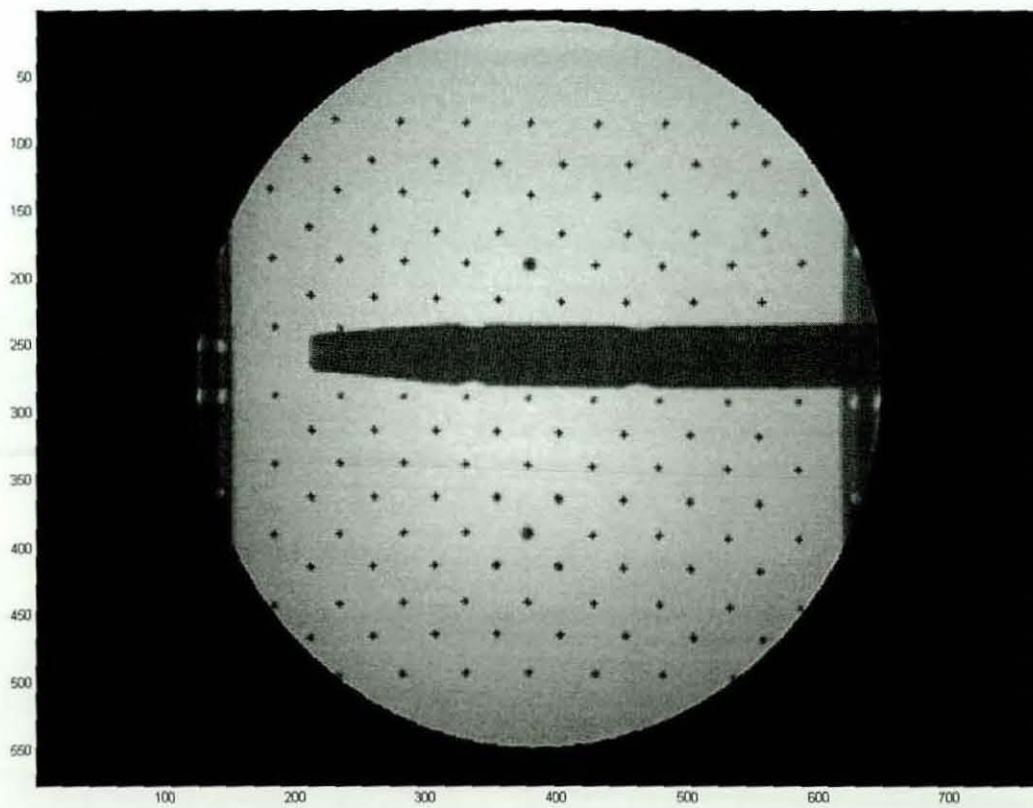


Figure 4-15 Fiducial recognition in AP view image.

4.2.3 Check for partially imaged fiducials

In order to convert 2-D image information into 3-D position information it is essential to determine the focal point (i.e. location of the X-ray source) in both the Lateral and AP views. Since, centres of the detected fiducials are used to compute focal point, therefore to avoid errors in computation of focal point and in turn reconstruction accuracy, it is desirable to identify partially imaged fiducials. For this purpose, the fiducials on the edges of the X-ray image (i.e. fiducials which are only partially imaged) and those touching the edges of the nail (shown in Figure 4-16) have been identified (as described in the following sub-section) and were discarded.

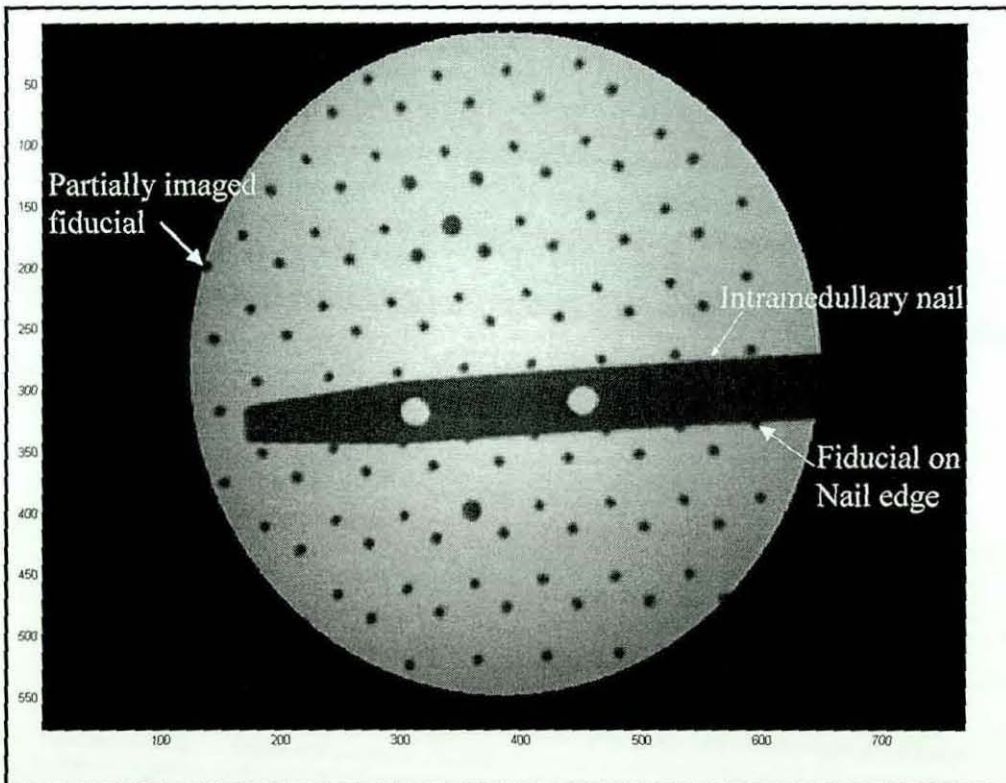


Figure 4-16 Lateral view X-ray image.

Partially imaged fiducials, for example along the edges of the X-ray image as shown in Figure 4-16 were identified by inspecting the cropped region containing the individual fiducial as shown in Figure 4-17.

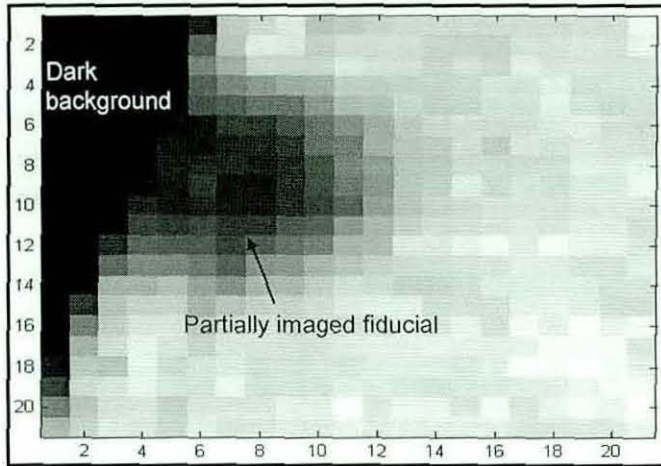


Figure 4-17 Cropped region containing the partially imaged fiducial at the edges of the X-ray image.

The grey level values of the pixels on the boundaries of the cropped region were checked for the presence of dark background. If some of these pixels have a grey level value equal to zero (i.e. indicating the presence of dark background), then the fiducial was classified as partially imaged. Also any fiducial at the nail edges, as shown in Figure 4-16, was identified by inspecting the boundaries of the cropped region of interest (i.e. region containing a fiducial) after thresholding. In case of the boundaries of a region of interest having a non-zero value as shown in Figure 4-18 (a) indicates the presence of the nail in the region, as the grey level values of a pixel belonging to the nail and the fiducial are similar.

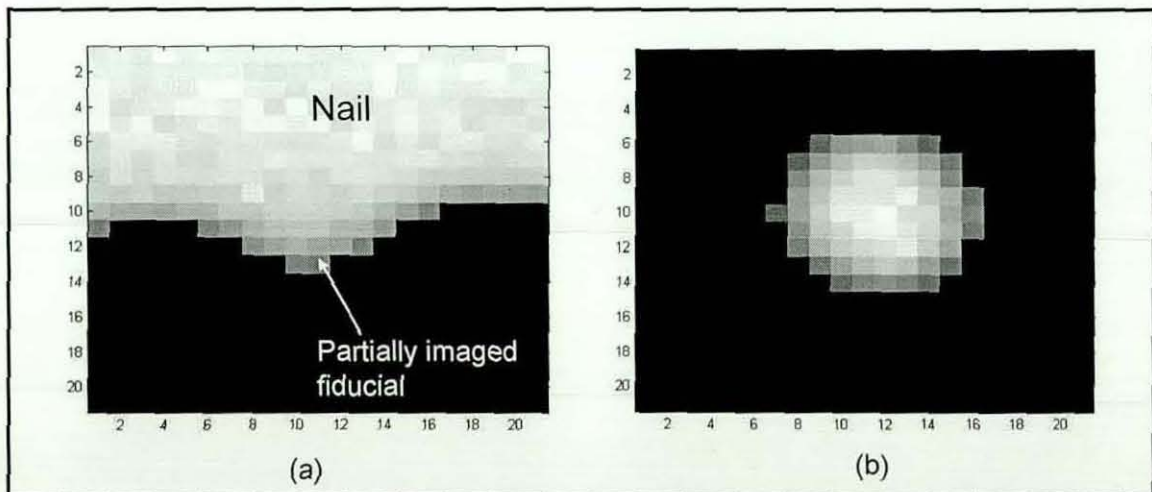


Figure 4-18 (a) Thresholded image of the cropped region containing fiducial at the nail edges (b) Thresholded image of the cropped region containing completely visible fiducial.

4.3 Localized distortion correction

Small ball bearings are widely used as fiducials for distortion correction of the X-ray image intensifier. In this study, localized distortion correction based on fiducial neighbourhood scanning [3] has been undertaken for intraoperative distortion correction of the X-ray images. Once the fiducial recognition has been performed, both the image and world coordinates of fiducials appearing within the field of view are known. Thus, for distortion correction, rather than calibrating the whole image, only those points which are of interest (i.e. image points on calibration plates, that are being used to construct focal lines, refer **Section 4.4**) were calibrated. In this way, much computational time is saved.

This approach allows data obtained directly from actual intraoperative images to be used to perform distortion correction. As a result assumptions do not have to be made with regard to magnetic influence in the operating room, the internal geometry of the Image Intensifier tube or to the orientation of the C-arm unit.

4.4 Location of X-ray source

Radiography can be considered to be a special case of central projection, in which all the rays pass through a perspective centre or focal point [78, 86]. This point is not identifiable as a physical feature of the X-ray machine but lies at a virtual point behind the X-ray tube. Therefore, in order to convert 2-D image information into 3-D position information it is essential to determine the focal point in both the Lateral and AP views. X-ray source point in both Lateral and AP views respectively will then be used in conjunction with points on the nail's centre line to define Lateral and AP view planes respectively. Intersection of these planes defines the nail axis in space as shown in Figure 4-36. Once fiducial recognition was performed, both the image and world coordinates of fiducials appearing within the field of view were known. Focal lines are then constructed to determine the location of the X-ray source. Construction of the focal lines was accomplished by selecting image points within the intraoperative X-ray image and assigning their corresponding world co-ordinates to a point on each of the two calibration plates in the relevant view. For this purpose, centres of some of the detected fiducials on the XR11 calibration plate (i.e. the

calibration plate nearest to the X-ray image intensifier) are selected as image points, as their world co-ordinates are already known, thereby avoiding any calculation error. For each of these image points a corresponding point on the adjacent source calibration plate (i.e. the calibration plate nearest to the X-ray source) was obtained using the localized interpolation technique described in [4]. This technique involves comparing the image coordinates of the given image point on the XRII plate with the image coordinates of fiducials on the Source plate. Three closest fiducials are determined that define a bounding triangle for the given image point, as shown in Figure 4-19. The white cross represent fiducial markers centre on the Source plate.

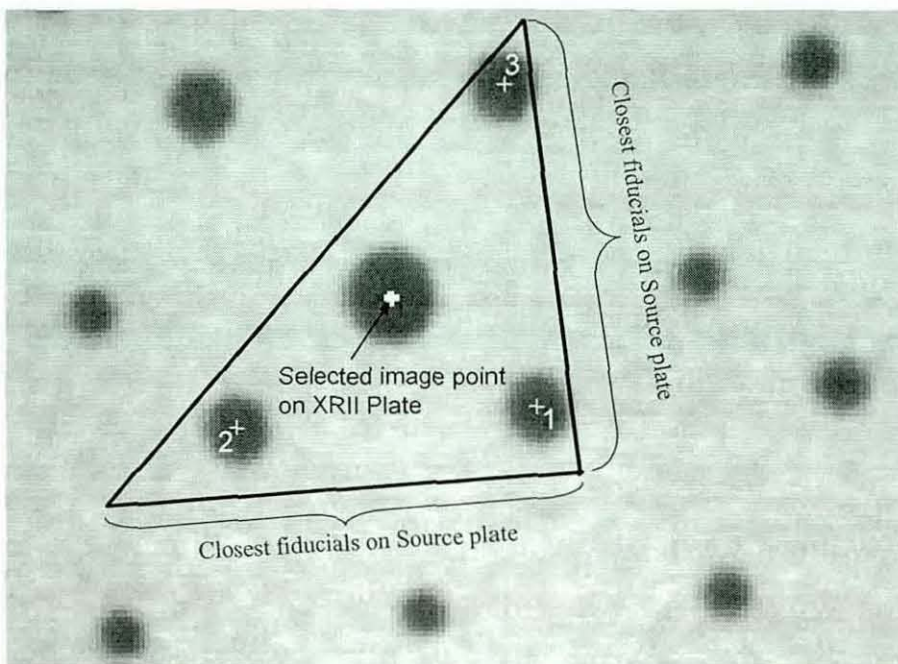


Figure 4-19 Division of intraoperative image into triangular sub-region.

4.4.1 Selection of three closest fiducials

For better accuracy the three closest fiducials for a given image point should enclose the given image point thereby avoiding extrapolation based photogrammetric reconstruction. However, sometimes while taking points on the nail centre line, the three closest fiducials may be collinear due to the positioning of the nail. For example, for an image point shown in Figure 4-20, the three closest fiducials on the source plate were searched so that image point's corresponding position can be determined. In this case, the source plate fiducials lying immediately above the image point were not

detected due to being in close proximity of the nail edges, therefore the three closest fiducial are actually collinear, as shown in Figure 4-20 (a).

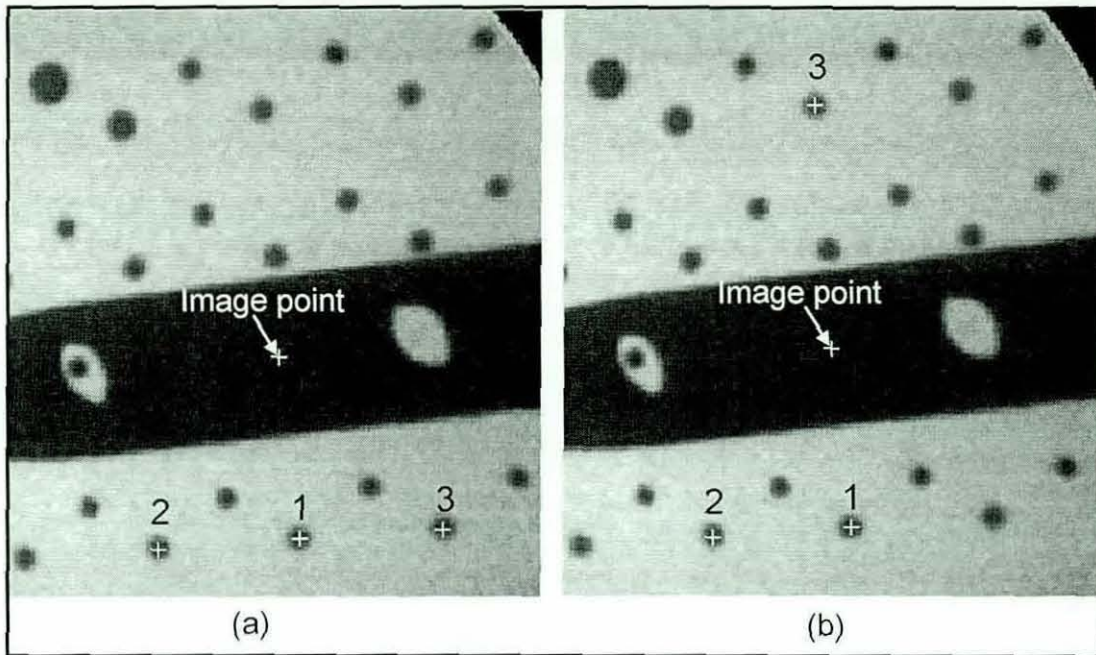


Figure 4-20 Determination of three closest fiducials for a given image point.

The author has therefore developed a novel algorithm that ensures that the selected three fiducials for a given image point on the Source plate always form a bounding triangle for a given image point on the XRII plate as shown in Figure 4-20 (b). Figure 4-21 describes this procedure in detail in the form of a flow chart. It should be noted that this algorithm was developed by the author in response to certain situations where while taking image points (points on the nail centre line), the three closest fiducials to a given image point may be collinear due to the positioning of the nail rather than forming a bounding triangle. In summary, once the first two closest fiducials were chosen, their location was used to check whether they are collinear or not. If they are not collinear, then third closest fiducial was chosen straightaway. However, if the first two fiducials are collinear then the location of the image point with respect to first two closest fiducials was used to determine whether they lie above or below the image point. Afterwards following procedure was adopted for selection of third fiducial:

- At first y co-ordinate of the potential third closest fiducial was compared with those of first two to ensure that all three fiducials are not collinear.

- Once three fiducial were found which were not collinear, it is required to ensure that they bound the given image point in a triangle. For example, as shown in Figure 4-20 if the first two closest collinear fiducials lies below the image point, the third closest fiducial was searched until one was found which lie above the image point. This was accomplished by comparing the y co-ordinate of image point with that of fiducial.

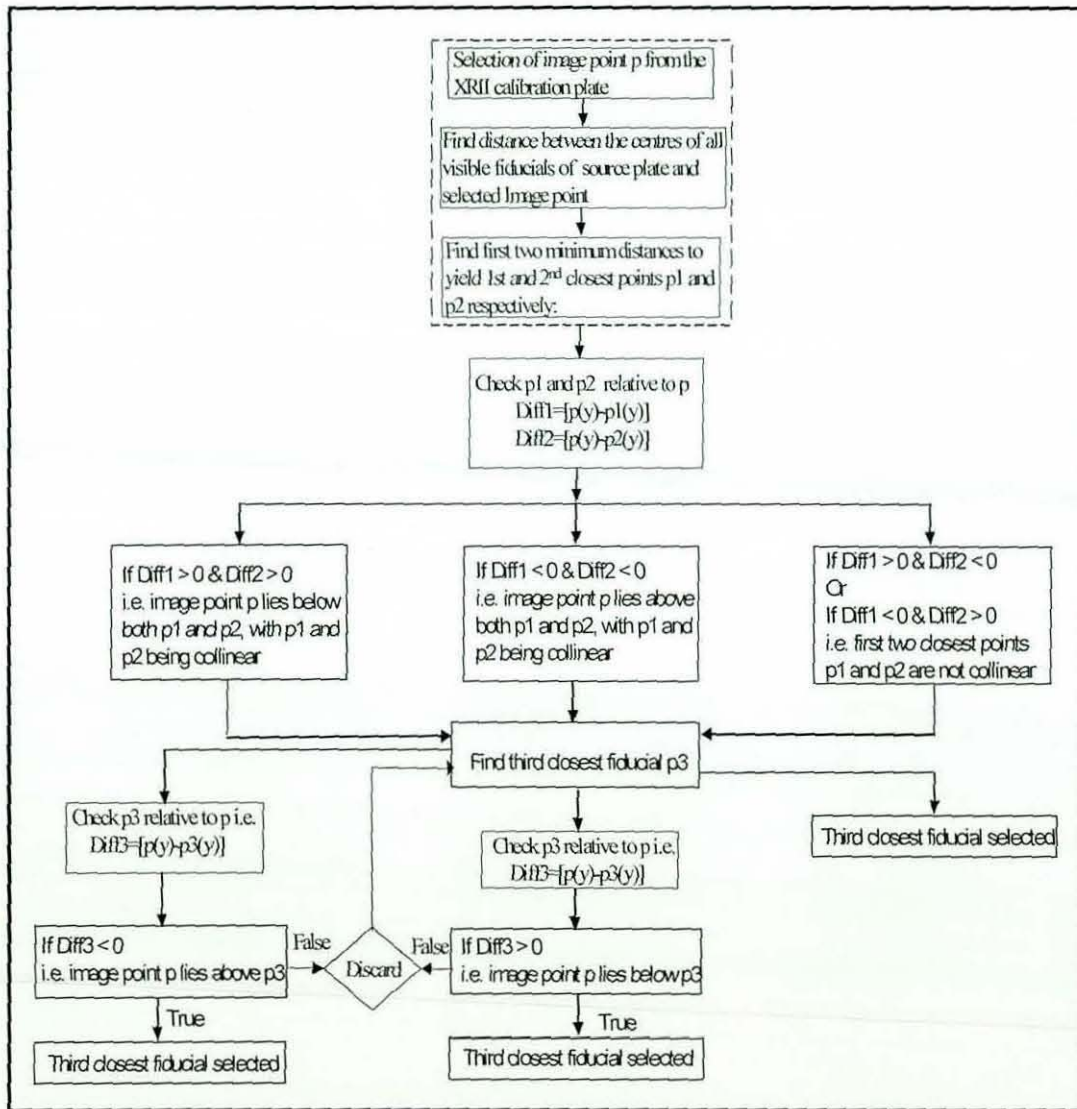


Figure 4-21 Flowchart of algorithm for selecting the bounding triangle for a given image point.

Ideally, focal lines should intersect at a true focal point, as depicted by Figure 4-22. However, due to the nature of X-ray imaging systems these focal lines do not intersect exactly in this way, thus an estimated focal point must be obtained.

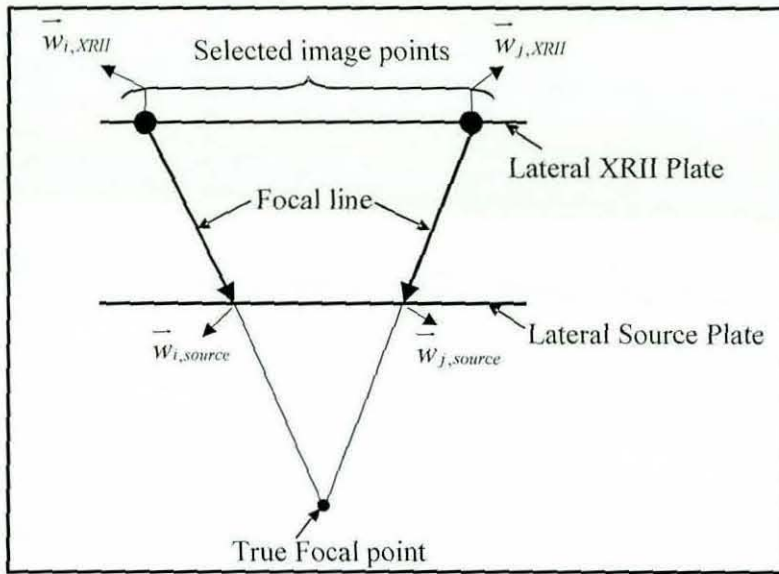


Figure 4-22 Ideal case of the focal point determination.

Therefore, the intersection of each pair of focal lines was obtained and, for pairs which do not intersect due to the nature of the X-ray imaging systems, the point of closest approach was determined as the intersection i.e. the smallest distance between two lines was obtained. The centre point of this distance was considered as their intersection point, as shown in Figure 4-23.

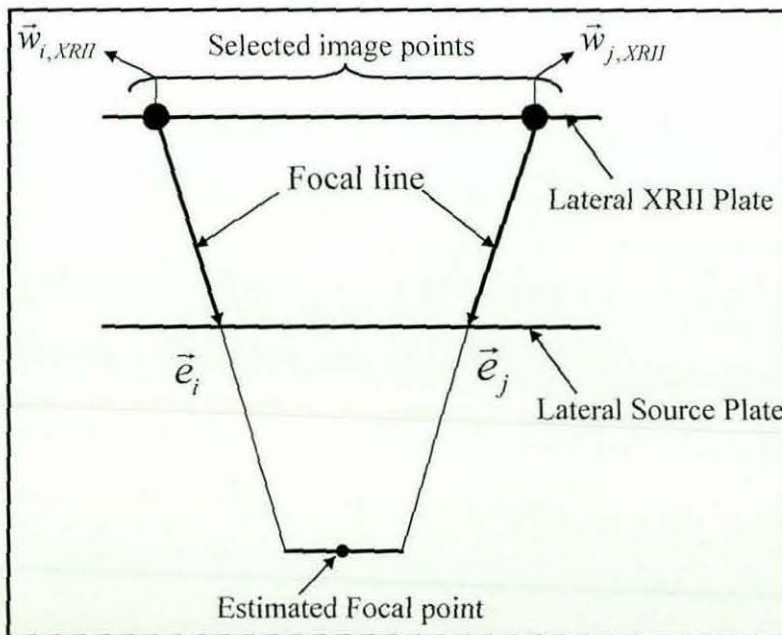


Figure 4-23 Determination of point of intersection between two focal lines using point of closest approach.

Therefore, if there are ' n ' focal lines to be intersected then total number of individual focal points ' N_{fp} ' will be given by:

$$N_{fp} = \frac{(n^2 - n)}{2}$$

The centre of gravity i.e. the mean co-ordinates of this set of intersection points is then obtained and used as an initial estimated focal point ' $F_{initial}$ ' i.e. the location of the X-ray source.

$$F_{initial} = \frac{1}{N_{fp}} \left[\sum_{i=1}^{N_{fp}} F_x \quad \sum_{i=1}^{N_{fp}} F_y \quad \sum_{i=1}^{N_{fp}} F_z \right]$$

However, in order to obtain a better estimation of the focal point, any points which were far off from the estimated focal point location were discarded from the set of intersection points. For this purpose the mean and standard deviation of the set of intersection points were determined, then any intersection point found outside the range i.e. ($mean \pm sd$) were discarded. The mean of the new set of intersection points was then determined and used as the final estimated focal point. Analysis on several X-ray images has shown that the difference in the initial and final estimated focal point locations is within 0.15 mm, which implies most of the individual intersection points were located near the true focal point location. In this study, numbers of image points chosen from the XRII plate for focal point determination were varied from 3 to 25. Results showed that 15 points were enough to obtain the position of the focal point without any loss of accuracy, as similar accuracies were obtained when using 15 or more image points. While selecting the image points on the XRII plate, effort has been made to choose the image points that were located towards the centre of the plate (as this section of the plate is least affected by distortion) while avoiding points that lie at the edges of the nail as shown in Figure 4-24.

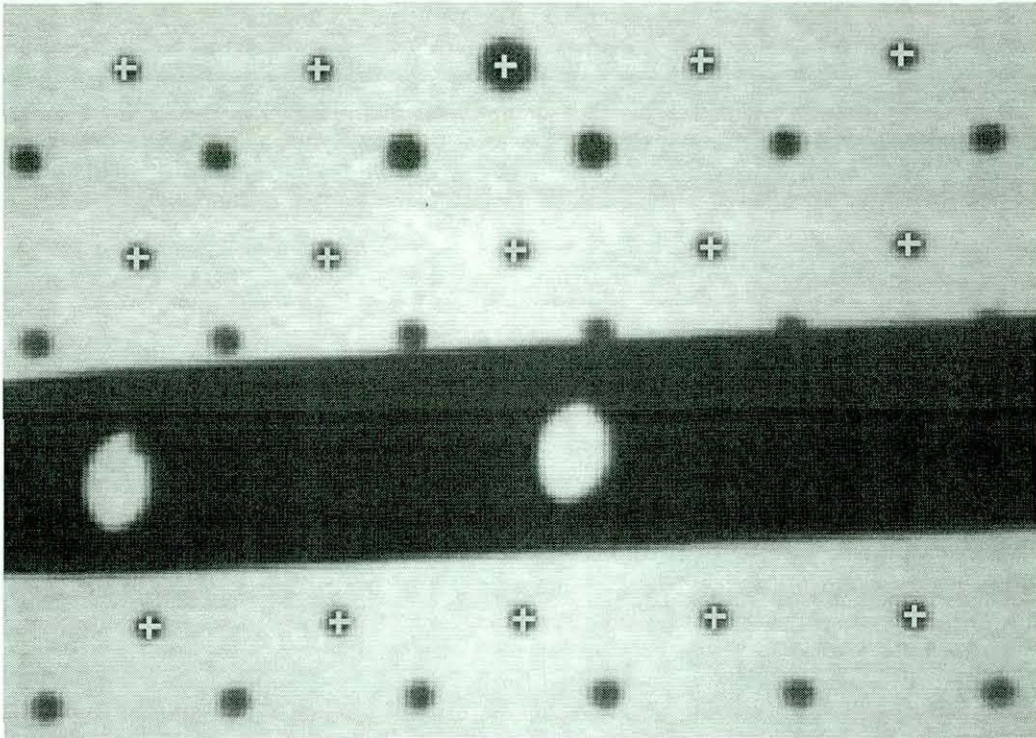


Figure 4-24 Selection of image points from XR11 Plate for focal point determination.

4.5 Recovery of the nail axis in space

In order to recover the nail axis in space, two X-ray images of the nail were used. These two images were taken from views which were roughly orthogonal, hence allowing a complete description of the 3-D position of the nail. In order to determine the nail axis in space, automatic nail border detection was first carried out in both the Lateral and AP views.

For the distal locking procedure, only the distal part of the nail, which contains the distal locking holes, is of importance. Detection of the nail edges is necessary to determine the diameter of the nail and the nail axis. The following assumptions were made:

- The nail axis is midway between the nail borderlines. Therefore, bisection of the nail borderlines will result in determination of the nail centerline in the relevant view.
- The intramedullary nail is straight i.e. has parallel edges at its distal end.

Since, in an X-ray image, the nail is darker than its surroundings, the borderline of the nail can be obtained by analyzing changes i.e. gradient in grey levels within a vertical line profile drawn across the nail. Apparently, there will be two major transitions in grey level values, corresponding to the nail edges, within this profile as shown in Figure 4-25.

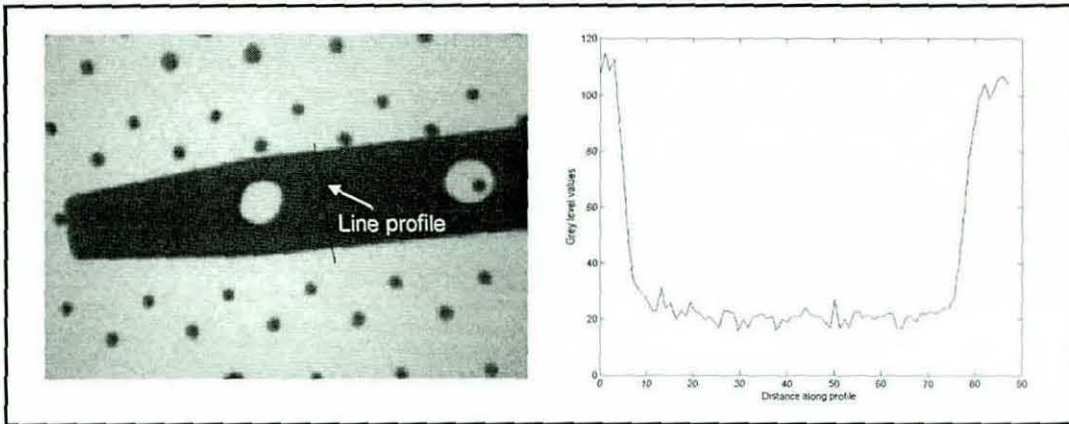


Figure 4-25 Line profile across the nail for nail border detection.

However, problems can be encountered if a fiducial is also present within the line profile (see Figure 4-28) as in such case the maximum grey level difference can be between the pixel related to the fiducial and the background, resulting in false nail edge detection. Therefore, multiple vertical line profiles were drawn across the nail for the purpose of edge detection as described in the following sub-sections.

4.5.1 Nail border detection in the Lateral view image

In the Lateral view image, once the location of the distal hole projection has been obtained automatically (see **Section 4.6.1**), multiple line profiles on both sides of the distal hole projection were generated as measuring the nail edges only once can lead to potential errors, such as the presence of a fiducial within the profile. These automatic line profiles were parallel to each other. Detection of the nail edges for each profile is performed in the following manner:

- Initially the length of the line profile to be drawn was determined by finding the approximate width of the nail from the thresholded image. For this purpose, once the extraction of the distal hole projection has been performed (see **Section 4.6.1**),

the information obtained from the bounding box of the distal hole projection was used to crop the region containing the distal end of the nail as shown in Figure 4-26. The cropped image was then thresholded and inverted (shown in Figure 4-27) so that the nail can be considered as an object (i.e. area of white pixels).

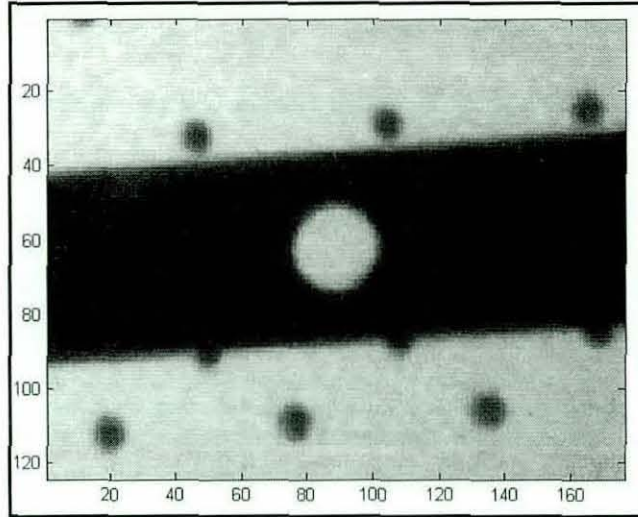


Figure 4-26 Cropping of image to determine nail width.

Any fiducials in the surrounding region of the nail were then discarded by only considering objects with area greater than 500 pixels as shown in Figure 4-27. The approximate width of the nail was then determined by using the co-ordinates of potential edges of the nail in the cropped region as shown in Figure 4-27. However, it can be seen that the presence of fiducials at the nail edges can induce an error in this approximation of the nail width, therefore multiple nail edges were used to estimated nail width.

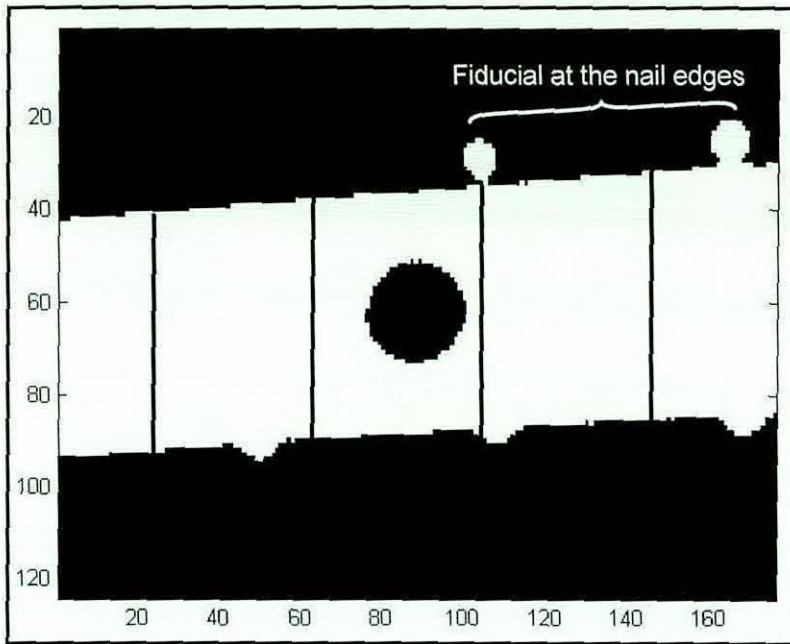


Figure 4-27 Determination of approximate nail width.

- Based on the location of the mid nail width point, the line profile was then divided into upper and lower halves for detecting upper and lower edges of the nail respectively, as shown in Figure 4-28.

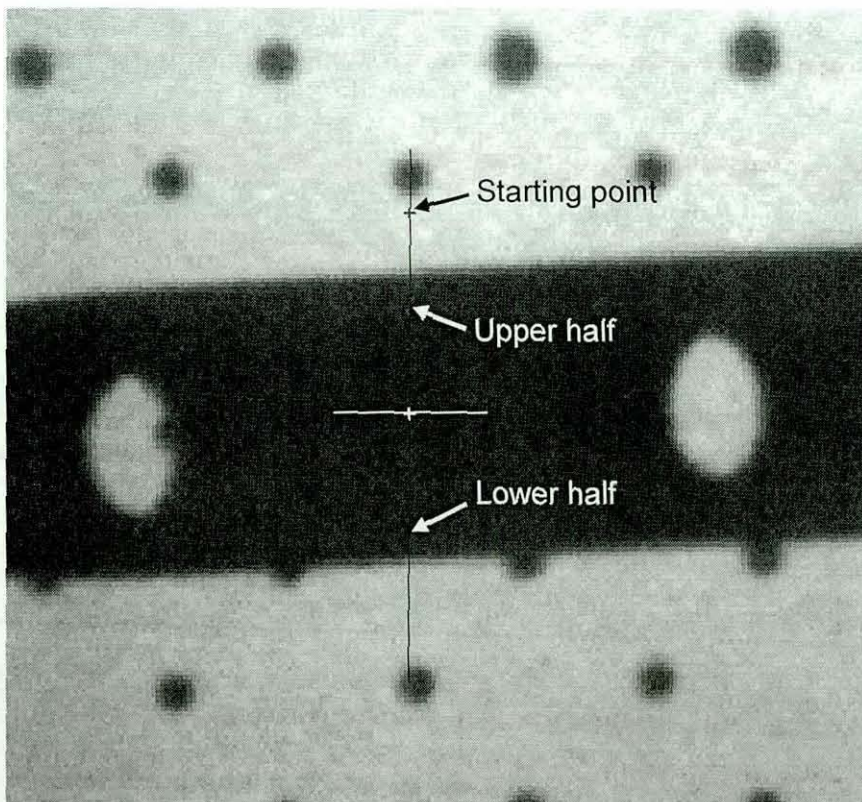


Figure 4-28 Division of line profile in two halves.

- For the upper half of the profile, the maximum value of grey level was determined, and then only the profile from that point i.e. starting point as shown in Figure 4-28, onwards was considered, while the rest of the profile above this point was discarded. Use of this approach eliminated any error which may be caused by presence of fiducial towards the end of the profile (as shown in Figure 4-28) as largest grey level gradient or derivative of the profile is used to determine nail edges.
- The grey level gradient or derivative of the profile was determined for all the pixels, within the remaining upper half profile.
- The point where this derivative is a maximum was then classified as an edge pixel as shown in Figure 4-29. However, in the case of two maxima, the lower pixel of the two was considered as an edge pixel, because the transition between consecutive grey levels across the nail was small in comparison to the transition between the nail and background or the fiducial and background. Therefore the upper of the two pixels (i.e. where the derivative is maximum) was classified as the transition between a fiducial and background.

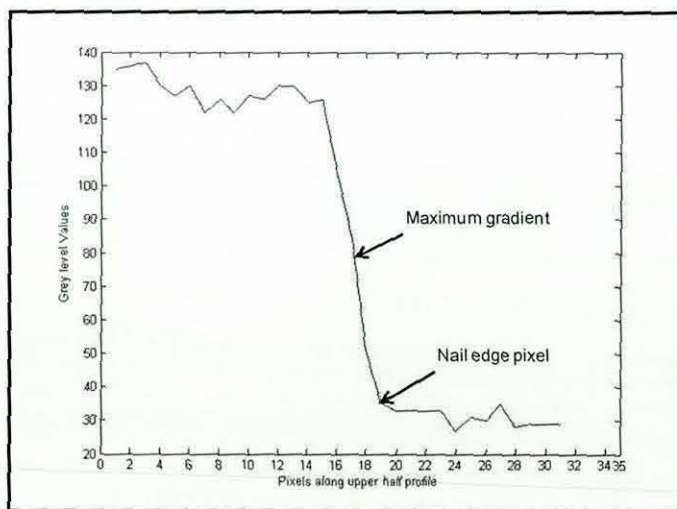


Figure 4-29 Determination of nail edge using gradient

- Then for the lower half of the profile, a maximum value of grey level was determined, and then only the profile from that point upwards was considered, while the rest of profile below that point was discarded. This was done because if

the line profile ends within a fiducial, then in this way only that part of the profile was considered which comes before a fiducial.

- As for the upper line profile, an edge pixel was obtained for the lower half of the line profile in a similar fashion. However, for the lower half of the line profile, in case of two maxima, the upper of the two pixels was considered as an edge pixel. Whereas, the lower pixel of the two was classified as the transition between a fiducial and the background.
- Once the upper and lower edges were determined for each individual profile, the profile length between the nail edges was determined. These profile lengths were then stored in an array called "profilelength_set".
- The mean and standard deviation (sd) of the "profilelength_set" were determined.
- Any value of profile length within "profilelength_set" found outside the range i.e. ($mean \pm sd$) were regarded as abnormal values and were discarded from "profilelength_set".
- The coordinates of edges obtained from "profilelength_set" were then averaged, to determine the nail edges. Similarly average profile length was determined by averaging the set of profile length obtained from "profilelength_set".
- Since vertical line profiles drawn across the nail were perpendicular to the x-axis of the image and not to the nail edges, to compute nail diameter it is essential to determine the slope of the nail axis (β) as shown in Figure 4-30. In order to determine the slope of the nail axis, nail border lines were obtained by using linear least square fit of a straight line to the data i.e. edges found on the nail border lines. Since, the nail is straight i.e. has parallel edges at the distal end of the nail, the nail axis will have the same slope as the nail borderlines.

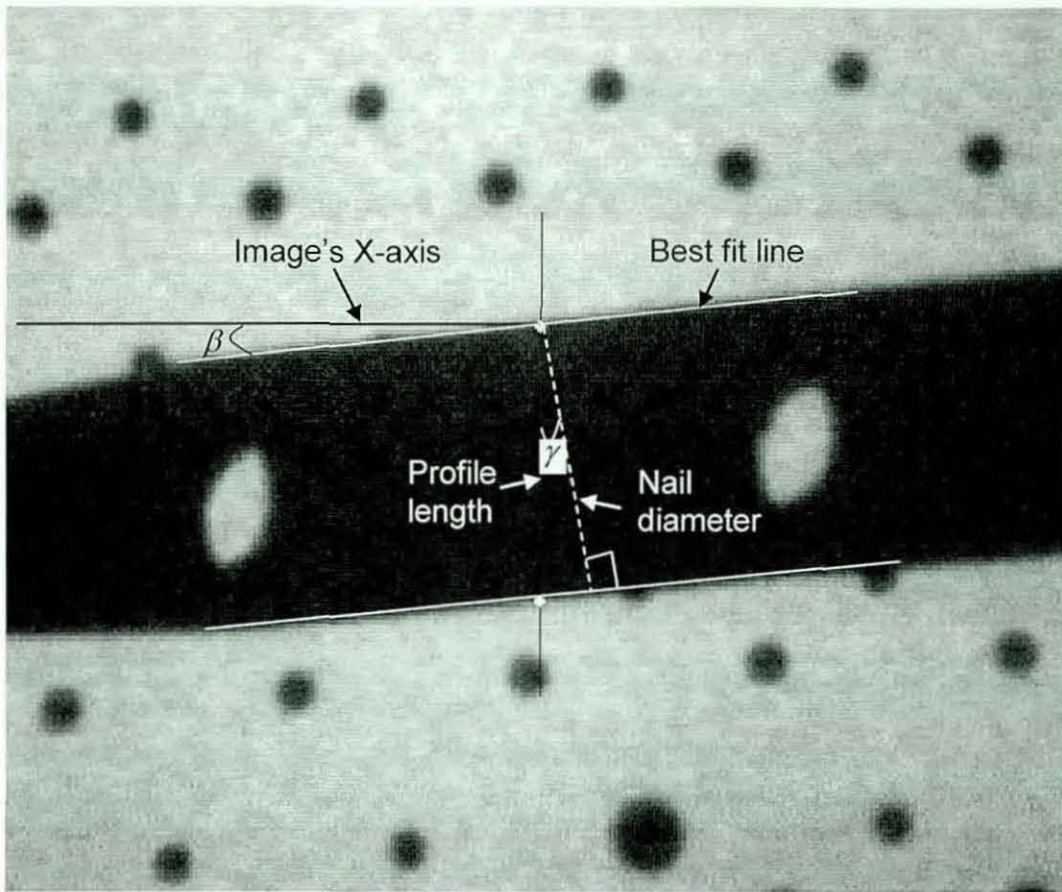


Figure 4-30 Determination of nail diameter.

It can be seen from Figure 4-30 that the nail diameter (ϕ) will be given by:

$$\phi = \text{Profile length} \times \cos \gamma$$

- By assuming that the nail axis coincides with the centre of the nail borderlines, the boundary edges of the nail, shown in Figure 4-31, were then bisected to determine the nail axis in the Lateral view image.

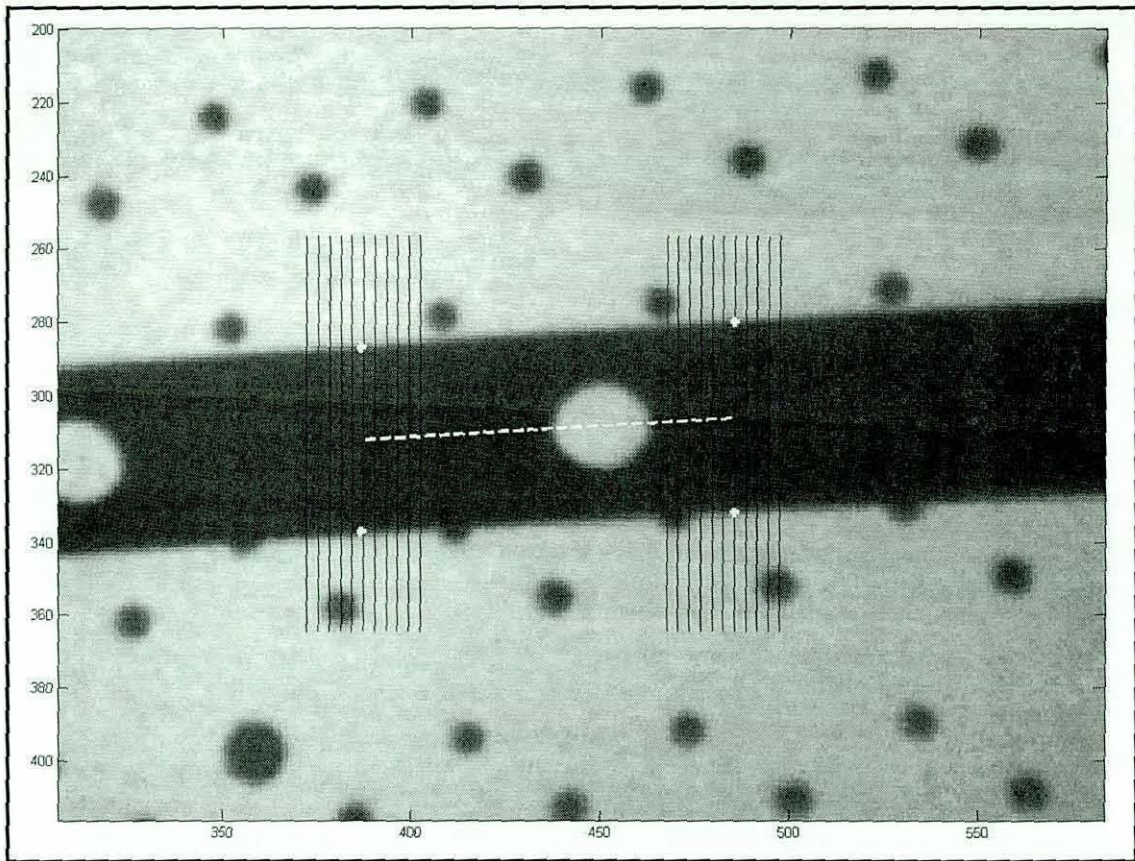


Figure 4-31 Detection of nail edges and nail centreline in the Lateral view.

4.5.2 Nail border detection in the AP view image

In the AP view image, the location of the nail was determined in the following manner:

- The primary condition for taking an AP view image is to have the nail lying between the central and orientation marker of the XRII AP plate. Therefore, once fiducial recognition was performed, location of the central and orientation markers along with the fiducials on their extreme right and left hand sides allows cropping of the part of the image that contains the distal end of the nail, as shown in Figure 4-32.

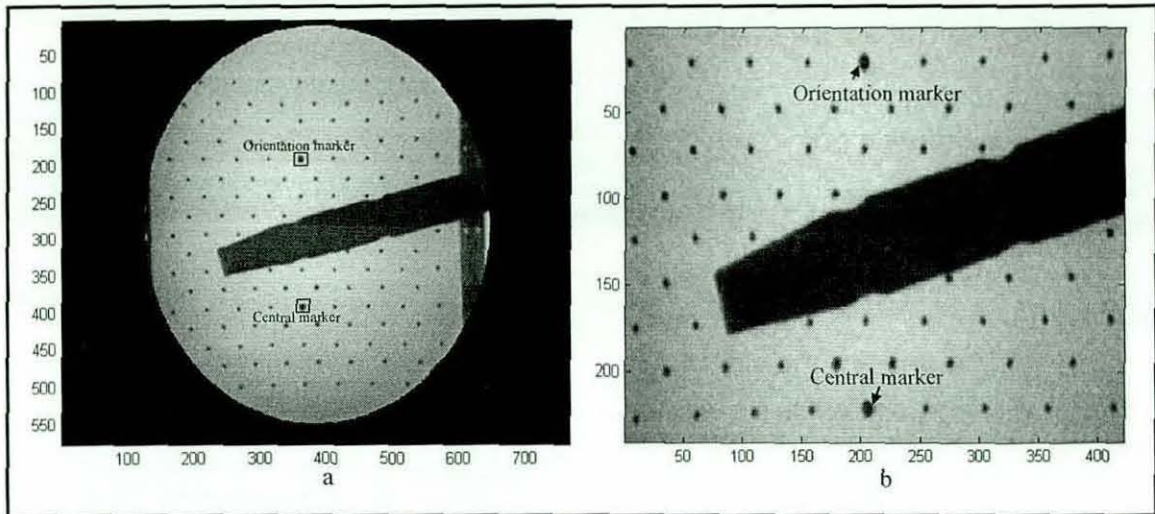


Figure 4-32 (a) AP view image (b) Cropping of the AP view image to locate the nail using central and orientation markers.

Where the nail obscures fiducials on either side of the central or orientation marker, the fiducials on the extreme right and left hand side of the line immediately above the line containing the orientation marker (say Line 1) were chosen to crop the image, for example as shown in Figure 4-33, where the extreme right and left hand side fiducials on Line 1 were used to crop the image.

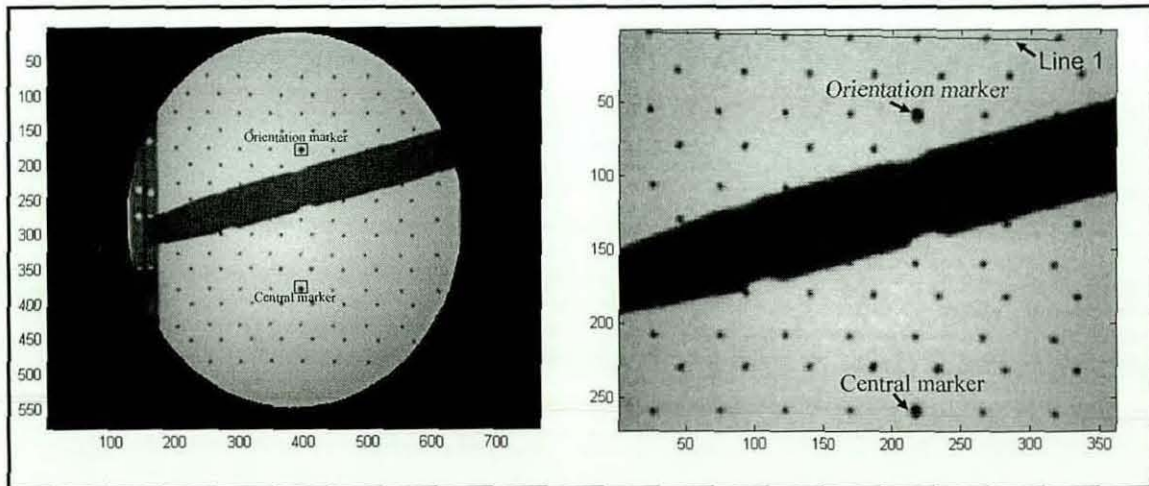


Figure 4-33 Location of nail in the AP view, when fiducials on extreme R.H.S. of the Orientation marker are hidden beneath the nail.

- The approximate width of the nail and slope of the nail axis were then determined in a similar fashion to that of the Lateral view image (see Section 4.5.1.).

- Then, several line profiles (at 10 pixel intervals) perpendicular to the nail axis were drawn from the starting point as shown in Figure 4-35. The starting point for drawing line profiles was obtained by determining the upper most nail edge from the thresholded image of the region containing the nail, as shown in Figure 4-34.

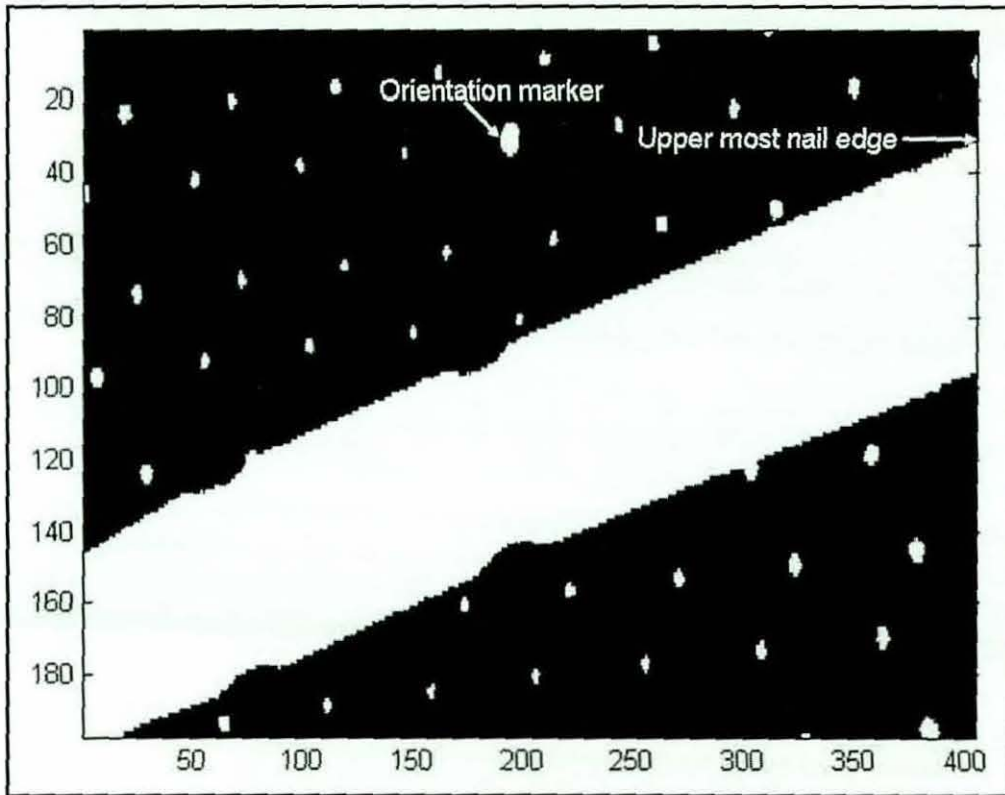


Figure 4-34 Determination of starting point for drawing line profiles.

The length of each line profile between the nail edges along that particular line was then determined to locate the positioning of the distal locking hole by finding the minima, so that this region can be avoided during the subsequent nail border detection process. Here it should be noted that during laboratory trials to cover a wide range of possible nail orientations likely to be encountered during the surgical procedure, the test rig was used to simulate different rotations (θ) of the nail about its own axis, with the nail at different orientations (ϕ) with respect to the X-ray imaging axis. There was always a minima (used to locate the positioning of the distal locking hole) on the AP view image.

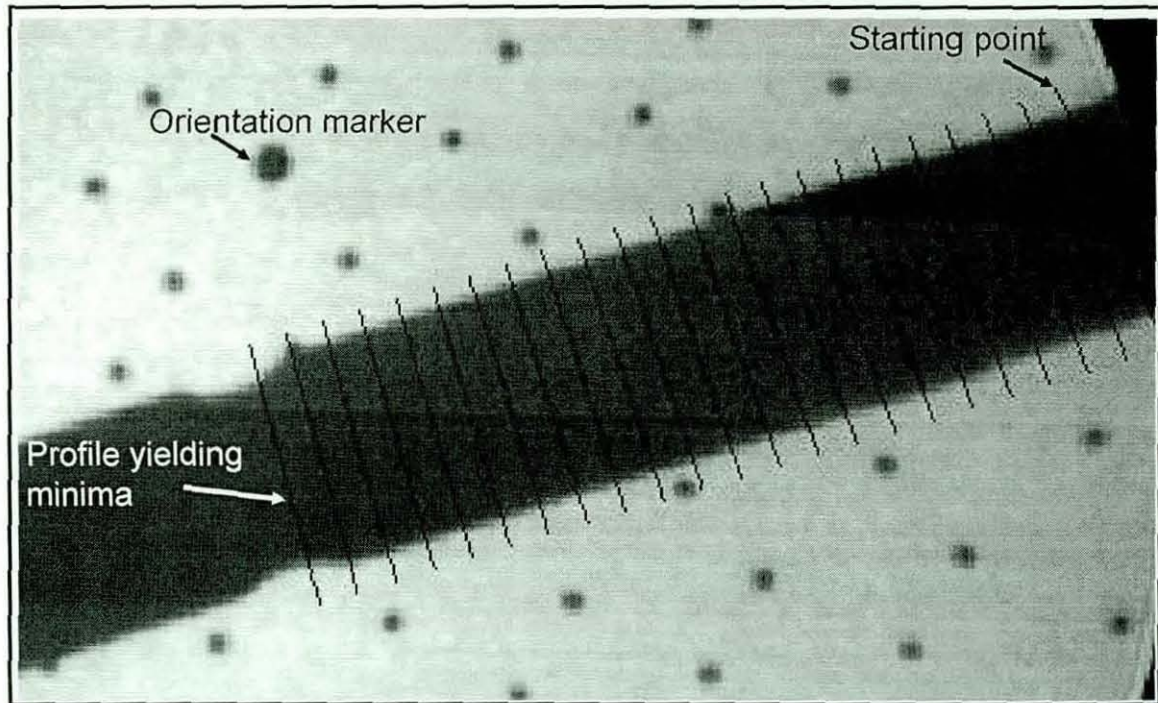


Figure 4-35 Drawing line profile across the nail to avoid a distal hole.

- The pixel co-ordinate information was obtained from the starting point of the line profile for which minima was found. It was then used in conjunction with the starting points of other line profiles to establish starting points for drawing line profiles on both sides of the distal locking hole. Then the nail border detection in the AP view image was carried out in a similar fashion as for the Lateral view image (see **Section 4.5.1**). Figure 4-36 represents nail edge detection in a typical AP view X-ray image. For robustness purposes, influence of noise on nail edge detection has been considered, details of which can be found in Section 6.6.

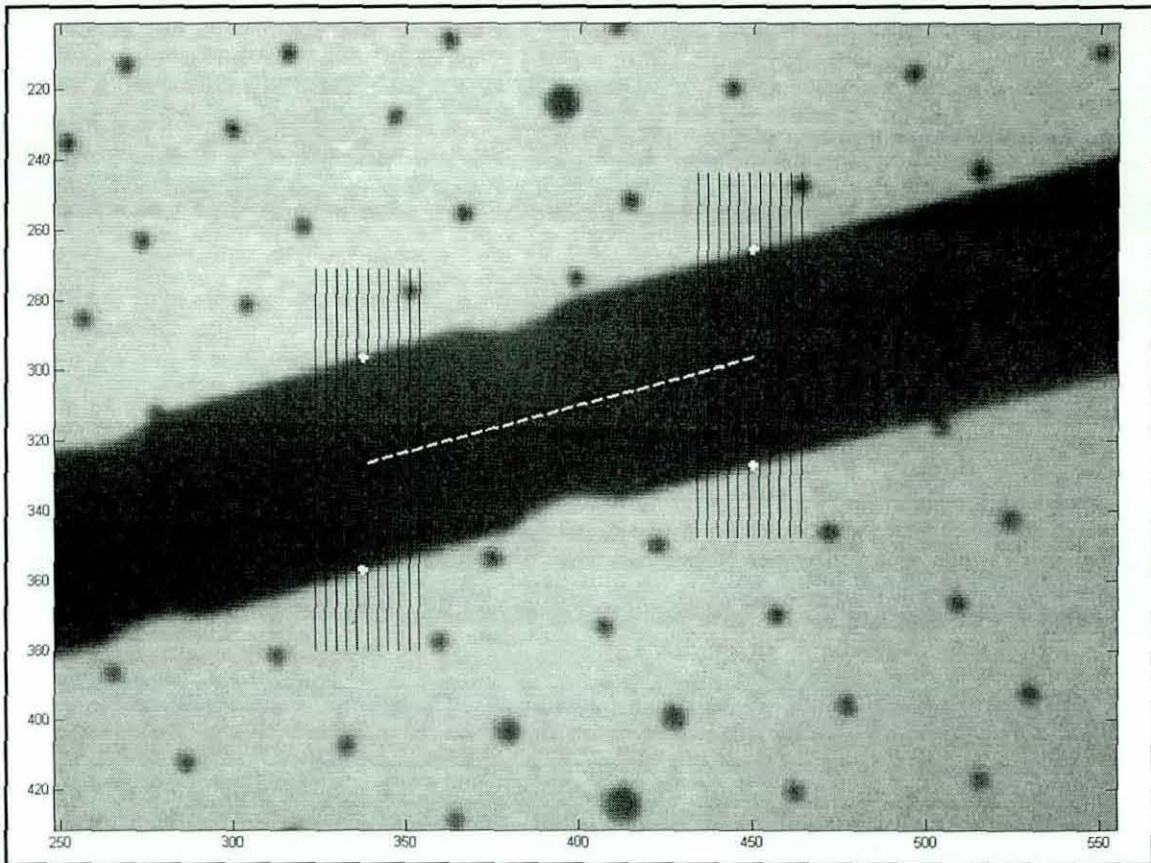


Figure 4-36 Detection of nail edges and nail axis in the AP view.

The procedure used in this study to obtain the nail axis in space has been described in [5, 85]. In the Lateral view, after nail border detection, it is possible to find points on the centre line of the nail. Once these points were known in the image plane, a localized interpolation technique using triangular sub-regions was used to find their corresponding world coordinates on the calibration plate. These two points in conjunction with the Lateral view focal point define a plane. A similar approach was carried out for the AP view. Once these planes were defined in the Lateral and AP views respectively, their intersection defines the nail axis in space as shown in Figure 4-37. This has been accomplished as follows:

At first defining Lateral view plane using Lateral view focal point (F_{lat}) and points Lat_{pt1} and Lat_{pt2} which lie on the nail centre line. Let $P(x_1, y_1, z_1)$ be a general point in the plane determined by the points F_{lat} , Lat_{pt1} and Lat_{pt2} . Now defining two vectors in plane as follows:

$$\vec{L}_{vec1} = (F_{lat} - Lat_{pt1}) \quad (\text{Equation 4-1})$$

$$\vec{L}_{vec2} = (F_{lat} - Lat_{pt2}) \quad \text{(Equation 4-2)}$$

Now the cross product of these two vectors will define a normal vector which is perpendicular to the plane determined by the points F_{lat} , Lat_{pt1} and Lat_{pt2} .

$$\vec{N}_{Lat} = (\vec{L}_{vec1} \times \vec{L}_{vec2}) \quad \text{(Equation 4-3)}$$

Since P is distinct from F_{lat} , therefore $F\vec{P}_{Lat}$ lies in the plane and is perpendicular to the vector ' \vec{N}_{Lat} '. Now the equation of the plane is:

$$F\vec{P}_{Lat} \cdot (\vec{L}_{vec1} \times \vec{L}_{vec2}) = 0 \quad \text{(Equation 4-4)}$$

Now similarly defining AP view plane using AP view focal point (F_{ap}) and points AP_{pt1} and AP_{pt2} which lies on the nail centre line. Let Q (x_2, y_2, z_2) be a general point in the plane determined by the points F_{ap} , AP_{pt1} and AP_{pt2} . Now defining two vectors in plane as follows:

$$\vec{A}_{vec1} = (F_{AP} - AP_{pt1}) \quad \text{(Equation 4-5)}$$

$$\vec{A}_{vec2} = (F_{AP} - AP_{pt2}) \quad \text{(Equation 4-6)}$$

Now the cross product of these two vectors will define a normal vector which is perpendicular to the plane determined by the points F_{ap} , AP_{pt1} and AP_{pt2} .

$$\vec{N}_{AP} = (\vec{A}_{vec1} \times \vec{A}_{vec2}) \quad \text{(Equation 4-7)}$$

Since Q is distinct from F_{ap} , therefore $F\vec{Q}_{AP}$ lies in the plane and is perpendicular to the vector ' \vec{N}_{Lat} '. Now the equation of the plane is:

$$F\vec{Q}_{AP} \cdot (\vec{A}_{vec1} \times \vec{A}_{vec2}) = 0 \quad \text{(Equation 4-8)}$$

Now, the vector or cross product of these two normal vectors i.e. \vec{N}_{Lat} and \vec{N}_{AP} gives a vector which is perpendicular to both of them and which is therefore parallel to the line of intersection of the two planes. So this cross product will give a direction vector ' \vec{V} ' for the line of intersection.

$$\vec{V} = (\vec{N}_{Lat} \times \vec{N}_{AP}) \quad \text{(Equation 4-9)}$$

In order to define the vector equation of the line of intersection, it is essential to find a position vector, say ' \vec{a} ' of a specific point on the line. This position vector ' \vec{a} ' can be found by setting y-component equal to zero in equation 4.4 and equation 4.8 for Lateral and AP planes respectively and solving these two equations simultaneously. Now the equation of the line of intersection can be given by:

$$r = \vec{a} + t\vec{V} \quad \text{(Equation 4-10)}$$

It should be noted that point that is obtained for any value of 't' will satisfy equation 4.4 and equation 4.8 for Lateral and AP planes respectively.

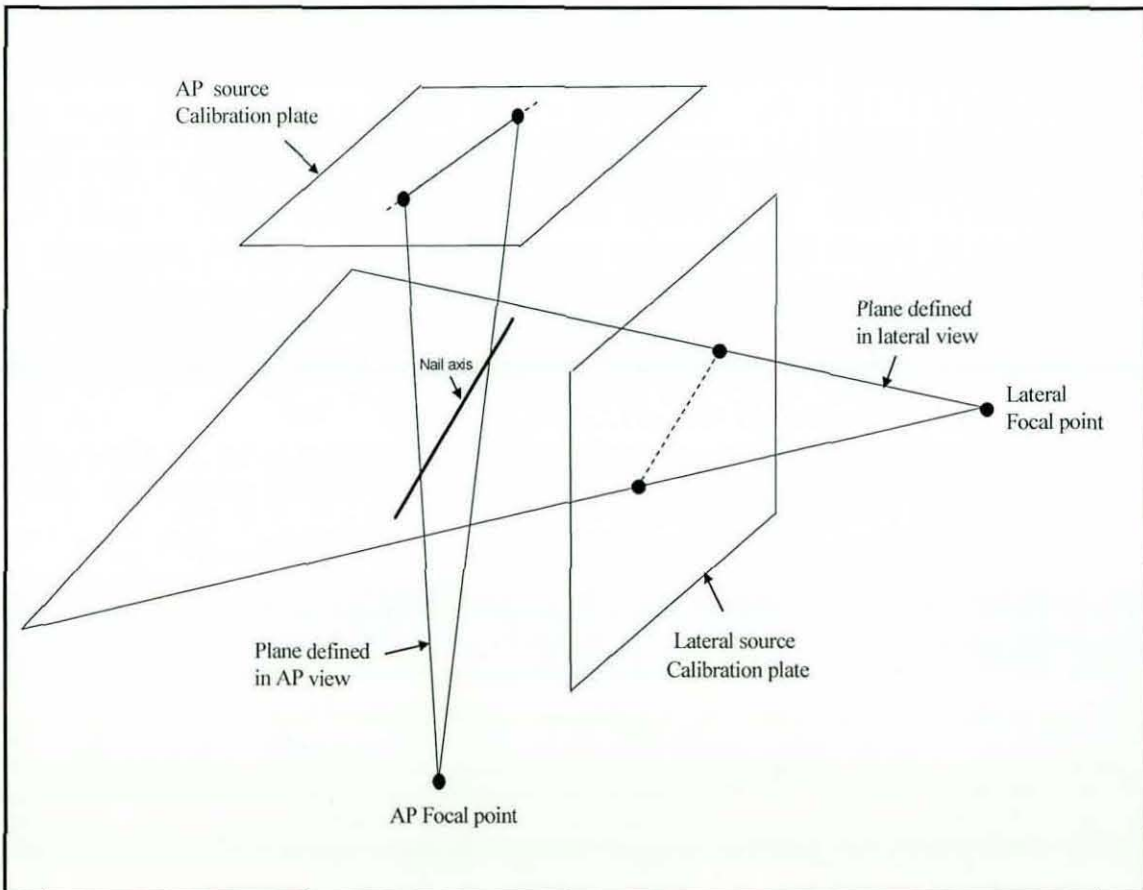


Figure 4-37 Recovery of the nail axis in space using extrapolation technique [5, 85]

4.6 Determination of the drilling axis for distal holes

The features that were used to determine the drilling trajectory were: the angle λ (shown in Figure 4-38) between the major axis of the distal hole's oval shaped projection and the nail axis or the dimensionless area of the distal hole projection, the

target point (which is the intersection of the distal hole axis and the nail axis) and the angle ϕ (shown in Figure 4-40) between the X-ray imaging axis and the nail axis. These features are described below.

Angle between major axis of the oval and the nail axis (λ)

Feature extraction from the distal hole projection is very critical, as its accuracy will influence the overall performance of the system. During rotation of the nail about its long axis, the angle of the major axis of the oval shaped distal hole projection changes significantly with respect to the nail axis. Therefore, the region containing the distal hole projection was selected from the Lateral view X-ray image and image segmentation was performed to extract the oval shape. The major axis of the oval was then determined using a least squares best fit approach [130]. The angle λ between the major axis of the oval and the nail axis was then determined as a characteristic measurement as shown in Figure 4-38. The angle λ is then used in conjunction with the Look-up tables (LUT) obtained from modelling of the intramedullary nail (described in detail in Chapter 5) to to predict rotation of the nail about its long axis i.e. θ .

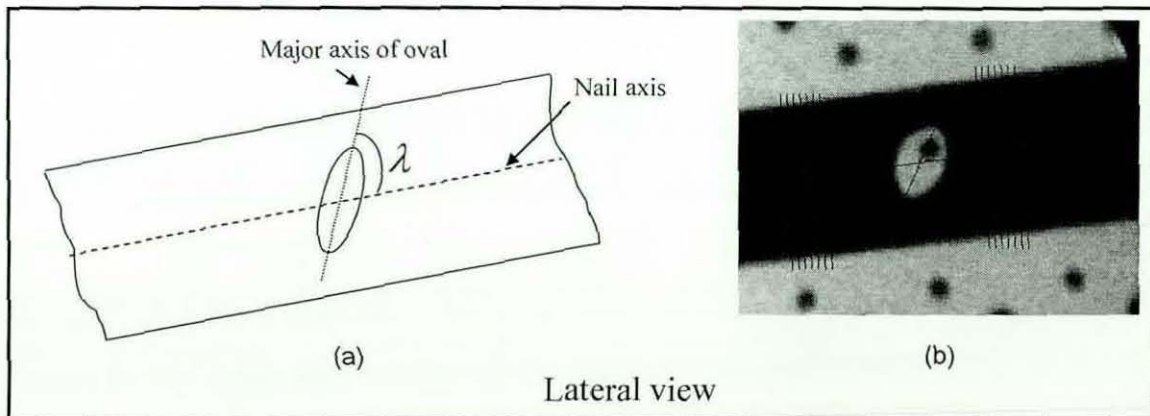


Figure 4-38 Angle between the major axis of the oval and the nail axis. (a) Concept (b) Implementation using image analysis

Dimensionless area calculation

When the nail is rotated about its long axis, the angle of the major axis of the oval-shaped distal hole projection changes significantly with respect to the nail axis, which

remains constant except when the nail axis is perpendicular to the X-ray imaging axis. In such a scenario it will not be possible to use λ as a characteristic measurement. Therefore in the light of the results obtained from modelling of the intramedullary nail (see **Section 5.5**) it is recommended to use a dimensionless area as a characteristic measurement in such scenarios. Therefore, once the distal hole's oval shaped projection was extracted from the Lateral view X-ray image (see **Section 4.6.1**); the area within the extracted boundary was calculated by counting the number of pixels having a value of 1 within the extracted boundary. Dimensionless area was then calculated by dividing this area by nail's diameter, which was obtained from the Lateral image as discussed in **Section 4.5.1** .

Determination of target point and angle ϕ

The desired drilling trajectory must pass through the centre of the distal hole, i.e. the target point, which is the intersection of the nail axis with the distal hole axis. This point was found by intersecting the nail axis with the line-of-sight that passes through the centre of the distal hole. In order to construct the line-of-sight that passes through the centre of the distal hole, the image (pixel) co-ordinates of the centre of the hole's oval shaped projection, shown in Figure 4-39 were determined using the Lateral view X-ray image.

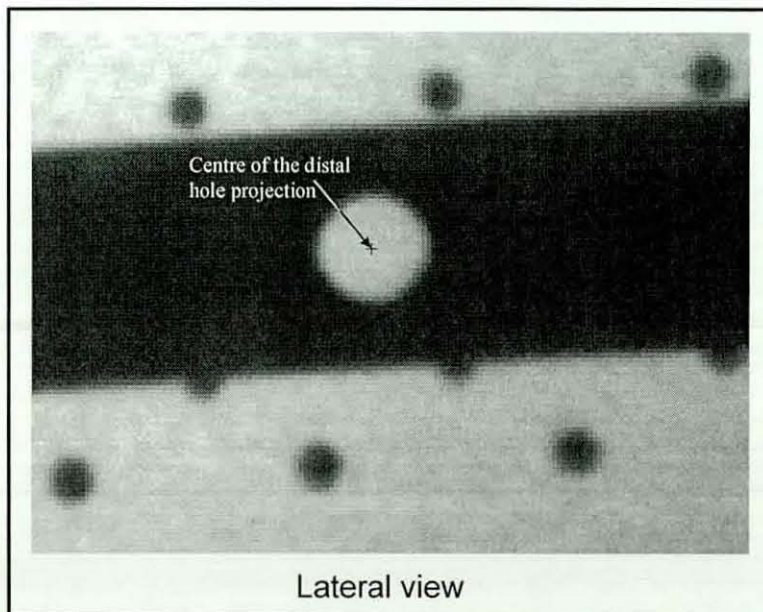


Figure 4-39 Location of the centre of the distal hole projection in image plane.

By applying a triangulation technique (described in **Section 4.4**) to this measured pixel location, the corresponding source calibration plate intersection point " P_{source} ", can be found. Now a line-of-sight can be defined using the focal point (determined in **Section 4.4**) in the Lateral view in conjunction with " P_{source} ", which passes through the centre of the distal hole i.e. "O" as shown in Figure 4-40.

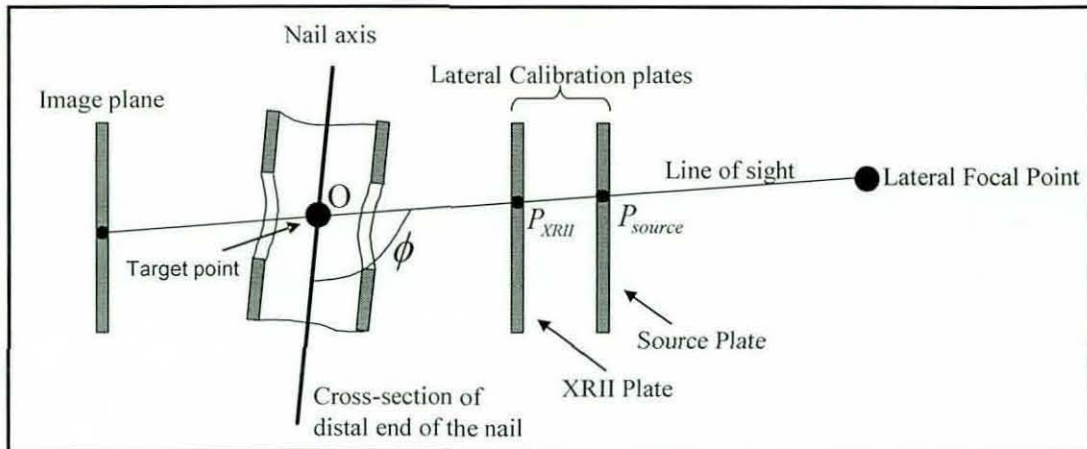


Figure 4-40 Determination of distal hole's centre and angle ϕ .

Angle ϕ is then determined by finding the angle between the nail axis and the line-of-sight (defined by the line passing through the target point "O" and Lateral focal point) as shown in Figure 4-40.

Investigation of the effect of nail rotation on the centre of the oval

An investigation was carried out to determine whether the centre of the oval changes or not, as the nail is rotated. The following results were obtained. Although image magnification or pixel/mm ratio is dependent on positioning of the X-ray source with respect to the calibration frame, however for a standard Lateral view image it was found to be around 0.2, i.e. 1 Pixel \approx 0.2 mm.

Reading Number (n)	Rotation of the nail about its long axis " θ " (Degrees)	Coordinates of centre (x_n, y_n) of the oval (Pixels)	Distance (Pixel) $\sqrt{(x_n - x_0)^2 + (y_n - y_0)^2}$
1	0	(450.5 , 308.2)	-
2	2	(450.6 , 308.3)	0.2
3	4	(450.8 , 308.1)	0.3
4	6	(450.9 , 308.6)	0.5
5	8	(450.8 , 308.6)	0.5
6	10	(450.8 , 308.4)	0.4
7	12	(451.0 , 308.4)	0.5
8	14	(450.5 , 308.4)	0.2
9	16	(450.8 , 308.7)	0.5

Table 4-5 Investigation into change in the centre of the oval.

It can be seen from Table 4-5, that there is no significant difference in the centre of the oval as the nail is rotated about its long axis; and the minor difference that occurs in the location of the centre of the oval is due to digitisation error.

Determination of angle ϕ

The angle ϕ between the nail axis and the line-of-sight (defined by the line passing through the target point "O" and Lateral focal point as shown in Figure 4-40), yields the rotation of the nail about the X-ray imaging axis.

Rotation of the intramedullary nail about its long axis

For determination of the drilling axis, in addition to the angles λ , ϕ and the coordinates of the target point, it is also necessary to determine the rotation of the nail θ about its long axis with respect to the line-of-sight as shown in Figure 4-41.

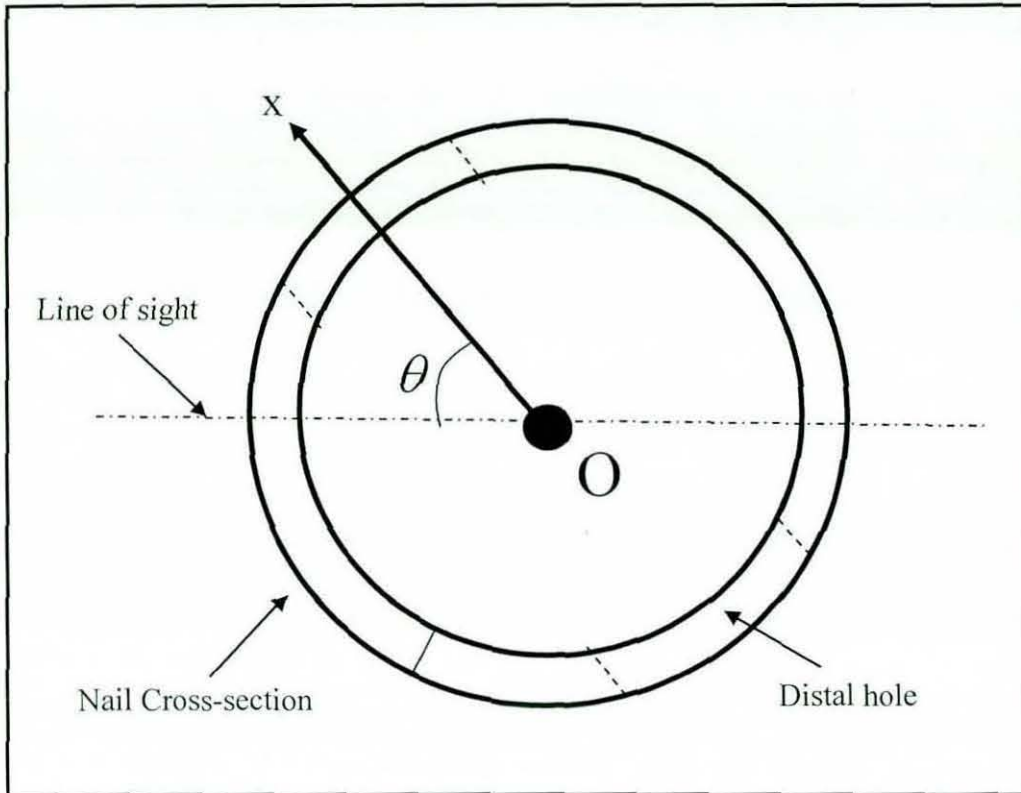


Figure 4-41 Rotation of the nail about its long axis.

4.6.1 Extraction of distal hole projection

As described earlier, the most challenging task faced by the surgeons during IMN is to locate the axes of the distal locking holes. During IMN, distal locking holes can only be seen in the Lateral X-ray image, as the nail is inside the canal of the patient's femur. Therefore, for the determination of rotation of the nail about its long axis, only the Lateral view is of importance.

Automatic extraction of the distal hole projection from the Lateral X-ray image was performed in the following manner:

- Firstly, the Lateral X-ray image was converted to a binary image as shown in Figure 4-42, by applying Otsu's thresholding technique (see **Section 4.2.1**).

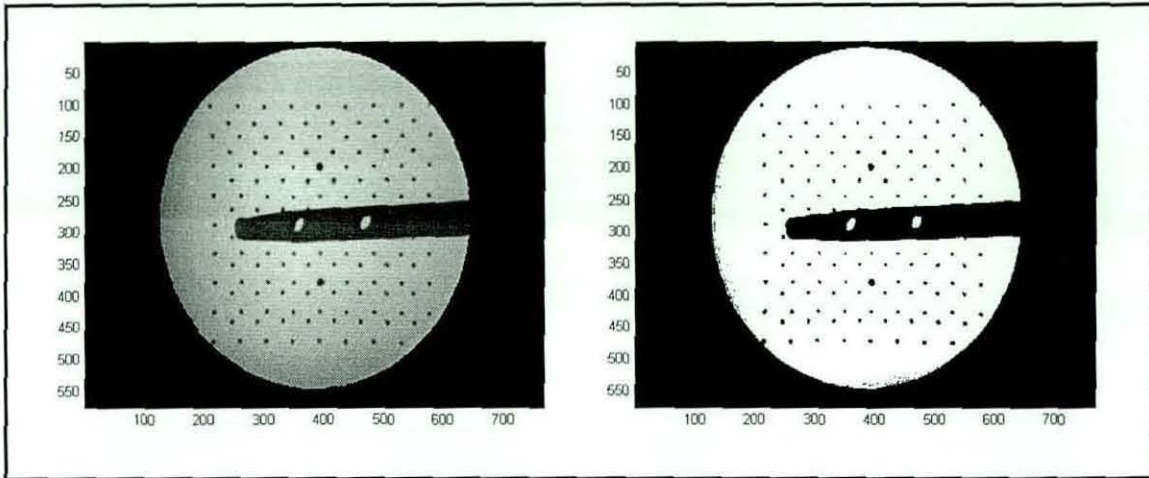


Figure 4-42 Lateral view image before and after thresholding.

- Pixel connectivity was then used for extraction of connected components in the binary image for individual identification of objects (i.e. clusters of white pixels). This was accomplished by using the Matlab IP toolbox function “bwlabel.m”.
- Then, the areas of all the labelled objects in the binary image were determined and stored in descending order. Any objects having smaller areas (i.e. other than background and two distal holes) were discarded.
- As can be seen from Figure 4-42, the two distal holes have the 2nd and 3rd largest area, whereas the white background has the largest area. However, in images where the nail is completely across the calibration frame, shown in Figure 4-43, the two distal holes will have 3rd and 4th largest area as the presence of the nail across the calibration frame divides the background into two parts. Therefore a check was made to determine the number of labelled objects in the binary image to determine positioning of the nail and two distal holes were identified accordingly based on their area.

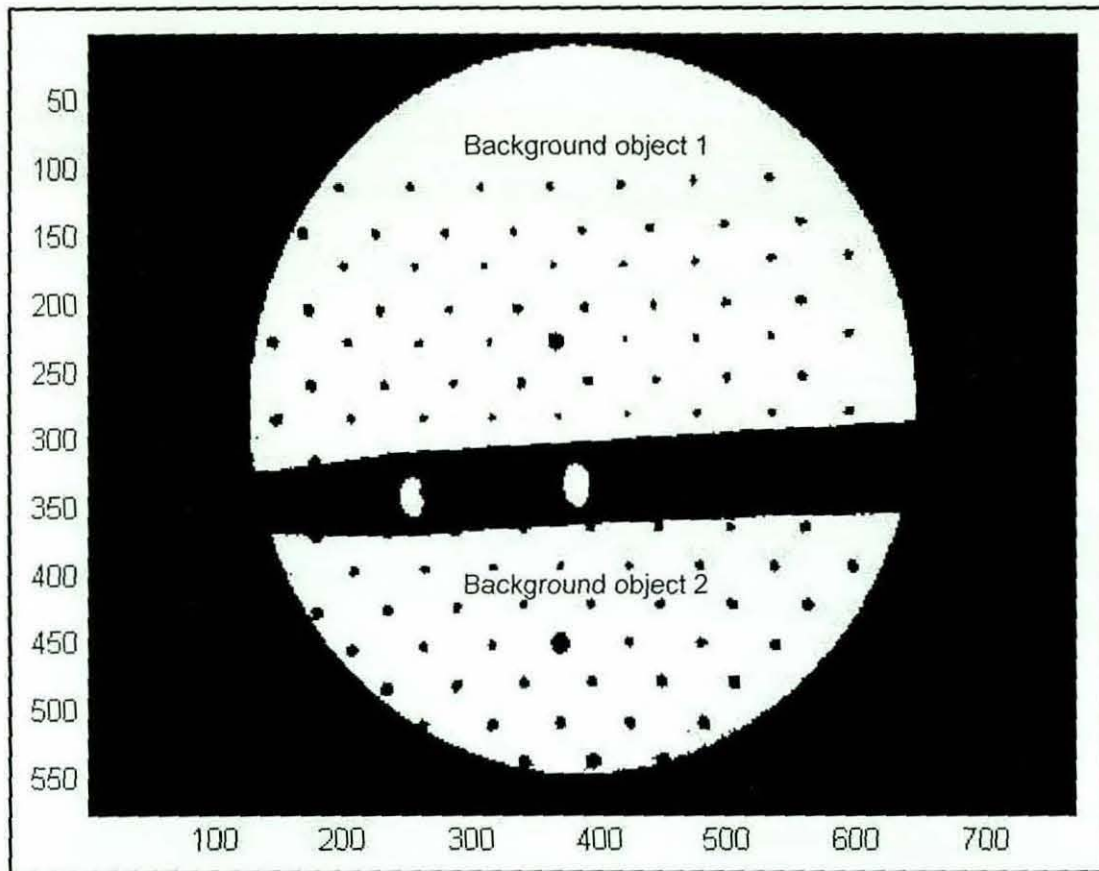


Figure 4-43 Lateral view X-ray image with nail completely across the calibration frame.

- The centroids of the objects representing the two distal holes were then determined, and distinction between the two distal holes was then made on the basis of the x-coordinate of the centroid, as the distal hole on the right hand side of the Lateral view image will always have higher value of x-coordinate.
- The area containing the distal hole projection was then cropped from the original image as shown in Figure 4-44. Then Otsu's thresholding method was applied to extract the distal hole oval shaped projection from the cropped region.

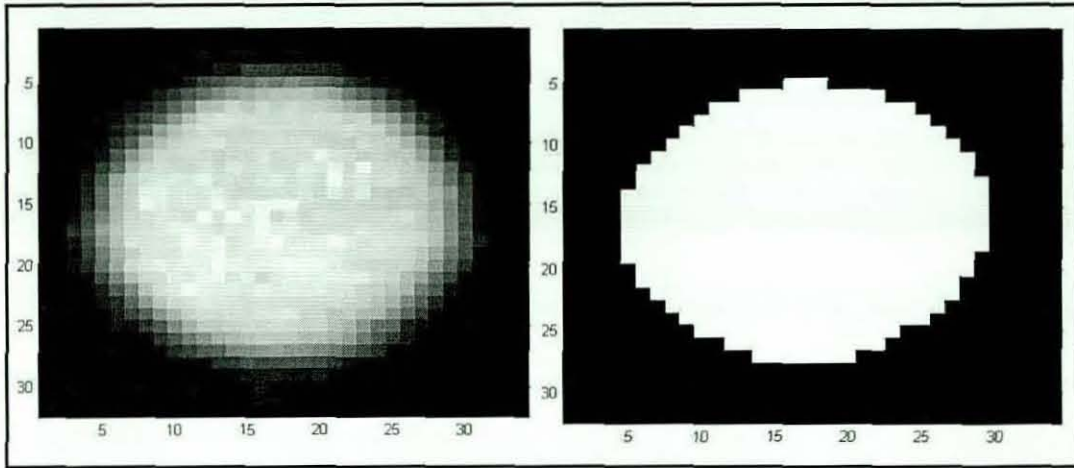


Figure 4-44 Oval before and after thresholding.

It should be noted that intramedullary nail used during x-ray image acquisition has diameter of 14 mm, with the distal locking hole of 7mm diameter. Some times during the distal locking process, the oval shape of the distal locking hole contains one or more fiducials at its edges or completely within it. This could result in false calculation of the major axis of the oval and hence inaccurate determination of the rotation of the nail about its long axis. Therefore, the oval shaped projection of the distal locking hole was analysed to check for the presence of fiducials within or at the edge of the oval. An automatic technique has been implemented which removes the effect of such fiducials in computing the area of the oval and the angle between the major axis of the oval and the nail axis; both of these measurements are necessary for derivation of the drilling trajectory. This technique is described in detail in the following sub-sections.

4.6.2 Fiducial within the oval

Once the region that contains the distal hole projection has been selected, Otsu's thresholding was applied to the region, to binarize the image, as shown in Figure 4-45.

- The thresholded image was then inverted, so that in the case of a fiducial being within the oval as shown in Figure 4-45, an inverted image will contain two objects representing background and the fiducial respectively, as shown in Figure 4-46.

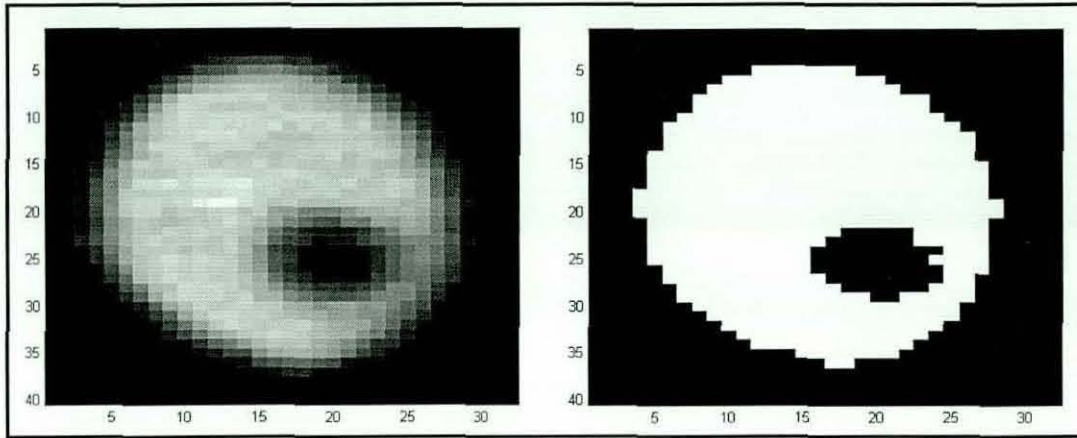


Figure 4-45 Presence of fiducial within the oval.

- Then labeling of the binary image was done, to determine the number of objects within the image. The presence of a fiducial within the oval was indicated when the number of objects within the binary image were greater than one, i.e. fiducial and the background as shown in Figure 4-46.

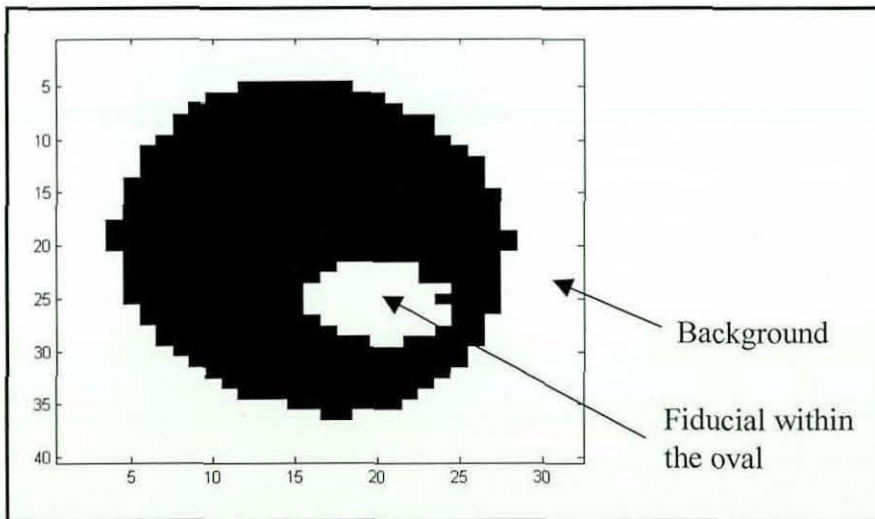


Figure 4-46 Inverted thresholded image.

- The pixels belonging to the fiducial were then identified based on area comparison between the two objects (i.e. fiducial and the background), and were assigned a value of zero, thus making the fiducial part of the oval.
- The image was then inverted again to determine the major axis of the oval, with the fiducial now being part of the oval, as depicted by Figure 4-47.

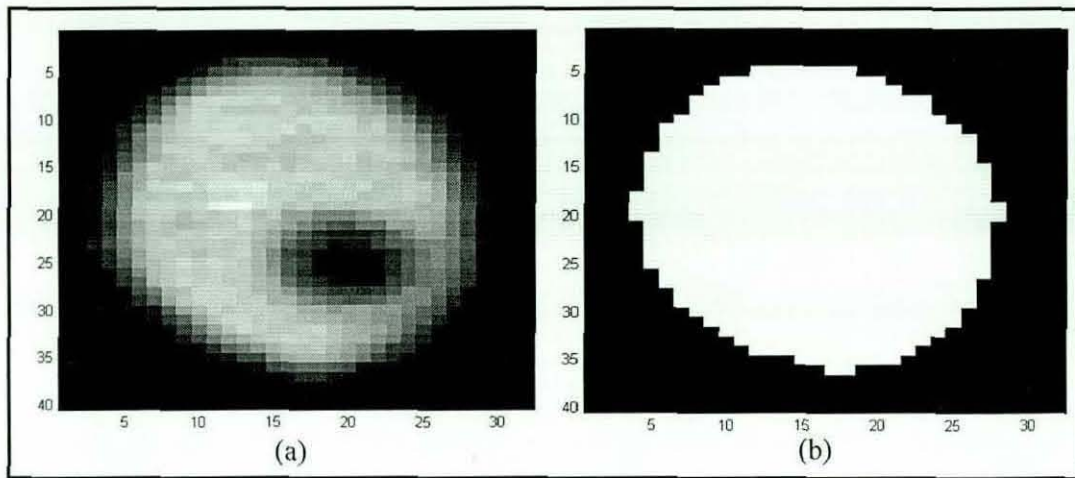


Figure 4-47 Removal of the fiducial within the oval. (a) Original (b) after fiducial removal and binarization

4.6.3 Fiducial at the edge of the oval

When the labeling of the inverted binary image results in the presence of only one object, then a check for the existence of any possible fiducial at the edges of the oval projection was carried out in the following manner:

- At first, using the information about the bounding box of the distal hole oval projection, a rectangle was cropped from the image, containing the oval projection, to check for the presence of a fiducial at the edge of the oval, as shown in Figure 4-48.

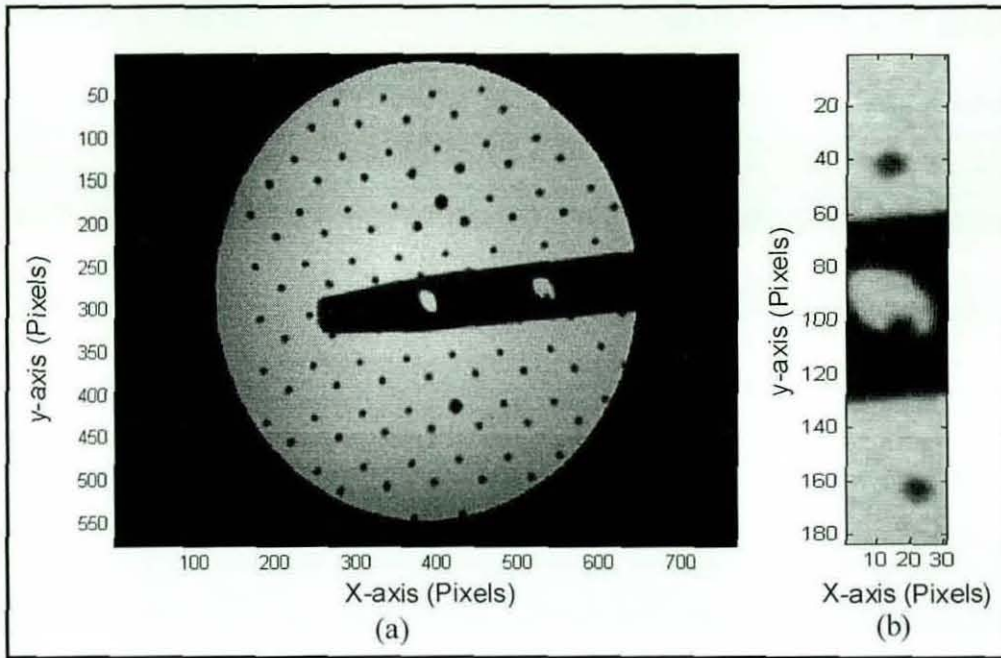


Figure 4-48 (a) Lateral intraoperative X-ray image (b) cropped region.

- The cropped image was then thresholded and inverted, to obtain the location and area of the fiducials present within the cropped image.
- The location of the fiducials within the cropped image was then used to distinguish between the upper and lower fiducial within the cropped region.
- Then, location of these fiducial was determined in terms of original image rather than the cropped region.
- The spacing along y-axis between the fiducials was then determined, and compared with the y-spacing obtained from the fiducial recognition program, to check for the possibility of number of fiducials lying between the upper and lower fiducial. Suppose that, as in this case (Refer Figure 4-48), it was found that there is a possibility of one fiducial lying between upper and lower fiducials. The bounding box of the target fiducial lying between the upper and lower fiducial was then determined in terms of the original image, by assuming that it lies midway between the upper and lower fiducial.
- The bounding box of the target fiducial was then compared with the bounding box of the oval, to determine whether it lies at the edge of the oval or not. If it was

found that the target fiducial lies at the edge of the oval then the following procedure was adopted to remove the fiducial region within the oval.

- At first, in order to obtain horizontal G_x and vertical G_y edge responses, edge detection of the region containing the distal locking hole projection was carried out using a Sobel operator.
- The horizontal and vertical edge responses were then used to find the absolute magnitude of the gradient at each point and the orientation of that gradient. The gradient magnitude is given by :

$$|G| = \sqrt{G_x^2 + G_y^2}$$

And angle of orientation of the edge (relative to the pixel grid) is given by:

$$\alpha = \tan^{-1}(G_y / G_x)$$

- Now adaptive thresholding based on gradient magnitude was applied until a closed image of the oval was obtained (i.e. without any gaps), as shown in Figure 4-49(b).

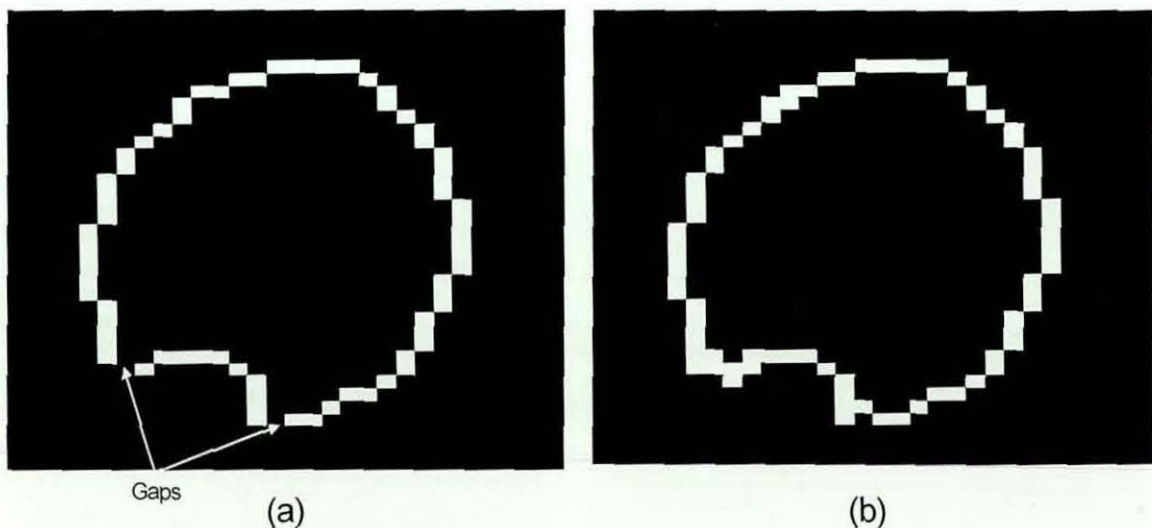


Figure 4-49 (a) Oval with gaps along its boundary (b) Closed oval obtained using adaptive thresholding.

- Edge co-ordinates and their respective orientation were then ranked in a counter-clockwise direction, so that a comparison can be made between consecutive edge co-ordinates. The starting point for the ordered edge co-ordinates is the edge co-

ordinate with the lowest column number, as in Figure 4-50, where the edge coordinate with column number 5 is the starting point.

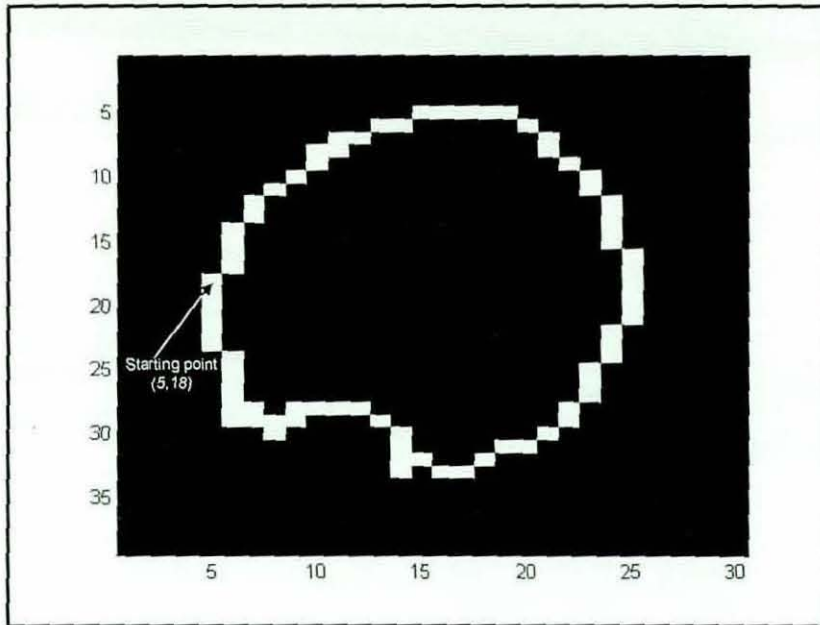


Figure 4-50 Starting point for the ordered edge co-ordinates.

- In the presence of a fiducial, there will be a sudden change in the direction of the gradient in close proximity rather than far apart, which is the case at upper/lower edges of the oval as depicted by Figure 4-51. However, it can also be seen from Figure 4-51 that sudden changes in the direction of the gradient were also found along the oval profile at locations where the fiducial is not present, which makes it impossible to use direction of the gradient alone to locate the fiducial.

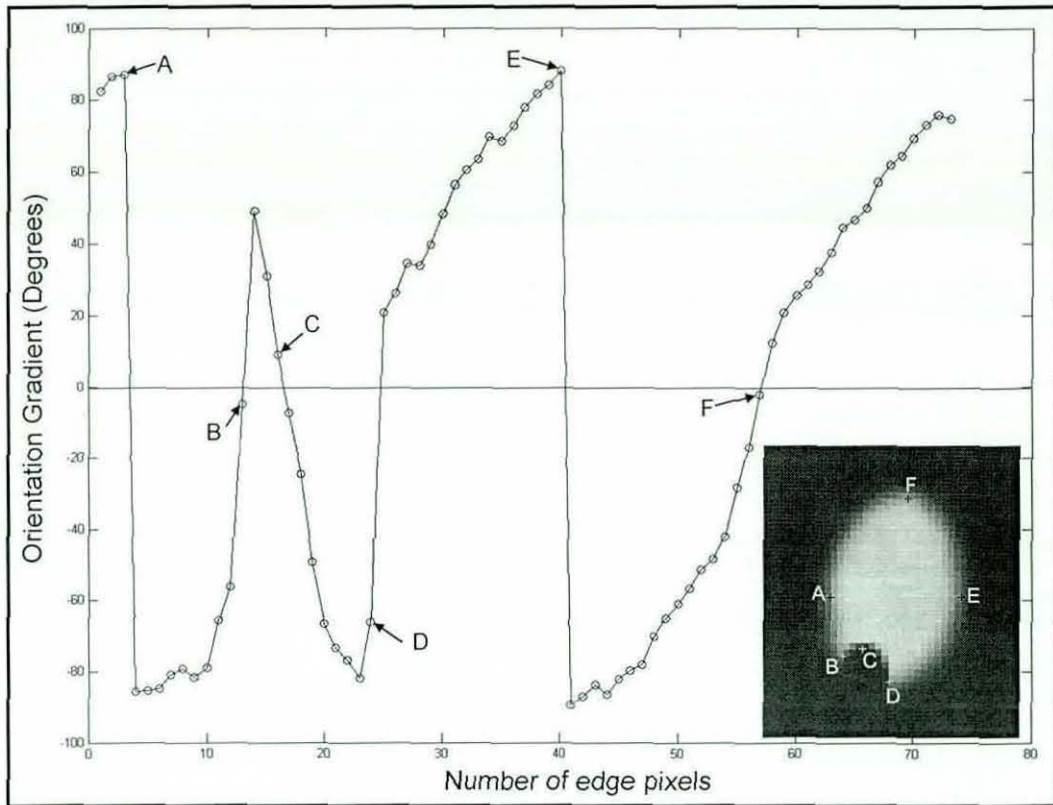


Figure 4-51 Use of gradient direction for detection of fiducial location at the oval edges.

Processing of several X-ray images exhibiting the scenario under investigation has shown that for an oval which contains a fiducial at its edge, the largest orientation difference between consecutive edge pixels usually occurs in the region containing the fiducial due to sharp gradient transitions along the fiducial profile as shown in Figure 4-52.

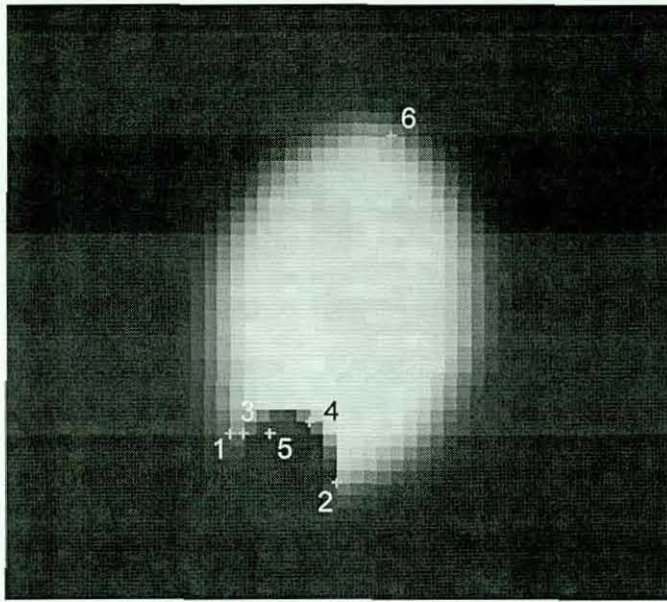


Figure 4-52 Plot of six largest orientation transitions along the edges of the oval.

Whereas in regions along the oval profile where no fiducial is present such as at points A, E and F of Figure 4-51, change in gradient direction is accompanied by a very small change in orientation difference between consecutive edge pixels. Therefore, for reliable location of the fiducial, it was decided to use gradient direction along with orientation difference between consecutive edge pixels i.e. orientation gradient. To accomplish this task, at first change in the gradient sign along the oval profile is used to locate potential regions containing the fiducial. For example, analysis of gradient direction from Figure 4-51 was made and pixels at which the direction of the gradient has changed, were extracted to yield the expected location of the fiducial.

Change in gradient direction	1st	2nd	3rd	4th	5th	6th
Pixel number at which gradient direction changed	3	13	16	24	40	57

Table 4-6 Estimation of expected fiducial locations using direction of the gradient.

Then, orientation gradient along the oval profile was determined (shown in Figure 4-53) and sorted in descending order.

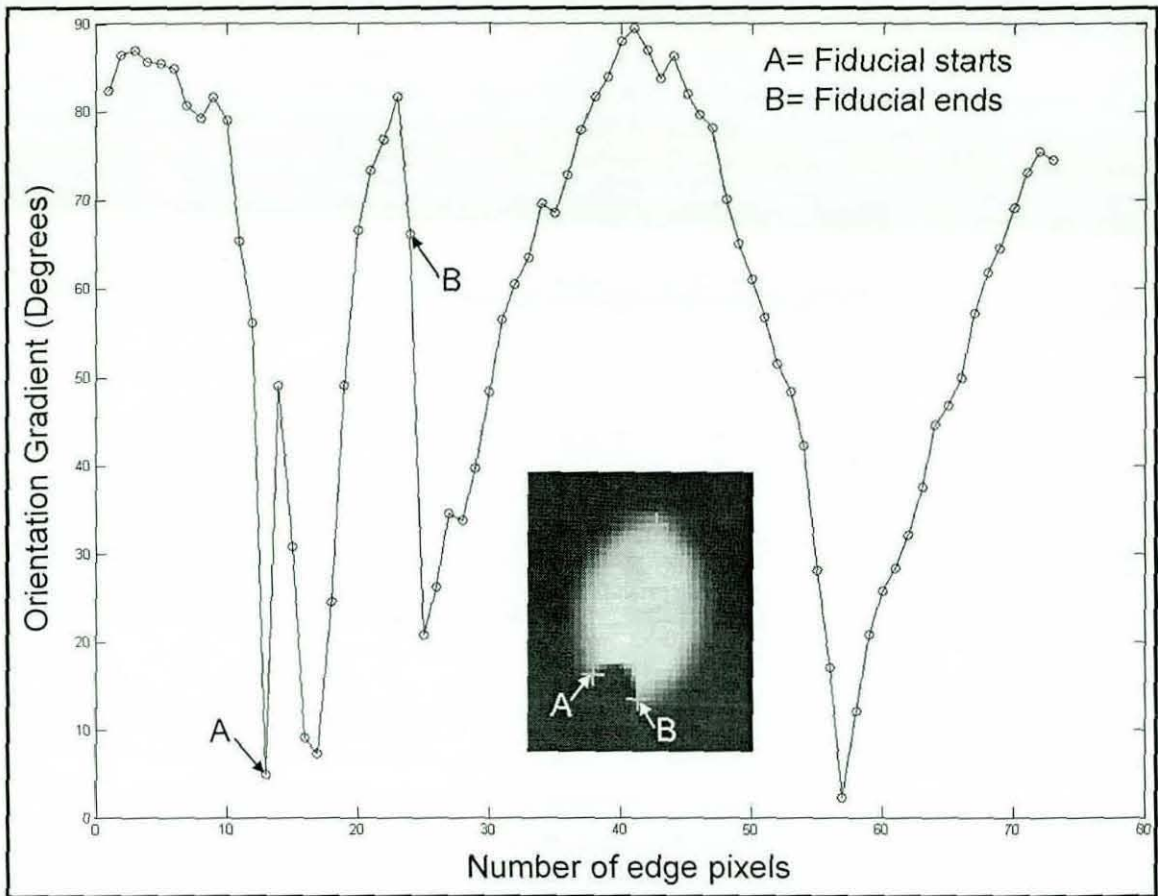


Figure 4-53 Use of orientation gradient for detection for fiducial location at the oval edges.

Through analysis of several images it has been found that usually the first two largest transitions in orientation between consecutive edge pixels (as shown in Table 4-7) provide sufficient information to locate the fiducial reliably. For example, by analysing Table 4-7 it can be verified that the fiducial lies between the 13th and 24th edge pixel. It is also evident from Table 4-7 that the first five largest orientation gradients lie along the fiducial profile as depicted by Figure 4-52.

	1st	2nd	3rd	4th	5th	6th
Orientation transition	51.3	45.4	44.2	24.6	21.8	18.3
Edge co-ordinates (Pixels)	13	24	18	19	16	57

Table 4-7 First six largest orientation gradients.

However, it is not always possible to reliably locate a fiducial at the edge of the oval by only using the first two largest orientation gradients. Therefore, analysis of several X-ray images was carried out and it was found out that for safety, the first six largest orientation gradients should be used in conjunction with the change in gradient direction for reliable fiducial location along the oval profile.

- It is possible that the starting point for the closed image lies in the region containing the fiducial as shown in Figure 4-54, in which case it will not be possible to locate the fiducial accurately based on the analysis of gradient direction and orientation gradient only once. Therefore, once fiducial location was obtained, a second pass was carried out along the oval profile from the opposite side to verify the location of the fiducial as shown in Figure 4-54.

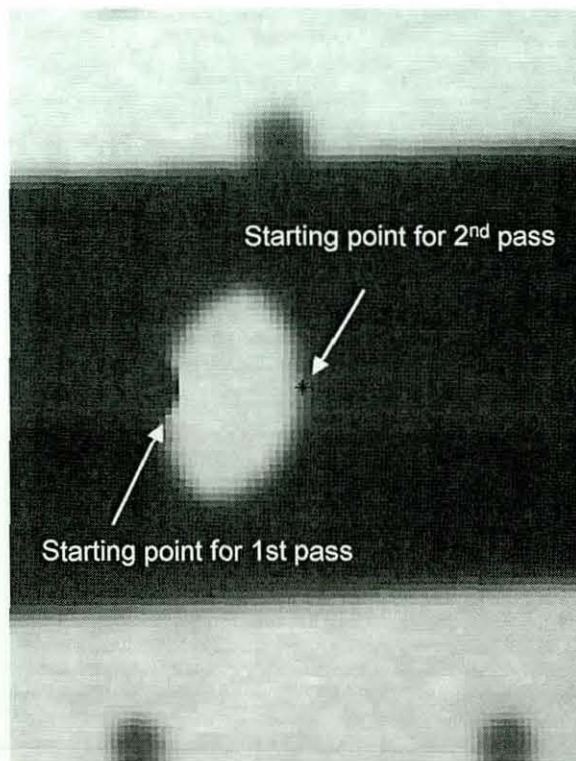


Figure 4-54 Starting points used during two passes for locating fiducial.

- The edge co-ordinates representing the fiducial that are common in both passes were then assigned as pixels belonging to the fiducial and were discarded from the list of edge co-ordinates obtained for the oval profile, while using the rest of the pixels along the profile to best fit an ellipse using least squares fitting.

4.6.3.1 Comparison between proposed technique and Convex Hull approach

In order to check the robustness of the proposed technique, it was tested against a convex hull approach (i.e. the use of points lying on the convex hull to best fit an ellipse using a least squares method) in terms of accuracy and reliability.

Convex Hull

The convex hull of a geometric object (such as a point set or a polygon) is the smallest convex set containing that object. For a two dimensional finite set the convex hull is a convex polygon. Figure 4-55 shows the convex hull for the set of points lying at the edge of the oval, which has a fiducial at its edge.

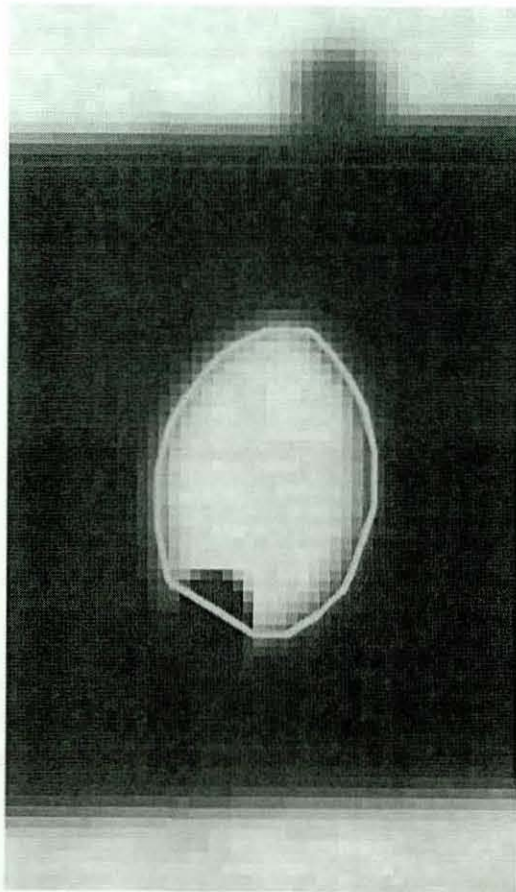


Figure 4-55 Convex Hull of a set of points.

For this purpose, an ideal image of the oval (i.e. without any fiducial at its edges) was used as datum. Then a fiducial was introduced at different locations of the oval to simulate different possible scenarios as shown in Figure 4-56. Both a convex Hull

approach and the proposed gradient technique were applied to these images to determine the rotation of the nail about its long axis (θ). The θ value obtained for each of the images was then compared with θ_{ideal} i.e. rotation of nail about its long axis obtained by analysing the oval with no fiducial at its edges.

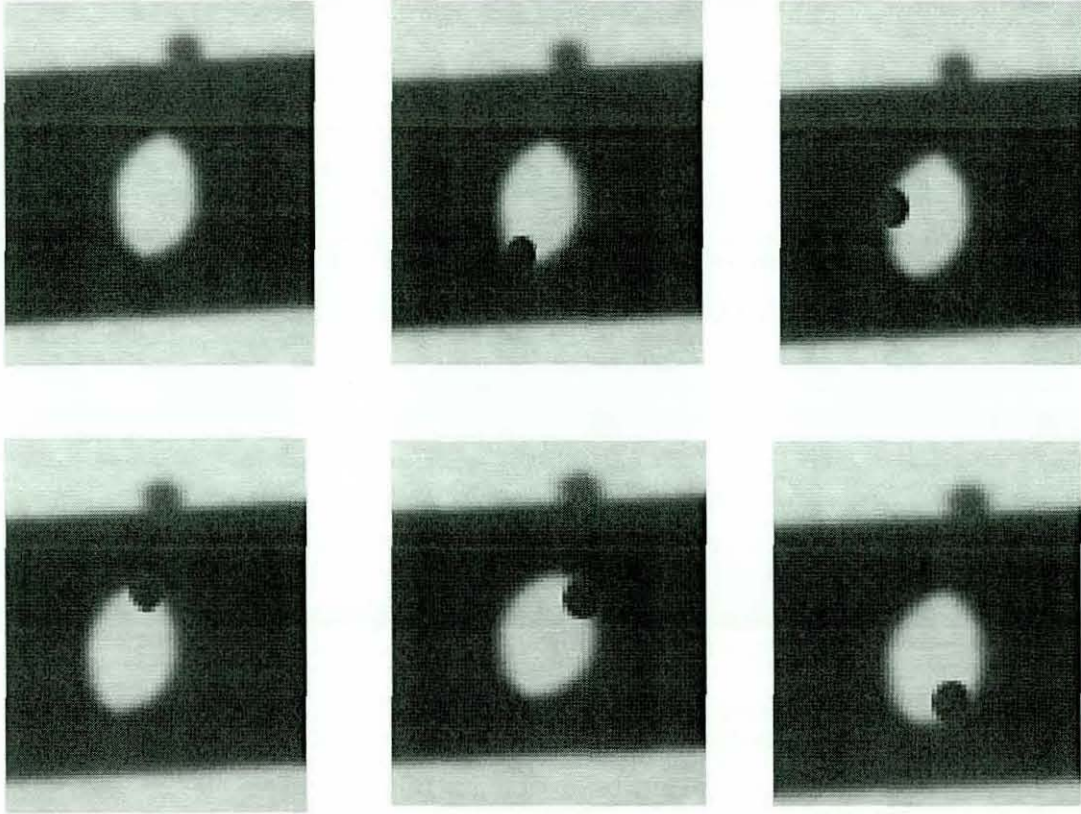


Figure 4-56 Introduction of fiducial at the edge of the oval.

Processing of several X-ray images containing a fiducial at the distal hole edges has shown that the proposed technique has been able to locate a fiducial lying at the edge of the oval reliably. In terms of accuracy it can be seen from Table 4-8, that while using the proposed or convex hull technique for predicting θ for oval with fiducial at its edges, almost similar results were obtained. A mean error of 0.05° (worst case being 0.14°) was obtained using the proposed approach in comparison to mean error of 0.12° (worst case being 0.24°) when using Convex Hull approach. Therefore, it has been decided to adopt the proposed approach for this system.

For ideal image, i.e. with no fiducial at the edge of the oval
 $\theta_i = 2.46^\circ$

Modified Image	Gradient approach		Convex Hull approach	
	θ_g	E_g	θ_c	E_c
1	2.35	0.11	2.22	0.24
2	2.47	0.01	2.51	0.05
3	2.32	0.14	2.35	0.11
4	2.46	0	2.42	0.04
5	2.41	0.05	2.37	0.09
6	2.44	0.02	2.42	0.04
7	2.5	0.04	2.61	0.15
8	2.6	0.14	2.7	0.24
9	2.4	0.06	2.37	0.09
10	2.52	0.06	2.64	0.18

where,

θ_g, θ_c = Rotation of the nail about its long axis ' θ ' obtained using gradient and convex hull approach respectively,

E_g, E_c = Error in determining θ using gradient and convex hull approach respectively.

Table 4-8 Comparison between proposed and Convex Hull approach.

4.7 GUI Development

The Graphical User Interface (GUI) for the distal locking procedure, shown in Figure 4-57, has been developed in the Matlab environment. The GUI has been developed by keeping in mind that computer assisted system have only been introduced in the recent past, therefore most surgeons have had very little interaction with computers. Hence, simplicity of the GUI is of paramount importance for the benefit of current orthopaedic surgeons. The steps involved in GUI operation are as follows:

- At first, the user is asked to provide the patient's name and National Health Service (NHS) number.
- The user is then asked to enter the nail specifications i.e. diameter of the intramedullary nail and the diameter of the distal locking holes.
- The user is then asked to enter the type of calibration frame that is being used.
- Then user is asked to select either an AP or Lateral view X-ray image from the stored X-ray images. Once the user has selected an image, he/she is given another chance to proceed with the selected image or to select a new image.
- The system then determines whether it is an AP or Lateral view image. The system then processes the image. Once the processing of the image has been performed, the user is again asked whether he/she wishes to continue or select the image again.
- Once the user is satisfied with the analysis of the first selected image, he/she is asked to select an AP/Lateral view image, depending upon which image was processed first. Again the user is presented with an option, whether to proceed with the selected image or to select a new image. Once the user is satisfied with the selected image, processing of the second image is performed.
- Once the analysis is complete, the system writes the trajectory data and the two X-ray images (i.e. Lateral and AP) to a unique directory. The name of this directory is based on the patient's name and NHS number provided by the user.
- During the entire process, a status window shown in Figure 4-57 is used to interact with the user.

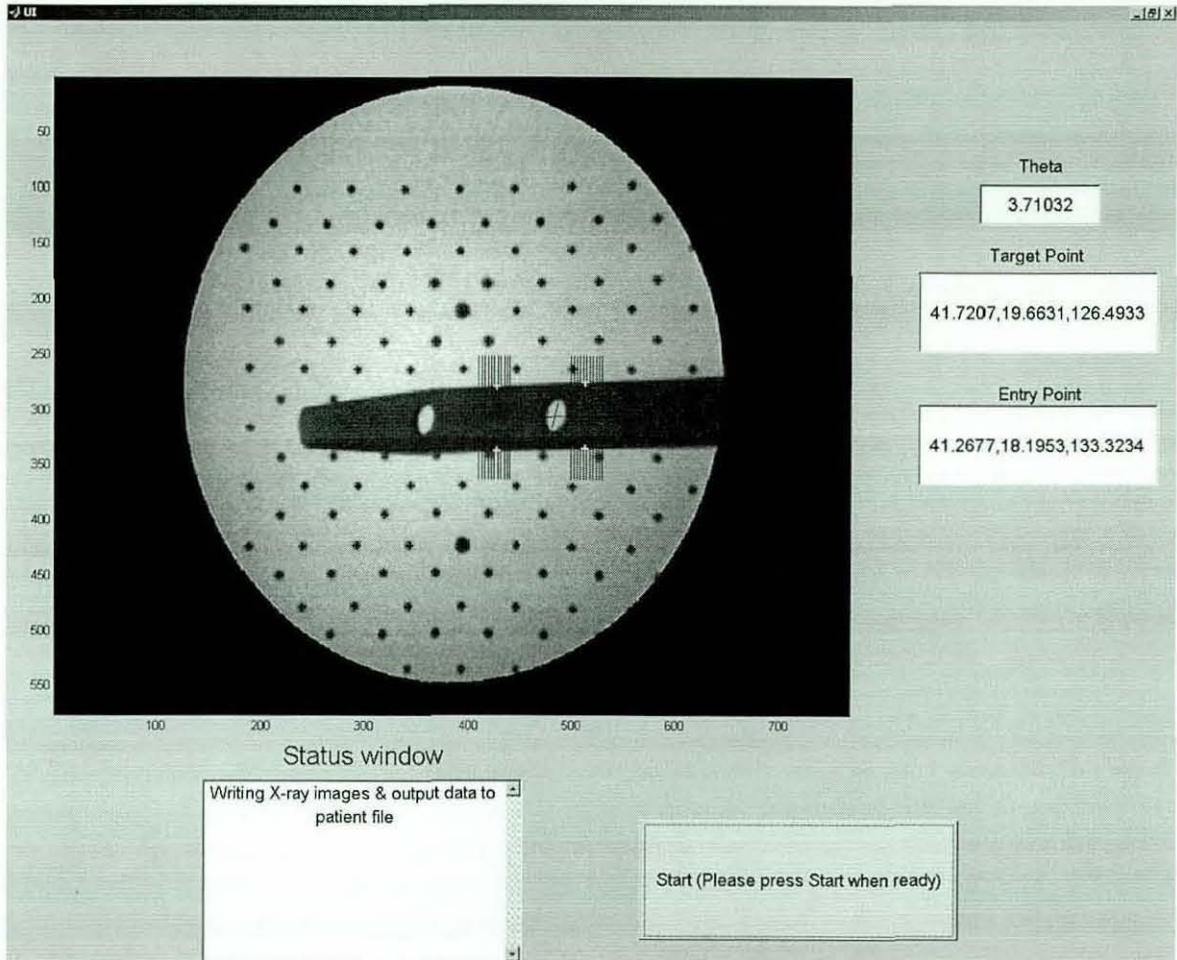


Figure 4-57 GUI for distal locking procedure.

It should be noted that the developed GUI program is reliable as it does not allow the user to input incorrect data for trajectory calculation. For example, if the user acquires a Lateral X-ray image first and then tries to acquire another Lateral X-ray image as second image, the system will inform the user that an AP X-ray image is required instead of a Lateral X-ray image.

4.7.1 Software flowchart of GUI

In this section, the steps involved during image analysis are shown in the form of a flowchart as depicted by Figure 4-58. More details about individual programs used during “GUI.m” can be found in **APPENDIX E**.

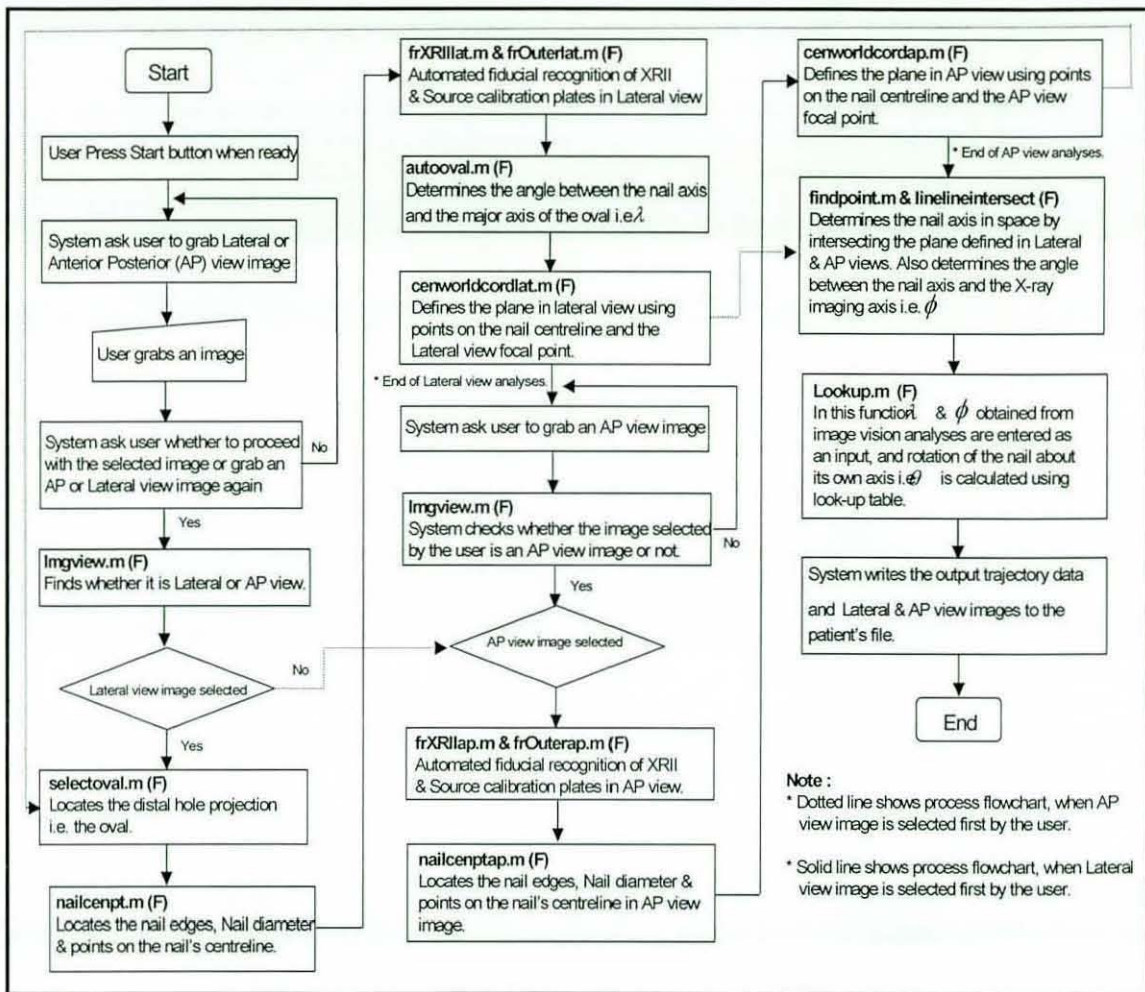


Figure 4-58 Matlab Software flowchart.

For intraoperative applications, it is necessary to acquire X-ray images and process them simultaneously. However, unfortunately due to a limitation of the frame grabber used in this research, it was not possible to acquire live images and process them in the Matlab environment. Therefore, software has been designed using Visual Basic (VB) to acquire X-ray images intraoperatively, followed by their processing in the Matlab environment. The Flowchart depicted in Figure 4-59 shows the step-wise process when using Visual Basic and Matlab to perform intraoperative trajectory calculation.

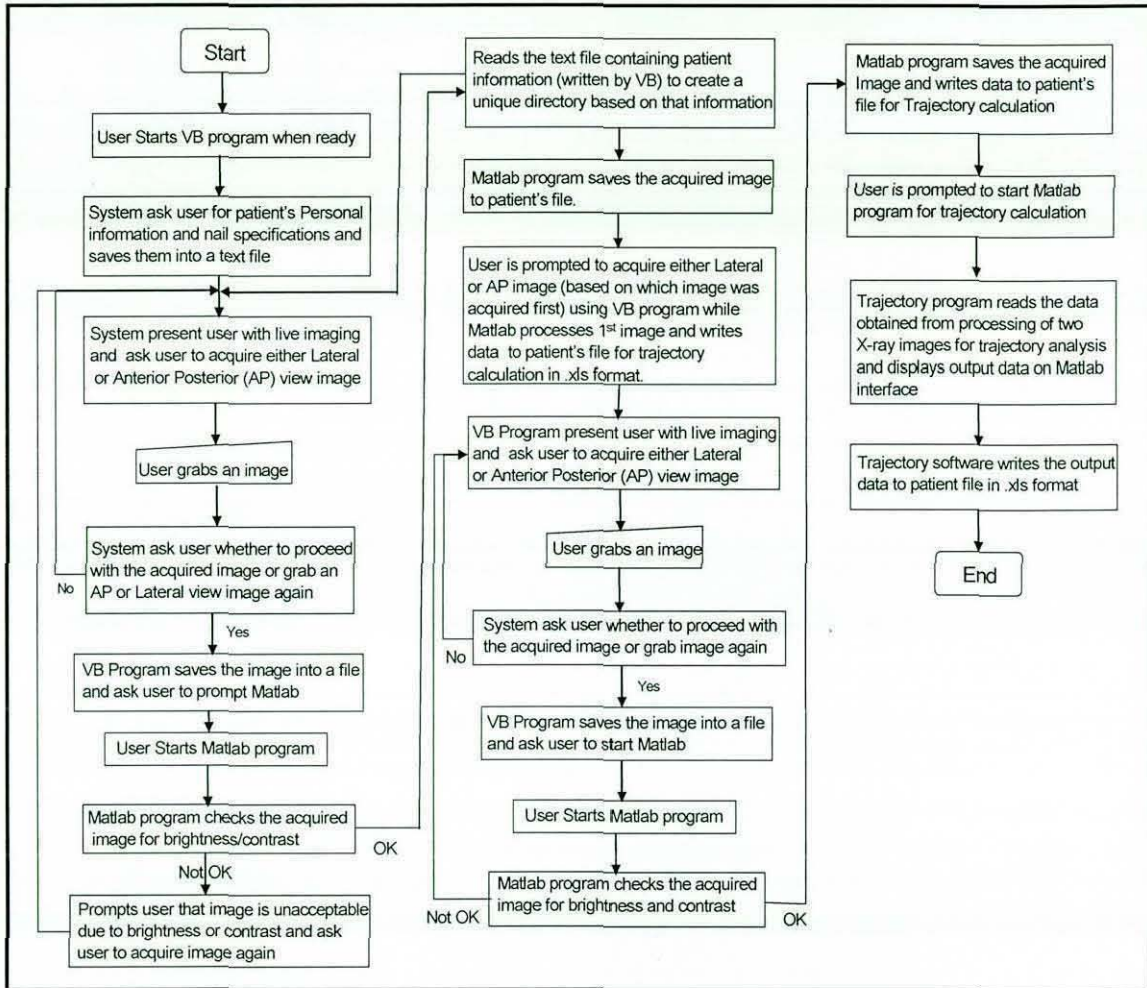


Figure 4-59 Intraoperative trajectory analysis using VB and Matlab interface.

4.8 Determination of nail specifications from the intraoperative X-ray image

Initially, in order to implement a look-up table (LUT) for trajectory analysis, the user was asked to enter the nail specifications i.e. nail diameter and distal locking hole diameter. However, in order to make the existing system more robust and user independent, the intraoperative Lateral X-ray image was used to estimate the nail specifications in the following manner:

- Firstly the fiducial spacing (in pixels) on the Lateral XR11 and Source plate was determined. Although the fiducial on the Source plate has a spacing of 9mm in comparison to that of 10mm on the XR11 plate, the fiducial spacing (in pixels) for the two plates, always appear very close to each other (for example, say 55 and

55.3 for Source and XRII plate respectively). This is because the XRII and Source plates are 50mm apart, with the Source plate being nearer to the X-ray source. Therefore, it experiences more magnification than the XRII plate.

- The diameter of the nail was determined (in pixels) from the Lateral X-ray image. In order to determine the diameter of the nail in mm, there is a need to quantify the nail magnification (i.e. pixels/mm ratio) at the place where the nail is lying with respect to X-ray source). This was achieved by using the known spacing (mm) between the two distal locking holes. By analysing nail specifications provided by different manufacturers, it has been found that the spacing between the two distal holes (i.e. centre to centre) is always either 25mm or 30mm. Therefore, at first, spacing between the centres of the two distal holes was determined in terms of pixels. Then using that pixel spacing pixel/mm ratios were determined for both 25mm and 30mm spacing respectively. These pixel/mm ratios are compared with pixel/mm ratio obtained independently for the Lateral source plate. Since, as the distance of the object from X-ray source increases, pixel/mm ratio decreases, therefore pixel/mm ratio will always be higher at the Lateral source plate in comparison to that obtained from distal hole spacing, because the Lateral source calibration plate lies closer to X-ray source in comparison to the intramedullary nail. Therefore, pixel/mm ratio that satisfies this condition was chosen to quantify the nail magnification. This pixel/mm ratio was used in conjunction with a known nail diameter (pixels) to determine the nail diameter (mm).

It has been found that determination of the distal hole diameter by analysing the distal hole projection is not reliable due to the different possible orientations of the nail. Therefore, once the diameter of the nail was determined, it was used in conjunction with different nail specifications provided by the nail manufacturer, to present the user with all possible nail specifications for that particular nail diameter. It should be noted that most of the time the diameter of the distal locking hole is kept uniform for a variable nail diameter, for example, a distal hole diameter of 5.3mm for 10mm, 11.5mm and 13mm intramedullary nails manufactured by Smith and Nephew [131].

4.9 Summary

Keeping in mind that robustness, reliability, and repeatability are of paramount importance when introducing any new technology into the operating theatre, all the steps involved during image analysis are fully automated, and hence the machine vision system is user independent. A potential problem with the proposed system is the appearance of one or more of the opaque markers within or on the edge the oval shaped distal hole projection. An automatic technique has been implemented which removes the effect of such fiducials in computing the area of the oval and the angle between the major axis of the oval and the nail axis; both of these measurements are necessary for derivation of the drilling trajectory. This technique therefore eliminates the need for repositioning the calibration frame or using a smaller number of opaque markers. In the next chapter, CAD modelling of the nail, which is used in conjunction with machine vision system to compute the drilling trajectory, is described in detail.

5 Modelling of intramedullary nails

In order to determine the rotation θ of the nail about its own axis, a model-based approach using look-up tables (LUTs) was employed. These LUTs were obtained using off-line CAD modelling of the intramedullary nail. This method allowed accurate modelling of any shape of intramedullary nail. LUT is a sampled model of the relationship between (θ, ϕ) and the shape properties of the oval shaped projection of the distal locking hole (clear aperture or overlap of the distal locking hole) as shown in Figure 5-1.

		ϕ			
		0	1	2	3
θ	0	(dA_{00}, λ_{00})	(dA_{01}, λ_{01})	(dA_{02}, λ_{02})	(dA_{03}, λ_{03})
	1	(dA_{10}, λ_{10})	(dA_{11}, λ_{11})	(dA_{12}, λ_{12})	(dA_{13}, λ_{13})
	2	(dA_{20}, λ_{20})	(dA_{21}, λ_{21})	(dA_{22}, λ_{22})	(dA_{23}, λ_{23})
	3	(dA_{30}, λ_{30})	(dA_{31}, λ_{31})	(dA_{32}, λ_{32})	(dA_{33}, λ_{33})

$\phi = \text{angle between nail axis \& x-ray imaging axis,}$
 $\theta = \text{rotation of the nail about its long axis,}$
 $dA_{mn} = \text{dimensionless area @ } \phi=m \text{ \& } \theta=n,$
 $\lambda_{mn} = \text{angle between major axis of the oval and}$
 $\text{the long axis of the nail @ } \phi=m \text{ \& } \theta=n.$

Figure 5-1 Look-up table format.

In order to build the LUTs the following steps were required:

- Construction of the distal end of the intramedullary nail according to the geometry data provided by manufacturers.
- Simulation for different nail orientations i.e. rotation θ of the nail about its own axis and rotation ϕ of the nail about the X-ray imaging axis.
- For each unique orientation of the nail, the oval shaped projection of the distal locking hole was analysed to determine measurements such as area, perimeter, major-axis length, and roundness. These measurements were then stored in the database to build the LUTs.
- The LUTs were then imported into the Matlab programme, and used in conjunction with image analysis to determine the drilling trajectory of the distal locking holes.

5.1 Selection of the CAD Package

The requirement is to create an intramedullary nail computer model with user defined inputs, then reposition the nail at different orientations and to store characteristic measurements, such as area, in a file to generate the LUTs. Since mathematical modelling can be time consuming and complex, another alternative is to model the intramedullary nail using its geometric properties in a CAD package using its scripting language. Several CAD packages offer scripting capabilities which can be used for this type of automated modelling.

Programming languages available for scripting in different CAD packages are shown below:

- AutoCAD, Mechanical Desktop : ObjectARX, AutoLISP, Visual BASIC for Applications
- Mcneel Rhinoceros : Rhino Script, Visual Basic, Microsoft Foundation Class (MFC), C++.

- Unigraphics (UG), Pro/Engineer (Pro/E), CATIA : C, C++, MFC, OpenGL, JAVA.

The learning curve for most CAD/CAM programming languages is high. Rhino 3D with Rhino Script and other CAD platform were tried but the Mechanical Desktop CAD platform with a programming language known as AutoLISP was preferred, as this option proved to be quicker due to the author's previous experience with the CAD package.

5.2 Tools used for Modelling

Modelling of the intramedullary nail to generate the LUT was carried out in AutoCAD Mechanical Desktop using its solid modelling capabilities. The programming language used for this purpose is known as AutoLISP, which is a versatile and flexible automated CAD language. These tools are described in following sub-sections:

5.2.1 AutoCAD

AutoCAD is a set of CAD software products for 2D and 3D design and drafting from Autodesk. It includes a full set of basic solid modelling and 3D tools. Like other CAD programs, AutoCAD is fundamentally a vector graphics drawing program. It uses primitive entities such as lines, polylines, circles, arcs, and text as the foundation for more complex objects. AutoCAD supports a number of application programming interfaces (APIs) for customization and automation, such as AutoLISP, Visual LISP, .NET etc.

5.2.2 Autodesk Mechanical Desktop

Autodesk has also developed overlay programs, called Desktops, for field specific enhancements. Such as AutoCAD Mechanical Desktop, AutoCAD Architectural Desktop and AutoCAD Electrical are examples of industry-specific CAD applications built on the AutoCAD kernel. Mechanical Desktop ® helps to create 3D designs in AutoCAD ® software by uniting 3D solid modelling with freeform surface and 2D/3D wireframe.

5.2.3 AutoLISP

AutoLISP is a scripting language for AutoCAD. The first version of AutoLISP was developed in 1986 and was developed directly from the LISP programming language (an interpreter) embedded within AutoCAD. It allows customization of AutoCAD into a more useful tool for a particular application. Aside from the core language, most of the primitive functions are for geometry or the manipulation of graphical entities in AutoCAD, as most AutoCAD commands can be called as AutoLISP functions. The properties of these graphical entities are revealed to AutoLISP as lookup tables in which AutoCAD "group codes" are paired with values that indicate properties such as points, radii, colours, layers, line types, etc. Since AutoLISP is an interpreter, it can be debugged by typing a line of the program and inspecting the results for that code. Other derivatives of AutoCAD like Mechanical Desktop, Autodesk Architectural Desktop and Autodesk Map 3D also uses AutoLisp. Other CAD packages that use AutoLisp are FelixCAD, IntelliCAD, BricsCAD.

5.3 Construction of an Intramedullary nail model

The first step during modelling was to create a model of the distal end of the nail conventionally in AutoCAD Mechanical Desktop; this was accomplished in the following manner:

- Based on the actual intramedullary nail specifications, two cylinders were created with the nail diameter 'D' and the distal hole diameter 'd' respectively. It was assumed that the hole is in the middle of the nail.
- The rotation ϕ , was created by rotating the nail about the hole axis (which is initially parallel to the X-ray imaging axis). A rotation θ of the nail about its own axis was applied to the cylinder, as shown in Figure 5-2.

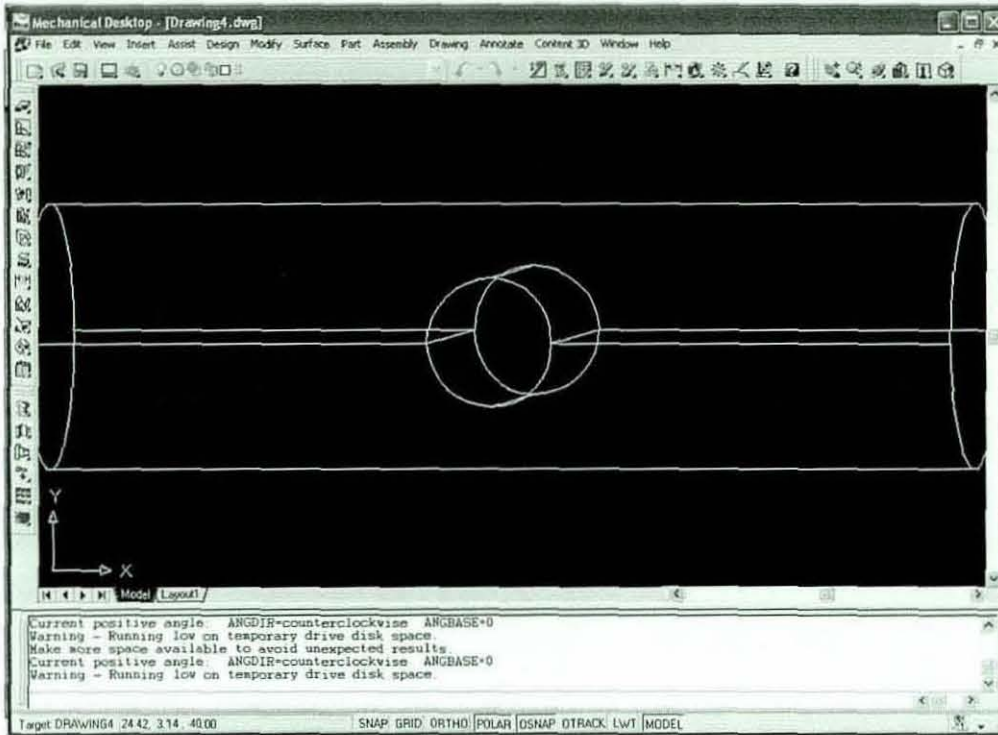


Figure 5-2 Modelling of the nail using AutoCAD Mechanical Desktop.

- The projection of both hole edges was then created on a plane for the given orientation of the nail. Trimming was done to obtain a projection of the hole, and then area and the major axis of the projected oval were calculated. Here it should be noted that this “oval” does not really exist. It is the result of a particular angle of view of two overlapping holes.

The next stage was to automate these steps using AutoLISP to generate the LUTs. This was achieved by employing the following procedure:

- First the user was asked to input nail dimensions i.e. nail diameter D and distal hole diameter d .
- The two variables D and d were then used to create two cylinders i.e. Cylinder1 (representing the nail) and Cylinder2 (representing the distal locking hole).
- Cylinder 2 was then subtracted from Cylinder 1 to simulate the distal region of an intramedullary nail as shown in Figure 5-3. The Cylinder2 entity was then deleted and a new entity was created in Mechanical Desktop representing the distal end of the nail.

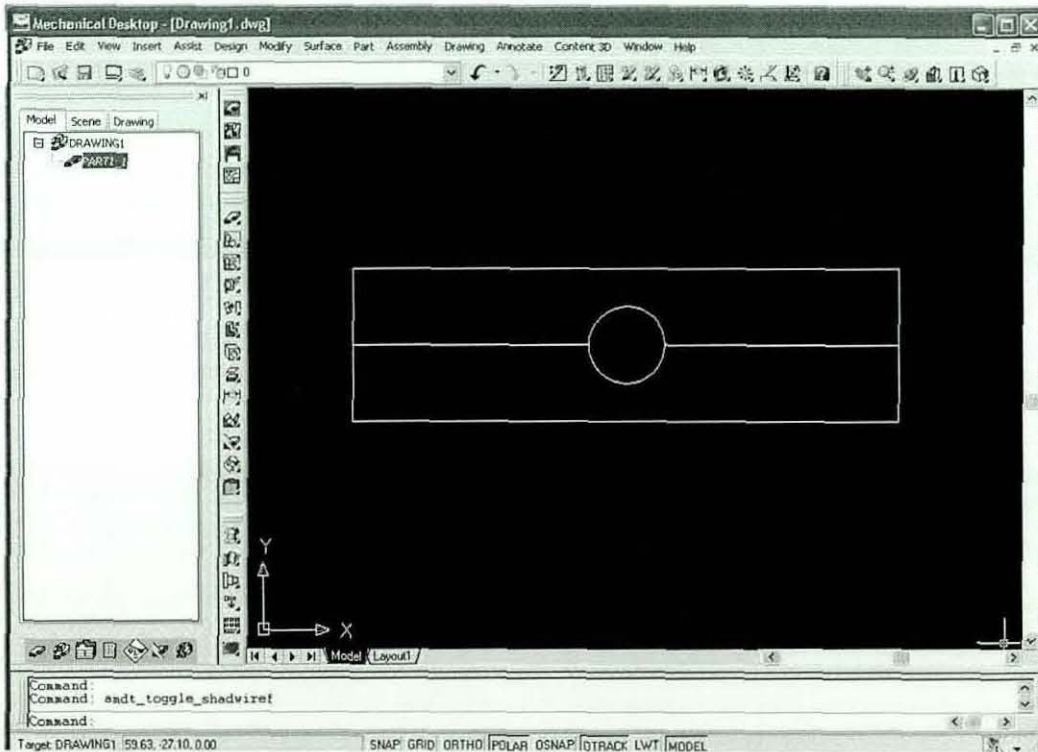


Figure 5-3 Front view of distal end of the intramedullary nail.

- Initially ϕ was set to zero, representing the scenario in which the nail axis is perpendicular to the X-ray imaging axis. A Universal co-ordinate system (UCS) was moved from the World co-ordinate System (WCS) to the intersection of nail and distal hole axes.

- For a given orientation ϕ , rotation of the nail about its own axis was initially set at zero (i.e. $\theta = 0$).
- A plane A was created by moving the UCS along the Z-axis which represents the distal hole axis. This plane is parallel to WCS's XY-Plane. Then a projection of the hole edges was created onto the plane A. After projecting the curves onto the plane for specified rotations of the nail (i.e. θ and ϕ) the curves were trimmed, as shown in Figure 5-4, to obtain the distal locking hole overlap projection.

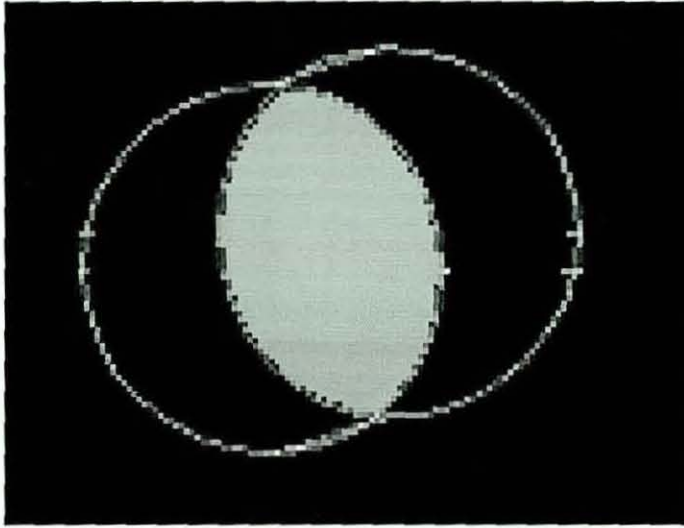


Figure 5-4 Shaded region representing projection of distal locking hole.

- This oval shaped overlap projection obtained using trimming was then analysed to extract different features such as area, perimeter, major-axis length, roundness and angle λ between major-axis of the oval and the nail axis.
- The results were then output into a Comma Separated File (CSV), which is in fact the LUT.
- The previous nail projection from the plane A' was then deleted and UCS was changed back to the intersection of nail and distal hole axes. The value θ was then incremented at 0.5° intervals for a specified value of ϕ , such as for $\phi = 0$ as shown in Figure 5-5.

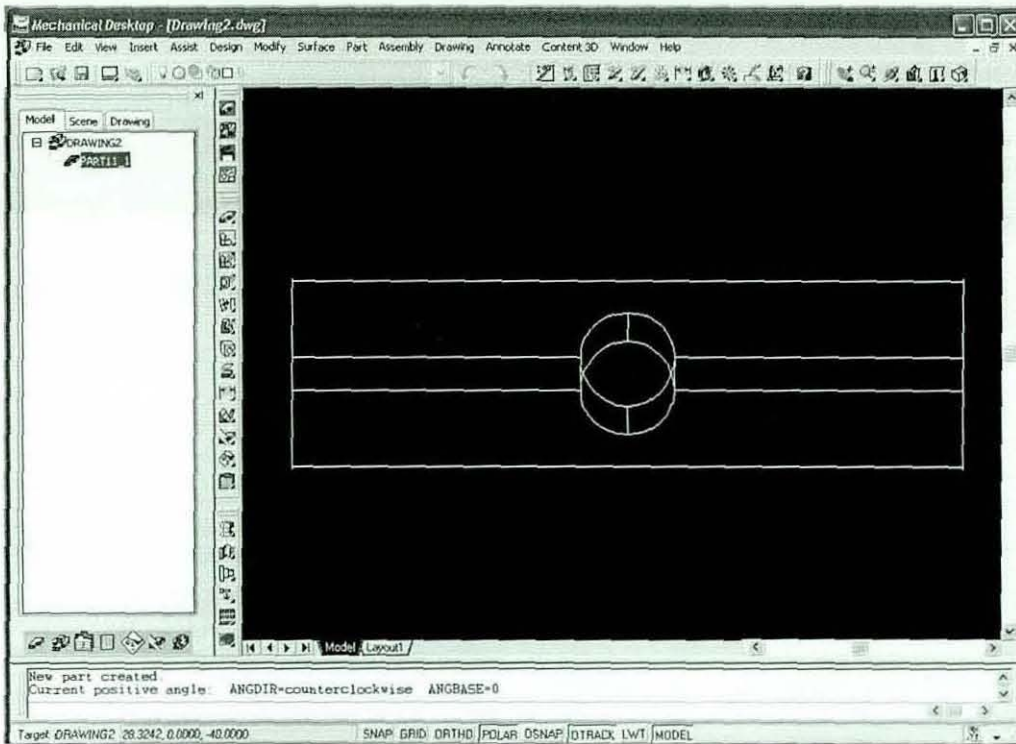


Figure 5-5 Rotation of the nail about its own axis at $\phi = 0$.

- The nail was rotated about its own axis in both directions, until the hole projection becomes very small, as depicted by Figure 5-6. At this stage value of ϕ was incremented by 0.5° and θ was again set at 0° .

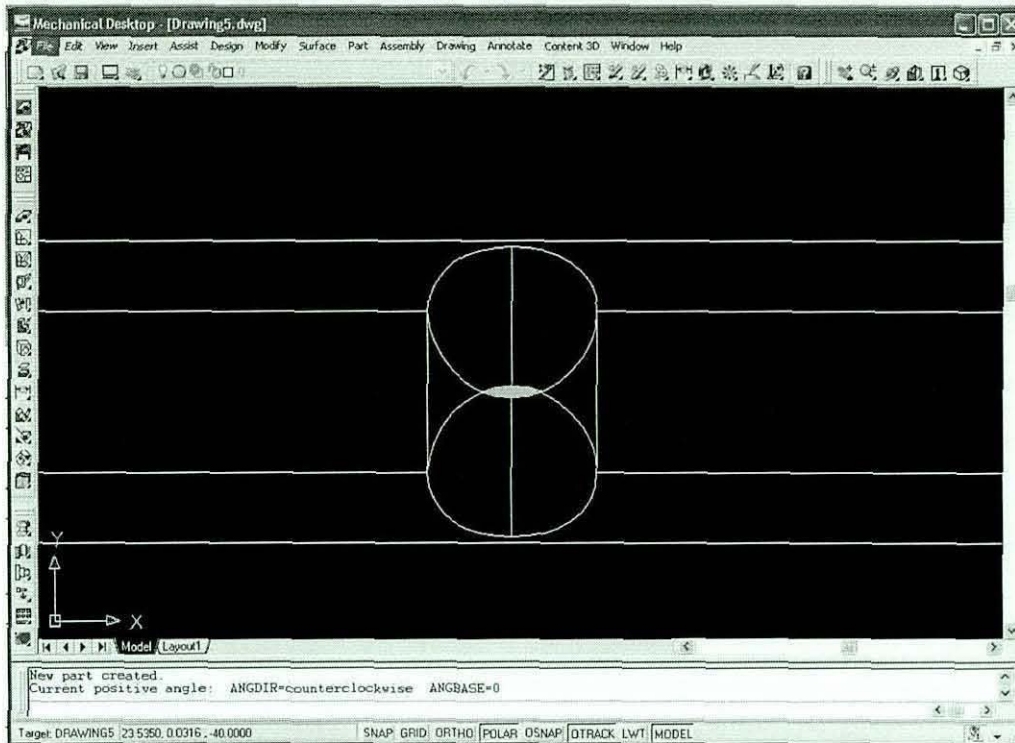


Figure 5-6 Small hole projection resulting in termination of angle " θ " increment.

- The value of ϕ is incremented by 0.5° until a specified value of ϕ (typically 15°) is reached.
- The CSV file i.e. LUT, was then saved in the directory based on the nail specifications.

Modelling of the intramedullary nail is summarized in the form of a flow chart, as depicted by Figure 5-7:

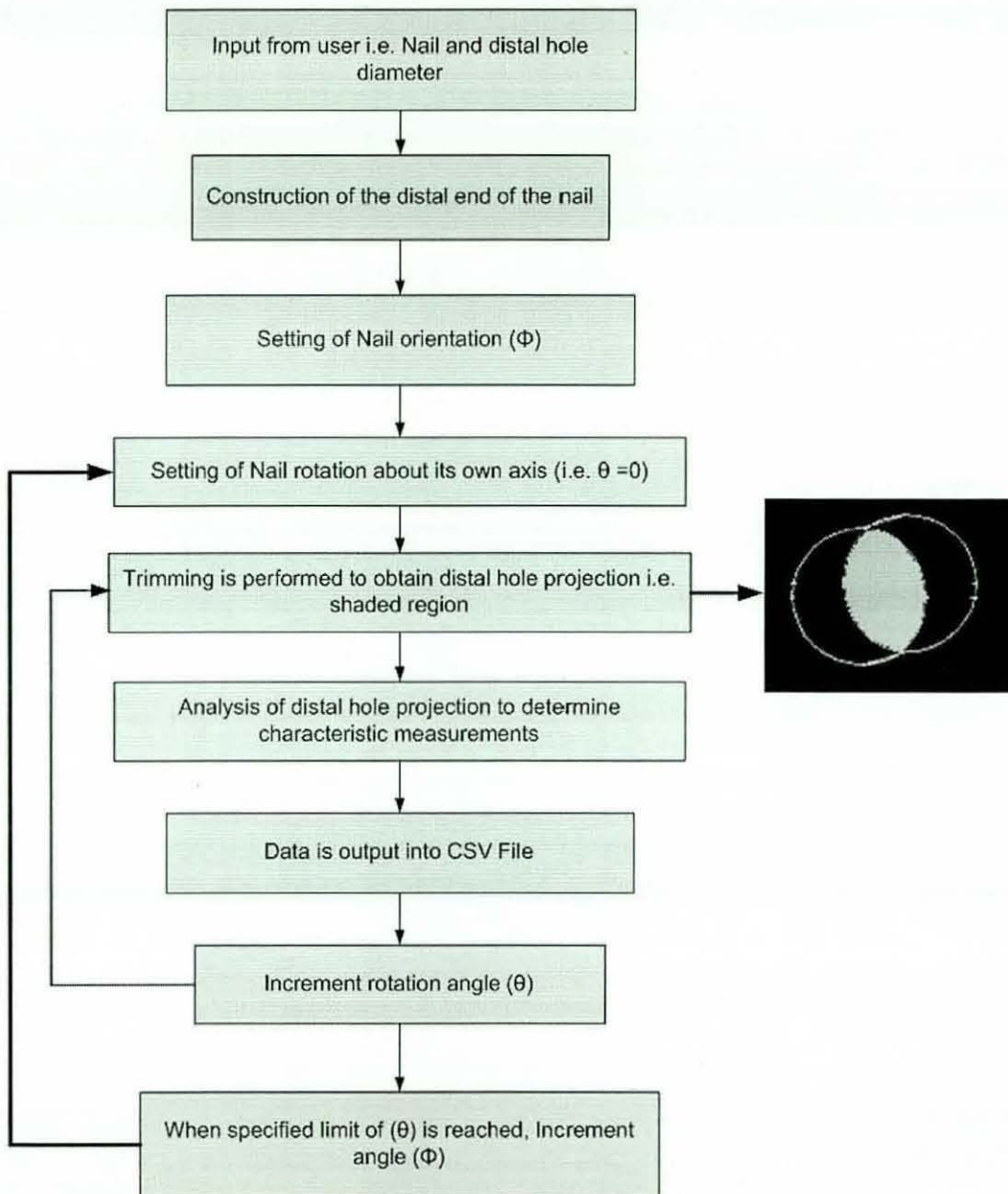


Figure 5-7 Flowchart of intramedullary nailing procedure.

5.4 Construction of delta nail

The main causes of failure or complication during closed intramedullary nailing are inappropriate entry point and inadequate nail size. These are especially important problems in the patient whose femoral canal diameter is very small (around 8mm or 9mm), such as such as adolescent patients and patients with congenital problems. In order to minimize the risk of insertion-related complications in the treatment of such

patients, nails with an anterior band of around 4° in the distal portion of the nail (shown in Figure 5-8) have been introduced [22].

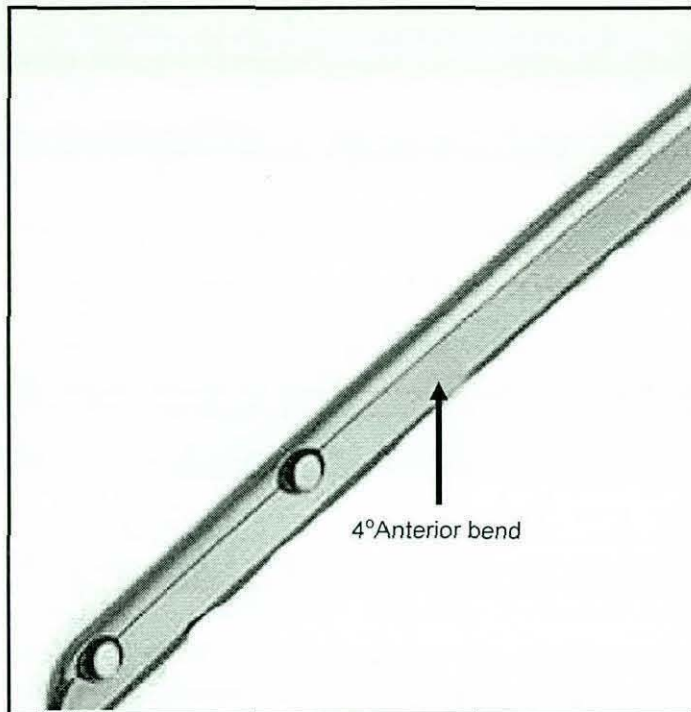


Figure 5-8 Distal end of the Delta nail

These nails are commonly known as Delta nails, and usually have diameter of 10mm and 11mm. However, proximal portion of the Delta nail (about 7cm from the proximal end) is thick (diameter 13mm) to gain enough strength for holding the insertion device and fixation of the interlocking screws [132]. According to T. Cannale in [22], the combination of strength and smaller size offered by delta nail has special advantages in the treatment of patients with smaller femoral canals, such as adolescent patients and patients with congenital problems.

In order to evaluate whether delta nails can be modelled as cylindrical nails or not, modelling of the delta and cylindrical nails of the same nail and distal hole diameter specification was performed. In order to determine the full extent of the difference between a cylindrical and delta nail, modelling of the delta nail was done from the smallest diameter nail (10mm) to the largest (13mm) used for IMN, at different orientations of the nail i.e. combinations of θ and ϕ .

A delta shaped intramedullary nail having an outer diameter of 10 mm and an inner diameter of 9.5 mm (i.e. diameter at the delta edges), as depicted by Figure 5-9, with a distal hole diameter of 5.2 mm was modelled as follows:

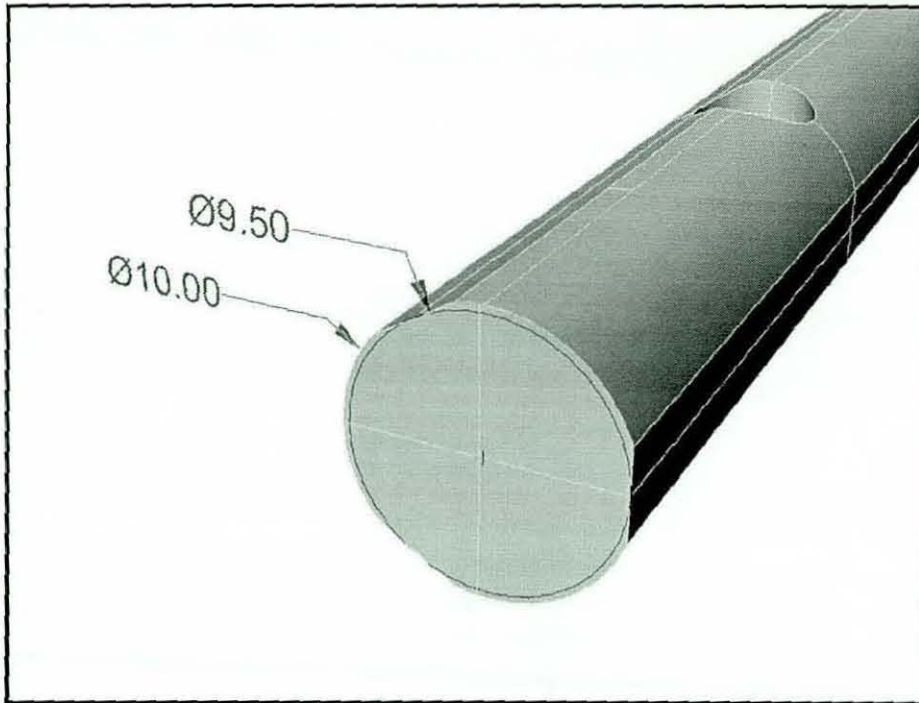


Figure 5-9 Delta nail model.

- At first, a cylinder of 10mm diameter was created to simulate the nail, and then another cylinder of 5.2mm was created to simulate the distal hole as shown in Figure 5-10.

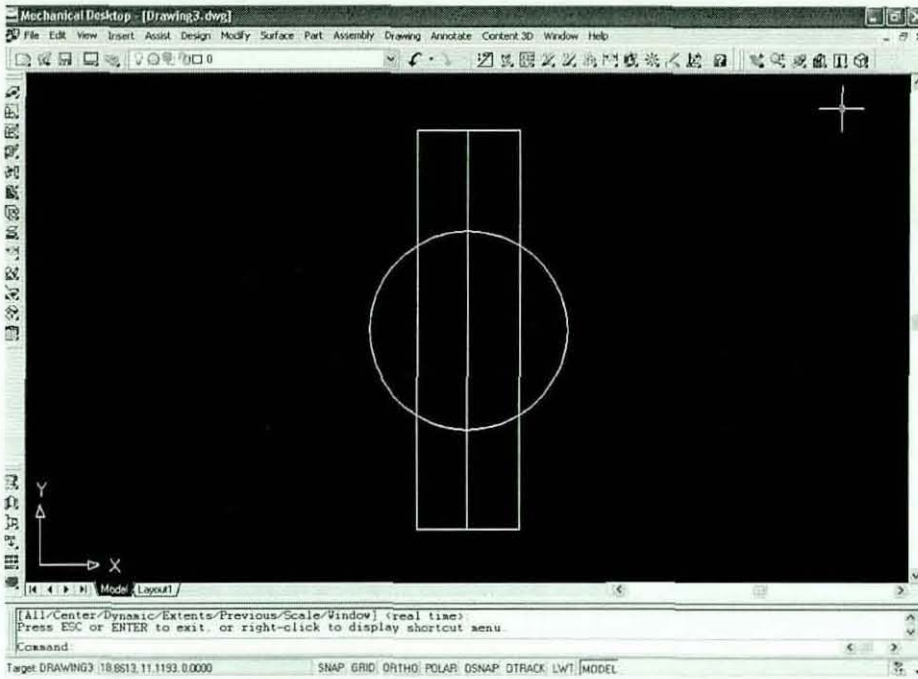


Figure 5-10 Creation of two cylinders to represent distal end of the nail.

- Now in order to create the delta shape, a rectangular box was created, based on the measurements made on the actual delta nail. The box was then rotated by 30° , as flat surfaces on the delta nail are at 120° to each other. A polar array of the rectangular box was then performed as shown in Figure 5-11.

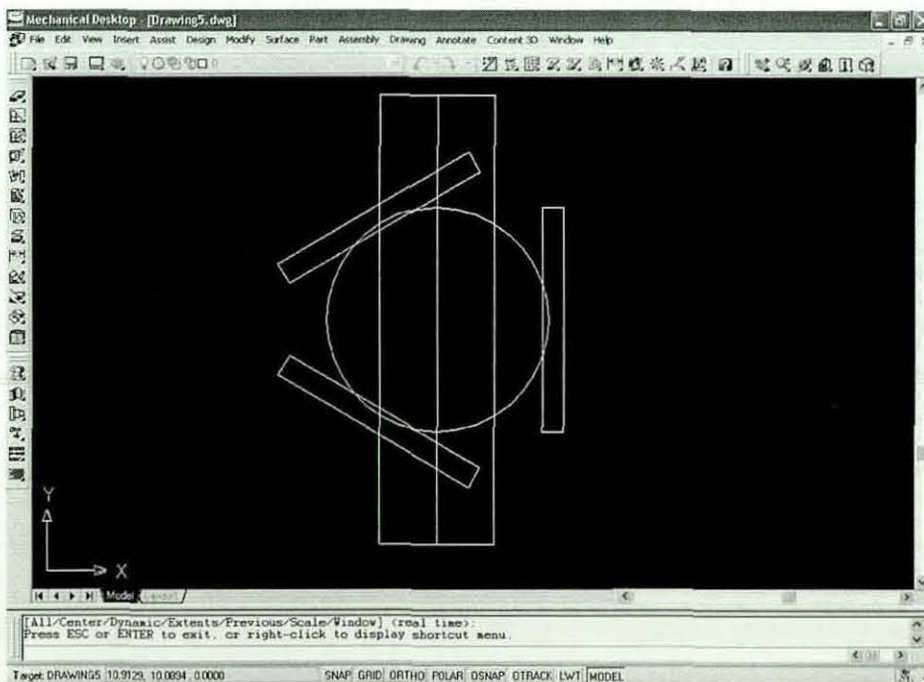


Figure 5-11 Polar array of rectangular box to obtain delta shape.

- All three rectangular boxes and cylinder representing the hole were then subtracted from the cylinder representing the nail. This results in the creation of a new entity in Mechanical Desktop which represents the delta nail as shown in Figure 5-12 and Figure 5-13.

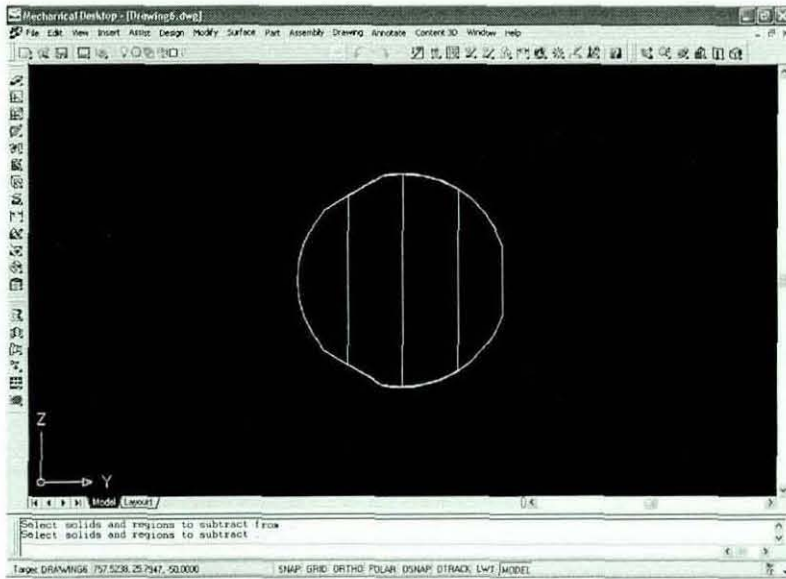


Figure 5-12 Right view of the delta nail.

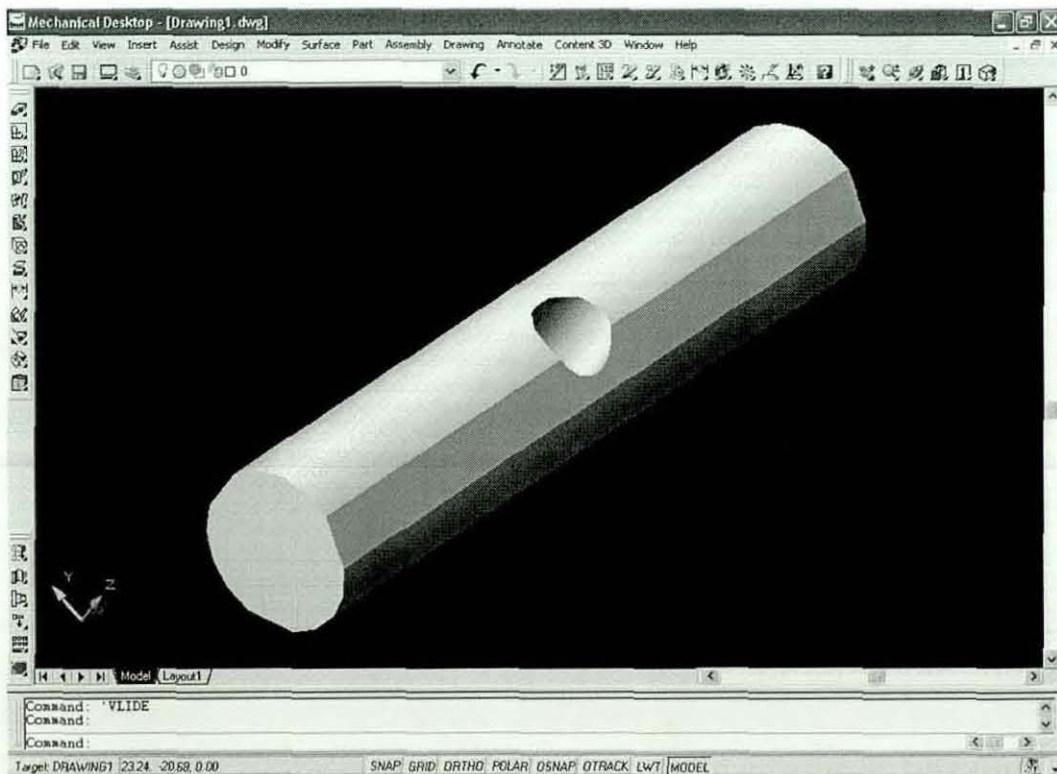


Figure 5-13 Front Isometric view of distal end of delta nail.

Once modelling of the delta nail has been performed, a cylindrical nail of the same specifications i.e. nail diameter of 10mm and hole diameter of 5.2mm was modelled as described in Section 4.2. A comparison was then made between the (λ) values obtained at different rotations of the nail (i.e. θ and ϕ) for both cylindrical and delta nail respectively. The following results were obtained:

For this analysis, following abbreviations are used:

D = Diameter of the nail,

d = Diameter of the distal locking hole,

θ = Rotation of the nail about its own axis,

λ = Angle between the major axis of the oval and the nail axis,

Difference = ($\lambda_{Delta} - \lambda_{Cylindrical}$),

$\phi = \hat{f}i$ = Angle between the nail axis and the ideal nail axis

where,

ideal nail axis = nail axis perpendicular to X-ray imaging axis.

θ	$\lambda_{Cylindrical}$	λ_{Delta}	$\lambda_{Difference}$
0	90	90	0
1	78.76	78.74	-0.02
2	68.34	68.32	-0.02
3	59.25	59.24	-0.01
4	51.6	51.63	0.03
5	45.32	45.33	0.01
6	40.2	40.24	0.04
7	35.98	36.01	0.03
8	32.5	32.49	-0.01
9	29.61	29.69	0.08
10	27.18	27.24	0.06
11	25.12	25.16	0.04
12	23.35	23.41	0.06
13	21.83	21.92	0.09
14	20.51	20.59	0.08
15	19.35	19.41	0.06

where, $\lambda_{Difference} = (\lambda_{Cylindrical} - \lambda_{Delta})$

*All dimensions are in Degrees.

Figure 5-14 Comparison between small diameter Delta and cylindrical nail at $\phi = 5^\circ$.

θ	$\lambda_{Cylindrical}$	λ_{Delta}	$\lambda_{Difference}$
0	90	90	0
1	84.43	84.41	-0.02
2	78.97	78.93	-0.04
3	73.72	73.7	-0.02
4	68.76	68.73	-0.03
5	64.12	64.17	0.05
6	59.86	59.87	0.01
7	55.95	55.97	0.02
8	52.41	52.51	0.1
9	49.2	49.32	0.12
10	46.31	46.39	0.08
11	43.7	43.74	0.04
12	41.36	41.39	0.03
13	39.24	39.32	0.08
14	37.34	37.37	0.03
15	35.6	35.64	0.04

where, $\lambda_{Difference} = (\lambda_{Cylindrical} - \lambda_{Delta})$

*All dimensions are in Degrees.

Figure 5-15 Comparison between small diameter Delta and cylindrical nail at $\phi = 10^\circ$.

θ	$\lambda_{Cylindrical}$	λ_{Delta}	$\lambda_{Difference}$
0	90	90	0
1	86.4	86.34	-0.03
2	82.83	82.77	-0.06
3	79.33	79.26	-0.04
4	75.91	75.94	0.03
5	72.62	72.68	0.01
6	69.45	69.55	0.02
7	66.43	66.57	0.03
8	63.58	63.64	0.02
9	60.88	61.12	0.08
10	58.34	58.54	0.06
11	55.97	56.19	0.06
12	53.75	54.04	0.1
13	51.68	51.88	0.06
14	49.76	50.04	0.1
15	47.97	48.16	0.07

where, $\lambda_{Difference} = (\lambda_{Cylindrical} - \lambda_{Delta})$

*All dimensions are in Degrees.

Figure 5-16 Comparison between small diameter Delta and cylindrical nail at $\phi = 15^\circ$.

It can be seen from Figure 5-14 to Figure 5-16 that for a small diameter nail over a range of rotation ϕ for the first few increments of θ , the difference in the value of measurement i.e. " λ " obtained from modelling of the delta and cylindrical nails was negligible. While, for higher values of θ (say greater than 6°) the difference in λ for the delta and cylindrical nails changes slightly. Similar results were obtained when a large delta shaped intramedullary nail having an outer nail diameter of 13 mm and a distal hole diameter of 6.7 mm was modelled and compared with a cylindrical nail of the same specifications, as depicted by Figure 5-17 and Figure 5-18. The maximum difference in λ obtained for the delta and cylindrical nails respectively at the same nail orientation was 0.15° (Refer Figure 5-18). This difference in λ will in turn causes an error of 0.04° in calculating the θ , while using λ as an input parameter from the machine vision system into the LUT. For simplicity purposes it was therefore decided to model the delta nail as cylindrical nail.

θ	$\lambda_{Cylindrical}$	λ_{Delta}	$\lambda_{Difference}$
0	90	90	0
1	78.76	78.74	-0.02
2	68.34	68.34	0
3	59.24	59.28	0.04
4	51.6	51.62	0.02
5	45.32	45.32	0
6	40.19	40.2	0.01
7	35.98	35.99	0.01
8	32.5	32.56	0.06
9	29.61	29.66	0.05
10	27.18	27.31	0.13
11	25.12	25.23	0.11
12	23.35	23.49	0.14
13	21.83	21.96	0.13
14	20.51	20.62	0.11
15	19.35	19.41	0.06

where, $\lambda_{Difference} = (\lambda_{Cylindrical} - \lambda_{Delta})$

*All dimensions are in Degrees.

Figure 5-17 Comparison between large diameter delta and cylindrical nail at $\phi = 5^\circ$.

θ	$\lambda_{Cylindrical}$	λ_{Delta}	$\lambda_{Difference}$
0	90	90	0
1	86.41	86.41	0
2	82.83	82.81	-0.02
3	79.33	79.34	0.01
4	75.91	75.92	0.01
5	72.62	72.65	0.03
6	69.45	69.47	0.02
7	66.43	66.43	0
8	63.58	63.6	0.02
9	60.88	60.98	0.1
10	58.34	58.38	0.04
11	55.97	56.03	0.06
12	53.75	53.9	0.15
13	51.68	51.8	0.12
14	49.76	49.91	0.15
15	47.97	48.01	0.04

where, $\lambda_{Difference} = (\lambda_{Cylindrical} - \lambda_{Delta})$

*All dimensions are in Degrees.

Figure 5-18 Comparison between large diameter delta and cylindrical nail at $\phi = 15^\circ$.

5.5 Selection of characteristic measurements

Due to the unconstrained nature of imaging geometry, in order to match the measurements from image analysis and the CAD model, the characteristic measurements must be scale invariant (i.e. constant and unaffected by transformation of coordinates, such as, in this case, from pixels to millimetres).

In order to identify characteristic measurements, i.e. measurements that can be used reliably to predict the rotation of the nail about its own axis, the distal hole projection was analysed to extract measurements such as dimensionless area, dimensionless perimeter, dimensionless major-axis length, roundness R and the angle λ . The reason for using λ is that during rotation of the nail, the nail axis remains constant while the major axis of the oval changes significantly, except when the nail axis is perpendicular to the X-ray imaging axis ($\phi = 90$). Dimensionless area was obtained by dividing area of the oval by the square of nail's diameter, whereas dimensionless perimeter and dimensionless major-axis length were obtained by dividing perimeter

and major-axis length by the nail's diameter respectively. It should be noted that roundness is given by:

$$R = \frac{P^2}{4\pi A}$$

where,

R = Roundness,

P = Perimeter,

A = Area

The response of all these measurements to changes in the angular orientation of the nail was then determined using the CAD model of the nail. The data obtained from the CAD model was then plotted to produce the measurements versus angular rotation of the nail graphs as shown in Figure 5-19. It should be noted that these measurement were obtained when the nail axis was perpendicular to the X-ray imaging axis ($\phi = 90^\circ$), therefore the major axis of the oval always remained parallel to the nail axis ($\lambda = 0^\circ$).

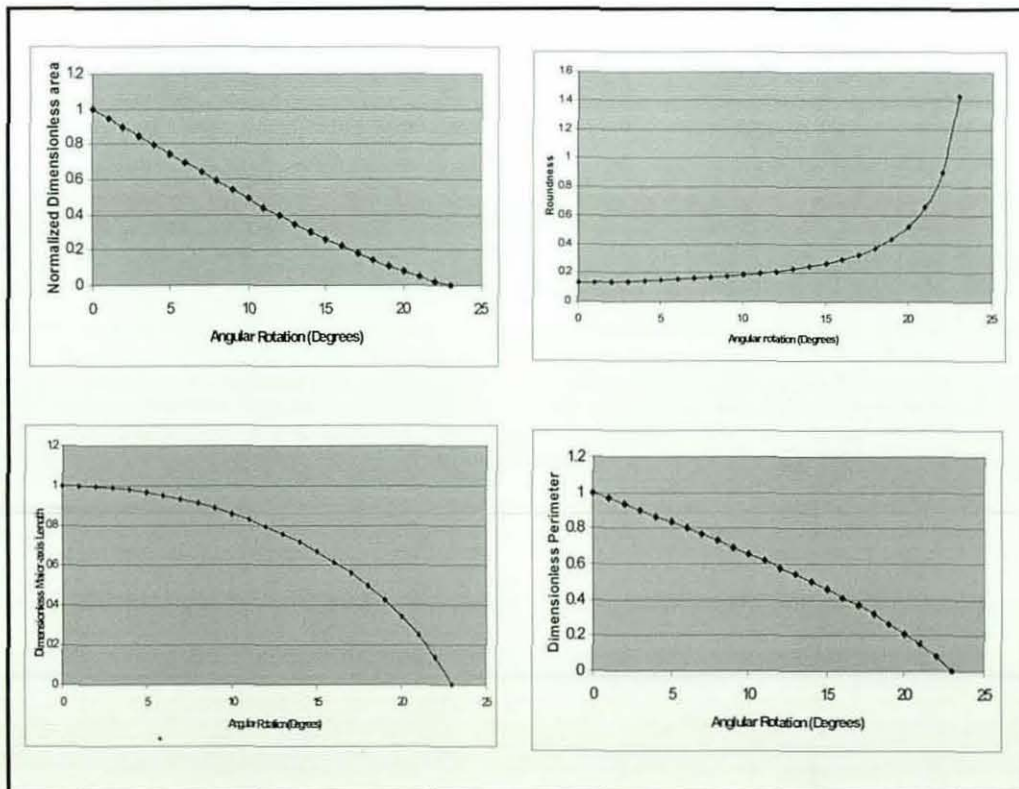


Figure 5-19 Graphical comparisons of different oval measurements with angular rotation " θ " of the nail.

It can be seen from Figure 5-19, that both dimensionless area and dimensionless perimeter show almost linear behaviour for the entire range of possible angular rotations of the nail. However, roundness and dimensionless major axis length do not change much for initial rotations of the nail, and therefore were deemed not suitable to be used as characteristic measurements. In the light of previous research by Browbank [78] and results from CAD modelling of intramedullary nails, it was decided to analyse the distal hole projection using dimensionless area and angle λ as characteristic measurements.

5.6 Building of Look-up tables

The LUT consisting of characteristic measurements of dimensionless area and λ , obtained from the modelling of the nail in Mechanical Desktop were then imported into Matlab in the manner depicted by Figure 5-1.

The angles λ and ϕ obtained from X-ray image analysis and the LUT obtained from modelling of the nail were entered as input into the software. Software was designed in such a way that when the value of ϕ obtained from X-ray image analysis did not match with the value ϕ of the LUT then interpolation was carried out to determine λ and the corresponding θ for entered value of ϕ . Then for this particular value of ϕ , angle λ obtained from X-ray image analysis was searched within the LUT to predict rotation of the nail about its own axis i.e. θ .

5.7 Accuracy evaluation of nail modelling

In order to evaluate the accuracy of the nail model, in the laboratory a specially designed test rig was used to physically simulate different nail orientations using combinations of angles ϕ and θ . Using the test-rig the nail was rotated by a known angle θ (so that θ values obtained by using the nail model in conjunction with the X-ray image analysis can be compared against a true value of θ).

5.7.1 Determination of nail rotation angle θ

At first, X-ray images of the nail with the calibration frame in position were taken in both Lateral and AP views. X-ray images were then processed using the Matlab Image Processing Toolbox to obtain characteristic features (dimensionless area of the oval, angle λ and angle ϕ). These measurements were then used as an input into the LUT obtained from the nail model developed in Mechanical Desktop to predict θ . Two methods were used to predict θ . These were:

5.7.1.1 Area method

In this method, for a given value of ϕ the dimensionless area of the oval extracted from X-ray image analysis was compared with the dimensionless area of the oval projection obtained from the nail model to predict θ . The major disadvantage of this area method is that it was not possible to distinguish in which direction the nail has been rotated, as a similar value of area was obtained for both positive and negative rotations of the nail.

5.7.1.2 Major angle method

In this method, for a given value of ϕ , the value of the angle λ obtained from X-ray image analysis was compared with λ obtained from the nail model to estimate rotation of the nail about its own axis. Using this method also enabled determination of the direction in which the nail is rotated. However, it can not be used when the nail axis is perpendicular to the X-ray imaging axis ($\phi = 90^\circ$), as in this case the major axis of the oval always remains parallel to the nail axis for all possible rotations θ of the nail.

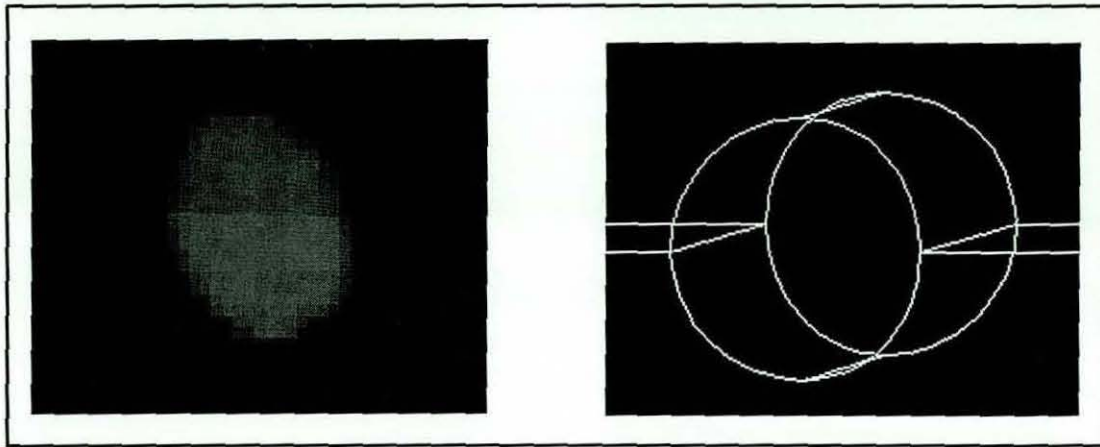


Figure 5-20 Matching between X-ray image and CAD Model.

5.7.1.3 Major angle v/s area method

Analysis has showed that the Major angle method was more accurate than the area method, as using this method rotation θ of the nail was predicted with a mean accuracy of 0.22° (worst case being 0.49°) as shown in Figure 5-21. It can be seen from Figure 5-20 that the edges of the oval in the X-ray image are not as sharp as in the model, the reason being that in digital images edges are represented by finite transition from dark background to object rather than sharp transitions. It can also be seen that the major axis of the oval in both the X-ray image and the CAD model is almost identical. Therefore, the major angle method proved to be more accurate than the area method.

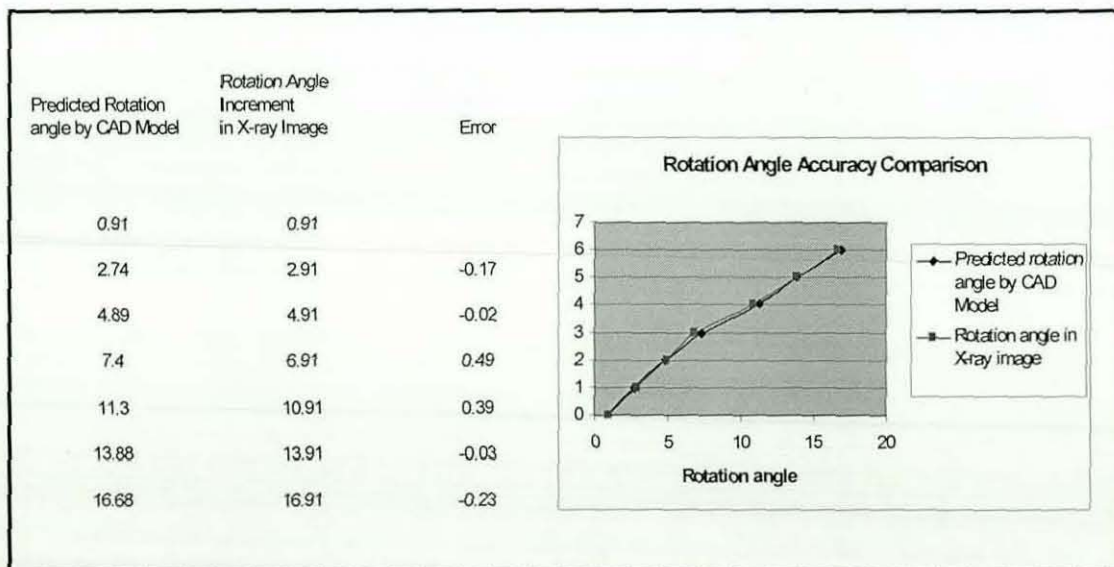


Figure 5-21 Rotation angle accuracy obtained using the Major angle method.

Using the area method a mean accuracy of 0.75° (worst case being 1.1°) was achieved as depicted by Figure 5-22.

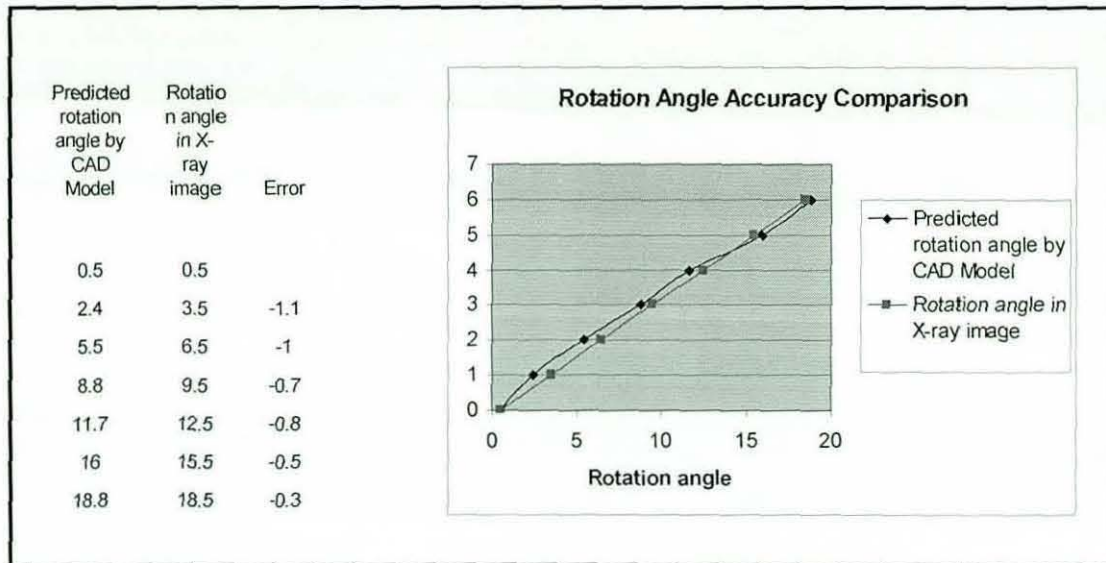


Figure 5-22 Rotation angle accuracy obtained using the Area method.

Therefore, in order to achieve better accuracy, it was decided to use the Major angle method for predicting θ to obtain optimum results from modelling of the nail. However, the area method can be used when the nail axis is perpendicular to the X-ray imaging axis. If possible this scenario should be avoided by creating an angle between the nail axis and the X-ray imaging axis, so that the Major angle method can be used to obtain better accuracy. From the analysis of the data obtained this angle of ϕ should be around 10° to achieve optimum results.

5.8 Summary

The novel method of off-line modelling of the nail to generate LUTs allows modelling of any shape of intramedullary nail (such as delta nails) accurately; therefore nails from different manufacturers can be modelled. Furthermore, this method reduces the length of time for the computation of the drilling trajectory and thus has the potential for reducing the overall time required for the surgical procedure. The major angle method proved to be more reliable in predicting θ in comparison to the area method. It should be noted that there are two types of intramedullary nails, slotted and solid nails. Slotted nails may have large insertion related deformation due to their relatively low stiffness compared to solid nails. The solid nails have virtually

negligible local deformation at the distal holes to affect the circularity of the holes. This work relates to solid intramedullary nails. In the following chapter, robustness of the machine vision system was evaluated.

6 Accuracy evaluation of the machine vision system

The use of a Co-ordinate Measuring Machine (CMM) was considered for accuracy evaluation of the machine vision system, however, it was found to be nearly impossible to transport the intramedullary nail and the calibration frame to the CMM machine while keeping the same spatial relationship as used while taking intraoperative x-rays for each set of measurement. Therefore, it was decided to use optical co-ordinate measurement by using theodolites for accuracy evaluation of the machine vision system.

6.1 Theodolite

The theodolite is a surveying instrument which is generally used in civil engineering. It consists of a small telescope mounted so as to move on two graduated circles, one horizontal and the other vertical, while its transverse axes pass through the centres of the circles as shown in Figure 6-1. The optical axis of the telescope, called the sight axis and defined by the optical centre of the objective and the centre of the cross-hairs in its focal plane, must similarly be perpendicular to the horizontal axis.

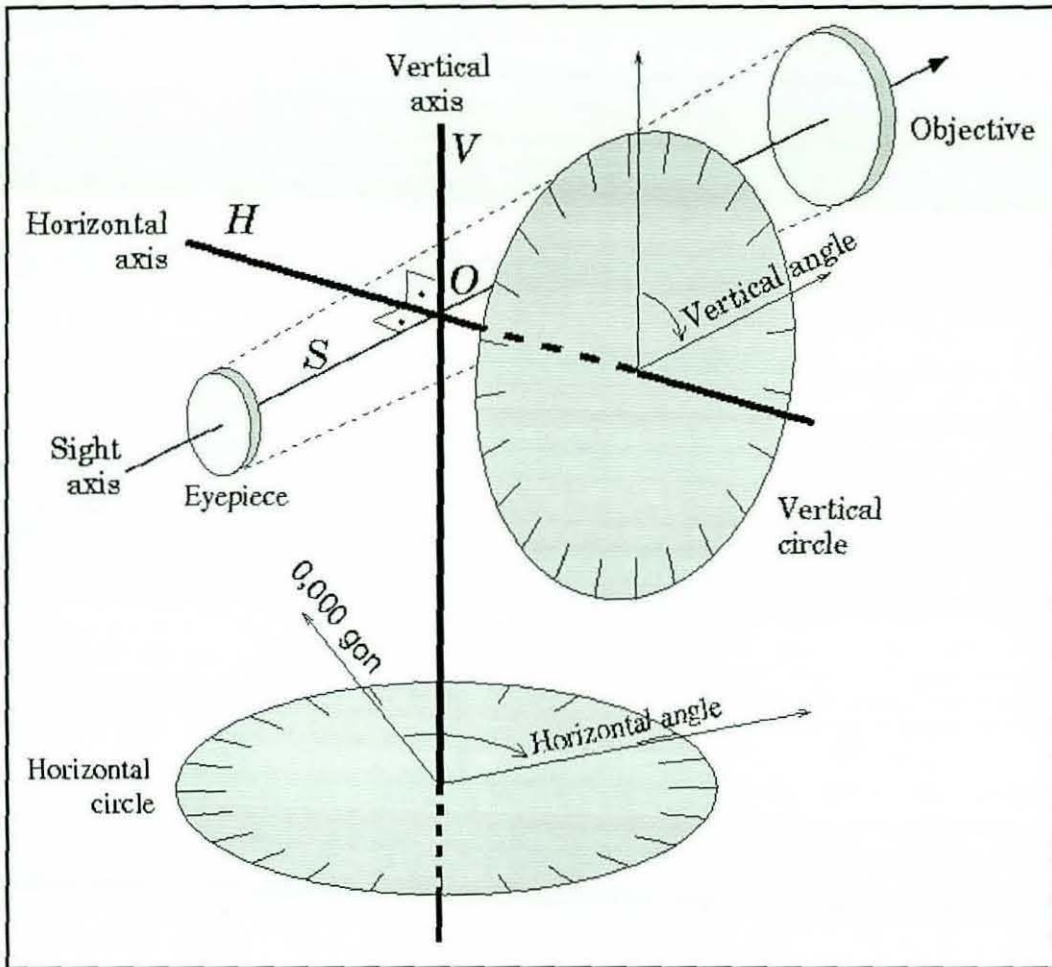


Figure 6-1 Internal Construction of theodolite.

6.1.1 The triangulation technique

Triangulation is a technique used in surveying to measure distances by using the properties of a triangle. It uses two theodolites, with one being used as the master theodolite while the other provides the radial information as shown in Figure 6-2.

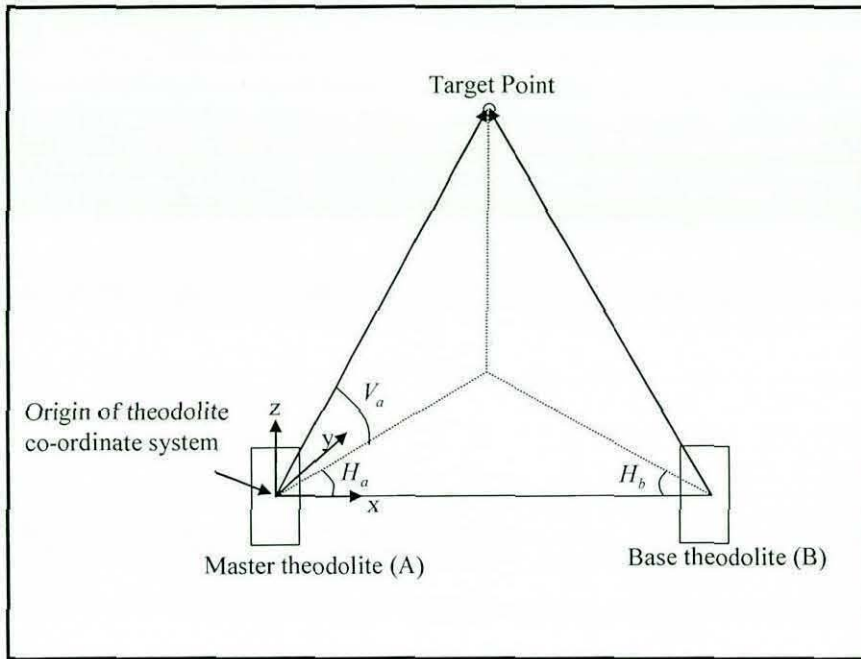


Figure 6-2 Application of triangulation technique.

Given that the distance between the two theodolites is known the 3-D position of the target point was determined with respect to the co-ordinate system of the master theodolite as described in **APPENDIX F**.

6.2 Accuracy evaluation of machine vision system using Γ calibration frame

In order to cover the wide range of possible nail orientations likely to be encountered during the surgical procedure, a specially designed test rig, shown in Figure 6-3, was used in laboratory trials to simulate different rotations θ of the nail about its own axis. This was carried out with the nail at different orientations ϕ with respect to the X-ray imaging axis. In order to obtain optimal lighting conditions while taking theodolite measurements, an incandescent lamp was used in the vicinity of the calibration frame.

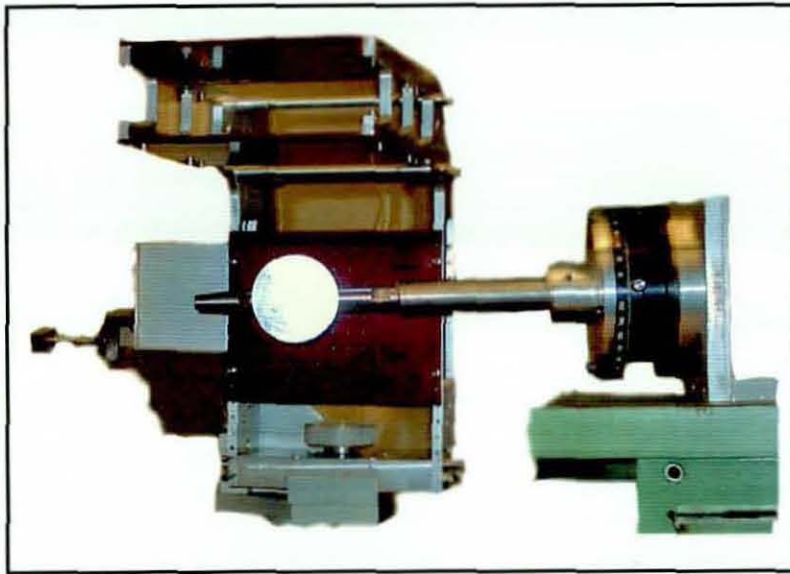


Figure 6-3 Experimental set up in the vicinity of calibration frame.

For theodolite measurement, two *Sokisha DT5* theodolites, with single frame attachment, were used as shown in Figure 6-4.



Figure 6-4 Sokisha DT5 Theodolite.

In order to obtain the best possible accuracy, a minimum distance between theodolites and calibration frame was obtained using the following measurements, while the C-arm unit was in position to acquire a Lateral view image:

Distance between calibration frame and control panel of C-arm unit to achieve a typical Lateral view image $\approx 1.4m$

Space required for manoeuvring C-arm via control panel $\approx 0.5m$

In the light of the above measurements the theodolites were placed at a distance of 2 metres from the calibration frame.

For theodolite measurement, determining the sample size (i.e. number of readings that should be taken for each measurement) is very important because samples that are too large can waste time and resources, while samples that are too small may lead to inaccurate results. Therefore, prior to laboratory trials sample size was determined using the following equation.

$$E = z_{\alpha/2} \cdot \frac{\sigma}{\sqrt{N}} \quad \text{(Equation 6-1)}$$

In Equation 6-1, 'E' is the margin of error (i.e. the maximum difference between the observed sample mean and the true value of the population mean), $z_{\alpha/2}$ is known as the critical value, the positive 'z' value that is at the vertical boundary for the area of $\alpha/2$ in the right tail of the standard normal distribution, ' σ ' is the population standard deviation and 'N' is the sample size. It was assumed that the data is normally distributed.

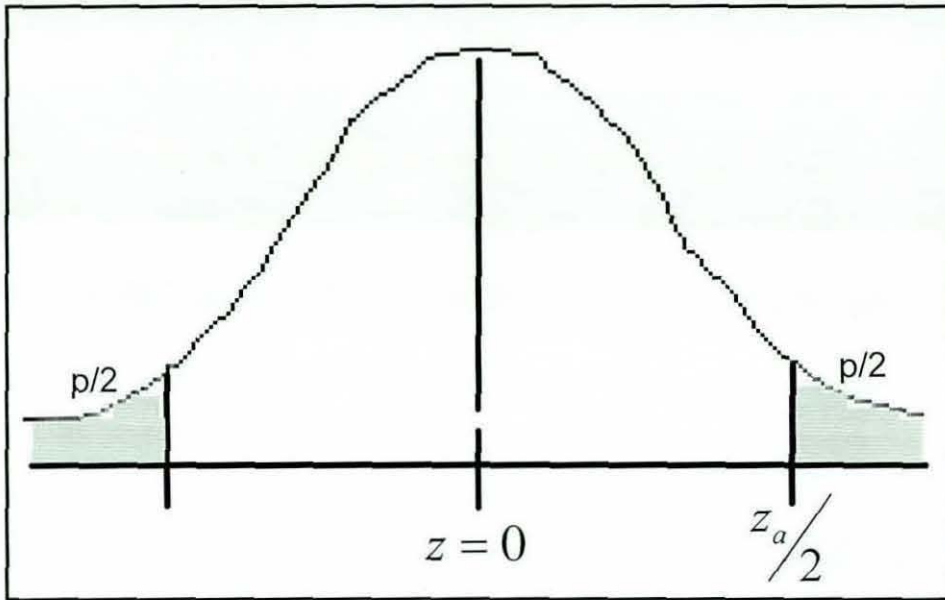


Figure 6-5 Standard normal distribution graph.

Equation 6-1 can be rearranged to determine sample size, which is necessary to produce results accurate to a specified confidence level, the mean value μ to within $\pm E$.

$$N = \left[\frac{z_{\alpha/2} \cdot \sigma}{E} \right]^2 \quad \text{(Equation 6-2)}$$

A confidence level of 95% which corresponds to a probability (p) value of 0.05 is used. Each of the shaded regions in Figure 6-5 has an area of $p/2 = 0.025$. The region to the left of $-z_{\alpha/2}$ and to the right of $z = 0$ is $0.5 - 0.025$, or 0.475. From the table of the Standard Normal (z) Distribution, an area of 0.475 corresponds to a value of 1.96. The critical value $-z_{\alpha/2}$ is therefore equal to 1.96. Theodolites used in this study have a resolution of 0.0122 mm/m, whereas encoder resolution of theodolites used in this study is 0.0025 mm/sec at 1 metre target distance. Since during laboratory trials theodolites were placed at a distance of 2 m from the calibration frame as described earlier. Therefore, resolution of theodolites is 0.0244 mm during laboratory trials. However, in order to allow for human error the margin of error was kept at 0.05mm. In order to determine the standard deviation five readings were taken for a single

measurement (i.e. centre of a cross hair was measured, each time once a measurement is obtained, theodolites were turned away and then centred back again onto the centre of a cross hair) as shown in Table 6-1.

Reading	x (mm)	y (mm)
1	657.93	493.13
2	657.89	493.19
3	657.95	493.21
4	657.9	493.14
5	657.93	493.21
Mean	657.92	493.18

Table 6-1 Theodolite readings to determine sample standard deviation.

Using the above data, standard deviations of $\sigma_x = 0.025$ and $\sigma_y = 0.039$ were obtained for the x and y co-ordinates respectively. Now the sample size was calculated as follows:

$$N_x = \left[\frac{1.96 \times 0.025}{0.05} \right]^2 = 0.99$$

and

$$N_y = \left[\frac{1.96 \times 0.039}{0.05} \right]^2 = 2.34$$

The above calculations yield that a sample size of 2 should be used during theodolite measurement; however, to be on the safe side it was decided to take 3 readings for each theodolite measurement as it would take only about 5 minutes of additional time.

6.2.1 Determination of drilling trajectory using theodolites

In order to determine the true drilling trajectory of the distal locking hole, the following measurements must be obtained using theodolites:

At first, there is a need to define the co-ordinate system of the calibration frame. The specified origin of the calibration frame does not lie on the surface of the Lateral XR11

plate (i.e. XY plane), because the centre of the ball bearing does not coincide with that plane as shown in Figure 6-6.

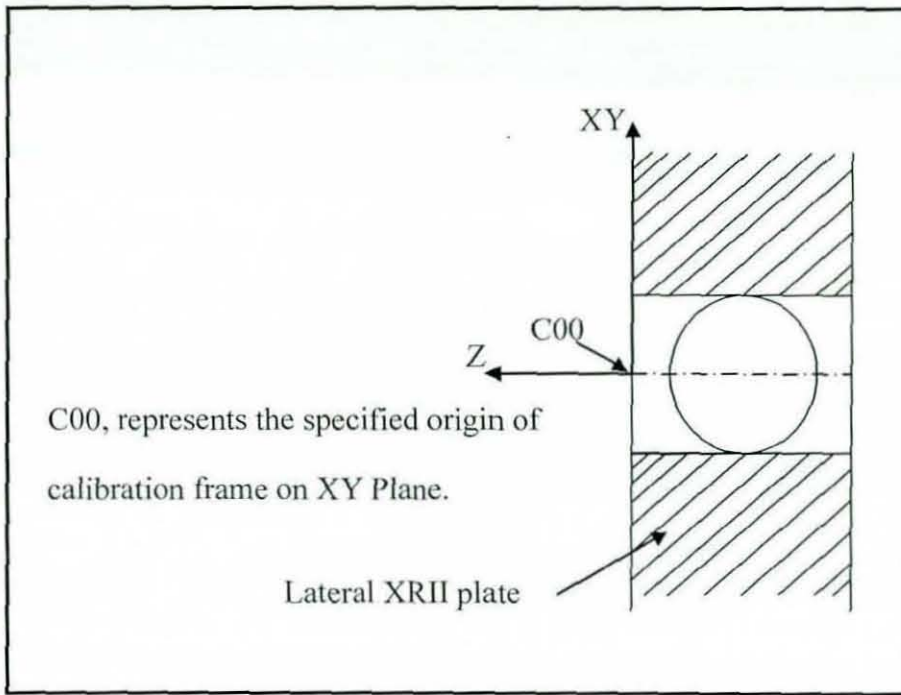


Figure 6-6 Positioning of specified origin of calibration frame.

Therefore, the points (R_0, R_1, R_2, R_3 & R_4) on the surface of the Lateral XRII calibration plates were measured with respect to the theodolite frame of reference as shown in Figure 6-7. Here it should be noted that on the surface of the XRII plate different cross hairs were drawn and centre of these cross hairs represented points R_0 : R_4 respectively

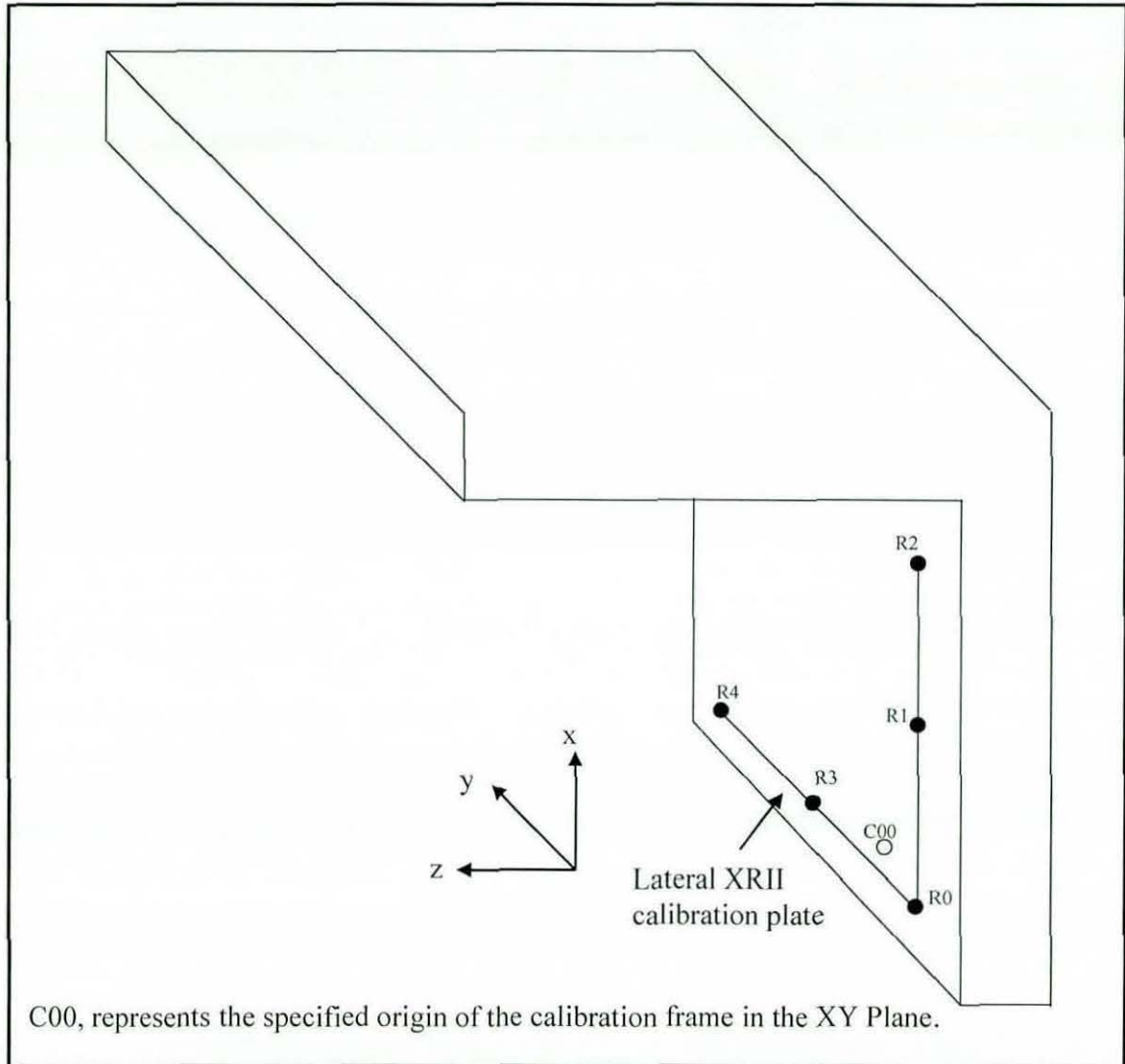


Figure 6-7 Theodolite measurements on the calibration frame.

Once all the above mentioned measurements were made using two theodolites, the calibration frame co-ordinate system can be defined with respect to the theodolite frame of reference (i.e. the homogenous transform ${}^{TH}_{CF}T$, where 'CF' and 'TH' refer to calibration frame and theodolite respectively) as shown in Section 6.2.1.1.

During laboratory trials, a simulation of the distal locking procedure was performed using a cylindrical nail of 14mm diameter containing two distal holes of 7mm diameter. In order to define the true trajectory of the distal locking hole, a test piece comprising a solid cylinder of $7_{-0.01}^{+0.00}$ mm diameter with an integral concentric disc of 50mm diameter at one end (as shown in Figure 6-8) was fitted into one of the nail holes.

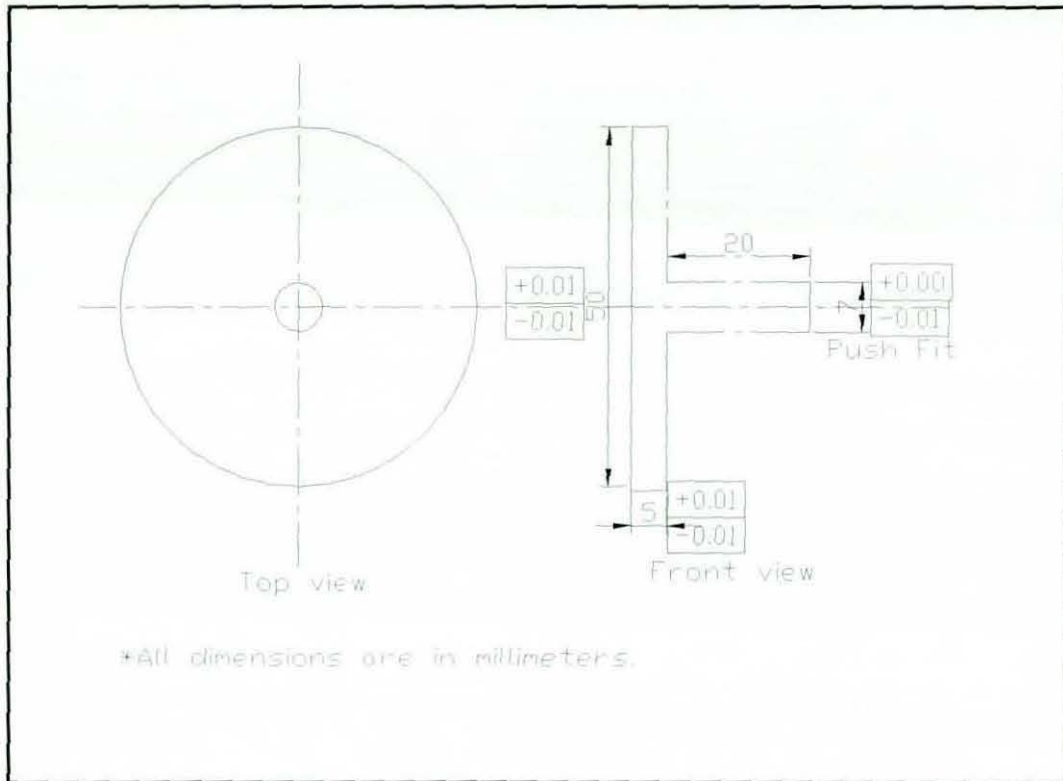


Figure 6-8 Solid cylinder with circular disc.

When inserted into the distal locking hole, as depicted by Figure 6-9, the solid cylinder fits the hole precisely, thus the axis of the solid cylinder represents the true drilling trajectory. The test piece was made of mild steel to reduce wear on the shaft due to multiple insertions.

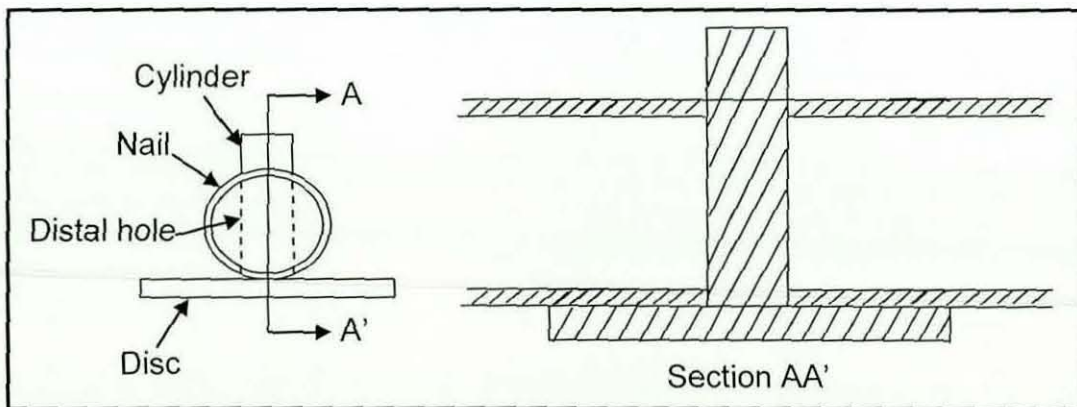


Figure 6-9 Insertion of solid cylinder into the distal locking hole.

In order to obtain the best possible accuracy, a computer assisted Ferranti Merlin 750 precision CMM, shown in Figure 6-10, was used to take measurements on the test piece to check whether its dimensions met the specified dimensions. The accuracy of

the CMM is 5 micron with 2 micron repeatability. The following results were obtained:

Diameter of the solid cylinder = 6.97 mm.

Angle between the cylinder axis and disc surface = 89.97° .

Deviation in concentricity between cylinder and disc = 0.026mm.



Figure 6-10 Ferranti Merlin 750 Co-ordinate measurement machine.

On the surface of this disc five points, marked as Cen, D_1, D_2, D_3 & D_4 (these points are physically marked as centre of different cross hairs on the target disc) as shown in Figure 6-11, were measured with respect to the theodolite frame of reference to determine the central axis $^{TH}_V$ of the test piece and thus the distal hole axis.

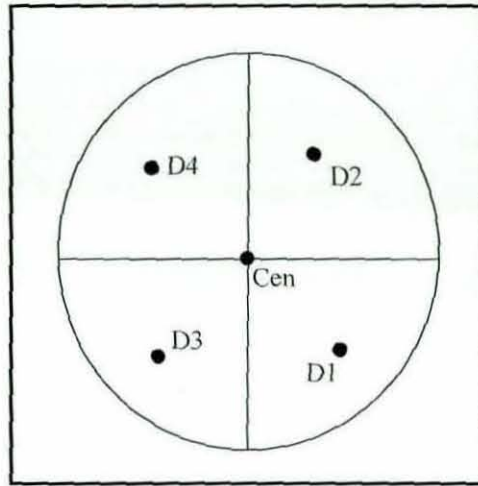


Figure 6-11 Points to be measured on the surface of the circular disc.

Using theodolites a study was conducted to determine whether to use the centre of the disc that was obtained using a centre-finder or to use centre of the disc that was obtained using perpendicular bisector method i.e. locating the point of intersection of the perpendicular bisectors of two chords of the circle. For this purpose, at first centre of the disc obtained using centre finder was measured and it was found out to be (665.50, 516.78) mm. Subsequently in order to determine centre of the disc using perpendicular bisector method, several chords were drawn on disc surface as shown in Figure 6-12.

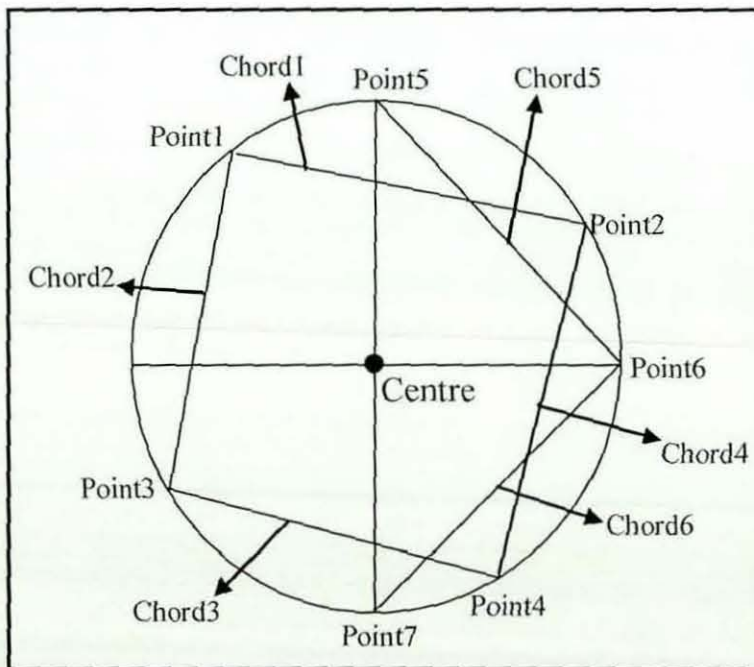


Figure 6-12 Drawing of several chords on disc surface to determine disc's centre

Initially, points forming the chords were measured as shown in Table 6-2.

Measurements	X (mm)	Y (mm)
Point1	657.93	493.12
Point2	688.59	507.74
Point3	641.85	524.50
Point4	670.25	541.26
Point5	665.89	492.00
Point6	690.38	517.13
Point7	665.21	541.71

Table 6-2 Theodolite measurements.

Using the data in Table 6-2, the following set of disc centres was obtained using perpendicular bisector method, as depicted by Table 6-3.

Chord intersection	Disc's centre	X (mm)	Y (mm)
Chord1 with chord2	Cen1	665.46	516.79
Chord1 with chord4	Cen2	665.45	516.81
Chord3 with chord4	Cen3	665.49	516.82
Chord2 with chord3	Cen4	665.52	516.76
Chord5 with chord4	Cen5	665.50	516.83
Chord5 with chord2	Cen6	665.53	516.81
Chord6 with chord1	Cen7	665.46	516.79
Chord6 with chord3	Cen8	665.51	516.81
	Mean Centre	$665.49^{+0.04}_{-0.04}$	$516.80^{+0.03}_{-0.04}$

Table 6-3 Disc's centre obtained using perpendicular bisector method.

It can be seen from Table 6-3, that the difference in centre co-ordinates obtained using a centre-finder i.e. (665.50,516.78) and perpendicular bisector method i.e. (665.49,516.80) is relatively insignificant. Therefore, it was decided to use the centre

of the disc that was obtained using centre-finder as it will involve fewer theodolite measurements and hence will be less time consuming without losing any accuracy.

Now the transformation matrix (i.e. ${}^{CF}_{Th}T$) that can be used to relate the theodolite frame of reference with respect to the calibration frame co-ordinate system with base point R_0 must be determined, as shown in Section 6.2.1.1. Once the transformation matrix ${}^{CF}_{Th}T$ was obtained the points Cen, D_1, D_2, D_3 & D_4 , measured on the circular disc with respect to the theodolite frame of reference, can be described relative to the calibration frame co-ordinate system with base point R_0 . The true drilling trajectory then can be determined with respect to the calibration frame co-ordinate system with base point R_0 , by finding the line which is perpendicular to the plane defined by D_1, D_2, D_3 & D_4 and passing through the point "cen".

Using the CMM measurement, transformation (i.e. only translation) from the base point R_0 to C_{OO} , i.e. specified origin of the calibration frame, was determined so that the true drilling trajectory obtained using the theodolite measurements can be described with respect to the calibration frame.

- Finally, the drilling trajectory of the distal locking hole relative to the calibration frame obtained from machine vision analysis and theodolite measurements can be compared to determine the angular and positional error of the drilling trajectory obtained from machine vision analysis.

6.2.1.1 Defining the Calibration frame co-ordinate system

The co-ordinate system of the calibration frame can be defined by a base point R_0 , then points R_1 and R_2 along the x-axis to define the direction of the unit vector. The plane then can be defined by using points R_3 and R_4 along the y-axis as shown in Figure 6-7. In order to obtain a more accurate definition of the plane, instead of using only three points (the minimum points required to define a plane), five points on the Lateral XRII plate were measured using theodolites as shown in Figure 6-7.

Consider $(\hat{e}_x, \hat{e}_y, \hat{e}_z)$ as a set of unit vectors that gives the principal directions of the coordinate system of the calibration frame with point R_0 as the origin. Now the unit vectors \hat{e}_{x1} , & \hat{e}_{x2} will be given by:

$$\hat{e}_{x1} = \frac{\vec{R}_1 - \vec{R}_0}{\|\vec{R}_1 - \vec{R}_0\|}; \text{ and } \hat{e}_{x2} = \frac{\vec{R}_2 - \vec{R}_0}{\|\vec{R}_2 - \vec{R}_0\|} \quad \text{(Equation 6-3)}$$

Where, \vec{R}_0, \vec{R}_1 & \vec{R}_2 are position vectors with respect to the Master theodolite coordinate system.

Now the unit vector \hat{e}_x will be determined by taking the average of \hat{e}_{x1} & \hat{e}_{x2} .

It cannot be assumed that the points R_3 & R_4 along y-axis form a right angle with respect to the vectors given by R_1 & R_2 along x-axis. Therefore, the unit vector \hat{e}_y was computed by fulfilling the requirement of orthogonality as follows:

\hat{e}_y is a unit vector which is orthogonal to \hat{e}_x and lies in the plane defined by points R_0, R_1, R_2, R_3 and R_4 as shown in Figure 6-13.

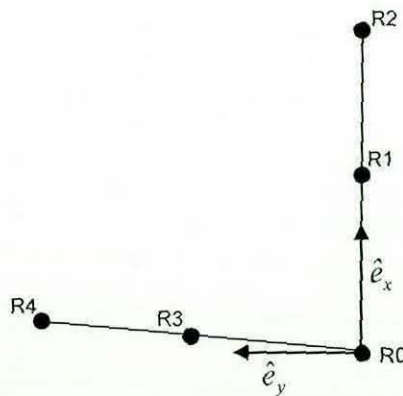


Figure 6-13 Datum coordinate system of calibration frame

Now an intermediate vector $\vec{n}_{\eta 1}$ is introduced which lies in the plane of R_0, R_1 and R_3 .

It defines \hat{e}_{y1} as follows:

$$\hat{e}_{y1} = \frac{\vec{n}_{\eta 1}}{\|\vec{n}_{\eta 1}\|} \quad \text{(Equation 6-4)}$$

Now $\vec{n}_{\eta 1}$ can be found by the following vector equation

$$\alpha \bar{e}_x + \bar{n}_{\eta 1} = \bar{R}_3 - \bar{R}_0 \quad (\text{Equation 6-5})$$

with the constraint of orthogonality i.e. $\bar{e}_x \cdot \bar{n}_{\eta 1} = 0$

Now Equation 6-5 can be divided into a set of four equations with

$$\bar{e}_x = [e_x \ e_y \ e_z]^T \text{ and } \bar{n}_{\eta 1} = [n_{x1} \ n_{y1} \ n_{z1}]^T$$

$$\alpha \begin{bmatrix} e_x \\ e_y \\ e_z \end{bmatrix} + \begin{bmatrix} n_{x1} \\ n_{y1} \\ n_{z1} \end{bmatrix} = \begin{bmatrix} R_{3,x} - R_{0,x} \\ R_{3,y} - R_{0,y} \\ R_{3,z} - R_{0,z} \end{bmatrix} \quad (\text{Equation 6-6})$$

$$e_x n_{x1} + e_y n_{y1} + e_z n_{z1} = 0 \quad (\text{Equation 6-7})$$

The above equation can be rewritten as follows:

$$\begin{bmatrix} 1 & 0 & 0 & e_x \\ 0 & 1 & 0 & e_y \\ 0 & 0 & 1 & e_z \\ e_x & e_y & e_z & 0 \end{bmatrix} \begin{bmatrix} n_{x1} \\ n_{y1} \\ n_{z1} \\ \alpha \end{bmatrix} = \begin{bmatrix} R_{3,x} - R_{0,x} \\ R_{3,y} - R_{0,y} \\ R_{3,z} - R_{0,z} \\ 0 \end{bmatrix} \quad (\text{Equation 6-8})$$

Or

$$A \cdot x = b \quad (\text{Equation 6-9})$$

The above equation will have a defined solution if:

- a) A is not singular, i.e. $\det A \neq 0$. This will be the case when $[e_{x1} \ e_{y1} \ e_{z1}]^T \neq 0$ which implies $\bar{e}_x \neq 0$, therefore it is always possible to find vector which is orthogonal to directing towards point R_3 and thus lying in the plane defined by R_0, R_1 and R_3 .
- b) $R_0 \neq R_3$, as if $R_0 = R_3$, then the plane can not be defined as in this case $A \cdot x = b = 0$ and thus the null vector will be the only solution.

Since $e_1^2 = e_{x1}^2 + e_{y1}^2 + e_{z1}^2$, the inverse of A will be given by:

$$A^{-1} = \begin{bmatrix} \left(1 - \frac{e_{x1}^2}{e_1^2}\right) & -\frac{e_{x1}e_{y1}}{e_1^2} & -\frac{e_{x1}e_{z1}}{e_1^2} & \frac{e_{x1}}{e_1^2} \\ -\frac{e_{x1}e_{y1}}{e_1^2} & \left(1 - \frac{e_{y1}^2}{e_1^2}\right) & -\frac{e_{y1}e_{z1}}{e_1^2} & \frac{e_{y1}}{e_1^2} \\ -\frac{e_{x1}e_{z1}}{e_1^2} & -\frac{e_{y1}e_{z1}}{e_1^2} & \left(1 - \frac{e_{z1}^2}{e_1^2}\right) & \frac{e_{z1}}{e_1^2} \\ \frac{e_{x1}}{e_1^2} & \frac{e_{y1}}{e_1^2} & \frac{e_{z1}}{e_1^2} & -\frac{1}{e_1^2} \end{bmatrix} \quad \text{(Equation 6-10)}$$

Since the aim was to determine components of $\vec{n}_{\eta 1} = [n_{x1} \ n_{y1} \ n_{z1}]^T$, that can be determined by calculating

$$x = A^{-1} \cdot b \quad \text{(Equation 6-11)}$$

which will results in

$$n_{x1} = \left(1 - \frac{e_{x1}^2}{e_1^2}\right)(R_{3,x} - R_{0,x}) - \frac{e_{x1}e_{y1}}{e_1^2}(R_{3,y} - R_{0,y}) - \frac{e_{x1}e_{z1}}{e_1^2}(R_{3,z} - R_{0,z}) \quad \text{(Equation 6-12)}$$

$$n_{y1} = \left(1 - \frac{e_{y1}^2}{e_1^2}\right)(R_{3,x} - R_{0,x}) - \frac{e_{x1}e_{y1}}{e_1^2}(R_{3,y} - R_{0,y}) - \frac{e_{x1}e_{z1}}{e_1^2}(R_{3,z} - R_{0,z}) \quad \text{(Equation 6-13)}$$

$$n_{z1} = \left(1 - \frac{e_{z1}^2}{e_1^2}\right)(R_{3,x} - R_{0,x}) - \frac{e_{x1}e_{y1}}{e_1^2}(R_{3,y} - R_{0,y}) - \frac{e_{x1}e_{z1}}{e_1^2}(R_{3,z} - R_{0,z}) \quad \text{(Equation 6-14)}$$

Now the orthogonal unit vector can be obtained as follows:

$$\hat{e}_{y1} = \frac{\vec{n}_{\eta 1}}{\|\vec{n}_{\eta 1}\|}, \text{ where } \|\vec{n}_{\eta 1}\| = \sqrt{n_{x1}^2 + n_{y1}^2 + n_{z1}^2}$$

Similarly \hat{e}_{y2} is obtained using points R_0 and R_4 . The unit vector \hat{e}_y was determined by taking the average of \hat{e}_{y1} & \hat{e}_{y2} .

Now to complete the calibration frame coordinate system the third unit vector i.e.

\hat{e}_z which is normal to both \hat{e}_x and \hat{e}_y will simply be calculated by taking their cross

product as follows:

$$\hat{e}_z = \hat{e}_x \times \hat{e}_y \quad (\text{Equation 6-15})$$

or

$$\hat{e}_z = \begin{bmatrix} e_{z,x} \\ e_{z,y} \\ e_{z,z} \end{bmatrix} = \begin{bmatrix} e_{x,x} \\ e_{x,y} \\ e_{x,z} \end{bmatrix} \times \begin{bmatrix} e_{y,x} \\ e_{y,y} \\ e_{y,z} \end{bmatrix} = \begin{bmatrix} e_{x,y} e_{y,z} - e_{x,z} e_{y,y} \\ e_{x,z} e_{y,x} - e_{x,x} e_{y,z} \\ e_{x,x} e_{y,y} - e_{x,y} e_{y,x} \end{bmatrix} \quad (\text{Equation 6-16})$$

From machine vision analysis the drilling trajectory was obtained with respect to the calibration frame co-ordinate system with point C_{00} as the origin. Using theodolite measurement on the disc as shown in Figure 6-11, the drilling trajectory was obtained with respect to the theodolite frame of reference. The aim is then to transform this trajectory in terms of the calibration frame co-ordinate system with point C_{00} as the origin.

To achieve this aim, at first there is a need to determine a transformation matrix that can be used to define the calibration frame co-ordinate system relative to the theodolite frame of reference. Since the co-ordinate system of the calibration frame ($\hat{e}_x \hat{e}_y \hat{e}_z$) is already defined with respect to the theodolite frame of reference using theodolite measurements, the transformation can be given as follows:

$${}_{C.F}^{Th}T = \begin{bmatrix} {}_{C.F}^{Th}R & {}_{C.F}^{Th}P_{C.F.Origin} \\ 0 & 0 & 0 & 1 \end{bmatrix} \quad (\text{Equation 6-17})$$

Where, ${}_{C.F}^{Th}R$ is the rotation matrix which describes calibration frame coordinate system relative to theodolite frame of reference.

$${}_{C.F}^{Th}R = \begin{bmatrix} {}_{C.F}^{Th}\hat{x} & {}_{C.F}^{Th}\hat{y} & {}_{C.F}^{Th}\hat{z} \end{bmatrix} \quad (\text{Equation 6-18})$$

$${}_{C.F}^{Th}R = \begin{bmatrix} \hat{e}_{xx} & \hat{e}_{yx} & \hat{e}_{zx} \\ \hat{e}_{xy} & \hat{e}_{yy} & \hat{e}_{zy} \\ \hat{e}_{xz} & \hat{e}_{yz} & \hat{e}_{zz} \end{bmatrix} \quad (\text{Equation 6-19})$$

It can be seen from the above rotation matrix that components of each vector ${}^{Th}\hat{x}_{C.F.}$, ${}^{Th}\hat{y}_{C.F.}$ and ${}^{Th}\hat{z}_{C.F.}$ are the projection of that vector onto the unit direction of the theodolite frame of reference.

In Equation 6-20 ${}^{Th}P_{C.F.Origin}$ is the translation vector describing the calibration frame coordinate system with base point R_0 relative to theodolite frame of reference. Since base point is measured using theodolite, so the translation is simply given by:

$${}^{Th}P_{C.F.Origin} = \begin{bmatrix} R_{0,x} \\ R_{0,y} \\ R_{0,z} \end{bmatrix} \quad \text{(Equation 6-21)}$$

Hence the transformation matrix which describes the calibration frame coordinate system with base point R_0 relative to theodolite frame of reference is given by:

$${}^{Th}T_{C.F.} = \begin{bmatrix} \hat{e}_{xx} & \hat{e}_{yx} & \hat{e}_{zx} & R_{0,x} \\ \hat{e}_{xy} & \hat{e}_{yy} & \hat{e}_{zy} & R_{0,y} \\ \hat{e}_{xz} & \hat{e}_{yz} & \hat{e}_{zz} & R_{0,z} \\ 0 & 0 & 0 & 1 \end{bmatrix} \quad \text{(Equation 6-22)}$$

Now taking the inverse of the above mentioned transformation will result in a transformation matrix that will describe the theodolite frame of reference relative to the calibration frame co-ordinate system as follows:

$${}^{C.F.}T_{Th} = \begin{bmatrix} {}^{Th}R_{C.F.}^t & -{}^{Th}R_{C.F.}^t {}^{Th}P_{C.F.Origin} \\ 0 & 0 & 0 & 1 \end{bmatrix} \quad \text{(Equation 6-23)}$$

Where ${}^{Th}R_{C.F.}^t$ is the transpose of the rotation matrix which describes the calibration frame coordinate system relative to theodolite frame of reference.

$${}^{Th}R_{C.F.}^t = \begin{bmatrix} \hat{e}_{xx} & \hat{e}_{xy} & \hat{e}_{xz} \\ \hat{e}_{yx} & \hat{e}_{yy} & \hat{e}_{yz} \\ \hat{e}_{zx} & \hat{e}_{zy} & \hat{e}_{zz} \end{bmatrix} \quad \text{(Equation 6-24)}$$

6.2.2 Determination of positional and angular error of machine vision drilling trajectory

Once the rotations " θ " and " ϕ " were obtained from machine vision analysis they were used in conjunction with the target point (i.e. point obtained by intersecting the nail axis with the line-of-sight that passes through the centre of the oval) and nail diameter to determine the entry point of the drilling trajectory. These two points i.e. "target point" and "entry point" defines the drilling trajectory obtained from the machine vision system with respect to the calibration frame co-ordinate system. This trajectory was then compared with the true drilling trajectory obtained from theodolite measurement to determine the angular and positional errors. Initial analysis showed that a mean angular error of 1.12° (worst case being 1.41°) and mean positional error of 1.04 mm (worst case being 1.52 mm) could be obtained.

In order to improve the quality of the input data, which in turn should result in an improvement in the overall accuracy of the system, instead of using the specified co-ordinates for ball bearing centres on the calibration plates, the centres of all the ball bearings were determined with respect to the calibration frame co-ordinate system using the CMM, as shown in Figure 6-14. CMM measurements were also performed to check the relative positions and orientation of all calibration plates. The data obtained via CMM measurement was then stored in a file and subsequently used for trajectory analysis. Details of these measurements are given in **APPENDIX G**.

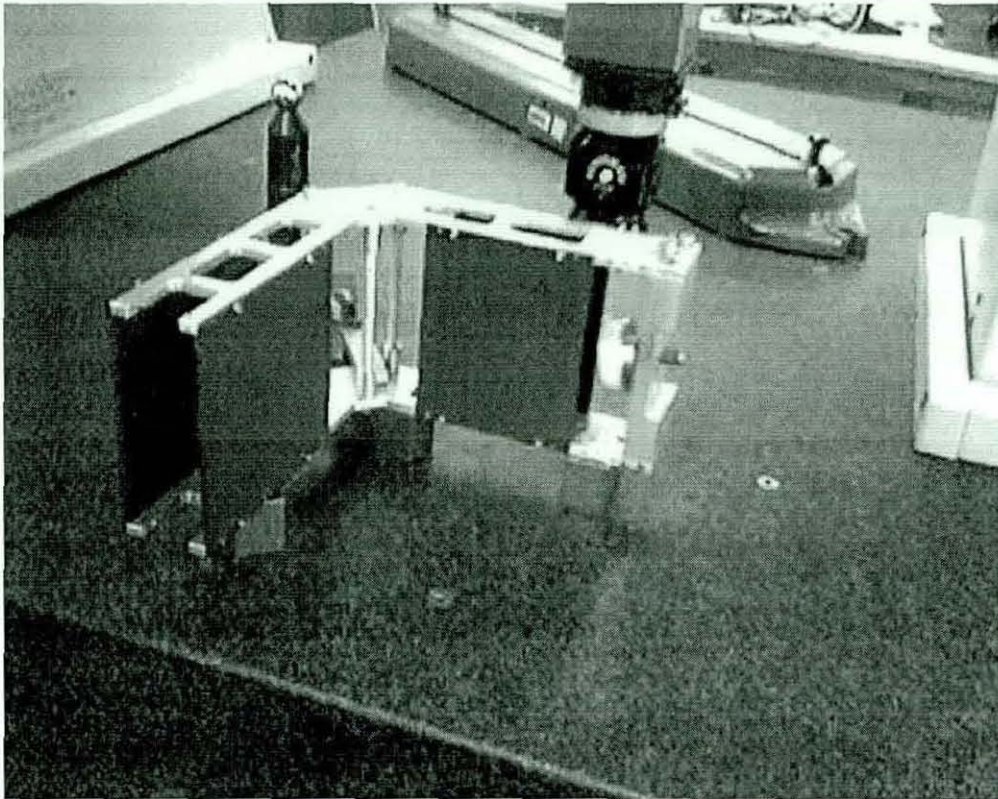


Figure 6-14 Calibration frame in position for CMM measurements (Front view).

After using the actual data obtained using CMM measurements, instead of specified data (i.e. specified fiducial co-ordinates), the results from the laboratory trials were summarized in Figure 6-15. The corresponding numbers in Figure 6-15(a) and Figure 6-15(b) represent the entry and exit points respectively for the various drilling trajectories. Analysis showed that a mean positional error of 0.81mm (worst case being 1.18 mm, as depicted by trajectory 5) and mean angular error of 1.01° (worst case being 1.25° , as depicted by trajectory 2) were obtained. These values were considered acceptable for inserting a guide wire of 2.5mm diameter into the distal locking hole of 7mm diameter (or even 5mm diameter distal locking hole) and the subsequent screw insertion. In the light of previous research by Phillips *et al* [113, 117] and consultation with our collaborating surgeons, it was found that successful drilling of the pilot hole for locking a screw using the guide wire indicates that successful locking of the distal holes of an intramedullary nail can be performed.

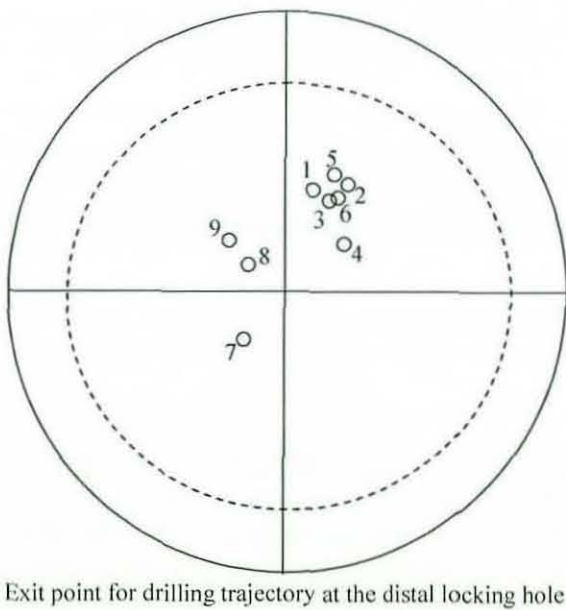
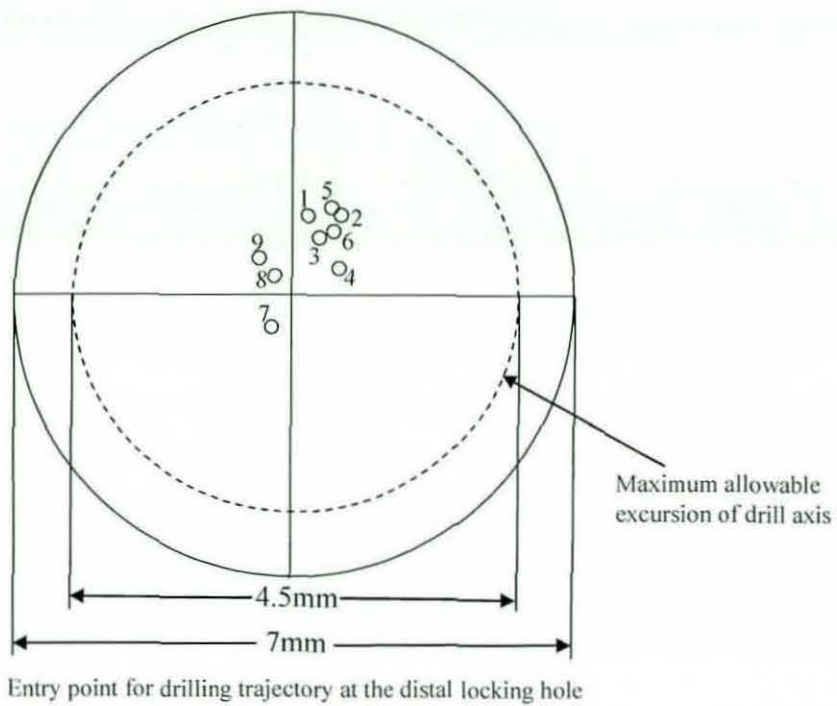


Figure 6-15 Results from accuracy evaluation of the machine vision system.

To evaluate the robustness of the system, the effect of the position of the C-arm X-ray unit with respect to the calibration frame and also contrast and noise variations in the X-ray images have been studied, as discussed below.

6.3 Effect of X-ray source position on the Lateral view image

In the adopted procedure the C-arm image intensifier was positioned as close as possible to the calibration frame plates in the AP view. However, in the Lateral view the position of the image intensifier (and thus the position of the X-ray source) can vary.

In X-ray imaging, object points nearer to the X-ray source experience higher magnification than object points nearer to the image plane. Therefore, during laboratory trials, in order to determine the robustness of the image analysis system in predicting nail rotation about its own axis at different magnifications, three different positions of the X-ray source with respect to the calibration frame (D) were used for each set of rotations (ϕ and θ) of the nail. During trials the three values of D (shown in Figure 6-16) used were 345, 395 and 445mm i.e. a difference of 50mm between each position. The latter distance represents a standard position of the X-ray source for the Lateral image.

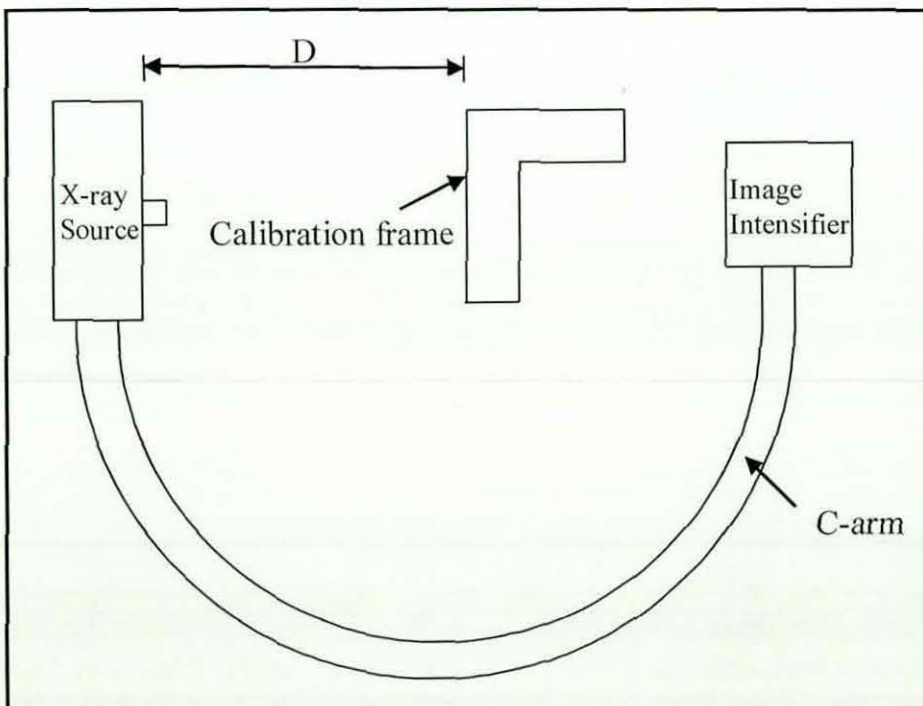


Figure 6-16 Positioning of the X-ray source relative to calibration frame.

Analysis showed that, for different values of D , the maximum deviation in predicting the rotation of the nail about its own axis was 0.08° . This shows that machine vision system has small invariance to the positioning of the X-ray source with respect to the calibration frame.

6.4 Influence of contrast and noise variations on image analysis

During this study, special attention has been given to the effect of variable contrast and noise in the X-ray images on machine vision analysis. To measure accurately the performance of the machine vision system, the combined effects of noise and contrast must be evaluated.

Noise

Inherent in any digital imaging chain, noise has long been recognized as a parameter that can have a dramatic impact on image quality, which degrades very quickly as noise increases. Since noise is a major limiting factor in object detectability, low noise is a prerequisite for good image quality [133]. According to Gonzalez *et al* [134] the principal sources of noise in digital images arise during:

- Image acquisition, as the performance of imaging sensors is affected by a variety of factors, such as environmental conditions during image acquisition, and by the quality of the sensing elements themselves.
- Digitisation or transmission, as image is corrupted during transmission principally due to interference in the channel used for transmission.

Quantum and electronic noise are random variations of a signal that can obscure useful information in a diagnostic image; *quantum noise* arises from variation in the number of X-ray photons detected. Quantum and electronic noise are unavoidable in a digital imaging chain. The effect, often expressed as signal-to-noise ratio (SNR), can vary widely from system to system.

$$\frac{\text{Signal}}{\text{Noise}} = \frac{\text{Useful image information}}{\text{Erratic information}}$$

High SNR, or low system noise, is therefore key to digital X-ray image quality. It can be seen from Figure 6-17 that as noise decreases, or SNR increases, object detectability increases rapidly.

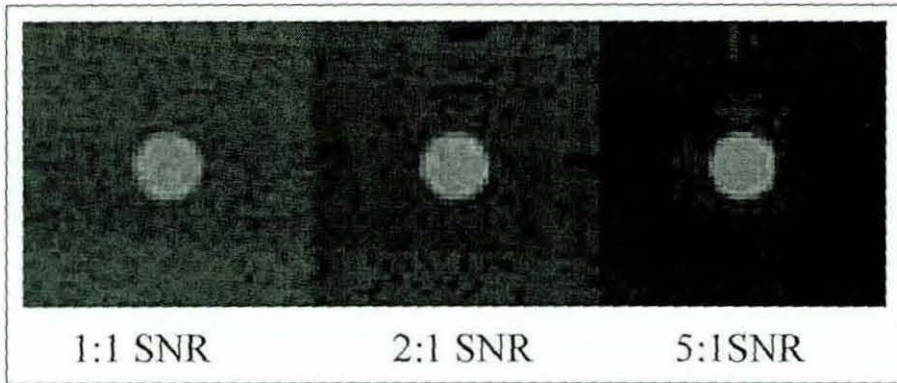


Figure 6-17 Images at different SNR Ratios [134]

Contrast

X-ray contrast is produced because X-ray penetration through an object differs from the penetration through the adjacent background tissue. Maximum (100%) contrast is produced when no radiation penetrates the object. Metal objects, for example use of stainless steel ball bearing as calibration marker on the Γ calibration frame is a good example. It should be noted that increased X-ray penetration through the object results in contrast reduction while decreasing the radiation dose to the patient [135], as shown in Figure 6-18.

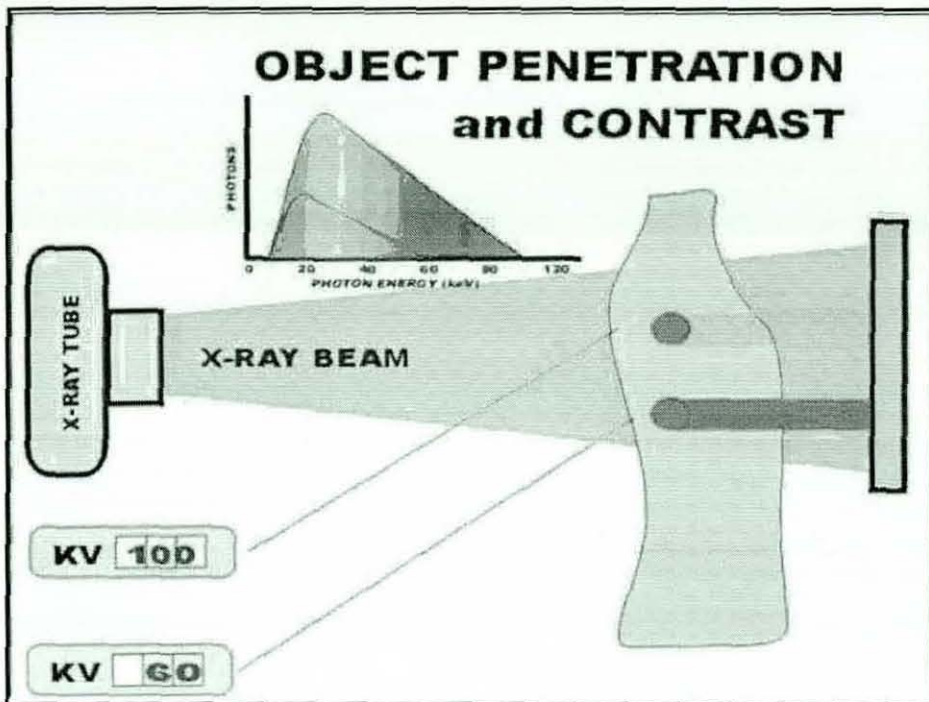


Figure 6-18 Influence of X-ray penetration on image contrast [135]

Since the contrast of an X-ray image is controlled by a combination of X-ray tube voltage and current [134], different combinations of voltage and current were used during laboratory trials to achieve a wide range of contrast in the images. Simulated Gaussian noise was added at various levels between 5% and 15% to each of the variable contrast images using a proprietary image processing package. Subsequent tests showed that good repeatability (less than 0.1° difference in measurement of the distal holes axes direction) could be obtained for up to 15% of gaussian noise across a wide range of contrast. For example, Figure 6-19 and Figure 6-20 depicts the performance of the machine vision analysis on noisy Lateral and AP view X-ray images with variable contrast respectively.

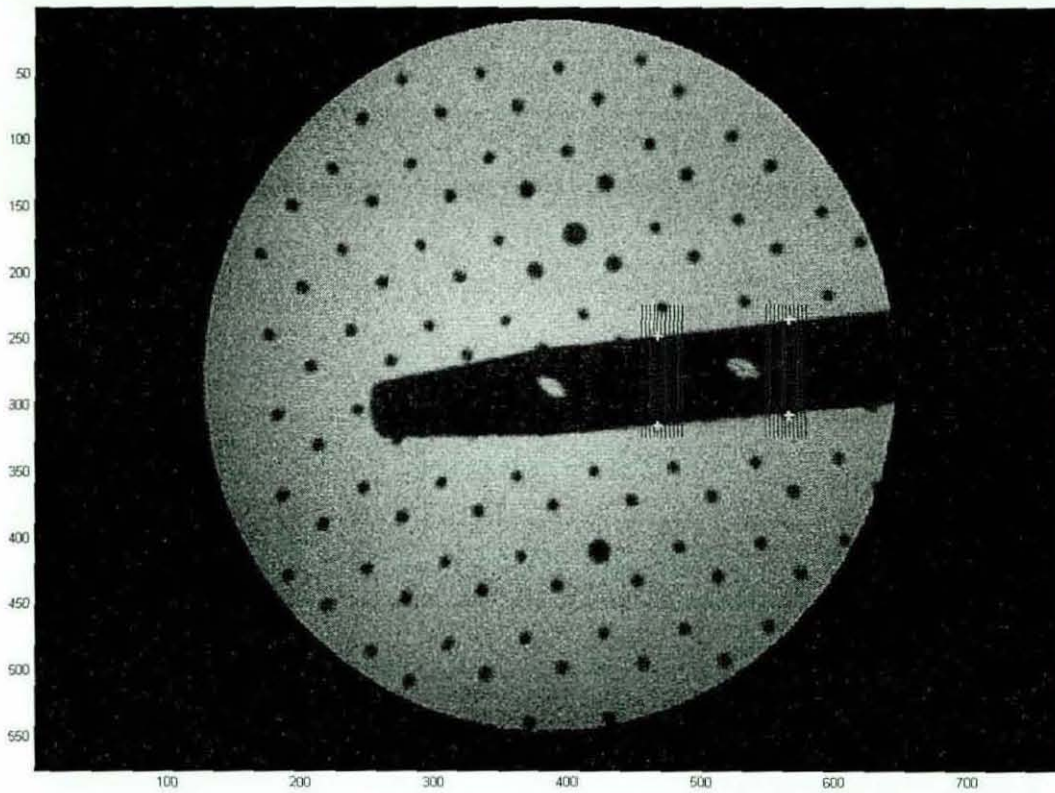


Figure 6-19 Machine vision analysis on the Lateral view image with variable noise and contrast.

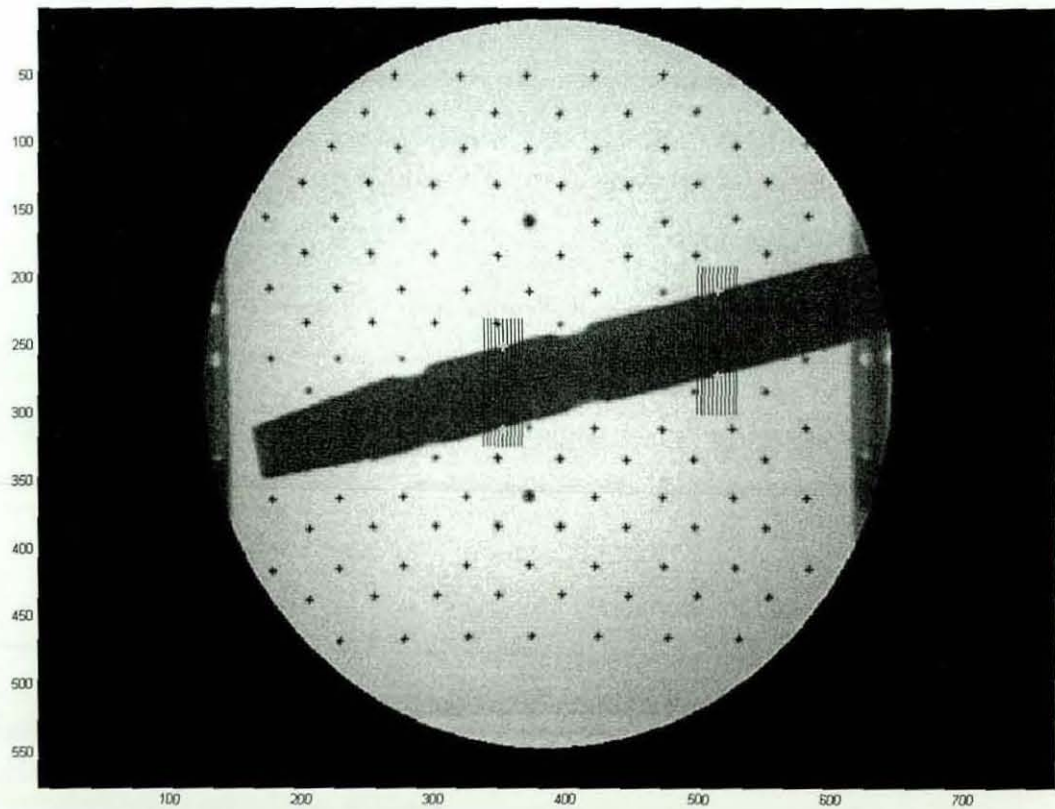


Figure 6-20 Machine vision analysis on the AP view image with variable noise and contrast.

6.5 Summary

In order to evaluate the accuracy of the machine vision system, the drilling trajectory for the distal locking hole computed with respect to the calibration frame using machine vision system was compared with the true drilling trajectory that was obtained with respect to the calibration frame using theodolite measurements.

During laboratory trials, the nail was placed at different orientations likely to be encountered during the surgical procedure using a specially designed test rig. Based on the results obtained from the laboratory trials presented in this chapter, it has been shown that the proposed system provides the accuracy required for successful insertion of distal locking screws. It has also been shown that the proposed system is very robust in the presence of variable noise and contrast in the X-ray images and in terms of variable magnification. The following chapter describes the development of a robust calibration frame in order to make the proposed system suitable for clinical use.

7 Design of a robust calibration frame

Existing calibration frame was designed to prove the concept. Therefore, to make it adaptable for clinical use it has been redesigned to:

- To investigate the optimal number of fiducials and their spatial distribution necessary to provide the required accuracy.
- Accommodate wide range of patient physiologies while taking into account swelling
- Issues such as robustness, ease of manufacture and calibration.

7.1 Investigation into Fiducial layout

The aim of this study was to *investigate the optimal number of fiducials and the spatial distribution required to obtain the desired accuracy*. It comprises the following stages:

1. In the first stage, a comparison between fiducials lying towards the centre of the plate and those near the periphery was made in terms of their influence on the overall accuracy of the machine vision system.
2. During the second stage, in the light of results obtained from the first stage, a search was made to determine the minimum number of fiducials and the spatial distribution that can be used to achieve the desired accuracy.

7.1.1 First stage investigation

In the Lateral view fiducials were used to:

- Construct focal lines for focal point determination,
- Determine points on the centre line of the nail, and
- Find corresponding position of the centre of the oval on two calibration plates.

In the AP view fiducials were used to:

- Construct focal lines for focal point determination and
- Determine points on the centre line of the nail.

In order to determine which fiducials of the AP and Lateral calibration plates have most influence on the overall accuracy of the system, the following changes have been made in the existing system:

a) Removal of centre fiducials from each line

In this scenario, the total numbers of fiducials on Lateral and AP calibration plates were kept the same (i.e. 15). However, two fiducials from the centre of the line were discarded while adding two fiducials towards the periphery of the calibration plates on either side of each line. Figure 7-1 shows the Lateral view image with discarded fiducials bounded in blocks.

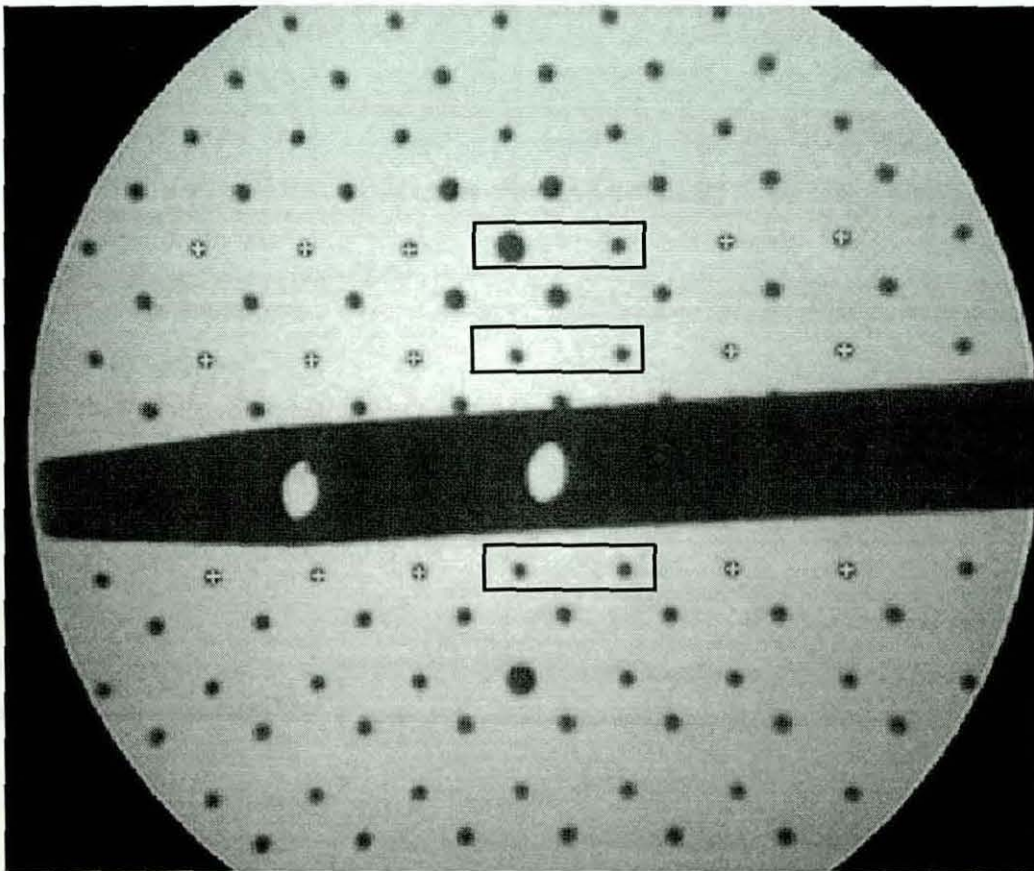


Figure 7-1 Removal of centre fiducials in the Lateral view image.

Analysis has shown that an increase of 0.12 mm and 0.09° is obtained in mean positional and mean angular error respectively, when the scenario depicted in Figure

7-1 was compared with the standard practice i.e. using all 15 fiducials as shown in Figure 7-2.

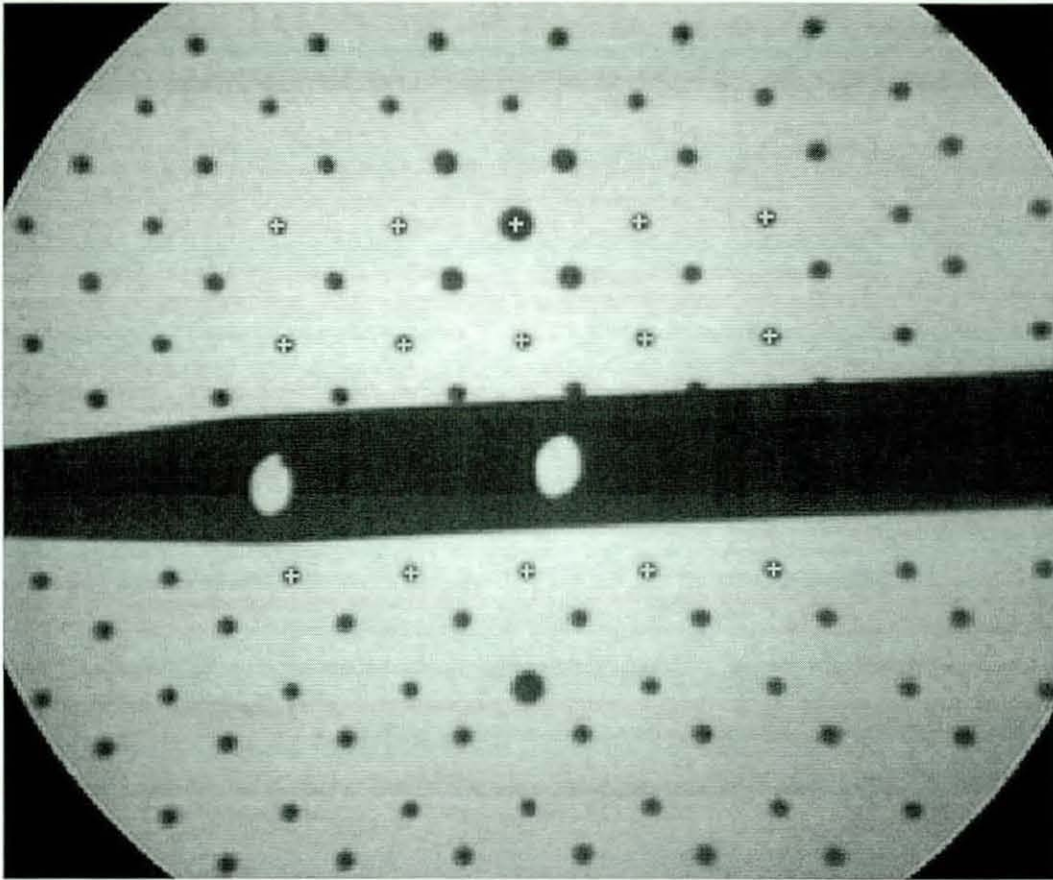


Figure 7-2 Fiducial used in standard practice image analysis.

b) Discarding of fiducials immediately above and below the intramedullary nail

In this scenario, the total number of fiducials on the Lateral and AP calibration plates were kept the same (i.e. 15), however, all the fiducials from the lines immediately above and below the intramedullary nail were discarded while using fiducials which lie towards the periphery of the calibration plates on either side of the nail, as shown in Figure 7-3 for the Lateral view image.

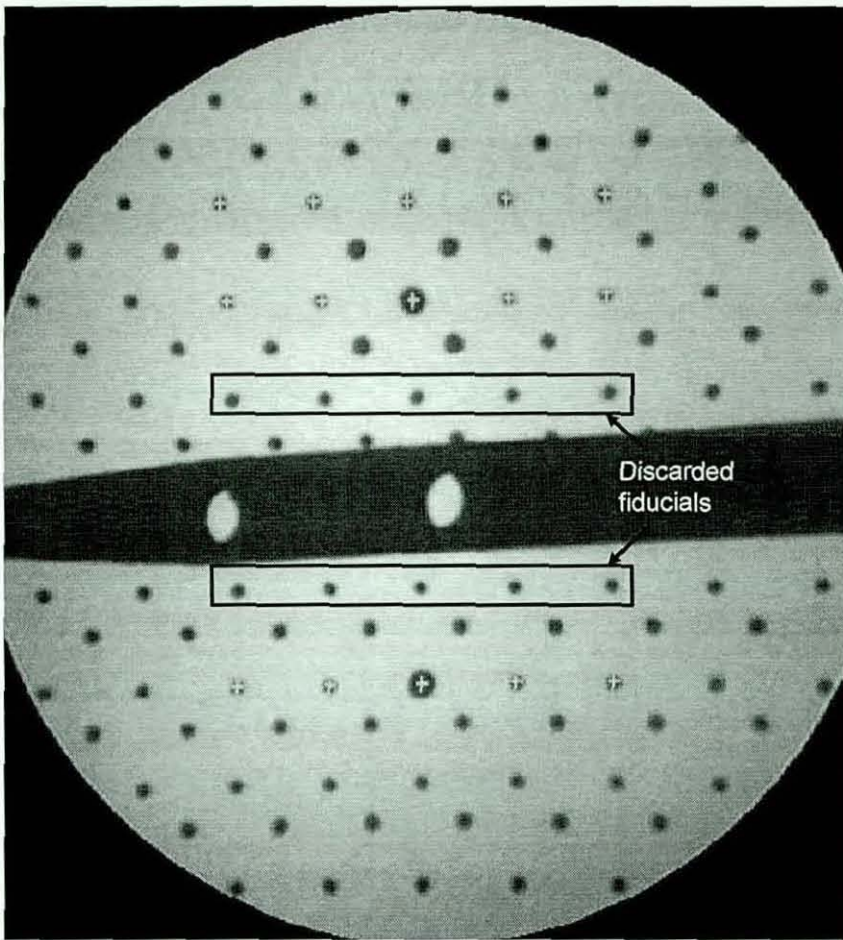


Figure 7-3 Discarding of fiducials immediately above and below the intramedullary nail.

Analysis has shown that an increase of 0.19 mm and 0.24° is obtained in mean positional and mean angular error respectively when compared with the standard practice as shown in Figure 7-2. This loss of accuracy is due to the fact that fiducials lying in the immediate surroundings of the nail were discarded, therefore the three closest points chosen to reconstruct given image points (i.e. points on the nail centre line in both Lateral and AP views, and a point representing the centre of the distal hole projection in the Lateral view) are further away from those points in comparison to their ideal location. As a result, a larger triangular sub-region was used for the interpolation process, which results in reduced reconstruction accuracy as a linear interpolation function is used to estimate non-linear distortion effects.

It can be seen from the analysis presented in this section that fiducials lying towards the centre of the plate are more influential on overall accuracy than fiducials lying at the periphery. Therefore, during the second stage, fiducials used to calculate the

drilling trajectory will be chosen such that they lie towards the centre of the calibration plates rather than at the periphery.

7.1.2 Second stage investigation

In order to determine the optimal number of fiducials and the spatial distribution required to achieve the desired accuracy, different fiducial configurations for AP and Lateral calibration plates were used on existing X-ray images. These configurations are discussed in detail in the following sub-sections.

Scenario 1

In the Lateral and the AP view, fiducials were used to reconstruct given image points on the centre line of the nail using the localized interpolation technique described in **Section 4.4**. Image points on the centre line of the nail were obtained by drawing multiple line profiles across the nail on either side of the distal locking hole as described in **Section 4.5.1** and **Section 4.5.2** for the Lateral and the AP views respectively. Therefore, a minimum of three visible fiducials were required on each calibration plate to include image points on the nail centre line in a bounding triangle, and to determine their corresponding position on the relevant calibration plate, as shown in Figure 7-4 and Figure 7-5 for the Lateral and AP views respectively.

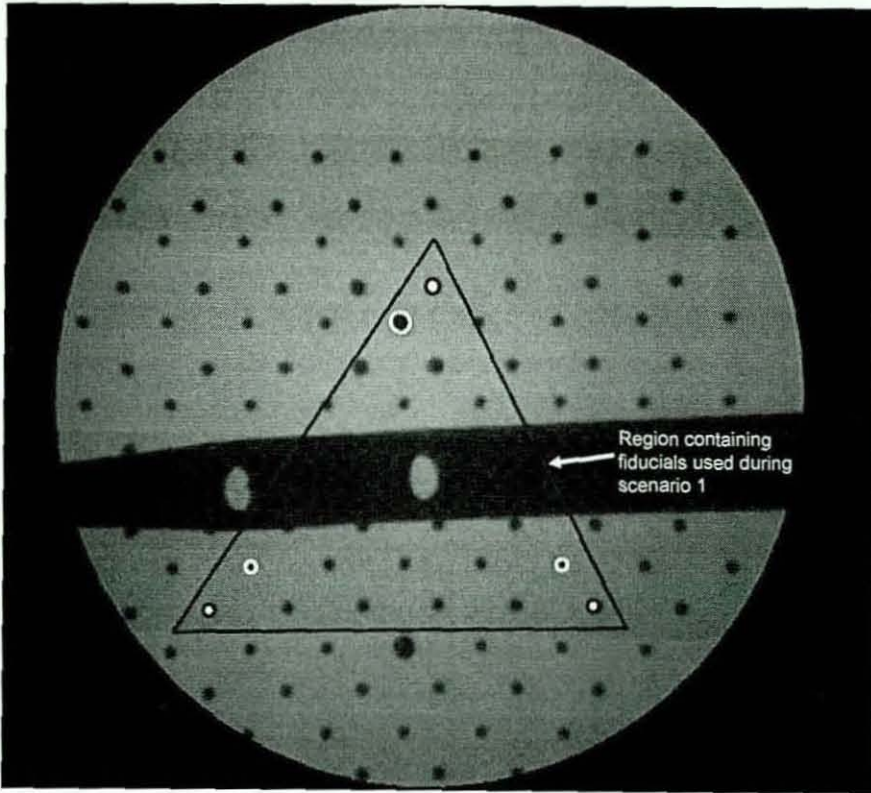


Figure 7-4 Fiducials used in the Lateral view image for Scenario 1.

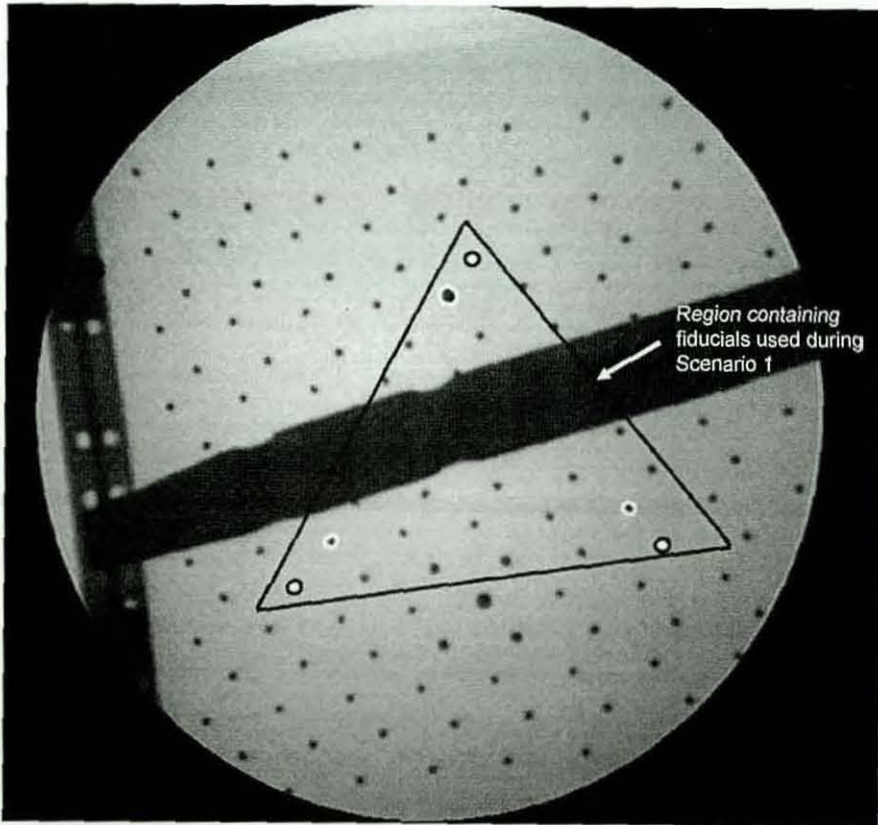


Figure 7-5 Fiducials used in the AP view image for Scenario 1.

It should be noted that in Figure 7-4 and Figure 7-5, fiducials belonging to the XRII plate are encircled with white circles, whereas fiducials belonging to the Source plate are filled with white and encircled with black circles. This description of fiducials is also valid for Figure 7-6 and Figure 7-7.

Analysis has shown that an increase of 0.71 mm and 0.68° was obtained in mean positional and mean angular error respectively, when the scenario 1 depicted in Figure 7-4 and Figure 7-5 was compared with the standard practice as shown in Figure 7-2. Therefore, scenario 1 was discarded as it does not provide the required accuracy.

Scenario 2

During this scenario, 4 fiducials on the XRII plate and 4 fiducials on the Source plate in both Lateral and AP views, shown by the rectangular sub-region of Figure 7-6 and Figure 7-7, were used to determine the drilling trajectory.

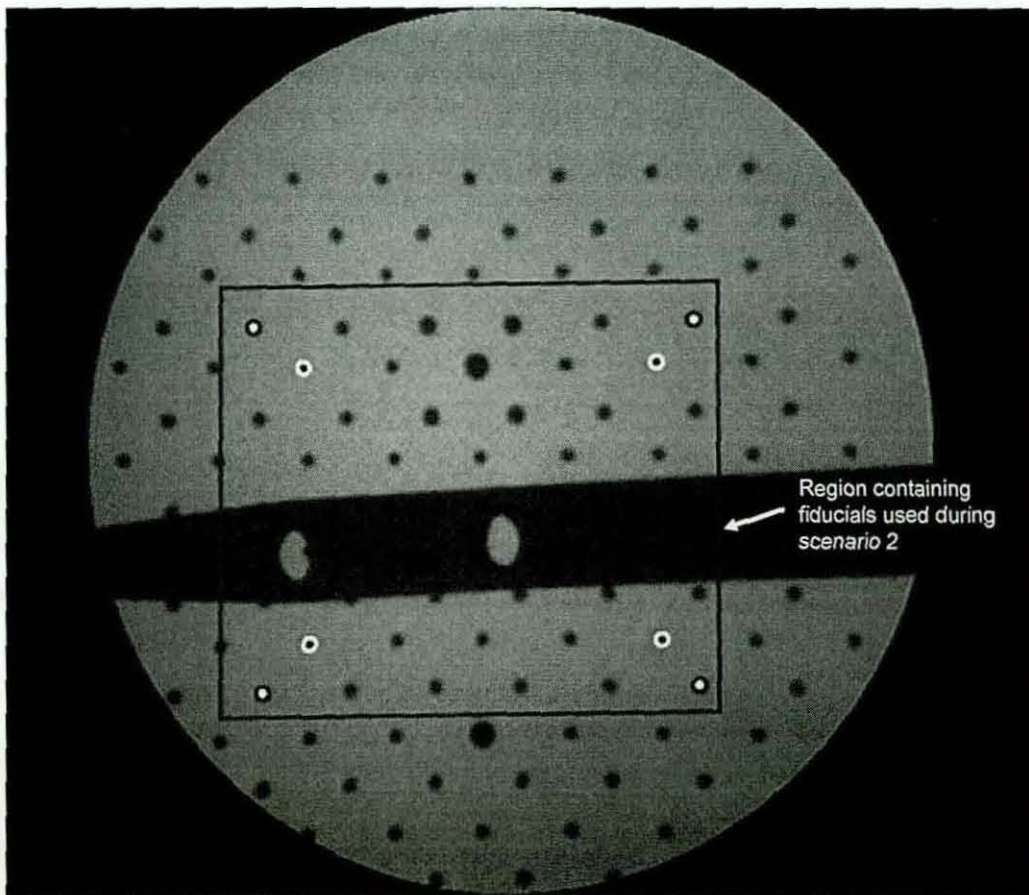


Figure 7-6 Fiducials used in the Lateral view image for Scenario 2.

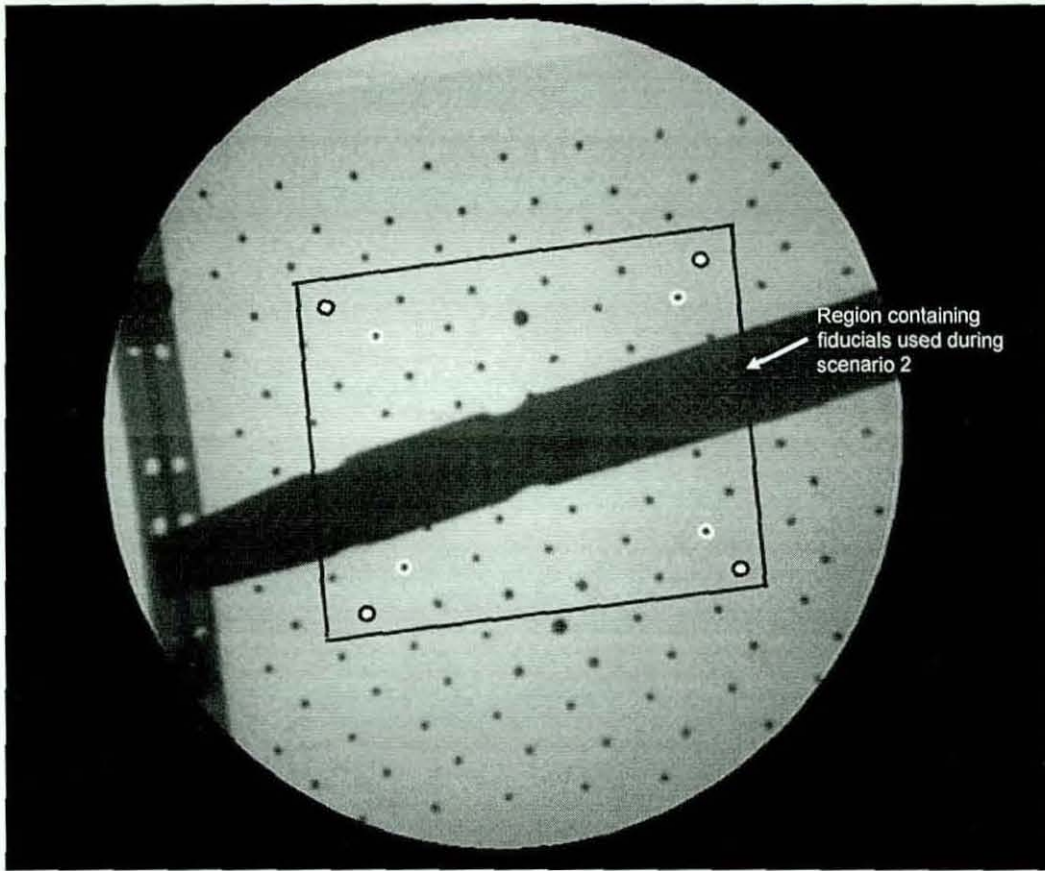


Figure 7-7 Fiducials used in the AP view image for Scenario 2.

Analysis has shown that an increase of 0.56 mm and 0.64° was obtained in mean positional and mean angular error respectively, when compared with the standard practice as shown in Figure 7-2. Therefore, scenario 2 was discarded as it does not provide the required accuracy.

In addition to loss of accuracy, one potential disadvantage of scenario 1 and scenario 2 was that the calibration frame would need to be positioned such that the distal end of the nail containing the locking hole would appear within the field of view bounded by the fiducials used for each Lateral and AP view. This method can also prove to be quite time consuming as excessive repositioning of the calibration frame may be required. This problem can be partially overcome by having the fiducials at a large distance from each other, in other words, having them towards the periphery of the calibration plates. However, in the light of the results obtained during the first stage, employing these scenarios with large spacings will result in a further loss of accuracy.

Scenario 3

In this scenario, 6 fiducials on the XRII plate and 8 fiducials on the Source plate in both Lateral and AP views, shown by rectangular sub-regions of Figure 7-8 and Figure 7-10 respectively, were used to determine the drilling trajectory. Fiducials used during the analysis of the Lateral view image for this scenario are bounded in the rectangular region of Figure 7-8. Those fiducials which surround the oval shaped distal hole projection, lie towards the centre of the calibration plates.

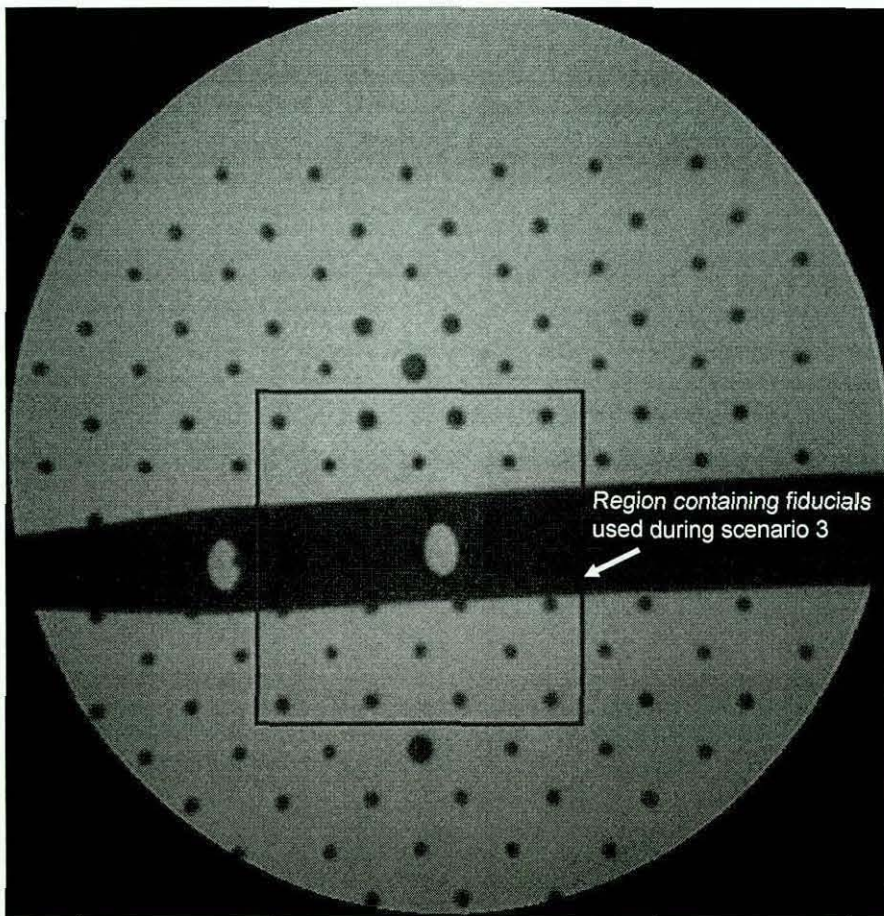


Figure 7-8 Fiducials used in the Lateral view image for Scenario 3.

From here on, it should be noted that partially imaged fiducials within the rectangular region (i.e. fiducials at the nail edges) were identified, and were not used during image analysis. A schematic view of the fiducial layout on the Lateral view plates used for this scenario is depicted by Figure 7-9.

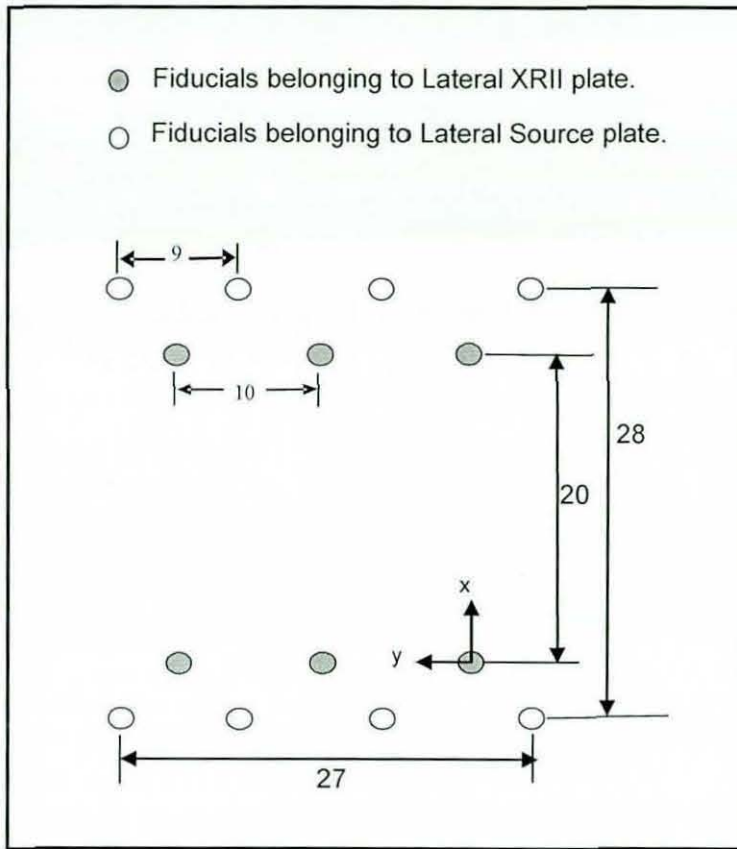


Figure 7-9 Schematic view of fiducial layout on the Lateral view using Scenario 3.

For the AP view X-ray image, fiducials used during image analysis for this scenario are depicted in the bounded rectangular region of Figure 7-10. These fiducials lie towards the centre of the calibration plates.

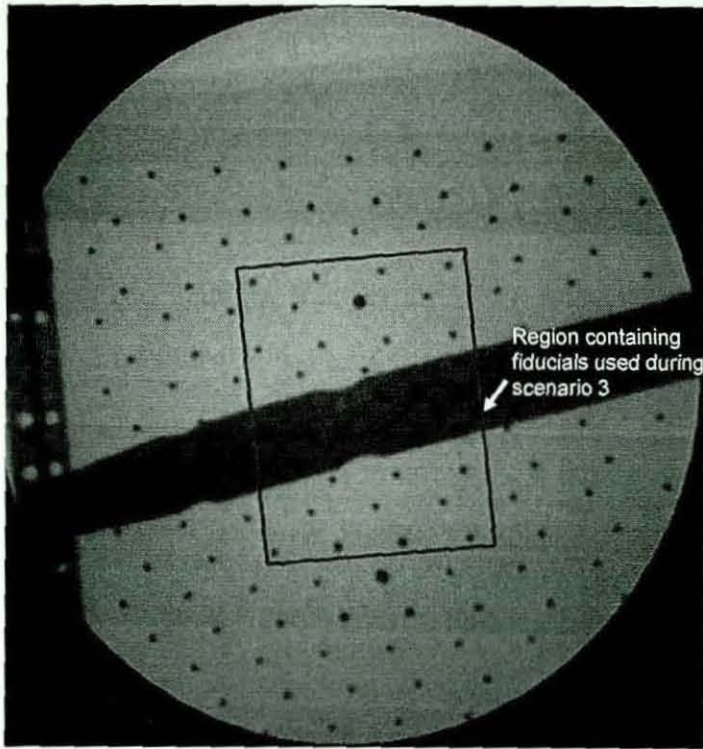


Figure 7-10 Fiducials used in the AP view image for Scenario 3.

A schematic view of the fiducial layout on the AP view plates used for this scenario is depicted by Figure 7-11.

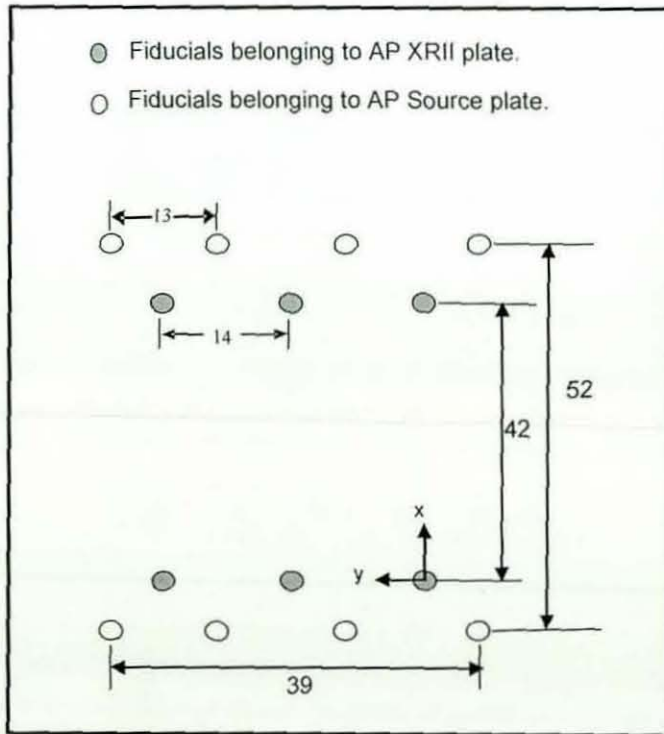


Figure 7-11 Schematic view of fiducial layout on AP view image using Scenario 3.

Analysis has shown that by employing this scenario, a mean positional error of 1.12 mm and mean angular error of 1.36° were obtained. This compares to a mean positional error of 0.81 mm and 1.01° obtained when the standard scenario or practice (i.e. using all 15 fiducials on XRII calibration plates and all 18 fiducials on Source calibration plate in both Lateral and AP views) was employed. Thus scenario 3 was discarded.

Scenario 4

In this scenario, 9 fiducials on the XRII plate and 12 fiducials on the Source plates in both Lateral and AP views, shown by the rectangular sub-region of Figure 7-12 and Figure 7-13 respectively, were used to determine the drilling trajectory. Fiducials used during image analysis of the Lateral view image for this scenario are bounded in the rectangular region of Figure 7-12.

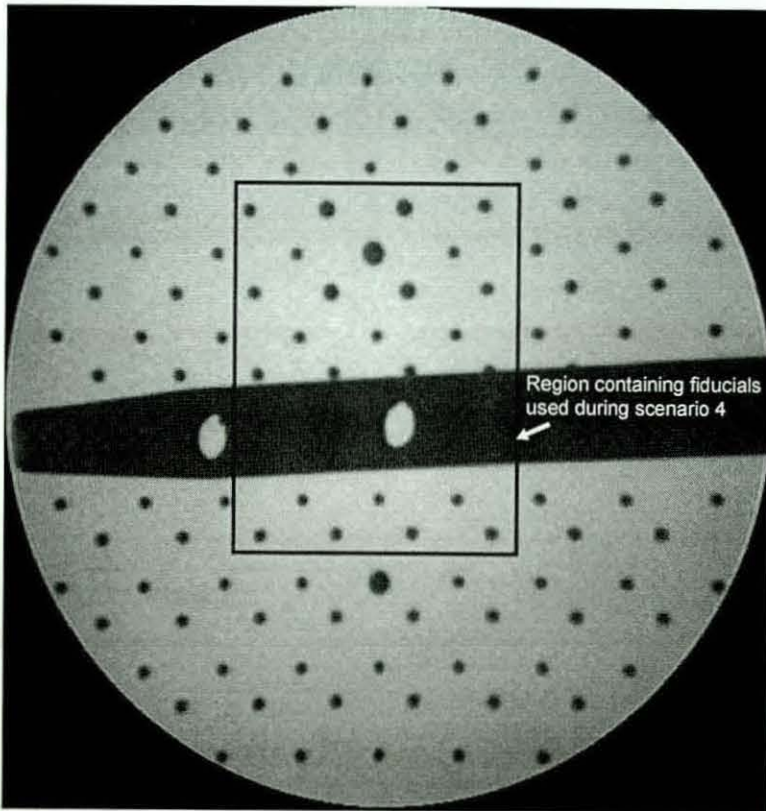


Figure 7-12 Fiducial used in the Lateral view for Scenario 4.

For the AP view, fiducials used for this scenario are shown in the bounded rectangular region of Figure 7-13.

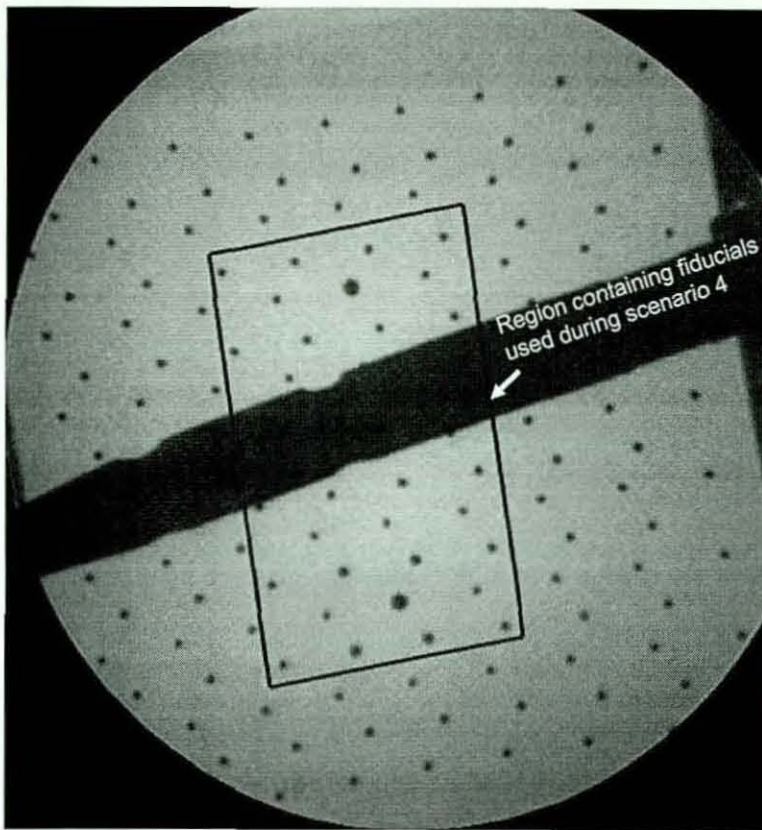
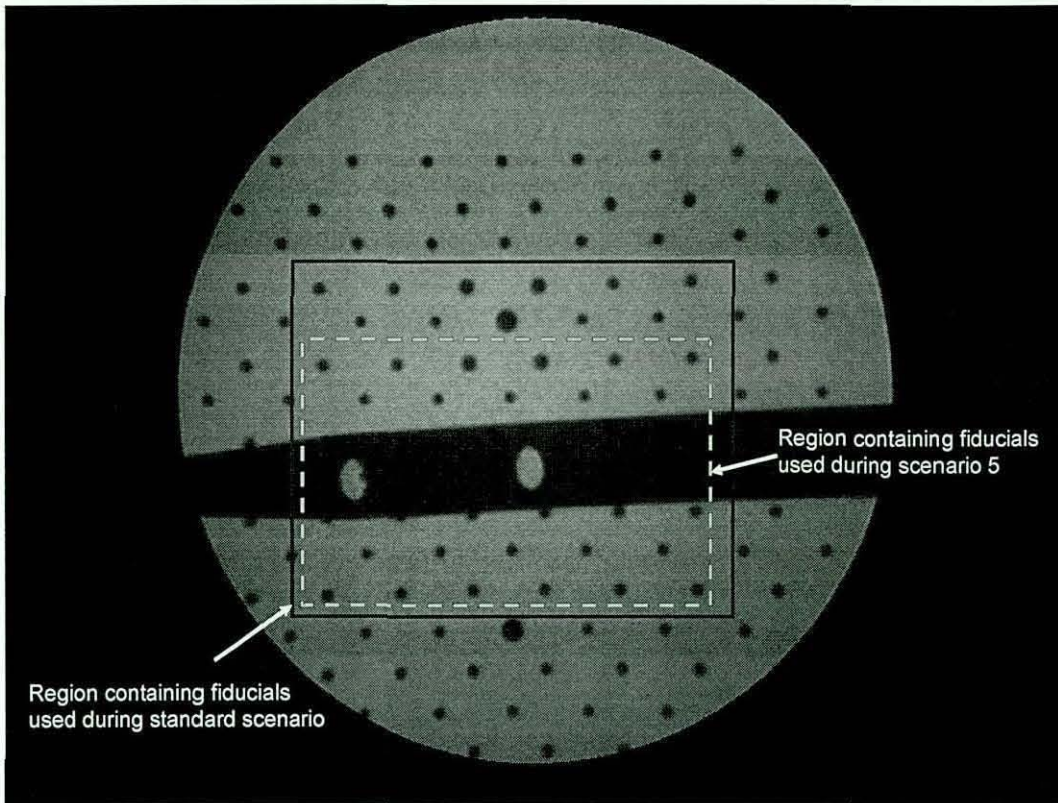


Figure 7-13 Fiducial used in the Lateral view for Scenario 4.

Analysis has shown a mean positional error of 0.91 mm and a mean angular error of 1.12° for this scenario, in comparison to mean positional error of 0.81 mm and 1.01° obtained when the standard scenario was employed. Thus scenario 4 was discarded.

Scenario 5

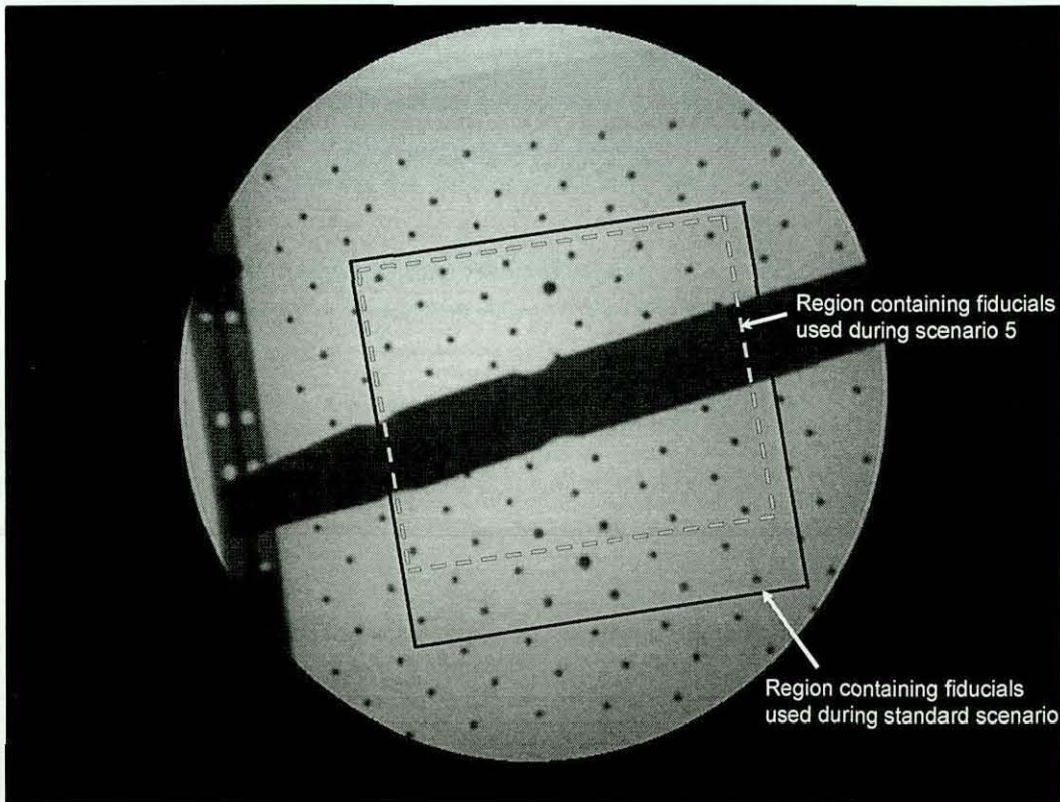
In this scenario, instead of using 15 fiducials on the XRII calibration plates and 18 fiducials on the Source calibration plates in both Lateral and AP views, the number of fiducials was reduced to 10 and 12 respectively, as shown in Figure 7-14 and Figure 7-15 for the Lateral and AP view respectively. These fiducials lie in the vicinity of the intramedullary nail, towards the centre of the calibration plates.



Region containing fiducials used during standard scenario

Region containing fiducials used during scenario 5

Figure 7-14 Fiducial used in the Lateral view image for Scenario 5.



Region containing fiducials used during scenario 5

Region containing fiducials used during standard scenario

Figure 7-15 Fiducial used in the AP view image for Scenario 5.

Analysis has shown that by employing this scenario, a mean positional error of 0.92 mm and a mean angular error of 1.08° were obtained, in comparison to a mean positional error of 0.81mm and 1.01° obtained when the standard scenario was employed and hence scenario 5 was discarded.

Scenario 6

In order to see whether an increase in the number of fiducials used during image analysis results in a significant improvement of results obtained from the machine vision system, the number of fiducials on the XR11 and Source calibration plates were increased from 15 to 20 and from 18 to 24 respectively, for both Lateral and AP views, as shown in Figure 7-16 and Figure 7-17.

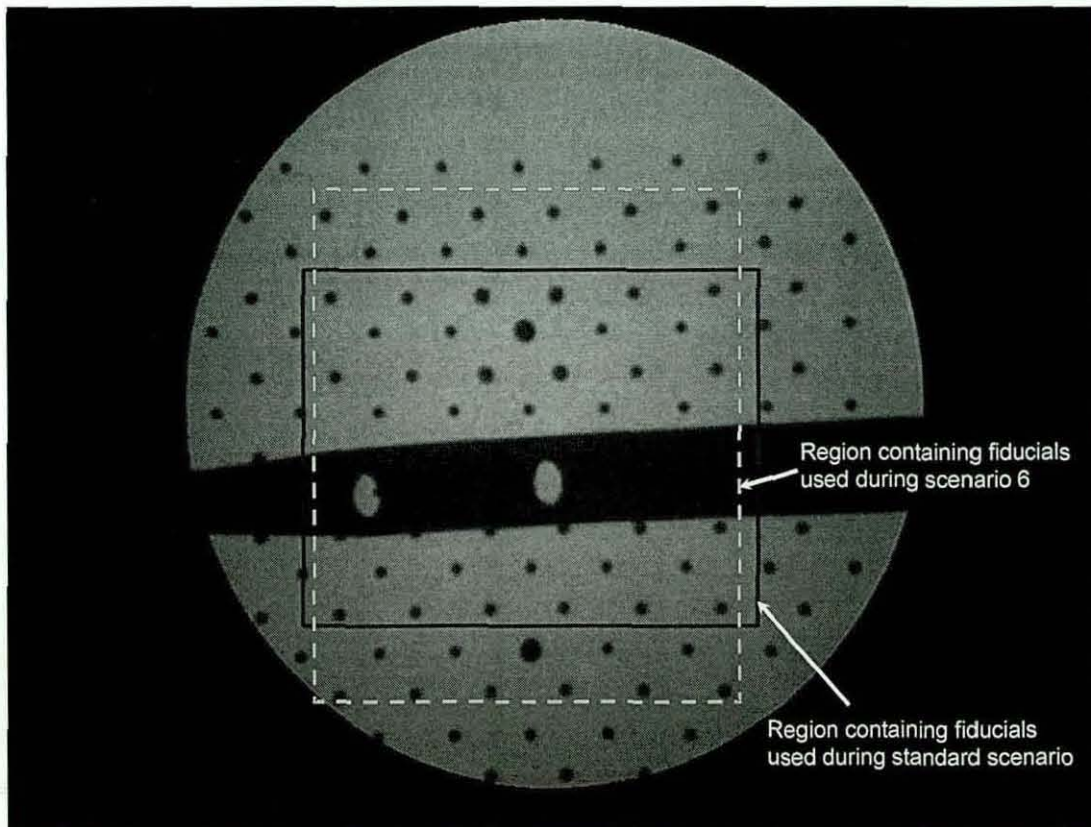


Figure 7-16 Fiducial used in the Lateral view image for Scenario 6.

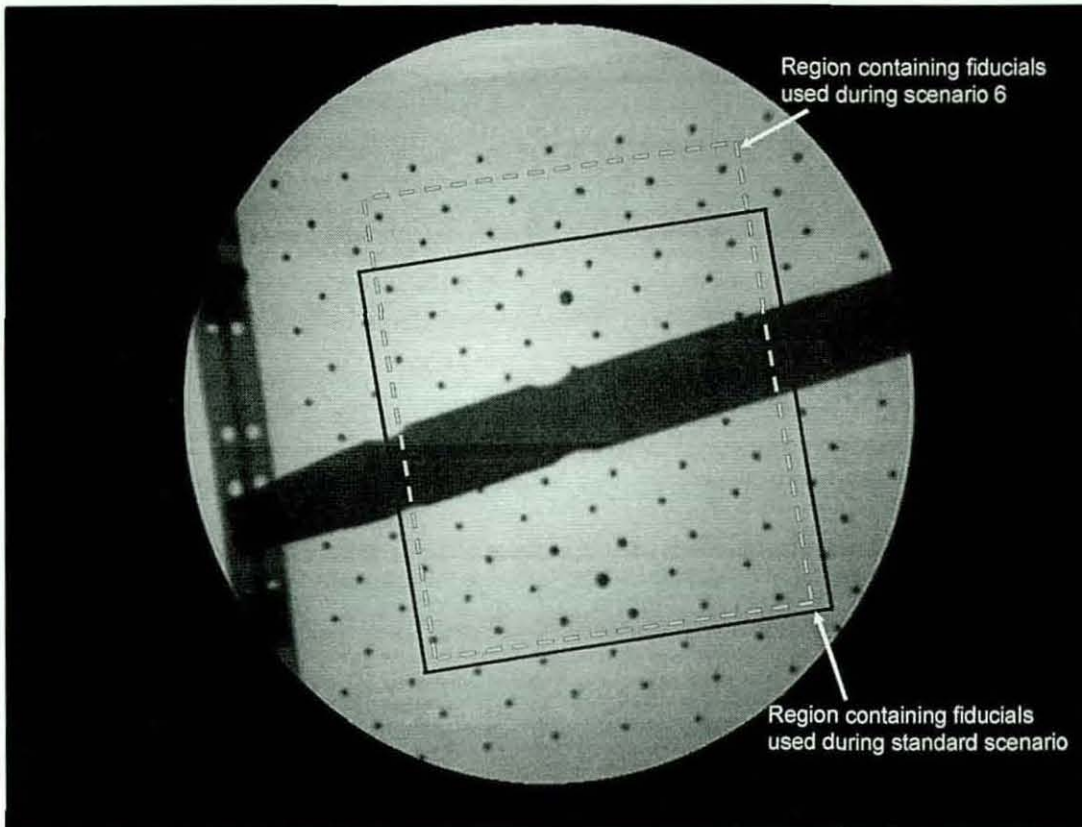


Figure 7-17 Fiducial used in the AP view image for Scenario 6.

Analysis has shown that using this scenario, a mean positional error of 0.80 mm and mean angular error of 1.01° were obtained, in comparison to a mean positional error of 0.81 mm and 1.01° obtained when the standard scenario was employed.

Conclusion

Since, similar results were obtained by employing both the standard scenario and scenario 6; it was decided to use the standard scenario to determine the drilling trajectory as it involves the use of fewer calibration markers, which will result in reduced manufacturing time and cost as well as faster processing.

7.2 Adaptability for patient physiology

In order to make the calibration frame more robust, it should be able to take into account variable patient physiology while acquiring X-ray images. Previous research by Stephenson *et al* [136] has shown that femoral cross-sectional geometry varies considerably along the length of the femoral shaft. Therefore, it is necessary to

determine the location of the femoral axis with respect to the upper surface of the leg (in the AP direction) and outside surface of the leg (in the medio-lateral direction) i.e. dimensions "D" and "W" (shown in Figure 7-18) at the distal end of the femur.

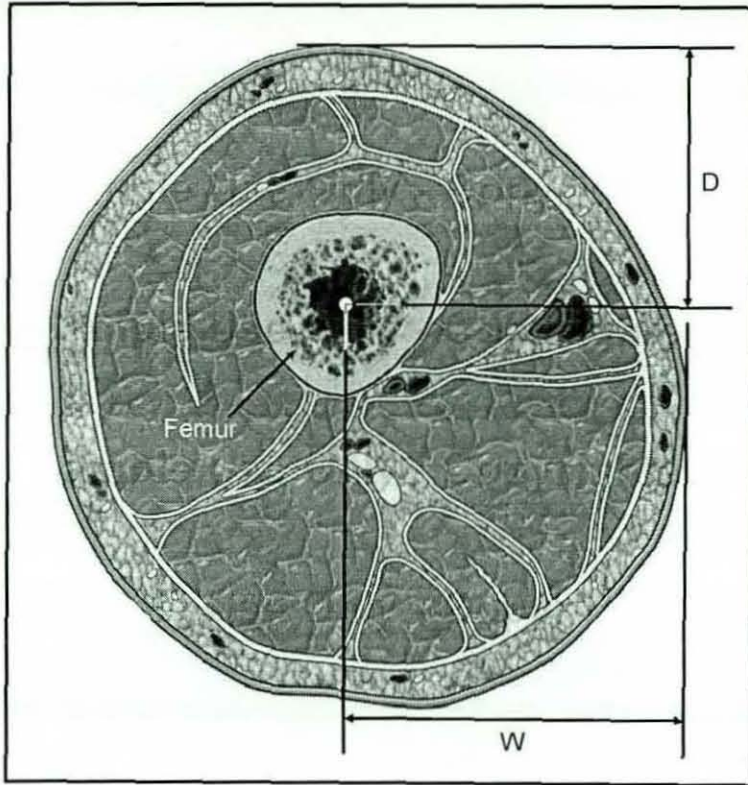


Figure 7-18 Femur Cross-section of left leg

In the initial phase, it was decided to use adult anthropometric data [137] to determine D and W. However, no anthropometric data for the area of interest (the distal end of the femur) was available, therefore, the closest available data (i.e. thigh depth behind knee while sitting, as shown in Figure 7-19) was used.

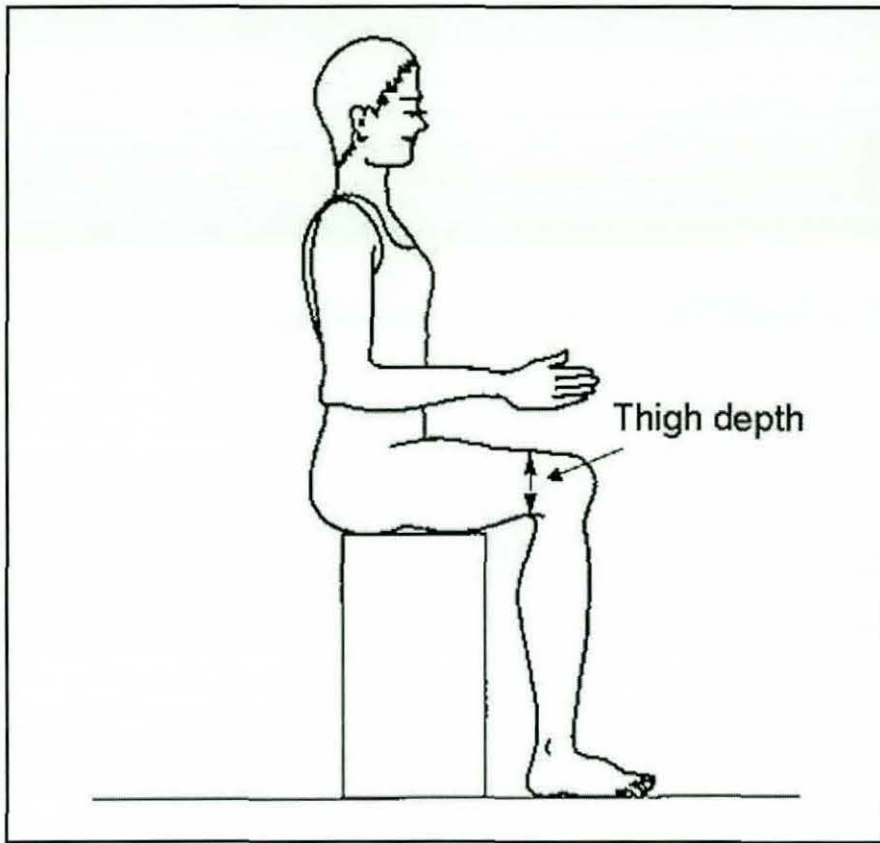


Figure 7-19 Measurement location of thigh depth, behind the knee

The anthropometric data, shown in Table 7-1 represents adults' aged between 18-64 years living in the UK and was obtained from PeopleSize 1998. PeopleSize is a computer anthropometry database that provides a visual interface to the data. The PeopleSize data set uses data from many sources, but in particular from the Department of Health and the HUMAG research group at Loughborough University. The data was obtained by *measuring vertically from the underside of the unsupported tendons to the upper surface of the thigh*. Although during IMN the leg would be extended, the extension doesn't significantly change the shape at the distal end of the femur. All dimensions presented in the tables of chapter 7 are in millimetres.

Sex	Mean	Standard Deviation (sd)	5th%ile	95th%ile
male	140.4	16.5	113.3	167.5
female	131.6	15.4	106.3	157

Table 7-1 Anthropometric data for thigh depth (mm), behind knee while sitting [137]

While compiling ergonomic data it is impossible to measure everyone. Therefore, the range of variability of human features is usually predicted by measuring a random selection of people among the target population. For Table 7-1 it should be noted that, within a gender, the 5th through 95th percentile range covers 90% of people (i.e. the top 5% and bottom 5% are excluded), as shown in Figure 7-20.

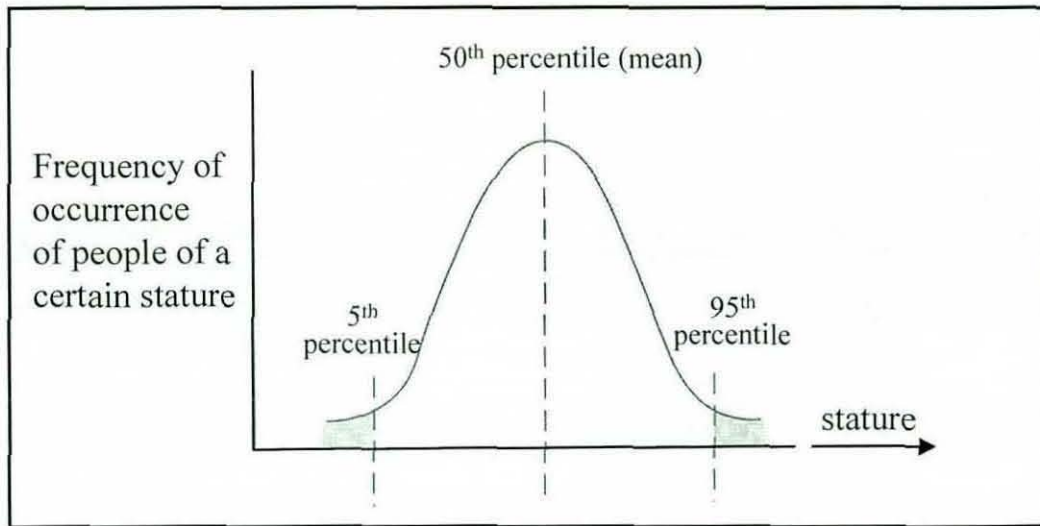


Figure 7-20 Standard normal distribution graph.

It should be kept in mind that ergonomic design cannot accommodate every user, and that typically it should be able to accommodate from a 5th percentile woman to a 95th percentile man, as theoretically this range will accommodate 9.5 out of 10 users [138]. Therefore the dimensions for 5th percentile female to 95th percentile male from Table 7-1 were considered while designing the calibration frame for the target population.

It should be noted that no anthropometric data of interest i.e. for the distal end of femur was available for older adults (i.e. 65 + years age) from [139] and data about thigh depth (where it is greatest while sitting) for people in the UK from Pheasant 1996 was the closest available data. This data is shown in Table 7-2.

Sex	Mean	Standard Deviation (sd)	5th%ile	95th%ile
male	150	15	125	175
female	145	16	115	170

Table 7-2 Thigh depth in mm (maximum, sitting) anthropometric data for older adults [139]

Pheasant 1996 represents the information reprinted from [140]. The data shown in Table 7-2 was obtained by measuring vertically from the seat surface to the upper, uncompressed, surface of the thigh where the thigh depth is greatest as shown in Figure 7-21.

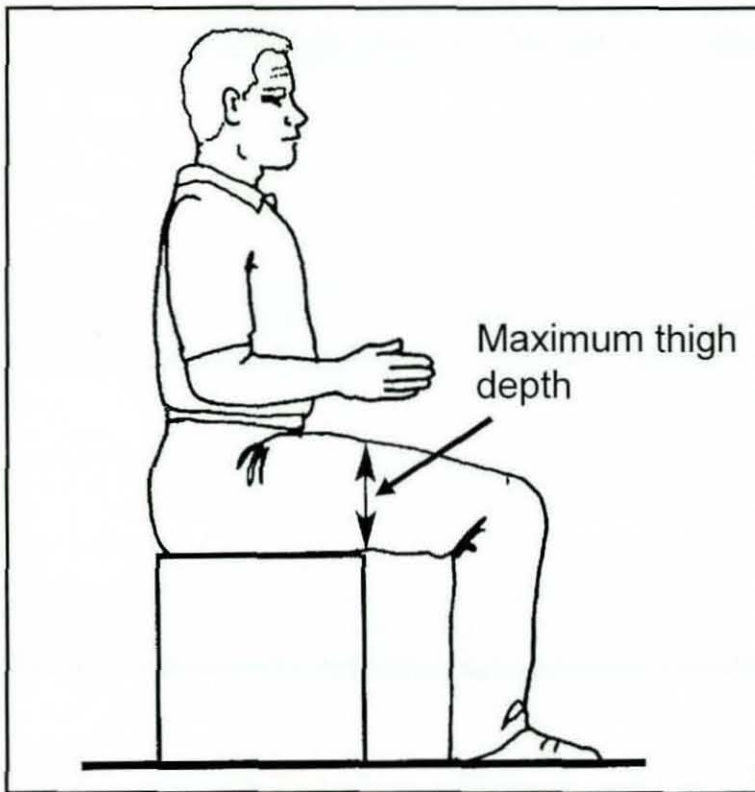


Figure 7-21 Measurement location of Thigh depth(maximum, sitting) for older adults [139]

In order to obtain a correlation or to establish a relationship between adult and older adult distal thigh dimensions, the maximum thigh depth dimension for older people in Table 7-2 was compared with that of younger adults (see Table 7-3) obtained from [137].

Sex	Mean	Standard Deviation (sd)	5th%ile	95th%ile
male	166.8	18.8	135.9	197.7
female	153.7	22.6	116.6	190.9

Table 7-3 Thigh depth in mm (maximum, sitting) anthropometric data for adults.

It can be seen from Table 7-2 and Table 7-3 that thigh depth for older adults almost lies within the range specified for younger adult data; therefore it can be assumed that older adults probably will have thigh depth (behind the knee) dimensions which lie within the dimensions reported in Table 7-1 for younger adults.

In the case of children with femoral shaft fractures, ideal treatment depends on the age, location, and type of fracture and to a lesser extent financial considerations. However, general recommended treatment guidelines are shown in Table 7-4 [22]. It has also been reported that cast bracing should only be used to treat fractures of the distal third of the femoral shaft, because it is difficult to control varus alignment by applying this technique to proximal shaft fractures.

Age	Recommended treatment
Birth to 6 years	Immediate cast/spica casting
6 to 12 years	Traction followed by cast/spica casting
12 years or older children	Intramedullary nailing

Table 7-4 General treatment guidelines in children with femoral shaft fractures.

For infants and younger children use of cast/spica casting is preferred in comparison to IMN, to avoid femoral head avascular necrosis (AVN). AVN can occur in young children undergoing IMN of femoral shaft fractures due to vulnerable blood supply of the femoral head. Later on it causes musculoskeletal disability [141, 142].

Gracilla *et al* [143] treated 20 children (aged between 3 and 12 years) for an isolated femoral shaft fracture using traction followed by a spica cast. Patients were discharged from the hospital at a mean time of 5.1 days following injury. All but one fracture healed in acceptable alignment, and there was no clinically significant leg-length discrepancy. Sahin *et al* [144] also reported use of closed reduction and early spica cast as a simple definitive method for treating femoral shaft fractures in children aged between 1 and 10 years.

However, in older children prolonged immobilization due to traction and cast/spica casting can result in limb shortening, malunion, loss of joint motion and muscle atrophy [22, 141]. Reeves *et al* [145] compared the use of traction and subsequent

casting with IMN in cases of adolescent femoral shaft fractures. It was found out that traction and casting group had a mean hospital stay time of 26 days in comparison to 9 days required for group treated with IMN. Group treated with IMN also had fewer complications. It was also reported that the cost of non-operative treatment is 40 % higher than IMN treatment, even after considering the necessity for another surgical procedure for intramedullary nail removal in case of IMN, largely because of a threefold difference in mean hospital stay. Therefore use of IMN has been recommended to treat adolescent femoral shaft fractures as it results in earlier walking, shorter hospital stays and decreased healing times [22, 148].

In the light of the above discussion it was essential to obtain anthropometric data for the distal end of the femur in older children (i.e. aged between 12 to 18 years). However no such anthropometric data was available for older children from [147]. Therefore, data for the thigh depth (where it is greatest when seated as shown in Figure 7-22) was used. This data is shown in Table 7-5 and Table 7-6 for male and female older children respectively.

Age	Mean	Standard Deviation (sd)	5th%ile	95th%ile
12	125	13	105	145
13	130	15	105	155
14	140	16	115	165
15	140	15	115	165
16	150	15	125	175
17	155	17	125	185
18	160	15	135	185

Table 7-5 Thigh depth in mm (maximum, sitting) anthropometric data for male older children

[147]

Age	Mean	ard Deviatio	5th%ile	95th%ile
12	130	17	100	160
13	135	15	110	160
14	140	14	115	165
15	140	14	115	165
16	145	14	120	170
17	145	16	120	170
18	145	14	130	170

Table 7-6 Thigh depth in mm (maximum, sitting) anthropometric data for female older children [147]

The data presented in Table 7-5 and Table 7-6 was obtained by measuring vertically from the seat surface to the highest point on the top surface of the thigh while the subject sits erect as shown in Figure 7-22.

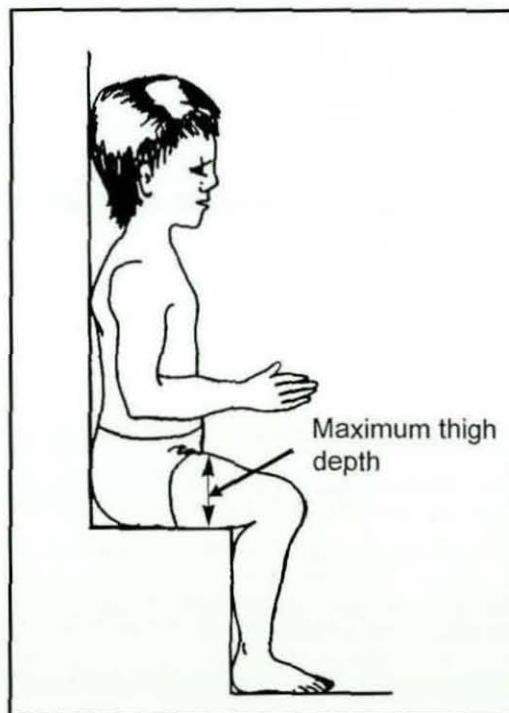


Figure 7-22 Measurement location of thigh depth(maximum, sitting) for older children [147]

In order to establish a relationship between adult and older children distal thigh dimensions, maximum thigh depth dimensions for older children depicted by Table 7-5 and Table 7-6 were compared with that of adult people (see Table 7-3).

It can be seen from Table 7-3, Table 7-5 and Table 7-6 that with the exception of 12 and 13 year old children, maximum thigh depth for older children lies within the range specified for adult data; therefore it is assumed that the majority of older children probably will have a thigh depth (behind the knee) dimension which lies within the dimensions reported in Table 7-1 for adults.

In order to estimate the required dimensions of the Calibration frame i.e. "D" and "W" (shown in Figure 7-18) cross-sectional views of the distal end of the thigh were used in conjunction with anthropometric data. For this purpose a human anatomy atlas titled "A cross-sectional anatomy" [148] by Eycleshymer and Schoemaker was chosen. It was first published in 1911 and the present volume is a reprint. In this study, serial sections of the entire body, made from formalin-hardened (i.e. by injecting formalin into the body through the femoral artery resulting in a thoroughly hardened body in a few days) cadavers are presented. This study sets the standard by which work of sectional anatomy is measured and compared, and is incorporated in standard textbooks [1, 149, 150]. It should be noted that reasonable assumptions were made throughout this process to allow progress as it was not possible to obtain data for each individual.

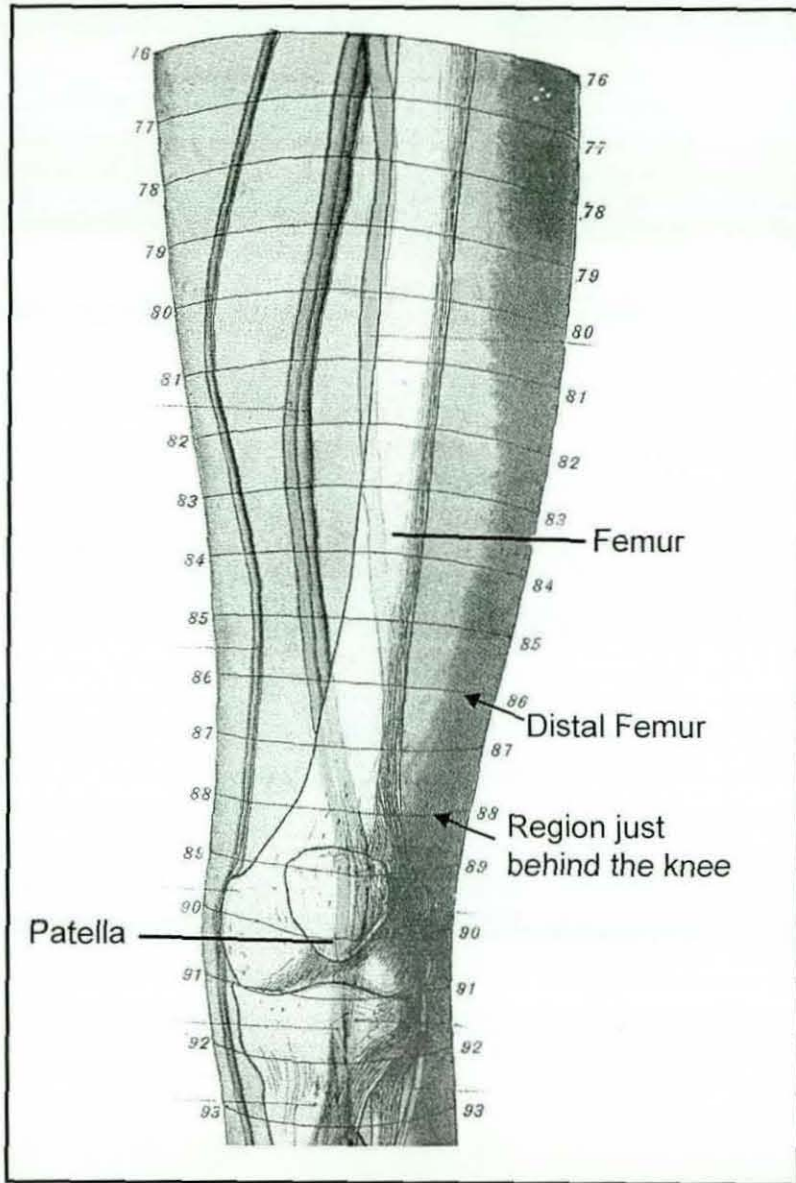


Figure 7-23 Front view of the upper left leg [148]

It can be seen from Figure 7-23 that the area of interest, i.e. the distal end of the thigh, is represented by cross section 86, whereas cross section 88 represents the region “just behind the knee” for which the data was available from [137] as depicted by Table 7-1. In order to obtain dimensions in meaningful units (mm), the cross-section 88 shown in Figure 7-24 was then used in conjunction with a grid (shown in Figure 7-24) to determine mm/square ratio as depicted by Table 7-7.

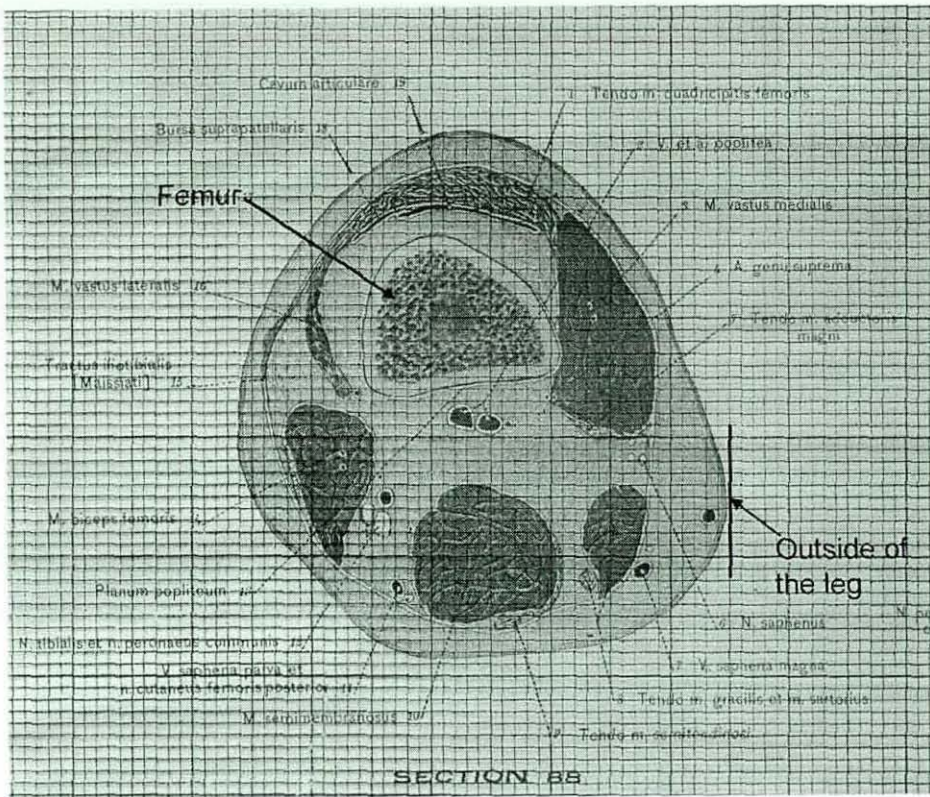


Figure 7-24 Femur cross section, just behind the knee region [148]

It was assumed that this cross section is representative of the mean thigh depth for both males and females. Therefore mean thigh depth dimensions were used from Table 7-1.

Sex	Mean depth (mm)	Mean Depth (squares)	mm/square
Male	140.4	44	3.19
Female	131.6	44	2.99

Table 7-7 Determination of mm/square ratio

A grid was then used for analysis of cross section 88 (shown in Figure 7-25) to determine depth and width dimensions respectively at the distal end of the femur.

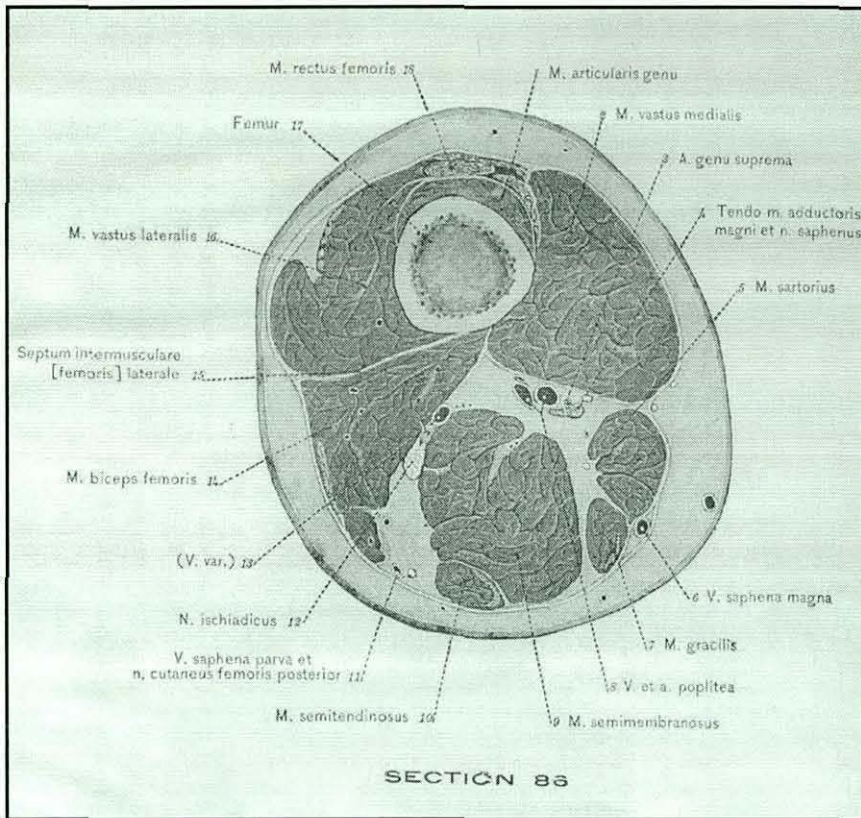


Figure 7-25 Distal femur Cross section [148]

It was found out that the leg was 45.5 squares in depth and 41.5 squares in width. These dimensions were then used with “mm/square” ratio obtained from Table 7-7 to obtain depth and width dimensions for the distal end of the femur as depicted by Table 7-8. The following assumptions were made for Table 7-8.

1. The standard deviation for the thigh depth at the distal section was assumed to be the same as that obtained from [137] for the thigh depth (just behind the knee) region. This was done due to the close proximity and similar composition of the two cross sections.
2. The standard deviation for the distal section width was assumed to be in the same proportion as that of the depth i.e.

$$Male_{SD(WIDTH)} = \frac{132.4}{145.1} \times 16.5 = 15.1mm$$

$$Female_{SD(WIDTH)} = \frac{124.1}{136} \times 15.4 = 14.1mm$$

Sex	Mean depth	SD (Depth)	Mean width	SD (Width)
Male	145.1	16.5	132.4	15.1
Female	136	15.4	124.1	14.1

Table 7-8 Depth and width dimensions for distal end of the leg.

Since the aim was to target the middle 95th percentile population (i.e. the top 2.5% and bottom 2.5% are excluded), therefore distal section dimensions (shown in Table 7-9) were obtained for the target population. Values in this table were rounded up to provide a small safety factor.

Sex	Depth (max)	Depth (min)	Breath (max)	Width (min)
Male	178	114	163	102
Female	167	105	152	96

Table 7-9 Depth and width dimensions at the distal section for middle 95th percentile population.

In order to acquire X-ray images for analysis, it is essential that the calibration frame is able to accommodate the location of the nail for different patient physiologies. Since the nail is inserted in the femoral canal, the soft tissue surrounding the femur does not require a reference from the calibration frame. However, it is essential to determine where the femur is located in relation to the top and outside of the leg as this information will help to determine the dimensions of the calibration plates needed for X-ray image acquisition. Therefore, after having determined the theoretical size of the leg at the distal section, the location of the femur relative to the outside and top of the leg at this distal section was determined using the grid. The femur can be seen to be almost circular, so the location relative to the top and outside of the leg was taken from its centre. This is the bone marrow canal which is where the intramedullary nail is inserted so it provides an ideal reference. The location was found to be;

total width = 41.5 squares,

Centre of femur to outside of leg = 22squares,

total depth = 45.5 squares,

Centre of femur to top of leg = 24 squares.

The range of the femur location for the target population was then obtained using the depth and width of the distal section (shown in Table 7-9) as follows:

$$W_{(max/min)} = \frac{22}{41.5} \times width_{(max/min)} = (51 \sim 87) mm$$

$$D_{(max/min)} = \frac{14}{45.5} \times depth_{(max/min)} = (32 \sim 55) mm$$

However, in order to validate the results obtained using the thigh cross section from [148], thereby making this study more conclusive, a recent cross sectional anatomy atlas by Bergman *et al* [149] was used. The study provides a high-quality colour photographic atlas of sectional anatomy. By presenting actual photographs of sections of the human body one of the major disadvantages of drawings that of possible inaccuracies due to artistic interpretation, is avoided. The specimens used in the preparation of this atlas have come from several bodies that were preserved by routine anatomical procedures and then thoroughly frozen. The bodies were sectioned using a band saw. The sections were then thawed and cleaned in a chilled solution. The sections were then refrozen and stored until they were photographed.

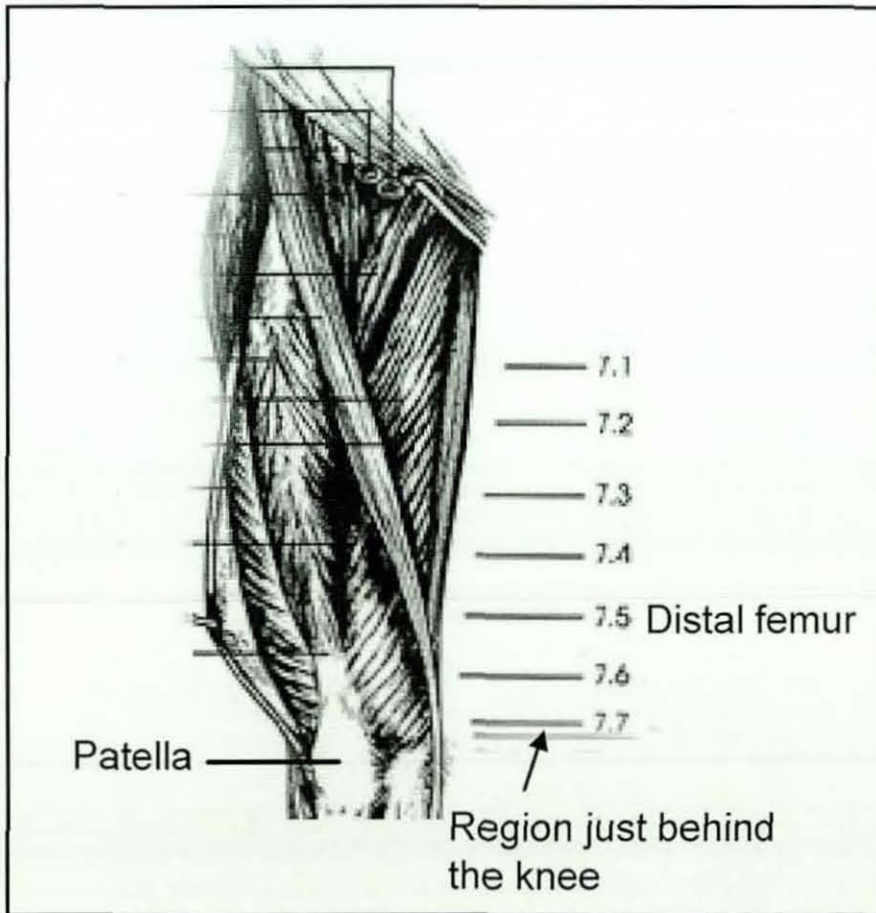


Figure 7-26 Front view of the upper right leg

It can be seen from Figure 7-26 that the area of interest is represented by cross section 7.5, whereas cross section 7.7 represents the region “just behind the knee” for which the data was available from [137] as depicted by Table 7-1. Now the “mm/square ratio” was obtained in a similar fashion as for [148] depicted by Table 7-10.

Sex	Mean depth (mm)	Mean Depth (squares)	mm/square
Male	140.4	52	2.7
Female	131.6	52	2.53

Table 7-10 Determination of mm/square ratio

A grid was then used for the analysis of cross section 7.5 (shown in Figure 7-27) to determine the depth and width dimensions at the distal end of the femur.

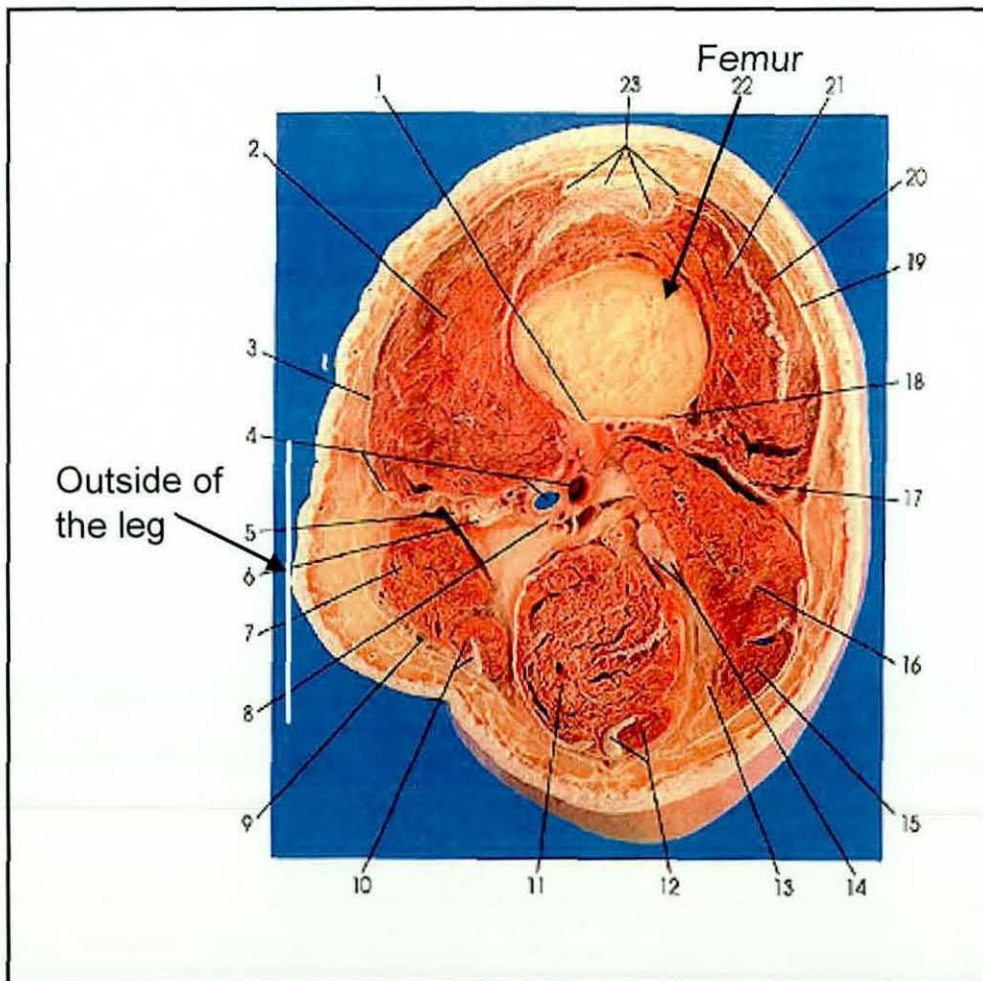


Figure 7-27 Cross sectional view of the distal femur [149]

It was found that the leg was 56 squares in depth and 46.5 squares in width. These dimensions were then used with “mm/square” ratio obtained from Table 7-10 to obtain depth and width dimensions for the distal end of the femur as depicted by Table 7-11. Standard deviation for the thigh depth and width at the distal section was obtained as described earlier for [148].

Sex	Mean depth	SD (Depth)	Mean width	SD (Width)
Male	151.2	16.5	125.5	13.7
Female	141.7	15.4	117.7	12.8

Table 7-11 Depth and width dimensions for distal end of the leg.

Distal section dimensions (shown in Table 7-12) were then obtained for the target population. Values in this table were rounded up to provide a small safety factor.

Sex	Depth (max)	Depth (min)	Breath (max)	Width (min)
Male	184	118	153	98
Female	173	111	144	92

Table 7-12 Depth and width dimensions at the distal section for middle 95th percentile population.

After having determined the theoretical size of the leg at the distal section, the location of the femur relative to the outside and top of the leg at this distal section was determined using the grid. The location was found to be;

$$\begin{aligned}
 \text{total width} &= 46.5 \text{ squares,} \\
 \text{Centre of femur to outside of leg} &= 26 \text{ squares,} \\
 \text{total depth} &= 56 \text{ squares,} \\
 \text{Centre of femur to top of leg} &= 16.5 \text{ squares.}
 \end{aligned}$$

The range of the femur location for the target population was then obtained using the depth and width of the distal section (shown in Table 7-12) as follows:

$$\begin{aligned}
 W_{(max/min)} &= \frac{26}{46.5} \times \text{width}_{(max/min)} = (51\sim 85)mm \\
 D_{(max/min)} &= \frac{16.5}{52} \times \text{depth}_{(max/min)} = (32\sim 54)mm
 \end{aligned}$$

As a result of the above analysis the essential measurements required for calibration frame dimensions are shown in Figure 7-28.

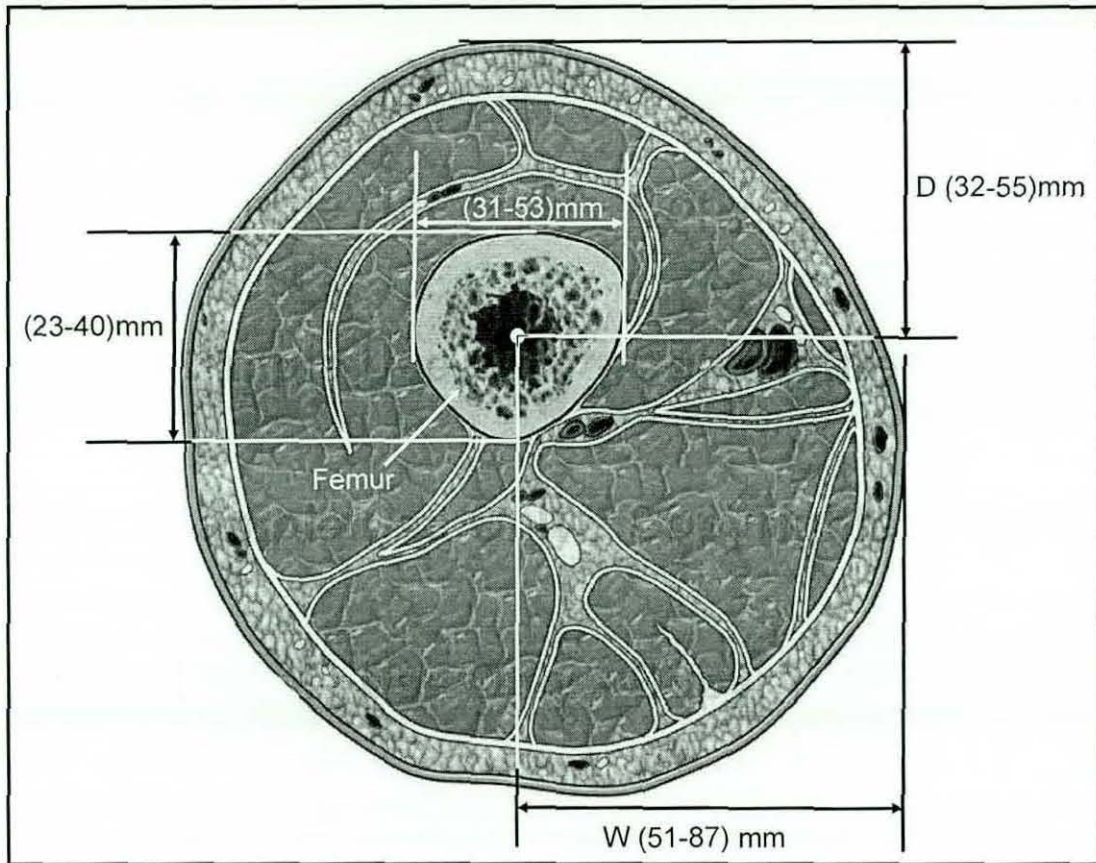


Figure 7-28 Femur location dimensions with respect to outside and top of the leg.

It should be noted that the above dimensions are only valid for legs without any swelling. Therefore, for robust design of the calibration frame, the influence of swelling on a patient's thigh size after femoral shaft fracture was also evaluated. The following section discusses swelling and its repercussions on femoral shaft fracture treatment in detail.

7.2.1 Swelling

Swelling, or edema, is a natural inflammatory reaction of the body to an injury. It involves the enlargement of organs, skin, or other body structures due to excessive build-up of fluid in the tissues. This build-up occurs due to damage to the small blood vessels (capillaries), which leak fluid into the surrounding tissue resulting in increased

blood flow inside the thigh. This rush of warm blood causes redness, heat, and swelling. This build-up of fluid can lead to a rapid increase in weight over a short period of time. Pressure from the swelling and the accumulation of immune cells, along with the destructive chemicals released by the cells, irritate local nerve endings, and cause pain. Swelling can occur throughout the body (generalized) or it may be limited to a specific part of the body (localized) such as to the thigh due to a femoral shaft fracture.

7.2.1.1 Localized swelling

Possible causes of localized swelling are as follows:

- Injury: Any physical damage to the body caused by violence or accident or fracture etc, such as in case of a femoral shaft fracture, due to significant loss of blood into the muscles of the thigh.
- Infections etc

In consultation with orthopaedic surgeons, it was discovered that, since operative treatment causes further trauma to an injury, therefore in the case of isolated fractures delayed nailing is necessary to prevent blood infection and further vascular destruction to injured tissues. This reduces the possibility of inactivating the biology of fracture repair, which leads to delayed union or to non-union. Hence, immediately after the fracture [22]:

- The patient's leg is kept in an elevated position to avoid further swelling
- Wait for 48-72 hours to see if the patient develops any fever, which is indicative of infection. In the case of fever, the surgeon will wait until the fever goes away before surgery.
- A blood test is taken and the surgeon waits until the white blood cell count returns to normal.

However, in the case of open fractures, [22] early nailing is recommended, such as A.P. Whittle [22] suggest that immediate nailing does not significantly increase the risk of infection, and all such cases should be treated within 8 hours of injury. Goose

et al [151] have demonstrated that open femoral fractures treated by immediate or early (i.e. within a few hours of injury) intramedullary nailing have a low overall complication rate and a very low infection rate. Therefore, early intramedullary fixation is a safe and efficient method of treating open femoral shaft fractures.

Femoral shaft fractures are usually high energy injuries, often associated with multiple injuries [49]. However, in case of multiple trauma patients, contradictory views are found in the literature about the timing of intramedullary fixation [22]. In the past, early fracture fixation was believed to be important as one of the major aims is rapid stabilization of their extremity injuries. Bone *et al* [152] found a high rate of pulmonary complications in patients who had delayed stabilization of fractures. In summary, the majority of studies in 1980s proposed early fracture stabilization as beneficial for multiple trauma patients. Recently, Susan *et al* [153] reviewed 1362 patients with a femoral shaft fracture over a 12-year period and reported that early femur fracture fixation (i.e. within 24 hours of injury) is associated with an improved outcome, even in patients with coexistent head and/or chest trauma. Whereas, fixation of femur fractures at 2 to 5 days was associated with a significant increase in pulmonary complications, particularly with concomitant head or chest trauma, and length of stay. Therefore, the author concluded, chest and head trauma are not contraindications to early fixation with reamed intramedullary nailing.

However, some recent reports suggest patients with more severe head injury, high Injury Severity Score (ISS) may get poorer outcomes if treatment of their musculoskeletal injuries includes early surgical intervention. Fakhry *et al* [154] reviewed 2805 patients with femoral fractures and divided them into 2 groups according to ISS i.e. ISS less than 15 or ISS greater than 15. In patients with ISS greater than 15, surgery within 1 day after trauma was associated with 3.8% mortality rate, while in patients operated 2-4 days after injury, mortality was 1.8% and in the group operated more than 4 days, mortality rate was 1.5%. It was also found that in the subgroup of patients with severe chest injury, mortality was as high as 4.6% in patients operated on day 1, while no patient died, even with severe chest injury, in the group of patients operated 2-4 days, or later, after the trauma. Pape *et al* [155] found a high incidence of Acute Respiratory Distress Syndrome (ARDS) in patients with chest trauma and early IMN of femoral fracture. In a group of patients with

comparable chest trauma but delayed femoral fracture fixation, the incidence of ARDS was low. The author concluded that the combination of multiple trauma chest injury and early reamed IMN is associated with higher risk of ARDS.

In the light of the above discussion and recommendations made in [22] and by the consultant orthopaedist Mr. G. Taylor, guidelines regarding the time frame for femoral shaft treatment can be summarized as follows:

Type of fracture	Recommended time frame for IMN
Isolated	Within 7 days
Multiple	Within 3 days
Open	Within 12 hours

Table 7-13 General treatment guidelines for femoral shaft fractures using IMN.

Consultation with orthopaedic surgeons revealed that swelling usually subsides in around 2 weeks, therefore in light of the treatment guidelines swelling influence on leg size during surgical procedure must be taken into account. This has been accomplished by using rough guidelines about swelling obtained from orthopaedic surgeons, according to which the maximum % enlargement, caused by swelling, with respect to normal upper leg dimensions in width and depth for different patient physiology is approximately twice the circumference. Since,

$$\text{Circumference} = \pi \cdot \text{diameter}$$

In this case width/ depth can be considered as diameter, therefore in order to take into account the worst case scenario, maximum depth and width dimensions shown in Figure 7-28 will become twice the normal. For robustness purposes, wide ranges of depth and width were established by keeping the minimum depth and width dimensions the same as when the leg is not swollen. Dimensional requirements for the calibration frame design are shown in Figure 7-29.

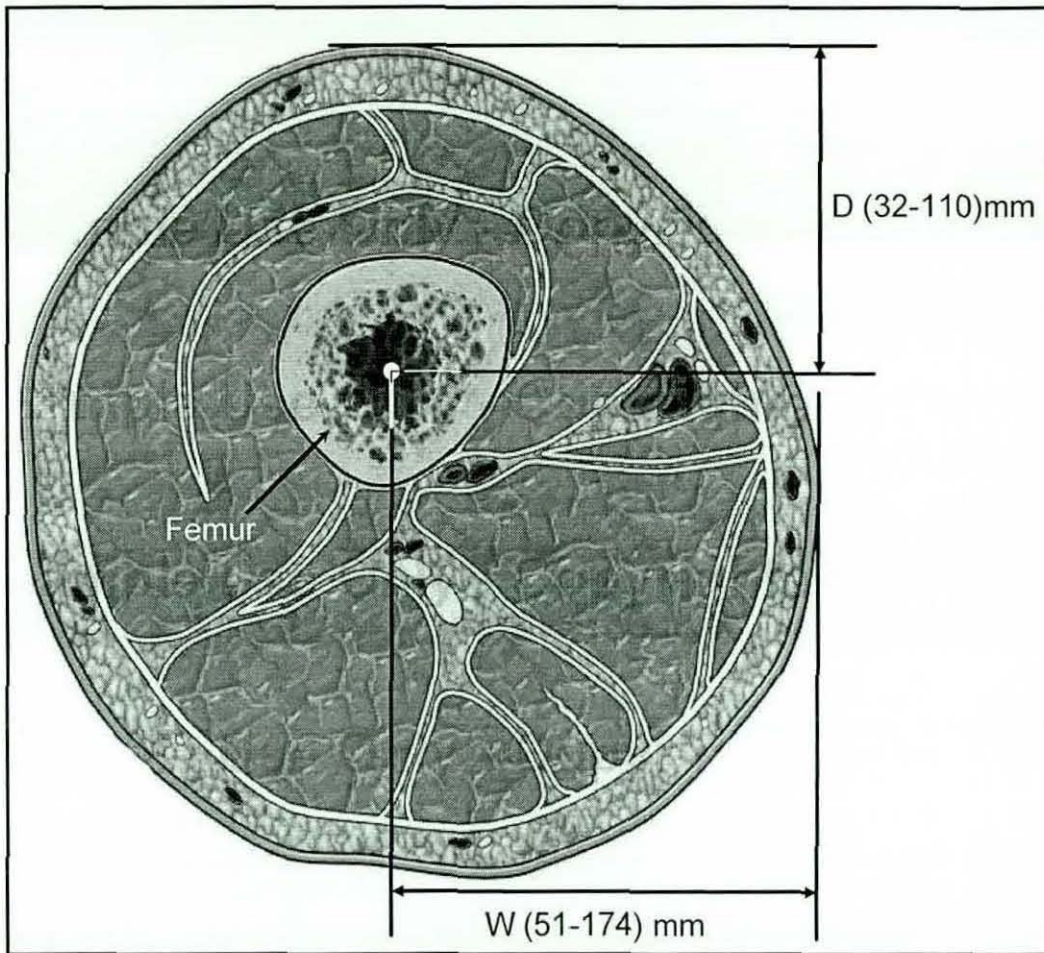


Figure 7-29 Calibration frame dimensional requirements.

7.3 Design of a modular calibration frame

A group of final year Undergraduate students (David *et al* [156]) were given the task of redesigning the Γ calibration frame to eliminate the associated problems of the existing design. These include:

- Design is only suitable for use on the right leg.
- Stainless steel attachment makes the calibration frame heavy, increasing deflection of the external support arm and loading on the patient.
- Results obtained from CAD modelling of the intramedullary nail have shown that optimum results were obtained when angle ϕ is around 10° . Therefore, it is required to design the calibration frame such that $\phi \approx 10^\circ$ is always obtained while positioning the calibration frame to acquire desired X-ray images.

The modular calibration frame designed by David *et al* [156] is shown in Figure 7-30. Details about the calibration frame design can be found in [156].

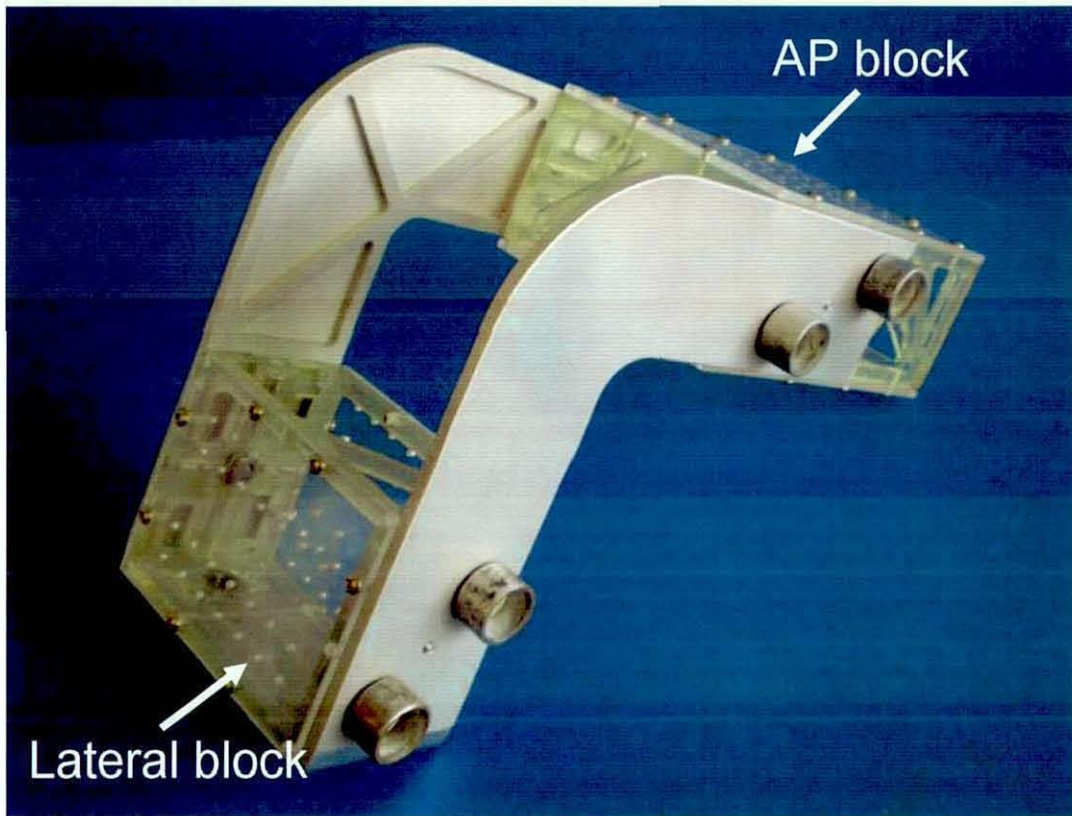


Figure 7-30 Assembled modular calibration frame [156]

The lateral block should be against the leg to achieve the desired X-ray image and must always be centred around the centre of the femur as shown in Figure 7-31.

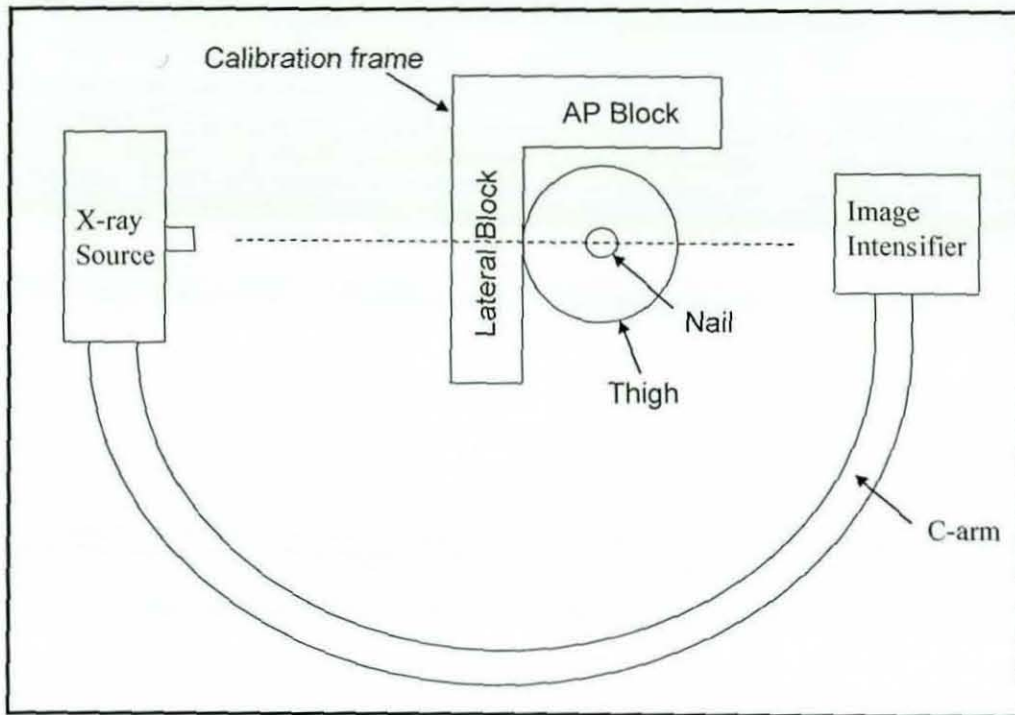


Figure 7-31 Desired patient position during the Lateral image acquisition.

Therefore, the fiducial area requirement of the Lateral block was derived in the light of the results obtained in Section 7.1, as swelling has no effect on this. However, the distance between the Lateral and AP blocks i.e. " H_x " (shown in Figure 7-32) is governed by the leg dimensions in the swollen condition. This is because the underside of the AP block must be at a distance above the centre of the Lateral block to sufficiently accommodate the tissue above the femur when swollen. It should be noted that calibration frame has been designed in such a way that during image acquisition the centre of the Lateral block is nearly in alignment with the intramedullary nail.

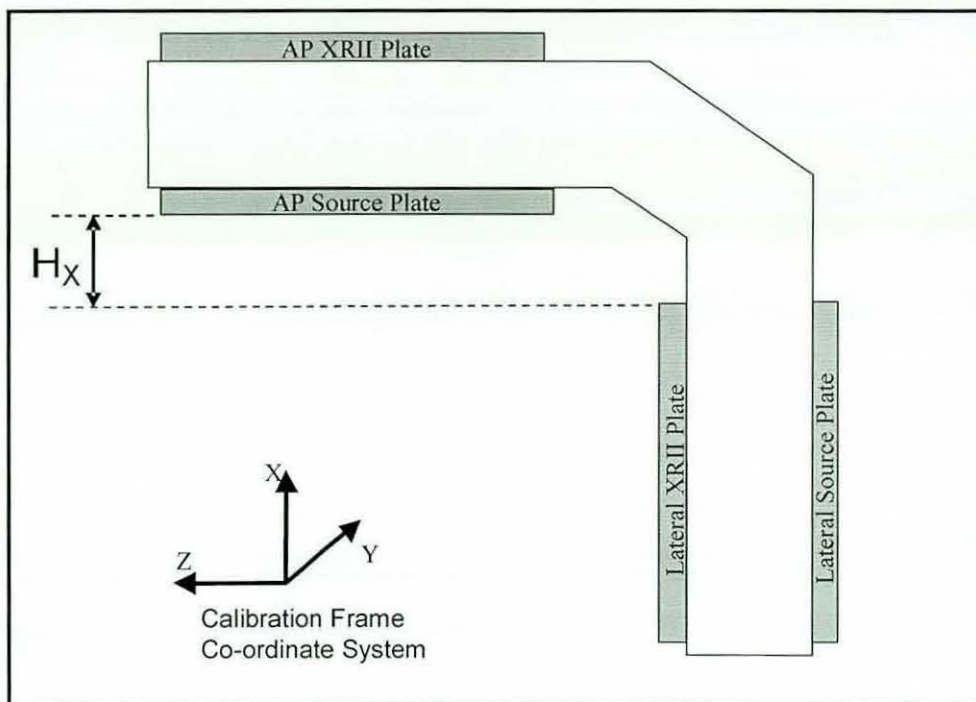


Figure 7-32 Separation between Lateral and AP plates along the X-axis.

Furthermore, the fiducial area of the AP block needed determining as swelling affects this significantly. Based on the dimensions obtained for the distal femur section (shown in Figure 7-29), the length of the AP calibration plates accommodate the target population was determined. Two configurations, “Medium” with length of 130 mm and “Large” with length of 190 mm, were proposed to accommodate the middle 50% and 95% population respectively. Both configurations have a uniform width of 90 mm (obtained from analysis presented in Section 7.1). The layout of the fiducials was then optimised for the available area of the calibration plates as shown in the following section.

7.4 Proposed fiducial layout

In order to allow ease of manufacture and to reduce manufacturing cost, it was decided to use fiducials (ball bearings) of the same diameter throughout the calibration frame. Hence, spacing between fiducials was used to uniquely identify each individual fiducial. It should be noted that the diameter of the ball bearings was kept at 2mm as, due to distortion large balls appear oval rather than circular in the X-ray image, thereby making it difficult to determine accurately the image centre. The diameter of the balls was therefore kept as small as possible, while ensuring that the

balls will be able to produce sufficient X-ray absorption to ensure their visibility in the image.

7.4.1 Fiducial layout for Lateral calibration plates

During the Lateral view image acquisition, irrespective of patient physiology, the calibration frame will be positioned such that the intramedullary nail will lie approximately in the centre of the calibration plates as shown in Figure 7-31. Therefore the Lateral view fiducial layout will be uniform, unlike that of the AP view for all patient physiologies. To assist operating theatre personnel in positioning of the nail around the centre of the calibration plates, a 24mm region in the middle of the Lateral calibration plates was kept clear of fiducials. The distance of 24mm was derived using existing Lateral view X-ray images to ensure placement of the largest available nail (i.e. diameter of 14mm) without occluding any of the fiducials. This arrangement is helpful in determining the distance along the X-axis between the Lateral calibration plates and the AP Source calibration plate (H_X in Figure 7-32), that can take into account different patient physiology (dimension D in Figure 7-29). In this way the distance between the intramedullary nail axis and the AP Source calibration plate will almost always remain the same thereby resulting in uniform magnification of the nail irrespective of the size of the patient's thigh in the AP view image. Therefore, fiducial layout for the Lateral calibration plates was designed in the light of the results obtained from Section 7.1. The fiducial layout for the Lateral calibration plates is shown in Figure 7-33.

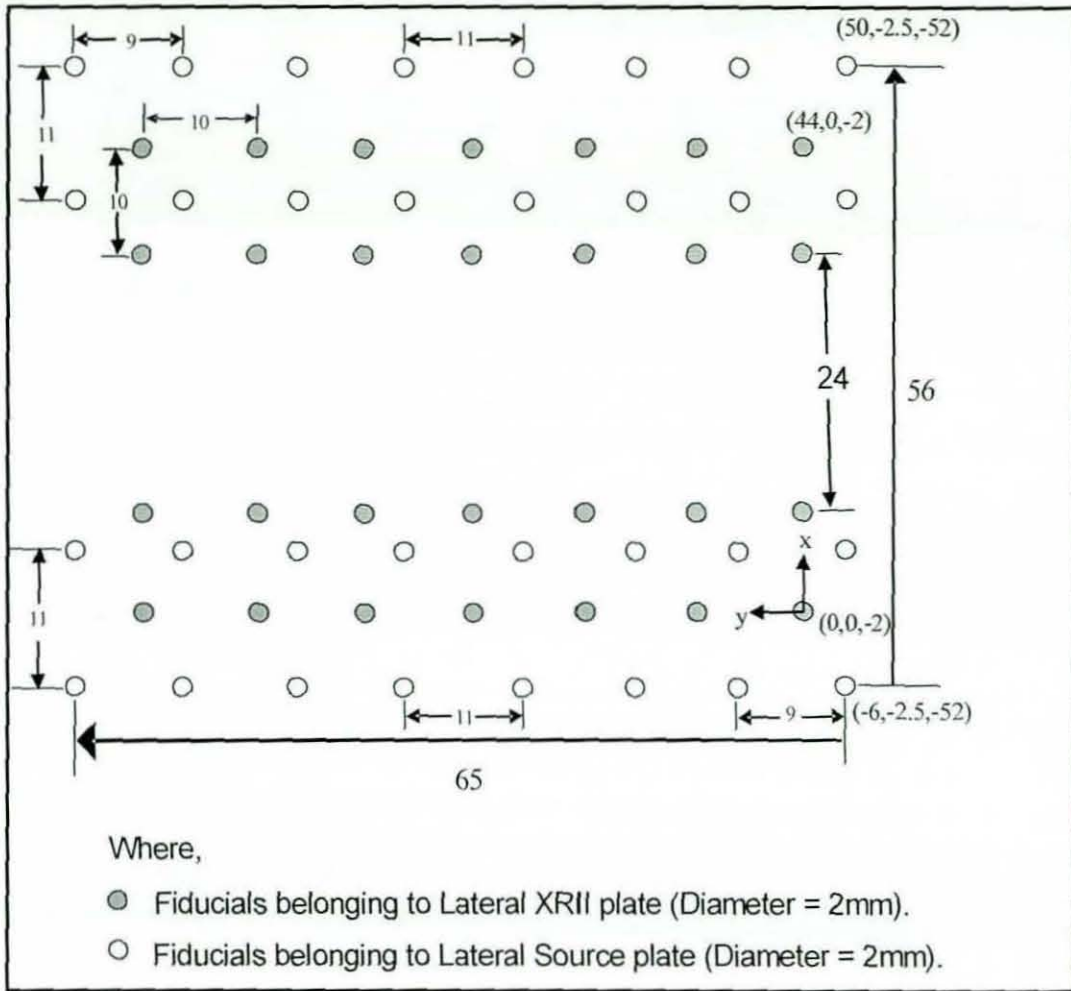


Figure 7-33 Fiducial layout for Lateral calibration plates.

In Figure 7-33, it should be noted that for:

Lateral XRII plate: Both horizontal and vertical spacing were kept at 10mm throughout.

Lateral Source plate: Any change in horizontal and vertical spacing from 9 mm to 11 mm is specified.

It should be noted that in the Lateral view both fiducials on the XRII plate (i.e. A and B as shown in Figure 8-1) are surrounded with Source plate fiducials having a unique spacing of 11 mm and will be used as reference markers.

7.4.2 Fiducial layout for AP calibration plates

In the light of the results obtained from Section 7.1 and Section 7.2, fiducial layout for the AP calibration plates for the medium and large calibration frames is shown in Figure 7-34 and Figure 7-35 respectively.

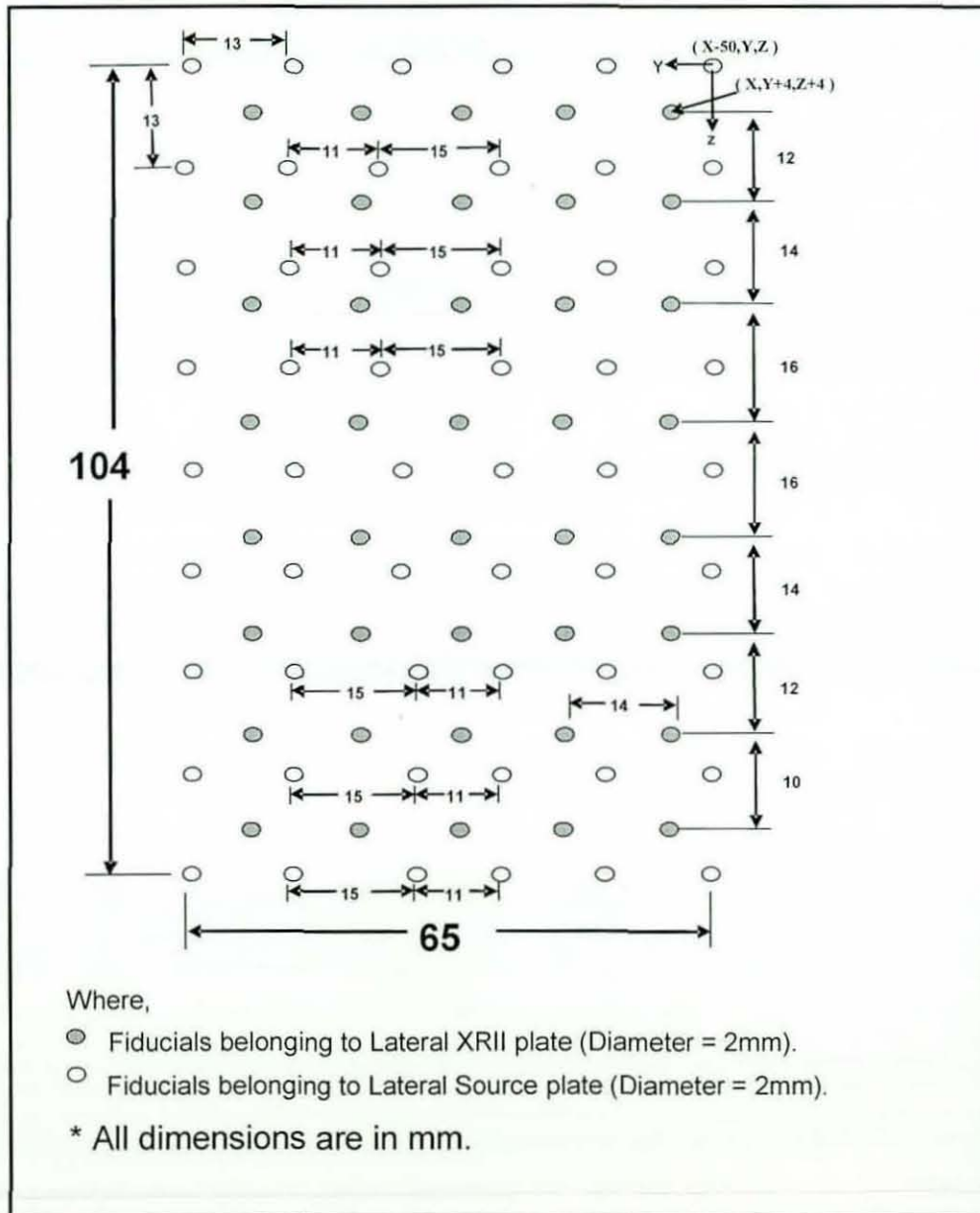


Figure 7-34 Fiducial layout for AP calibration plates (Medium frame).

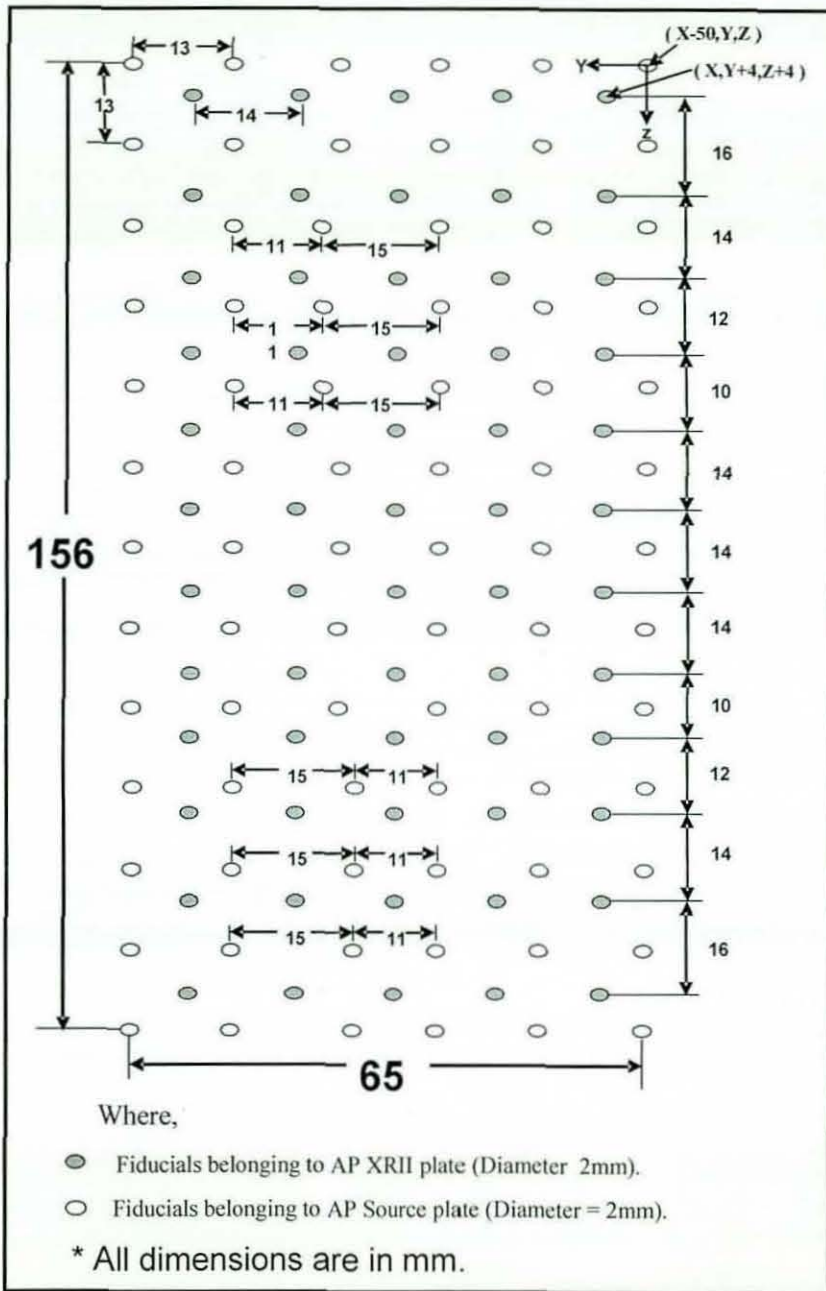


Figure 7-35 Fiducial layout for AP calibration plates (Large frame).

In Figure 7-34 and Figure 7-35, it should be noted that for:

AP Source plate: Vertical spacing is kept at 13mm throughout; whereas, any change from 13mm in horizontal spacing is specified.

AP XRII plate: Horizontal spacing is kept at 14mm throughout; whereas, vertical spacing is varied from 10 to 16mm, in order to achieve unique identification of the fiducials.

7.5 Summary

In order to make the calibration frame robust, a comprehensive redesign was proposed. At first an optimal number of fiducials and their spatial distribution necessary to provide the required accuracy of 1 mm and 1° were determined using existing X-ray images. During the second stage dimensions of the calibration frame that will make it suitable to be used for a target population (middle 95% of the population) were determined. To accomplish this task, cross sectional images of the upper leg and anthropometric data were used to determine the maximum and minimum dimensions of the leg at the distal section across the target population. These dimensions were then adjusted to take into account the worst case of swelling. Towards the end of the chapter, two calibration frames configurations namely "Medium" and "Large" are proposed to accommodate the middle 50% and 95% population respectively. In the next chapter, image analysis protocol and accuracy evaluation of the proposed calibration frame are discussed.

8 Image analysis and accuracy evaluation of the proposed calibration frame

In laboratory trials, two nearly orthogonal (Lateral and AP) X-ray images of the distal end of the intramedullary nail were taken with the calibration frame in position as shown in Figure 4-1 and Figure 4-2 respectively. Since use of reference markers has been abandoned, therefore extensive modifications were required to fiducial recognition program. Section 8.1 and 8.2 provides description of Lateral and AP view image analysis respectively.

8.1 Image analysis protocol for Lateral calibration plates

Once a Lateral view image was acquired, it was divided into two regions using the nail location as shown in Figure 8-1.

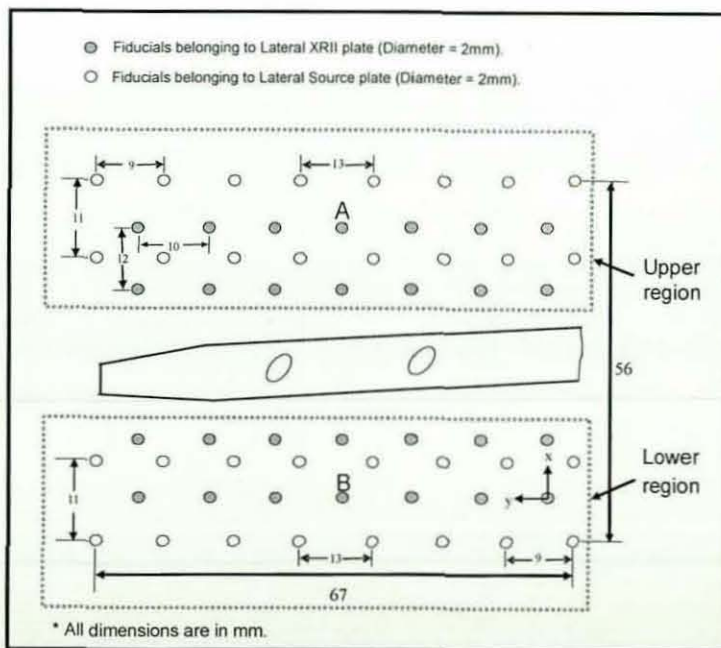


Figure 8-1 Division of fiducials on Lateral calibration plates into two regions.

This has been accomplished as follows:

- Once a Lateral X-ray image (shown in Figure 8-2) was acquired, locations of all pixels with grey level values greater than zero was determined to get rid of the dark background i.e. cropping part of the image which is of interest i.e. contains calibration markers as shown in Figure 8-3.

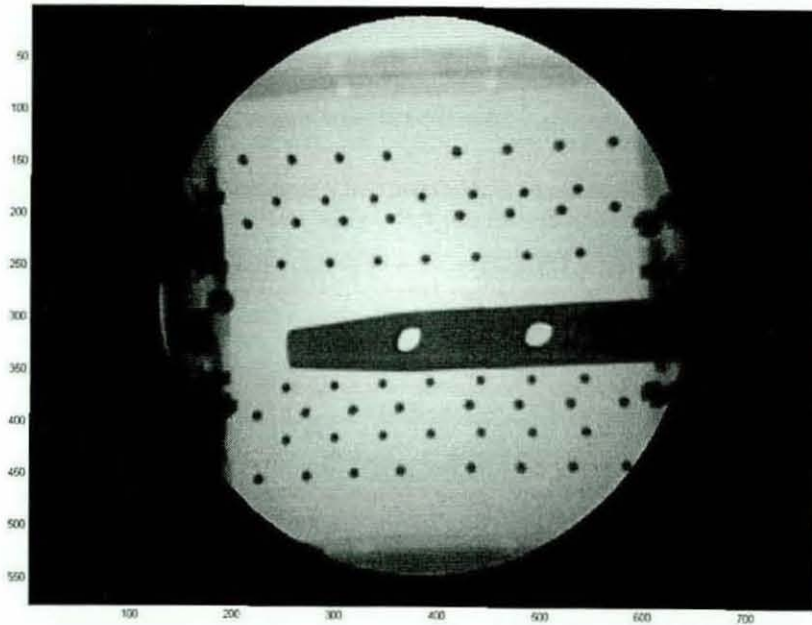


Figure 8-2 Lateral view image

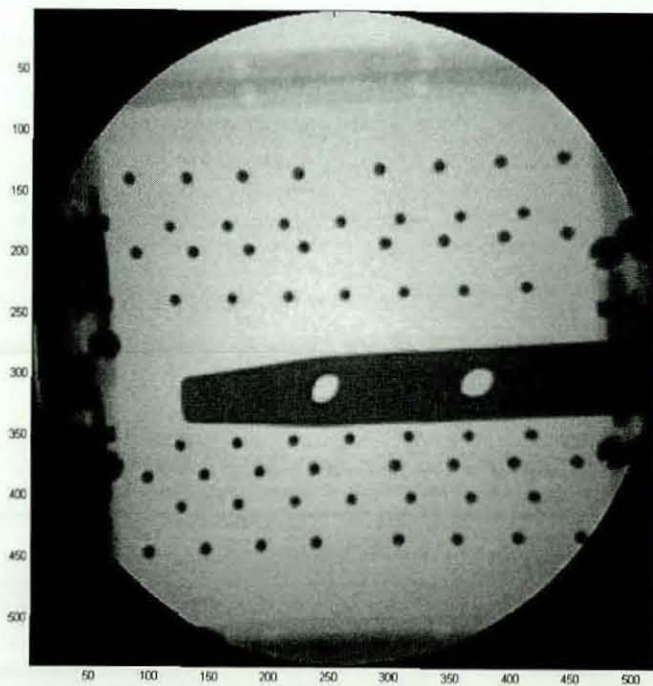


Figure 8-3 Cropped Lateral view image

- Now in order to determine the location of the nail, mid region of Figure 8-3 was cropped (shown in Figure 8-4) using the image size along x and y axes.

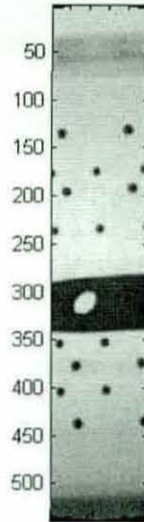


Figure 8-4 Cropping of the image to obtain nail's location

- Thresholding was applied to binarize the image. The binary image was then inverted, so that all the fiducials and nail becomes white i.e. having a value of 1.
- Then, objects within the inverted binary image were labelled on the basis of connectivity, and their properties i.e. area and bounding box were determined.
- The objects were then sorted in descending order based on their area (pixels), with ideally the nail having the largest area among all objects. However, use of area alone in presence of external objects (as shown in Figure 8-5) can cause error in nail's location. Therefore, starting point of objects bounding box was also used in addition to area. Initially, fiducials within the cropped region were discarded based on their area, then if only one object was left (as in Figure 8-4) it was classified as nail, whereas if two or more objects were left (as in Figure 8-5) then y-coordinate of each object bounding box's starting point was compared with y-coordinate of cropped region's centre (shown in Figure 8-5b).

Object whose bounding box's starting point lies nearest to the cropped region's centre along y-axis was classified as nail.

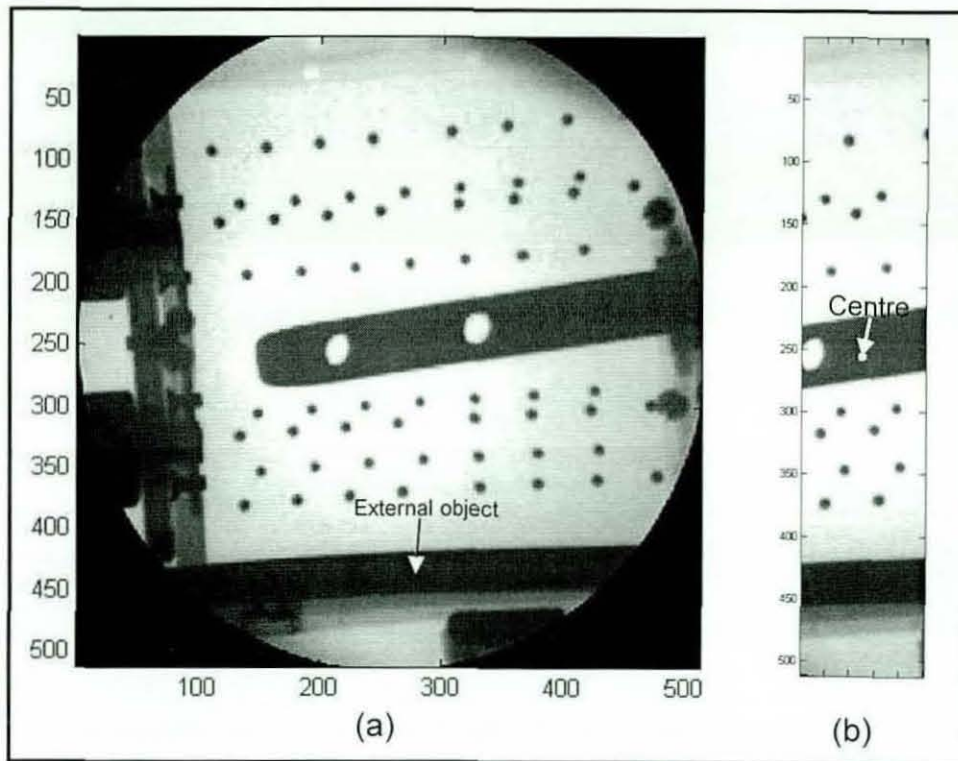


Figure 8-5 (a) Lateral view image with external object (b) Cropped region to obtain nail's location

Based on the location of the nail, the fiducials on Lateral calibration plates were then divided into two regions i.e. upper and lower region as depicted by Figure 8-1. Then in order to determine whether the acquired image is a useful image (i.e. image that can be used to determine characteristic measurements described in chapter 4 to determine drilling trajectory of the distal locking holes) or not, following checks were carried out on the acquired image.

Check 1: Determination of number of visible fiducials in the Upper and lower region.

Check 2: Confirmation of presence of fiducials with unique spacings (i.e. Lateral source plate fiducials with horizontal spacing of 13mm).

Check 3: Presence of fiducial overlapping.

The acquired image is not deemed suitable for processing if any of the above mentioned checks fails and the user is asked to acquire image again until a useful image is obtain.

Check 1: Determination of number of visible fiducials in the Upper and lower region

To determine location of the X-ray source using triangulation technique (described in section 4.4), it is essential to have XRII and Source plate fiducials' visible in both upper and lower region respectively. Any Lateral view image which fails to fulfil this criterion, for example image shown in Figure 8-6 does not fulfil this criteria for the upper region, was discarded and the user was asked to acquire image again. However, if the acquired image passes check 1, then check 2 was carried out.

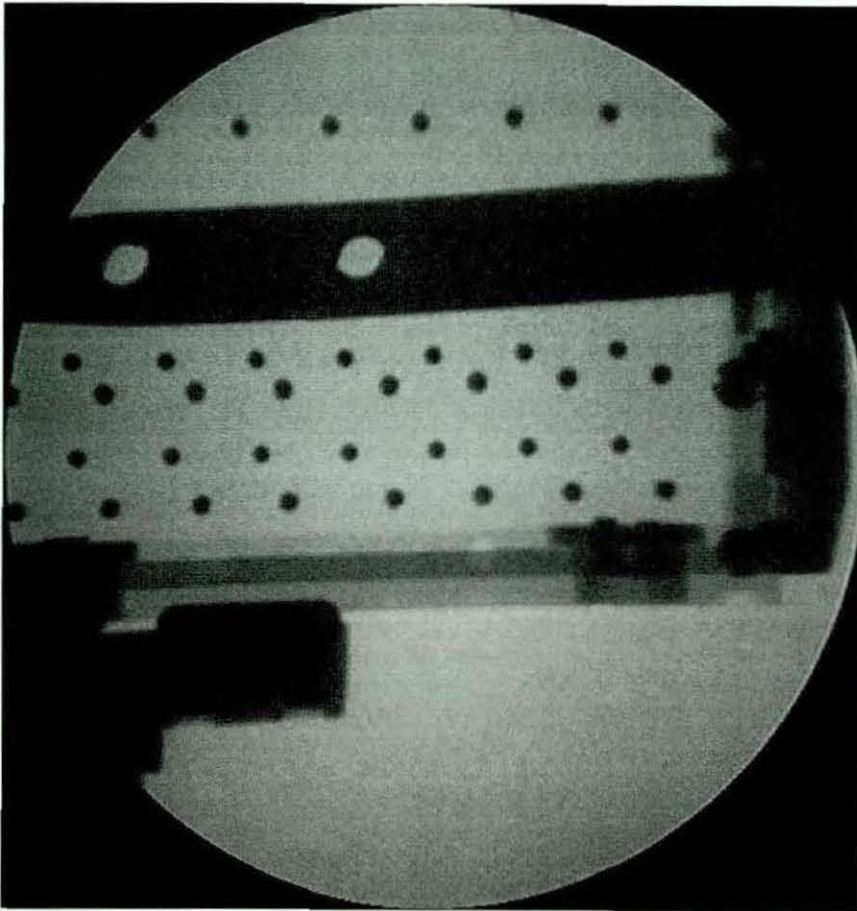


Figure 8-6 Discarded Lateral image due to insufficient number of fiducials.

Check 2: Confirmation of presence of fiducials with unique spacings

Since spacing between fiducials was used for unique identification of each fiducial. In order to carry out fiducial recognition, it was therefore essential that fiducials with unique spacings are visible in both regions. Any Lateral view image which does not fulfil this condition, for example image shown in Figure 8-7 only contains fiducials

with unique spacing in the upper region, was discarded and the user was asked to acquire image again.

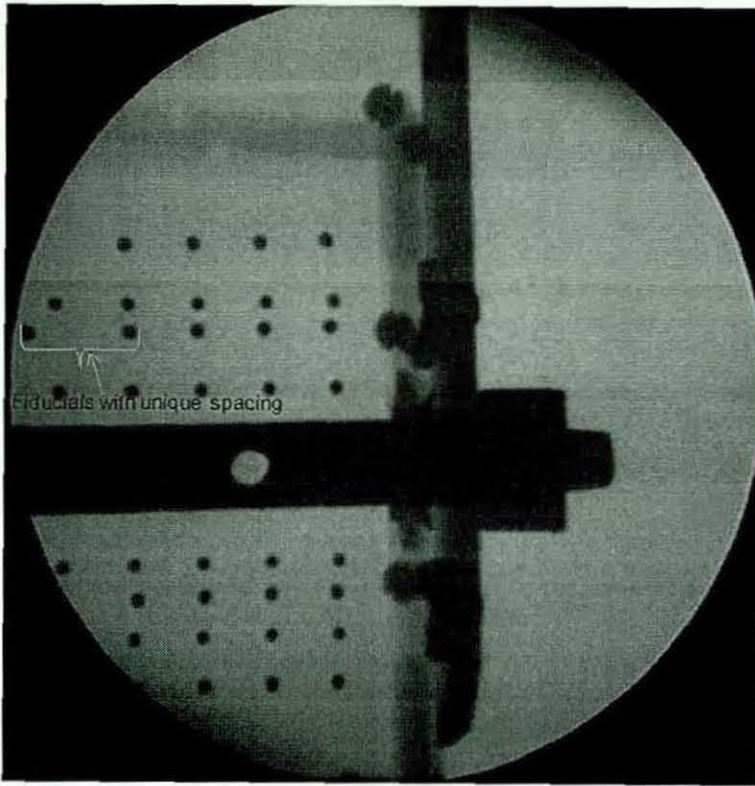


Figure 8-7 Discarded Lateral image due to absence of fiducials with unique spacing.

Check 3: Presence of fiducial overlapping

It can be seen from Figure 8-8 that some fiducials in the upper region have although not overlapped but are very close to each other, in such case fiducial recognition has been carried out successfully as shown in Figure 8-8.

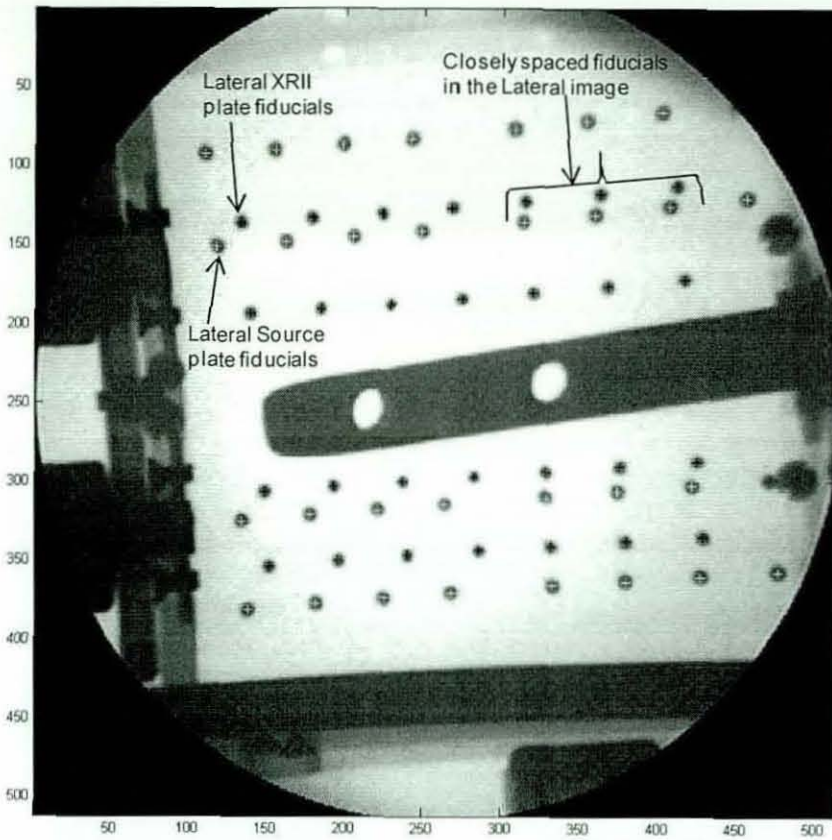


Figure 8-8 Lateral view image with fiducials very close to each other.

It should be noted that for Lateral view image acquisition, X-ray imaging axis should ideally be nearly perpendicular to calibration frame axis as shown in Figure 8-9; otherwise sometimes fiducial overlapping may occur.

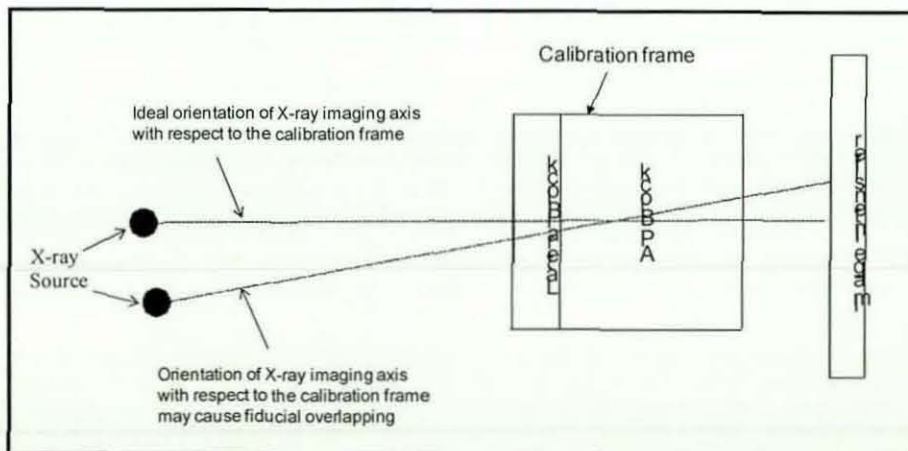


Figure 8-9 X-ray imaging axis with respect to calibration frame for the Lateral image acquisition (Top view)

Since overlapping of fiducial causes an error in determination of fiducial's centre, which in turn will result in loss of accuracy, therefore it is essential detect fiducial overlapping. To accomplish this aim, at first all fiducials in the upper region were identified as shown in Figure 8-10.

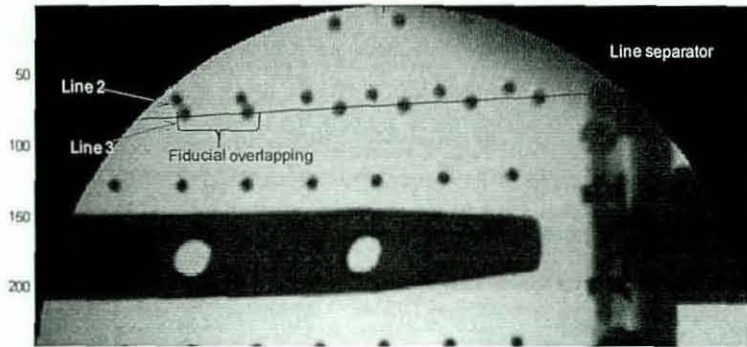


Figure 8-10 Fiducial overlapping in Lateral view image

Then, number of fiducials along each line were counted and in case of an abnormality (i.e. a line having fewer fiducials in comparison to an adjacent line, for example in Figure 8-10 line3 only contains 4 fiducials in comparison to 6 of line2) the user was asked to acquire image again by adjusting the C-arm with respect to the calibration frame. However, if the acquired image passes this check in the upper region then same procedure was repeated for the lower region.

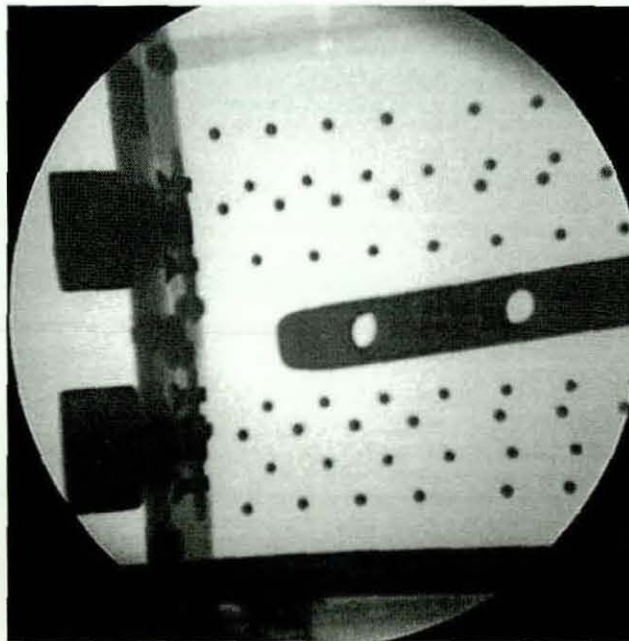


Figure 8-11 Useful Lateral view image

Once a useful image, for example shown in Figure 8-11 was obtained, fiducial recognition was carried out in following manner:

Initially, each region has been assigned a reference marker (i.e. calibration marker "A" and "B" in upper and lower region respectively) surrounded with unique spacing. Initially fiducial recognition was carried out in the upper region (shown in Figure 8-12).

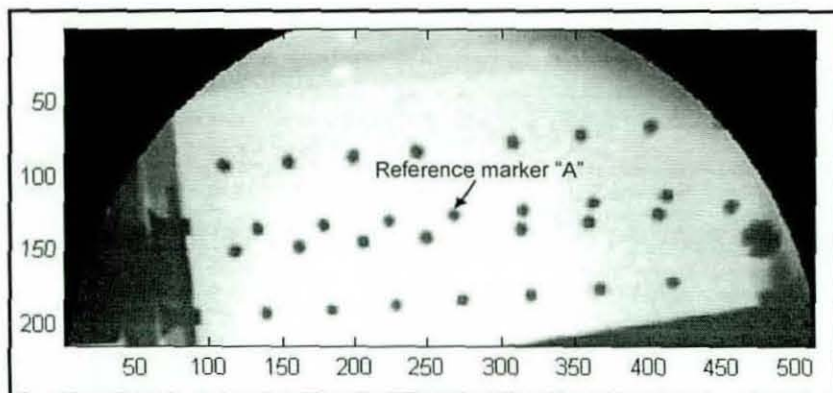


Figure 8-12 Lateral image's upper region

Since spacing between fiducials was used for unique identification of each fiducial. Therefore, at first the aim was to find fiducials with unique horizontal spacing of 13 mm on Source plate. This was accomplished as follows:

- Thresholding was applied to binarize the image; the binary image was then inverted, shown in Figure 8-14, so that fiducials can be classified as objects. Object properties such as area and circularity were then used to identify all visible fiducials.
- Among the visible fiducials, distinction was made between XRII and Source plate fiducials based on their area. Since Source plate lies closer to X-ray source in comparison to XRII plate, therefore Source plate fiducials experience more magnification than XRII plate fiducials. As a result area of Source plate fiducials is slightly greater area than that of XRII plate fiducials.
- Once all fiducials belonging to Source plate were identified, their respective bounding boxes were used to identify upper most left hand side fiducial as shown in Figure 8-14. In order to ensure that selected fiducial belongs to Source plate,

this fiducial was used as starting point to determine horizontal spacing (in pixels) between horizontally lying consecutive fiducials while scanning from left to right of the image. This scanning will continue until “unusual transition” in spacing i.e. from 9mm to 13mm was found along the line. However, if no “unusual transition” in spacing was found then this fiducial was regarded as XRII plate fiducial. For example, starting point shown in Figure 8-13 belongs to Source plate.

- Then fiducials lying immediately below (vert_fiducial) and to the immediate right (hor_fiducial) of starting point fiducial on the same calibration plate were located as shown in Figure 8-13. These fiducials were then used to determine horizontal and vertical spacings.

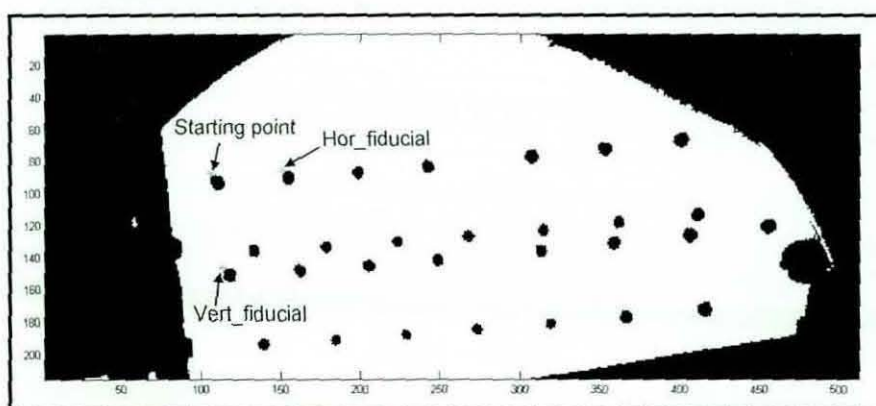


Figure 8-13 Determination of horizontal and vertical spacings.

- These spacings were then used while comparing bounding box of the starting point with those of all visible fiducials in the upper region to establish starting point for each individual line in upper region as shown in Figure 8-14.

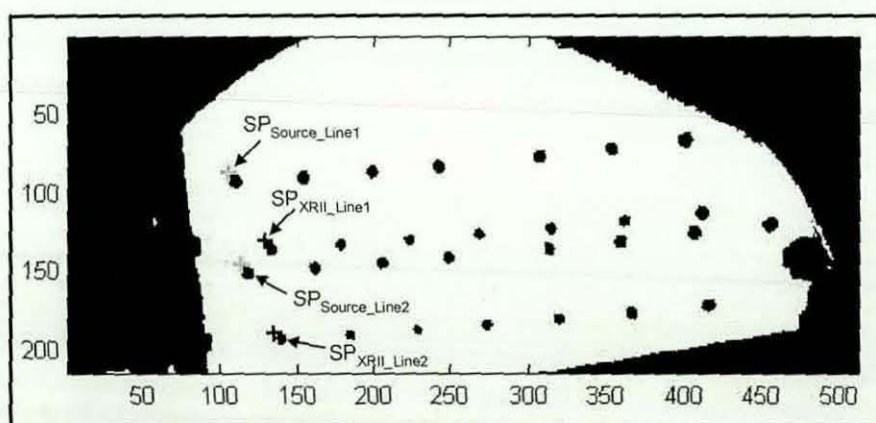


Figure 8-14 Establishment of Starting points on Source plate.

- Fiducial recognition along each line was accomplished (shown in Figure 8-15) using its own starting point and spacings. The program uses this information to establish central fiducial along each line. Then image was divided into sub-regions and each fiducial was processed individually while scanning from central fiducial of each line to the left and right of the image.

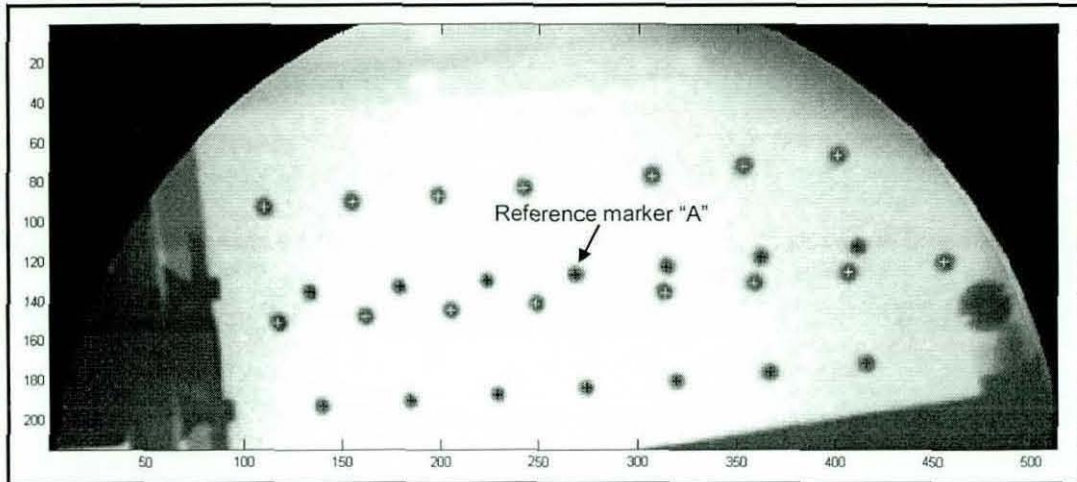


Figure 8-15 Fiducial recognition in Lateral view upper region.

It should be noted that if a line is missing (i.e. hidden beneath the nail or in close proximity of the nail), for example in Figure 8-16 fiducials along XR11_Line2 are in close proximity of the intramedullary nail, which makes it impossible to detect fiducial centre accurately along that line, in such case these fiducial's centers were assigned image coordinates (0,0).

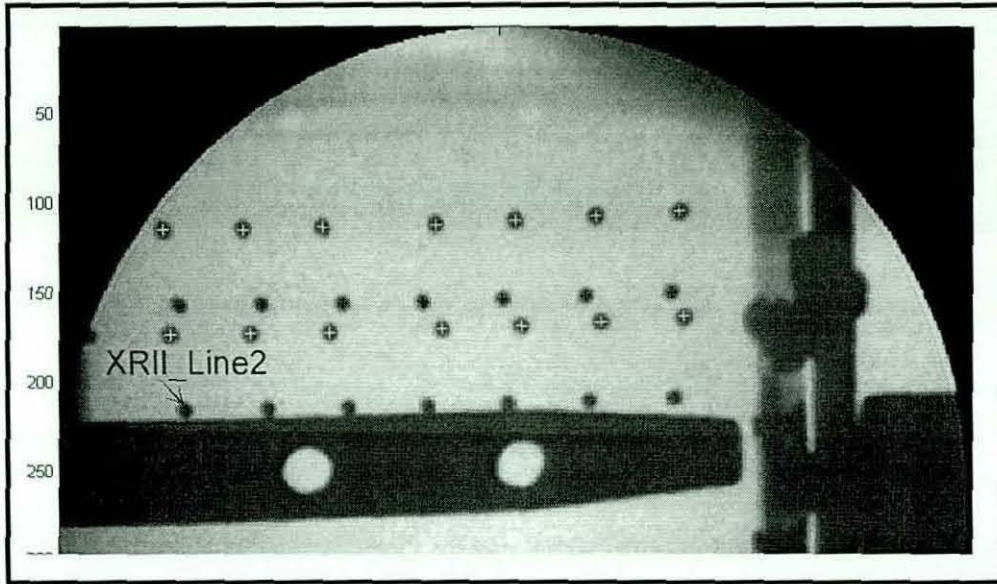


Figure 8-16 Fiducial recognition in Lateral view upper region when XR11_Line2 is in close proximity of the nail.

- Similarly, fiducial recognition was carried out in the lower region of the Lateral view image as shown in Figure 8-17.

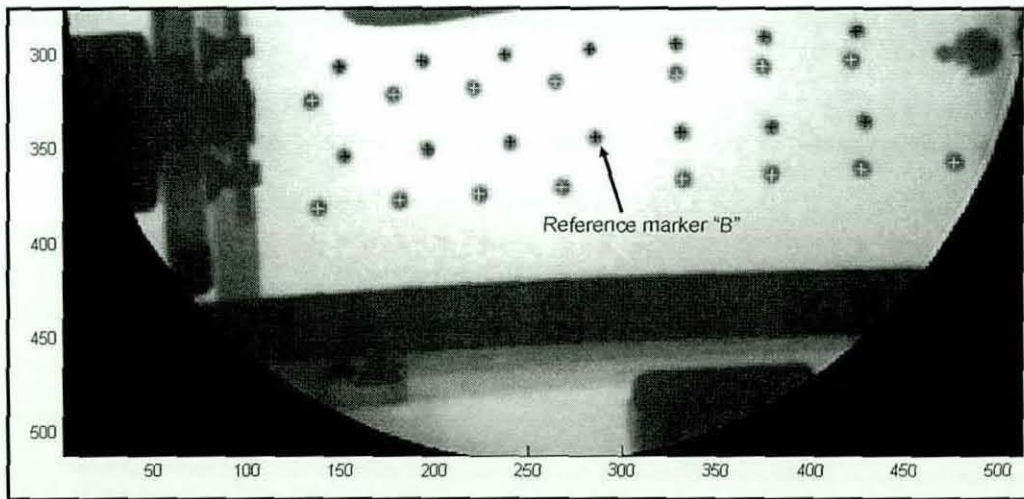


Figure 8-17 Fiducial recognition Lateral view lower region

Once fiducial recognition was completed, nail border detection (shown in Figure 8-18) and features that are used to determine the drilling trajectory i.e. the angle λ (shown in Figure 4-37) between the major axis of the distal hole's oval shaped projection and the nail axis or the dimensionless area of the distal hole projection, the target point (which is the intersection of the distal hole axis and the nail axis) and the

angle ϕ (shown in Figure 4-39) between the X-ray imaging axis and the nail axis were determined in similar manner as described in chapter 4 for Lateral view image.

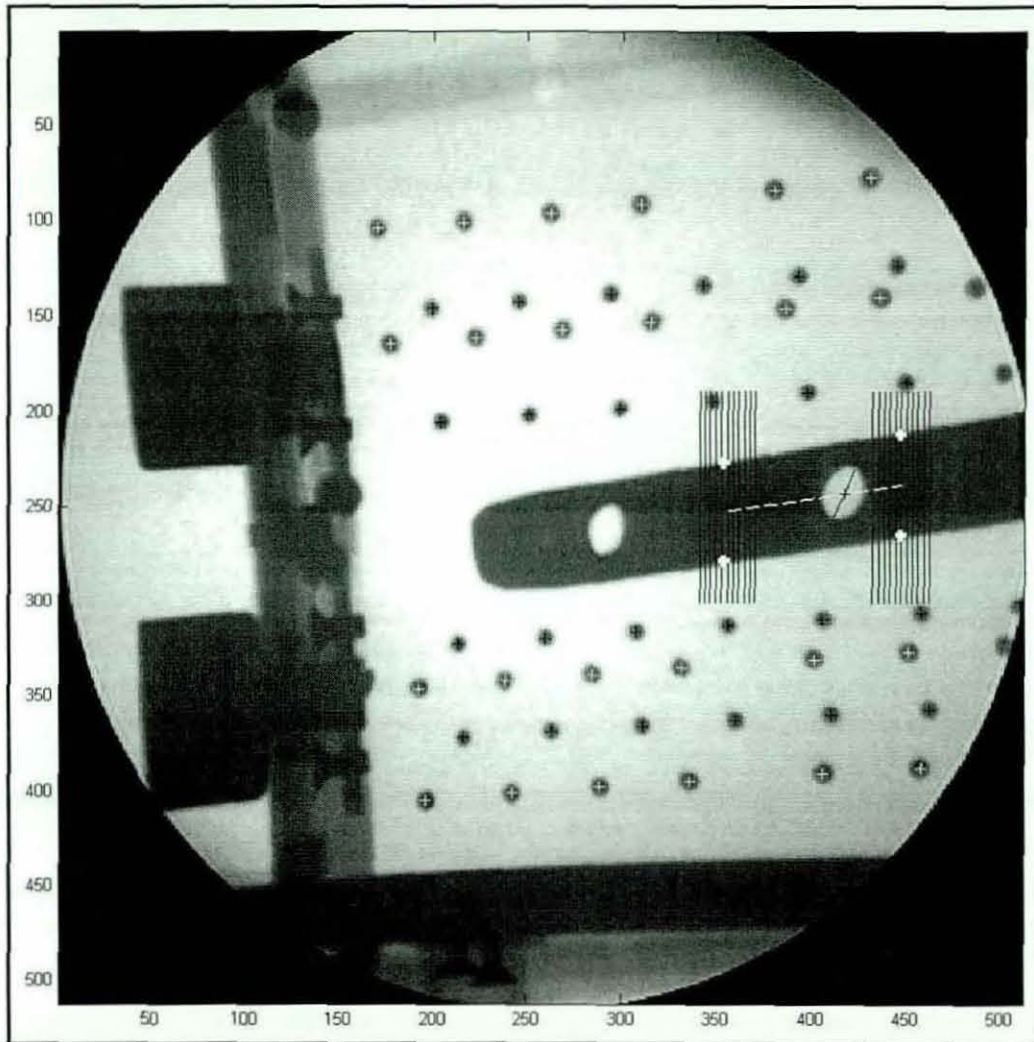


Figure 8-18 Lateral view image analysis

8.2 Image analysis protocol for AP calibration plates

Once an AP X-ray image (shown in Figure 8-19) was acquired, locations of all pixels with grey level values greater than zero was determined to get rid of the dark background i.e. cropping part of the image which is of interest i.e. contains calibration markers as shown in Figure 8-20.

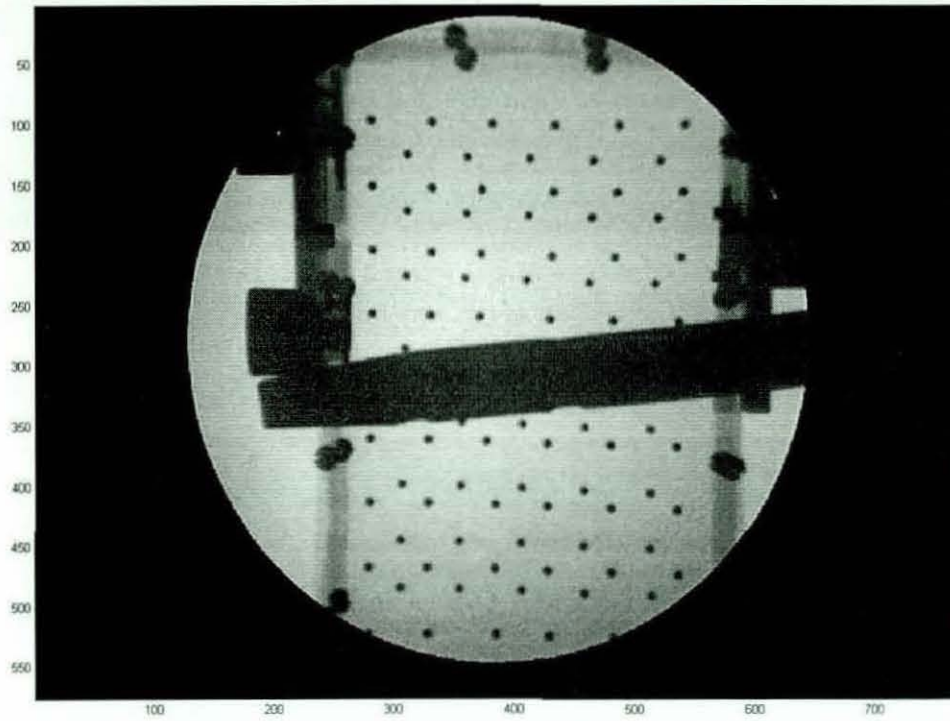


Figure 8-19 AP view image

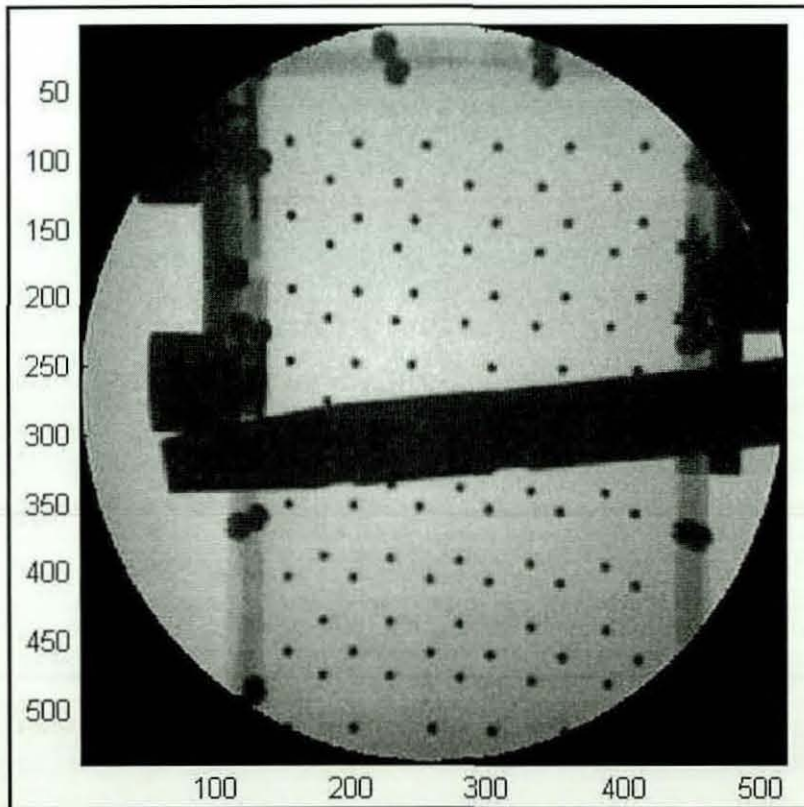


Figure 8-20 Cropped AP view image

At first location of the nail was determined in similar manner as described for Lateral view image. Based on the location of the nail, the fiducials on AP calibration plates were then divided into two regions i.e. upper and lower region as depicted by Figure 8-21 and Figure 8-22 respectively.

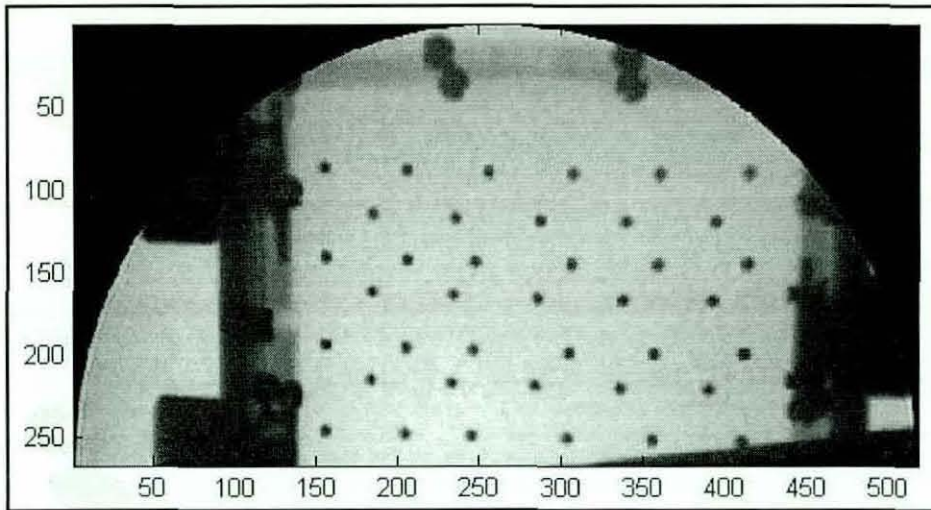


Figure 8-21 AP view upper region

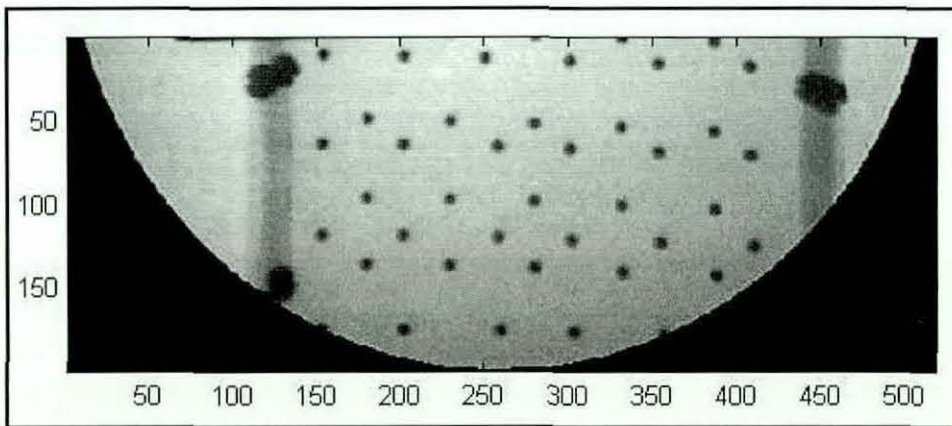


Figure 8-22 AP view lower region

Then in order to determine whether the acquired image is a useful image or not, checks similar to that made on the Lateral view image were carried out on the acquired image. The acquired image is not deemed suitable for processing if any of the checks fails and the user is asked to acquire image again until a useful image is obtain.

Since different horizontal spacings between Source plate fiducials was used for unique identification of each fiducial. The aim was therefore to find line of fiducials

belonging to the AP Source plate with unique horizontal spacing. For this purpose, search was made from upper most visible line in the image and going downwards until the aim was achieved. This was accomplished as follows:

- At first thresholding was applied to binarize the image, the binary image was then inverted, shown in Figure 8-14, so that fiducials can be classified as objects. Object properties such as area and circularity were then used to identify all visible fiducials.
- The respective bounding box of all visible fiducials are then analysed to establish initial starting point i.e. upper most left hand side fiducial in upper region (shown in Figure 8-23).

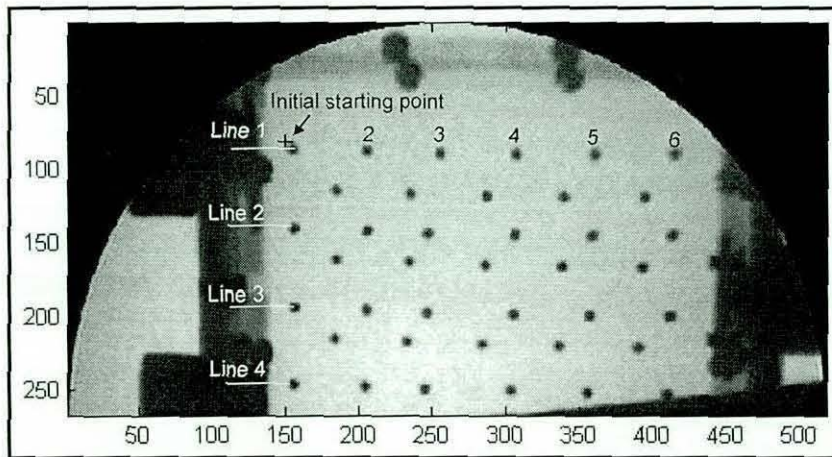


Figure 8-23 Selection of initial starting point

- In order to identify which calibration plate this fiducial belongs, the line containing the starting point fiducial was analysed to determine number of visible fiducials along this line. As presence of six fiducials along the line will indicate that starting point fiducial belongs to the AP Source plate (as in Figure 8-23). However, if there are five or fewer than five fiducials are present (shown in Figure 8-24) than this line can belong to either Source or XRII plate. In such cases, horizontal spacing between consecutive fiducials along a line was determined until an “unusual transition” in horizontal spacing was found as shown in Figure 8-24. The extreme left hand side fiducial of that line was then chosen as starting point.

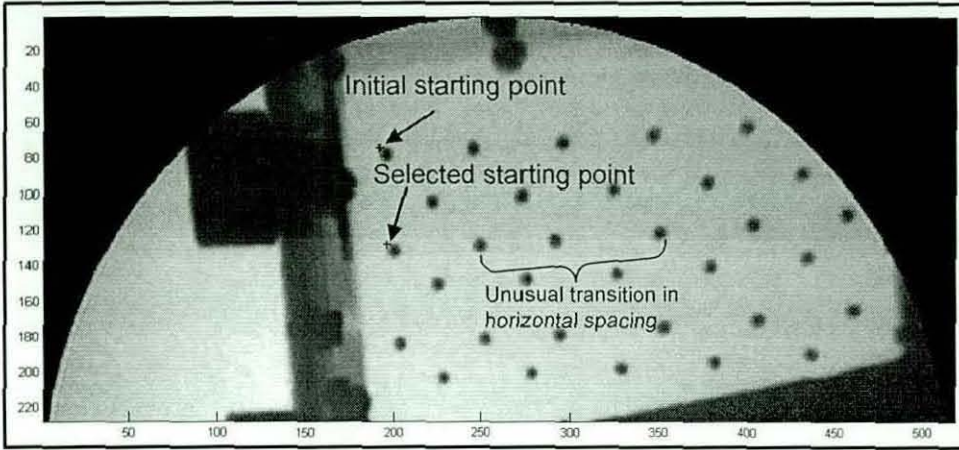


Figure 8-24 Selection of starting point

- Once starting point on the AP Source plate is selected, it needs to be determine which line of the Source plate this starting point belongs to. For this purpose at first horizontal spacing between consecutive fiducials along the line containing starting point was determined. If no “unusual transition” in horizontal spacing was found (as in case of Figure 8-23), then it was classified as Line 1 of the Source plate (refer Figure 8-23). However, if an “unusual transition” in horizontal spacing was found (as in Figure 8-24) then it can either be Line 2, 3 or 4 as these lines have similar fiducial pattern. In such case, horizontal spacing between consecutive fiducials along lines lying immediately above and below the selected line (i.e. line containing the selected stating point) was analysed to distinguish between line 2, 3, and 4 as shown in Figure 8-25. For example, for Figure 8-24 when line lying immediately above the selected line was analysed, no unusual transition in horizontal spacing was found which indicates that the selected line is line 2 of the Source plate.

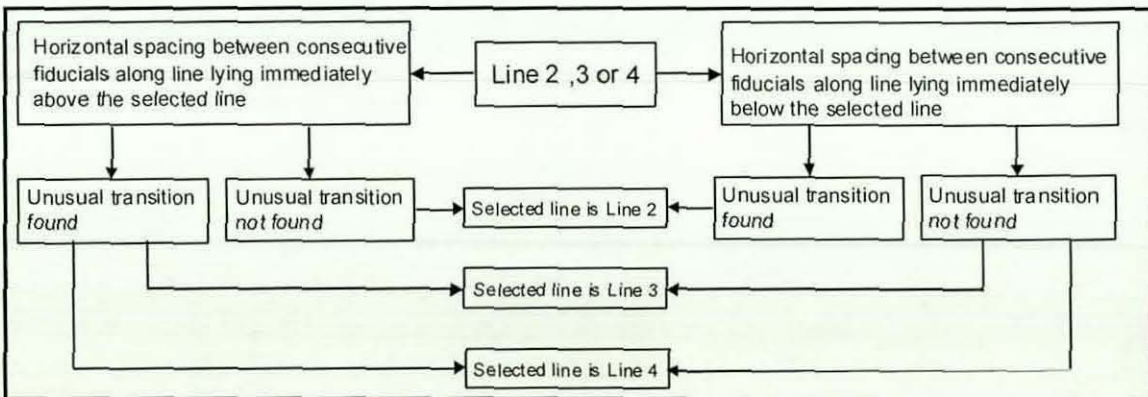


Figure 8-25 Distinction between line 2, 3 or 4 of Source plate

- Once the line containing the starting point on the Source plate was identified, central fiducial of that line was determined. The program uses this information to establish central fiducial along each line. Now fiducial recognition along each line was accomplished (as shown in Figure 8-26) by dividing image into sub-regions and each processing each fiducial individually while scanning from central fiducial of each line to the left and right of the image. Once fiducial recognition was completed, nail border detection (shown in Figure 8-26) was carried out in similar manner as described in chapter 4 for the AP view image.

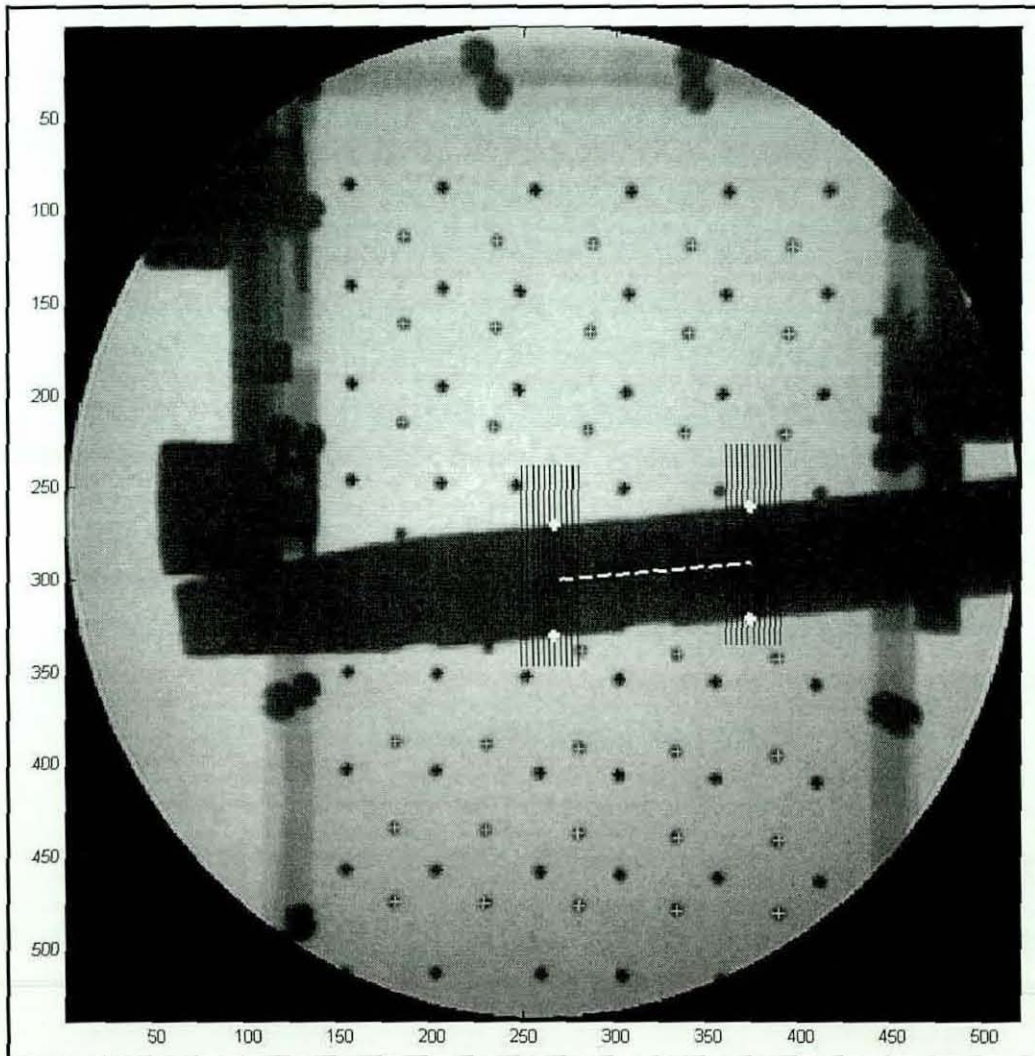


Figure 8-26 AP view image analysis with starting point chosen in upper region

- However if distinction can not be made between line 2,3 or 4 due to line immediately above and/or below the selected line being invisible due to presence

of nail or positioning of the calibration frame with respect to C-arm as shown in Figure 8-27.

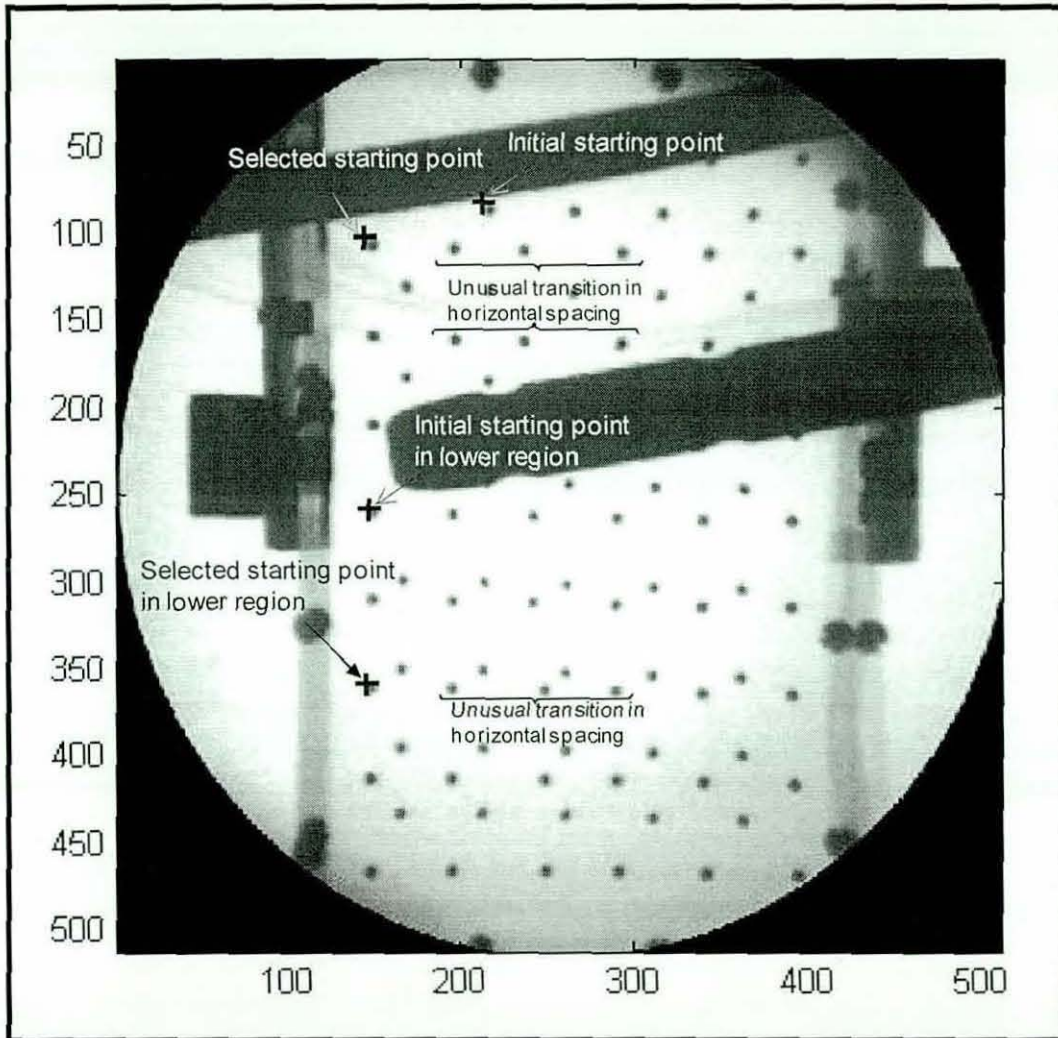


Figure 8-27 Selection of starting point from lower region.

For example, in Figure 8-27 initial starting point is chosen on XRII plate, however then as described earlier a starting point was established on Source plate as shown in Figure 8-27. The starting point was selected along a line with unusual transition; however distinction can not be made whether it is line 3 or 4 as line immediately below it also has unusual transition, whereas line immediately above this line is invisible. In such case, lower region of the image was analysed to establish the starting point (shown in Figure 8-27). At first, upper left most fiducial was chosen as an initial starting point. Then horizontal spacing between consecutive fiducials along each line was determined until a line with unusual transition in horizontal spacings

was found. Unique identification of Source plate line was then obtained by carrying out checks similar to those of described above.

Once unique identification of Source plate line was obtained rest of the AP image analysis (shown in Figure 8-28) carried out in similar manner as described above.

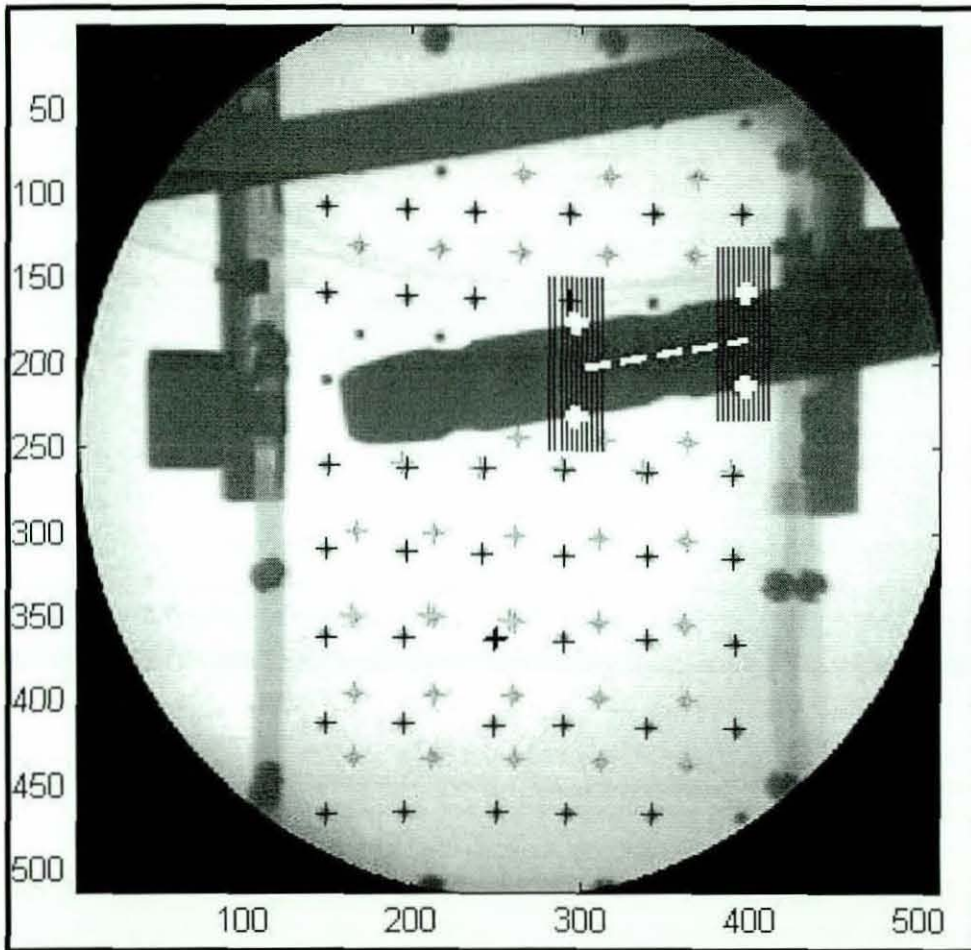


Figure 8-28 AP view image analysis with starting point chosen in lower region.

8.3 Accuracy evaluation of machine vision system using proposed calibration frame

Accuracy evaluation of the machine vision system for proposed calibration frame was carried out using theodolite measurement in similar manner as described for Γ calibration frame in chapter 6. During laboratory trials, in order to cover the range of intramedullary nails used during distal locking procedure two cylindrical nails of 14mm and 11mm diameter containing two distal holes of 7mm and 5.3mm diameter

respectively were used in conjunction with specially designed test rig (shown in Figure 8-29).

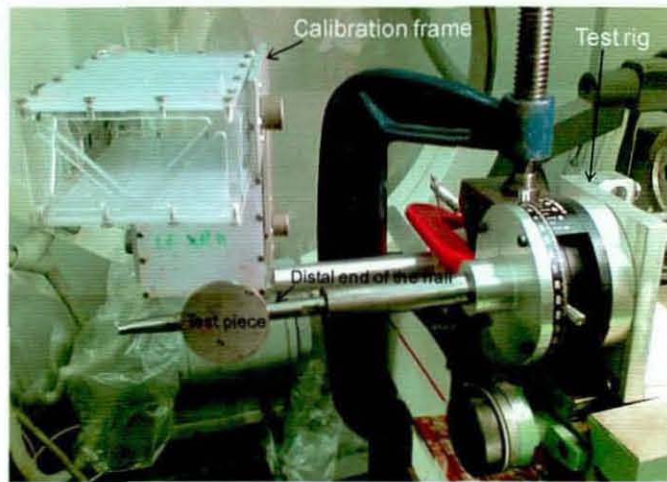


Figure 8-29 Nail and calibration frame set-up during laboratory trials.

For theodolite measurement, two *Sokisha DT5* theodolites, with single frame attachment, were used as shown in Figure 8-30.

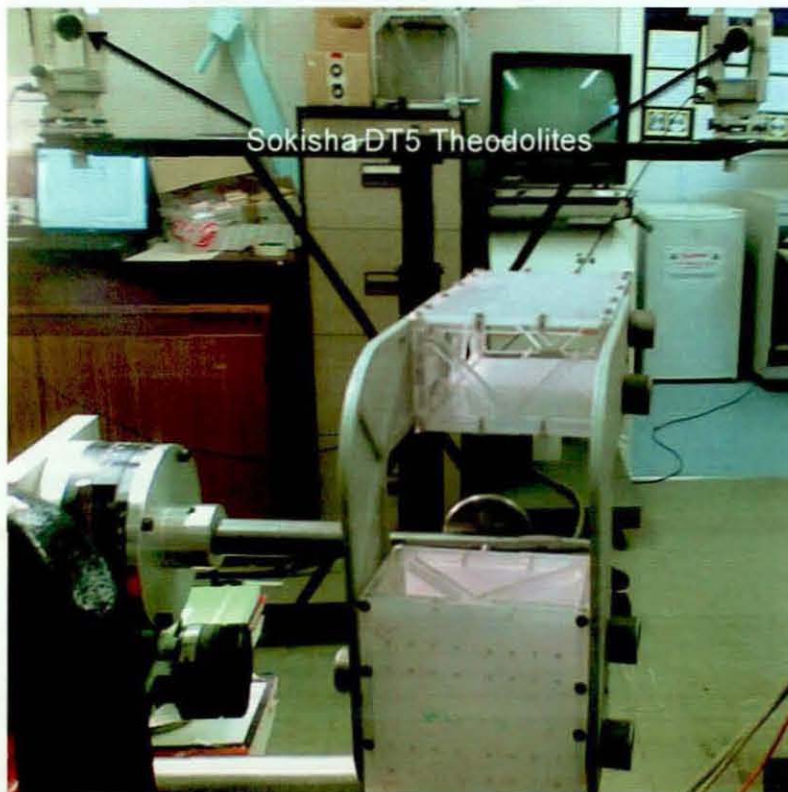
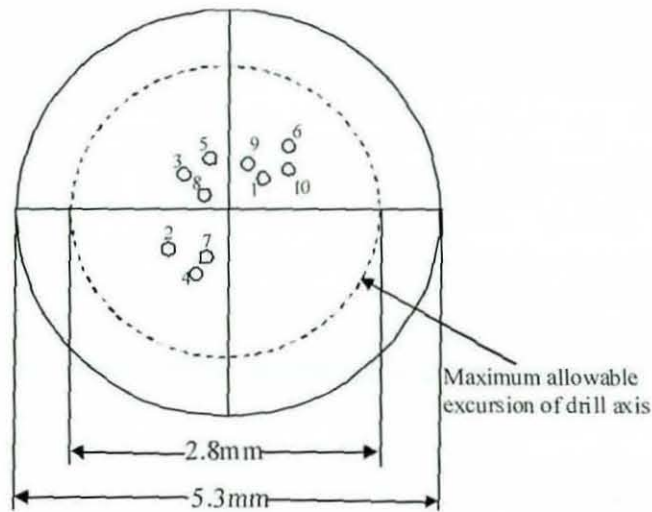
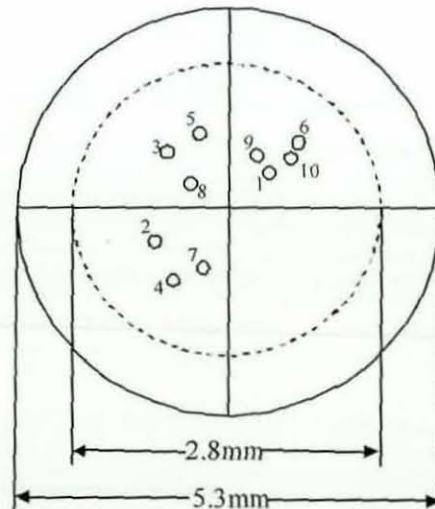


Figure 8-30 Theodolite set-up for optical measurement during laboratory trials.

The results obtained for small cylindrical nail (i.e. nail with nail diameter of 11mm and distal hole diameter of 5.3mm) from laboratory trials are summarized in Figure 8-31. The corresponding numbers in Figure 8-31(a) and Figure 8-31(b) represent the entry and exit points respectively for the various drilling trajectories. Analysis showed that a mean positional error of 0.75mm (worst case being 1.10 mm, as depicted by trajectory 6) and mean angular error of 0.92° (worst case being 1.22° , as depicted by trajectory 4) were obtained. These values were considered acceptable for inserting a guide wire of 2.5mm diameter into the distal locking hole of 5.3mm diameter and the subsequent screw insertion.



(a) Entry point for drilling trajectory at the distal locking hole



(b) Exit point for drilling trajectory at the distal locking hole

Figure 8-31 Results obtained for small cylindrical nail during accuracy evaluation of the machine vision system.

The results obtained for large cylindrical nail (i.e. nail with nail diameter of 14mm and distal hole diameter of 7mm) from laboratory trials are summarized in Figure 8-32. The corresponding numbers in Figure 8-32(a) and Figure 8-32(b) represent the entry and exit points respectively for the various drilling trajectories. Analysis showed that a mean positional error of 0.68mm (worst case being 1.02 mm, as depicted by trajectory 3) and mean angular error of 0.90° (worst case being 1.17° , as depicted by trajectory 4) were obtained. These values were considered acceptable for inserting a guide wire of 2.5mm diameter into the distal locking hole of 7mm diameter and the subsequent screw insertion.

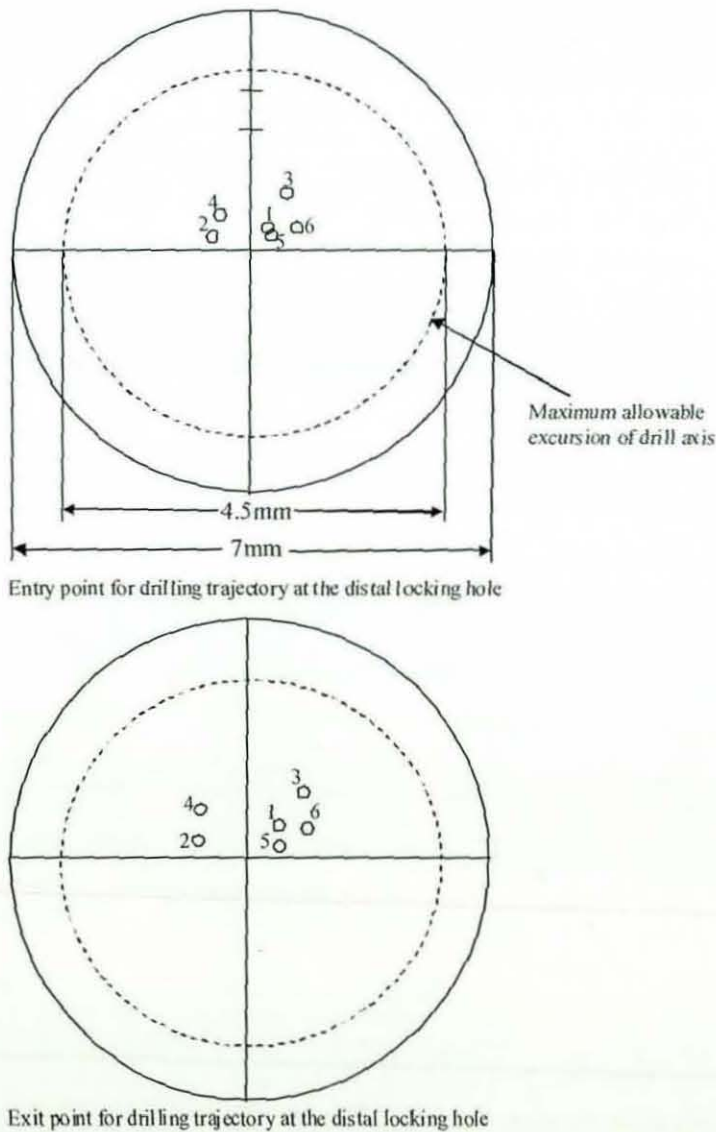


Figure 8-32 Results obtained for large cylindrical nail during accuracy evaluation of the machine vision system.

8.4 Robustness evaluation of Machine vision system for clinical use

Having established the required accuracy for successful drilling of distal locking hole during laboratory trials, more realistic trials using flesh covered sheep femur were conducted in order to evaluate the robustness of the machine vision system during clinical use. For this purpose, distal end of an intramedullary nail of 11mm diameter with distal locking hole diameter 5.3mm, was inserted into a sheep femoral canal as shown in Figure 8-33.

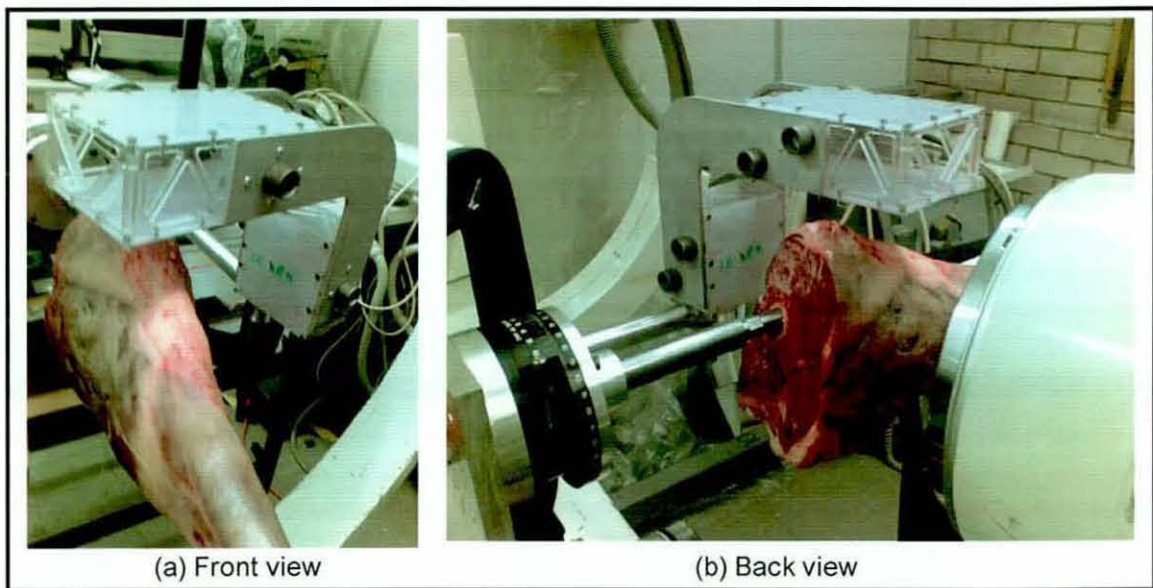


Figure 8-33 Insertion of distal end of the nail into sheep femur.

It can be seen from Figure 8-34 that introduction of flesh-covered femur in X-ray image has influenced the image contrast with the edges of the image considerably brighter than the rest of the image due to geometry of the femur, which is thicker towards the middle.

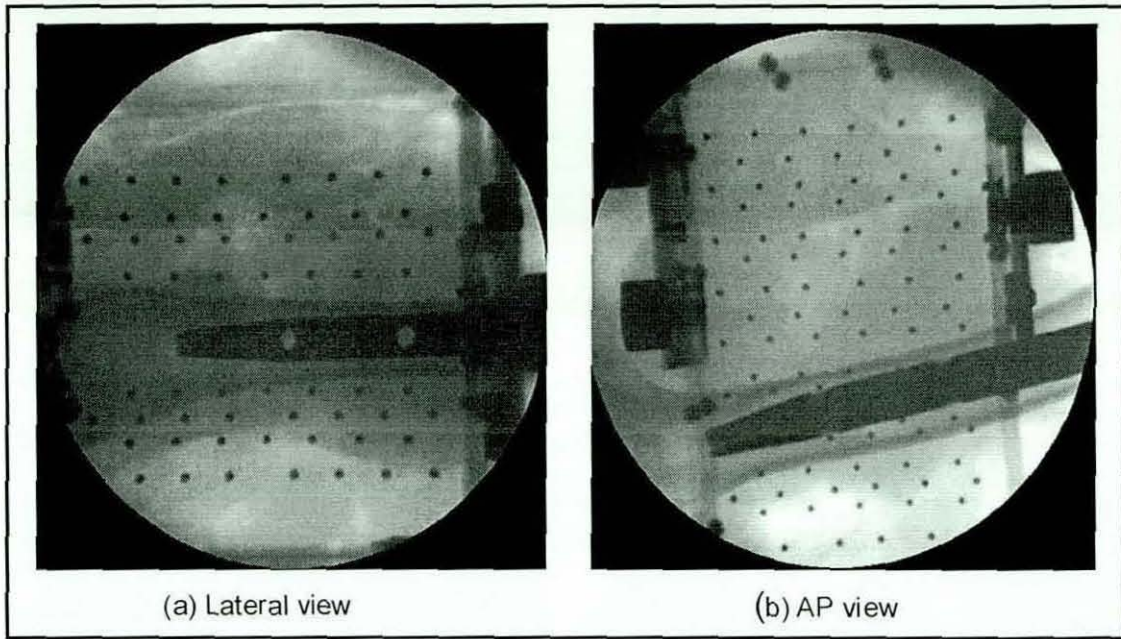


Figure 8-34 X-ray images acquired with flesh-covered sheep femur.

Therefore, in order to minimize influence of contrast variations across the image, slight modification was made in image analysis protocol for both Lateral and AP view image. This modification is discussed below.

After image acquisition, once the X-ray image was divided into two regions (i.e. upper and lower regions) based on the location of the nail as described in section 8.1 and 8.2 for Lateral and AP view image respectively), each region was further cropped to only include area of the calibration plate covered by the fiducials. For upper region this was accomplished by analysing the bounding boxes of all fiducials and determining the location of upper most fiducial and fiducials on the extreme right and left hand side of the upper region. This information was then used for further cropping of the image, for example as shown in Figure 8-35 for the AP view image.

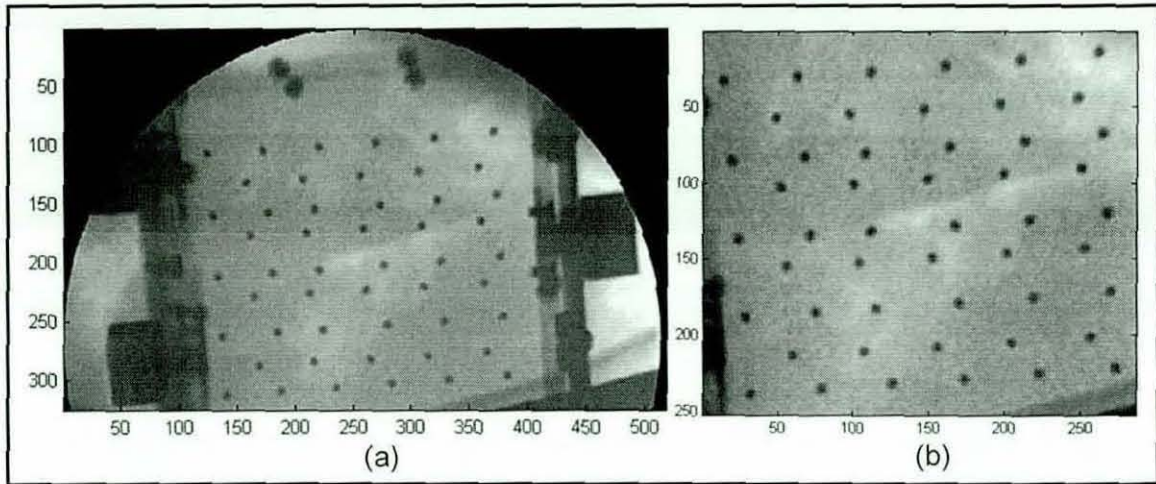


Figure 8-35 (a) Initially cropped upper region (b) Further cropping of the upper region

Similarly, for lower region, location of the lower most fiducial and fiducials on the extreme right and left hand side of the lower region was determined. This information was then used for further cropping of the image, for example as shown in Figure 8-36 for the Lateral view image.

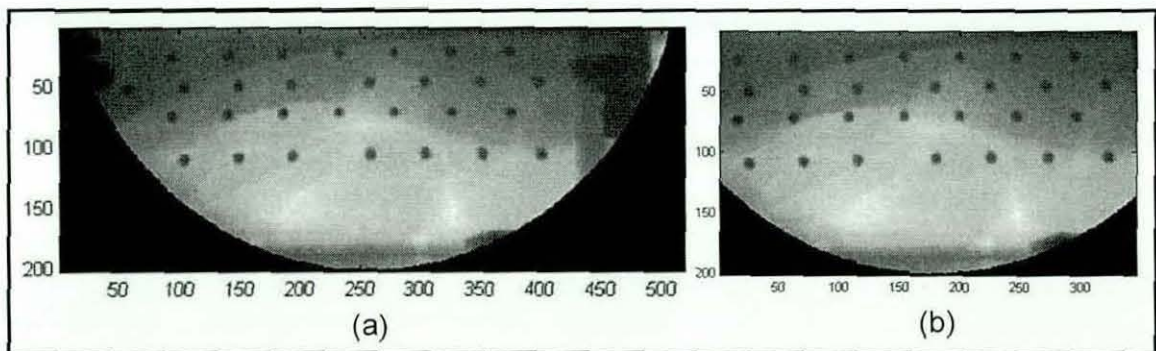


Figure 8-36 (a) Initially cropped lower region (b) Further cropping of the lower region.

Rest of the image analysis were carried out in similar fashion as described in section 8.1 and 8.2 for Lateral and AP view image respectively. Figure 8-37 and Figure 8-38 depicts the image analysis performed on Lateral and AP view X-ray images respectively.

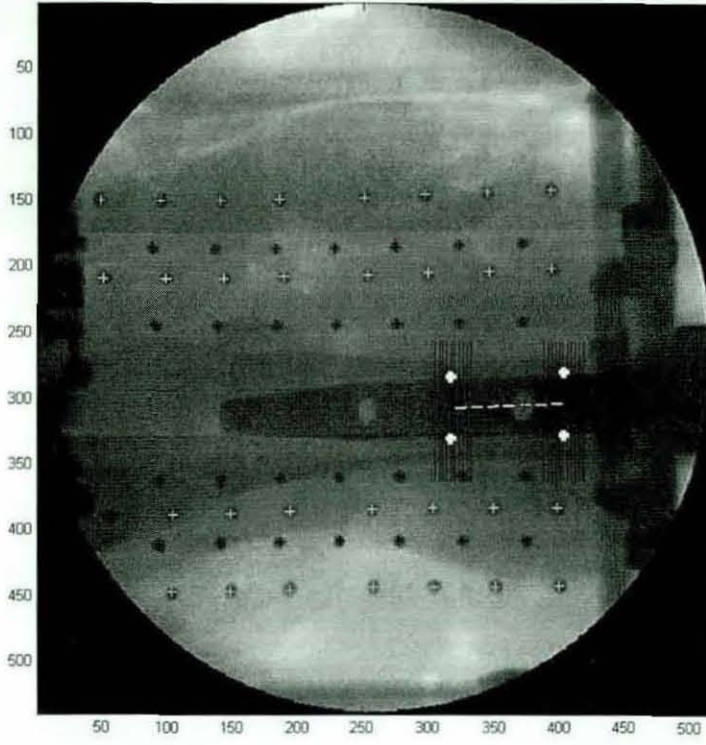


Figure 8-37 Image analysis on the Lateral view image.

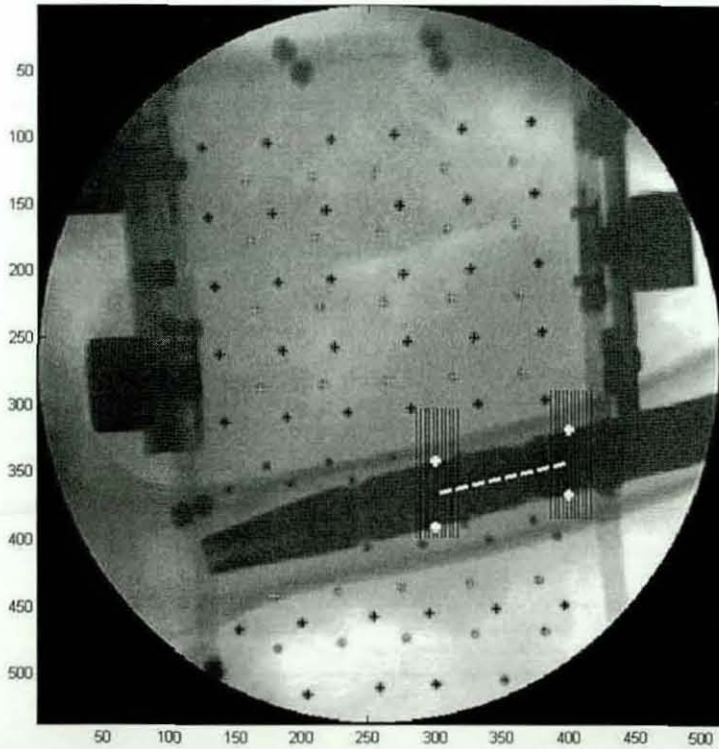


Figure 8-38 Image analysis on the AP view image.

Results from laboratory tests (summarized in Figure 8-39) showed that a mean positional error of 0.92mm (worst case being 1.17 mm, as depicted by trajectory 3) and mean angular error of 0.98° (worst case being 1.18° , as depicted by trajectory 6) were obtained. These values were considered acceptable for successful drilling of distal locking hole and the subsequent screw insertion as shown in Figure 8-39. It is also evident from Figure 8-39 that almost similar accuracies to those shown in Figure 8-32 and Figure 8-31 are obtained when the nail is inserted in a flesh-covered sheep femur, hence shows the robustness of the machine vision system used and is an indication of its suitability for clinical application.

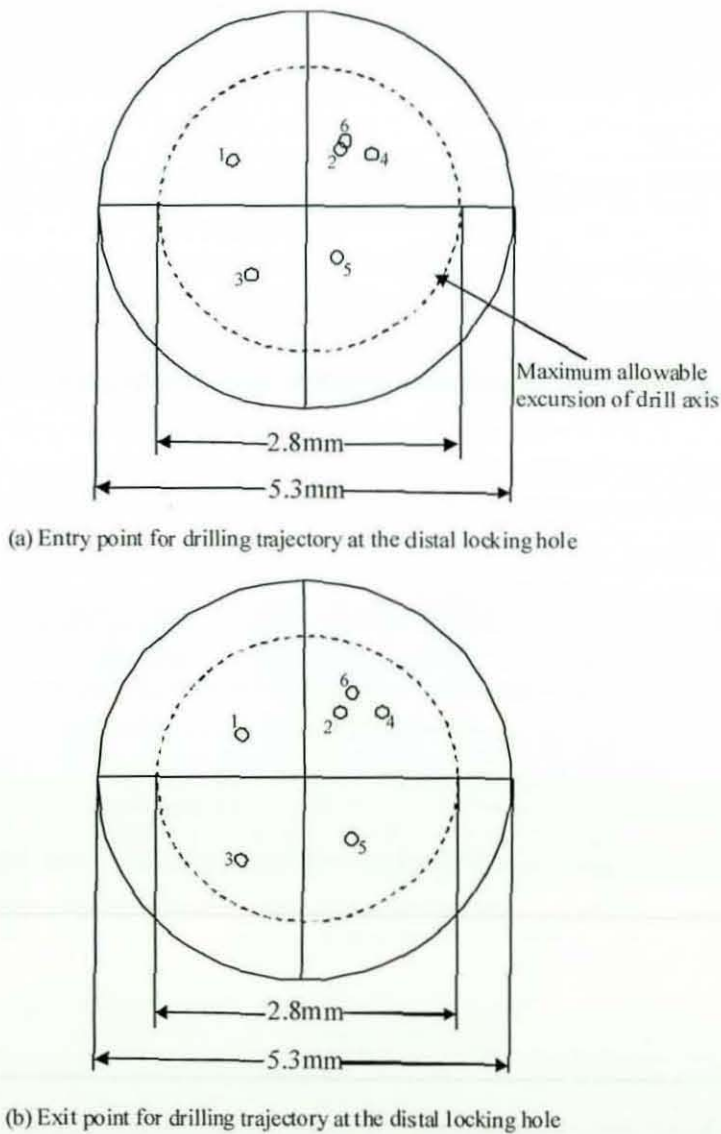


Figure 8-39 Results obtained during accuracy evaluation of the machine vision system for clinical use.

Phillips *et al* [116] at Hull University have reported a mean positional error and a mean angular error within 0.3mm and 0.2° respectively. Although the accuracy achieved by the Hull system is better compared to the LOAS results, the image analysis protocol and system set-up are user-dependent. The system requires the surgeon (or user) to manually select some features on the intraoperative Lateral and AP images, and most importantly it requires optical tracking equipment which results in a more involved and time consuming set-up. The LOAS reduced accuracy, which is acceptable for distal locking of intramedullary nails, is a result of a simplified (practical) system which involves the use of a Γ shaped calibration frame instead of a frame which fits around the leg. That is, the increased errors are mainly due to the adopted extrapolation technique instead of the preferred, but practically difficult to implement, interpolation technique. It should also be noted that image intensifier used during this research for acquiring X-ray images during laboratory trials is fairly old (around 15 years old), therefore it presented an ideal opportunity to evaluate the robustness of the system.

8.5 Summary

At the beginning of this chapter machine vision system developed for proposed calibration frame is described in detail. Then, in order to evaluate the robustness of the machine vision system using proposed calibration frame during clinical use, realistic trials using flesh-covered sheep femur were conducted. For this purpose, distal end of an intramedullary nail was inserted into a sheep femoral canal. Based on the results obtained from the laboratory trials presented in this chapter, it has been shown that the proposed system provides the accuracy required for successful insertion of distal locking screws. Therefore, the outcome of the procedure will be improved as the system has the potential to reduce the occurrence of screw misplacement, as demonstrated by Figure 8-32, Figure 8-31 and Figure 8-39.

9 Conclusions and Future Work

9.1 Conclusions

In order to provide clinically acceptable solutions to the research problems identified in Section 1.4 the current thesis has proposed the use of an Automated X-ray machine vision system based upon X-ray photogrammetry principles. This system minimises the changes to current surgical procedures and takes into account the physical constraints of the operating theatre, adopting a novel approach based on the use of a calibration frame in conjunction with offline modelling of the nail. It should be noted that photogrammetric reconstruction is usually a time consuming process, therefore the key to the successful implementation of the proposed system is the acquisition and quick analysis of intraoperative X-ray images.

Having inherited a digital X-ray photogrammetry system (LOAS), the calibration frame design and software modules have subsequently been developed in order to meet the clinical requirements of the osteosynthesis procedure targeted in this thesis. Although this research was restricted to *in vitro* laboratory trials, clinical requirements such as anatomical compatibility and compliance with surgical sterility have been fully addressed. The following section provides an evaluation of the main stages of this thesis.

9.1.1 Modelling of the IMN

Look-up tables (LUTs) are used to determine the rotation of the nail about its long axis θ . These LUTs are obtained by off-line CAD modelling of nails of different shapes and dimensions. These LUTs were used in conjunction with machine vision system to determine the drilling trajectory of the distal locking holes.

Accuracy evaluation of the nail model in the laboratory was carried out using a specially designed test rig. This test rig was used to physically simulate different nail

orientations using combinations of angles ϕ and θ . Using the test-rig the nail was rotated by a known angle θ , so that θ values obtained by using the nail model in conjunction with the X-ray image analysis can be compared with the true value of θ . Analysis has shown that the rotation θ of the nail was predicted with a mean accuracy of 0.22° (worst case being 0.49°). The adopted off-line modelling of the nail to generate look-up tables reduces the length of time for the computation of the drilling trajectory and thus has the potential for reducing the overall time required for the surgical procedure. Furthermore, this approach allows modelling of any shape of intramedullary nail accurately; therefore nails from different manufacturers can be modelled.

9.1.2 Automated machine vision system

In order to perform the photogrammetric reconstruction process, two sets of accurate input data are required, i.e. the real-world (millimetres) coordinates of the fiducial markers on the calibration frame, and their corresponding image (pixels) coordinates. Given the obvious time constraints associated with an intraoperative application, in particular the need to avoid prolonging the surgical procedure, the extraction of this image data must be performed with the minimum possible level of user intervention. The image analysis protocol has therefore been fully automated to make the vision system user independent and very efficient in terms of time taken to determine the drilling trajectory. Analysis has shown that once Lateral and AP x-ray image acquisition is performed, around 20 seconds are taken for computation of drilling trajectory of the distal locking hole. This time is considerably smaller than time taken using traditional free hand technique using perfect circle approach, which ranges between 1.61mins to 4.64 mins as reported by Sanjeev *et al* [13], Coetzee *et al* [89] and Muller *et al* [93] respectively.

A potential problem with the LOAS is the appearance of one or more of the opaque markers (embedded in the calibration frame plates) within or on the edge of the oval shaped distal hole projection. An automatic technique has been implemented which removes the effect of such markers in computing the area of the oval and the angle between the major axis of the oval and the nail axis, both of these measurements being necessary for derivation of the drilling trajectory. This technique has

successfully eliminated the need for repositioning the calibration frame or using a smaller number of opaque markers.

A graphical user interface (GUI) has been developed that assists and updates the user throughout the procedure. It has also been shown that the automated vision system is very robust in the presence of variable noise and contrast in the X-ray images and in terms of variable magnification.

9.1.3 Design of a robust calibration frame

For robustness purposes the existing Γ calibration frame has been redesigned. At first an optimal number of fiducials and their spatial distribution necessary to provide required accuracy of 1 mm and 1° are determined using existing X-ray images. During the second stage dimensions of the calibration frame that will make it suitable to be used for the target population (middle 95% of the population) were determined. To accomplish this task, cross sectional images of the upper leg and anthropometric data were used. These dimensions were then adjusted in light of recommendations made by orthopaedic surgeons to take into account worst cases of swelling. Initially based on different physiologies two calibration frames are proposed namely "Medium" and "Large" to accommodate the middle 50% and 95% population respectively.

Complexity of the fiducial recognition software during image analysis is directly related to the image being scanned and therefore, from the software viewpoint, a carefully designed fiducial pattern can greatly simplify the image analysis process. Keeping in mind that there is a need to uniquely identify each fiducial marker appearing within the field-of-view, reference markers with unique horizontal and/or vertical spacings are used. Initially a search of reference fiducial markers is therefore performed based on the spacings between consecutive fiducial markers. Identifying the locations of these reference markers allows the "predicted" locations of the remaining fiducial markers to be calculated.

9.1.4 Computation of drilling trajectory

Theodolites were used for accuracy evaluation of the LOAS during laboratory trials. In order to cover the wide range of possible nail orientations likely to be encountered

during the surgical procedure, a specially designed test rig, shown in Figure 6.3, was used in laboratory trials to simulate different rotations θ of the nail about its own axis. This was carried out with the nail at different orientations ϕ with respect to the X-ray imaging axis.

Having established the required accuracy for successful drilling of a distal locking hole during laboratory trials (see Section 6.2 and Section 8.3), more realistic trials using a flesh covered sheep femur were conducted in order to evaluate the robustness of LOAS in clinical environment. Analysis showed that a mean positional error of 0.92mm and a mean angular error of 0.98° were obtained in planning the drilling trajectory for the insertion of distal locking screws for different orientations of the nail. These values are considered acceptable for successful drilling of distal locking hole and the subsequent screw insertion

In summary, aims of this thesis outlined in Section 1.5 have been met, as the LOAS has the potential of reducing significantly the X-ray irradiation during distal locking procedures, while the outcome of the procedure will be improved as the system has the potential to reduce the occurrence of screw misplacement, as demonstrated in Chapter 6 and Chapter 8 respectively. Additionally the LOAS has the potential to reduce the surgical time and to make the procedure more consistent, irrespective of variations in the skill levels and experience of clinical staff.

9.2 Contributions

- The adopted off-line modelling of the nail to generate look-up tables reduces the length of time for the computation of the drilling trajectory and thus has the potential for reducing the overall time required for the surgical procedure.
- The outcome of the procedure will be improved as the system has the potential to reduce the occurrence of screw misplacement, as demonstrated by results from laboratory trials.
- The vision system is user-independent as all the steps involved during image analysis are fully automated, thereby making outcome of the procedure more consistent.

- It has also been shown that the LOAS is very robust in the presence of variable noise and contrast in the X-ray images and in terms of variable magnification, thus making it suitable for clinical use.
- The newly designed calibration frame can accommodate wide range of patient physiologies.

9.3 Future work

In the light of the results obtained from *in vitro* laboratory trials following recommendations are made.

9.3.1 Proposed Calibration frame configurations

The calibration frame used during laboratory trials employs a spacing of 50 mm between the XRII and Source plates for both Lateral and AP views. In an attempt to improve the overall accuracy of the system, an increment in the spacing between the XRII and Source calibration plate can be explored as, theoretically, increased plate separation should result in better accuracy. This is because a given image point error in pixels yields a calibration plate intersection point error in millimetres, depending on image magnification, as described in Section 3.5.1. An increment in plate separation will result in the Source plate being closer to the X-ray source causing an increase in the pixel/mm ratio. Hence an increase in the plate separation should decrease the reconstruction errors associated with the Source plate, whereas errors associated with the XRII plate remain the same due to the location of the XRII plate being unchanged.

It should also be noted that in order to obtain better reconstruction accuracy, more fiducials should be visible in the X-ray image *i.e.* to avoid fiducial occlusion, as shown in Figure 3-38. To accomplish this task during image acquisition it is essential to obtain angular alignment of the C-arm X-ray imaging axis with planes of the calibration frame *i.e.* X-ray imaging being nearly at 90° to the calibration frame. It can be seen from Figure 4-2 that, for the AP view image acquisition, the X-ray image intensifier lies in close proximity to the AP block, thereby making it relatively easier to obtain the angular alignment between the X-ray imaging axis and the calibration

frame. Conversely for the Lateral view image acquisition shown in Figure 4-1, due to the design of the calibration frame, the X-ray image intensifier lies slightly away from the Lateral block, thereby making it more difficult to obtain angular alignment between the X-ray imaging axis and the calibration frame.

For this purpose, the modular calibration frame (shown in Figure 7-30) can be used to evaluate the influence of different spacings between XRII and Source plates on the overall system accuracy. In the light of the above discussion, the following modular calibration frame configurations, shown in Figure 9-1 are proposed.

- a. (Lat-50, AP-100) implies plate spacing of 50 mm and 100 mm for Lateral and AP block respectively.
- b. Standard (Lat-100, AP-100) implies plate spacing (spacing between XRII and Source plate) of 100 mm for both Lateral and AP blocks.

As described earlier, it is difficult to obtain angular alignment between the C-arm X-ray imaging axis with planes of the calibration frame i.e. X-ray imaging being nearly at 90° to the calibration frame during the Lateral image acquisition in comparison to the AP image acquisition. Therefore, excessive repositioning of the calibration frame may be required to acquire the desired Lateral X-ray image if 100mm spacing between calibration plates is used. Therefore the configuration of (Lat-50, AP-100) is proposed as a compromise for ease of use.

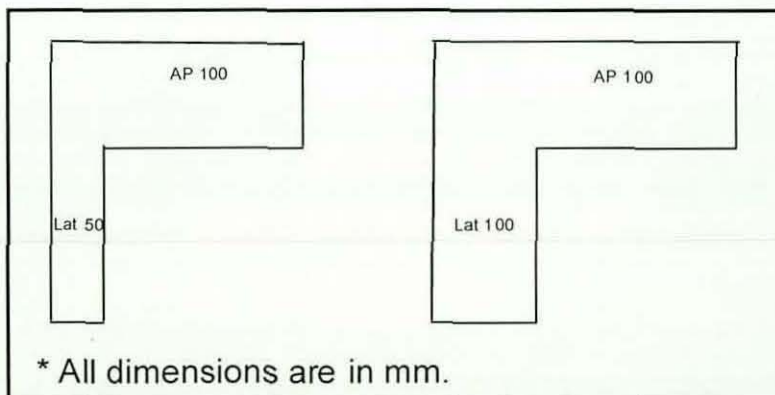


Figure 9-1 Proposed modular calibration frame configurations.

It should be noted that the use of a modular calibration frame is ideally suited to laboratory trials; however this design is not suitable for clinical use as over time,

frequent attachment and detachment of the Lateral and AP blocks can result in a change in the relative positions and orientations of the blocks i.e. accurate knowledge of the fiducials on the calibration frame may be lost, reducing the overall system accuracy. Furthermore, assembling of the modular calibration frame using attachment thumb screws, alignment rods and Lateral/AP blocks is *time consuming and difficult* for operating theatre staff. Therefore, in order to achieve consistent accuracy and ease of use, a solid calibration frame (i.e. the Lateral and AP blocks permanently fixed to the frame) is proposed for clinical use.

9.3.2 LOAS Commercialization

Commercialising the LOAS is a challenge and could be the emphasis of any further work on this project. To accomplish this task the following issues need to be addressed:

- The automatic machine vision system has been developed in a Matlab environment, which is ideal for development purposes, however it is not suitable for the commercial application purposes as a Matlab license is required. Hence conversion of Matlab coding to Visual C++/Visual Basic is desirable to make LOAS a platform-independent application. For this purpose the author has made detailed flowcharts of the Matlab software modules (see **APPENDIX E**), which can be used to accomplish this task.
- Accurate positioning of calibration markers is of paramount importance to achieve the required accuracy. Therefore, in order to make the LOAS more robust and cost-effective it is desirable to develop an automated calibration technique that can be used to check the positioning of calibration markers before each surgical use against their specified location, thereby taking into account any misplacement of calibration markers, without causing any additional time. This check can be carried out to ensure that the calibration frame is correct prior to clinical use.

Other osteosynthesis applications

In addition to the distal femur locking procedure, LOAS is also applicable to other osteosynthesis procedures involving the extremities. Therefore, application of the

system could be expanded to include other surgical procedures such as tibial distal locking and humeral shaft fracture treatment.

References

1. **H. Gray**, *Gray's Anatomy : The anatomical basis of clinical practice*. 39th ed, ed. S. Standring. 2005: Elsevier Churchill Livingstone.
2. **R. Bucholz and A. Jones**, *Fractures of the shaft of the femur*. Journal of Bone and Joint Surgery (Am), 1991. **73**: p. 1561-1566.
3. **I. Browbank, K. Bouazza-Marouf and J. Schnabler**, *Robotic-assisted internal fixation of hip fractures: a fluoroscopy-based intraoperative registration technique*. Proc. Instn. Mech. Engrs, Part H, Journal of Engineering in Medicine, 2000. **214(H2)**: p. 165-179.
4. **J. Schnabler**, *Robotic assistance in Orthopaedic Surgery*. MSc Thesis, Supervised by Dr. K Bouazza Marouf, Loughborough University, 1997.
5. **M.J. Hochrainer**, *Repair of femoral shaft fractures, M.Sc Thesis*. 1997, Supervised by Dr K. Bouazza Marouf, Loughborough University,.
6. **K. Bouazza-Marouf, I. Browbank and JR. Hewit**, *Robotic-Assisted Invasive Surgery*. Journal of Mechatronics, 1996. **6(4)**: p. 381-387.
7. **K. Bouazza-Marouf, I. Browbank and J.R. Hewit**, *Robotic-assisted internal fixation of femoral fractures*. Proc. Instn. Mech. Engrs, Part H, Journal of Engineering in Medicine, 1995. **209 (H1)**: p. 51-58.
8. **D. Robert and B. George**, *Mercer's Orthopaedic Surgery*. 9th edition, 1996: Hodder Arnold Publication. (ISBN: 0340551631)
9. **J.J. Gartland**, *Fundamentals of Orthopaedics*. 4th ed. 1987: W B Saunders Co Philadelphia, PA, USA.
10. **G. Kuntcher**, *Die Marknagelung von Knochenbruchen*. Arch Klin Chir., 1940. **200**: p. 443-455.
11. **S. Weller**, *Internal fixation of fractures by intramedullary nailing. Introduction, historical review and present status*. Injury, 1993. **24(3)**: p. 1-6.
12. **R. Hofstetter, M. Slomczykowski, M. Sati and LP. Nolte**, *Fluoroscopy as an imaging means for computer assisted surgical navigation*. Computer Aided Surgery, 1999. **4(2)**: p. 65-76.

13. **S. Madan and C. Blakeway**, *Radiation exposure to surgeon and patient in intramedullary nailing of the lower limb*. *Injury*, 2002. **33**(8): p. 723-727.
14. **GM. Whatling and LD. Nokes**, *Literature review of current techniques for the insertion of distal screws into intramedullary locking nails*. *Injury*, 2006. **37**(2): p. 109-119.
15. **R. Sanders, K.J. Koval, T. DiPasquale, G. Schmelling, S. Stenzler and E. Ross**, *Exposure of the orthopaedic surgeon to radiation*. *J Bone Joint Surg Am.*, 1993. **75**: p. 952-953.
16. **B. Badman, L. Rill, B. Butkovich, M. Arreola and R. Griend**, *Radiation Exposure with Use of the Mini-C-Arm for Routine Orthopaedic Imaging Procedures*. *Journal of Bone and Joint Surgery (Am)*, 2005. **87**(1): p. 13-17.
17. **M.E. Miller, M.L. Davis, C.R. MacClean, J.G. Davis, B.L. Smith and J.R. Humphires**, *Radiation exposure and associated risk to operating room personnel during use of fluoroscopic guidance for selected orthopaedic surgical procedures*. *Journal of Bone and Joint Surgery (Am)*, 1983. **65**: p. 1-4.
18. **T. Pun, G. Guido and R. Osman**, *Image analysis and Computer vision in Medicine*. *Computerized Medical Imaging and Graphics*, 1994. **18**(2): p. 85-96.
19. **H. Yuehuei and R.A. Draughn**, *Mechanical Testing of Bone - Implant Interface.*, 1st edition. 2000: CRC Press LLC. (ISBN: 0849302668)
20. **A.G. Apley and L. Solomon**, *Concise system of Orthopaedics and fractures*. 1991: Butterworth-Heinemann Ltd.
21. **B. Eastwood, H.K. Biggs, T. Knutson and F.T. Editors: S.I. Rabin, A. Corces, D. Patel and C.J. Lavernia**. *Diaphyseal Femur Fractures*. www.emedicine.com 2006
22. **S.T. Canale**, *Campbell's Operative Orthopaedics, Third Volume*, 9th edition, 1998: Mosby-Year Book, Inc. (ISBN: 03023012409)
23. **A. Shezar, N. Rosenberg and M. Soudry**, *Technique for closed reduction of femoral shaft fracture using an external support device*. *Injury*, 2005. **36**(3): p. 450-453.
24. **A. Gaffey and M. Blakemore**, *Femoral shaft fractures*. *Trauma*, 2003. **5**(2): p. 103-115.
25. **C.K. Yiannakopoulos, A.D. Kanellopoulos, C. Apostolou, E. Antonogiannakis and D.S. Korres**, *Distal intramedullary nail interlocking:*

- the flag and grid technique*. Journal of Orthopaedic Trauma 2005. **19**(6): p. 407-411.
26. **C.J. Hindley, R.A. Evans, E.M. Holt and J.W. Metcalfe**, *Locked intramedullary nailing for recent lower limb fractures*. Injury, 1990. **21**(4): p. 239-244.
27. **R.A. Winquist**, *Locked femoral nailing*. The Journal of the American Academy of Orthopaedic Surgeons, 1993. **1**(2): p. 95-105.
28. **I. Kempf, A. Grosse and G.J. Beck** *Closed locked intramedullary nailing*. Bone Joint Surg Am., 1985. **67**(5): p. 709-720.
29. **R. G. Deshmukh, K. K. Lou, C. B. Neo, K. S. Yew, I. Rozman and J. George**, *A technique to obtain correct rotational alignment during closed locked intramedullary nailing of the femur*. Injury, 1998. **29**(3): p. 207-210.
30. **D.A. Wiss, W.W. Brien and W.B. Stetson**, *Interlocking nailing for treatment of segmental fractures of the femur*. Journal of Bone and Joint Surgery (Am), 1990. **72**: p. 724-728.
31. **P. Rokkanen, P. Slätis and E. Vanka**, *Closed or open intramedullary nailing of femoral shaft fractures?* The Journal of bone and joint surgery (British volume), 1969 **51**(2): p. 313-323.
32. **L. Joskowicz, C. Milgrom, M. Shoham, Z. Yaniv and A. Simkin**. *Robot-Guided Long Bone Intramedullary Distal Locking: Concept and Preliminary Results*. in *2nd International Conference on Computer Assisted Orthopaedic Surgery*. 2002. CAOS 2002,USA.
33. **R.J. Brumback**, *The rationales of interlocking nailing of the femur, tibia, and humerus*. Clinical Orthopaedics And Related Research, 1996(324): p. 292-320.
34. **P. Wolinsky, N. Tejwani, J. Richmond, K. Koval, K. Egol and D. Stephen**, *Controversies in Intramedullary Nailing of Femoral Shaft Fractures*. Journal of Bone and Joint Surgery (Am), 2001. **83**: p. 1404-1415.
35. **S. Larsen, K. Nielsen, M. Larsen and S. Kristensen**, *Treatment of femoral shaft fractures with Grosse-Kempf intramedullary nail*. Journal Of Orthopaedic Science: Official Journal Of The Japanese Orthopaedic Association, 2000. **5**(4): p. 328-332.
36. **A. Alho, K. Stromsoe and A. Ekeland**, *Locked intramedullary nailing of femoral fractures*. The journal of Trauma. **31**(1): p. 49-59.

37. **M.E. Muller, M. Allgower, R. Schneider and H. Willenegger**, *Manual of Internal Fixation: Techniques recommended by the AO-ASIF Group*. 3rd ed, ed. M. Allgower. 1991.
38. **C.M. Moein, M.H.J. Verhofstad, R.L. Bleys and C. Van-der Werken**, *Soft tissue injury related to choice of entry point in antegrade femoral nailing: piriform fossa or greater trochanter tip*. *Injury*, 2005. **36**(11): p. 1337-1342.
39. **L. Joskowicz, C. Milgrom, A. Simkin, L. Tockus and Z. Yaniv**, *FRACAS: a system for computer-aided image-guided long bone fracture surgery*. *Computer Aided Surgery: Official Journal Of The International Society For Computer Aided Surgery*, 1998. **3**(6): p. 271-288.
40. **S.A. Riley**, *Exposure of the orthopaedic surgeon to radiation*. *The Journal Of Bone And Joint Surgery (Am)*, 1994. **76**(6): p. 952-953.
41. **R. F. Ostrum**, *Retrograde femoral nailing: Indications and techniques* *Operative Techniques in Orthopaedics*, 2003. **13**(2): p. 79-84.
42. **V. Bühren, J.D. DiCicco III and T.G. DiPasquale**, *T2TM Femoral Nailing System: Operative Technique*, in *Osteosynthesis*. 2006, Stryker[®], Germany.
43. **L. Handolin, J. Pajarinen, J. Lindahl and E. Hirvensalo**, *Retrograde intramedullary nailing in distal femoral fractures-results in a series of 46 consecutive operations*. *Injury*, 2004. **35**(5): p. 517-522.
44. **A.J. Starr and W. B. Robert**, *Retrograde nailing of fractures of the femoral shaft* *Current Orthopaedics*, 1999. **13**(3): p. 237-241.
45. **S.B. Antekeier, R.L. Burden Jr, M.J. Voor and C.S. Roberts**, *Mechanical study of the safe distance between distal femoral fracture site and distal locking screws in antegrade intramedullary nailing*. *Journal of Orthopaedic Trauma*, 2005. **19**(10): p. 693-697.
46. **P. Tornetta III and D. Tiburzi**, *Antegrade or retrograde reamed femoral nailing: A Prospective, randomised trial*. *Journal of Bone and Joint Surgery (Br)*, 2000. **82**(5): p. 652- 654.
47. **G. M. Spence, M.T. Dunning, S.R. Cannon and T.R. Briggs**, *The hazard of retrograde nailing in pathological fractures: Three cases involving primary musculoskeletal malignancy*. *Injury*, 2002. **33**(6): p. 533-538.
48. **M.V.D. Elst and C.V.D. Werken**, *Bilateral retrograde femoral nailing in an obese patient* *Injury: Short Communication*, 1999. **30**(5): p. 371-373.

49. **G. Papadokostakis, C. Papakostidis, R. Dimitriou and P.V. Giannoudis**, *The role and efficacy of retrograding nailing for the treatment of diaphyseal and distal femoral fractures: a systematic review of the literature*. *Injury*, 2005. **36**(7): p. 813-822.
50. **R.F. Ostrum, J. DiCicco, R. Lakatos and A. Poka**, *Retrograde intramedullary nailing of femoral diaphyseal fractures*. *Journal of Orthopaedic and Trauma*, 1998. **12**(464-468).
51. **C.M. Court-Brown**, *The management of femoral and tibial diaphyseal fractures: Review article*. *Journal of the Royal College of Surgeons of Edinburgh* 1998. **43**: p. 374-380.
52. **J.C. Taylor**, *Campbell's Operative Orthopaedics, Second Volume*, ed. S.T. Canale. Vol. 9th. 1998: Mosby-Year Book, Inc. (ISBN 0-8151-2087-7).
53. **R.J. Brumback, S. Uwagie-Ero, R.P. Lakatos, A. Poka, G.H. Bathon and A.R. Burgess**, *Intramedullary nailing of femoral shaft fractures. Part II: Fracture healing with static interlocking fixation*. *Journal of Bone and Joint Surgery (Am)*, 1988. **70**: p. 1453-62.
54. **M.C. Forster, A.S. Aster and S. Ahmed**, *Reaming during anterograde femoral nailing: is it worth it?* *Injury*, 2005. **36**(3): p. 445-449.
55. **R.J. Brumback, T.R. Toal Jr, M.S. Murphy-Zane, V.P. Novak and S.M. Belkoff**, *Immediate weight-bearing after treatment of a comminuted fracture of the femoral shaft with a statically locked intramedullary nail*. *Journal of Bone and Joint Surgery (Am)*, 1999. **81**: p. 1538-1544.
56. **R.J. Brumback and W.V. Walter**, *Intramedullary Nailing of the Femur: Reamed Versus Nonreamed*. *The American Academy of Orthopaedic Surgeons*, 2000. **8**: p. 83-90.
57. **M.W. Chapman**, *The effect of reamed and nonreamed intramedullary nailing on fracture healing*. *Clinical Orthopaedics and Related Research* . 1998. **355**(Suppl): p. 230-238.
58. **M.G. Clatworthy, D.I. Clark, D.H. Gray and A.E. Hardy**, *Reamed versus unreamed femoral nails. A randomized prospective trial*. *Journal of Bone and Joint Surgery (Br)*, 1998. **80**: p. 485-489.
59. **P.R. Wolinsky, E McCarty, Y. Shyr and K. Johnson**, *Reamed intramedullary nailing of the femur: 551 cases*. *Journal of Trauma*, 1999. **46**: p. 392-399.

60. **P.V. Giannoudis, A.J. Furlong, D.A. Macdonald and R.M. Smith**, *Reamed against unreamed nailing of the femoral diaphysis: a retrospective study of healing time*. *Injury*, 1997. **28**(1): p. 15-18.
61. **P. Tornetta and D. Tiburzi**, *Reamed Versus Nonreamed Anterograde Femoral Nailing*. *Journal Of Orthopaedic Trauma*, 2000. **14**(1): p. 15-19.
62. **M. Bhandari, HG. Guyatt, D. Tong, A. Adili and SG. Shaughnessy**, *Reamed Versus Nonreamed Intramedullary Nailing of Lower Extremity Long Bone Fractures: A Systematic Overview and Meta-analysis*. *Journal of Orthopaedic Trauma*. , 2000. **14**(1): p. 2-9.
63. **R. Praveen, S. Kumar and S. Venkat**, *Complications in locked intramedullary nailing: A series of 406 cases: Part-1 Femur*. *Orthopaedic Update (India)*, 1997. **7**(2).
64. **M. Shantanu, S. Malik and J. Jeffery**, *The importance of stable distal locking in intramedullary nail stabilisation of proximal femoral metastatic deposits*. *Injury Extra.*, 2005. **36**(10): p. 442-444.
65. **T.J.S. Chesser, P.S. Kerr and A.J. Ward**, *Pathological fracture after prophylactic reconstruction nailing of the femur. The need for distal locking*. *International Orthopaedics*, 1996. **20**: p. 190-191.
66. **C. Krettek, J. Mannss, T. Miclau, P. Schandelmaier, I. Linnemann and H. Tscherne**, *Deformation of femoral nails with intramedullary insertion*. *Journal Of Orthopaedic Research: Official Publication Of The Orthopaedic Research Society*, 1998. **16**(5): p. 572-575.
67. **C. Krettek, B. Konemann, T. Miclau, R. Kolbli, T. Machreich and H. Tscherne**, *A mechanical distal aiming device for distal locking in femoral nails*. *Clinical Orthopaedics And Related Research*, 1999(364): p. 267-275.
68. **J. D. Goodall**, *An image intensifier laser guidance system for the distal locking of an intramedullary nail*. *Injury*, 1991. **22**(4): p. 339.
69. **J.A. Goulet, F. Londy, C.L. Saltzman and L.S. Matthews**, *Interlocking intramedullary nails. An improved method of screw placement combining image intensification and laser light*. *Clinical Orthopaedics And Related Research*, 1992(281): p. 199-203.
70. **T. Ohe, K. Nakamura, T. Matsushita, M. Nishiki, N. Watanabe and K. Matsumoto**, *Stereo fluoroscopy-assisted distal interlocking of intramedullary nails*. *Journal Of Orthopaedic Trauma*, 1997. **11**(4): p. 300-303.

71. **K.A. Steriopoulos, G.M. Kontakis, P.G. Katonis, I. A. Galanakis and E.K. Dretakis**, *Placement of the distal locking screws of the femoral intramedullary nail without radiation*. Archives Of Orthopaedic And Trauma Surgery, 1996. **115**(1): p. 43-44.
72. **S.N. Azer, W.R. Krause and N.N. Salman**, *Self-guiding interlocking intramedullary nail*. Contemporary Orthopaedics, 1992. **25**(1): p. 22-28.
73. **A.D. Kanellopoulos, C.K. Yiannakopoulos, I. Vossinakis and L.S. Badras**, *Distal locking of femoral nails under direct vision through a cortical window*. Journal of Orthopaedic Trauma, 2003. **17**(8): p. 574-577.
74. **M. MacMillan**, *Operative technique: a new distal aiming device for locking nail fixation*. Orthopedics, 1989. **12**(11): p. 1456.
75. **S S. Kelley, S. Bonar, O.D. Hussamy and J.A. Morrison**, *A simple technique for insertion of distal screws into interlocking nails*. Journal Of Orthopaedic Trauma, 1995. **9**(3): p. 227-230.
76. **E F. Barrick**, *Distal locking screw insertion using a cannulated drill bit: technical note*. Journal Of Orthopaedic Trauma, 1993. **7**(3): p. 248-251.
77. **M.Shoham, M.Burman, E. Zehavi, J. L, B. E and Y. Kunicher**, *Bone-Mounted Miniature Robot for Surgical Procedures: Concept and Clinical Applications*. IEEE Transactions on Robotics and Automation, 2003. **19**(5): p. 893-901.
78. **I. Browbank**, *Intraoperative Registration for Robotic-assisted Orthopaedic Surgery: A Digital X-ray photogrammetry based technique*, in *Wolfson School of mechanical and manufacturing engineering*. PhD Thesis, 1998, Loughborough University: Loughborough, UK.
79. **M. MacMillan and R.H. Gross**, *A simplified technique of distal femoral screw insertion for the Grosse-Kempf interlocking nail*. Clinical orthopaedics and related research, 1988. **226**: p. 252-259.
80. **C.J. Knudsen, G.P. Grobler and R.E. Close**, *Inserting the distal screws in a locked femoral nail*. The Journal of bone and joint surgery (Br), 1991. **73**(4): p. 660-661.
81. **T.D. Owen and J. Coorsh**, *Insertion of the distal locking screws in femoral nailing: a simplified technique*. Injury, 1993. **24**(2): p. 101-103.

82. **L.K. Wagner and O.R. Mulher**, *Radiation attenuating surgical gloves: Effects of scatter and secondary electron production*. *Radiology*, 1996. **200**: p. 45-48.
83. **M.H. Noordeen, N. Shergill, R.S. Twyman, J.P. Cobb and T. Briggs**, *Hazard of ionizing radiation to trauma surgeons: reducing the risk*. *Injury*, 1993. **24**(8): p. 562-564.
84. **S. Skjeldal and S. Backe**, *Interlocking medullary nails--radiation doses in distal targeting*. *Archives of Orthopaedic and Trauma Surgery*, 1987. **106**(3): p. 179-181.
85. **R. Phillips, W.J. Viant, A.M.M.A. Mohsen, J.G. Griffiths, M.A. Bell, T.J. Cain, K.P. Sherman and M.R.K. Karpinski**, *Image guided orthopaedic surgery design and analysis*. *Transactions of the Institute of Measurement and Control*, 1995. **17**(5): p. 251-264.
86. **K. Bouazza-Marouf, I. Browbank and J. R. Hewit**, *Robot-assisted invasive orthopaedic surgery*. *Mechatronics*, 1996. **6**(4): p. 381-397.
87. **N. Theocharopoulos, K. Perisinakis, J. Damilakis, G. Papadokostakis, A. Hadjipavlou and N. Gourtsoyiannis**, *Occupational exposure from common fluoroscopic projections used in Orthopaedic Surgery*. *Journal of Bone and Joint Surgery (Am)*, 2003. **85**: p. 1698-1703.
88. **T.P. Barry**, *Radiation exposure to an orthopedic surgeon*. *Clinical Orthopaedics And Related Research*, 1984(182): p. 160-164.
89. **J.C. Coetzee and E.J. Van Der Merwe**, *Exposure of surgeons-in-training to radiation during intramedullary fixation of femoral shaft fractures*. *The South African Medical Journal* 1992. **81**(6): p. 312-314.
90. **Proceedings of the ACR/FDA workshop**, *Fluoroscopy strategies for improvement in performance, radiation safety and control*. American college of Radiology, 1992.
91. **MA. Hafez, RM. Smith, SJ. Matthews, G. Kalap and KP. Sherman**, *Radiation exposure to the hands of the surgeons: are we underestimating the risk ?* *Archives Of Orthopaedic And Trauma Surgery*, 2005. **125**: p. 330-335.
92. **D. Herscovici and R. Sanders**, *The effects, risks, and guidelines for radiation use in orthopaedic surgery*. *Clinical Orthopaedics and Related Research*, 2000. **375**: p. 126-132.

93. **L.P. Muller, J. Suffner, K. Wenda, W. Mohr and P.M. Rommens,** *Radiation exposure to the hands and the thyroid of the surgeon during intramedullary nailing.* Injury, 1998. **29**(6): p. 461-468.
94. **G. Singer,** *Occupational Radiation Exposure to the Surgeon.* Journal of the American Academy of Orthopaedic Surgeons, 2005. **13**(1): p. 69-76.
95. **T. Blattert, U. Fill, E. Kunz, W. Panzer, A. Weckbach and D. Regulla,** *Skill dependence of radiation exposure for the orthopaedic surgeon during interlocking nailing of long-bone shaft fractures: a clinical study.* Archives of Orthopaedic and Trauma Surgery., 2004. **124**(10): p. 659-664.
96. **C.T. Mehlman and T.G. DiPasquale,** *Radiation exposure to the orthopaedic surgical team during fluoroscopy: "how far away is far enough?"* Journal Of Orthopaedic Trauma, 1997. **11**(6): p. 392-398.
97. **I.D. Sugarman, I. Adam and T.D. Bunker,** *Radiation dosage during AO locking femoral nailing.* Injury., 1988. **19**(5): p. 336-338.
98. **G.P. Graham and I.G. Mackie,** *Experience with the A.O. locking femoral nail.* Injury., 1988. **19**(4): p. 249-253.
99. **P.E. Levin, R.W. Schoen and R.W. Browner,** *Radiation exposure to the surgeon during closed interlocking intramedullary nailing.* The Journal Of Bone And Joint Surgery. (Am), 1987. **69**(5): p. 761-766.
100. **N. Suhm, P. Messmer, I. Zuna, L. Jacob and P. Regazzoni,** *Fluoroscopic guidance versus surgical navigation for distal locking of intramedullary implants; A prospective, controlled clinical study.* Injury, 2004. **35**(6): p. 567-574.
101. **HR. Maxon, SR. Thomas, EL. Saenger, CR. Buncher and JG. Kereiakes,** *Ionizing irradiation and the induction of clinically significant disease in the human thyroid gland.* The American Journal of Medicine, 1977. **63**(6): p. 967-978.
102. **E. Hazan and L. Joskowicz,** *Computer-assisted image-guided intramedullary nailing of femoral shaft fractures.* Techniques in Orthopaedics, 2003. **18**(2): p. 191-200.
103. **P.R. Wolf and B. A. DeWitt,** *Elements of Photogrammetry.* 2000, London: McGraw-Hill.
104. **Z. Wang,** *On the renaming of the discipline 'photogrammetry'.* ISPRS Journal of Photogrammetry and Remote Sensing, 1996. **51**(1): p. 1-4.

105. **M. Hans-Gerd**, *Concepts of real-time photogrammetry*. Human Movement Science, 1997. **16**(2-3): p. 189-199.
106. **K.B. Atkinson**, *Close Range Photogrammetry and Machine vision*. Whittles Publishing, Scotlnd, UK, 1996. ISBN 1-870325-46-X.
107. **H. L. Mitchell and I. Newton**, *Medical photogrammetric measurement: overview and prospects*. ISPRS Journal of Photogrammetry and Remote Sensing, 2002. **56**(5-6): p. 286-294.
108. **M. Carbonnel, W. Faig and S.K. Ghosh**, *Handbook of Non-Topographic Photogrammetry*. American Society of Photogrammetry, 1979.
109. **J.A. Garrett and P.H. Smithson**, *Conventional X-ray imaging*. IEEE Proceedings, Physical Science, Measurement and Instrumentation, Management and Education, 1987. **134**(2): p. 107-114.
110. **R.R. Liu, S. Rudin and D. Bednarek**, *Super-global distortion correction for a rotational C-arm X-ray image intensifier*. Medical physics, 1999. **26**(9): p. 1802-1810.
111. **D. Soimu, C. Badea and N. Pallikarakis**, *A novel approach for distortion correction for X-ray image intensifiers*. Computerized Medical Imaging and Graphics, 2003. **27**(1): p. 79-85.
112. **S. Paul and R. Johnson**, *Automated detection of Ball Bearings pixel clusters in digital fluoroscopic images*. Physics in medicine and biology, 1998. **43**: p. 2677-2683.
113. **W.J. Viant, R. Phillips, J.G. Griffiths, T.O. Ozanian, A.M. Mohsen, T.J. Cain, M.R. Karpinski and K.P. Sherman**, *A computer assisted orthopaedic surgical system for distal locking of intramedullary nails*. Proc Instn Mech Engrs, 1997. **211**(Part H: J Engineering in Medicine): p. 293-300.
114. **N. Schep, I. Broeders and Chr. Van der Werken**, *Computer assisted orthopaedic and trauma surgery: State of the art and future perspectives*. Injury, 2003. **34**(4): p. 299-306.
115. **A. Mohsen, K P. Sherman, T J. Cain, M. R. K. Karpinski, F. R. Howell, R. Phillips, W. J. Viant, J. G. Griffiths, K. D. F. Dyer**, *End user Issues for Computer Assited Surgical Systems. International Workshop on advanced robotics and intelligent machines*. 1995. Manchester.
116. **S Malek, R Phillips , A Mohsen , W Viant, M Bielby and K Sherman**, *Computer Assisted Orthopaedic Surgical System for Insertion of Distal*

- Locking Screws in Intra-medullary Nails: A valid and Reliable Navigation System.* International Journal of Medical Robotics and Computer Assisted Surgery, 2006. 1(4): p. 34-44.
117. **Y. Zhu, R. Phillips, J.G. Griffiths, W.J. Viant, A.M. Mohsen and M. Bielby,** *Recovery of distal hole axis in intramedullary nail trajectory planning.* Proc. Instn. Mech. Engrs, Part H, Journal of Engineering in Medicine, 2002. 216(H5): p. 323-332.
118. **Z. Yaniv and L. Joskowicz,** *Precise robot-assisted guide positioning for distal locking of intramedullary nails.* IEEE Transactions on Medical Imaging, 2005. 24(5): p. 624-635.
119. **L. Joskowicz, C. Milgrom, M. Shoham, Z. Yaniv and A. Simkin,** *A robot-assisted system for long bone intramedullary distal locking: concept and preliminary results.* Computer Assisted Radiology and Surgery, 2003: p. 485-491.
120. **M.A. Slomczykowski, R. Hofstetter, M. Sati, C. Krrettek and L.P. Nolte,** *Novel Computer-assisted Fluoroscopy system for Intraoperative guidance: Feasibility study for distal locking of femoral nails.* Journal Of Orthopaedic Trauma, 2001. 15: p. 122-131.
121. **N. Suhm, A L. Jacob, L P. Nolte, P. Regazzoni and P. Messmer,** *Surgical navigation based on fluoroscopy--clinical application for computer-assisted distal locking of intramedullary implants.* Computer Aided Surgery: Official Journal Of The International Society For Computer Aided Surgery, 2000. 5(6): p. 391-400.
122. **C. B. Bose. and I. Amir.** *Design of Fiducials for Accurate Registration Using Machine Vision.* in *IEEE Transactions on Pattern Analysis and Machine Intelligence.* 1990.
123. **J.T. Lea, D. Watkins, A. Mills, M. Peshkin., T. Kienzle and S.D. Stulberg.,** *Registration and immobilization in robot-assisted surgery.* First International Symposium on Medical Robotics and Computer Assisted Surgery, Pittsburgh, PA, 1994.
124. **Y. Feixiang, Z. Hong and C.K. Ronald,** *A multistage adaptive thresholding method.* Pattern Recognition Letters, 2005. 26(8): p. 1183-1191.

125. **S. Mehmet and S. Bulent**, *Survey over image thresholding techniques and quantitative performance evaluation*. Journal of Electronic Imaging., 2004. **13**(1): p. 146-165.
126. **T. Abak, U. Baris and B. Sankur**, *The performance of thresholding algorithms for optical character recognition*. International Conference on Document Analysis and Recognition. ICDAR'97., 1997. Ulm., Germany.
127. **M. Sezgin and R. Tasaltin**, *A new dichotomization technique to multilevel thresholding devoted to inspection applications*. Pattern Recognition Letters, 2000. **21**(151-161).
128. **N. Otsu**, *A threshold selection method from gray-level histograms*. IEEE Transactions on Systems, Man, and Cybernetics, 1979. **9**(1): p. 377-393.
129. **L. Cao, Z. Shi and E.K.W. Cheng**, *Fast automatic multilevel thresholding method*. Electronics Letters, 2002. **38**(16): p. 868-870.
130. **A.W. Fitzgibbon, M. Pilu and R.B. Fischer**, *Direct least squares fitting of ellipses*. in *In Proc. of the 13th International Conference on Pattern Recognition*. 1996. Vienna.
131. **R. Thomas and R. Sander**, *TRIGEN Trochanteric Antegrade nail by Smith & Nephew: Surgical Technique*. 2006.
132. *Zimmer Sirius. ®. Intramedullary Nail System Brochure*, 1997.
133. *Introduction to Digital X-ray technology, General Electronics Healthcare Brochure*. 2008.
134. **R. Gonzalez and R. Woods**, *Digital image processing*, 2nd Edition, 2002, Prentice Hall, Upper Saddle River, N.J. (ISBN:0201180758)
135. **P. Sprawls**, *The Physical Principles of Medical Imaging*. . 2nd Edition. 2008: Medical Physics Publishing, Madison, Wisconsin
136. **P. Stephenson and B.B Seedhom**, *Cross-Sectional Geometry of the Human Femur in the Mid-Third Region*, Proceedings Institution of Mechanical Engineers, 1999. **213**(Part H: J Engineering in Medicine): p. 159-166.
137. *Adult data: the handbook of adult anthropometric and strength measurements- Data for Design safety*, Department of Trade and Industry, Government Consumer Safety Research, 1998.
138. **Prof. A. Hedge**, *Anthropometry and Workspace Design* 2007, Dept. Design and Environmental Analysis, Cornell University, Ithaca, USA.

139. **Older data: the handbook of adult anthropometric and strength measurements- Data for Deign safety**, Department of Trade and Industry, Government Consumer Safety Research, 1998.
140. **S. Pheasant**, *Bodyspace: Anthropometry, Ergonomics and the Design of the Work*. 2nd Edition. 1996: Taylor & Francis CRC Press (ISBN 0748403264).
141. **J.B. Hunter**, *Femoral shaft fractures in children*. *Injury*, 2005. **36**(1): p. 86-93.
142. **J.M. Buckaloo, H.J. Iwinski and S.L. Bertrand**, *Avascular necrosis of the femoral head after intramedullary nailing of a femoral shaft fracture in a male adolescent*. *Journal of the Southern Orthopaedic Association*, 1997. **6**(2): p. 97-100.
143. **R.V. Gracilla, H.M. Diaz, N.R. Penaranda, J.M. Pagsisilgan, D.A. Spiegel, D. Quirapas and E.R. Reyes**, *Traction spica cast for femoral-shaft fractures in children*, *International Orthopaedics*, 2003. **27**(3): p. 145-148.
144. **V. Sahin, A. Baktira, C. Yildirim-Turk, E.S. Karakas and S. Aktas**, *Femoral shaft fractures in children treated by closed reduction and early spica cast with incorporated supracondylar Kirschner wires: a long-term follow-up results* *Injury*, 1999. **30**(2): p. 121-128.
145. **R.B. Reeves, R.I. Ballard and J.L. Hughes**, *Internal fixation versus traction and casting of adolescent femoral shaft fractures*. *Journal of Pediatric Orthopedics*, 1990. **10**(5): p. 592-595.
146. **D.G. Stewart, R.M. Kay and D.L. Skaggs**, *Open Fractures in Children. Principles of Evaluation and Management*, *The Journal of Bone and Joint Surgery (Am)*, 2005. **87**: p. 2784-2798.
147. **Child data: the handbook of adult anthropometric and strength measurements- Data for Deign safety**, Department of Trade and Industry, Government Consumer Safety Research, 1998,
148. **C. Eycleshymer and D.M. Shoemaker**, *A cross-section anatomy*. 1970: Appleton-Century-Crofts, New York. (ISBN:0517223651)
149. **R A. Bergman, A.K. Afifi, J. J. Jew and P.C. Reimann.**, *Atlas of Human Anatomy in Cross Section* 1991: Lippincott Williams & Wilkins,US. (ISBN: 0683006002)
150. **O. J. Lewis**, *Review: A Cross-section Anatomy*, *Journal of Anatomy*, 1971. **108**(1): p. 200.

151. **A. Grosse, J. Christie, G. Taglang, C. Court-Brown and M. McQueen,** *Open adult femoral shaft fracture treated by early intramedullary nailing.* The Journal of bone and joint surgery (Br)., 1993 **75**(4): p. 562-565.
152. **L.B. Bone, K.D. Johnson and J. Weigelt,** *Early versus delayed stabilization of fractures.* Journal of Bone and Joint Surgery (Am), 1989. **71**(336-339).
153. **B. Susan, M. Ryan, J. Gregory, M. Chris and M. Ronald,** *Timing of femur fracture fixation: effect on outcome in patients with thoracic and head injuries.* The Journal of Trauma, 2002 **52**(2): p. 299-307.
154. **S.M. Fakhry, R. Rutledge, L.E. Dahners and D. Kessler,** *Incidence, management and outcome of femoral shaft fracture: a statewide population-based analysis of 2805 adult patients in rural state.* The Journal of trauma, 1994. **37**(2): p. 255-261.
155. **H.C. Pape, F. Hildebrand, S. Pertschy, B. Zelle, R. Garapati, K. Grimme, C. Krettek and R.L. Reed,** *Changes in the management of femoral shaft fractures in polytrauma patients: from early total care to damage control orthopedic surgery.* The Journal of trauma, 2002. **53**(3): p. 452-462.
156. **D.M. Luscombe, N.G.E. Aitken, I. Gray and I.W. Smith.,** 2007, Loughborough University.
157. **C.T. Blauvelt and F.R.T. Nelson,** *A Manual of Orthopaedic Terminology.* 6th ed. 1998: Mosby, (ISBN 0-8151-2787-1).
158. **P.D. Holtom and M.J. Patzakis,** *Open fractures and postoperative orthopedic infections.* Current treatment options in infectious diseases, 2000.
159. **C. Brown, S. Rimmer and U. Parakash,** *The epidemiology of open long bone fractures.* Injury, 1998. **29**: p. 529-534.
160. **T. Tsukayam and A.H. Schmidt,** *Open fractures.* Current treatment options in infectious diseases, 2001. **3**: p. 301-307.
161. **I. kevau and D.A.K. Watters,** *Conservative management of femoral shaft fractures.* Papua New Guinea Medical Journal, 1996. **39**: p. 143-151.
162. **D.K. Nikolicacute, Z. Jovanovicacute, G. Turkovicacute, R. Vulovicacute and M. Mladenovicacute,** *Supracondylar missile fractures of the femur.* Injury, 2002. **33**(2): p. 161-166.
163. **L. B. Bone, K. D. Johnson, J. Weigelt and R. Scheinberg,** *Early versus delayed stabilization of femoral fractures: a prospective randomized study. .* Clinical Orthopaedics And Related Research, 2004(422): p. 11-16.

164. **M.R.P. Van-den Bossche, P. L. Broos and P. M. Rommens**, *Open fractures of the femoral shaft, treated with osteosynthesis or temporary external fixation*. *Injury*, 1995. **26**(5): p. 323-325.
165. **J. Coupland**, *Notes on Optical CO-ordinate measurement*. Loughborough University, 2005.

APPENDIX A: Functional anatomy of the femur

The femur mainly consists of three parts, these parts are:

- Proximal femur,
- Femoral shaft or diaphysis and
- Distal femur.

Figure A- 1 represents the anatomy of a femur from both anterior and posterior views.

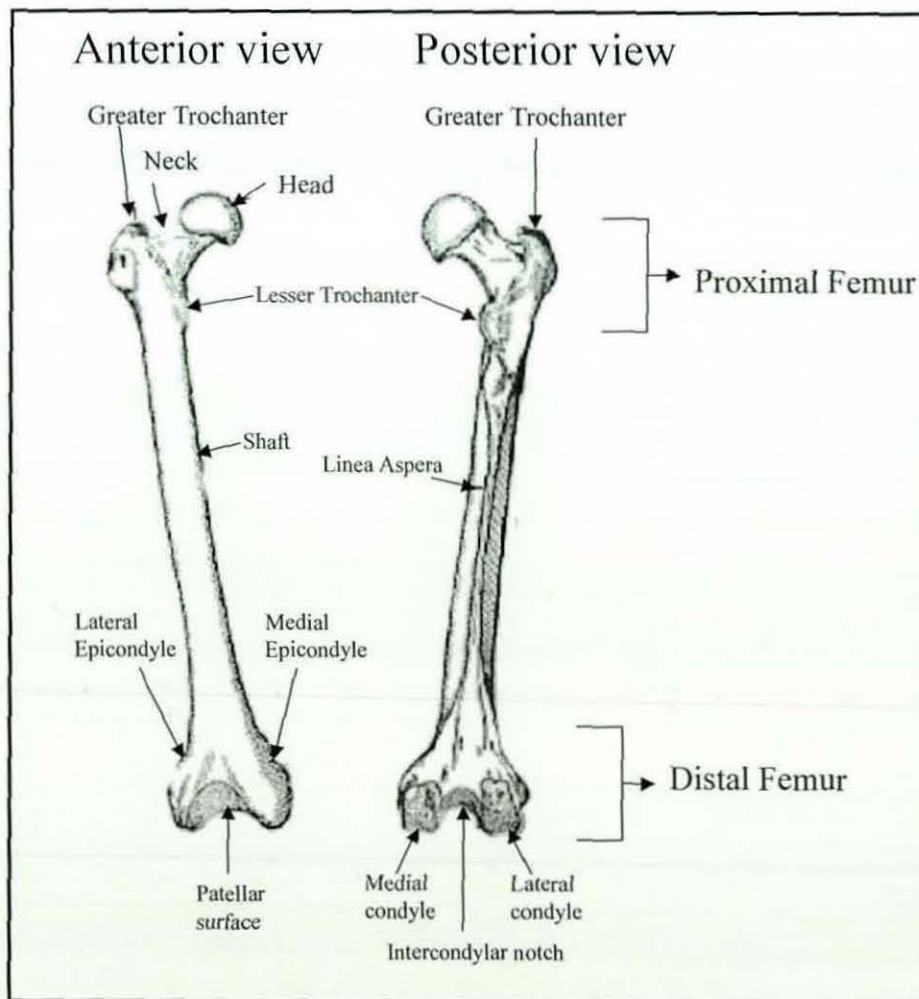


Figure A- 1 Femur anatomy [1]

A.1 Proximal femur

The proximal femur incorporates *femoral head*, which is rather more than half a 'sphere', as shown in Figure A- 2.

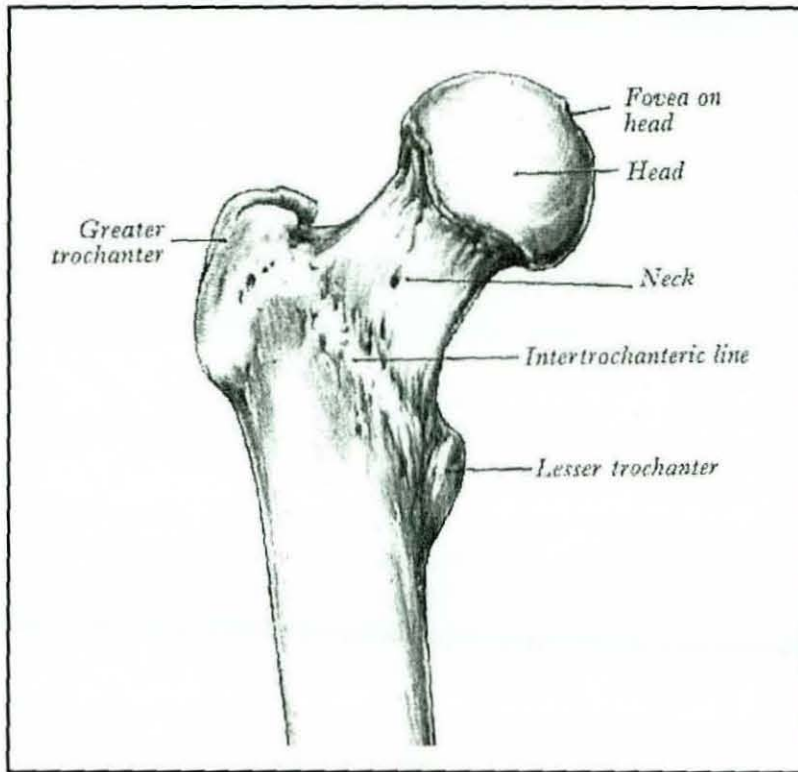


Figure A- 2 Proximal femur [1]

Femoral head is directed upwards, medially and slightly forward, to articulate with the acetabulum³ to form the ball-and-socket of the hip joint. The femoral head is attached to the femoral shaft, at an approximate angle of 125° , through a short piece of bone, called *femoral neck*, in order to facilitate the movement of the hip joint and to enable the lower limb to swing clear of the pelvis. The femoral neck is narrowest at its middle and wider at its lateral than its medial end. Its two borders are rounded. Immediately distal to the femoral neck, the bone widens into two large prominences, which acts as an attachment sites for the muscles of the upper leg. The lower of these prominences (i.e. on the medial side of the femur) is called *lesser trochanter*, while the prominence on the lateral side of the femur is called *greater trochanter*. The *intertrochanteric line* marks the junction of the anterior surface of the neck with the

³Acetabulum i.e. cup shaped depression in the pelvis

femoral shaft, whereas the *intertrochanteric crest* marks the junction of the posterior surface of the neck with the femoral shaft [157].

A.2 Femoral Shaft or Diaphysis

The femoral shaft is tubular with a slight anterior bow as in the standing position, the femoral shaft normally inclines about 10° from the vertical axis of tibia. It surrounds a central region (medullary cavity) of soft, fatty bone marrow and spongy (*cancellous*) bone. It extends from the lesser trochanter to the flare of the femoral condyles i.e. medial and lateral condyle. The anterior bow during weight bearing produces compression forces on the medial side and tensile forces on the lateral side. Therefore, in order to withstand the concentration of these forces there is ridge (i.e. increase in bone thickness) of bone (the *linea aspera*) running down the posterior aspect. Femoral shaft also connects two extremities (or epiphyses), which are wider than the shaft itself. Now use of the above mentioned orthopaedic terminologies leads to use of the term *proximal femur*, to indicate the extremity in the vicinity of the hip joint, and the term *distal femur*, to indicate femoral extremity in the vicinity of knee joint as shown in Figure A- 1.

A.3 Distal Femur

The distal end of the femur is widely expanded and thus provides a good bearing surface for the transmission of the weight of the body to the top of the tibia. The distal femur consists of two prominent masses of bone, known as *lateral* and *medial condyles*. Both lateral and medial condyles are articulate (i.e. jointed) with the *patella* (knee-cap) and the *tibia* (shin bone), in order to provide the kinematics of the knee joint. Anteriorly the two condyles are united and are continuous with the front of the femoral shaft, whereas, posteriorly they are separated by a deep gap, the *intercondylar fossa* (*intercondylar notch*), as shown in Figure A- 3 to make room for the cruciate (i.e. sharped) ligaments within the capsule of the knee joints. The distribution of weight from the femur to the tibia is therefore divided between two articular surfaces.

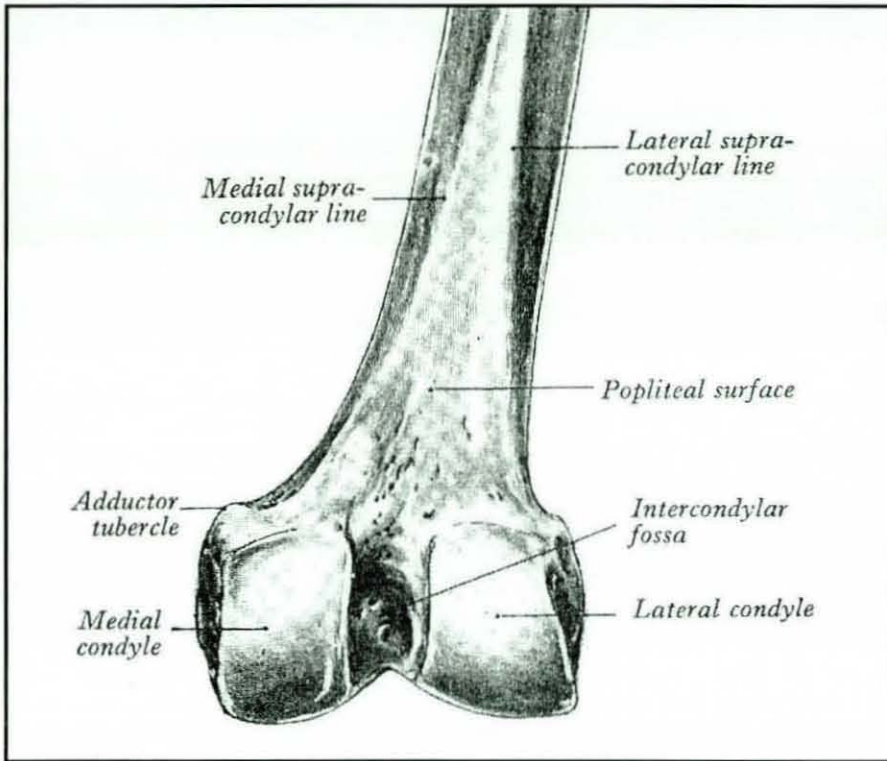


Figure A- 3 Distal Femur [1]

APPENDIX B: Types of femoral shaft fracture

B.1 Femoral shaft Fracture

The femur is the largest and strongest bone [1] and is essential for normal ambulation. Because of this and its protective surrounding muscle, the femoral shaft requires a large amount of force to fracture. Therefore, femoral shaft fractures result from significant force transmitted by a direct blow or from indirect force transmitted at the knee. However, once a fracture does occur, this same protective musculature usually is the cause of displacement, which commonly occurs with femoral shaft fractures.

The spectrum of femoral shaft fractures is wide and ranges from non-displaced stress fractures to fractures with severe comminution and soft tissue injury, possibly requiring amputation. Femoral shaft fractures are usually the result of violent high-energy forces sufficient to fracture the strongest bone in the body.

High-energy fractures are most often associated with multisystem injury and other bony injuries. Isolated fractures occur with lesser-velocity forces or with pathologic bone. Femoral shaft fractures are the result of motor vehicle accidents, pedestrian/auto accidents, gunshot wounds, sports-related trauma, falls from heights, plane crashes, and primary bone or metastatic disease.

Generally, femoral fracture patterns vary according to the direction of the force applied and the quantity of force absorbed. The most common site for a femoral shaft fracture is in the middle third of the shaft i.e. the narrowest part of the shaft [20].

There are various types of femoral shaft fractures, which are as follows:

- Transverse fractures,
- Oblique fracture,
- Spiral fracture,

- Comminuted fractures,
- Segmental or wedge fracture and
- Open fracture.

B.1.1 Transverse Fracture

Angular forces, resulting from a violent blow to the bone, produce a *transverse fracture*, which is approximately perpendicular to the axis of the femoral shaft. Fracture surfaces may be smooth or serrated but the bone is broken cleanly in two as shown in Figure B- 1. Sixty percent of all adult fractures are transverse.

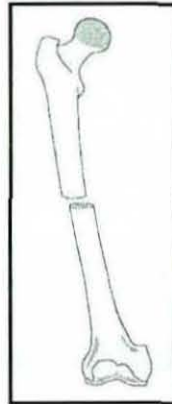


Figure B- 1 Transverse Fracture [11]

Given that the femoral shaft is essentially a tubular structure, torsional forces arising from violent twisting about the axis of the bone, are also common causes of fracture. In such cases, either an *oblique* or a *spiral fracture* is generally produced.

B.1.2 Oblique Fracture

These fracture results from bending with some degree of superimposed axial compression. The fracture line runs oblique to the long axis of the bone i.e. the fracture line is on a slant as shown in Figure B- 2. The cortical fracture surfaces of each fragment are in the same plane. This is a difficult fracture for orthopaedists to manage because the ends of the broken bone tend to slide past each other and causes shortening of the bone itself. About 15 percent of all fractures are oblique.

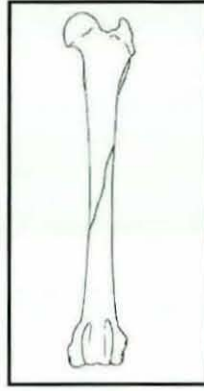


Figure B- 2 Oblique Fracture [11]

B.1.3 Spiral Fracture

This is a long, curved, coil-like fracture as shown in Figure B- 3. These fractures are usually the result of torsional forces. The fracture line runs oblique to the long axis of the bone but the cortical fracture surfaces of each fragment are in different planes. The edges and ends of the fracture tend to be sharp and pointed. This fracture is commonly seen in skiers whose bodies rotate in a fall while their feet remain fixed. Spiral fractures have much less soft-tissue injury than others. They heal quickly because there is a large area of fracture to mend. About 5 percent of all fractures are spiral.



Figure B- 3 Spiral fracture [11]

B.1.4 Comminuted Fractures

Generally are the result of high-energy trauma i.e. associated with multisystem injury and other bony injuries. It results from large impaction force, caused for example by

direct blow to the flexed knee joint. Comminuted means that there are at least three fragments and the fracture lines interconnect. Comminuted fractures are often open fractures, with the bone sticking up through the skin. It takes tremendous force to break a bone in this fashion. About 20 percent of all adult fractures are this type.

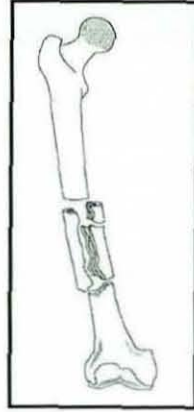


Figure B- 4 Comminuted Fracture [11]

B.1.5 Segmental or Wedge Fracture

They are also called multiple fractures. A large angular force can produce either a *segmental fracture* i.e. two transverse fractures leaving a section of the femur isolated or a *wedge fracture* i.e. two transverse fractures producing a “butterfly” fragment [11]. These types of fracture imply three or more fracture fragments in a single bone; however, unlike the comminuted fractures, the fracture lines do not interconnect.

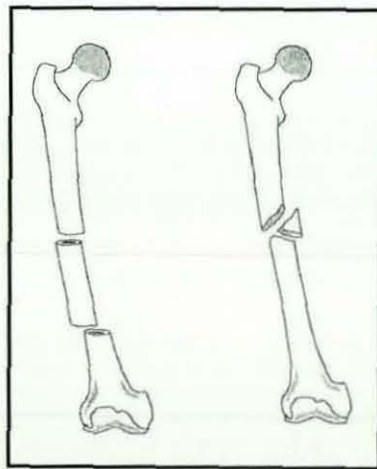


Figure B- 5 Segmental Fracture (L.H.S) or Wedge Fracture (R.H.S) [11]

B.1.6 Open fracture

Open fracture, also known as compound fracture. Because of the levels of violence associated with femoral shaft fracture, it is not uncommon for the patient to suffer additional fractures and significant soft tissue damage. In severe cases, bone fragments can also penetrate the skin from within, thus producing an *open or a compound* fracture [11]. All open fractures are surgical emergencies that need prompt therapy. Open long bone fractures occur with a frequency of 11.5 per 100,000 persons per year [158, 159]. Open fracture wounds are classified according to size, the degree of soft tissue crushing, the severity of bone devitalisation, and the time to treatment [160]. Prevention of infection, fracture healing, and restoration of function are the goals of the management of open fractures. Infection can result in non-union of the fracture, chronic osteomyelitis⁴, amputation, or even death.

In case of *Open fractures*, surgical treatment that is mandatory includes the early and complete debridement⁵ from the fracture wound, along with stabilization of the fracture. Even as little as a 5-hour delay in debridement is associated with increased infection rates. For most open, long bone fractures, immediate definitive fixation with closed intramedullary nailing is appropriate as by using intramedullary nailing, the risk of infection and non-union is low, the incidence and severity of malunion are reduced, the hospital stay is short, and early mobilization of the patient is possible [28].

B.2 Complications of Femur Fracture

Complications associated with femoral fractures are as follows:

B.2.1 Malunion and shortening of the leg

The most common complication of fracture of the femur is malunion due to the improper correction of the lateral angulation. If overriding is not corrected, the

⁴Osteomyelitis: Bacterial infection of bone in which the resulting inflammation can lead to a reduction of blood supply to the bone

⁵ Debridement: Surgical excision of dead, devitalised, or contaminated tissue and removal of foreign matter

malunion occurs with marked shortening. If the shortening is more than 1 and 1/2" it will need surgery by osteotomy⁶ and internal fixation.

B.2.2 Stiffness of the knee joint

Knee stiffness occurs due to the prolonged immobilisation, particularly in older patients. The causes are:

- Adhesions inside the joint (tibio femoral),
- Adhesion of patella to the femur and
- Adhesion of quadriceps muscle to the fracture site more particularly in cases treated by open operation.

B.2.3 Non-union

Non-union is usually due occurs as a result of shortening as well as external rotation of the distal fragment. Shortening occurs due to interposition (i.e. overlapping) of soft tissues between the fragments. This needs an operative reduction and internal fixation with IMN, supplemented with bone grafts.

⁶ Osteotomy: Surgical operation in which a bone is divided or a piece of bone is removed or cut in order to correct a deformity

APPENDIX C: Femoral Shaft fracture treatment

C.1 Skeletal traction

Skeletal traction of femoral shaft fractures involves insertion of a metal wire or pin through the bone distal to the fracture (i.e. proximal tibia), so as to exert a continuous pull in the long axis of the bone for the reduction of fracture [20]. Weights are then attached to this pin, via a series of Ropes and pulleys as shown in Figure C- 1, to provide a traction force, which is strong enough to overcome the contraction of the leg muscles. While applying traction, following must be practiced [161].

- The weight must be off the bed rail and not sitting on the floor. The amount of weight to be suspended should be one tenth of the body weight, which is sufficient to pull the bones out to length but not over distract (i.e. excessive traction).
- Friction should be avoided, as it causes reduction in effective traction.
- Direction of traction must be as horizontal as possible.

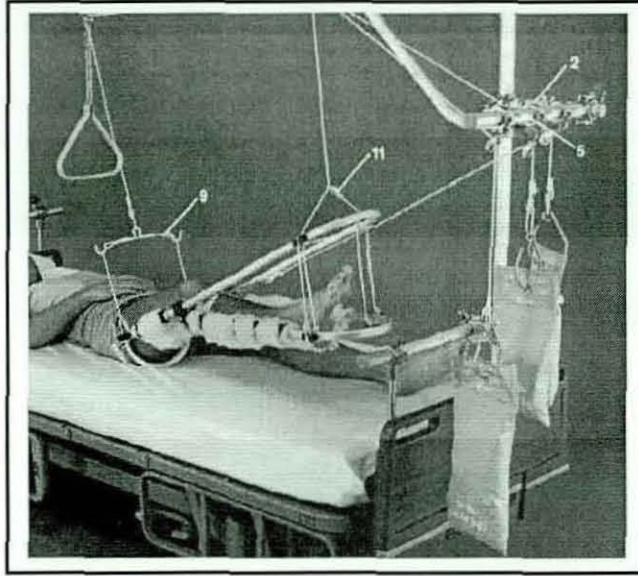


Figure C- 1 Skeletal Traction treatment of femoral shaft fracture

A prolonged period of hospitalisation is then required, in order to allow the bone healing process to take place. Therefore, skeletal traction is an expensive form of treatment and can also result in number of complications associated with prolonged bed rest such as muscle atrophy etc [161]. The use of this technique is, therefore, generally restricted to spiral or oblique fractures that are easily displaced by muscle contraction [20]. The period of hospitalisation can however be shortened by applying a cast bracing when the fracture becomes stable, as indicated radiographically by the appearance of the callus⁷.

C.2 Cast or Functional bracing

Cast or functional bracing, using either plaster of Paris or one of the lighter materials, is one way of overcoming the fracture, while still permitting fracture splintage and loading. Segments of the cast are applied only over the shafts of the bone, leaving the joints free; the cast segments are connected by metal or plastic hinges which allow movements in one plane [20].

In the context of femoral shaft fractures, it is widely used in the treatment of children's femur fractures, as it is less invasive than many alternatives for treating children's femur fractures. It requires a general anaesthetic, but the only surgically

⁷ Callus: The hard bony tissue that develops around the ends of a fractured bone during healing.

invasive portion of the procedure is placement of a single Steinmann pin in the distal femur under fluoroscopic guidance. The fracture is then reduced closed and appropriate moulding is applied to the cast brace. There is minimal risk of injury to the distal femoral growth plate, negligible risk of infection, no pin tract scarring from external fixation, and no risk of *avascular necrosis*⁸ of the femoral head as a result of the procedure. The cast brace can be removed in clinic and a return trip to the operating room is not required. For patients in mid-childhood (between 6 and 10), especially with any comminution of the fracture, the cast brace is a reliable, proven method. However, for many children over age ten, flexible nails may be a more attractive option.

As with any treatment there are a number of disadvantages related to cast bracing. Cast brace treatment of paediatric femur fractures can be labour intensive for the orthopaedist. Placement of the cast brace requires great attention to detail. The fracture must be adequately reduced, followed by correct moulding of the plaster to allow for stability at the fracture site. Also, the patient in the cast brace requires close follow up when discharged from the hospital. The patient is followed at weekly intervals with radiographs for the first two to four weeks to evaluate fracture alignment. Finally, a high degree of patient and family cooperation is required. The patient must not sit upright for approximately the first three weeks of treatment, as femur shortening may result. The patient is must be in traction when not walking.

C.3 External Fixation

External fixation is used for fracture associated with severe soft-tissue injuries. Two or three metal pins are driven through the bone above the fracture and two or three below it as shown in Figure C- 2, the fracture is reduced and the pins are attached to the bars which hold the bone rigid while leaving the soft tissues exposed and accessible for treatment. The external fixation devices can be adjusted externally to ensure the bones remain in an optimal position during the healing process.

⁸ Avascular necrosis : Death of bone tissue due to impaired or disrupted blood supply, marked by severe pain in the affected region and by weakened bone that may flatten and collapse.

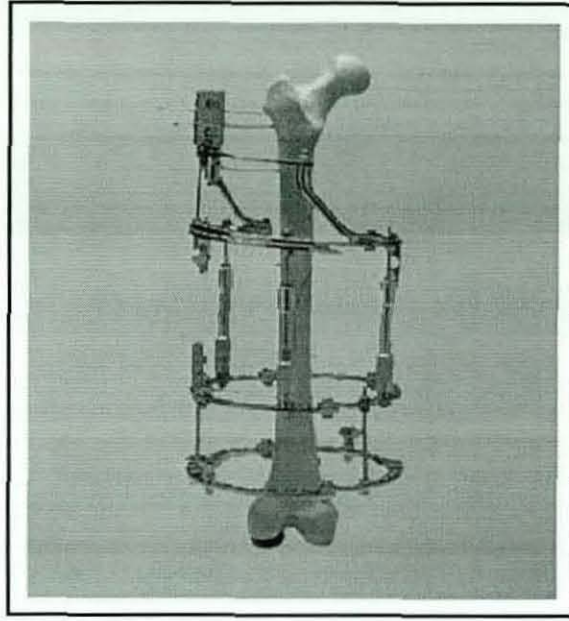


Figure C- 2 External fixation treatment of femoral shaft fracture

However, in the context of femoral shaft fractures, the use of external fixation devices tends to be limited to contaminated or unstable fractures as closed reduction and stabilization of such fractures are usually impossible, and surgical treatment with fixation by plates and screws is required [162]. In such cases, external fixation device provides temporary stabilization of the fracture while the contaminated wound is being treated. Upon closure of the wound, the external fixation device is then replaced by internal fixators. Therefore, in summary, external fixation in cases of multiple injuries offers a quick method of stabilization, resulting in better outcome of the fracture as well as better rehabilitation of the associated injury [163, 164].

APPENDIX D: Overview of the X-ray imaging

imaging

D.1 X-ray Tube

X-rays are a form of electromagnetic wave with a wavelength range from 0.001 nm to 10 nm. X-rays are produced in a device known as X-ray tube. Within the X-ray tube, electrons are accelerated from the hot cathode filament (the cathode typically employs a heated tungsten filament as the source of the electrons) towards the anode surface, where X-rays are produced mainly by *Bremsstrahlung process*. The Bremsstrahlung process is due to the deceleration of the incident electrons by coulomb interactions with the electrons and nuclei of the target material. This process gives a continuous spectrum.

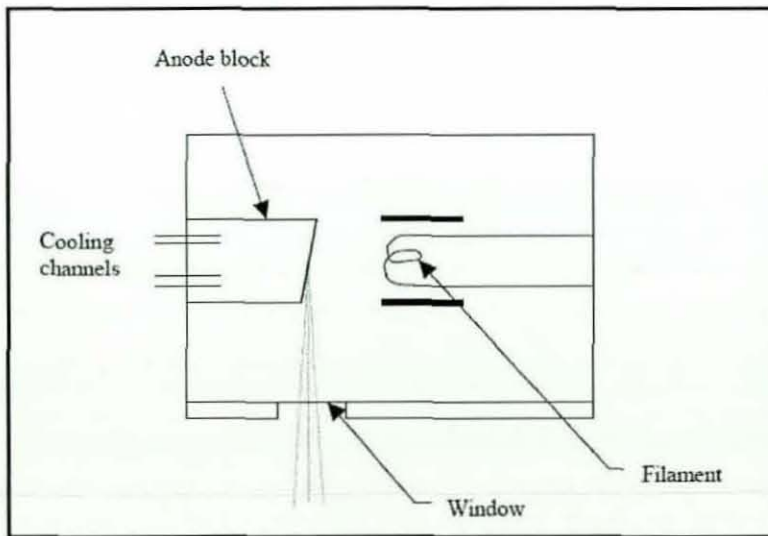


Figure D- 1 Schematic diagram of X-ray tube

The intensity of the X-ray beam decreases as the square of the distance from the focal spot increases. Thus, the further away from the X-ray tube the patient is located the less radiation per square meter and the less likely hood of radiation burn. This is

especially important in the Lateral view since the X-ray tube is usually much closer to the patient than in the AP view.

A high voltage generator powers the X-ray tube. An increase in voltage results in an increase in image density, which in turn decreases image contrast. Image density in the radiograph is also controlled by combination of amount of current in the cathode used to produce the electrons, which strikes the focal point, and the duration of exposure. Therefore, by controlling the X-ray tube voltage and current, a continuous spectrum of the X-ray radiation may be obtained, whose penetrative properties are suitable for specific radiographic examination. Therefore, the proper combination of current-time-voltage is the responsibility of the X-ray technician [108].

In order to reduce radiation exposure to the patient, *collimation* and *filtration* of the X-ray beam emerging from the X-ray tube is performed.

D.1.1 Collimation

Collimation involves restricting the size of the useful X-ray field to the region of clinical interest using lead shutters, because, larger the X-ray field size, the larger the amount of scatter, which degrades the image quality. By tightly collimating the X-ray beam to the area of interest reduces the amount of scatter, reduces the volume of tissue exposed, and improves the quality of the image.

D.1.2 Filtration

Filtration is performed using an aluminium exit window in the X-ray tube, to absorb the lower-energy X-ray photons emitted by the tube before they reach the patient. Filtration results in cleaner image due to absorption of the lower energy X-ray photons that tend to scatter more, and therefore do not contribute to radiographic image.

Because of heterogeneous nature of human body, the primary X-ray beam, which leaves the X-ray tube housing, is subjected to a series of different attenuation processes as it passes through the patient's body. This attenuation is directly related to thickness, atomic number, and density of the tissues in the way of the X-ray beam.

The attenuated beam emerging from patient therefore represents information about internal anatomical structures in the form distribution of X-ray radiation intensities. Since, anatomical information is only provided by x-rays, which passes straight through the patient, therefore if any of the deflected rays reaches the image plane, it adds the noise i.e. information not related to area of interest. In order to avoid noise addition in X-ray images, a grid is placed in front of the image plane, which contains lead vanes that are parallel with one another in one direction and converge towards the nominal position of the focal point of the X-ray tube. This grid is called "Bucky". The lead vanes absorb virtually all deflected rays. The bucky also moves back and forth in its own plane during radiation exposure to eliminate shadows of the vanes [108].

D.2 X-ray Image Intensifier

An X-ray image intensifier is a large image tube that converts a low intensity X-ray image into visible image, as shown in Figure D- 2.

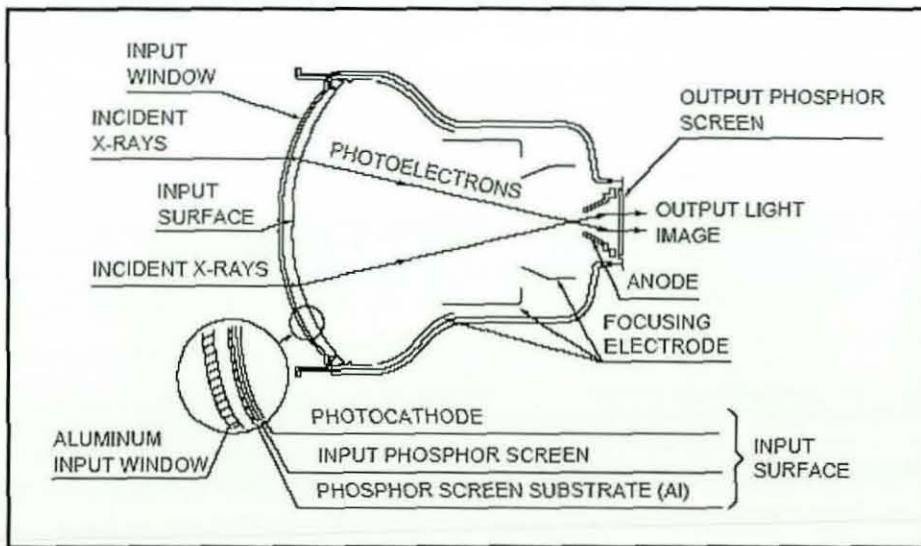


Figure D- 2 Construction and operation of X-ray image intensifier

X-rays incident on the X-ray image intensifier are transmitted through an aluminum metal input window with high X-ray transmittance and less scattering. They are then absorbed by an input phosphor screen and converted into a light image. The input phosphor is typically 15 to 40 cm in diameter, depending on the image intensifier. An intermediate layer (less than 0.001 mm thick) is evaporated onto the inner surface of

the input phosphor and photocathode, which is about 2 nm thick. The intermediate layer has a high optical transmission and is used to chemically isolate the input phosphor and photocathode materials. Light photons emitted by the input phosphor are absorbed via the photoelectric effect in the photocathode to release photoelectrons. The vacuum is then required so that the electrons can travel unimpeded. A voltage of 25 to 35 kV is used to accelerate the electrons. An electric lens (electric field) that consists of an input window, focused electrodes and an anode as shown in Figure D-2, is used for focussing them onto the output phosphor. A current of about 10^{-8} to 10^{-7} Amperes results in the acceleration and focussing of these electrons which gives rise to the image intensification. The output phosphor screen then, again, converts this photoelectron into a visible light image. The output phosphor emits a green light when it absorbs the accelerated electrons, and is typically about 0.005 mm thick and 25 to 35 mm in diameter. Since the photoelectron image is condensed by the electric lens, to increase the density of electrons, and simultaneously accelerated by a high electric field to collide with the output phosphor screen, the output image is approximately 10000 times brighter than it would be obtained when the phosphor screen is placed at the input surface position of the X-ray image intensifier due to electron acceleration and image reduction process.

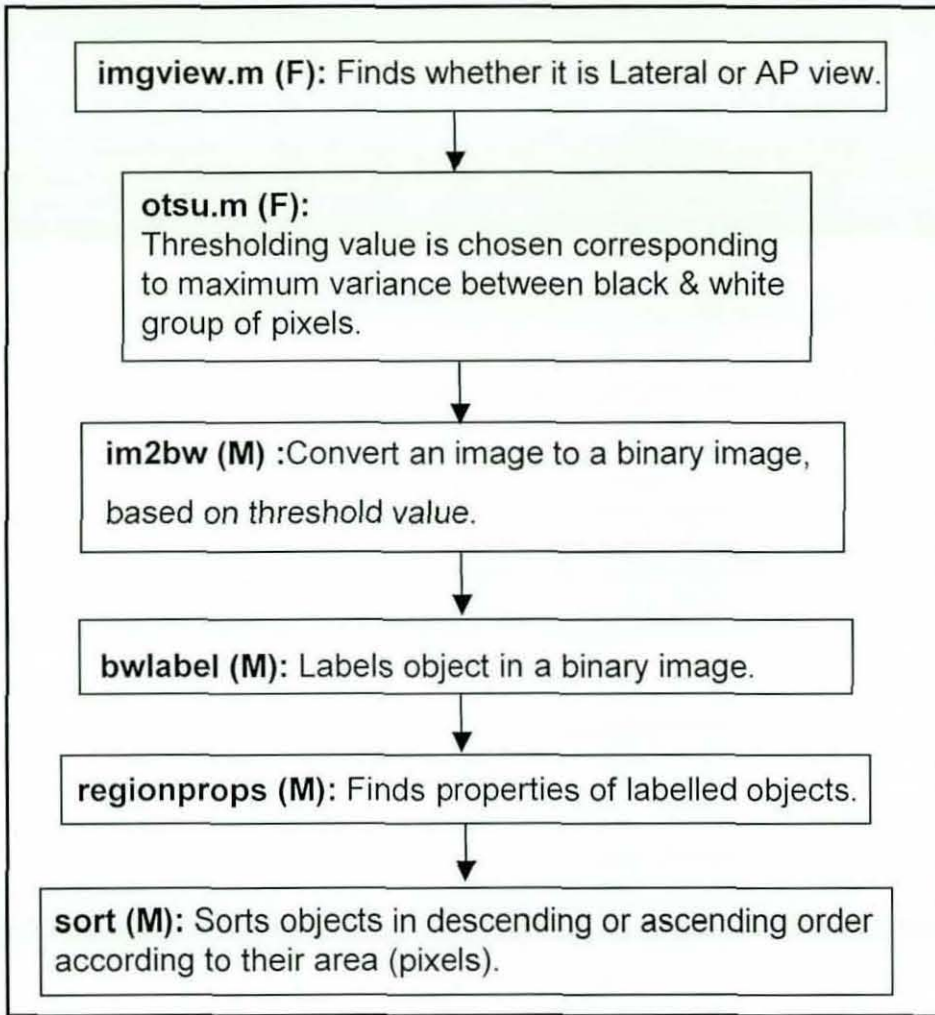
The fluoroscopic image, which is formed at the output window of image intensifier, is too small to be of any useful clinical use as diameter of output screen is usually 2.5cm. Therefore, the output image from the output window is viewed using television technology, which uses lens system to focus output image onto the photoconductive surface of either a television camera or CCD camera. The amplified output from the camera is transmitted as a video signal and can be viewed on the television screen in real time.

APPENDIX E: Software details

In this section, in order to give a better understanding of machine vision system, the functions and sub-functions developed by the author in Matlab environment to obtain the drilling trajectory of distal locking hole are discussed in details. It should be noted that (F) represents the functions developed by the author, whereas (M) represents the Matlab built-in functions that author have used. It should be noted that conversion of machine vision system from Matlab to *Visual C++/Visual Basic environment* can be accomplished by converting functions represented by (M) in these flowcharts into *Visual C++/Visual Basic code*.

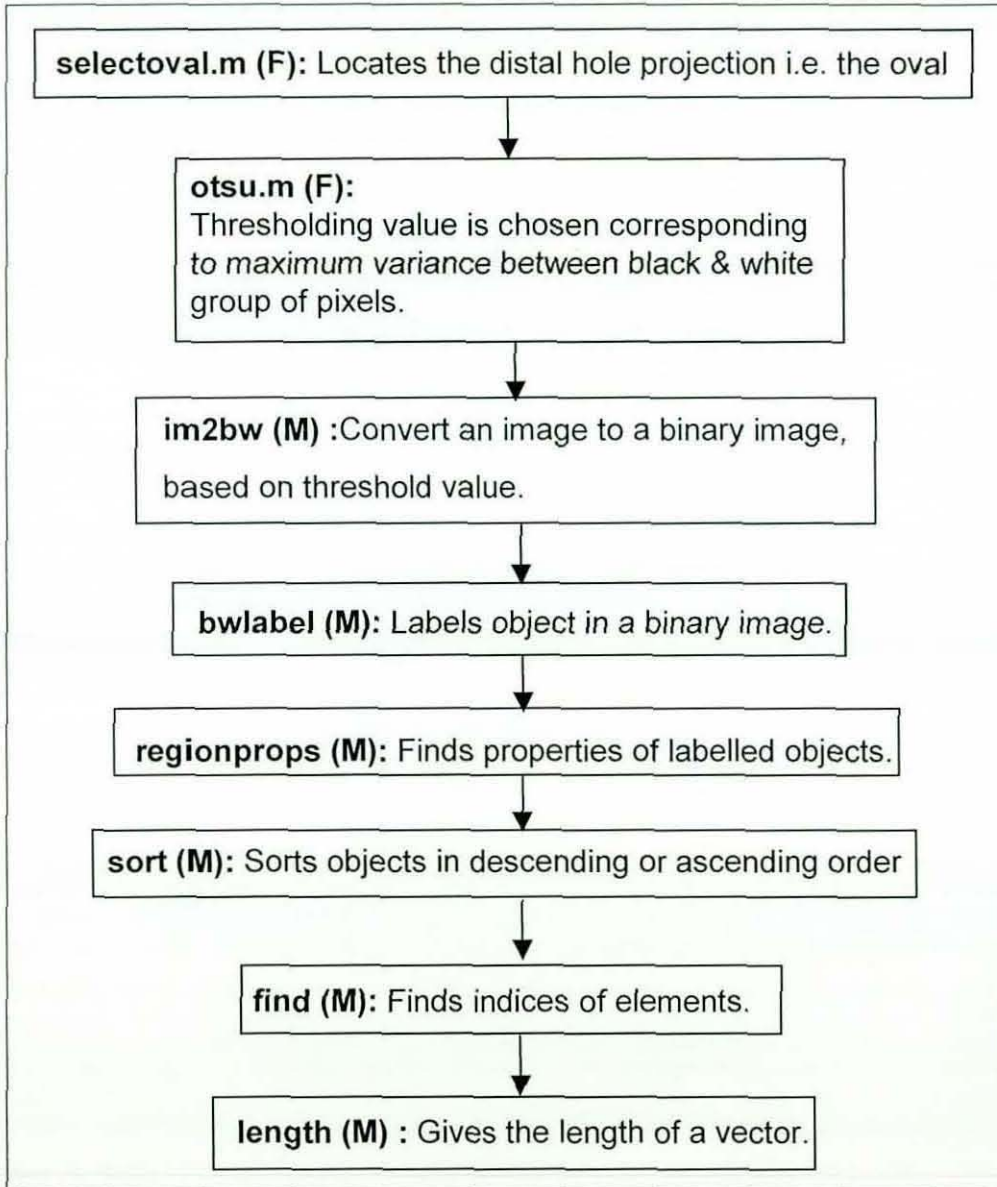
E.1.1 *imgview.m*

Once the user have grabbed an intraoperative X-ray image, and ready to proceed with it, *imgview.m* determines whether it is a Lateral or AP view image based on the location of the oval shaped distal hole projection.



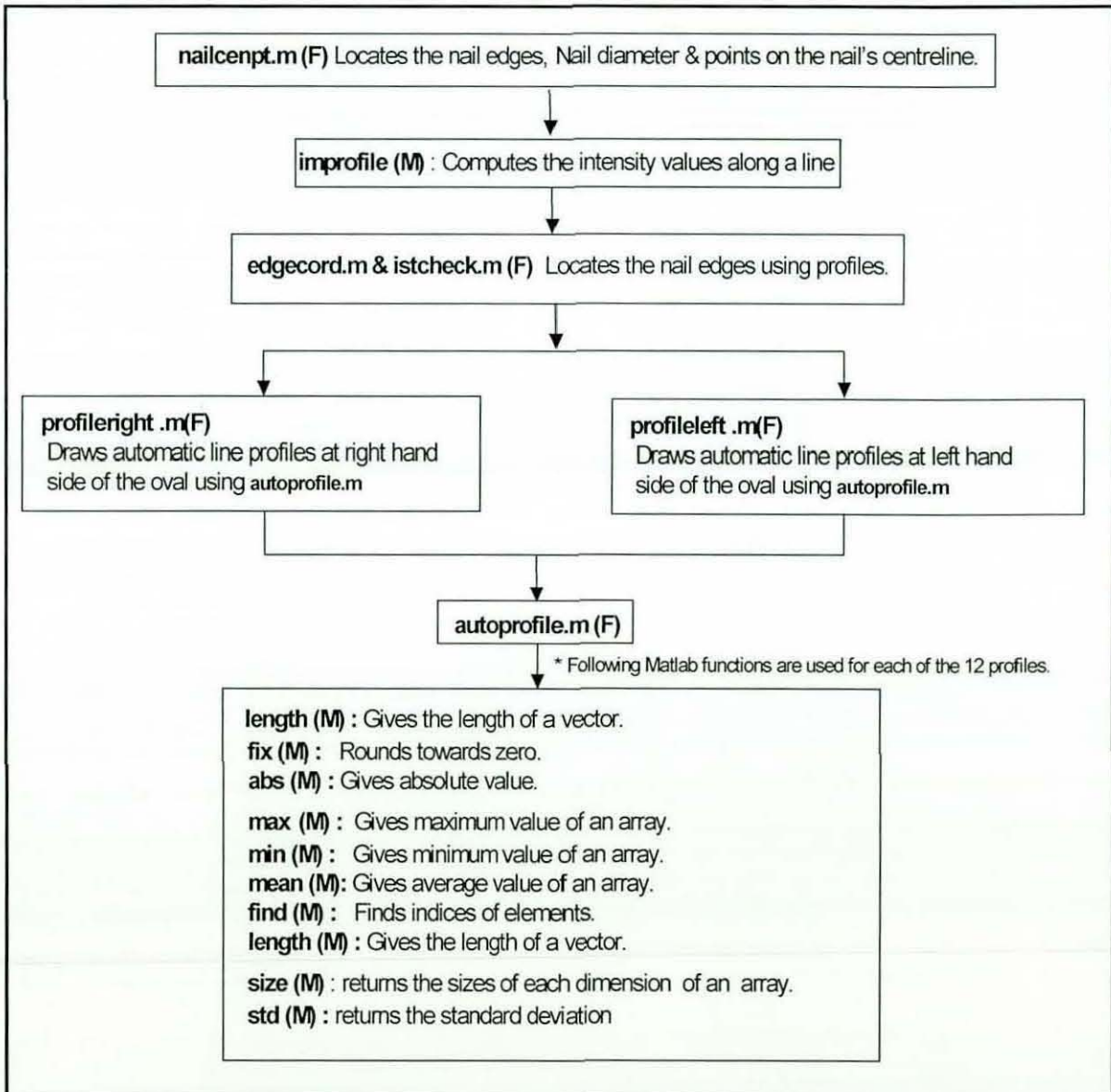
E.1.2 selectoval.m

This function automatically locates the position of two distal locking holes from the Lateral view X-ray image.



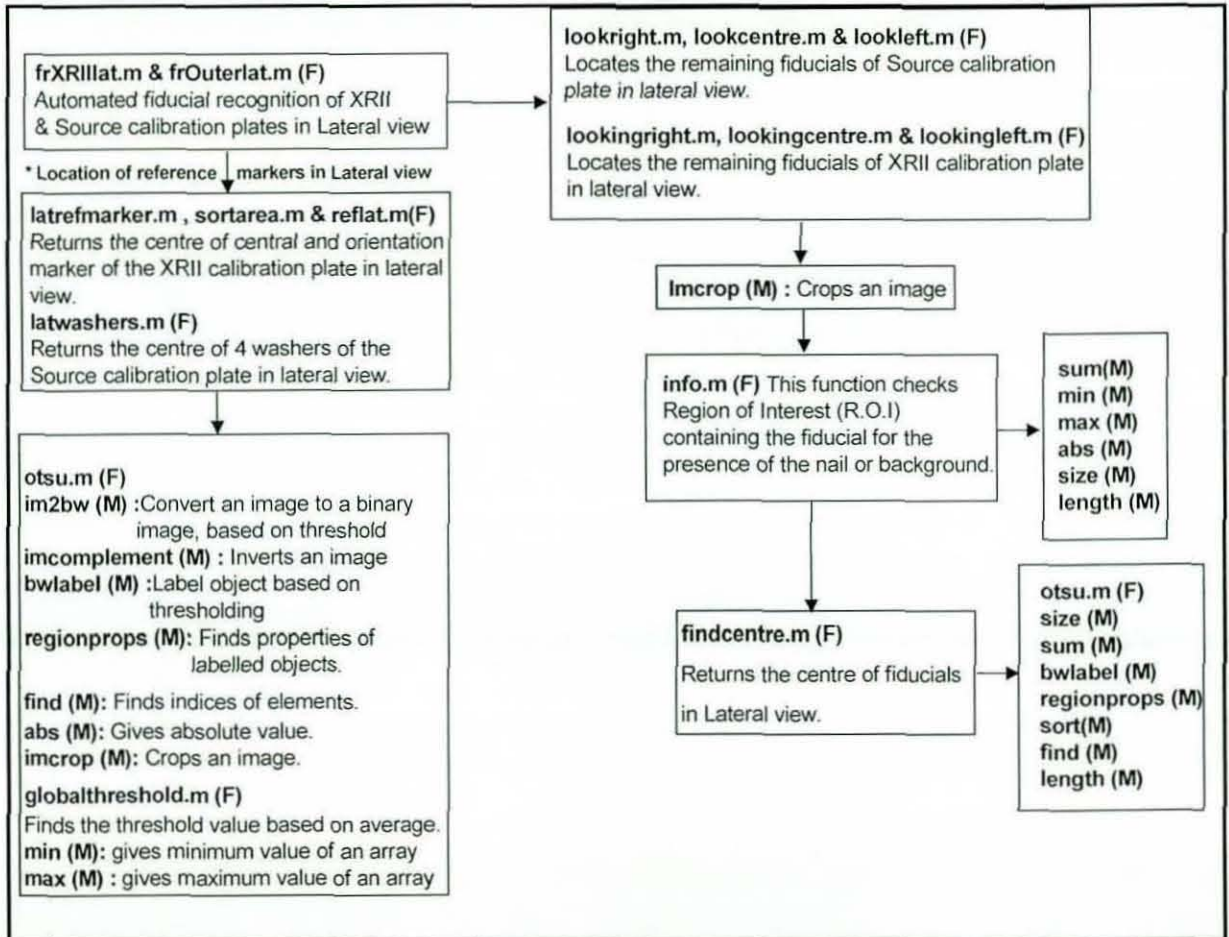
E.1.3 nailcenpt.m

This function uses the information about the location of distal locking hole in the Lateral view image, obtained from “selectoval.m” to draw automatic line profiles across the nail on both sides of the distal locking hole to detect the nail edges, which in turn results in determination of nail diameter and points on the centreline of the nail in Lateral view.



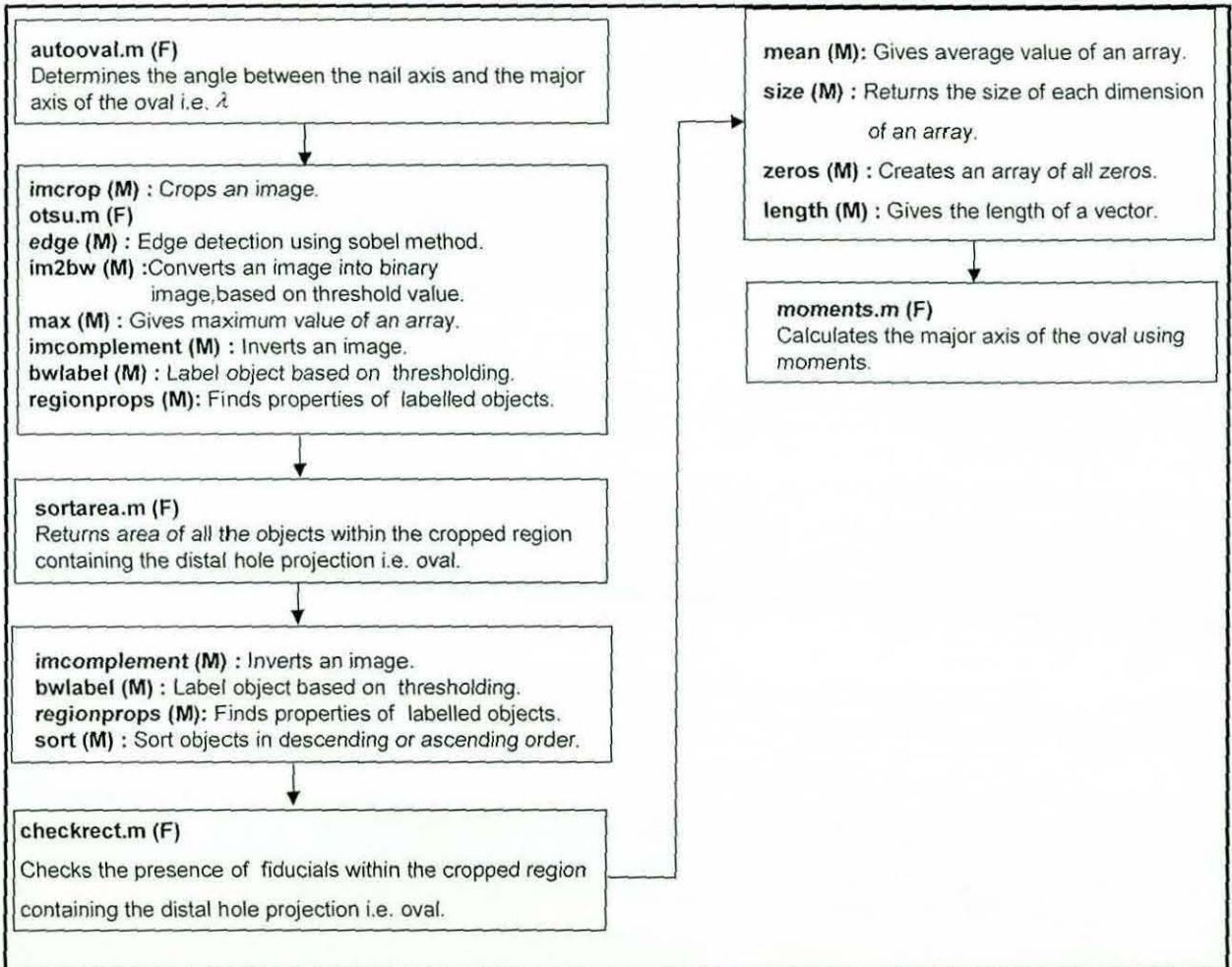
E.1.4 frXRllat.m & frOuterlat.m

This function is used to carry out fiducial recognition of XRll and Source calibration plates in the Lateral view image.



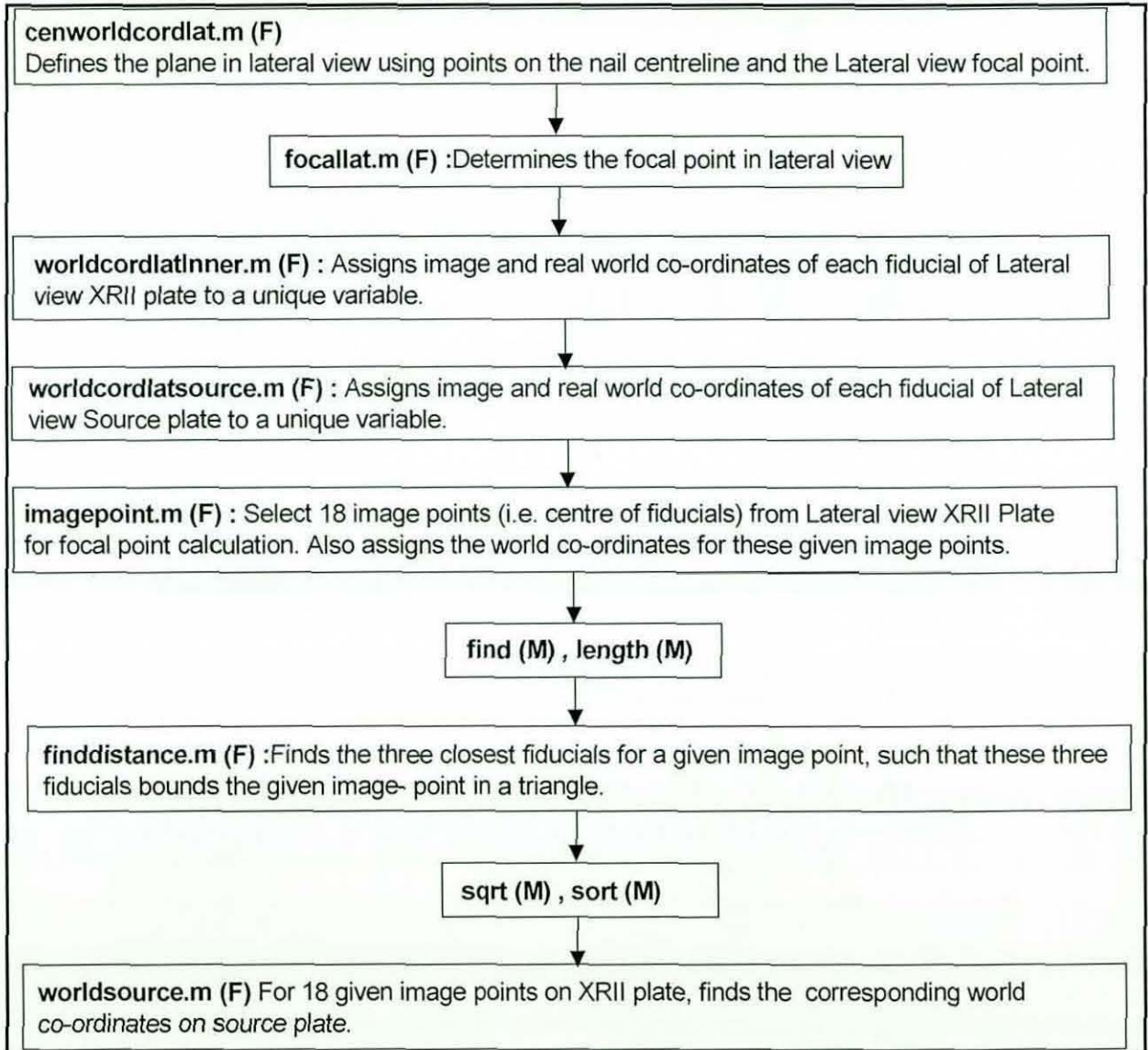
E.1.5 autooval.m

This function is used to determine the angle between the major axis of the oval and the nail axis.



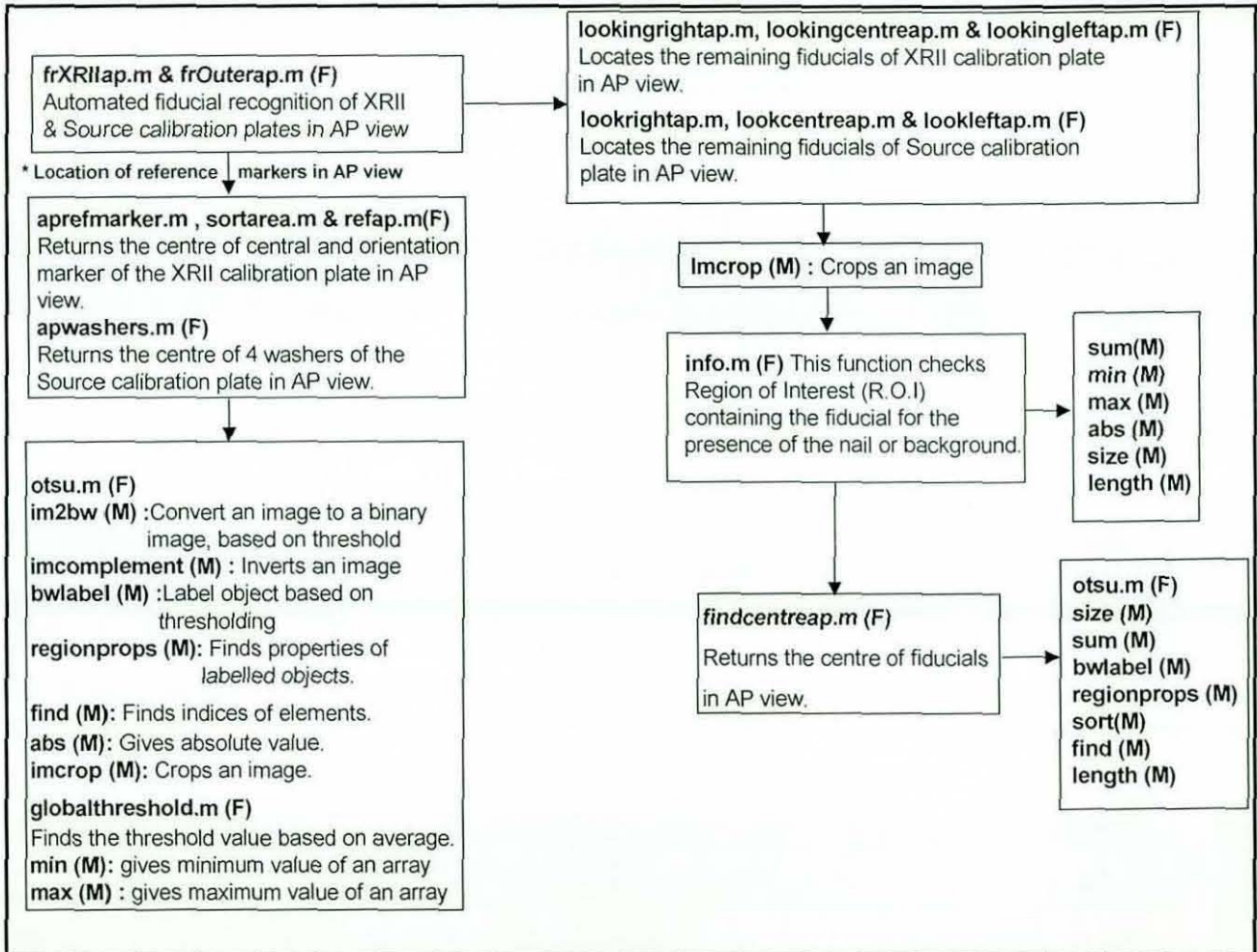
E.1.6 cenworldcordlat.m

This function is used to define the plane in the Lateral view using points on the nail centreline and the Lateral view focal point.



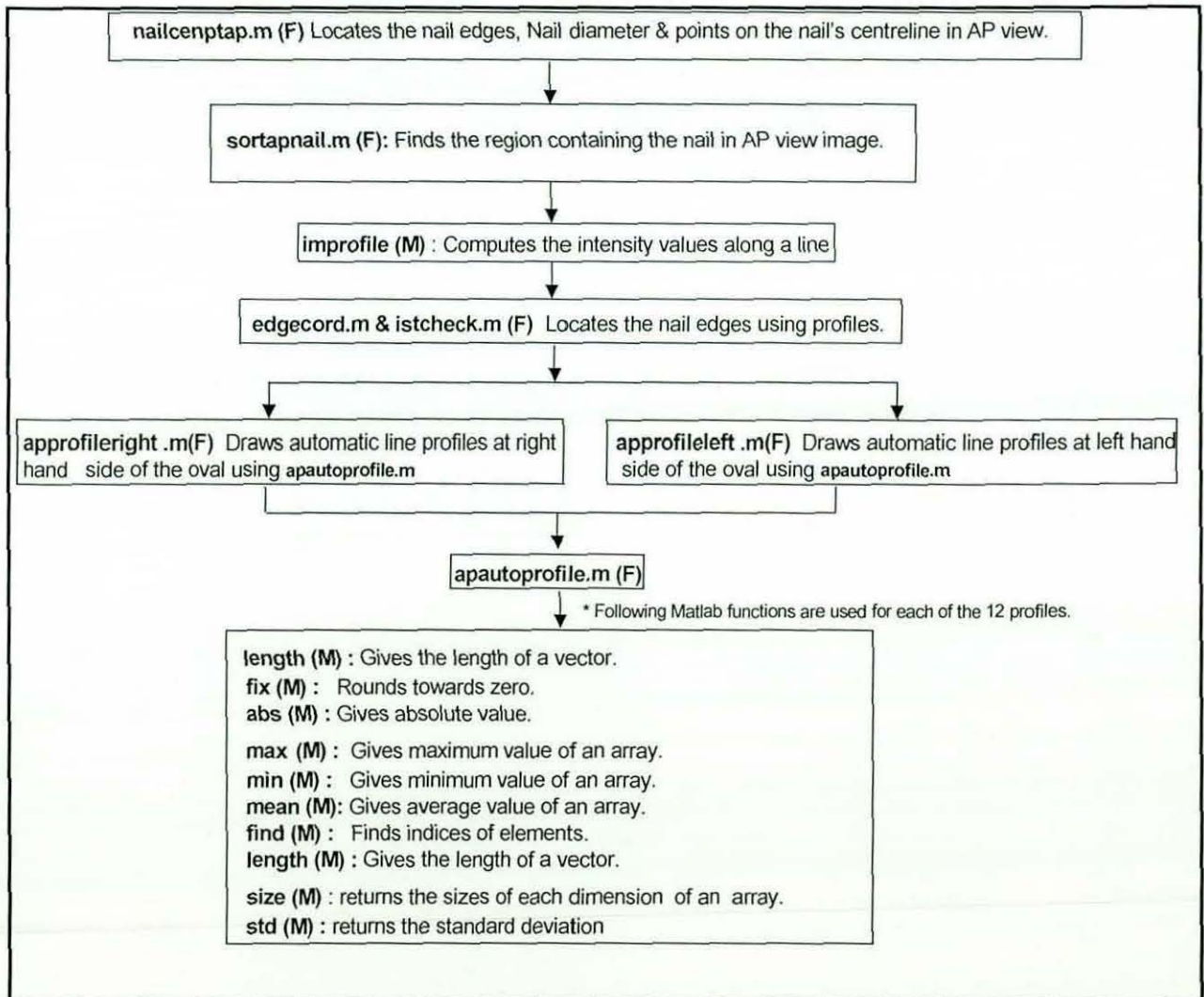
E.1.7 frXRIIap.m & frOuterap.m

This function is used to carry out fiducial recognition of XRII and Source calibration plates in the AP view image.



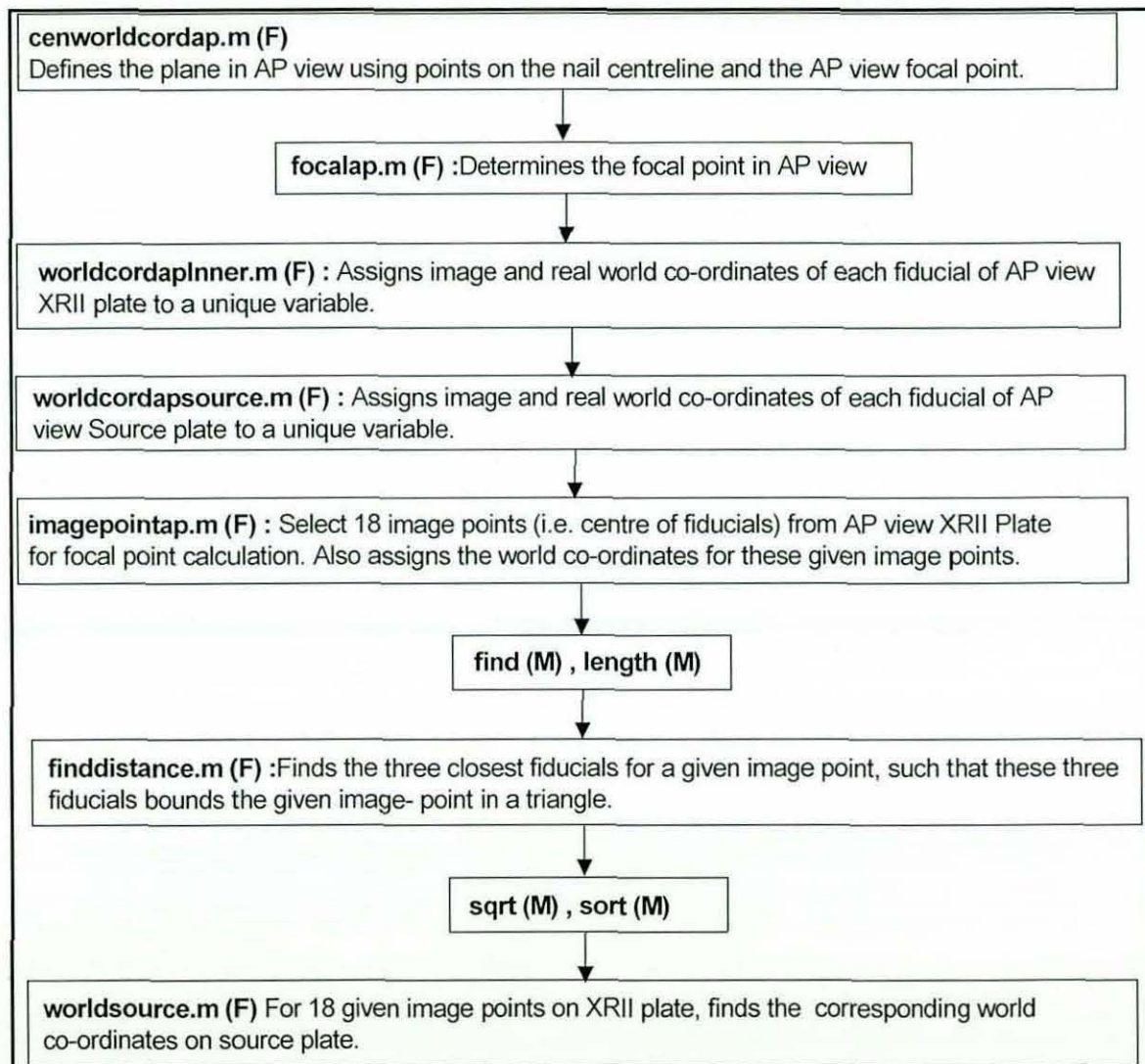
E.1.8 nailcenptap.m

This function at first uses the information about the location of central and orientation marker in the AP view image, obtained from “frXRIIap.m” to crop the image such that it contains the nail. Then bounding box for the nail is obtained, and line profiles across the nail are drawn at short intervals, so that distal hole can be avoided while drawing line profiles to determine the nail centreline in the AP view image.



E.1.9 cenworldcordap.m

This function is used to define the plane in the AP view using points on the nail centreline and the AP view focal point.



E.1.10 findpoint.m & linelineintersect.m

“findpoint.m” determines the nail axis in space by intersecting the planes defined in Lateral and AP views. Whereas, “linelineintersect.m” is used to determine the target point of the drilling trajectory by intersecting nail axis with the line-of-sight passing through the centre of the oval. It also determines the angle between the nail axis and the X-ray imaging axis.

E.1.11 Lookup.m

The angle between major axis of oval and nail axis i.e. " λ " and angle between nail axis and the X-ray imaging axis i.e. " ϕ ", obtained from X-ray image analysis are entered as input and rotation of the nail about its own axis i.e. " θ " is calculated using Look-up table, which is obtained by modelling of the nail in AutoCAD Mechanical Desktop.

APPENDIX F: Theodolite measurement procedure

Given that the distance between the two theodolites is known the 3-D position of the target point is determined with respect to the co-ordinate system of the master theodolite in the following manner:

1. First it is necessary to achieve precise levelling of each theodolite. This is achieved by rotating the theodolite until its plate bubble is parallel to any two foot screws (say A and B), then adjusting A and B to centre the bubble. The left thumb rule applies as usual (the bubble will travel in the direction of the left thumb). Now rotate the theodolite body by 90° , and centre the bubble with the third foot screw (C) only. This procedure is repeated for each 90° revolution of the instrument until the bubble is centred for all four positions.
2. Alignment of the two theodolites is then achieved by turning both theodolites such that they face each other, then in order to set their respective horizontal angle to zero, their cross hair are centred over one another. It should be noted that both theodolites should measure positive rotation in opposite directions. For example, if the Master theodolite measures positive rotation in a clock-wise direction, then the other theodolite should measure positive rotation in a counter Clock-wise direction. The two theodolites should be positioned such that their optical axes converge at approximately 90° .
3. The two theodolites should also be positioned as close as possible to the object, as they measure angular values, hence doing so will increase their resolution in terms of distance. The only limitation for this is to get in-focus views of the desired point. Theodolites used in this study (Sokisha DT5) can focus objects down to 1 metre in front of the object lens.
4. Then the calibration is performed, i.e. the length between the two theodolites is measured, to provide a base line as described in the following section:

Calibration

Calibration for the distance between theodolites is carried out using a metre ruler. As in usual practice, the distance between the two theodolites is not known accurately; therefore, two points at each end of a known length scale bar are measured by centering to determine theodolite separation as follows [165]:

- At first determining the dimensionless co-ordinates of the two target points on the scale bar by simply using Horizontal and vertical angles of master theodolite and horizontal angle of the other theodolite, i.e. (x_1, y_1, z_1) & (x_2, y_2, z_2) respectively.
- Since the spacing between the two target points on the scale bar, say " l ", is known, the spacing between the two theodolites can be determined as follows:

$$d = \frac{l}{\sqrt{(x_2 - x_1)^2 + (y_2 - y_1)^2 + (z_2 - z_1)^2}}$$

- Then, from each end of this base line, an angle is measured to a distant (i.e. target) point using a particular theodolite. Therefore, now a triangle is formed in which the length of one side and two adjacent angles are known. By using trigonometry it is possible to work out the lengths of the other two sides.
- The co-ordinates of a point sighted by two mutually level theodolites can be found using the following equations:

$$X = \frac{d \sin H_b \cos H_a}{\sin(H_a + H_b)},$$

$$Y = \frac{d \sin H_b \sin H_a}{\sin(H_a + H_b)} \text{ and}$$

$$Z = \frac{d \sin H_b \tan V_a}{\sin(H_a + H_b)}$$

Where,

H_a, V_a = Horizontal & Vertical angle for master theodolite "a".

H_b = Horizontal angle for theodolite "b".

d = separation between theodolites "a" & "b".

Uncertainty in measurement occurs due to the errors in the calibration length and angular errors caused by:

- Levelling and calibration,
- Setting the telescope on the target (i.e. centering) and
- Accuracy of angular encoders.

The angular error in setting the telescope is limited by angular (Rayleigh) resolution of the telescope, which is given by [165]:

$$\Delta\theta = \frac{1.22\lambda}{D} = 1.22 \times 10^{-5} \text{ radians}$$

Where,

λ = wavelength of visible light = 0.5 Micron and

D = Diameter of the objective lens = 50mm.

Now, assuming that the measurement triangle is well conditioned and taking the distance "L" to the object being 1 metre, the positional error will be given by:

$$\text{Pos_error} = L\Delta\theta = 0.0122\text{mm}$$

I.e. if the two points are closer than 0.0122mm, while they are located at a distance greater than 1 metre to the theodolite object lens, they will be observed as one single point rather than 2 distinct points.

APPENDIX G: CMM measurements on calibration frame

Based on the hypothesis that an improvement in the quality of the input data should result in an improvement in the overall accuracy of the system, an inspection of the calibration frame was undertaken using CMM, as shown in Figure G- 1.

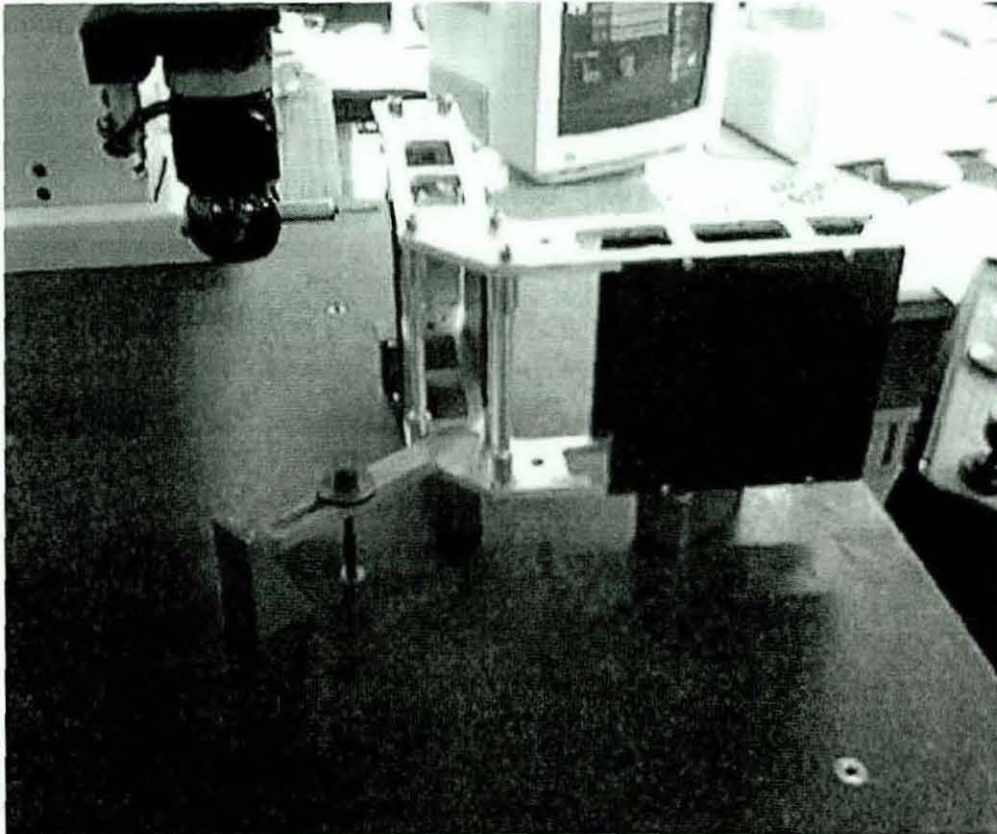


Figure G- 1 Calibration frame inspection using CMM

Following measurements were obtained using CMM:

Relative positions of the individual calibration plates with respect to the Lateral XRII Plate

Several Points (in order to avoid errors, due to measuring once only) on the surface of each individual calibration plate were used in order to determine the relative positions

of the individual calibration plates with respect to the Lateral XRII Plate (i.e. datum plate, as the specified origin of the calibration frame lies on this calibration plate).

Perpendicularity between Lateral and AP calibration plates

Several points on the surface of the Lateral and AP calibration plates were used to define a plane in each view respectively. Then angle between those two planes was determined to find the perpendicularity between Lateral and AP plates, this angle was found to be 89.98° .

Parallelism between XRII and Source calibration plates in Lateral and AP views respectively

Lateral view = 0.03° , AP view = 0.01° .

In order to obtain actual positioning of calibration markers (fiducials), location of each individual fiducial's centre is determined with respect to an arbitrarily defined calibration frame co-ordinate system. It should be noted that since, the specified centre of the fiducials does not lie on the surface of the respective calibration plate (i.e. XY plane for Lateral plates fiducials, whereas, YZ plane for the AP plates fiducials), therefore, multiple points along the circumference of each fiducial are used to determine the centre of fiducial.

G.1 Lateral XR11 Calibration plate

Figure G- 2 shows the fiducial layout on the Lateral XR11 calibration plate, which each fiducial being given a unique identity. Whereas, Table G- 1 and Table G- 2 depicts the comparison between the specified and measured location of each fiducial embedded on the Lateral XR11 calibration Plate. It should be noted that all dimensions are in millimetre.

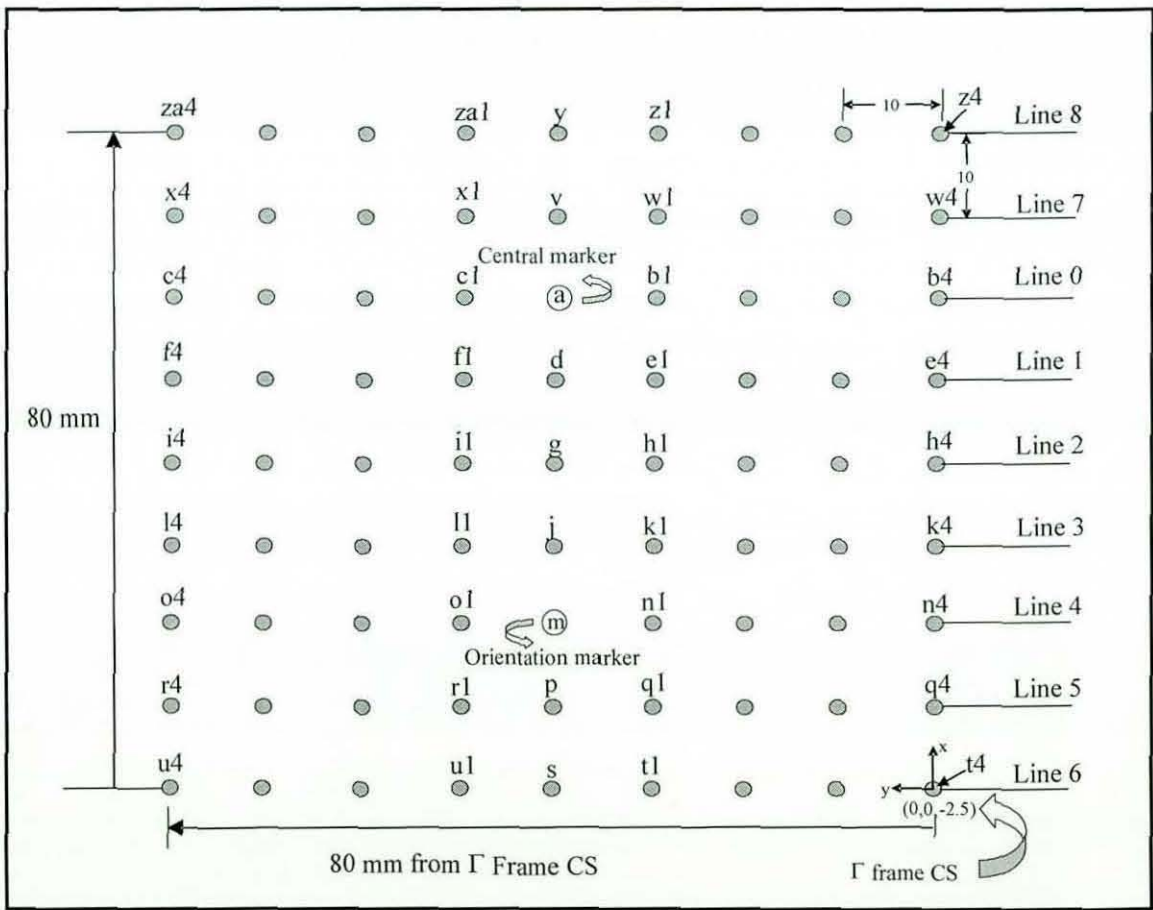


Figure G- 2 Fiducial layout on the Lateral XR11 calibration plate

Line	Fiducial	Specified values		CMM Measurements	
		X	Y	X	Y
0	a	60	40	60.1	40.04
0	b1	60	30	60.02	29.95
0	b2	60	20	60.05	20.03
0	b3	60	10	59.99	10
0	b4	60	0	60.02	0.07
0	c1	60	50	60.18	49.88
0	c2	60	60	60.17	59.97
0	c3	60	70	60.22	70.04
0	c4	60	80	60.23	79.99
1	d	50	40	50.07	39.94
1	e1	50	30	50.08	29.96
1	e2	50	20	50.06	19.98
1	e3	50	10	49.93	9.94
1	e4	50	0	50.04	0.01
1	f1	50	50	50.02	49.96
1	f2	50	60	50.06	59.95
1	f3	50	70	50.15	69.98
1	f4	50	80	50.2	80
2	g	40	40	40.12	39.99
2	h1	40	30	40.08	30.01
2	h2	40	20	40.04	20.03
2	h3	40	10	40.04	9.9
2	h4	40	0	40.02	0.01
2	i1	40	50	40.05	49.92
2	i2	40	60	40.08	60.02
2	i3	40	70	40.07	70.02
2	i4	40	80	40.11	80.06
3	j	30	40	30.1	40.04
3	k1	30	30	30.01	30.05
3	k2	30	20	30.08	20.03
3	k3	30	10	29.93	10
3	k4	30	0	30.07	0.01
3	l1	30	50	30.09	49.94
3	l2	30	60	30.05	59.94
3	l3	30	70	30.14	69.98
3	l4	30	80	30.09	80.06
4	m	20	40	20.04	40
4	n1	20	30	20.09	30.01
4	n2	20	20	20.04	20.05
4	n3	20	10	20.03	10.08
4	n4	20	0	19.91	0.02
4	o1	20	50	19.98	50.09
4	o2	20	60	20.12	60.03
4	o3	20	70	20.08	70.13
4	o4	20	80	20.19	80.01

Table G- 1 Comparison between specified and measured fiducial centre for the Lateral XRII

Plate - 1

Line	Fiducial	Specified values		CMM Measurements	
		X	Y	X	Y
5	p	10	40	10.06	40.05
5	q1	10	30	10.08	30.05
5	q2	10	20	10.07	19.99
5	q3	10	10	10.08	10.08
5	q4	10	0	9.92	0.01
5	r1	10	50	10	50.04
5	r2	10	60	10.11	60.11
5	r3	10	70	10.13	70
5	r4	10	80	10.17	80.06
6	s	0	40	0.05	40.02
6	t1	0	30	0.06	30.11
6	t2	0	20	0.05	20.13
6	t3	0	10	0.02	10.01
6	t4	0	0	0	0
6	u1	0	50	0.1	50
6	u2	0	60	0.12	60.11
6	u3	0	70	0.09	70.11
6	u4	0	80	0.07	80.06
7	v	70	40	70.06	40
7	w1	70	30	70	29.89
7	w2	70	20	69.97	19.96
7	w3	70	10	70	9.88
7	w4	70	0	70.02	0.14
7	x1	70	50	70.12	50.05
7	x2	70	60	70.1	59.98
7	x3	70	70	70.08	69.94
7	x4	70	80	70.18	79.9
8	y	80	40	80.04	39.92
8	z1	80	30	80.05	29.9
8	z2	80	20	80.15	19.93
8	z3	80	10	80.1	9.84
8	z4	80	0	80.09	0.16
8	za1	80	50	80.21	49.94
8	za2	80	60	80.18	59.87
8	za3	80	70	80.14	69.9
8	za4	80	80	80.17	79.92

Table G- 2 Comparison between specified and measured fiducial centre for the Lateral XR11

Plate - 2

9.4 G.2 Lateral Source Calibration plate

Figure G- 3 shows the fiducial layout on the Lateral Source calibration plate, which each fiducial being given a unique identity. Whereas, Table G- 3 and Table G- 4 depicts the comparison between the specified and measured location of each fiducial embedded on the Lateral Source calibration Plate. It should be noted that all dimensions are in millimetre.

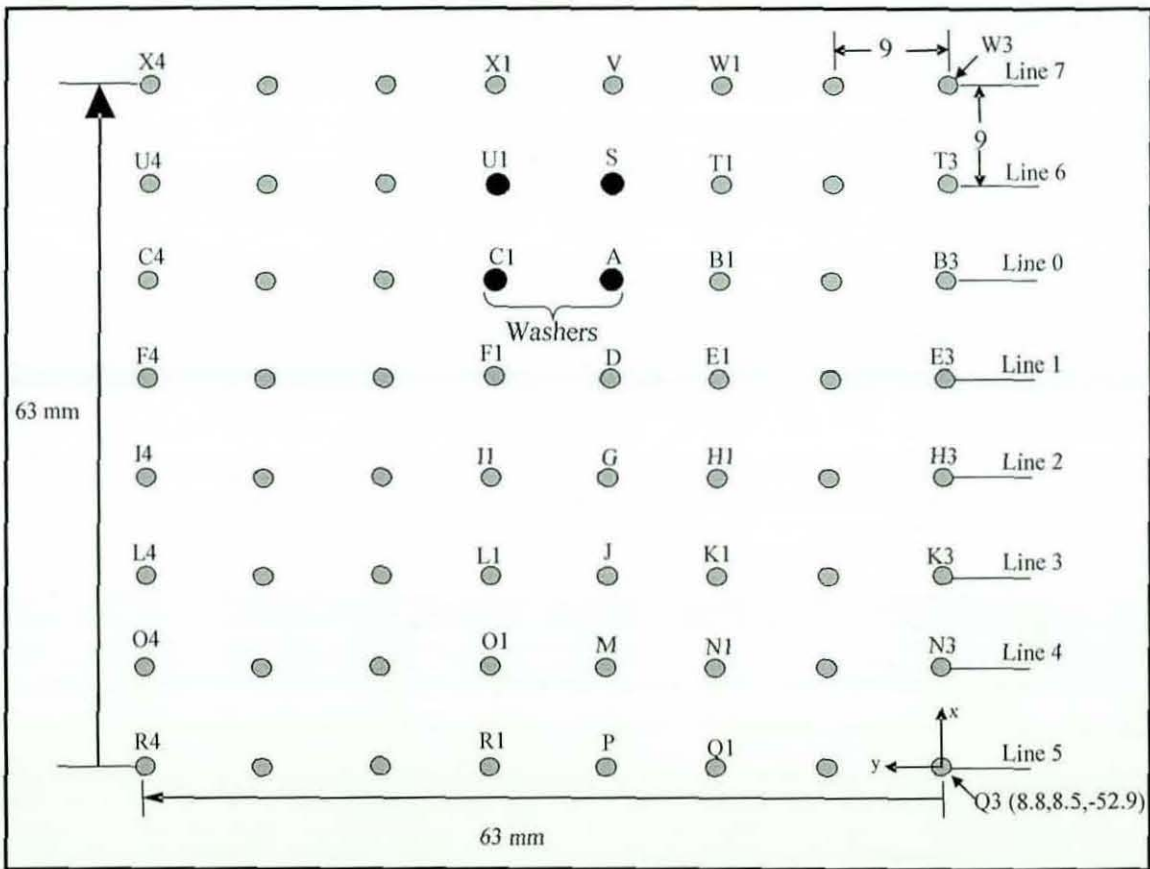


Figure G- 3 Fiducial layout on the Lateral Source calibration plate

Line	Fiducial	Specified values		CMM Measurements	
		X	Y	X	Y
0	A	53.8	35.5	53.8	35.39
0	B1	53.8	26.5	53.85	26.4
0	B2	53.8	17.5	53.87	17.37
0	B3	53.8	8.5	53.83	8.36
0	C1	53.8	44.5	53.8	44.38
0	C2	53.8	53.5	53.81	53.37
0	C3	53.8	62.5	53.72	62.4
0	C4	53.8	71.5	53.73	71.39
1	D	44.8	35.5	44.87	35.36
1	E1	44.8	26.5	44.8	26.34
1	E2	44.8	17.5	44.86	17.4
1	E3	44.8	8.5	44.9	8.42
1	F1	44.8	44.5	44.86	44.35
1	F2	44.8	53.5	44.75	53.36
1	F3	44.8	62.5	44.75	62.35
1	F4	44.8	71.5	44.7	71.39
2	G	35.8	35.5	35.9	35.32
2	H1	35.8	26.5	35.87	26.32
2	H2	35.8	17.5	35.86	17.31
2	H3	35.8	8.5	35.85	8.33
2	I1	35.8	44.5	35.81	44.35
2	I2	35.8	53.5	35.82	53.34
2	I3	35.8	62.5	35.81	62.35
2	I4	35.8	71.5	35.7	71.35
3	J	26.8	35.5	26.85	35.33
3	K1	26.8	26.5	26.84	26.25
3	K2	26.8	17.5	26.86	17.31
3	K3	26.8	8.5	26.84	8.26
3	L1	26.8	44.5	26.86	44.3
3	L2	26.8	53.5	26.78	53.3
3	L3	26.8	62.5	26.76	62.3
3	L4	26.8	71.5	26.74	71.32

Table G- 3 Comparison between specified and measured fiducial centre for the Lateral Source

Plate - 1

Line	Fiducial	Specified values		CMM Measurements	
		X	Y	X	Y
4	M	17.8	35.5	17.85	35.22
4	N1	17.8	26.5	17.88	26.26
4	N2	17.8	17.5	17.83	17.29
4	N3	17.8	8.5	17.87	8.29
4	O1	17.8	44.5	17.78	44.31
4	O2	17.8	53.5	17.82	53.27
4	O3	17.8	62.5	17.74	62.28
4	O4	17.8	71.5	17.71	71.29
5	P	8.8	35.5	8.87	35.2
5	Q1	8.8	26.5	8.82	26.25
5	Q2	8.8	17.5	8.85	17.28
5	Q3	8.8	8.5	8.85	8.27
5	R1	8.8	44.5	8.83	44.2
5	R2	8.8	53.5	8.7	53.26
5	R3	8.8	62.5	8.72	62.24
5	R4	8.8	71.5	8.71	71.26
6	S	62.8	35.5	62.77	35.42
6	T1	62.8	26.5	62.79	26.46
6	T2	62.8	17.5	62.83	17.38
6	T3	62.8	8.5	62.88	8.45
6	U1	62.8	44.5	62.81	44.42
6	U2	62.8	53.5	62.74	53.44
6	U3	62.8	62.5	62.72	62.44
6	U4	62.8	71.5	62.72	71.43
7	V	71.8	35.5	71.88	35.4
7	W1	71.8	26.5	71.87	26.5
7	W2	71.8	17.5	71.95	17.4
7	W3	71.8	8.5	71.95	8.35
7	X1	71.8	44.5	71.84	44.42
7	X2	71.8	53.5	71.78	53.44
7	X3	71.8	62.5	71.73	62.44
7	X4	71.8	71.5	71.69	71.5

Table G- 4 Comparison between specified and measured fiducial centre for the Lateral Source

Plate - 2

G.3 AP XRII Calibration plate

Figure G- 4 shows the fiducial layout on the AP XRII calibration plate, which each fiducial being given a unique identity. Whereas, Table G- 5 and Table G- 6 depicts the comparison between the specified and measured location of each fiducial embedded on the AP XRII calibration Plate. It should be noted that all dimensions are in millimetre.

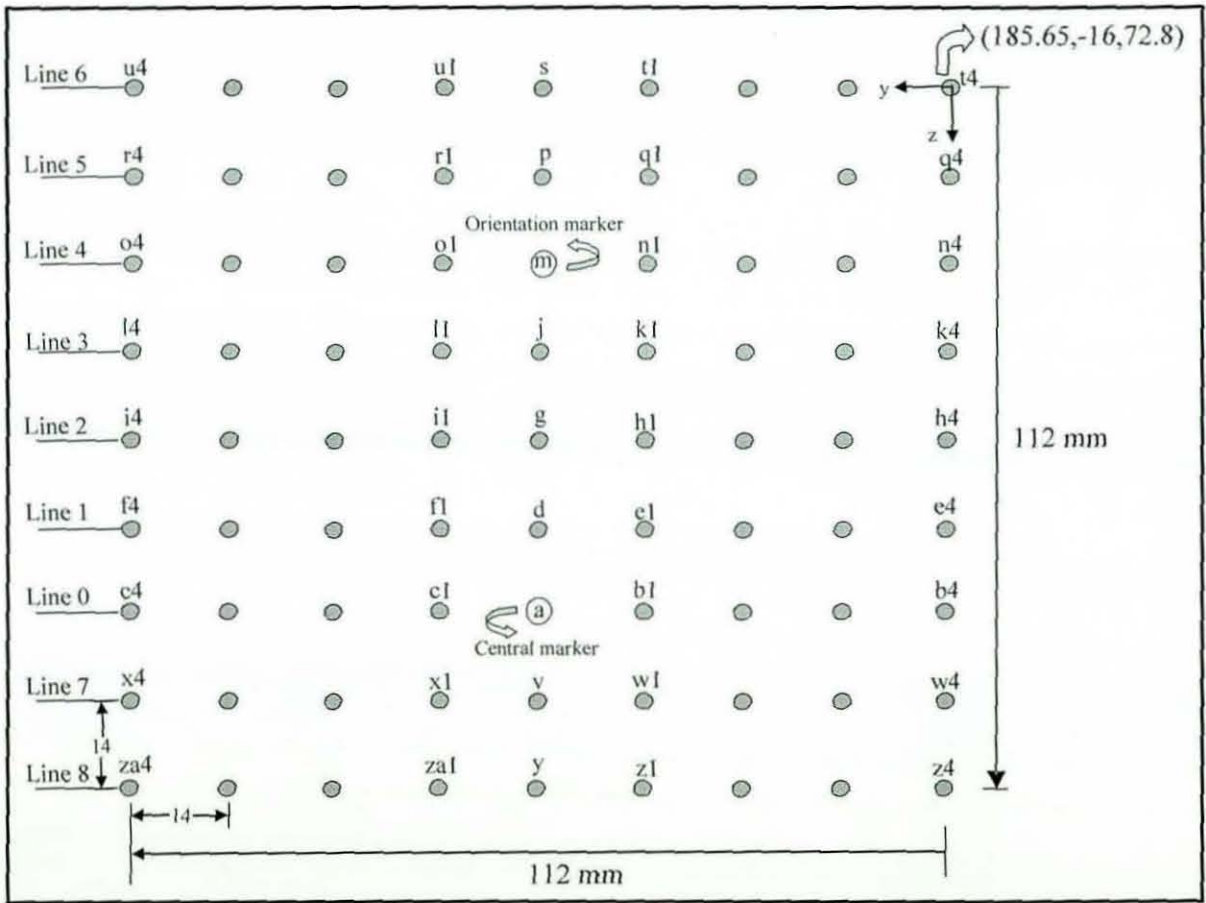


Figure G- 4 Fiducial layout on the AP XRII calibration plate

Line	Fiducial	Specified values		CMM Measurements	
		Y	Z	Y	Z
0	a	40	156.8	40.34	157.12
0	b1	26	156.8	26.33	157.19
0	b2	12	156.8	12.25	157.13
0	b3	-2	156.8	-1.73	157.17
0	b4	-16	156.8	-15.74	157.12
0	c1	54	156.8	54.26	157.15
0	c2	68	156.8	68.32	157.13
0	c3	82	156.8	82.39	157.07
0	c4	96	156.8	96.39	157.06
1	d	40	142.8	40.28	143.08
1	e1	26	142.8	26.3	143.16
1	e2	12	142.8	12.31	143.18
1	e3	-2	142.8	-1.69	143.13
1	e4	-16	142.8	-15.75	143.08
1	f1	54	142.8	54.29	143.18
1	f2	68	142.8	68.29	143
1	f3	82	142.8	82.36	142.98
1	f4	96	142.8	96.26	142.96
2	g	40	128.8	40.19	129.15
2	h1	26	128.8	26.17	129.11
2	h2	12	128.8	12.2	129.11
2	h3	-2	128.8	-1.79	129.15
2	h4	-16	128.8	-15.77	129.19
2	i1	54	128.8	54.21	129.1
2	i2	68	128.8	68.33	129.06
2	i3	82	128.8	82.28	129.01
2	i4	96	128.8	96.22	129.01
3	j	40	114.8	40.24	115.1
3	k1	26	114.8	26.21	115.17
3	k2	12	114.8	12.24	115.15
3	k3	-2	114.8	-1.74	115.07
3	k4	-16	114.8	-15.82	115.13
3	l1	54	114.8	54.2	115
3	l2	68	114.8	68.27	114.97
3	l3	82	114.8	82.23	114.98
3	l4	96	114.8	96.15	115.01
4	m	40	100.8	40.26	101.08
4	n1	26	100.8	26.27	101.07
4	n2	12	100.8	12.24	101.17
4	n3	-2	100.8	-1.79	101.09
4	n4	-16	100.8	-15.73	101.09
4	o1	54	100.8	54.3	101.09
4	o2	68	100.8	68.16	101.04
4	o3	82	100.8	82.25	101.09
4	o4	96	100.8	96.26	101.05

Table G- 5 Comparison between specified and measured fiducial centre for the AP XR11 Plate - I

Line	Fiducial	Specified values		CMM Measurements	
		Y	Z	Y	Z
5	p	40	86.8	40.15	87.1
5	q1	26	86.8	26.29	87.13
5	q2	12	86.8	12.15	87.12
5	q3	-2	86.8	-1.79	87.11
5	q4	-16	86.8	-15.8	87.08
5	r1	54	86.8	54.26	87.09
5	r2	68	86.8	68.2	87.15
5	r3	82	86.8	82.21	87.11
5	r4	96	86.8	96.27	86.99
6	s	40	72.8	40.07	73.07
6	t1	26	72.8	26.14	73.11
6	t2	12	72.8	12.19	73.12
6	t3	-2	72.8	-1.92	73.13
6	t4	-16	72.8	-15.86	73.17
6	u1	54	72.8	54.18	73
6	u2	68	72.8	68.25	72.98
6	u3	82	72.8	82.2	72.96
6	u4	96	72.8	96.28	72.94
7	v	40	170.8	40.35	171.13
7	w1	26	170.8	26.32	171.21
7	w2	12	170.8	12.31	171.18
7	w3	-2	170.8	-1.72	171.2
7	w4	-16	170.8	-15.7	171.25
7	x1	54	170.8	54.34	171.08
7	x2	68	170.8	68.31	171.15
7	x3	82	170.8	82.35	170.99
7	x4	96	170.8	96.42	171.01
8	y	40	184.8	40.34	185.14
8	z1	26	184.8	26.4	185.15
8	z2	12	184.8	12.23	185.16
8	z3	-2	184.8	-1.76	185.32
8	z4	-16	184.8	-15.68	185.2
8	za1	54	184.8	54.29	185.1
8	za2	68	184.8	68.39	185.11
8	za3	82	184.8	82.39	185.07
8	za4	96	184.8	96.39	185.12

Table G- 6 Comparison between specified and measured fiducial centre for the AP XR11 Plate - 2

G.4 AP Source Calibration plate

Figure G- 5 shows the fiducial layout on the AP XRII calibration plate, which each fiducial being given a unique identity. Whereas, Table G- 7 and Table G- 8 depicts the comparison between the specified and measured location of each fiducial embedded on the AP XRII calibration Plate. It should be noted that all dimensions are in millimetre.

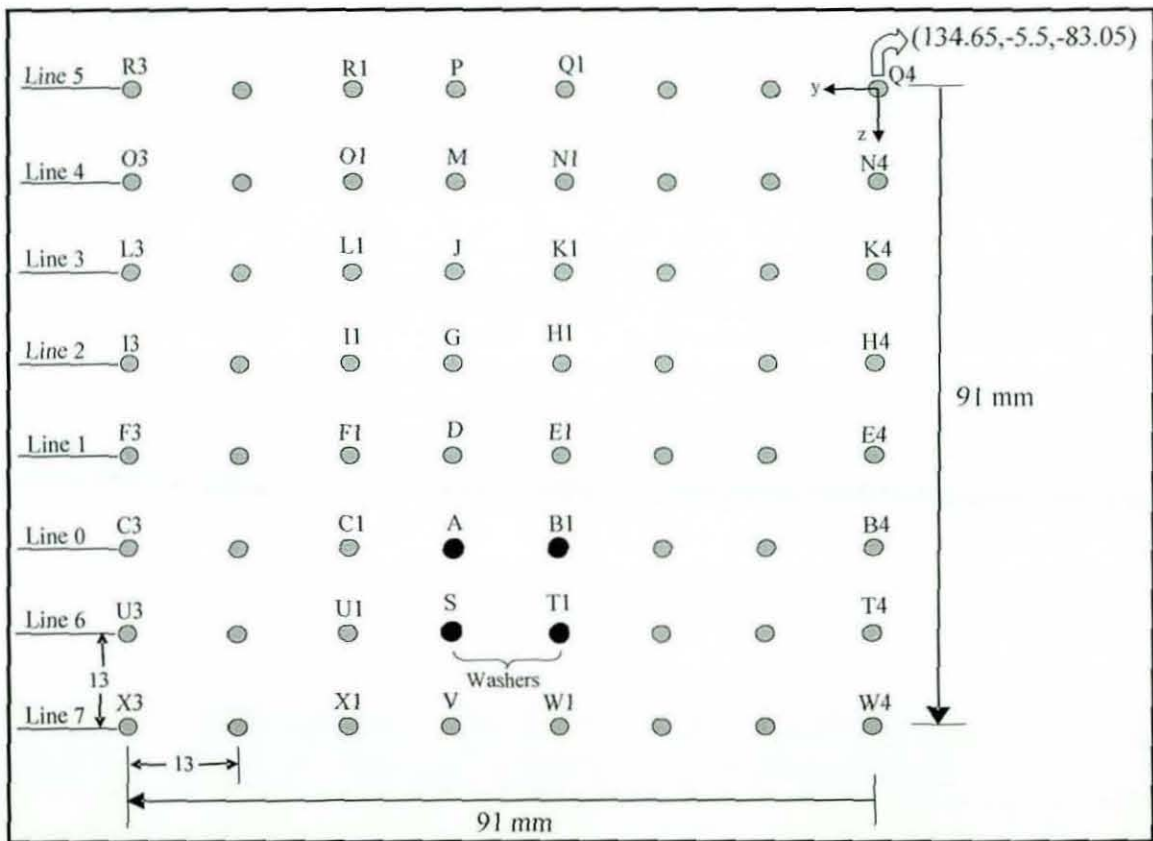


Figure G- 5 Fiducial layout on the AP Source calibration plate

Line	Fiducial	Specified values		CMM Measurements	
		Y	Z	Y	Z
0	A	46.5	148.05	46.96	148.63
0	B1	33.5	148.05	33.95	148.69
0	B2	20.5	148.05	20.9	148.72
0	B3	7.5	148.05	7.93	148.74
0	B4	-5.5	148.05	-5.07	148.79
0	C1	59.5	148.05	59.9	148.59
0	C2	72.5	148.05	72.88	148.58
0	C3	85.5	148.05	85.92	148.55
1	D	46.5	135.05	46.87	135.68
1	E1	33.5	135.05	33.9	135.66
1	E2	20.5	135.05	20.88	135.68
1	E3	7.5	135.05	7.89	135.69
1	E4	-5.5	135.05	-5.13	135.75
1	F1	59.5	135.05	59.86	135.61
1	F2	72.5	135.05	72.85	135.6
1	F3	85.5	135.05	85.89	135.56
2	G	46.5	122.05	46.87	122.63
2	H1	33.5	122.05	33.87	122.68
2	H2	20.5	122.05	20.86	122.68
2	H3	7.5	122.05	7.89	122.72
2	H4	-5.5	122.05	-5.09	122.72
2	I1	59.5	122.05	58.88	122.6
2	I2	72.5	122.05	72.89	122.59
2	I3	85.5	122.05	85.88	122.6
3	J	46.5	109.05	46.87	109.63
3	K1	33.5	109.05	33.83	109.68
3	K2	20.5	109.05	20.85	109.66
3	K3	7.5	109.05	7.82	109.7
3	K4	-5.5	109.05	-5.16	109.74
3	L1	59.5	109.05	59.88	109.61
3	L2	72.5	109.05	72.85	109.63
3	L3	85.5	109.05	85.85	109.59

Table G- 7 Comparison between specified and measured fiducial centre for the AP Source Plate -

Line	Fiducial	Specified values		CMM Measurements	
		Y	Z	Y	Z
4	M	46.5	96.05	46.87	96.62
4	N1	33.5	96.05	33.84	96.64
4	N2	20.5	96.05	20.83	96.66
4	N3	7.5	96.05	7.84	96.67
4	N4	-5.5	96.05	-5.17	96.67
4	O1	59.5	96.05	59.84	96.65
4	O2	72.5	96.05	72.88	96.58
4	O3	85.5	96.05	85.85	96.58
5	P	46.5	83.05	46.84	83.63
5	Q1	33.5	83.05	33.79	83.65
5	Q2	20.5	83.05	20.79	83.67
5	Q3	7.5	83.05	7.83	83.68
5	Q4	-5.5	83.05	-5.19	83.71
5	R1	59.5	83.05	59.84	83.6
5	R2	72.5	83.05	72.87	83.61
5	R3	85.5	83.05	85.85	83.62
6	S	46.5	161.05	46.89	161.65
6	T1	33.5	161.05	33.92	161.71
6	T2	20.5	161.05	20.93	161.71
6	T3	7.5	161.05	7.91	161.74
6	T4	-5.5	161.05	-5.04	161.74
6	U1	59.5	161.05	59.89	161.59
6	U2	72.5	161.05	72.91	161.58
6	U3	85.5	161.05	85.92	161.57
7	V	46.5	174.05	46.95	174.64
7	W1	33.5	174.05	33.92	174.7
7	W2	20.5	174.05	20.92	174.69
7	W3	7.5	174.05	7.91	174.73
7	W4	-5.5	174.05	-5.04	174.74
7	X1	59.5	174.05	59.94	174.61
7	X2	72.5	174.05	72.93	174.59
7	X3	85.5	174.05	85.96	174.56

Table G- 8 Comparison between specified and measured fiducial centre for the AP Source Plate -

APPENDIX H: Publications

Conference paper titled as **“X-Ray based Machine vision system for Robotic Assisted Orthopaedic Surgery”** published in 9th Annual Conference on Medical Image Understanding & Analysis by BMWA, held in Bristol, UK
19-20, July 2005.

X-Ray based Machine vision system for Robotic Assisted Orthopaedic Surgery

F. Junejo⁹, K. Bouazza-Marouf, D. Kerr and A.J. Taylor

Wolfson School of Mechanical and Manufacturing Engineering, Loughborough University, UK

Abstract

In surgical procedures for femoral shaft fracture treatment, current techniques for locking of distal holes on an intramedullary nail (i.e. distal locking) rely heavily on the use of two-dimensional X-ray images, to guide three-dimensional bone drilling processes. Therefore, a large number of X-ray images are required as the surgeon uses his/her skills and experience to locate the distal hole axes. Since the long term effects of X-ray radiation and their relation to different types of cancer still remains unknown, there is a need to develop a surgical technique that can limit the use of X-rays during the distal locking procedure. A Robotic-Assisted Orthopaedic Surgery System has been developed at Loughborough University to assist orthopaedic surgeons by reducing the irradiation involved in such operations. This system employs a novel approach of using a calibration frame with an X-ray based vision system to measure the direction of the distal holes axes. The system simplifies the current approach, as it uses only two near-orthogonal X-ray images, thereby considerably reducing the irradiation to both surgeon and patient. Laboratory test results have shown that the proposed system is very robust in the presence of variable noise and contrast in the X-ray images.

1. Introduction

Nowadays, intramedullary nailing is the best available method for femoral shaft fracture treatment [1], as it provides adequate stabilization for the mid-shaft fractures. However, in order to provide a more effective fixation, i.e. rotational and axial stability, concept of distal locking has been introduced [2]. The intramedullary nail is in the form of a stainless steel tube with fixation holes at the proximal and distal ends. The deformation of the intramedullary nail during surgical procedure makes the insertion of

⁹ Corresponding author. Wolfson School of Mechanical and Manufacturing Engineering, Loughborough University, LE11 3TU, Loughborough, UK. Tel.: +44-1509-227579; Email address: F.Junejo@lboro.ac.uk

the distal locking screws the most demanding step. Many devices have been developed to assist orthopaedic surgeons during distal locking. Examples include proximally mounted targeting devices [3], image intensifier mounted devices [4], laser devices [5] and mechanical guides [6]. However, all of these devices and techniques have deficiencies, for example, they are only selectively applicable, are cumbersome and difficult to use, time consuming, or are not sufficiently accurate. Due to their simplicity, free hand techniques are used nowadays by most of the surgeons as the best available method for the distal locking procedure [7]. However, the free hand technique uses the so-called “perfect circle approach” i.e. the position of the C-arm on the stationary leg is adjusted with continuous X-ray imaging until the two distal holes appear as near perfect circles rather than simply as ellipses. The surgeon then adjusts the entry point and orientation of the drill so that its axis coincides with the corresponding distal hole axis. Drilling proceeds incrementally, with each advance verified with a new pair of X-ray images. The major disadvantages of this technique are excessive irradiation to both surgeon and patient and lengthy operational time which depends extensively on the experience of the surgeon.

2.Method

The aim of this study is to develop a system which can eliminate the conventional “perfect circle approach”, thus reducing surgery time and the surgeon’s cumulative radiation exposure. Furthermore, the outcome of the distal locking procedure will be improved by ensuring that the drill and the axes of the distal holes are in alignment, thereby eliminating geometric errors and their associated complications. The system determines the direction of the two distal holes axes with respect to a calibration frame, which contains two Lateral and two AP calibration plates as shown in Figure 1(a). These calibration plates have an array of fiducial markers embedded on them. The adopted technique is implemented in the following manner:

2.1 Capture of Intraoperative X-ray images

In laboratory trials, two nearly orthogonal i.e. Lateral and Anterior-Posterior (AP) view X-ray images of the distal end of the intramedullary nail are taken together with the calibration frame as shown in Figure 1(b).

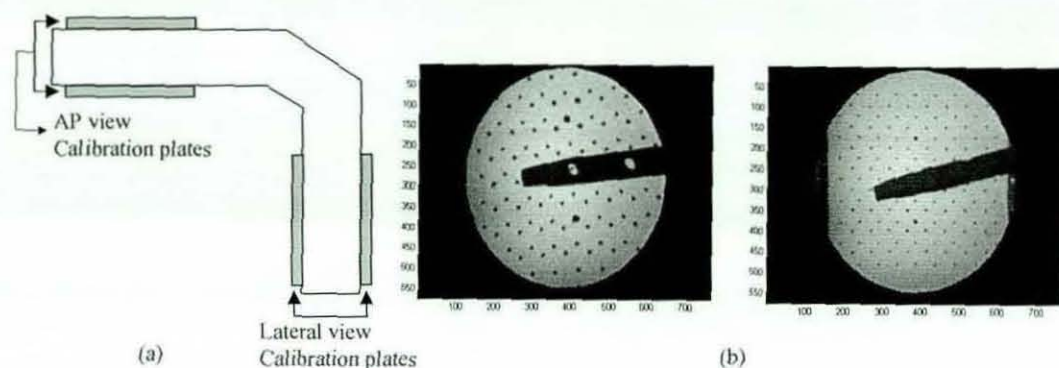


Figure 1 (a) Calibration frame (b) Typical Lateral view (L.H.S) and AP view X-ray images during laboratory trials

A simulation of the distal locking procedure is performed using a cylindrical nail of 14mm diameter containing two distal holes of 6.8mm diameter that are 3cm apart to represent a standard intramedullary nail. The nail is rotated by known angles (so that results obtained from image vision analyses can be verified) using a specially designed test-rig.

Keeping in mind that robustness, reliability and repeatability are of paramount importance when introducing new technologies in operating theatres, all the steps involved during image vision analyses are fully automated, and hence the image vision system is user independent. Once intraoperative X-ray images are obtained, image vision analyses are performed in the following manner:

2.2 Fiducial Recognition

X-ray Photogrammetry techniques work by introducing fiducials in radiographic images to reconstruct 3D locations of imaged object points. Therefore, at first, automatic fiducial recognition is carried out to determine the image (pixel) co-ordinates of all the visible fiducials, in Lateral and AP X-ray images. These fiducials link the real world and the 2D image space, due to their presence in both.

2.3 Localized Distortion correction

X-ray images have inherent distortion, mainly due to the internal geometry of the image intensifier and the influence of magnetic fields on the electron acceleration within the X-ray tube. Therefore, localized distortion correction based on fiducial neighbourhood scanning has been undertaken for intraoperative distortion correction of the X-ray images [8]. Using localized distortion correction implies that data

obtained directly from actual intraoperative images is used to perform distortion correction. As a result, assumptions do not have to be made with regard to magnetic influence in the operating room, the internal geometry of the Image Intensifier tube or the orientation of the C-arm unit.

2.4 Location of X-ray Source

X-rays can be considered to be a special case of central projection [8], in which all the rays pass through a perspective centre i.e. focal point. Therefore, in order to convert 2-D image information into 3-D position, it is essential to determine the focal point in both Lateral and AP views. After fiducial recognition, focal lines are constructed. Construction of the focal lines is accomplished by selecting an image point within the registration image, and assigning its corresponding world co-ordinate to a point on each of the two calibration plates in the relevant view. In this way, for a single image point, two corresponding world co-ordinates form a line in space, i.e. a focal line. Ideally these focal lines should intersect at a true focal point. However, due to the nature of X-ray imaging system, the lines do not intersect in this way, thus an estimated focal point must be obtained. Therefore, to obtain the focal point, the intersection of each pair of focal lines is obtained. For pairs which do not intersect, the point of closest approach is determined as the intersection. The centre of gravity of this set of intersection points is used to determine the estimated focal point.

2.5 Location of the nail axis

In order to determine the nail axis in space, automatic nail border detection is first carried out in both Lateral and AP views. By assuming that the nail axis coincides with the centre of the nail borderlines, the two boundary edges for the nail are then bisected to determine the nail axis in both views. In the Lateral view it is possible to find points on the centre line of the nail. Once these points are known in the image plane, a triangulation technique [9] is used to find their corresponding world coordinates on the calibration plate. Both these points in conjunction with the Lateral view focal point define a plane. A similar approach is carried out for AP view. Once these planes are defined in the Lateral and AP views, their intersection defines the nail axis in space [10,11], as shown in Figure 2.

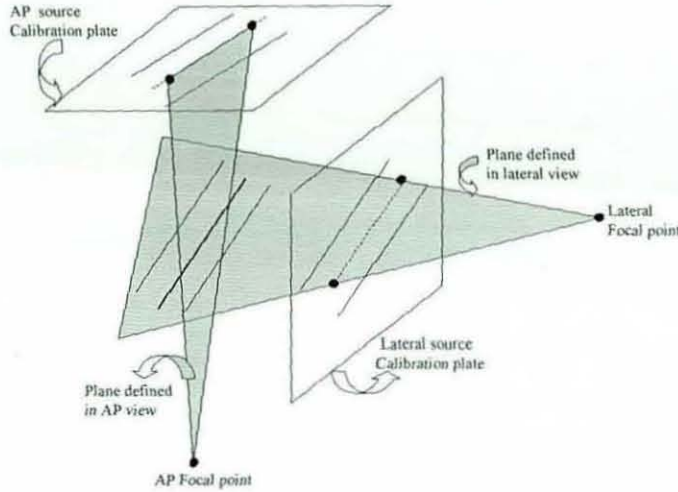


Figure 2 Location of the nail axis in space

2.6 Feature extraction to determine drilling trajectory

During the rotation of the nail, the angle of the major axis of the oval-shaped distal hole projection changes significantly, whereas the nail axis remains constant. Therefore, the region containing the distal hole projection is selected from the Lateral view. Image segmentation is then performed to extract the oval, the major axis of which is then determined using moments. The angle λ between the major axis of the oval and the nail axis, is then determined as a characteristic measurement, as shown in Figure 3.

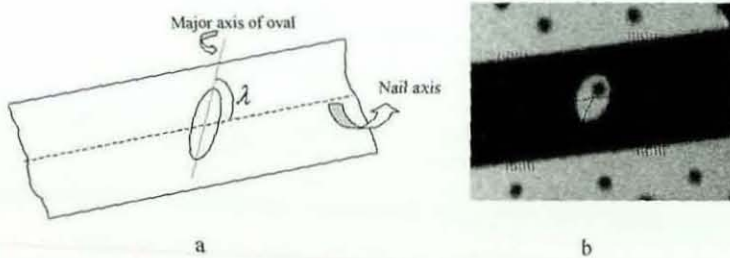


Figure 3 Angle between the major axis of the oval and the nail axis. (a) Concept. (b) Implementation using image vision analyses

The desired drilling trajectory must pass through the centre of the distal hole, which can be obtained from the intersection of the nail axis with the distal hole axis. This is achieved by intersecting the nail axis with the line-of-sight that passes through the centre of the distal hole. In order to construct this line-of-sight, the image (pixel) co-ordinates of the centre of the oval-shaped distal hole projection are

measured using lateral view X-ray image. Then application of triangulation technique [9] to this measured pixel location, allows the corresponding calibration plate intersection point " P_{Source} " to be calculated. Therefore, a line-of-sight is defined using the known focal point of the lateral view in conjunction with " P_{Source} ", which passes through the centre of the distal hole "O" as shown in Figure 4.

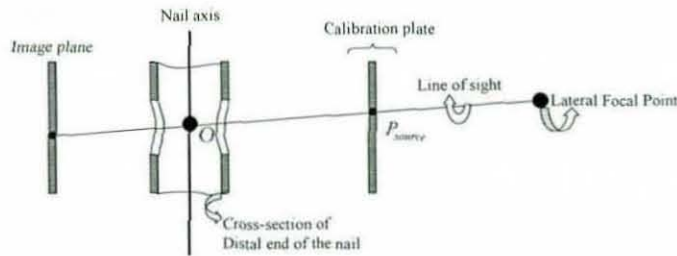


Figure 4 Determination of distal hole's centre

The angle ϕ , between the nail axis and the line-of-sight yields the rotation of the nail about the X-ray imaging axis in the Lateral view. The characteristic measurements, λ and ϕ , are then used in conjunction with a model of the nail (obtained using Manufacturer's data) to determine the direction of the axes of the distal holes.

2.7 Influence of contrast and noise variations

During this study, special attention has been given to the effect of variable contrast and noise in the X-ray images on image vision analyses. To measure accurately the performance of vision system, the combined effects of noise and contrast must be evaluated. Since the contrast of an X-ray image is controlled by a combination of X-ray tube voltage and current, different combinations of voltage and current are used during laboratory trials to achieve a wide range of contrast in the X-ray images. Noise can prove to be a major limiting factor in image segmentation. Simulated Gaussian noise of known mean and standard deviation was added to each of the variable contrast images. Subsequent tests showed that good repeatability (less than 0.1° difference in measurement of the distal holes axes direction) could be obtained for up to 15% of gaussian noise across a wide range of contrast.

3. Results and Conclusion

In this study, an automated image vision system is presented to determine the position and orientation of the axes of the distal holes of the intramedullary nail by using only two intraoperative X-ray images. The system is tested with data obtained through laboratory trials as described in section 2.1. The analyses have shown that the proposed algorithm is able to predict the rotation of the nail about its long axis with a mean accuracy of 0.20° (worst case being 0.35°) which is well within the acceptable limit of $\pm 1^{\circ}$. Therefore, the aim of reducing X-ray radiation exposure to the minimum possible in locating accurately the axes of the distal holes of intramedullary nail has been successfully achieved.

References

1. J. Lin, S.J. Lin, P.Q. Chen & et. al, "Stress analysis of the distal locking screws for femoral interlocking nailing", *J.Orthop Res.* 19(1), pp. 57-63, 2001.
2. I. Browbank, "Intraoperative Registration for Robotic-Assisted Orthopaedic Surgery", PhD Thesis, Loughborough University, UK. 1998.
3. C. Krettek, B. Konemann, T. Miclau & et. al, "A mechanical aiming distal device for distal locking in femoral nails", *Clin Orthop Relat Res.* (364), pp. 267-275, 1999.
4. S. Tyropoulos, C. Garmavos, "A new distal targeting device for closed interlocking nailing", *Injury.* 32 (9), pp. 732-735, 2001.
5. J.A. Goulet, F. Loday, C.L. Saltzman & et. al, "Interlocking Intramedullary nails. An improved method of screw placement combining image intensification and laser light", *Clin Orthop Relat Res.* (281), pp. 199-203, 1992.
6. K.A. Steriopoulos, G.M. Kontakis, P.G. Katonis & et. al, "Placement of the distal locking screws of the femoral intramedullary nail without radiation", *Arch Orthop Trauma Surg.* 115(1), pp. 43-44, 1996.
7. E.F. Barrick, "Distal locking screw insertion using a cannulated drill bit", *Journal of Orthopaedic Trauma.* 7(3), pp. 248-251, 1993.
8. I. Browbank, K. Bouazza-Marouf & J. Schanbler, "Robotic assisted internal fixation of hip fractures: A fluoroscopy based Intraoperative technique", *Proc Instn Mech Engrs. Part H, Journal of Engineering in medicine* 214 (2), pp. 165-179, 2000.
9. J. Schanbler, "Robotic Assistance in Orthopaedic Surgery", MSc Thesis. Loughborough University, UK. 1997.
10. M.J. Hochrainer, "Repair of femoral shaft fracture", MSc Thesis. Loughborough University, UK. 1997.
11. W.J. Viant, R. Philips, J.G. Griffiths & et. al, "A computer assisted orthopaedic surgical system for distal locking of intramedullary nails", *Proc Instn Mech Engrs. Part H,* (211), pp. 293-300, 1997.

Journal paper titled as **“X-Ray based
Machine vision system for distal locking
of intramedullary nail”** published in
Proc. IMechE Part H: Journal of
Engineering in Medicine, Volume 221(4),
2007, pp. 365-374

X-ray based machine vision system for distal locking of intramedullary nails

F. Junejo¹, K. Bouazza-Marouf¹, D. Kerr¹, A.J. Taylor¹ and G.J.S. Taylor²

¹ The Wolfson School of Mechanical and Manufacturing Engineering, Loughborough University, UK

² Department of Orthopaedic Surgery, Glenfield Hospital, Leicester, UK

Abstract

In surgical procedures for femoral shaft fracture treatment, current techniques for locking the distal end of intramedullary nails, using two screws, rely heavily on the use of two-dimensional X-ray images to guide three-dimensional bone drilling processes. Therefore, a large number of X-ray images are required, as the surgeon uses his/her skills and experience to locate the distal hole axes on the intramedullary nail. The long term effects of X-ray radiation and their relation to different types of cancer still remain uncertain. Therefore, there is a need to develop a surgical technique that can limit the use of X-rays during the distal locking procedure. A Robotic-Assisted Orthopaedic Surgery System has been developed at Loughborough University to assist orthopaedic surgeons by reducing the irradiation involved in such operations. The system simplifies the current approach as it uses only two near-orthogonal X-ray images to determine the drilling trajectory of the distal locking holes, thereby considerably reducing irradiation to both the surgeon and patient. Furthermore, the system uses robust machine vision features to reduce the surgeon's interaction with the system, thus reducing the overall operating time. Laboratory test results have shown that the proposed system is very robust in the presence of variable noise and contrast in the X-ray images.

Keywords: robotic/computer-assisted orthopaedic surgery, intramedullary nailing, distal locking

Notation

D	Distance between the X-ray source and the calibration frame
O	Centre of the distal hole
P_{Source}, P_{XRII}	Corresponding points on the Source and XRII plate for image point representing the centre of the oval
${}_{Th}^{CF}T$	Homogenous transformation matrix describing the theodolite frame of reference relative to calibration frame co-ordinate system
λ	Angle between the major axis of the oval and the nail axis
ϕ	Angle between the nail axis and X-ray imaging axis
θ	Rotation of the nail about its own axis

1 Introduction

The femur, or thigh bone, is the longest, largest and strongest bone of the human body [1]. Femoral-shaft fractures commonly occur as a result of road accidents, falls, and gunshot wounds. In addition, osteoporosis in elderly people dramatically increases the risk of femur fracture. Closed intramedullary nailing (IMN) has shown its efficacy in the treatment of diaphyseal fractures of long bones, especially of complex fractures of the femur. The concept behind IMN is to insert a nail (a stainless steel tube) into the bone canal from the proximal end. This allows the surgeon to perform both the reduction and stabilization procedures without the complications of opening the fracture site, thereby reducing further damage to the traumatized area. This results in lower blood loss, lower infection risk, shorter hospitalisation time and reduced morbidity. Due to these advantages, IMN has become the standard treatment for long bone fractures.

Although conventional IMN with only proximal locking may provide adequate stabilization of mid-shaft fractures, the concept of distal locking was introduced in order to provide more effective fixation. Distal locking involves attaching the nail to the bone fragment at the distal end of the femur by means of screws, as shown in Figure 1, to provide rotational and axial stability.



Figure 1 Femoral shaft fracture treatment using Intramedullary Nailing

A number of problems are faced by orthopaedic surgeons during distal locking of intramedullary nails, the most serious being:

- The intramedullary nail may deform by several millimetres on its passage through the medullary canal to conform to the bone canal shape [2]. Therefore, without compensation for nail deformation, it is impossible to place the distal locking screws correctly using an external guide attached to the proximal end of the nail, as is used for proximal locking screws.
- The use of two-dimensional X-ray images to guide three-dimensional bone drilling procedures means that a large number of X-ray images are required. The surgeon has to mentally correlate the surgical tool and desired drilling trajectory without direct visual feedback. Hence sets of X-ray images must be frequently acquired to ascertain each new position of the surgical tool.

These difficulties make the insertion of the distal locking screws the most demanding step of the IMN operation [2]. In order to overcome these difficulties many devices have been developed to assist orthopaedic surgeons in performing distal locking. Examples include proximally mounted targeting devices [3], image intensifier mounted devices [4], laser devices [5], stereo fluoroscopy [6], magnetic [7] and mechanical guides [8]. However, all of these devices and techniques have deficiencies. For example, they lack versatility (i.e. only selectively applicable), are unstable and not easy to use, are time consuming or are not sufficiently accurate.

Free-hand techniques are currently used by most surgeons as the best available method for the distal locking procedure. However, surgeons rely heavily on hand-eye coordination during the entire procedure and therefore both the duration and outcome of the procedure are highly dependent upon the skill and the experience of the surgeon. Madan *et al* [9] have demonstrated that the average time of radiation exposure during femoral nailing reduces to one-third when performed by a consultant rather than a middle-grade surgeon. The free-hand technique uses the so-called "perfect circle approach" in which the position of the C-arm fluoroscopy unit in relation to the stationary leg is adjusted using X-ray imaging until the two distal holes appear as near perfect circles rather than as ellipses. The surgeon then uses additional X-ray images to adjust the entry point and orientation of the drill bit to align it with the corresponding distal hole axis. Drilling proceeds incrementally, with each advance verified with a new pair of near orthogonal X-ray images resulting in excessive irradiation to the surgeon and patient. According to Mehlman *et al* [10] the total radiation exposure time for femoral intramedullary nailing with proximal and distal locking varies between 3.1 and 31.4min, with distal locking alone occupying up to 30 to 50 percent of the total radiation exposure time. Therefore, there is concern among orthopaedic surgeons about the high levels of exposure to radiation associated with intraoperative C-arm fluoroscopy during the distal locking procedure [11], as there is evidence that carcinogenic potential exists from low-dose, low-energy radiation [12].

The risk of intraoperative radiation to orthopaedic surgeons has recently been the impetus for many researchers to develop surgical techniques that would limit the need for fluoroscopy during distal locking of intramedullary nails. Nolte *et al* [13, 14] developed a computer-assisted free-hand navigation system that uses intraoperative X-ray images as a basis for real-time navigation of surgical tools. It separates image acquisition from the surgical procedure, as it offers continuous intraoperative guidance to surgeons by producing real time positioning of the surgical tool overlaid

on stored X-ray images. The system consists of an optical tracking system; optically tracked calibration grid attached to the image intensifier of the C-arm and optically tracked markers placed on both the implant and the surgical tool. There are other commercially available computer-assisted fluoroscopy based surgical navigation systems, such as SurgiGATE (Medivision, Switzerland) and Fluoronav (Medtronic, USA). Phillips *et al* [15, 16] have developed a computer-assisted orthopaedic surgery system which also uses optical tracking cameras and includes a lockable passive arm. The arm is used to align a drill guide with the computed trajectory using a graphical display. However, although these surgical assist systems reduce the irradiation to the surgeon they may result in a longer overall procedure time in comparison to the free-hand technique [17]. Furthermore, these systems require an unobstructed line-of-sight between the optical tracking cameras and infrared LEDs mounted on the image intensifier and the surgical tool (or drill guide), resulting in a limitation of free movement by the surgical personnel.

The system, developed at Loughborough University by Bouazza-Marouf *et al* [18-21] for robotic assisted internal fixation of hip fractures and distal locking of intramedullary nails uses a calibration frame, shown in Figure 2, and a C-arm X-ray unit. The calibration frame contains two Lateral and two AP (Anterior-Posterior) calibration plates, with each plate containing an array of embedded fiducial markers (stainless steel balls). The drilling trajectory is computed from two near orthogonal intraoperative X-ray images taken with the calibration frame in position around the body part of interest. The radiopaque reference markers (inserted in the radiolucent plates of the calibration frame) which are visible on each X-ray view and image points of interest (e.g. as shown in Figure 3) are used to establish the drilling trajectory with respect to the calibration frame co-ordinate system. Speed, robustness, reliability and repeatability are of paramount importance when introducing any new technology into the operating theatre. Therefore, the novelty of the work presented in this paper lies in the robustness of the machine vision system and the offline CAD Modelling of the intramedullary nail. Look-up tables are obtained by off-line CAD modelling of nails of different shapes and dimensions, and all the steps involved during image analysis have been fully automated to make the vision system user independent and very efficient in terms of time taken to determine the drilling trajectory.

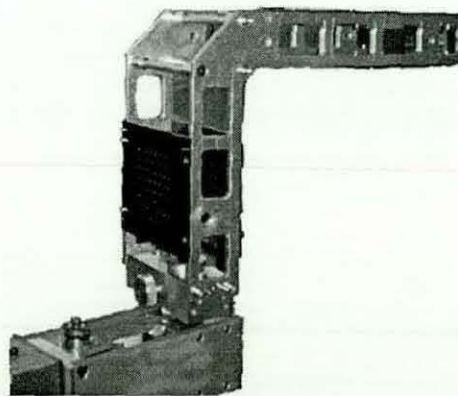


Figure 2 Calibration frame

Furthermore, the adopted machine vision system, is shown in Section 3 to be very robust in the presence of variable noise and contrast in the X-ray images and in terms of variable magnification. Therefore, the benefits of this approach are:

- The use of off-line modelling of the nail reduces the length of time of the surgical procedure.
- The method allows modelling of any shape of intramedullary nail accurately; therefore nails from different manufacturers can be modelled.
- User independent image analysis, and
- Robustness of the machine vision system.

It should be noted that there are two types of intramedullary nails, slotted and solid nails. Slotted nails may have large deformation due to the relative low stiffness as compared to solid nails. The latter nails have virtually negligible local (at the distal holes) deformation to affect the circularity of the holes. This work relates to solid intramedullary nails.

2 The Loughborough Orthopaedic Assistant System: X-ray Image analysis

The Loughborough robotic-assisted orthopaedic surgery system, described in Section 1, uses a calibration frame for calibration and registration purposes rather than relying on an optical tracking system such as Optotrak. Two near orthogonal Lateral and AP X-ray images of the distal end of the intramedullary nail are taken with the calibration frame in position. The calibration frame and typical X-ray images are shown in Figure 3.

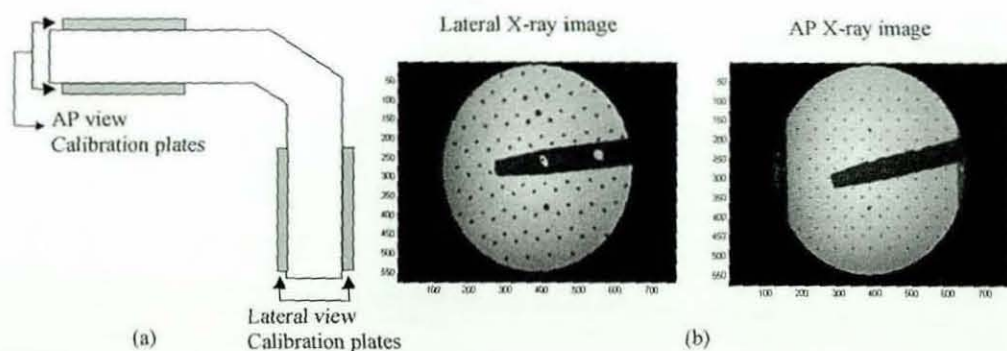


Figure 3 (a) Calibration frame (b) Typical Lateral and AP X-ray images

Simulation of the distal locking procedure was performed using a specially designed test-rig incorporating a cylindrical nail of 14mm diameter containing two distal holes of 7mm diameter spaced 30mm apart to represent a typical intramedullary nail. The nail can be rotated accurately by known angles so that results obtained from image analysis could then be verified. The experimental results are given in Section 3. For clarity, the remainder of this section describes the machine vision system together with the enhancements made in order to reduce the length of time of the surgical procedure in determining the drilling trajectory for IMN distal locking. The image

analysis protocol depicted by the flow diagram of Figure 4 is followed once the Lateral and AP intraoperative X-ray images are acquired.

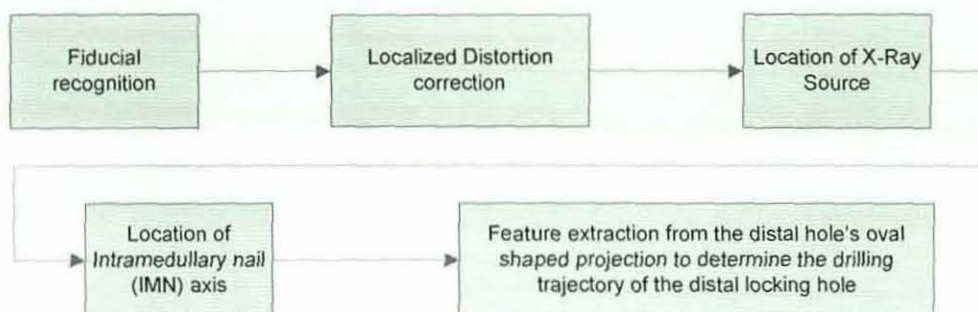


Figure 4 Flow diagram of X-ray image analysis

Fiducial Recognition

X-ray Photogrammetry techniques work by introducing fiducials in radiographic images to reconstruct 3D locations of known object points. Therefore, firstly, automatic fiducial recognition is carried out to determine the image (pixel) coordinates of all the visible fiducials, in both Lateral and AP X-ray images. For fiducial recognition this study employs a localized thresholding approach by dividing the whole image into small sub-regions in which each fiducial is processed individually. Any error in fiducial recognition can induce errors in distortion correction and focal point determination. Therefore, any partially imaged fiducials on the edge of the X-ray image and fiducials touching the edges of the nail (shown in Figure 5) are automatically identified and are not considered in the subsequent analysis.

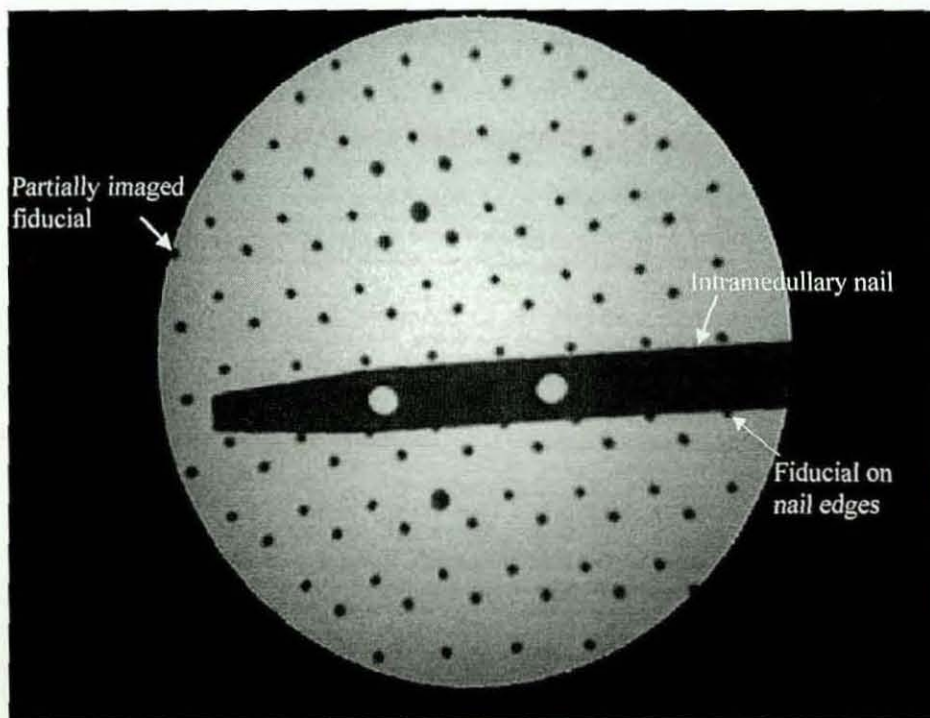


Figure 5 Fiducial Recognition in Lateral X-ray image

Localized Distortion correction

X-ray images have inherent distortion, mainly due to the internal geometry of the image intensifier and the influence of magnetic fields on the electron acceleration within the X-ray tube. Therefore, localized distortion correction based on fiducial neighbourhood scanning has been undertaken for intraoperative distortion correction of the X-ray images [19, 21]. This approach allows data obtained directly from actual intraoperative images to be used to perform distortion correction. As a result, assumptions do not have to be made with regard to magnetic influence in the operating room, the internal geometry of the image intensifier tube or the orientation of the C-arm unit.

Location of the X-ray Source

X-rays can be considered to be a special case of central projection, in which all the rays pass through a perspective centre, or focal point [19, 21]. This point is not identifiable as a physical feature of the X-ray machine but lies at a virtual point behind the X-ray tube. Therefore, in order to convert 2-D image information into a 3-D position, it is essential to determine the focal point in both Lateral and AP views. Once fiducial recognition has been performed both the image (pixel) and world (mm) coordinates of fiducials appearing within the field of view are known. Focal lines are then constructed to determine the location of the X-ray source. Construction of the focal lines is accomplished by selecting image points within the intraoperative X-ray image and assigning their corresponding world co-ordinates to a point on each of the two calibration plates in the relevant view. For this purpose, centres of some of the detected fiducials on the XR11 calibration plate (i.e. the calibration plate nearest to the X-ray image intensifier) are selected as image points, as their world co-ordinates are already known, thereby avoiding any calculation error. For each of these image points a corresponding point on the adjacent source calibration plate (i.e. the calibration plate nearest to the X-ray source) is obtained, as described in [21]. The intersection of each pair of focal lines is obtained and, for pairs which do not intersect due to the nature of X-ray imaging systems, the point of closest approach is determined as the intersection. The centre of gravity of the volume of this set of intersection points is then used as the focal point i.e. the estimated location of the X-ray source.

Location of the nail axis

In order to determine the nail axis in space, automatic nail border detection is carried out in both Lateral and AP views. The borderlines of the nail can be obtained by analysing the two major transitions in grey level values within a profile drawn across the nail. However, measuring the nail edges only once can lead to potential errors, such as presence of a fiducial within the selected profile. Therefore, for nail edge

detection, multiple parallel line profiles on both sides of the distal hole projection are generated as shown in Figure 6.

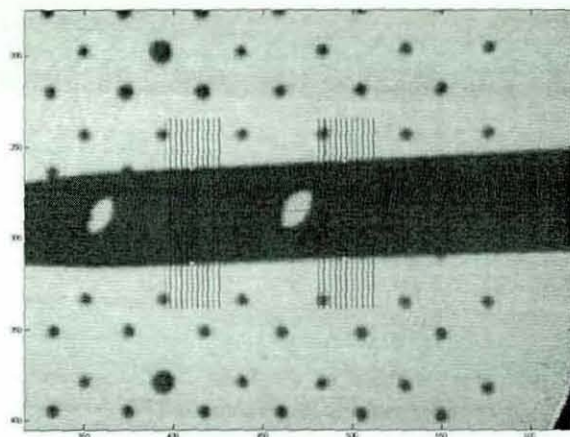


Figure 6 Nail edge detection in Lateral view

By assuming that the nail axis coincides with the centre of the nail borderlines, the two boundary edges for the nail are bisected to determine the nail axis in both the Lateral and AP views. In the Lateral view it is possible to find two points on the centre line of the nail. Once these points are known in the image plane the triangulation technique described in [21] is used to find their corresponding world coordinates on the calibration plate. Both these points in conjunction with the Lateral view focal point define a plane. A similar approach is carried out for the AP view. Once these planes are defined in the Lateral and AP views, their intersection defines the nail axis in space [16, 20], as shown in Figure 7.

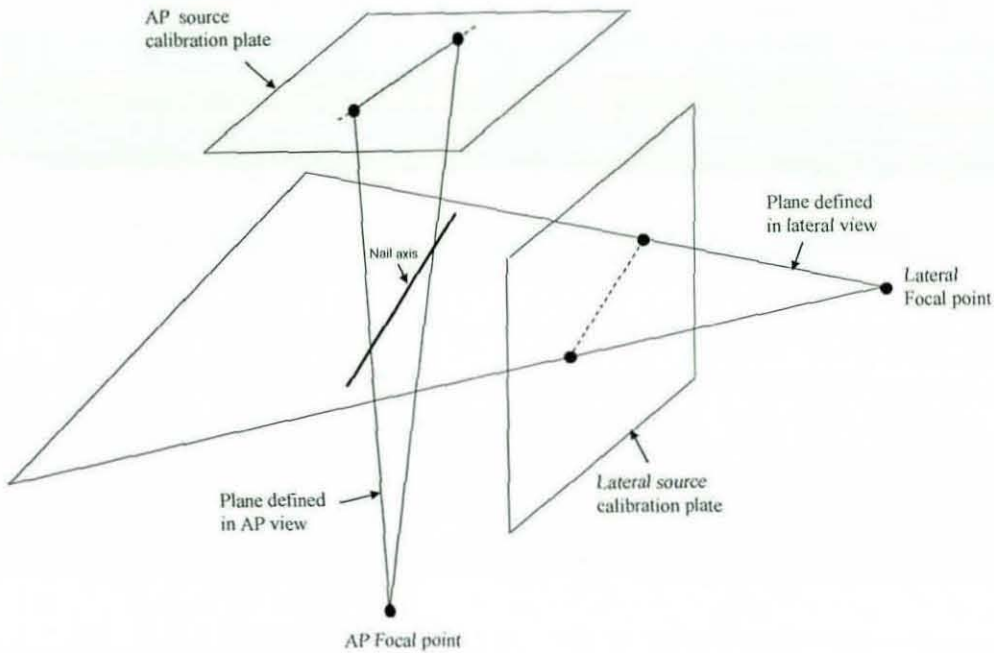


Figure 7 Recovery of the nail axis in space

Determination of the drilling axis for distal holes

The features that are used to determine the drilling trajectory are: the angle λ (shown in Figure 8) between the major axis of the oval and the nail axis, target point (which is the intersection of the distal hole axis and the nail axis) and the angle ϕ (shown in Figure 10) between the x-ray imaging axis and the nail axis. These features are described below.

The angle of the major axis of the oval-shaped distal hole projection changes significantly with respect to the nail axis, when the nail is rotated about its own axis. Therefore, the region containing the distal hole projection is automatically selected from the Lateral view X-ray image and image segmentation is performed to determine the major axis of the oval. The angle λ between the major axis of the oval and the nail axis is then determined as a characteristic measurement.

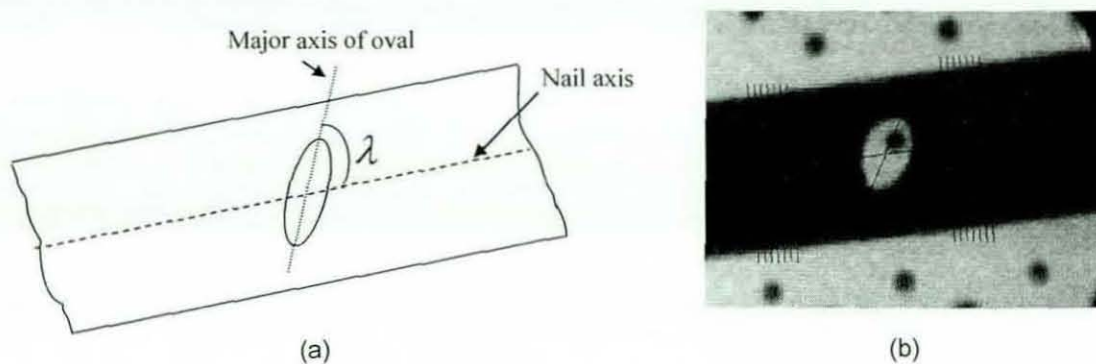


Figure 8 Angle between the major axis of the oval and the nail axis. (a) Concept. (b) Implementation using image analysis

On occasions, however, the image of the hole will contain a fiducial at the edge or entirely within the oval. Therefore, once the region containing the distal locking hole is selected, a check is made in the surroundings of the oval to determine the presence of any fiducial. In the case of a fiducial lying completely within the oval it is relatively easy to convert that fiducial into part of the oval. However, in the case of a fiducial lying on the edge of the oval, e.g. as shown in Figure 9, an algorithm has been developed to remove the fiducial region within the oval.

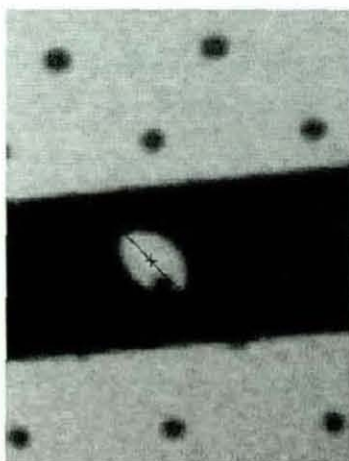


Figure 9 Major axis determination of the oval when a fiducial lies at the edge of the oval.

The desired drilling trajectory must pass through the centre of the distal hole, i.e. the target point, which is the intersection of the nail axis with the distal hole axis. This point is found by intersecting the nail axis with the line-of-sight that passes through the centre of the distal hole. In order to construct this line-of-sight, the image (pixel) co-ordinates of the centre of the oval-shaped distal hole projection are determined using the Lateral X-ray image. Then application of the triangulation technique to this measured pixel location allows the corresponding calibration plate intersection point, "P_{Source}", to be calculated. Therefore a line-of-sight is defined using the known focal point of the Lateral view in conjunction with "P_{Source}" which passes through the target point "O", as shown in. The angle ϕ between the nail axis and line-of-sight (defined by the line passing through the target point "O" and Lateral focal point), as shown in Figure 10, yields the orientation of the nail with respect to the X-ray imaging axis.

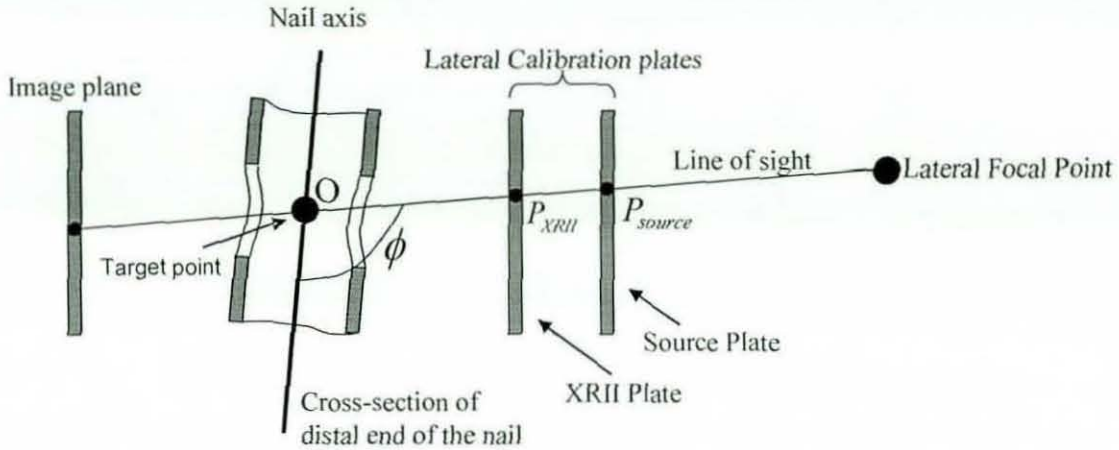


Figure 10 Determination of the centre of the distal hole and ϕ

With the adopted technique, in addition to the angles λ , ϕ and the coordinates of the centre of the distal hole (target point), it is also necessary to determine the rotation of the nail θ about its long axis with respect to the line-of-sight as shown in Figure 11. For this purpose 3D modelling of the nail is done using the manufacturer's data, then, using this model, simulation for a range of values of θ and ϕ is performed. For each unique rotation of the nail the oval shaped projection of the distal locking hole is automatically analysed to determine the angle between the major-axis of the oval and the nail axis i.e. λ . This value of λ , obtained from the modelling of the nail, together with the corresponding values of θ and ϕ , is then imported into Matlab to build a look-up table. The angles λ and ϕ obtained from the image analysis are then entered as input into the look-up-table software to obtain the rotation angle θ .

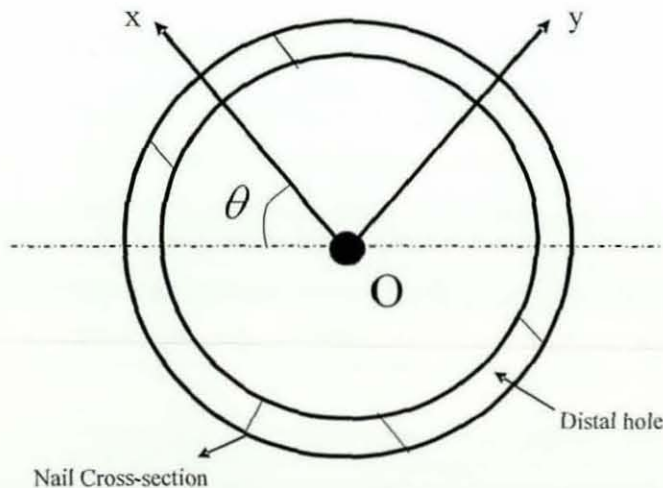


Figure 11 Rotation of the nail about its long axis

The drilling trajectory is then defined using the derived position of the centre of the distal hole (target point) and the angles θ and ϕ .

3 Accuracy evaluation of the machine vision system

In order to evaluate the accuracy of the computer vision system, the drilling trajectory, as computed with respect to the calibration frame, was compared with the true drilling trajectory obtained using theodolite measurements. The following procedure was adopted:

1. Several points on the surface of the Lateral XRII calibration plate were measured using two theodolites to define the calibration frame co-ordinate system with respect to the theodolite frame of reference, i.e. to obtain the homogenous transform ${}^{TH}T_{CF}$, where 'CF' and 'TH' refer to calibration frame and theodolite respectively.
2. A cylindrical nail of 14mm diameter containing two distal holes of 7mm was attached to a test rig. To cover a wide range of possible nail orientations likely to be encountered during the surgical procedure, this test rig was used to simulate different rotations (θ) of the nail about its own axis, with the nail at different orientations (ϕ) with respect to the X-ray imaging axis. In order to define the true trajectory of the distal locking hole, a test piece comprising a solid cylinder of $7_{-0.01}^{+0.00}$ mm diameter with an integral concentric disc of 50mm diameter at one end was fitted in the hole. On the surface of this disc five points, including the centre, were measured with respect to the theodolite frame of reference to determine the central axis ${}^{TH}v$ of the test piece and thus the distal hole axis with respect to the theodolite frame of reference.
3. The central axis of the distal locking hole with respect to the calibration frame obtained as:

$${}^{CF}v = {}^{CF}T_{TH} \cdot {}^{TH}v = {}^{TH}T_{CF}^{-1} \cdot {}^{TH}v$$

was then compared to the computed drilling trajectory described in Section 2.

Additionally, the position of the Lateral X-ray source was varied, as discussed in Section 0, to evaluate the influence of X-ray magnification on the accuracy of the vision system.

The results from the laboratory trials are summarized in Figure 12. The corresponding numbers in Figure 12 (a) and 12 (b) represent the entry and exit points respectively for the nine drilling trajectories. Analysis has shown that a mean positional error of 0.81mm (worst case being 1.18 mm, as depicted by trajectory 5) and mean angular error of 1.01° (worst case being 1.25° , as depicted by trajectory 2) were obtained. These values are considered acceptable for inserting a guide wire of 2.5mm diameter into the distal locking hole of 7mm diameter (or a 5mm diameter distal locking hole) and the subsequent screw insertion.

In light of previous research by Phillips *et al* [15, 16], and in consultation with orthopaedic surgeons, successful drilling of the pilot hole (for locking screw) using a guide wire will result in the successful locking of distal holes of an intramedullary nail. Therefore, based on the results obtained from the laboratory trials presented in this paper, the proposed system provides the accuracy required for a successful insertion of distal locking screws.

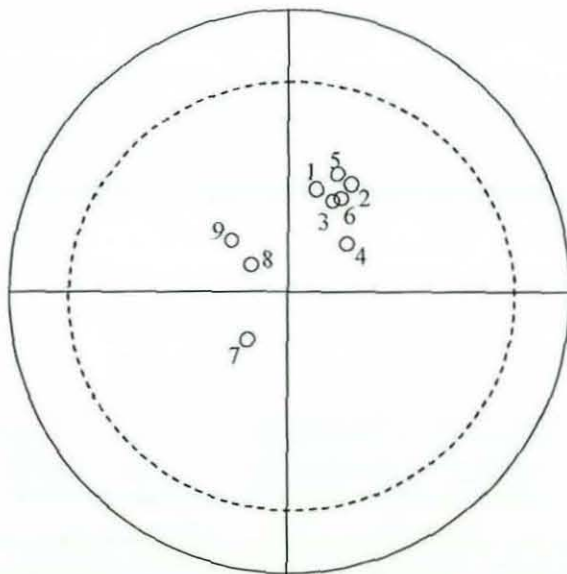
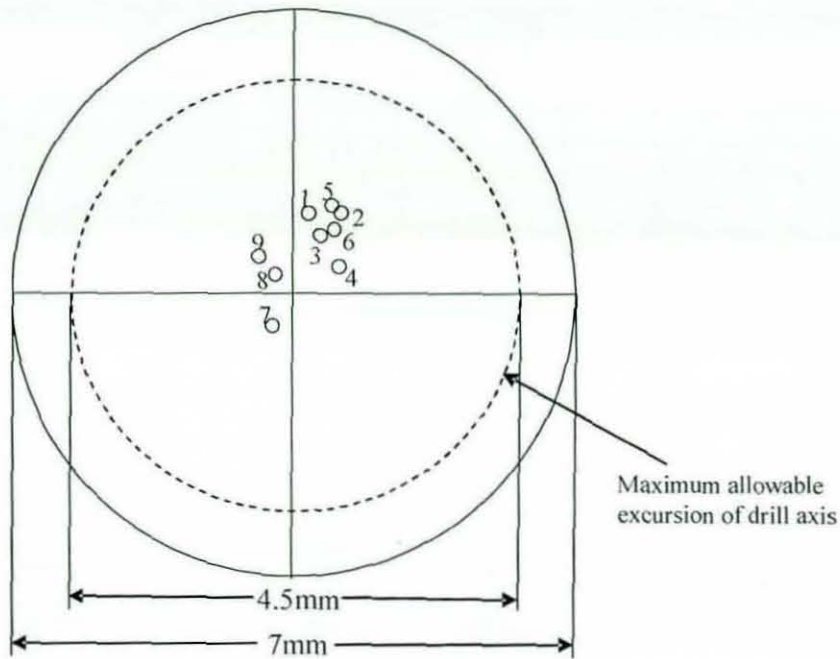


Figure 12 Results from accuracy evaluation of the computer vision system

To evaluate the robustness of the system, the effect of the position of the C-arm X-ray unit with respect to the calibration frame, and also contrast and noise variations in the X-ray images, have been studied, as discussed below.

Effect of X-ray source position on the Lateral view image

In the adopted procedure the C-arm image intensifier is positioned as close as possible to the calibration frame plates in the AP view, however, in the Lateral view the position of the image intensifier (and thus the position of the X-ray source) can vary. Therefore the effect of positioning of the X-ray source has been evaluated.

In X-ray imaging, object points nearer to the X-ray source experience higher magnification than object points nearer to the image plane. Therefore, during laboratory trials, in order to determine the robustness of the image analysis in predicting nail rotation about its long axis at different magnifications, three different positions of the X-ray source with respect to the calibration frame were used for each set of rotations (φ and θ) of the nail. During the trials three values of "D" (shown in Figure 13) used were 345, 395 and 445mm i.e. a difference of 50mm between the positions. The latter distance represents a standard position of the X-ray source for the Lateral image.

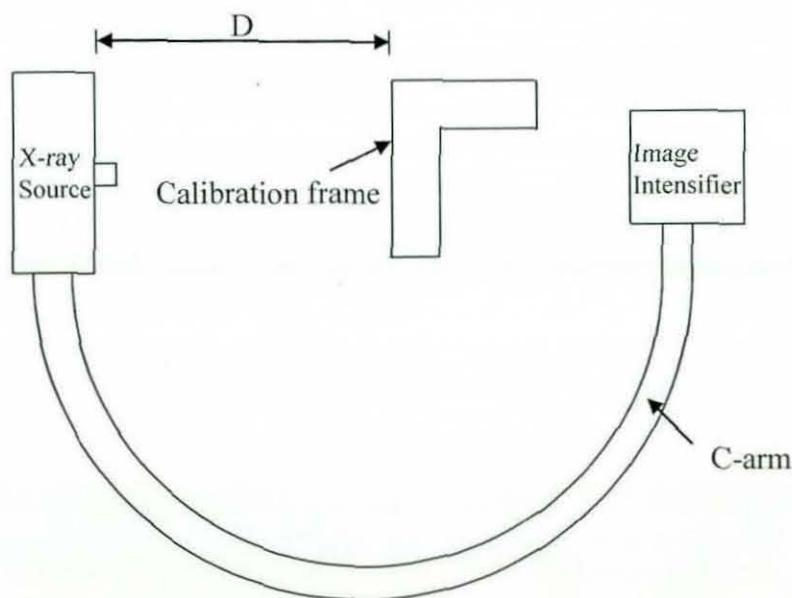


Figure 13 Positioning of X-ray source relative to calibration frame

Analysis showed that, for different values of D, the maximum deviation in predicting the rotation of the nail about its long axis is found to be 0.08° . This shows the robustness of the image segmentation techniques used and is an indication of its suitability for clinical application.

Influence of contrast and noise variations on image analysis

During this study, special attention has been given to the effect of variable contrast and noise in the X-ray images on the image analysis. To measure accurately the performance of the vision system the combined effects of noise and contrast must be evaluated. Since the contrast of an X-ray image is controlled by a combination of X-ray tube voltage and current, different combinations of voltage and current were used

during laboratory trials to achieve a wide range of contrast in the images. Noise can prove to be a major limiting factor in image segmentation, as image quality degrades very quickly when noise increases. Simulated Gaussian noise was added at various levels between 5% and 15% to each of the variable contrast images using a *proprietary image processing package*. Subsequent tests showed that good repeatability (less than 0.1° difference in measurement of the distal holes axes direction) could be obtained for up to 15% of gaussian noise across a wide range of contrast.

4 Discussion

Current free-hand techniques employed for distal locking of intramedullary nails use a large number of x-ray images during each step, resulting in excessive irradiation to both the surgeon and patient. Also the outcome of the procedure is largely dependent upon the surgeon's skills and experience, resulting in variable operating time and, occasionally, misplacement of screws. To reduce surgery time and the surgeon's cumulative radiation exposure, and to improve the accuracy and repeatability of the distal locking procedure, an automated X-ray based vision system has been developed at Loughborough University. This system minimises the changes to current surgical procedures and takes into account the physical constraints of the operating theatre, adopting a novel approach based on the use of a calibration frame in conjunction with offline modelling of the nail.

A potential problem with the Loughborough Orthopaedic Assistant System (LOAS) is the appearance of one or more of the opaque markers (embedded in the calibration frame plates) within or on the edge of the oval-shaped distal hole projection. An automatic technique has been implemented which removes the effect of such markers in computing the area of the oval and the angle between the major axis of the oval and the nail axis, both of these measurements being necessary for derivation of the drilling trajectory. This technique eliminates the need for repositioning the calibration frame or using a smaller number of opaque markers. Also, the adopted off-line modelling of the nail to generate look-up tables reduces the length of time for the computation of the drilling trajectory and thus has the potential for reducing the overall time required for the surgical procedure. Furthermore, the vision system is user-independent as all the steps involved during image analysis are fully automated. A graphical user interface (GUI) has been developed that assists and updates the user throughout the procedure. It has also been shown that the LOAS is very robust in the presence of variable noise and contrast in the X-ray images and in terms of variable magnification, thus making it suitable for clinical use.

The LOAS differs from existing computer-assisted orthopaedic surgery systems, as it eliminates the need for optical tracking equipment which tends to clutter the operating theatre environment and requires care in maintaining the line of sight. Additionally use of optical tracking equipment makes such systems an expensive method for surgical guidance in distal locking of intramedullary nails. In contrast, the LOAS can be implemented by adopting the simplified approach of using a standard C-arm in conjunction with the calibration frame (shown in Figure 2). Therefore the LOAS is more cost-effective and more suitable for clinical applications.

During laboratory trials of the LOAS, a mean positional error of 0.81mm and a mean angular error of 1.01° were obtained, in planning the drilling trajectory for the insertion of distal locking screws for different orientations of the nail. Whereas, Phillips *et al* [16] at Hull University have reported a mean positional error and a mean angular error within 0.3mm and 0.2° respectively. Although the accuracy achieved by the Hull system is better compared to the LOAS results, the image analysis protocol and system set-up are user-dependent. The system requires the surgeon (or user) to manually select some features on the intraoperative Lateral and AP images, and most importantly it requires optical tracking equipment which results in a more involved and time consuming set-up. The LOAS reduced accuracy, which is acceptable for distal locking of intramedullary nails, is a result of a simplified (practical) system which involves the use of a Γ shaped calibration frame (shown in Figure 2) instead of a frame which fits around the leg. That is, the increased errors are mainly due to the adopted extrapolation technique instead of the preferred, but practically difficult to implement, interpolation technique.

Nowadays, there is a trend towards applying computer-assisted free-hand navigation systems for different surgical procedures, including distal locking of intramedullary nails. These systems are based on the optical tracking of the C-arm, implant and surgical tools. However, they do not take into account the bending of the nail during insertion and therefore rely on the re-alignment of the C-arm to obtain perfect circles of the distal hole during the surgical procedure, which is time consuming and requires a pre-calibration of the C-arm. Unlike the surgical navigation systems, the LOAS does not require the intraoperatively acquired Lateral view image to show perfect circles, and does not need the pre-calibration of the C-arm. Also, use of surgical navigation systems requires expertise and additional personnel to set up the navigation system.

In summary, the LOAS has the potential of reducing significantly the X-ray irradiation during distal locking procedures, while the outcome of the procedure will be improved as the system has the potential to reduce the occurrence of screw misplacement, as demonstrated by Figure 12. Additionally the LOAS, which is also applicable to other osteosynthesis procedures, such as tibial distal locking and humeral shaft fracture treatment, has the potential to reduce the surgical time and to make the procedure more consistent, irrespective of variations in the skill levels and experience of clinical staff.

References

1. H. Gray, *Gray's Anatomy: The anatomical basis of clinical practice*. 39th ed, ed. S. Standring. 2005: Elsevier Churchill Livingstone.
2. GM. Whatling and LD. Nokes, *Literature review of current techniques for the insertion of distal screws into intramedullary locking nails*. *Injury*, 2006. **37**(2): p. 109-119.
3. C. Krettek, B. Konemann, T. Miclau, R. Kolbli, T. Machreich, and H. Tscherne, *A mechanical distal aiming device for distal locking in femoral nails*. *Clinical Orthopaedics And Related Research*, 1999(364): p. 267-275.
4. S. Tyropoulos and C. Garnavos, *A new distal targeting device for closed interlocking nailing*. *Injury*, 2001. **32**(9): p. 732-735.

5. J. D. Goodall, *An image intensifier laser guidance system for the distal locking of an intramedullary nail*. *Injury*, 1991. **22**(4): p. 339.
6. T. Ohe, K. Nakamura, T. Matsushita, M. Nishiki, N. Watanabe, and K. Matsumoto, *Stereo fluoroscopy-assisted distal interlocking of intramedullary nails*. *Journal Of Orthopaedic Trauma*, 1997. **11**(4): p. 300-303.
7. L. Catamo, R. Rotini, M. Rocca, R. Giardino, and G. Fontanesi, *Distal centering in locked intramedullary osteosynthesis of the femur: use of a magnet-resistant probe*. *La Chirurgia Degli Organi Di Movimento*, 1998. **83**(4): p. 375-379.
8. C. Krettek, B. Konemann, T. Miclau, R. Kolbli, T. Machreich, A. Kromm, and H. Tscherne, *A new mechanical aiming device for the placement of distal interlocking screws in femoral nails*. *Archives Of Orthopaedic And Trauma Surgery*, 1998. **117**(3): p. 147-152.
9. S. Madan and C. Blakeway, *Radiation exposure to surgeon and patient in intramedullary nailing of the lower limb*. *Injury*, 2002. **33**(8): p. 723-727.
10. C.T. Mehlman and T.G. DiPasquale, *Radiation exposure to the orthopaedic surgical team during fluoroscopy: "how far away is far enough?"* *Journal Of Orthopaedic Trauma*, 1997. **11**(6): p. 392-398.
11. MA. Hafez, RM. Smith, SJ. Matthews, G. Kalap, and KP. Sherman, *Radiation exposure to the hands of the surgeons: are we underestimating the risk?* *Archives Of Orthopaedic And Trauma Surgery*, 2005. **125**: p. 330-335.
12. HR. Maxon, SR. Thomas, EL. Saenger, CR. Buncher, and JG. Kereiakes, *Ionizing irradiation and the induction of clinically significant disease in the human thyroid gland*. *The American Journal of Medicine*, 1977. **63**(6): p. 967-978.
13. R. Hofstetter, M. Slomczykowski, M. Sati, and LP. Nolte, *Fluoroscopy as an imaging means for computer assisted surgical navigation*. *Computer Aided Surgery*, 1999. **4**(2): p. 65-76.
14. M.A. Slomczykowski, R. Hofstetter, M. Sati, C. Krettek, and L.P. Nolte, *Novel Computer-assisted Fluoroscopy system for Intraoperative guidance: Feasibility study for distal locking of femoral nails*. *Journal Of Orthopaedic Trauma*, 2001. **15**: p. 122-131.
15. Y. Zhu, R. Phillips, J.G. Griffiths, W.J. Viant, A.M. Mohsen, and M. Bielby, *Recovery of distal hole axis in intramedullary nail trajectory planning*. *Proc. Instn. Mech. Engrs, Part H, Journal of Engineering in Medicine*, 2002. **216**(H5): p. 323-332.
16. S Malek, R Phillips, A Mohsen, W Viant, M Bielby, and K Sherman, *Computer Assisted Orthopaedic Surgical System for Insertion of Distal Locking Screws in Intra-medullary Nails: A valid and Reliable Navigation System*. *International Journal of Medical Robotics and Computer Assisted Surgery*, 2006. **1**(4): p. 34-44.
17. N. Schep, I. Broeders, and Chr. Van der Werken, *Computer assisted orthopaedic and trauma surgery: State of the art and future perspectives*. *Injury*, 2003. **34**(4): p. 299-306.
18. K. Bouazza-Marouf, I. Browbank, and J.R. Hewit, *Robotic-assisted internal fixation of femoral fractures*. *Proc. Instn. Mech. Engrs, Part H, Journal of Engineering in Medicine*, 1995. **209** (H1): p. 51-58.
19. K. Bouazza-Marouf, I. Browbank, and JR. Hewit, *Robotic-Assisted Invasive Surgery*. *Journal of Mechatronics*, 1996. **6**(4): p. 381-387.

20. M.J. Hochrainer, *Repair of femoral shaft fractures, M.Sc Thesis*. 1997, Supervised by Dr K. Bouazza Marouf, Loughborough University.
21. I. Browbank, K. Bouazza-Marouf, and J. Schnabler, *Robotic-assisted internal fixation of hip fractures: a fluoroscopy-based intraoperative registration technique*. Proc. Instn. Mech. Engrs, Part H, Journal of Engineering in Medicine, 2000. **214(H2)**: p. 165-179.

